A Study of the Structure and Dynamics of Smectic 8CB Under Mesoscale Confinement Using the Surface Forces Apparatus

by

James Benson

A thesis
presented to the University of Waterloo
in fulfillment of the
thesis requirement for the degree of
Doctor of Philosophy
in
Physics

Waterloo, Ontario, Canada, 2012

Author's Declaration

I hereby declare that I am the sole author of this thesis. This is a true copy of the thesis, including any required final revisions, as accepted by my examiners.

I understand that my thesis may be made electronically available to the public.

Abstract

The structure and dynamics of the smectic-A liquid crystal 8CB (4 cyano-4′

octylbiphenyl) when sheared and confined to mesoscale gaps (with crossed cylindrical

geometry and mica confining surfaces) were studied using a Surface Forces Apparatus

(SFA). Triangular shear patterns with frequencies of 0.01, 0.1, 1.0 and 10 Hz, and

amplitudes of 62.5 nm, 625 nm and 6.25 μm were applied to samples at gap sizes of 0.5

and 5.0 μm. The study was performed at room temperature (20.5°C) and at two higher

temperatures (22°C and 27°C).   In order to minimize the thermal fluctuations within the

test chamber and hence to allow for the rapid re-initialization of test runs, the SFA was

modified to allow for quick, precise and remote control of the confining surfaces. The

procedure maximized the number of tests that could be undertaken with a single pair of

surfaces so that a single gap geometry could be maintained for the duration of the test

run. In order to run the SFA remotely, scripts written with a commercial software

package, LabVIEW, were used to control of the SFA components, its FECO-monitoring

camera and all its peripheral electronic equipment as well. Samples were agitated to

disrupt any shear-induced liquid crystal domain alignment from previous testing

following each shear test, and methodologies were developed to ascertain the extent of

confinement quickly and remotely following agitation. Separate methods were

developed for gap sizes at each extreme of the mesoscale regime, where the transition

from bulklike structure and dynamics to nano-confinement occurs (between 1 and 10

microns for smectic-A 8CB).

The results revealed that the greater amplitude-gap aspect ratio and surface-to-domain contact associated with smaller gaps facilitated reorientation of the domains in the shear direction. Evidence was also presented of domains at the higher end or outside of the mesoscale regime that, while straining and accreting, were unable to reorient and thereby led to an overall increase of viscoelastic response. The effective viscosity was found to obey a simple power law with respect to shear rate, $\eta(\dot{\gamma}) = K\dot{\gamma}^{n-1}$, and the flow behaviour indices, n, slightly in excess of unity indicate shear thickening occurs with large enough shear amplitude, and that the viscosity reached a plateau near unity over shear rates of 0.005 to 500 s^{-1} within the mesoscale regime. Different K and n values were observed depending on the shear amplitude used.

Unlike bulk smectic 8CB, whose domains do not align well in the shear direction with large shear-strain amplitude, at mesoscale levels of confinement large amplitude shearing (up to 12.5 shear strain amplitude) was found to be very effective at aligning domains. In general domain reorientation is found to be much more rapid within the mesoscale regime than has been reported in bulk. Aggressive shearing was found to result in a complete drop in viscoelastic response within seconds, while gentler shearing is found to produce a very gradual increase that persists for more than six hours, with individual shear periods exhibiting frequent and significant deviations from the expected smooth shear path that may be a product of discrete domain reorientations.

From these findings, certain traits of the smectic 8CB domain structures under mesoscale confinement were deduced, including how they respond to shear depending on

the level of confinement, and how their reorientation due to shear varies not only with shear rate but also independently with shear amplitude. An equation describing the viscosity change as a function of both shear rate and shear amplitude is proposed. The shear amplitude dependence introduces the notion of shearing beyond the proposed smectic 8CB "viscoelastic limit", which was shown to exhibit behaviour in accordance with Large Amplitude Oscillatory Shear (LAOS) techniques developed for Fourier Transform rheology. The findings provided an understanding of the behavioural changes that occur as one reduces the level of confinement of smectic materials from bulk to nanoconfinement.

Acknowledgements

The extraordinary length of this degree can only mean that I have had the good fortune to have met many kind souls that have helped me along the way. I would first like to thank my committee members, Jamie Forrest, Bae-Yeun Ha, John Medley, and my supervisor, Stefan Idziak, for their help and guidance in the project from beginning to end. I would also like to thank my external examiner, Professor Jeff Hutter, for taking the time to read my thesis and for offering his helpful comments and suggestions for improvement.

So many friends and colleagues have passed through the lab over the years that I worry I may forget to thank everyone here. Jonathan Teichroeb, Ryan Speller, Zahra Fakhraai, Sarah Guthrie, James Chan, Dongping Qi, Mark Ilton, William Toews, Brad Moores, Patrick McVeigh, Gianfranco Mazzanti, Chad Daley, Kanwarjeet Kaur, Maria Khomenko, Gavin MacDonald, Valentina Ngai, Howard Siu, Marsha Kisilak, Gaven MacDonald, Chris Collins, Kristine Dalton, Jen Hunter, Katarina Ilic, Kevin Head, Paul McGrath, William Ngo, Jane Robinson, Reyhaneh Nazarian, Francis Hane, Erin Fraught, Liz Drolle and Yongsong Liu, each of you have been with me through the highs and lows of the degree and have seen me at my best and worst, and I thank you all not only for the countless memories and all your help along the way, but also for putting up with me and my many eccentricities.

This thesis is dedicated to Sisyphus.

The presupposition of scientific work: belief in the unity and perpetuity of scientific work, so the individual may work at any part, however small, confident that his work will not be in vain.

There is one great paralysis: to work *in vain*; to struggle in vain.—

Friedrich Nietzsche
The Will to Power
Section 597 (1886-1887)

Table of Contents

List of Figures

Chapter 1: Introduction

Chapter 2: The Surface Forces Apparatus

Chapter 3: Experimental Details

Chapter 4: Results

Chapter 5: Discussion

Appendices

List of Tables

Introduction

This thesis will examine the structure and dynamics of sheared smectic-A 8CB under mesoscale confinement, which for this material occurs in gap sizes of approximately 1-10 µm. It follows experiments involving similar shear parameters and performed using an X-ray Confinement Cell (XCC), the results of which indicate that domain reorientation occurs discretely over the course of several hundred or thousands of seconds when sheared using small shear amplitudes and frequencies at the lower end of the mesoscale (0.5 µm gap size). All three oscillatory shear parameters, including gap size, shear frequency and amplitude, are varied. Two gap sizes representing the extremes of the mesoscale regime, 0.5 µm and 5.0 µm, were selected, corresponding to the two values used in the XCC experiments so that direct comparisons could be made. Shear tests were performed over all combinations of three shear amplitudes (62.5 nm, 625 nm and 6.25 µm) and four shear frequencies (0.01, 0.1, 1.0 and 10 Hz) as well, so that shear rates of from 0.0005 to 500 s^{-1} and shear-strain amplitudes of from 0.0125 to 12.5 were examined. Triangular shear profiles were used to provide a constant strain rate.

Because variations in the confining volume geometry can lead to measurable differences in response, it is desirable to use a single pair of confining surfaces for the duration of a test run. In an effort to minimize the thermal settling time within the test room and thereby maximize the life of the delicate confining surfaces, the SFA was modified to allow for quick, precise and remote control of the confining surfaces. Specifically, a remotely controlled DC stepper motor was affixed to the differential

micrometer via a custom-built coupler to enable the user to reach gap sizes in the mesoscale range within a few seconds. Also, the standard spring connecting the fine micrometer to the pivot stage was replaced by a stiffer spring to allow for more rapid fine adjustments in the mesoscale regime. Finally, two equations given by Israelachvili determining gap size at each end of the mesoscale were adopted in the gap size acquisition process in such a way that by aligning specific fringes to pre-assigned markers overlaid on the camera output feed, the exact gap size could be determined within a few seconds.

The strain gauge response to shearing is demonstrated to be proportional to the effective viscosity of the material under shear, and the observed drop in this viscosity during aggressive shearing is attributed to the annealing of smectic 8CB domains and their reorientation in the direction of shear. The SFA mesoscale results are compared to bulk results reported by other groups, and the influence of gap size on domain realignment is evidenced by how much faster asymptotic viscosity is reached while shearing within the mesoscale regime. The characteristic turbidity indicative of randomly oriented domains reported for bulk smectic 8CB undergoing large amplitude oscillatory shearing (strain amplitude of 5 or more) is not observed in the mesoscale, which may indicate domains are more constrained by confining walls as the gap size approaches the length scale of the smectic domains.

For the gentlest shearing conditions (for all combinations of smaller amplitudes and lower frequencies, and for both gap sizes tested), very slight time-dependent thickening is

observed, suggesting that domains within the sample are becoming less ordered. This is contrasted with earlier tests under similar conditions and performed using an X-Ray Confinement Cell (XCC) in which domains were observed to align and anneal, smoothly nearer the higher end of the mesoscale regime and in discrete jumps nearer the lower end. It is argued that because the XCC results are restricted to the vicinity of tightest confinement while the SFA results consider the entire sample, that the bulklike domains are being strained and are annealing but do not have sufficient energy imparted to them to fully realign in the shear direction and hence will tend to increase the overall effective viscosity. Thus, while domains within the mesoscale tend to reorient slowly, this contribution does not outweigh the bulklike contribution which tends to increase with time.

The effective viscosity is observed to undergo shear thinning only at smaller shear amplitudes (62.5 nm for the results presented here), while slight shear thickening is observed for shear amplitudes on the order of the length scale of the smectic 8CB domains. This amplitude-dependent effect is attributed to the stiffening of the material once it has been drawn beyond its viscoelastic limit, the point at which the material ceases to exhibit viscoelastic behaviour and begins to flow freely. This limit has been associated with a characteristic kink only becomes apparent when shearing at larger amplitudes (625 nm and 6.25 μm), which marks the switchover from viscoelastic response to purely viscous response. The onset of the kink varies depending on the shear parameters used, and tends to be sharper with gentler shearing and broader with more aggressive shearing.

The response data is fitted with the Burgers Model, a viscoelastic model consisting of Kelvin-Voigt and Maxwell element in series with one another. The fits indicate a post-viscoelastic limit viscosity that drops significantly during aggressive shearing but rises very slightly during gentler shearing. The kink, described primarily by the Kelvin-Voigt term, tends to soften over time regardless of the aggressiveness of shearing, indicating that a spectrum of viscoelastic limits are being exceeded as shearing proceeds, as might be expected in a geometry in which the gap size varies throughout the sample volume. The softening of the kinks with time indicates that the viscoelastic limit of domains further out radially from the crossed cylindrical center are being exceeded, which may be a direct result of domain reorientation progressing into the bulklike regime.

One drawback to the Burgers model is its assumption that pure viscous behaviour (associated here with sliding behaviour) begins immediately upon reversal of the shear direction. For this reason, a second model is proposed, the Split Model, in which early behaviour within the half-cycle is described using a Kelvin-Voigt Model and later, purely viscous behaviour is essentially linear (with weakly-weighted higher order terms handling fluctuations in the signal due to noise) beginning at a predetermined 'kink time' within the half-cycle.

The influence of shear amplitude also appears in the evolution of effective viscosity over time. Viscosity vs. time curves for the various shear parameters are fitted to two exponential fits, and the smaller time constant is plotted vs. shear rate, revealing similar

but distinct log-log relationships for different shear amplitudes. By extracting the fit parameters from the latter, an equation demonstrating the shear amplitude dependence of effective viscosity over time is developed, reinforcing the idea that shear amplitude plays a quantifiable role in the evolution of smectic-A 8CB viscosity.

The large shear amplitude results are Fourier Transformed to compare them with results obtained using FT rheology, in which sinusoidal shear profiles produce responses with odd-harmonics containing information on the material undergoing shear. Deviations from the fundamental higher harmonic amplitudes of the SFA response data are seen to increase with shear amplitude at all shear frequencies and for both gap sizes. This indicates that the techniques being developed within FT rheology are likely applicable to SFA results. Further, by Fourier Transforming data during testing methodologies may be developed to determine the amplitude at which the viscoelastic limit is exceeded and the onset of LAOS occurs.

Chapter 1

A History of the Study of Confined Liquid Crystals

The history of scientific study of liquid crystals (LCs), while relatively brief (spanning only one and one-quarter centuries), is nonetheless a complex and interesting one that involves several key figures from diverse scientific and cultural backgrounds. Only a general overview is provided here, including those topics most germane to our current understanding of the liquid crystal 4-cyano-4'-octylbiphenyl (8CB) as a smectic under various levels of confinement, from nano-confinement, where only a few layers of material are present and the confining walls play a significant role in the molecular behaviour, out to bulklike confinement. Included as well is the as yet not fully understood regime known as mesoscale (or mesoscopic) confinement, encompassing a gap size of approximately 1 to 10 μm, where the transition from bulklike to extreme confinement structure and dynamics occurs. This dissertation hopes to shed light on this latter confinement regime via an analysis of shear tests upon 8CB under various levels of confinement using a Surface Forces Apparatus (SFA).

The early history of the scientific investigation of liquid crystals by Reinitzer[1], Friedel[2], Lehmann[3], Mauguin[4, 5] and Grandjean[6, 7], including their attempts at orienting them is given in Sections 1.1 and 1.2.1-1.2.3. A brief discussion of the most common varieties of liquid crystals is also given here, along with Fréedericksz and Zolina's[8] pioneering work on the competition of surface and magnetic forces on nematic materials and, hence, the varieties of motion available to them. Zöcher[9, 10], Oseen[11], Tsvetkov[12]

and Frank's[13] treatments of the elastic theory of liquid crystals is detailed in Section 1.2.3, and ELP Theory is outlined in Section 1.2.4. The work done by Tsvetkov Tsvetkov, 1942 #324}, Maier[14, 15], Saupe[16, 17], Lippmann[18] and de Gennes[19-25] on characterizing liquid crystals in terms of an Order parameter is described in Sections 1.2.5-1.2.6. The experimental work of Dreyer[26], Sheng[27, 28], Jérôme[29-32] and Pieranski[33] and others on liquid crystal ordering near surfaces is discussed in Section 1.2.7. This leads naturally to the research done on liquid crystals under confinement, beginning with the fundamental work of Mięsowicz[34-36] (Section 1.3.1), which in turn leads to the more modern work on cyanobiphenyls by Israelachvili[37-40], Horn[41, 42], Klein[43-46] and others using the Surface Forces Apparatus (Section 1.3.3), a device that has also been used extensively in the research presented in this dissertation. Other methods of exploring the role surfaces have on liquid crystal behaviour are also described (Sections 1.3.4 to 1.3.10).

The structure and dynamics of layered systems (such as smectic liquid crystals) is next discussed, beginning with de Gennes'[19, 20] landmark treatment using energy and entropy (Sections 1.4.1-1.4.2), leading to the concept of layer distortions and undulations, first seen experimentally by Clark[47, 48] and developed into testable experimental parameters by Helfrich (Section 1.4.3)[49-51]. These parameters were used to test cyanobiphenyls and other smectic materials by several groups, both experimentally and theoretically (Sections 1.4.4-1.4.6). Finally, Section 1.5 is dedicated to the research performed on the material more specific to the dissertation, smectic 8CB, while under confinement, using the SFA and XSFA (also used for the present research). Safinya[52, 53] demonstrated the

presence of fluctuational forces using x-ray scattering (Section 1.5.1), while Idziak[54] demonstrated using x-ray patterns from the X-ray Surface Forces Apparatus (XSFA) that under mesoscale confinement, sheared 8CB domains exhibited the three Mięsowicz orientations (Section 1.5.2). Of the two gap sizes sheared (0.5 μm and 5 μm), only the smaller, if sheared gently enough, tended to re-orient in the shear direction in a step-like fashion, and showed a periodic tilting of the mosaic at the same frequency as the shear rate. This was attributed to discrete domain reorientation. The current study investigates this level of confinement and hence this shearing phenomenon directly (via strain gauge response) using the Surface Forces Apparatus.

1.1 Confined Liquid Crystals: An Introduction and Early History

The history of liquid crystal studies begins with Austrian botanist Friedrich Reinitzer who, while researching the chemical properties of cholesterol derivatives in carrot roots in 1888, found one (cholesteryl benzoate) that exhibited two distinct melting temperatures: one, at 145.5ºC, was a cloudy material, while another, at 178.5ºC, was clear[1, 55]. Both transitions were preceded by a colour change, from cloudy (145.5ºC) or clear (178.5ºC) to violet-blue, which disappeared after the transition was complete. Although the results were presented at a meeting of the Vienna Chemical Society that year, the field did not advance significantly until decades later when, in 1922, French crystallographer Georges Friedel published his seminal treatise, *The Mesomorphic States of Matter*, cementing the notion that what was being studied and discussed was a new phase of matter, the liquid crystal phase[2, 56]. During this tumultuous early period, much of the publicity for these novel materials was undertaken by crystallographer Otto Lehmann, who despite his young age had recently taken over as department head for Heinrich Hertz at the University of Karlsruhe. Reinitzer sought Lehmann's advice in March and April of 1888, with the hope that the latter's polarizing microscope might shed some light on the mystery he had uncovered. Lehmann in turn performed several experiments over the next few decades, characterizing the growing number of similarly-behaving materials, of which thirty-five had been documented by 1906; in addition, he founded the first liquid crystal summer school in 1912, through which he directly influenced many of the luminaries that would follow him (such as Grandjean, Mauguin and Friedel), and openly espoused his Haeckelian belief that liquid crystals were the

origin of many life processes. Ultimately, though, he died a few months short of seeing the publication of Friedel's widely influential treatise[56].

Thanks in part to this pioneering work it is now known that liquid crystals come in a variety of types, distinguishable by the position and orientation of their constituent molecules. In the nematic phase (Figure 1a), for example, they are devoid of positional order but have long-range orientational order. That is, while the center of mass distribution follows no specific pattern, the molecules tend to align in a specific direction, represented by the dimensionless unit vector, $\vec{n}$, known as the director. Smectics, meanwhile, have both orientational order and one-dimensional positional order, a result of the molecules' tendency to arrange themselves in parallel layers while maintaining isotropy within each layer. These layers, or lamina, are often able to slide easily with respect to one another, making smectics a frequent candidate for lubricants. There are several types of smectics, the two most common of which are smectic-A and smectic-C. With the former, molecules are aligned with their lengths perpendicular to the smectic layer (Figure 1b), while the latter have their molecules tilted some angle with respect to the layer (Figure 1c)[55]. Maurice de Broglie (the less famous brother of physicist Louis de Broglie) and Edmond Friedel (son of the aforementioned Georges Friedel) in 1923 demonstrated the existence of smectic layering by performing the first liquid crystal x-ray experiments, in their case on a sodium oleate-water mixture[56-58] with a stack of layers they determined to be equally 43 Å thick[57]. Over the next half century many more varieties of smectics were discovered, and the smectic notational convention, largely

developed by Sackmann and Demus[59], lists the materials alphabetically (Smectic-A, Smectic-B, etc.) based on their order of discovery[60].
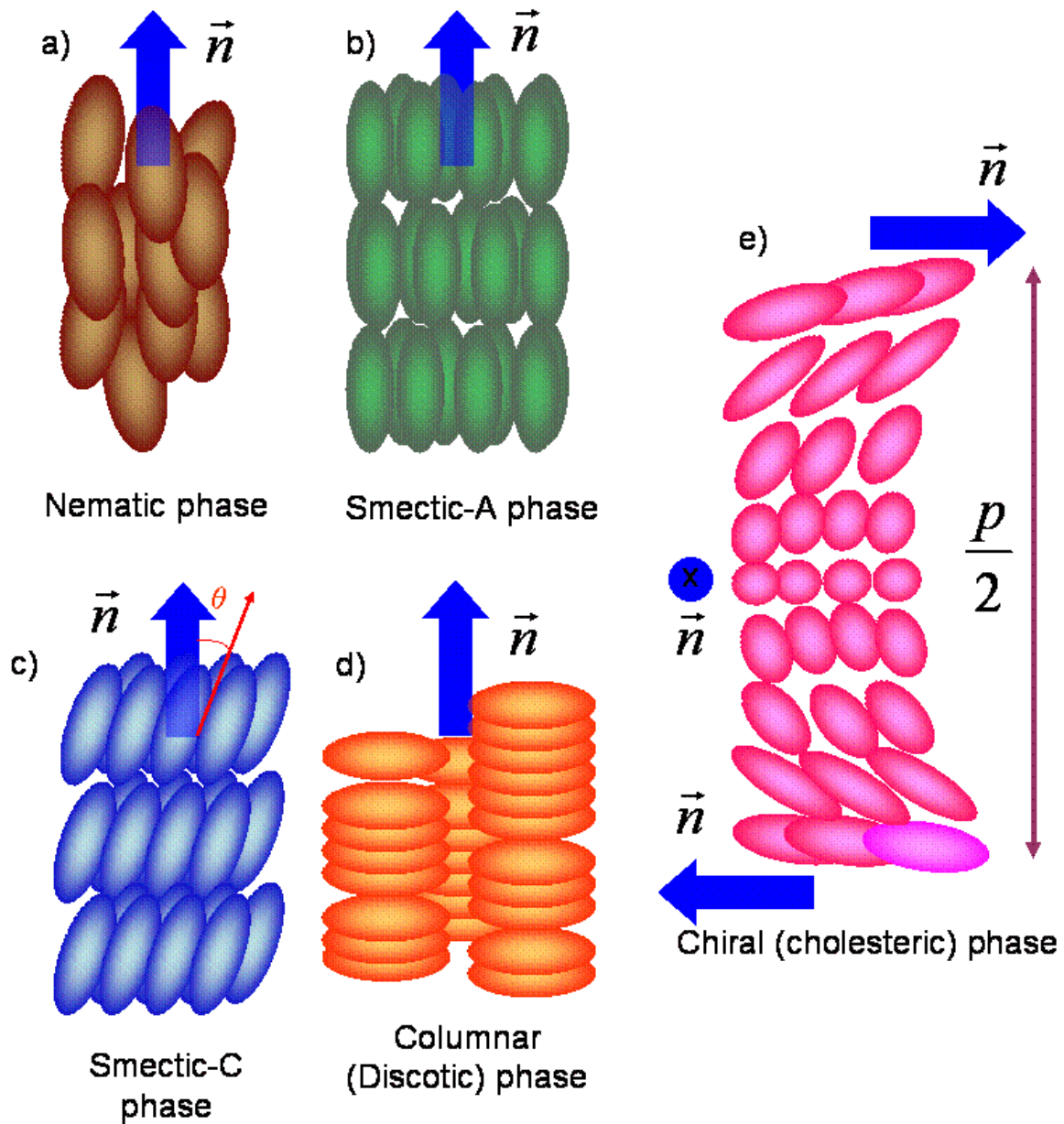
Figure 1.1: Common types of liquid crystals.

The chiral phase describes an arrangement wherein the molecules are positioned about a chiral center (Figure 1e); the director in this case rotates helically about the center, and if it does so sinusoidally the material may also be called a cholesteric. The full length of the sinusoid is known as the pitch (the half-pitch *p/2* is shown in the figure). The pitch often falls within the range of visible wavelengths, and since it is also very temperature-sensitive, chiral materials generally display vibrant reflective colours that themselves vary with temperature, a property which makes them useful to the electro-optical industry. Both smectics and nematics can be chiral [55], and those phases which exhibit a chiral structure have traditionally been labeled with an asterisk (e.g. Smectic-C*) to differentiate them from non-chiral phases[60]. The first studies on molecular chirality were performed in 1848 by Louis Pasteur in his doctoral work describing the chiral separation of tartaric and pantartaric acids in the sediments of fermenting wine, although it wasn't until 1893 that Lord Kelvin first defined a chiral body as an object 'that cannot be superimposed on its mirror image'[61].

A more recent discovery in the field of liquid crystals is that of the columnar phase, first studied by Sivaramakrishna Chandrasekhar in 1977[62]. Often referred to early on as the discotic phase, this term has in recent years fallen into disfavour following the discovery of several columnar systems not made up of discoid components[19, 63-65]. In such systems, the liquid-like direction is to be found along the column (as represented in Figure 1d by randomly-spaced discs within each column), while orientational ordering (along the stack) and two-dimensional positional ordering (due to the hexagonal placement of the columns in the plane perpendicular to the director) is present.

1.2 Methods of Orienting Liquid Crystals

1.2.1 Early Experiments in Orientation

While the first seventy-five years of the history of liquid crystals remained relatively uneventful, the discovery by Richard Williams in 1963 that such materials often exhibit interesting electro-optical properties led to a resurgence of interest in the field[66], ultimately culminating in the development of the now-ubiquitous Liquid Crystal Display (LCD). Attempts at manipulating liquid crystals in order to orient them began much earlier than this, however. In 1911 French mineralogist Charles-Victor Mauguin published results commenting on his findings using a petrographic microscope equipped with a stage temperature-controlled by a high current (5-10 amps), with the samples (azoxyanisole and azoxyphenetole) sandwiched between two glass slides[4]. In addition to noting that liquid crystals had birefringences in excess of those found in liquids in electric and magnetic fields (the Kerr and Cotton-Mouton effects, respectively), he found that the cleanliness of the glass alone could change the optical properties of the samples considerably. Furthermore, he reported that by adjusting the size of the gap and training monochromatic convergent light on the sample, he could change the number of interference fringes observed from two (with 10 µm sample thickness) to twelve (with 150 µm sample thickness). Finally, he described an experiment wherein the cover slide was rotated with respect to the sample slide and noted that the visible domains were relatively insensitive to the motion of the slide, providing a rudimentary example of a shear experiment involving liquid crystals[4].

In a paper later in the year, he presented his findings on the orientation of azoxyanisole in the presence of a magnetic field[5] and in a similar setup as before save for the addition of a small electromagnet pierced so that the microscope would have an aperture to observe the sample. The magnet was positioned such that the lines of magnetic force would be perpendicular to the glass slides. He found that without the magnetic field gap sizes exceeding 0.2 mm would never yield material of uniform optical alignment, while with a field of 2500 Gauss applied alignment was rapid and uniform, resulting in an optical axis parallel to the lines of force. Similar results were found with a magnetic field of similar magnitude placed parallel to the glass slides, and in both orientations strong birefringence was detected using the microscope; this birefringence increased as the field was increased to 5000 Gauss, at which point it stopped increasing. He finished his paper by mentioning an experiment wherein a magnetic field was applied to a thin film containing 'residual crystallites' adhering to the surface which, unlike the rest of the film, resist reorientation by the applied field, a topic taken up five years later by French mineralogist and geologist François Grandjean.

In 1916 Grandjean presented a survey of five liquid crystals and the surface effects observed when they were deposited on nine different minerals, each with a cleavage plane exposed. During this series of experiments he made the discovery of what he called the *terrace phenomenon* (made up of what are known today as *Grandjean terraces*)[56]: a series of plateaus laid one on top of another, with each successive layer smaller in surface area. The layers were always of constant thickness, flat-topped, and all had well-defined contours[6].
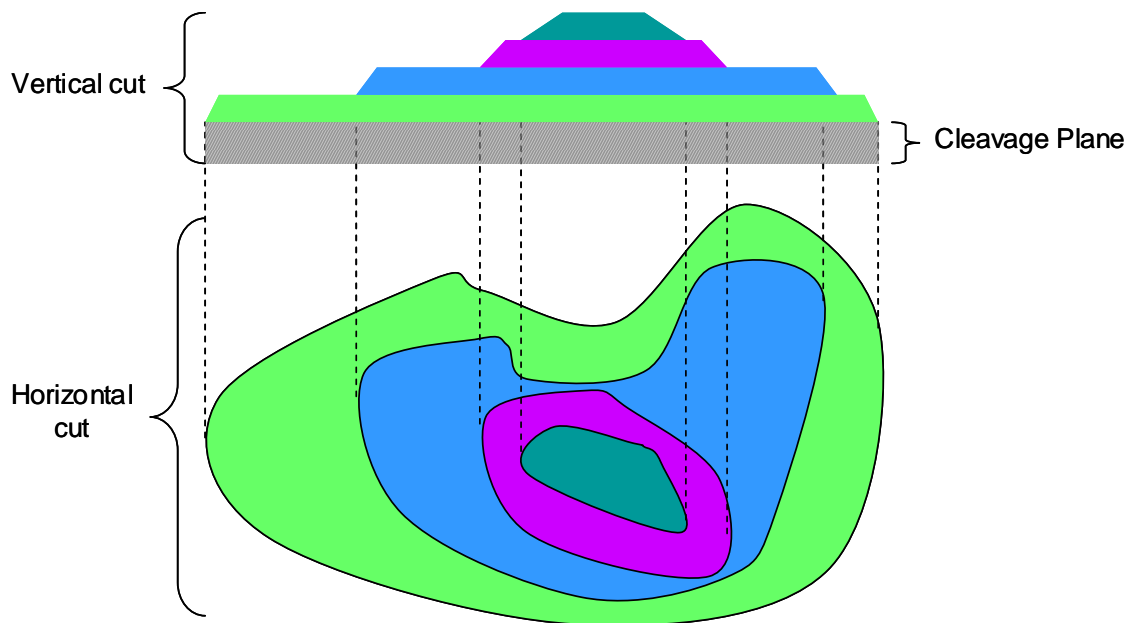
Figure 1.2: Grandjean terraces (recreation of the original figure in Grandjean[6])

This series of experiments was the first to identify smectics as a distinct type of liquid crystal (given this name in 1922 by Grandjean's collaborator, Friedel[2]), and at the same time showed the significant effect surface forces have on orienting such materials. It is also interesting to note that Grandjean published a very early discussion of an order parameter in liquid crystals[7], a quarter-century before Russian physicist Viktor Tsvetkov's important work (discussed in Section 1.2.5), but the treatment seems to have been either forgotten or dismissed by his contemporaries[56].

1.2.2 The Fréedericksz Transition and Frank Constants

In 1929 Russian physicist Vsevolod Fréedericksz presented his landmark paper quantifying the competition between confinement and electromagnetic force in liquid

crystals[8] at the 55th annual meeting of the American Electrochemical Society in Toronto. Fréedericksz and Zolina had developed an experiment wherein three materials (p-acetoxybenzaline, p-asoxyphenetole and anisaldazine) were confined between a flat glass plate and a convex glass lens, and a magnetic field was applied perpendicular to the plane. In this way a well-defined transition radius could be determined for each material to test the role surface forces play in orienting the liquid crystal. The Fréedericksz transition can be thought of as the product of two competing forces: surface forces that tend to keep the director aligned parallel to the confining surfaces and magnetic field forces that tend to re-align the director perpendicular to the surfaces. A derivation following Jones' treatment of a confined nematic in a magnetic field follows[67]. The free energy per unit volume of a single domain oriented in the z-direction would consist of the two aforementioned competing energy terms:

$$F = \frac{1}{2} K_{splay} \left(\frac{\partial \vec{\delta n}(z)}{\partial z} \right)^2 - \frac{1}{4\pi} \int \vec{D} \cdot d\vec{E}$$

where a splay elastic modulus term, K_{splay}, and a slight shift to the director in the z-direction, $\partial \vec{\delta n}(z)/\partial z$, have been introduced to describe the director's re-orientation elastically. The field, $\vec{D} = \varepsilon_a \left(\vec{\delta n} \cdot \vec{E} \right) \vec{\delta n}$, oriented in the z-direction as well, can be substituted into the above by letting $x = \vec{\delta n} \cdot \vec{E}$ so that $dx = \vec{\delta n} \cdot d\vec{E} + \vec{\delta dn} \cdot \vec{E} = \vec{\delta n} \cdot d\vec{E}$, giving:

$$F = \frac{1}{2} K_{splay} \left(\frac{\partial \vec{\delta n}(z)}{\partial z} \right)^2 - \frac{1}{4\pi} \int \varepsilon_a x dx$$

$$= \frac{1}{2} K_{splay} \left(\frac{\partial \vec{\delta n}(z)}{\partial z} \right)^2 - \frac{\varepsilon_a}{8\pi} \left(\vec{\delta n} \cdot \vec{E} \right)^2$$

And since $\delta\vec{n}$ and $\vec{E}$ are parallel to one another:

$$F = \frac{1}{2} K_{splay} \left(\frac{\partial \delta\vec{n}(z)}{\partial z} \right)^2 - \frac{\varepsilon_a E^2 |\delta\vec{n}|^2}{8\pi}$$

One must decide on an appropriate distortion shape for $\delta\vec{n}(z)$ to proceed further.

Considering the boundary conditions of $\delta\vec{n}(0) = \delta\vec{n}(d) = 0$ (where d is the thickness of the sample) and the assumption that the greatest field effect occurs at the center (i.e. furthest from both surfaces and hence least affected by them), a sinusoid fits the requirements well. That is, $\delta\vec{n}(z) = \delta n \sin(\pi z/d)$ and the total free energy can be obtained by integrating the above over the film:

$$E_{tot} = \int_0^d \left[\frac{\pi^2}{2d^2} K_{splay} (\delta n)^2 \cos^2\left(\frac{\pi z}{d}\right) - \frac{\varepsilon_a E^2}{8\pi} (\delta n)^2 \sin^2\left(\frac{\pi z}{d}\right) \right] dz$$

$$= \frac{\pi^2}{4d^2} K_{splay} (\delta n)^2 - \frac{\varepsilon_a E^2}{16\pi} (\delta n)^2$$

When the competing forces are balanced, $E_{tot} = 0$, so the critical field E_{crit} can now be solved:

$$E_{crit} = \frac{2\pi}{d} \sqrt{\frac{\pi K_{splay}}{\varepsilon_a}} \tag{1}$$

It should be noted that the more complicated situation of a twisted nematic system follows the same derivation, and yields results usable for the development of liquid crystal display technology (although generally alternating electric fields are used instead, as they have a greater effect on liquid crystal orientation; the principles for both, however, are the same[56]). The critical field is given by:

$$E_{crit} = \frac{2\pi}{d} \sqrt{\frac{\pi}{\varepsilon_a}\left[K_{splay} + \frac{1}{4}(K_{bend} - 2K_{twist}) \right]} \tag{2}$$

where two new elastic constants must be introduced to represent the additional motions possible in a twisted nematic, the twist and bend[67], shown in Figure 1.3:
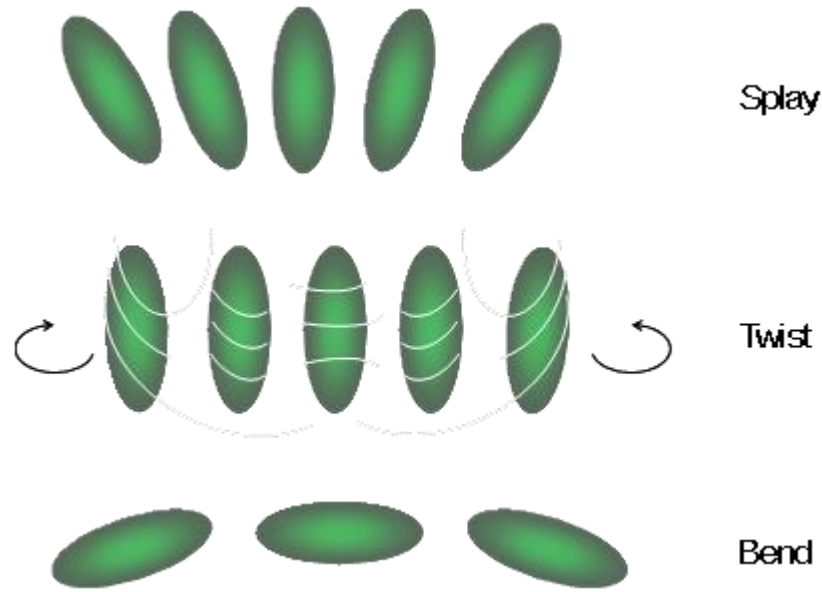
Figure 1.3: The three types of motion in nematic liquid crystals: Splay, Twist and Bend.

The concept of treating liquid crystals as elastic materials was first proposed at the 1933 Faraday Symposium in London[56]. Both German chemist Hans Zöcher and Swedish physicist Carl Oseen presented papers (the former in person and the latter in absentia) that considered the molecules from a mechanical point of view[10, 11]. This mechanical theory ultimately replaced the only widely-accepted theory of liquid crystals that existed at that time, and one that was a central focus at the 1933 Symposium: Swarm Theory. The now largely-abandoned theory, in which large-scale order comes about by dipole-dipole interactions between molecules, leading to approximately micron-sized, relatively stable, randomly assorted regions, each with a constant director[56, 68], was first proposed by Emil Bose in a series of papers published between 1907 and 1909[69-71], and first

established as a viable quantitative theory by Max Born in 1916[68, 72]. Despite Zöcher and

Oseen's introduction of this novel way of considering the problem, Swarm Theory

persisted for many years with many scientists in the field falling into one camp or the

other, and it remained a topic of discussion even into the 1970s, as evidenced by de

Gennes' (albeit disdainful) treatment of it in his seminal 1973 work, *The Physics of*

Liquid Crystals, in which he refers to it as "the so-called Swarm Theory which has

plagued the field of nematic liquid crystals for thirty years." [19, 68]

Russian polymer physicist Viktor Tsvetkov[12] made some preliminary measurements

of liquid crystal elastic constants in p-azoxyanisole in the early 1940's, but the notion of

an elastic theory of liquid crystals only truly took root after a treatment in 1958 by the

British physicist Frederick (Charles) Frank[13]. Frank used the above elastic moduli

explicitly in his revision and reformulation of Oseen's theory of nematics, smectics and

cholesterics, and gave them their current nomenclature as splay, twist and bend

coefficients, and as a result today they are known as Frank constants[55]. He proposed that

for small changes (relative to molecule size) to the director's orientation, the free energy

density can be represented entirely by elastic terms[13, 55, 67]:

$$F_{tot} = \frac{1}{2} K_{splay} \left(\nabla \cdot \vec{n} \right)^2 + \frac{1}{2} K_{twist} \left(\vec{n} \cdot \nabla \times \vec{n} \right)^2 + \frac{1}{2} K_{bend} \left(\vec{n} \times \vec{\nabla} \times \vec{n} \right)^2 \qquad (3)$$

Often, the splay, twist and bend subscripts are replaced by the numbers 1, 2 and 3 (using

Zöcher's notation) or 11, 22 and 33 (after Frank's original tensor notation). Frank's

derivation did not preclude the existence of what he called a saddle-splay term (K_{24}), but

he noted that in bulk nematic materials its effect would be negligible[13]. In 1991 and 1992

deuteron NMR experiments on nematic 5CB performed by Crawford, Allender and

Doane[73] demonstrated that the K_{24} term could, in fact, be measured under weak anchoring conditions within high-curvature (submicron diameter) cylindrical cavities, and that the director pattern is dependent on K_{24} under such conditions[74]. Oseen's derivation had one further term, K_{12}, which he assumed in all simple cases could be approximated to zero[11], and this assumption has been used as well by Frank. In the event that larger changes to the director occur, the above treatment can be modified to allow higher-order terms of $\nabla \vec{n}$ than are shown[67].

1.2.3 Surface-Induced Order: Early Experimental Work

It is often stated that, aside from the two notable contributions of Tsvetkov[12] and Mięsowicz[34-36] (discussed later in separate sections), very little progress was made in liquid crystal science over the quarter century period of 1933-1958[56, 68]. During the Second World War, however, French mineralogist and crystallographer Pierre Chatelain performed important experiments in epitaxial ordering of azoxyanisole due to the rubbing of substrates. While he was not the first to develop this technique[9, 10], his results represent the first published systematic attempt at quantifying the relationship between experimental preparation parameters and the resultant orientation. The amount of rubbing and the rubbing agent, the method of cleaning, the type of substrate, the type and age of liquid crystal used were all varied and the results recorded[75], and the reasons for varying results were discussed[7], giving future scientists techniques for preparation that are still in use today[56]. By 1962, with the publication of Gray's text on liquid crystals, it was well established that the substrate on which a liquid crystal is placed and the means

of preparing it could markedly affect its behaviour and structure several microns out from the surface[76].

1.2.4 Ericksen, Leslie-Ericksen and ELP Theory

The problem of fluid flow has been a topic of interest to scientists and engineers for centuries, garnering the interest of no less than Sir Isaac Newton, who posited that the stress, F, and rate of strain, $\frac{d\varepsilon}{dy}$, in liquids are linearly proportional to one another:

$$F = \eta \frac{d\varepsilon}{dy} \tag{4}$$

where η is the viscosity of the fluid. Fluids that obey the above relation are known as Newtonian Fluids, but there are several fluids that do not follow this simple model, liquid crystals being one example. Apart from an early and only partially successful attempt in 1933 by Oseen's student, Adolf Anzelius[77], it wouldn't be until 1960 that the problem of how to describe the motion of nematics (see Section 1.1 for details on this liquid crystal phase) undergoing shear would be tackled by American physicist Jerald Ericksen[78, 79]. He began by assuming the nematic consisted of an ensemble of rigid, rod-like molecules, and then further assumed an infinitesimal perturbation (that is, a force much smaller than the interaction forces between molecules in the ensemble) on this volume, V, of rods with surface area S, could be described by the Work-Energy Theorem. By assuming that nematics are incompressible and rigid, and with considerable mathematical perspicacity, he was able to express his solution in a remarkably succinct form, similar to Oseen's and Anzelius' solution[77]:

$$\frac{d}{dt} \int_V \sigma \frac{d\vec{n}}{dt} dV = \int_V \left(\vec{G} + \vec{g} \right) dV + \int_S \vec{s} \, dS \tag{5}$$

where $\vec{n}$ is the director, $\vec{G}$ and $\vec{s}$ are the perturbative body and surface forces causing the flow, and $\vec{g}$ is the intrinsic director body force[60, 68] which arises from the interaction of the director with external (for example, gravitational and electromagnetic) fields[80]. This equation, combined with the conservation of energy, mass, linear momentum and angular momentum equations[81], allows one to write a set of four differential equations, which, when thermal equilibrium is assumed, reduces to:

$$\vec{g} = \gamma \vec{n} - \frac{\partial W}{\partial \vec{n}} \tag{6}$$

where W is the work done on the system and γ is a proportionality constant[68].

Ericksen's theory assumes the rods generally lie in the same direction, however, and do not take into consideration surface influences which will lead to distortions in the nematic. This more generalized case, where Ericksen's flow equations would be coupled with Frank's elastic constants, was derived by Scottish physicist and mathematician Frank Leslie and first published in 1966[82]. By assuming the material properties of the system were single-valued and indifferent to the frame of reference, and by assuming the system was incompressible and isothermal, Leslie was led to the following constitutive equation, expressed by Larson in terms of tensors[55]:

$$= \alpha_1 \mathbf{nnnn} \, \mathbf{D} + \alpha_2 \mathbf{nN} + \alpha_3 \mathbf{Nn} + \alpha_4 \mathbf{D} + \alpha_5 \mathbf{nn} \, \mathbf{D} + \alpha_6 \mathbf{D} \, \mathbf{nn} \tag{7}$$

where σ is the viscous stress tensor, $\mathbf{n}$ is the director field, $\mathbf{N}$ is the rotation rate of $\mathbf{n}$, $\mathbf{D}$ is the symmetric part of the velocity gradient tensor, and the α_i terms are what are known as the *Leslie viscosities*, a mostly independent set of terms that describe the possible

22

viscosities affecting the splay, twist and bend motions given by Frank during nematic flow. Although the original theory predicted six terms, Parodi later showed that only five are independent, leading to a simplified Ericksen-Leslie-Parodi (ELP) theory[83]. If the director field is not uniform, Frank distortional stresses arise, leading to (after assuming the angular momentum of the system is conserved):

$$\mathbf{n} \times \mathbf{h} - (\alpha_6 - \alpha_5)(\mathbf{n} \cdot \mathbf{D} - \mathbf{n}\mathbf{n}\mathbf{n} \cdot \mathbf{D}) - (\alpha_3 - \alpha_2)\mathbf{N} = 0 \tag{8}$$

where **h** represents what is referred to as the molecular field, made up of the three Frank components[19]:

$$
\begin{aligned}
\mathbf{h}_{splay} &= K_{splay} \nabla (\nabla \cdot \mathbf{n}) \\
\mathbf{h}_{twist} &= -K_{twist} [(A \nabla \cdot \mathbf{n} + \nabla \times (A \mathbf{n}))] \\
\mathbf{h}_{bend} &= K_{bend} [\mathbf{B} \times (\nabla \times \mathbf{n}) + \nabla \times (n \mathbf{B})]
\end{aligned}
\tag{9}
$$

where $A = \mathbf{n} \cdot (\nabla \times \mathbf{n})$ and $\mathbf{B} = \mathbf{n} \times (\nabla \times \mathbf{n})$. It should be noted that in the special case of $\mathbf{N} = 0$, Leslie-Ericksen theory reduces to Ericksen theory[55]. If a magnetic field strong enough to keep the director in place were applied as was done in Mięsowicz's original experiments (see Section 1.3.1 for more details), the α_i viscosities reduce to Mięsowicz viscosities in the following way[84]:

$$\eta_a \equiv \frac{\alpha_4}{2} \qquad \eta_b \equiv \frac{\alpha_3 + \alpha_4 + \alpha_6}{2} \qquad \eta_c = \frac{-\alpha_2 + \alpha_4 + \alpha_5}{2} \tag{10}$$

If the director is not held in place by an external electric or magnetic field, of course, the overall stresses in the system are not necessarily proportional to the shear rate, and in fact the Leslie-Ericksen equations anticipate the possibility of shear thinning because they contain nonlinear terms that are functions of the gradient of the director field, **n**[55].

Leslie-Ericksen theory has been used with considerable success to describe nematics under shear since its development in the 1960's and 1970's[85-101]. Despite the relative simplicity of the five-fold viscosity, Leslie-Ericksen theory does also allow for the possibility of many types of interesting behaviours in nematics. While the topic is far too vast to be discussed here, one commonly occurring resultant phenomenon, *director tumbling*, has been studied in some detail, with thorough discussions having been published by Burghardt and Fuller [102, 103].

1.2.5 The Order Parameter

In practice, liquid crystals will not be perfectly ordered, and it is useful to introduce a long-range order parameter, *S*, to describe how well oriented a sample is, ranging from 0 for a perfectly isotropic material to 1 for a perfectly ordered material. Values in between are described using the second Legendre Polynomial, first proposed by Russian polymer physicist Viktor Tsvetkov[12]:

$$S = \left\langle P_2\left(\cos\theta\right)\right\rangle = \left\langle \frac{3\cos^2\theta - 1}{2}\right\rangle \tag{11}$$

where θ is the angle between the director and the long molecular axis in the region being studied. The polynomial chosen is second order since, were the first order chosen ($P_1 = \cos\theta$), the cosine term would average to zero since the director $\vec{n}$ and its negative are equivalent to one another (that is, liquid crystals are symmetric about their preferred axis). The order parameter has been related to various experimentally verifiable values, from early studies of birefringence by Chatelain[56] and diamagnetism via linear dichroism

by Saupe and Maier[104], to more recent experiments using Raman scattering[105], as well as EPR[106, 107] and NMR[108] spectroscopy.

German physicist Wilhelm Maier and his doctoral student, Alfred Saupe[12, 14], worked with Tsvetkov's order parameter definition in an attempt to relate it to the free energy of the system by making the assumption that the interaction energy between any two molecules and the order parameter are quadratically related while the entropy can be obtained from the standard Boltzmann treatment, integrating over all space, so that a transition from isotropy to anisotropy would lead to a change in free energy of[67]:

$$\Delta F = -\frac{uS^2}{2} + k_B T \int f(\theta) \left[\ln 4\pi f(\theta) \right] d\Omega \tag{12}$$

where u is a molecular coupling term—larger values of u represent increasingly favourable interactions between molecules—and $f(\theta)$ is a function representing the fraction of molecules in solid angle Ω; note that for a completely isotropic system the number of molecules in any given volume will be constant and so $f_{iso}(\theta) = 1/4\pi$. Also note that the above equation provides justification for a material to convert from a higher to a lower entropy state, through its favourable energy interaction term leading to a potentially overall lower free energy. After some calculations in which values of $f(\theta)$ are determined that will minimize free energy for a given fixed S, one can determine the relationship between the free energy per molecule and the order parameter, and from it characteristics of the isotropic-nematic transition may be determined. The above is known as Maier-Saupe Theory, and was first used in 1958 to make sense of experimental data on the phase transition of p-azoxyanisole collected by Tsvetkov in 1937[14, 67].

A more generalized order parameter was later developed for nematics[16, 109], wherein each molecule is represented by a tensor $\overset{=}{s}$ with elements S_{ij} given by its molecule-fixed Euler coordinates. French physicist and Nobel Laureate Pierre-Gilles de Gennes took a similar approach, generalizing Tsvetkov's order parameter so that:

$$S_{ij}^{\alpha\beta} = \left\langle \frac{1}{2}\left(3\ddot{p}_\alpha \ddot{p}_\beta - \delta_{ij}\delta_{\alpha\beta}\right)\right\rangle$$

where $\ddot{p}$ and $\ddot{p}$ are orthonormal vectors describing the orientation of the molecule, while α and β are indices representing the laboratory frame. By introducing what he refers to as the Order Parameter Tensor for magnetic susceptibility:

$$Q_{\alpha\beta} = \chi_{\alpha\beta} - \frac{1}{3}\chi_{\gamma\gamma}\delta_{\alpha\beta}$$

and using it to perform a Landau Expansion of the free energy per unit volume:

$$\overline{F} = F_0 + \frac{1}{2}AQ_{\alpha\beta}Q_{\beta\alpha} + \frac{1}{3}BQ_{\alpha\beta}Q_{\beta\gamma}Q_{\gamma\alpha} + O(Q^4) - \frac{1}{2}Q_{\alpha\beta}H_\alpha H_\beta \tag{13}$$

where H is the external magnetic field, $\overline{F}$ can be minimized with respect to the order parameter to obtain the birefringence of a given anisotropic medium. In a similar fashion, by assuming an order parameter that varies gently over space so that elastic components of F may be added, one can derive expressions for the anisotropic scattering intensities $I_\perp$ and $I_\parallel$[22].

1.2.6 Orientation through Spinning

German physicist Hans Lippmann[18] performed some of the first tests on the orientation of liquid crystals by spinning the sample, during his experiments involving

the NMR of nematics in 1958. He showed that there exists a critical speed above which

orientation due to a magnetic field disappears. The potential energy per unit volume, E_P,

of a nematic in a magnetic field, H, can be expressed easily combining Saupe's equation

with the first-order Zeeman dipole-dipole interaction energy term for two rigid rods of

identical spin:

$$E_P = -\left\{\frac{1}{3}\Delta\chi H^2\right\}\left\{\frac{1}{2}\left[3\cos^2\alpha - 1\right]\right\} \tag{14}$$

where $\Delta\chi$ is the anisotropy of the magnetic susceptibility and α is the angle between the

nematic director and the main magnetic field. The potential gives rise to a torque given

by Courtieu as[110]:

$$\tau_m = \frac{1}{2}\Delta\chi H^2 \sin 2\alpha \tag{15}$$

The realignment of the rods will not be instantaneous; rather, it will take a finite,

measurable time due to viscous effects, described by Leslie[82, 111] in terms of viscous

torque, τ_v:

$$\tau_v = \gamma_1 \dot{\alpha} \tag{16}$$

where γ_1 is a viscosity coefficient and $\dot{\alpha}$ is the rate of change of direction of the director.

Equating the two torques gives:

$$\dot{\alpha} = \frac{\Delta\chi H^2}{2\gamma_1}\sin 2\alpha \tag{17}$$

With this equation one can determine the rate at which a sample must spin in order to

counteract the torque exerted by a magnetic field, and hence one can orient a bulk sample

to be studied by NMR. With confidence buoyed by conversations with Saupe and

Englert[112], Diehl and Khetrapal undertook NMR experiments on nematics with

Lippmann's derivation in mind, and were able to show experimentally via NMR that the order parameter, S, of anisole azophenyl-n-capronate depends both on temperature and on concentration, as well as spinning speed.[113]. They later demonstrated that an electric field could effectively reorient a nematic director despite the presence of the main magnetic field, providing an alternative to Lippmann's method[114]. The first experimental success of homogenously orienting a nematic at any angle with respect to an external NMR magnetic field was performed by Courtieu in 1982, using nematic p-pentylphenyl 2-chloro-4-(p-pentylbenzoyloxyl)benzoate[110].

1.2.7 Surface-Induced Order: Working Towards a Theoretical Model

Dreyer[26, 115] reported in 1971 that even simulated rubbed surfaces can sometimes induce orientation in nematics, suggesting that the cause of surface-induced alignment is geometrical in nature rather than chemical or intermolecular. Berreman assumed a sinusoidally-ridged surface roughness and a nematic material approximately equal Frank constants in order to derive an expression for energy density, $u_\perp$, and total energy per unit area, $\rho_\perp$[116]. Taking typical experimental parameters (quartz glass of roughness amplitude 1 nm, a rub-induced sinusoidal roughness wavelength of 20 nm and all elastic constants equally 10^{-6} (cgs units), typical for p-azoxydianisole[13]), he calculated an energy density discrepancy of 5×10^5 erg/cm^2 and a total energy per unit area of 0.08 erg/cm^2 at the surface ($z = 0$). That is, it would take 0.08 erg/cm^2 more energy to align *across* the ridges than *parallel* to them, corresponding to an aligning electric field of 6×10^8 N/C or magnetic field of 700 T, both much higher than would be used in typical experiments. Hence, he concluded, with the simple assumptions he has made one can expect a strong

surface-induced ordering of nematic materials. He stressed that both $\rho_\perp$ and temperature

will affect nematic surface orientation, and presented his own data where, for p-

azoxydianisole on rubbed glass, the surface molecules aligned parallel to the rub

direction at 134°C and vertically at 136°C[116].

   Sheng[27] published early results on the effect that substrates have upon phase

transitions in nematics. Working from Landau-de Gennes theory[19, 21, 22], he was able to

show that there is a critical thickness above which the phase transition exhibits critical

behaviour (one example of which, a divergent specific heat capacity, is discussed in

Section 1.3.6 within Iannacchione et al's results) and below which the phase transition is

continuous. Sheng calculated as an example, the critical thickness of nematic MBBA,

which he found to be 100 nm[27].   This property of nematics was extended to curved

substrates by Kralj[117]. Sheng later demonstrated that the nematic-smectic phase transition

temperature will shift downwards with the presence of impurities and elastic strains, and

will shift upwards due to surface-induced ordering in the nematic within a range of

substrate potentials that are dependent on the substrate properties[28].

   Experiments on nematic domain orientation via crystalline substrates (generally alkali

halides) continued in static systems with Tikhomirova et al[118, 119] and Frolova[120], who

showed that anisotropic surfaces play a major role in the orientation of nematics.

Dynamic domain reorientation studies of n-4'-methoxybenzylidene-n-butylanilin

(MBBA) and 5CB were performed by Blinov and Sonin[121] by placing a single drop (0.1-

1.0 mm diameter) on a muscovite mica substrate and observing the reorientation into

domains using optical microscopy, a process that generally took only a few seconds. It was observed that the mica divided the drops into six domain sectors, and similar experiments with NaCl revealed four domain sectors. The group also performed experiments confining the nematics between two aligned NaCl surfaces and applying an electric field to trigger a Fréedericksz transition to test the field needed to reorient the material from one preferred domain direction to another. Finally, they tested local Fréedericksz transitions by depositing Langmuir-Blodgett staircases of stearic acid (on which the nematics would adopt a parallel alignment, due to short-range steric forces) on a mica substrate (which, due to van der Waals interactions, aligns the nematics homeotropically) followed by a drop of the nematics (MBBA and 5CB) to find at what thickness of acid the liquid crystal switched from planar to hometropic orientation, and hence the range at which the dispersive forces from the mica substrate were screened. The phenomenon, first proposed by Dubois-Violette and de Gennes[122], was shown to follow the relation $r_c = \sqrt{A/2W}$, where r_C is the range of the dispersive force, A is the Hamaker constant of the mica/nematic interaction, and W is the anchoring energy of the nematic with the stearic acid[121]. The principle that 5CB (and, as it turns out, other cyanobiphenyls) tends to adopt either a planar or homeotropic orientation on mica has often been used by liquid crystal experimentalists, particularly those using the surface forces apparatus (SFA) and surface forces balance (SFB)[123-130], discussed in Section 1.5.

Jérôme and Pieranski[31] studied the interaction of nematics with two types of mica (muscovite and phlogopite), and stressed that the substrate must be considered from a three-dimensional point of view. Noting that the mica cleavage plane is along the K^+

layer, beneath which lies an SiO_4 tetrahedral hexagon substrate with octahedral cavities containing either three Mg^{2+} (for muscovite) or two Al^{3+} (for phlogopite) ions, they considered the symmetries involved in each case and concluded that the surface is effectively hexagonal C_{6V} (also known as hexagonal pyramid) symmetry for phlogopite mica and C_S (also known as reflective) symmetry for muscovite. In the former, the sublayer is considered since it is nearer to the surface (5 Å beneath the top layer) while in the latter it is ignored since it is further away from the surface (13.9 Å beneath the top layer). The symmetries lead ultimately to four possible anchoring positions in muscovite, two of them stable and two quasi-stable, and one tristable anchoring position in phlogopite. They also performed microscopy experiments of nematics on various substrates and demonstrated the dependence of anchoring on relative humidity[131], noting that at a critical humidity point the liquid crystal orientation may jump from one anchoring position to another. The behaviour is explained by deriving a formula for the grand potential of the system dependent on the chemical potential, temperature and azimuthal angle, and then using Landau-Ginzburg theory to develop a second-order anchoring transition[131]. A later study by Jérôme, Pieranski and Bechhoefer using second-harmonic generation techniques revealed that for cyanobiphenyls (5CB and 5OCB were used) on muscovite, bulk samples maintained a single orientation 30° from the γ axis, while monolayers of the material oriented in several possible directions, as discussed above. Non-mesogenic impurities were found to align when present in the aforementioned liquid crystals[132]. Lejcek, Bechhoefer and Oswald calculated a critical volume for smectic drops deposited on substrates below which the layers lie parallel to one another, creating facets and surface steps, and above which angular matching can

occur at the surface, creating a smooth, drop-like shape. Edge dislocations can occur within the volume at intermediate volumes as well[133].

Barberi et al[134] performed experiments on the wetting and surface-induced premelting (that is, material diffusion that occurs in a solid due to interactions with the substrate) properties of both smectic-A and solid 8CB on three surface types (glass coated with silver, SiO_x and silicon wafer). Small drops of 8CB were deposited on each surface and their thicknesses and radii were observed using optical microscopy and ellipsometry over time at various temperatures. In general, the radii were found to vary with time as $R = \sqrt{Dt}$ where t is the time and D is the diffusion constant; D was found to increase with temperature. The solid phase was found to spread out as well in a precursor film in accordance with premelting behaviour predicted by Xue et al[135].
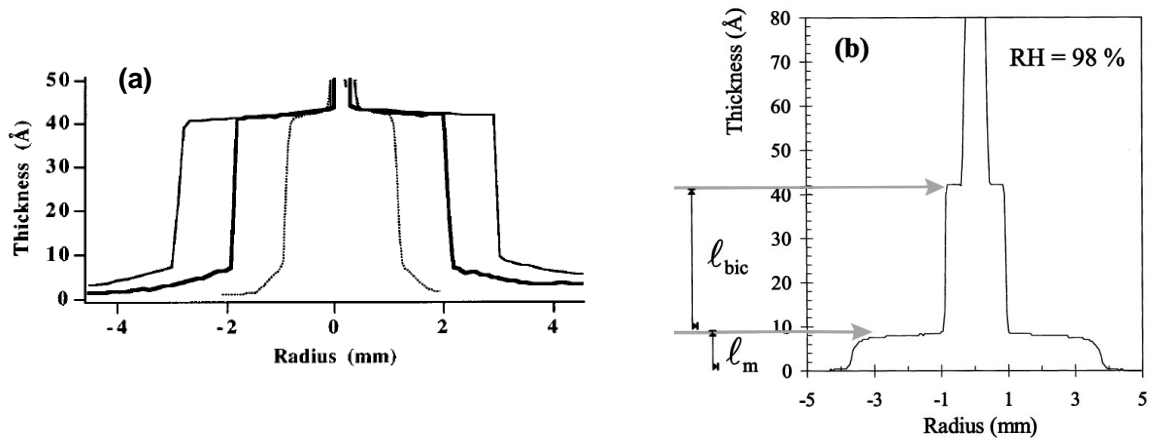
Figure 1.4: a) Solid 8CB near the solid-smectic-A phase transition premelting on a solid substrate at three different times following deposition. Reproduced from Barberi[134]. b) Smectic 8CB prewetting on a silicon wafer after three days of spreading. Symbols ℓ_m and ℓ_{bic} refer to the thickness of a monolayer and bilayer (together forming a trilayer) respectively. Reproduced from Bardon[136].

In their paper, Xue et al[135] predicted that the 8CB –CN end group would be absorbed by the polar surface and subsequently covered by a homeotropic interdigitated bilayer of 8CB, creating a thin fluid layer surrounding the solid. Bardon et al[136] studied prewetting phenomena of smectic 8CB microdrops on silicon wafers using ellipsometry and x-ray reflectivity. The gradual but continuous increase in thickness at the edges of the structure was attributed to an increase in density or tilt in the material. The outer plateau thickness corresponds to a monolayer of material tilted $63 \pm 6°$, while the middle plateau corresponds to the thickness of a bilayer atop the bottommost monolayer, together effectively forming a trilayer[136].

Alkhairalla et al investigated the role the surface field has in anchoring monolayers of liquid crystals by using evanescent wave ellipsometry[137], following earlier experiments performed on 5CB and 8CB by Evans et al[138]. The field, h_1, was modified by varying the chemical composition of the substrate, isotropic and nematic nCB (with $n = 5 - 9$) were used and an evanescent wave ellipsometric technique developed by the group were used to measure the Brewster-angle as a function of temperature. In all cases, the Brewster angle changed sharply at the isotropic-nematic transition, and the group was able to construct a phase diagram with temperature, n and h_1 for the axes. Notably, the anchoring transition from planar to homeotropic alignment as the surface became more hydrophobic was observed in the nematic phase and was mapped out. For a given temperature, this anchoring transition occurs upon less hydrophobic surfaces as n increases[137].

Olenik et al[139] studied the evaporation of thin layers of 8CB on polymeric (poly(vinyl cinnamate), or PVCN) and glass substrates using Brewster-angle reflection ellipsometry. They found that the first layer deposition is dominated by adsorption onto polar sites on the surface, with the 8CB head groups pointed toward the surface. When the polar sites are saturated, areas in between them are then filled with pairs of molecules, one pointed away from the surface and the other towards it[139].

1.3 Liquid Crystals under Confinement

1.3.1 Early work and Mięsowicz Orientations

Within a decade of Reinitzer's discovery, experiments were already underway to understand why the properties of liquid crystals seemed to change when proximal to surfaces. Otto Lehmann, in 1904, successfully suspended tiny (submicron diameter) droplets of nematic liquid crystal droplets within a viscous material and presented the results in his *Flüssige Kristalle* (Liquid Crystals)[3]. He differentiated between several phases as a result of these and other experiments, such as 'Fliessende Kristalle' (flowing crystals, spherical and rod-shaped molecules corresponding to smectics and cholesterics, respectively), 'Kristalline Flüssigkeit' (crystalline liquids) and 'Tropfbar flüssige Kristalle' (droplet-forming liquid crystals, corresponding to nematics) differentiating them by the shapes he could see under his microscope[58]. He also documented for the first time what is now known as the *Memory Effect*, where properties of the liquid crystal under confinement (in Lehmann's case, light extinction through the microscope slides) reappear after having been removed by heating and subsequently cooled to the original temperature. While he attributed this effect to residual crystals adhering to the surfaces, it is now known that the surfaces themselves order the liquid crystal near to them[56], a phenomenon that will be discussed in this section.

Marian Mięsowicz's work on magnetic-field-affected liquid crystals under confinement during the period 1934-1935 produced a trio of papers that laid the basis for understanding viscosity in such systems. The first, published in a Polish journal, received little attention, but was followed up with an article in Nature[34, 35]; both described the

method and equipment Mięsowicz used to conduct his experiments. A 48 mm $\times$ 24 mm glass plate was immersed in a temperature-controlled bath of the sample liquid and allowed to oscillate with a period of five seconds at amplitudes of up to 0.5 cm, creating a shear measured by analytical balance. The sample vessel was straddled by the two poles of an electromagnet[56]. The preliminary results showed a field of 2400 Gauss caused the viscosity of p-azoxyanisol to increase by a factor of 3.5, but it is with the third paper containing his follow-up results, written roughly in 1938 but with publication delayed until after WWII, that the concept of orientation-dependent viscosity began[36]. Three possible director orientations for the layered material were given: one in the direction of shear flow; one in the direction of the velocity gradient; and one perpendicular to both shear flow and velocity gradient. The three possible orientations are shown in Figure 1.5, for both nematic and smectic systems. The lavender dividers in the smectic diagrams represent lamellar layers.
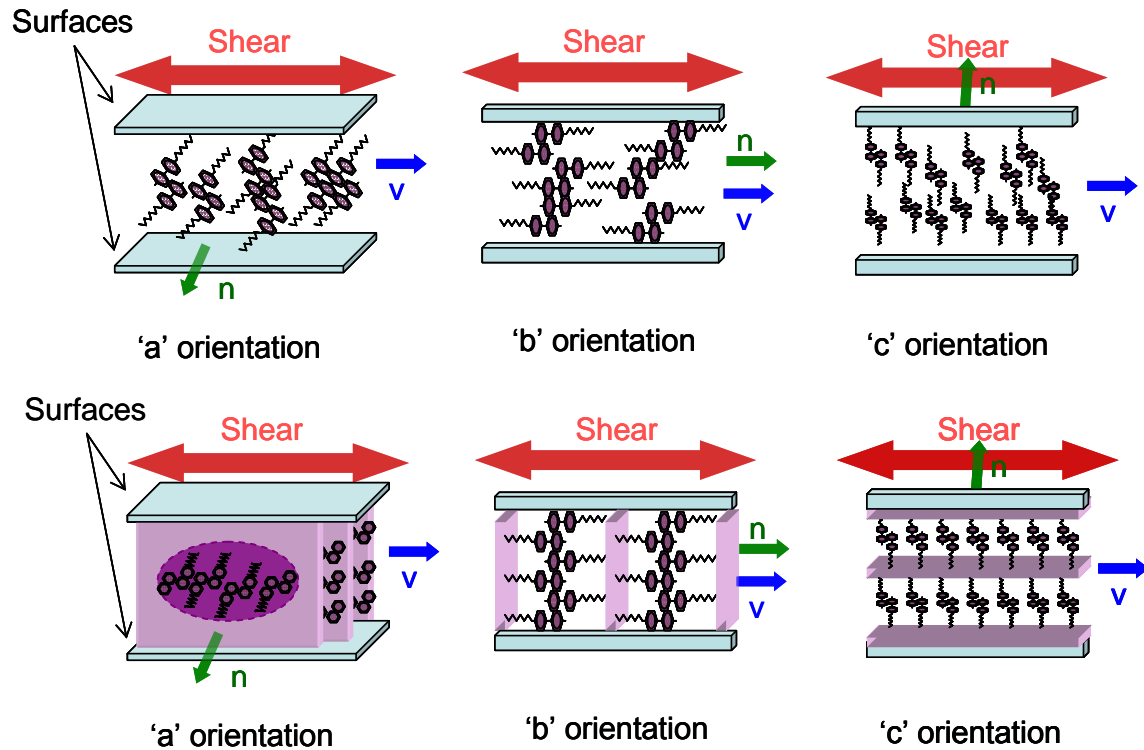
Figure 1.5: The three possible confined liquid crystal orientations, using the modern a-b-c nomenclature for (top) Nematics and (bottom) Smectics. Here, 'v' is the shear (velocity) direction and 'n' is the director.

The three orientations are now known as *Mięsowicz orientations* and the three resulting viscosities, η_a, η_b and η_c as *Mięsowicz viscosities* in his honour. Anisotropic dielectric permittivities originating from these three orientations, ε'_a, ε'_b and ε'_c are also of scientific relevance[140]. While he remained interested in the field up until his death in 1992 (he attended conferences on liquid crystals in Bordeaux in 1978 and Bangalore in 1982), the destruction of his lab by invading German forces during the Second World War led to Mięsowicz changing fields entirely and he became a professor of nuclear physics in Kraków after the war[56]. Section 1.4 contains more information on the theories behind the phenomena observed with smectics undergoing shear, as developed by de Gennes[19] and others.

1.3.2 Liquid Crystal Technology and Williams Domains

Richard Williams[66], during his time at RCA laboratories, in 1963 published the
advancements he had made in the study of the influence electric fields (both ac and dc)
have on confined liquid crystals. He used p-azoxyanisole confined between glass plates
with a spacing varying from 10 to 200 μm, and an electric potential of 10 V (the ac
frequency used was 1 kHz as, he mentions, it produced more stable patterns). At fields
above 1000 V/cm, he found that within about 2 milliseconds patterns formed in the
nematic, readily apparent due to their distinct optical properties: Sections outside the field
appeared dark, but sections immediately adjacent to it and inside the field transmitted
light. Upon removing the field the patterns disappeared within about 20 milliseconds.
He named the sections domains (now sometimes also referred to as *Williams Domains*),
and stressed that because of the rapidity of the transformation the phenomenon is not the
result of multiple phases; rather, it is the result of molecular reorientation. He added that
the reorientation cannot be due solely to a shift in the Boltzmann factor, *B*, since, using
the experimental parameters he provides:

$$\Delta B = \frac{\mu \Delta E}{k_B T} \approx \frac{\left(3.3356 \times 10^{-30}\ C \cdot m\right)\left(3 \times 10^{5}\ V/m\right)}{\left(1.38 \times 10^{-23}\ J/K\right)\left(400\ K\right)} \approx 1.81 \times 10^{-4}$$

which implies that only one in $\left(1.81 \times 10^{-4}\right)^{-1} \approx 5500$ molecules has been aligned by the
field, far fewer than what one might expect would be necessary to create a macroscopic
effect. He postulated that the effect is due to a torque exerted by the field on the net
dipole moment per unit volume in the area that was, before the field was applied, aligned
parallel to the confining wall. Since areas adjacent to that exposed to the field have no

torque upon them, they do not reorient, and this sharp divide between the two sections leads directly to domain formation.
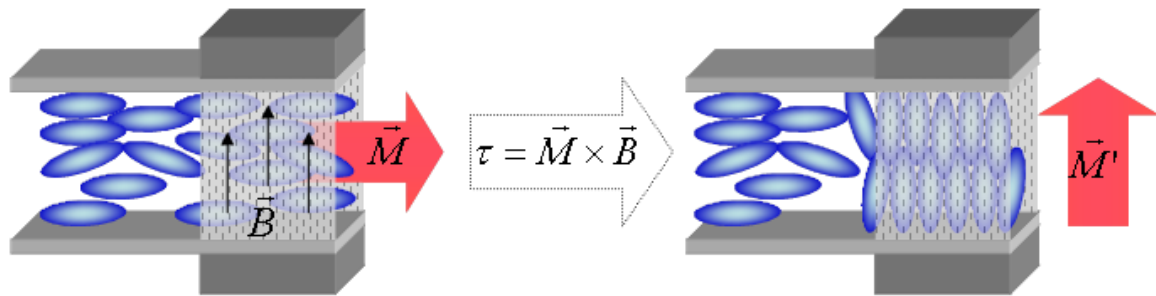
Figure 1.6: Confined nematic in a magnetic field; the field $\vec{B}$ and magnetic dipole $\vec{M}$ produce a torque which aligns the molecules with the field.

Williams also proposed a reason for nematic 'threads', which appear as sharp but irregular disclination lines that often result during the transition from the isotropic to nematic state and at low shear rates. He hypothesized that growing neighbouring domains whose boundaries abut will minimize their collective surface energy, and to do so they must align their directors either parallel or perpendicular to one another, which will lead to the densest packing of boundary molecules. Parallel alignment would lead to a coalescence of the domains, and perpendicular alignment would lead to a nematic thread or similar structure[66]. With the help of Williams' pioneering work in liquid crystal display technology, RCA was able to produce a prototype of the world's first working liquid crystal display in 1968.

1.3.3 Modern Methods of Studying Confinement: The Surface Forces Apparatus

Horn and Israelachvili performed experiments with the SFA on both an isotropic liquid[129] (octamethylcyclotetrasiloxane, or OMCTS) and a nematic liquid crystal[41] (4'-n-pentyl 4-cyanobiphenyl, or 5CB), to study the nature of structural forces (also known as solvation forces). The samples were confined to several monolayers by mica surfaces glued to cylindrical lenses. The top lens was mounted on a piezoelectric tube which, with a pair of micrometers, could control the separation between the surfaces to sub-Angstrom levels. The bottom surface was mounted on a spring mount with known stiffness, k, and by adjusting the lower disc by a specific amount (using either the micrometers or the piezoelectric tube) and recording the actual displacement (determined optically from the FECO fringes produced by white light passing through the sample and confining surfaces—see Chapter 2 for more details), the difference between the two measurements multiplied by k gave the normal force exerted by the sample via Hooke's law. By decreasing the gap size and recording the resulting force, the group was able to observe the solvation forces as a function of separation. In particular, oscillatory behaviour was recorded below a certain separation (which varies depending on the material being tested), representing the ejection of individual layers. As a layer is being ejected, it will exert a repulsive force, but once the layer is ejected there will be a jump inwards to the next stable layer.
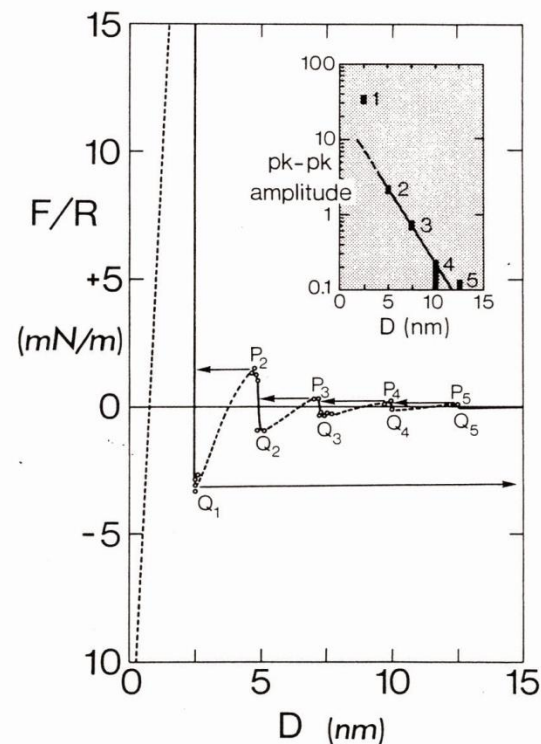
Figure 1.7: Force-measurement for nematic 5CB. Inset shows the amplitude of the oscillations as a function of separation. Reproduced from Horn et al[41].

The amplitude increase that occurs as the separation is reduced was attributed to the increased ordering at each successive layer. The pattern is analogous to the radial distribution function about any point in the immediate vicinity of a molecule in a liquid[141-143]. Horn, Israelachvili and Perez's aforementioned experiments represent the first to study thermotropic liquid crystals using an SFA[144]. Similar experiments have been performed since then on 5CB and 8CB by Ruths et al, using mica as a substrate[125] and gold[145], and both show similar behaviour. Presmectic ordering was first observed using the force-measurement technique in 1994 by Moreau, Richetti and Barois[146] using a mixture of water and caesium perfluorooctanoate (CsPFO) as the sample confined by two identical mica surfaces and later by one bare mica and one coated (by homeotropy-inducing poly-*l*-lysine) mica surface[147]. According to Frink and van Swol[148], oscillatory

solvation forces have been detected in several liquid materials since then, including water[149], ethanol[150], cyclohexane and *n*-pentane[151] and tetradecane and hexadecane[152]. Frink and van Swol treated the problem theoretically, using a grand canonical Monte Carlo simulation of a rough but patterned walled system interacting with a fluid obeying a Lennard-Jones potential, and found solvation oscillations that decreased proportionally to the degree of roughness of the surfaces[148].

Janik, Tadmor and Klein[123, 124] reported on shear experiments performed on nematic 4-cyano-4'hexylbiphenyl (6CB) under crossed cylindrical confinement between mica sheets, studied with a surface forces balance (SFB), a device similar in design and performance to the SFA. Both planar and homeotropic orientations were studied (the former using mica with minimal exposure to air and the latter using mica exposed for more than three hours); two types of planar orientation were used, simple (with the mica sheets parallel to one another) and twisted (with the mica sheets perpendicular to one another), as shown in Figure 1.8:
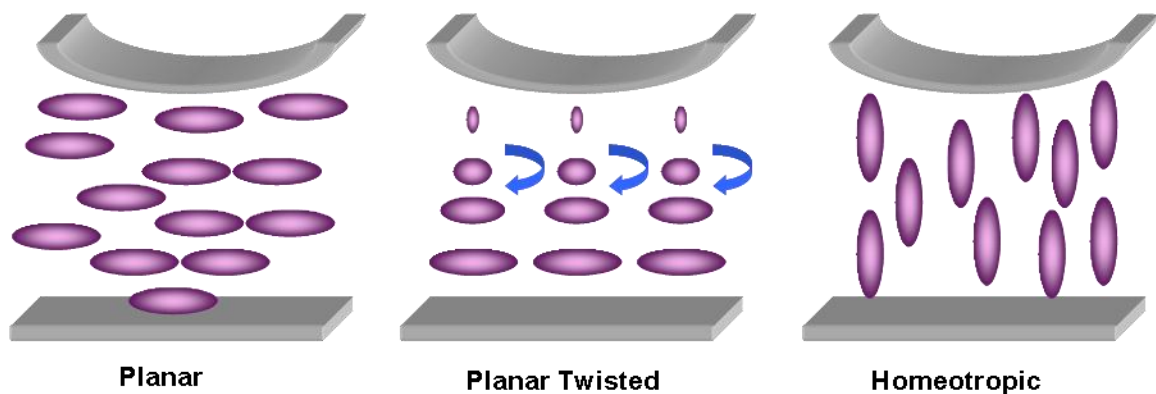
Figure 1.8: The three orientations of nematics on mica: Planar, Planar Twisted and Homeotropic. Adapted from Janik, Tadmor and Klein[123].

The different orientations were readily identifiable by the FECO patterns they create and the force profile they produce: Planar orientations create FECO whose doublets are closely spaced resulting from the two distinct refractive indices (the ordinary and extraordinary) arising from the sample geometry; planar twisted and homeotropic orientations both produce widely spaced doublets, but while the former exhibits monotonic repulsion roughly below 30 nm gap size, the latter exhibits an attractive well when the gap size reduces to roughly the dimer length.

The group reported that the orientation of the sample, as determined by their characteristic FECO pattern, can reorient over time due to exposure to air; Pieranski and Jérôme had demonstrated previously that water can penetrate nematic films and reach dry mica substrates over time, and ultimately nucleate oriented nematic domains above them[33]. Janik et al showed that this effect can be achieved from atmospheric water over the course of days. Initially homeotropically-oriented 6CB, for example, would begin to shift to a planar orientation, although only the onset of the effect could be detected after three days. The reorientation would generally occur on a timescale shorter than this, typically one to three days. Similar phenomena were also observed with 8CB and the non-polar nematic 4-hexyl-4-ethylazoxybenzene[123]. Lateral shear behaviour of confined 6CB was later reported by the group as well (with gap size typically below about 30 nm)[124]. They found that there was a measurable anisotropy in the friction across the nematic, believed to be a product of the Mięsowicz viscosities; they reported a 20-30% variation in response depending on the direction of shear relative to orientation. The shear response was found to vary roughly linearly with the normal load placed on the

sample, suggesting a solidlike system which would imply pinning of the molecules near to the surface. Shear tests were also performed in which, after the surfaces were brought together under a large load and sheared in one direction, they were separated and sheared in a direction perpendicular to the first. The anisotropy persisted during the latter shear, indicating that at the levels of confinement tested (smaller than 10 nm) the shear (of frequency 1 Hz and amplitude 560 nm) was unable to reorient the sample in the original direction[124].

Ruths and Granick[126] reported results on the effect surface alignment has on the static and dynamic behaviour of nematic 4'-n-pentyl-4-cyanobiphenyl (5CB) under shear while confined to a few molecular layers. The mica layers were rotated relative to one another an angle, θ, and this angle was measured according to McGuiggan and Israelachvili's relationship[153]:

$$\cos \theta = \frac{\lambda_{\gamma,\theta} - \lambda_{\beta,\theta}}{\Delta \lambda_{\theta=0^\circ}} \qquad (18)$$

where $\lambda_{\gamma,\theta}$ and $\lambda_{\beta,\theta}$ are the wavelengths of doublet fringes γ and β when the mica sheets are oriented at an angle θ to one another, and $\Delta \lambda_{\theta=0^\circ}$ is the maximum separation of γ and β. Force-measurement experiments revealed oscillatory forces similar in quality to those described by Horn and Israelachvili[41] were present, but with oscillatory amplitudes dependent on twist angle θ.
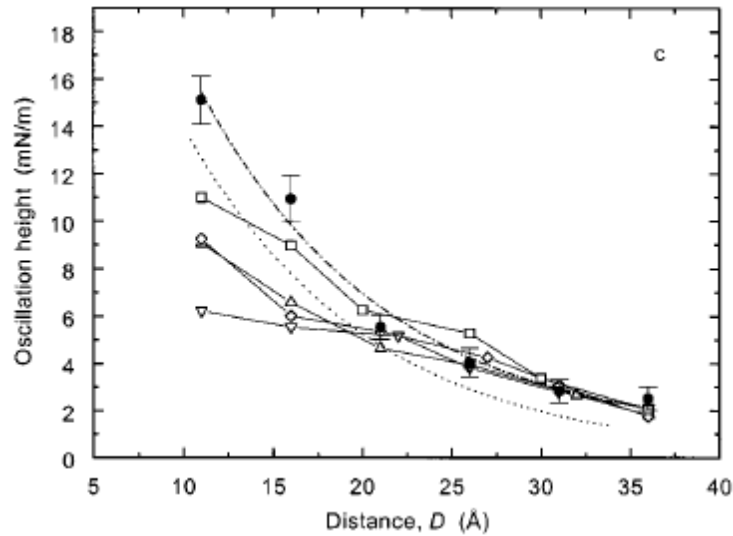
Figure 1.9: Oscillation amplitude of planar 5CB as a function of distance for various twist angles. Solid circles: $\theta = 2 \pm 2°$; squares: $\theta = 19 \pm 1°$; diamonds: $\theta = 40.2 \pm 0.5°$; triangles: $\theta = 60.4 \pm 0.3°$; inverse triangles: $\theta = 72.6 \pm 0.1°$. The dotted line represents an exponential decay with decay constant of 10 Å. Reproduced from Ruths and Granick[126].

The oscillation amplitude for twist angles below 10° decays exponentially with gap size. The variance of load force with twist angle reinforces Jérôme and Shen's conclusions that above the bottommost monolayer several orientations may be present[32].

Oscillatory shear experiments were performed as well, at two film thicknesses (10 ± 1 and 15 ± 1 Å, corresponding to two and three layers, respectively), with shear amplitudes of a few Angstroms and in the frequency range 0.13 to 130 Hz. The effective storage and loss moduli are large (indicating a rubbery material) and stay relatively constant over the range of shear rates save for high twist angles and low frequencies in the two layer system, where the viscous response dominates over the elastic, indicating liquid-like behaviour is present; the moduli also generally decrease with increasing twist angle. In experiments where frequency is kept constant (2.6 Hz) and the amplitude is varied over

the range of 0.2 to 1900 Å, however, both of the above film thicknesses exhibited nonlinear viscoelastic behaviour[126]:
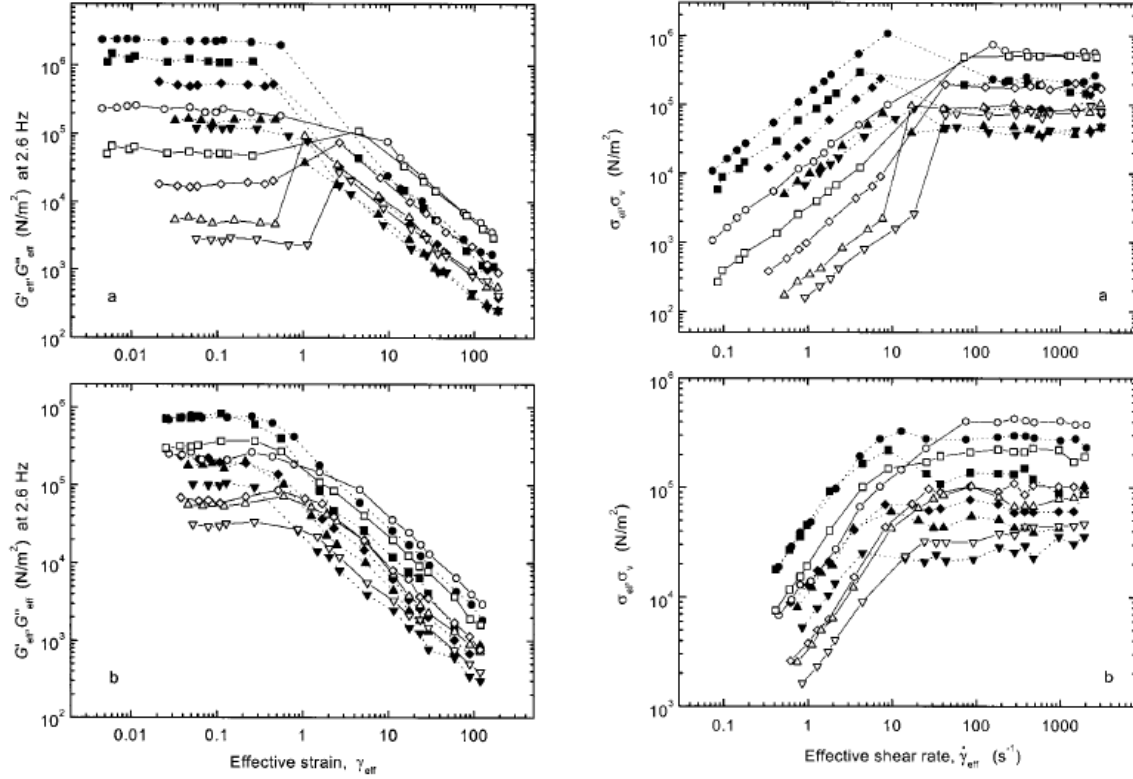
Figure 1.10: Viscous and elastic moduli for 5CB films of 10±1 Å (top) and 15±1 Å (bottom) thickness. Solid symbols represent the elastic moduli and open symbols the viscous moduli. Circles: $\theta = 2 \pm 2°$; squares: $\theta = 19 \pm 1°$; diamonds: $\theta = 40.2 \pm 0.5°$; triangles: $\theta = 60.4 \pm 0.3°$; inverse triangles: $\theta = 72.6 \pm 0.1°$. Reproduced from Ruths and Granick[126].

By comparing the shear moduli and asymptotic shear stress for the two films and finding them to be lower in general for the thicker film than the thinner one, and by noting that larger limiting strains occur for the thicker film, they concluded that the molecules one layer further out from the surface are noticeably less strongly confined. In addition, the shear response profiles for the three-layer film showed smooth sliding while that of the two-layer film showed stick-slip, indicating once again that the third layer is less strongly confined[126].

Kitaev and Kumacheva[144] performed SFB experiments on mesoscopically confined 5CB and 6CB (gap sizes of 200 to 1200 nm) to investigate their optical properties for the orientations described by Janik, Tadmor and Klein[123]. They measured the birefringence as a function of film thickness for a twist angle of 27° between the liquid crystal and the fully aligned mica. The results were in agreement with birefringence predictions calculated by the group for an anisotropic, uniform material. The results were, however, less satisfactory for mica surfaces oriented 15° with respect to one another, with a 10% disagreement between theory and experiment, and the group attributed this to the formation of surface-oriented domains. Deviations between theory and experiment (specifically, for gap sizes below 60 nm where the experimental FECO fringes become singlets while the theory predicts doublets, and above 1450 nm where the experimental birefringence values begin to fall while theory predicts they should continue increasing) for the case where the mica sheets were aligned perpendicular to one another were attributed once again to the presence of domains and to equipment limitations[144]. Following Janik et al's conclusions[123], Kitaev and Kumacheva[144] monitored the birefringence of 6CB and observed that while, in a crossed mica setup exposed to ambient air, the birefringence decreases but remains a doublet (indicating a planar molecular orientation), if the same system is exposed to saturated air the nematic shifts from a doublet to a singlet, and hence from a planar orientation to a homeotropic one.

Cho and Granick[154, 155] combined a home-built SFA with an impedance analyzer in order to study the dielectric spectra of both static and sheared nematic 5CB[156]. In

addition to comparing planar and homeotropic monolayer dielectric spectra and finding

the homeotropic peak to be three orders of magnitude slower than the 10 Hz planar peak

(attributed to dielectric anisotropy), they reported that shear has little effect on the

dielectric profile for homeotropic monolayers of 5CB, with the only difference (a 15%

shift) between the shear and no shear profiles occurring where the dielectric frequency

and shear frequency correspond, in their case, approximately 10^6 sec^{-1}. Tests at other

shear frequencies never resulted in shifts larger than the 15% seen at 10^6 sec^{-1} [156].

Zappone, Richetti and Barberi et al[157] performed experiments on nematic 5CB and 4'-

n-pentylphenyl-4-methoxybenzoate (ME10.5/ZLI-0245) confined between mica surfaces

separated by up to 250 nm. Both planar and homeotropic orientations (the latter from a

cetyl-trimethyl-ammonium-bromide (CTAB) coating) were studied. By considering the

anchoring geometry of the system and developing Barbero and Barberi's model for

confinement-induced anchoring transitions[158] (itself a product of Frank-Oseen theory[13]),

they were able to re-develop the theory for a curved surface as occurs in the SFA system

and found the vertical force in such a system to be given by:

$$F = 2\pi \left(\frac{\pi}{2} \right)^2 \frac{K}{\delta} - 4\pi \frac{K}{\sqrt{\delta}} \tag{19}$$

where K is the Frank elastic constant (which assumes $K \approx K_{Splay} \approx K_{Twist} \approx K_{Bend}$) and

$\delta = 2D/R$ where D is the separation and R is the surface radius. The first term on the

right is the anchoring contribution and the second is the curvature contribution, and

together they lead to a possibly attractive or repulsive force depending on δ. The

observed strong attraction at separations below 10 nm could not, however, be explained

by the theory as it predicts a repulsive force at that length scale, nor could it be explained by van der Waals interactions, since the range is too short. A theory was proposed in which a confinement-induced structural transition to a thin biaxial layer system may have occurred leading to the attractive force, but a full solution to the mystery has not yet been put forth[157].

Mizukami et al[159] reported results on a study of nematic 6CB confined between mica surfaces within the SFA using shear resonance. By laterally moving one of the surfaces with respect to the other by a piezoelectric element using a sinusoidal shear pattern and measuring the deflection of the other surface, they obtained the resonance response for both 6CB and, for comparison, the liquid octamethylcyclotetrasiloxane (OCMTS). Differences in resonance patterns between the two materials at various levels of confinement (from 104 nm down to 3.9 nm gap size) indicated that the sample-mica and intermolecular interactions differed between the two materials. In the confinement range of 5.7 to 7.9 nm coupling between the surfaces was observed for 6CB, resulting in the resonance peak's disappearance; the peak reappeared and increased in amplitude as the gap size was decreased below 5.7 nm, indicating the sample was becoming more structured.

1.3.4 X-ray studies

In order to study liquid crystals with x-ray scattering it is necessary to understand the scattering cross-section associated with it. Following the treatment by Als-Nielson et

al[160, 161] and others[162, 163] of Caillé's derivation[164], one may begin with the general

formula for the Fourier Transform of the structure factor, $S(\vec{r})$:

$$S(\vec{r}) = \left\langle e^{iq_0[u(r)-u(0)]} \right\rangle \tag{20}$$

where $u(r) - u(0)$ is an undulation representing a Helfrich deformation (described in

Sections 1.4.2 and 1.4.3) shifting the position from 0 to r, and q_0 is the displacement in

reciprocal space. Assuming $u(r)$ is randomly distributed one can apply a Gaussian

distribution to get:

$$S(\vec{r}) = e^{I(\vec{q})} = e^{-\frac{1}{2}q_0^2 \left\langle |u(r)-u(0)|^2 \right\rangle} \tag{21}$$

where $I(\vec{q})$ is the scattering intensity. Making use of the Equipartition Theorem,

$\left\langle |u_q^2| \right\rangle = \frac{1}{2}k_B T$, with equation (21) and assuming no magnetic field ($H \approx 0$), the

scattering intensity can be written as:

$$I(\vec{q}) = \frac{q_0^2}{V} \int_V \frac{d^3q}{(2\pi)^3} \left\langle |u_q^2| \right\rangle [1 - \cos(\vec{q} \cdot \vec{r})], \text{ where } \left\langle u_q^2 \right\rangle = \frac{Vk_B T}{B\left(q_\parallel^2 + \lambda^2 q_\perp^4\right)}$$

Integrating over reciprocal space, the scattering intensity becomes:

$$I(\vec{q}) = \frac{k_B T q_0^2}{(2\pi)^3 B} \int_{q_{min}}^{q_{max}} \int_0^{2\pi} \int_0^\infty \frac{[1 - \cos(q_\parallel z + \vec{q}_\perp \cdot \vec{\rho})]}{q_\parallel^2 + \lambda^2 q_\perp^4} dq_\parallel d\theta dq_\perp$$

where θ is the angle between $\vec{q}_\perp$ and the density function, $\vec{\rho}$. Using

$$\int_0^\infty \frac{\{1 - \cos[a(b-x)]\}}{x^2 + c^2} dx = \frac{\pi}{2c}\left[1 - e^{-ac}\cos(ab)\right], \text{ the first integral disappears:}$$

$$I(\vec{q}) = \frac{k_B T q_0^2}{(2\pi)^3 B} \int_{q_{min}}^{q_{max}} \int_0^{2\pi} \frac{\pi}{2\lambda q_\perp^2}\left[1 - \exp\left(-\lambda q_\perp^2 z\right)\cos\{\vec{q}_\perp \rho \cos\theta\}\right] d\theta dq_\perp$$

50

Applying Bessel relationship $J_0(x) = \pi^{-1} \int_0^{\pi} \cos(x \cos(\theta)) d\theta$, the intensity becomes:

$$I(\vec{q}) = \frac{k_B T q_0^2}{(2\pi)^3 B}\left(\frac{\pi}{2}\right) \int_{q_{min}}^{q_{max}} \left\{ \frac{2\pi - 2\pi \exp\left(-\lambda q_\perp^2 z\right) J_0(q_\perp \rho)}{\lambda q_\perp^2} \right\} dq_\perp$$

And by substituting the series expansion of the Bessel function,

$$J_0(q_\perp \rho) = \sum_{n=0} \left[\frac{(q_\perp \rho)^{2n}(-1)^n}{2^{2n}(n!)^2} \right] , \text{ the integral simplifies somewhat to:}$$

$$I(\vec{q}) = \frac{k_B T q_0^2}{(2\pi)^3 B}\left(\frac{\pi}{2}\right) \int_0^{q_0} \left\{ \frac{1}{\lambda q_\perp^2}\left[1 - \exp\left(-\lambda q_\perp^2 z\right)\sum_{n=0}\left(\frac{(q_\perp \rho)^{2n}(-1)^n}{2^{2n}(n!)^2}\right)\right] \right\} dq_\perp$$

where the integration bounds have been replaced by 0 and q_0 to represent the layer

dimensions over which the scattering occurs. The integral must be performed term by

term. With the help of the exponential function $E(x) = \int_x^{\infty} \frac{e^{-u}}{u} du$, which has solution

$E(x) = -\gamma - \ln x + \int_0^x \frac{1 - e^{-u}}{u} du$ (where γ is Euler's constant), the integral can be re-written

as $\int_0^{q_0} \frac{1 - e^{-\lambda q_\perp^2 z}}{\lambda q_\perp^2 z} d\left(\lambda q_\perp^2 z\right) = E(q_0) + \gamma - \ln(q_0)$, and, by way of an expansion of the Bessel

function, the structure factor can now be written as:

$$S(\vec{r}) = e^{I(\vec{r})} \approx e^{-2\eta\gamma}\left(\frac{4d^2}{\rho^2}\right)e^{-\eta E(q_0)/4\lambda z} \tag{22}$$

where $\eta = \frac{q_0^2 k_B T}{8\pi B \lambda}$. In the asymptotic limit as $\rho \ll \sqrt{\lambda z}$ and $\rho \gg \sqrt{\lambda z}$ (that is, very

large and very small penetration depths relative to the smectic layer dimensions), the

structure factor reduces to:

$$S(\vec{r}) \cong \begin{cases} (d^2/\lambda z)^{\eta} & \text{for} \quad \rho \ll \sqrt{\lambda z} \\ (2d/\rho)^{2\eta} & \text{for} \quad \rho \gg \sqrt{\lambda z} \end{cases} \qquad (23)$$

In the above $\rho \ll \sqrt{\lambda z}$ corresponds to the longitudinal limit and $\rho \gg \sqrt{\lambda z}$ corresponds to the transverse limit. This asymptotic behaviour results in structural factor singularities about q_m (where m is any integer), resulting in:

$$\vec{S} \cong (q_{\parallel} - q_0)^{-2+\eta} \qquad (24a)$$

for the longitudinal mode (with $q_{\perp} \approx 0$), and

$$\vec{S} \cong q_{\perp}^{-4+2\eta} \qquad (24b)$$

for the transverse mode (with $q_0 - q_{\parallel} \approx 0$). These singularities will show up as wings in the scattering profile[160-164]. In this way one can study smectics by way of their perturbative Helfrich undulations, as discussed in section 1.4.4.

Different types of liquid crystals will produce different scattering profiles as shown in Figure 1.11. Here, the double ring indicates scattering from two length scales: the outer, from the width of the molecule and the inner from the length. Hence, even in the isotropic phase (Figure 1.11a) one expects to see the concentric scatter rings unless the constituent molecules are spherical.
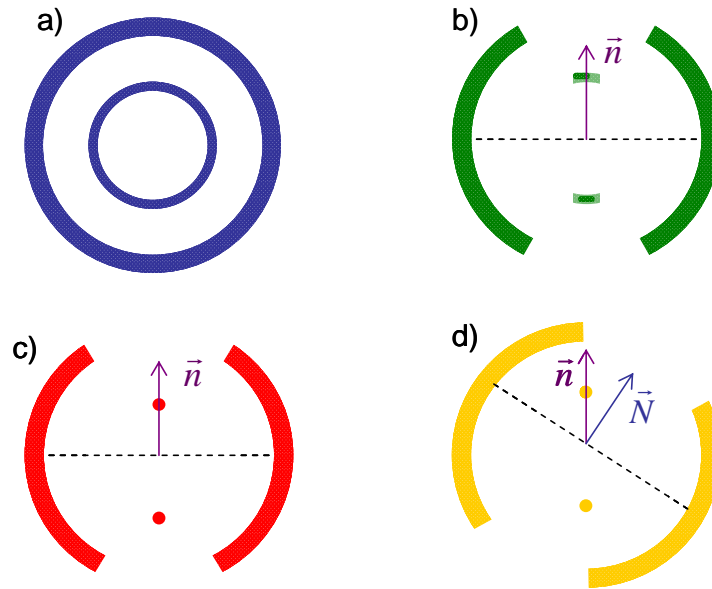
Figure 1.11: X-ray scattering profiles for: a) an isotropic liquid; b) a nematic; c) a smectic-A and; d) a smectic-C. Reproduced from Chaiken and Lubensky[165].

In the nematic phase (Figure 1.11b) the preferred direction of the molecules restricts scattering so that a diffuse arc segment will be all that remains of the inner ring at the position of the director, $\vec{n}$, while the outer ring will be devoid of intensity in that direction (since the majority of molecular widths will be aligned perpendicularly to the director and hence won't scatter in that direction). The smectic-A (Figure 1.11c) will resemble the nematic except the inner scattering peak will be better-aligned and hence appear as a spot, while the smectic-C (Figure 1.11d) will have a tilt angle between the inner spot representing the director and the outer ring section's center, given by $\vec{N}$ and representing the molecular alignment relative to the director[165].

Als-Nielsen and Safinya[160, 161] performed x-ray scattering experiments on magnetic field-aligned octyloxycyanobenzylidene (8OCB) in the smectic-A mesophase, demonstrating that it was a suitable example of a Landau-Peierls system in that its Bragg line peaks, particularly near to the smectic-nematic transition temperature, exhibited wings describable by the structure factors given above in equation (1). Similar results were found with N-p-cyanobenzylidene-p-octyloxyanilene (CBOOA)[166]. Later studies with 4-n-pentyl-phenylthiol-4'-octyloxybenzoate ($8\overline{S}5$) near the second order smectic-C to smectic-A transition once again demonstrated the presence of the Helfrich undulations, and revealed both planar spacings and molecular tilt in the sample. The ratio of spacings in the two states was found to remain constant through the transition[167]. Still later, experiments with smectic-A and smectic-C heptylphenyl nitrobenzoloxybenzoate (DB7NO$_2$) reveal regions of period-varying translational symmetry (incommensurability)[168] while tests of the multilayer membrane system consisting of sodium dodecyl sulfate (SDS), pentanol, water and dodecane showed the characteristic Landau-Peierels structure factor power-law dependence, indicating Helfrich fluctuations dominate the intermembrane interactions[169].

A study of homeotropically-oriented smectic-A 8CB and ferroelectric smectic-A/smectic-C* materials ZLI-3041 and CBC confined to 25 μm diameter glass pores by Mang, Sakamoto and Kumar[170] demonstrated that while the smectic-C* layers are formed parallel to the confining walls, the 8CB molecules form a chevron-shaped layer structure; the size of the layers themselves, furthermore, are dependent on temperature.

Clark and Bellini et al[171] performed x-ray experiments on 8CB confined to low-density silica Aerogel (with a volume fraction, or fraction of 8CB volume to total volume, of 0.79) while undergoing the nematic to smectic-A phase transition. The experiments followed light scattering and calorimetry experiments (discussed in Section 1.3.6), and showed an evolving scattering peak as the temperature is decreased through the isotropic-nematic transition, as well as coexistence of smectic and crystalline 8CB during the smectic-A-crystalline transition. In the former phase change, smectic-A domains increased in size with decreasing temperature, but were found to be restricted by the surfaces to 4 nm correlation lengths, well below the pore size of 17.5 nm, and this restriction persists even well below the transition point. Conversely, in the latter phase change, the length scales are on the order of the pore size, indicating an individual pore is either occupied by smectic-A or crystalline material, but not both simultaneously.

Panizza et al[172] performed x-ray scattering experiments on smectic 8CB within a Couette cell geometry, which will give a constant shear rate $\dot{\gamma} = v/D$, where v is the rotor velocity and D is the gap size. Here the gap size was 500 μm and the shear rate was varied from approximately 3 sec^{-1} to 1150 sec^{-1}. It was noted that upon lowering the temperature from the smectic-nematic transition point that the 'a' Mięsowicz orientation evolves to a mix of the 'a' and 'c' orientations, and that if the shear rate is increased to a critical point (700 sec^{-1}), this 'a' and 'c' mix of orientations reverts to a purely 'a' orientation. The shear stress, σ, vs. shear rate curves for these bulk samples showed nonlinear behaviour at low shear rates (below 700 sec^{-1}) where $\sigma \propto \dot{\gamma}^{1/2}$, while at high shear rates (700 to 1150 sec^{-1}), $\sigma \propto \dot{\gamma}$, indicating that the sample phase is Newtonian.

Similar results were found by Negita and Uchino using a viscometer and 8CB confined to a 1 mm gap a few years later[173].

Martinez-Miranda[174] performed grazing-incidence x-ray scattering (GIXS) experiments on the smectic-C* mixture mx5112 deposited on a glass substrate with 9 μm period gratings of 1.6 μm depth and 6.0 μm width, and with this technique found that two regions of confinement were observable. The first, from one to five microns in thickness, was associated with the geometry of the grooves, while the other, from five to twenty microns in thickness, was associated with the cooperative alignment of the grooves as a whole. This behaviour was attributed to the density of the grating channels and to the thermal history of the sample[175].

Leheny et al[176] studied nematic and smectic 8CB-aerosil dispersions with varying densities using x-ray scattering, and found in all cases (with densities varying from 0.025 g silica/cm^3 8CB to 0.341 g silica/cm^3 8CB) that the correlations remained short-range, indicating that the dispersion had disrupted order within the system and thereby dramatically altered the nematic to smectic transition.

A theoretical treatment of nematic 8CB under small amplitude shear was undertaken by de Andrade Lima and Rey[86] to characterize the temperature dependence and to understand the shear alignment transition. They used ELP theory (discussed earlier in the Ericksen and Leslie-Ericksen Theory section) to describe the oscillatory Poiseuille flow observed, and found that 8CB is flow-aligning above a temperature of 38.36 K and non-

aligning below that temperature, obtained by finding the point at which the loss angle

$\delta = \tan^{-1}(G''/G')$ (where G' and G'' are the storage and loss moduli, respectively) is

invariant with respect to frequency. The storage and loss moduli were found to be

characteristic of a viscoelastic material with a single relaxation time[86]. A similar

approach was developed earlier by Rey to describe cholesterics under small amplitude

shear[177, 178].

Hamley, Castelletto and Parras[88] used x-ray scattering to study 8CB confined to a

home-built capillary flow device. By lowering the temperature to the nematic tumbling

transition temperature of 38.36 K, calculated by de Andrade Lima (where the Leslie

viscosity coefficient α_3 changes sign[86], they were able to observe the transition from the

'b' Mięsowicz orientation to the 'c' Mięsowicz orientation at a flow rate of 0.1 ml/min,

and a similar transition at a lower temperature with a flow rate of 6.0 ml/min[88].

1.3.5 NMR studies

Nuclear magnetic resonance offers the possibility of studying in situ samples non-

invasively, since it gives information about molecular structure and dynamics solely by

the monitoring of spin properties while in a large (usually 0.1-20 T) magnetic field. The

prime difference between the NMR of liquids and the NMR of liquid crystals is that,

while in the former, motional averaging of the interactions between spins averages the

local magnetic field vector to zero[179-181], in the latter the partially oriented molecules, and

hence non-zero local field, become a major factor in determining the NMR spectrum[182],

similar to solid samples. NMR can be used not only to obtain information on the director

field, but the density of singular point defects, on the strength of surface anchoring, and on the surface elastic constants[183]. The history of NMR and liquid crystals begins with Spence, Moses and Jain who, in 1953, collected a proton spectrum of nematic p-azoxyanisole and published a brief article of it, interpreting the triple peak they had found as a product of rotational hindrance of methyl groups[184]. A paper later that year by the same group corrected their misinterpretation and indicated that because the triple peak was field-independent it arose from ordering in the material[112, 185]. The field of liquid crystal NMR did not take off until 1963, however, when Saupe and Englert[16] published their landmark paper proposing that liquid crystals might be used as solvents for studying small molecules.

In 1989 the NMR study of liquid crystals under confinement was improved by the implementation of controlled pore glass (CPG), originally developed for use in chromatography experiments in 1965 by Haller[186, 187]. CPG consists of small (usually borosilicate) glass beads; borates of well-defined size are leached from the silicates either by heat or acid treatment, leaving cylindrical cavities of narrow pore size distribution. Commercially available CPG comes in a wide variety of diameters and hence surface to volume ratios, making it a very useful tool in understanding surface physics via NMR.
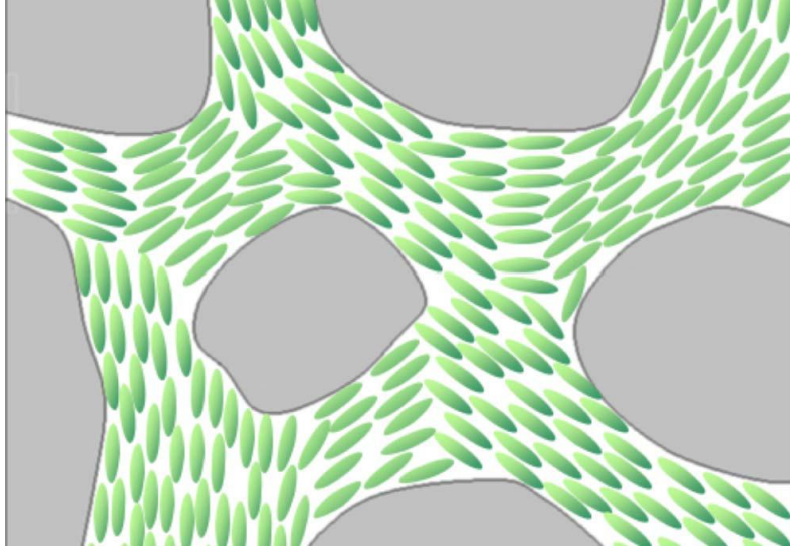
Figure 1.12: Schematic representation of a nematic liquid crystal confined to CPG. Reproduced from Vilfan et al[188].

Variations of CPG include Aerogel, Nuclepore and Anopore membranes. Alternatively, a polymer dispersion can be prepared in which the liquid crystal is combined with a polymeric network (4,4'-bis-acryloylbiphenyl, or BAB, for example) of fibres to act as a surface which tends to align the liquid crystal in which it is immersed. In general, in such systems the amount of surface-induced ordering will be proportional to the amount of polymer dispersed in the sample[183].

A brief description of the basic equations of liquid crystal NMR follows, focusing on applications to samples under confinement using frequency- and time-domain NMR. Traditionally two nuclei have been used as probes in the NMR study of liquid crystals: Protons (spin ½) and deuterons (spin 1). The Zeeman splitting of isolated protons and deuterons in rigid molecules, Δv, is given by Vilfan[183]:

$$\Delta v = \frac{3}{2} C \left\{ \frac{1}{2} \left(3 \cos^2 \Theta - 1 \right) \right\} \tag{25}$$

where Θ is the angle between the interproton vector (for protons) or the electric field gradient tensor symmetry axis (for deuterons) and the magnetic field, and C is a proportionality constant equal to $C_P = \dfrac{\gamma^2 \hbar}{\pi r^3}$ for protons and $C_D = \dfrac{e^2 qQ}{h}$ for deuterons. Here, γ is the proton gyromagnetic ratio, r is the interproton distance, and C_D is the static quadrupole coupling constant. In a nematic, however, the term in braces is averaged for molecular motions faster than the angular splitting frequency $(2\pi\Delta v)^{-1}$. The uniaxiality of the system leads to a more complicated equation given by Doane[189]:

$$\Delta v = \frac{3}{2} C \left\{ \frac{1}{2} \left(3\cos^2\alpha - 1 \right) \right\} \left[S \left\langle \frac{1}{2} \left(3\cos^2\beta - 1 \right) \right\rangle + \frac{1}{2} \left(S_{xx} - S_{yy} \right) \left\langle \sin^2\beta \cos 2\delta \right\rangle \right] \qquad (26)$$

where S is the order parameter, α is the angle between the director and the magnetic field, β and δ are the azimuthal and polar angles of the interproton vector (for protons) or of the electric field gradient tensor symmetry axis (for deuterons) and the long molecular axis, and $S_{xx} - S_{yy}$ describes the deviation of the molecular shape from perfect cylindrical symmetry. Because this last value is generally an order of magnitude smaller than S, the latter term can usually be disregarded. In practice, because of non-equivalent proton pairs in most systems, proton NMR spectra often result in broad backgrounds that can obscure peak details, and so deuteron NMR experiments are usually preferred, if possible. Equation (26) indicates that the order (via the order parameter) and the director angle are both a function of Zeeman splitting and so both can be monitored via standard NMR techniques.

Vilfan[183] gives the modification to line splitting of a nematic under constraint:

60

$$\Delta \nu_D(\vec{r}) = \Delta \nu \left\{ \frac{1}{2} \left[3 \cos^2 \alpha(\vec{r}) - 1 \right] \right\} S(\vec{r}) \tag{27}$$

where $\Delta \nu$ is given by equation (26) with $S = 1$ and $\alpha = 0°$, replaced by the local order parameter $s(\vec{r})$ and director angle $\alpha(\vec{r})$ to accommodate reorientations due to surface effects or other perturbations. Examples of line splitting for various nematic director fields are given by Crawford[190]:
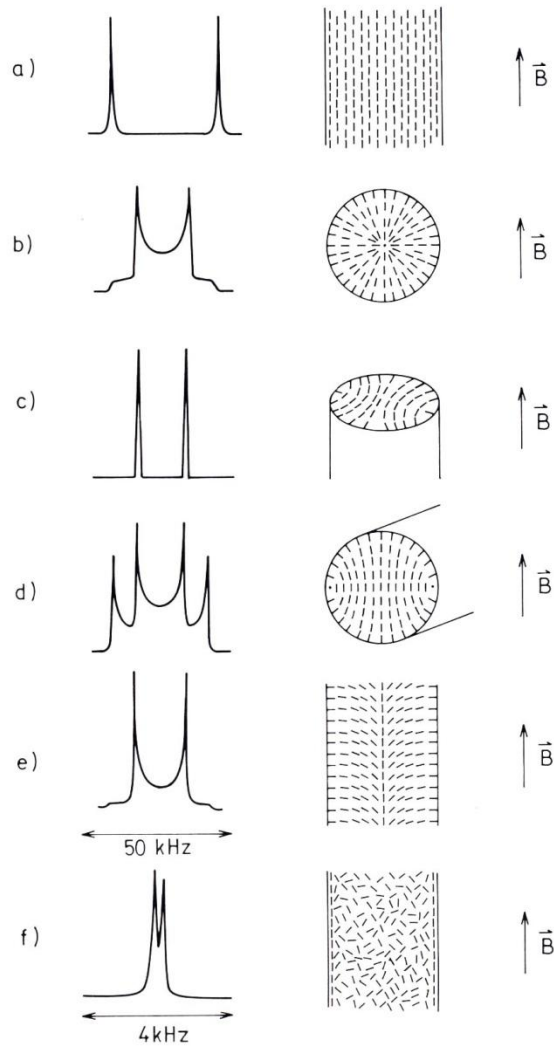
Figure 1.13: Deuteron NMR line splitting characteristics for various nematic cylindrical and spherical confinement scenarios. $\vec{B}$ refers to the external magnetic field. a) Parallel-axial structure in a cylindrical cavity; b) Radial distribution in a spherical cavity; c) Planar-polar structure in a cylindrical cavity, director perpendicular to $\vec{B}$; d) Cylindrical cavity, director parallel to $\vec{B}$; e) Escaped-radial structure in a cylindrical cavity; f) Isotropic phase in a cylindrical cavity. Reproduced from Crawford[190, 191].

It should be noted that the external magnetic field may distort surface effects according to the magnetic coherence length:

$$\xi_B = \sqrt{\frac{K}{\Delta \chi B^2}} \tag{28}$$

62

where K is the relevant liquid crystal elastic constant, $\Delta\chi$ is the anisotropy of the magnetic susceptibility, and B is the magnetic field strength. The above equation indicates that line distortion will occur in pores with diameters larger than ξ_B or at distances larger than ξ_B from the surface, and Crawford cites 5CB in a 1T field as having a magnetic coherence length of 8 μm[191].

The three most common measurements obtained from time-based NMR are the spin-spin relaxation times, T_2, spin-lattice relaxation times, T_1, and spin-lattice relaxation times in the rotating frame, $T_{1\rho}$. The first represents the decay of magnetization transverse to the external magnetic field due to energy exchange between spins, the second represents the decay of magnetization due to energy exchange with the environment (i.e. the lattice) and the third represents the decay of magnetization while it is spin-locked to the rf magnetic field[179, 192]. Together, they yield information on local magnetic fields within a sample since any local inhomogeneities present will either facilitate or retard relaxation compared to that which takes place within the rest of the sample, thereby affecting the overall relaxation. In a sample that contains bound molecules (close to a surface, for example), the exchange of bound and free molecules will lead to two (ideally) distinct relaxation rates so that the overall rate, T_2, will be a weighted average of the two constituent rates[183]:

$$\frac{1}{T_2} = \frac{\eta}{T_{bound}} + \frac{1-\eta}{T_{free}}$$

(29)

where η represents the fraction of bound molecules in the sample. Similar relations may be made for T_1 and $T_{1\rho}$. From equation (29) a simple relaxation experiment can give

information on the strength and extent of molecular binding in a known geometry. The technique is useful not only for confinement experiments, but for transition experiments as well; Martin et al observed a temperature-dependent increase of T_2 when decreasing the temperature to within 5 K of the bulk p-methoxybenzylidene-p-n-butylaniline (MBBA) nematic-isotropic transition, for example, and attributed the shift to nematic fluctuations in the isotropic phase[193].

Crawford et al[194] performed experiments comparing the spin-spin relaxation behaviour of parallel and perpendicularly-oriented 8CB-αd_2 confined within cylindrical glass pores (note that the -αd_2 suffix here refers to the first, or 'α', hydrocarbon chain position having been deuterated). They found that in the isotropic phase, the two orientations differed significantly in behaviour, in that while the parallel-anchored molecules were relatively temperature-invariant, the perpendicularly-oriented molecules varied considerably[195].
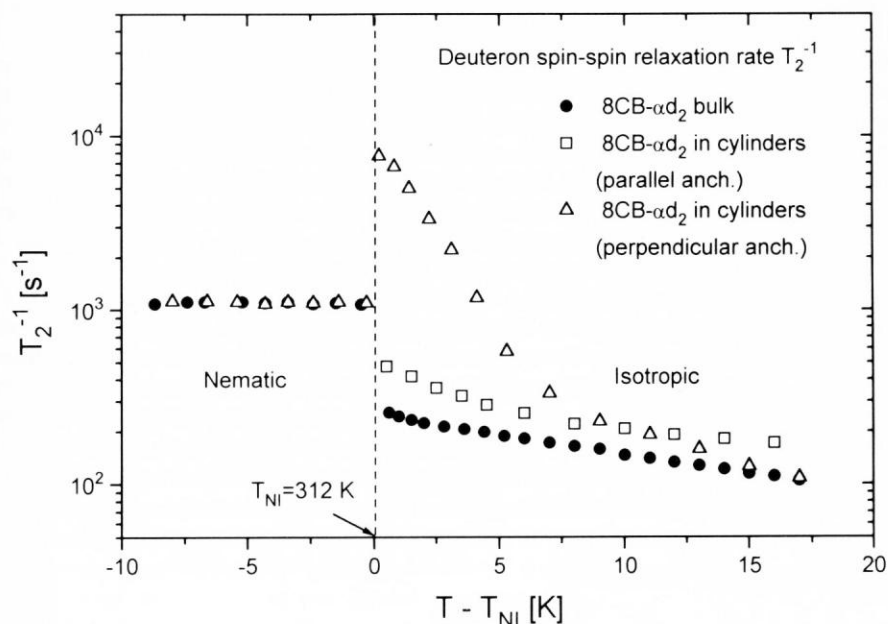
Figure 1.14: 8CB-αd$_2$ confined to 100 nm radius nanopores. Reproduced from Vilfan et al[195].

This phenomenon was not seen in nematic 8CB-αd2, and indicates a diminished surface-8CB interaction for the latter case, likely due to the $(CH_2)_{15}COOH$ coating on the pore walls being used to achieve the perpendicular orientation. For 5CB-αd$_2$, it was found that both proton and deuteron T_1's were generally the same for bulk and dispersion samples, while the T_2 and $T_{1\rho}$ values were higher in dispersion than in bulk. This indicates one or more dynamical relaxation processes were occurring in the dispersion. A relaxation time of 4 ± 1 μsec was calculated for the isotropic phase, likely related to the average lifetime of a surface molecule, and the surface order parameter was found to be approximately 0.1 and did not fluctuate near the isotropic-nematic transition[195]. A later study of 8CB by Vilfan et al[188] within 15 nm diameter CPG pores revealed spin-lattice relaxation values an order of magnitude larger than that found in bulk, a property

attributed to molecular reorientations that are mediated by translational displacement of the molecules. While the group was unable to conclude anything with certainty on long range diffusion, they were able to determine that the local translational diffusion of molecules, despite the confined environment, was just as high as that observed in the bulk state.

Cramer et al[196] performed ^{13}C and proton NMR as well as broadband dielectric spectroscopy on 5CB confined to 2.5, 5.0 and 10 nm diameter CPG to study its transition temperature suppression and found that even within the smallest pores nematic dynamics similar to that found in bulk was still detectable; the dielectric spectra indicate that the system is best described as being of two states, one of which is bulklike and the other surface-influenced, whose relaxation rate is slowed down 30-100-fold from that of the bulklike material. The transition to the crystalline phase occurred at no higher a temperature than 220 K.

Kralj et al[197] reported on deuteron NMR on 5CB and 8CB confined to CPG of various pore sizes. They concluded that in pore sizes of radius smaller than 25 nm the isotropic-nematic transition is retarded by an amount roughly inversely proportional to radius, $\Delta T_{NI} \propto R^{-1}$, which they attributed to an increase in the order parameter, S. Tests were done on 8CB treated with silane, which promotes homeotropic orientation, and it was determined that the degree of smectic ordering was much more suppressed by the confining surfaces while in the planar orientation than when in the homeotropic orientation[197]. These results are in agreement with those obtained on 8CB within 100 nm

radius Anopores using calorimetry by Iannacchione and Finotello[198]. A later joint NMR and SAXS study on parallel-aligned 8CB confined to CPG with a much larger diameter (400 nm) by Kralj's group revealed that the average smectic order parameter and layer spacing under such confinement is very similar to that found in bulk, while homeotropically-aligned 8CB in the same system showed a smectic ordering that increased with increasing temperature[199].

   Ogaki et al[200] performed NMR measurements on deuterated smectic 8CB confined between two glass slides separated by 96.0 μm and fitted with electrodes to produce an alternating electric field between the plates. The electrode field, placed at 45° to the main magnetic field, creates a well-defined director orientation in the sample, which is weakly coupled with the untreated electrode surface. They performed an experiment which started with the electrode field off so that the director aligned with the main field. The electrode field was then turned on and the sample left for a time varying from zero to two days, after which a free-induction decay was performed. By measuring the change in quadrupolar splitting of the phenyl and backbone groups, they were able to determine that the smectic exponential relaxation time constant within a main field of 7.05 T and ac electrode field of 100 V_{RMS} at 10 kHz was approximately one million times larger than that found with equivalent experiments on nematic 8CB[201], on the order of 1100 seconds at 30°C and 2000 seconds at 25°C. The phenomenon was attributed to the introduction of long range translational order introduced at the nematic-smectic phase transition[200].

1.3.6 Calorimetry

The principles behind the calorimetric study of smectic-A phase transitions

(particularly second order) in pores began in 1971[202] and 1972[23] with de Gennes' and

McMillan's analogy of their behaviour to that of superconductors. In his brief

communication, De Gennes drew a parallel between the phase behaviour of the two

materials while near phase transitions (both can be described in terms of one-dimensional

mass-density waves with complex phase, so that $\psi = |\psi| e^{i\phi}$; for smectics, the wave vector

is in the direction of the director, and the period represents the layer spacing), and by

performing a Landau-Ginzburg expansion of the free energy of the liquid crystal about

the nematic-smectic transition point he was able to derive relations between specific heat,

C_P, and temperature, T, summarized by Johnson[203]:

$$C_P = \begin{cases} \dfrac{A'}{\alpha'} \left[|t'|^{-\alpha'} - 1 \right] + B' + C_0(T) & T < T_c' \\ \dfrac{A}{\alpha} \left[|t|^{-\alpha} - 1 \right] + B + C_0(T) & T > T_C \end{cases} \qquad (30)$$

where the transition temperature range is bounded by T_c' and T_C, the fitting parameters

below T_c' are A', B' and α' and above T_C are A, B and α (with critical exponents α and

α' approximately zero), $C_0(T)$ is a background parameter that is well-behaved (fitted by

$C_0(T) = a_0 + a_1 T + a_2 T_2$, where a_0, a_1 and a_2 are fitting parameters) and spans the

transition zone, and t is a reduced temperature parameter defined by $t = (T - T_c)/T_c$.

Johnson et al performed early liquid crystal calorimetry experiments on

octyloxycyanobiphenyl (8OCB). The technique they used had been used many times

previously on other materials, and was developed by Sullivan and Seidel[204]. It works on

the principle that the sample, kept in thermal contact with a heater, thermometer and bath, if given small enough oscillatory doses of heat by the former (typically a few mK at most), will have a constant specific heat capacity which allows a steady state solution to be written. The solution contains two terms, one that depends on the bath's thermal conductance, and the other an oscillatory term inversely proportional to the specific heat capacity of the sample[204]. With this technique, Johnson et al were able to confirm that the nematic-smectic transition generally follows de Gennes' superfluid description, and is weakly first-order in nature; inconsistencies with de Gennes' predictions were attributed to the transition being of 1st order and to impurities in the sample.

Bellini and Clark et al[205] reported on both the light scattering and calorimetric properties of 8CB confined to silica aerogel over the temperature range 68º C to 7º C. By comparing the plots of specific heat capacity for confined 8CB to those of bulk and finding them qualitatively similar but with the confined isotropic-nematic and nematic-smectic-A transition peaks suppressed to 59% of the bulk peak amplitude, they were able to conclude that 41% of the material had been 'pinned' in some way to the surface and hence could not undergo the transitions. The transition peaks were found to be continuous rather than divergent, as one sees in the bulk state, and a slight 'smearing' of the nematic-smectic peak (compared to the bulk peak) was attributed to local smectic ordering occurring within the pores. It was also reported that crystallization of the sample, which would normally occur at about 21ºC in bulk, was suppressed to below 0ºC while confined to the silica aerogel. From Puglielli and Ford[206] the turbidity obtained from light scattering could be converted to a correlation length, and this was found to

vary continuously from 3 nm at the isotropic-nematic transition to 18 nm at the nematic smectic transition. This latter value did not greatly exceed the pore size, 17.5 nm, indicating the sample is multi-domain with domains limited to the dimensions of the pores[205]. The Bellini model was used by Olenik et al to explain the glassy reorientation observed in a nematic 5CB aerogel system within an alternating electric field[207].

Finotello and Iannacchione[208] performed a series of experiments looking at phase transitions within the *n*CB group under various degrees of confinement with axial and homeotropic anchoring, primarily using AC calorimetry. Their first publication looked at confinement in 200 nm aluminum oxide Anopores, and the general trends reported include, for the isotropic-nematic transition in 5CB, 7CB and 8CB: a non-divergent specific heat capacity at the transition point (an effect predicted earlier by Sheng[27]); a rounder, shorter peak for radially-oriented than for axially-oriented material; peaks from axial orientations exhibit a sharp post-transitional drop, indicating the material remains bulklike, while those from radial orientations are shorter and symmetric, indicating continuous nematic ordering; the peaks also exhibit a pre-transitional increase, larger for radial orientation than for axial orientation, indicating pre-transitional nematic ordering is occurring (likely near the surface) and that it extends deeper into the pore in the radial orientation; the transition temperature is suppressed for materials under confinement, more so for radial orientation than axial orientation, attributed to surface-oriented molecules forcing more central nematic molecules to arrange themselves to minimize elastic energy (an effect proposed a decade earlier by Kuzma and Labes for nematic p-cyano-p'-n-nonylbiphenyl (K27) and p-cyano-p'-n-pentylbiphenyl (K15) within

cylindrical pores studied using optical microscopy)[209]; and the larger the molecule, the broader the transition.
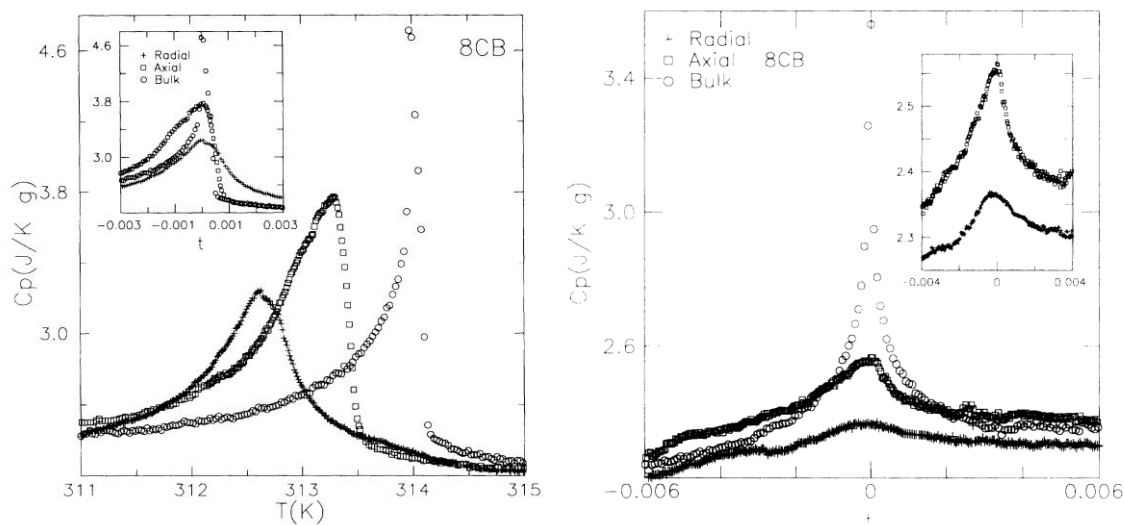
Figure 1.15: Specific heat capacity as a function of (a) temperature and (b) reduced temperature, $t = (T - T_c)/T_c$, for radially-, axially-oriented and bulk 8CB in 200 nm Anopores, about the (a) isotropic-nematic transition and (b) nematic-smectic-A transition. The inset shows the same data (bulk data removed in (b)) as a function of the reduced temperature. Reproduced from Iannacchione[208].

The peak suppression is attributed to the 'pinning' of molecules due to inhomogeneous surfaces which, as a result, fail to undergo transition with the rest of the material. The nematic-Smectic A transition results are shown for 8CB, and demonstrate behaviour similar to the previous transition. The peak suppression was found to be considerable, from which they concluded the transition to smectic ordering may only have been occurring near the surface, while molecules closer to the center remained nematic. They attributed this to the high energy cost of transitioning to the smectic state as the molecules attempt, unsuccessfully, to form a single layer spanning the pore diameter[210]. The transition from isotropic to smectic-A in 10CB and 12CB was also studied; results showed only weak surface effects (as evidenced by the slight peak broadening), with no

71

peak or transition temperature suppression[208]. Similar behaviour was found for 8CB

confined to CPG with diameters ranging from 20 nm to 400 nm using calorimetry[211].

A later study using AC and differential scanning calorimetry (ACC and DSC,

respectively) as well as small angle neutron scattering (SANS) involved 8CB confined to

Vycor glass containing 70 Å cylindrical pores[212]. The AC calorimetry work showed that,

despite crossing both the bulk isotropic-nematic and nematic-smectic-A transition points,

no signs of a phase transition were apparent (a result similar to that obtained with 5CB

and 7CB previously[213]), indicating a continuous increase of ordering is occurring with

decreasing temperature. The DSC results show a broad hump below the bulk isotropic-

nematic transition, likely further evidence of this continuous evolution. SANS

measurements were made slightly above and below the bulk smectic-A-crystalline

transition and showed no evidence of smectic ordering being present[212]. Finally, an ACC

and SANS study of 9CB liquid crystals confined to cellulose acetate Millipore filters of

300 nm cylindrical diameter was published. The calorimetry data showed a prominent

peak at the nematic-smectic-A transition, differing from the aforementioned results of

8CB in 200 nm Anopores[208]. The difference was ascribed to the different substrates:

while the aluminum oxide Anopore membranes provided a solid substrate which

introduced considerable elastic constraints, thereby constraining the smectic order, the

fibrous Millipore substrate allowed the smectic layer to form relatively unhindered. The

SANS results confirmed the presence of smectic ordering in the system[214]. A later study

of 8CB and 9CB confined to Millipore filters of various diameters tracked this nematic-

smectic-A transition temperature as function of pore size, from bulk (306.95 K and

72

321.21 K, respectively) down to 25 nm diameter (306.18 K and 320.81 K, respectively)[215, 216].

A combined calorimetry and small-angle x-ray scattering (SAXS) study of 8CB confined to CPG was performed by Kralj et al[199]. From the calorimetry results they concluded that the nematic-smectic transition is strongly suppressed for 8CB within pore diameters smaller than 24 nm; the isotropic-nematic transition is similarly affected below diameters of 11.5 nm, but the effect disappears below diameters of 7.5 nm. From the SAXS results they concluded that the order parameter obeys similar confinement-related temperature behaviour below diameters of 24 nm; the order parameter-transition behaviour relation obtained here is similar to those results obtained by Kralj et al using NMR (discussed in the NMR section)[197, 199].

1.3.7 Polarization and Atomic Force Microscopy

Kočevar, Blinc and Muševič[217] used Atomic Force Microscopy (AFM) to study presmectic layering of isotropic 8CB on a glass substrate coated with homeotropy-inducing N,N-dimethyl-N-octadecyl-3-aminopropyltrimethoxysilyl chloride (DMOAP). By using the AFM in force sensor mode with a DMOAP-coated glass tip and measuring *F/R* (where R is the tip radius) as a function of tip-surface separation (similar to what has been described before for SFA force-measurement tests), they were able to determine that the 8CB layer closest to the confining surface exhibited a stiffness two orders of magnitude larger than the layer above it, with a compressibility modulus, *B*, of 10^7 N/m^2, typical of smectic 8CB. From the second layer upward, regular oscillatory forces with a

period of the molecular long axis indicated that the system was ordered well away from the substrate, despite the bulk portion of the sample being in the isotropic phase. The results were later corroborated by the group using ellipsometry[218]. Carbone et al[143, 143, 219] later performed this same experiment with an improved AFM system, measuring the presmectic force by cantilever deflection and applying the Derjaguin approximation. In addition to the presmectic force, the smectic correlation length and smectic order parameter were also measured as a function of temperature[220]. A similar test was also performed on isotropic 5CB by Kočevar and Muševič[221, 222], and the temperature dependence of the amplitude and range of an observed prenematic force were reported.

Bračič et al[223] studied capillary condensation (the phenomenon wherein a phase change occurs solely as a result of confinement) in 5CB and 8CB using AFM on a DMOAP-coated glass substrate coated. The capillary condensation was induced by periodically increasing the confinement, and the transition was detected using the AFM in force sensor mode via deflection of the cantilever. By keeping the temperature a constant temperature above the isotropic-nematic transition they were able to reduce the gap size until they found a sudden jump in attractive force, which they interpret as being due to a structural change within the system, detectable even at separations above one micron. From these force curves the surface charge density, surface potential and Debye screening length were all determined by fitting to a superposition of the approximate Poisson-Boltzmann solutions for constant surface charge density and surface potential, respectively[223].

Pfohl et al[224] reported on two techniques they had developed, microcontact printing
and polyelectrolyte adsorption, to confine and align biological materials and liquid
crystals on microstructured surfaces. To demonstrate the effectiveness of the method,
they deposited nematic and smectic 8CB in channels 3 μm and 20 μm wide and 2 μm
deep on a silicon substrate coated with poly(ethylene imine) (PEI) to promote
homeotropic alignment with the surface and studied the structures present within the
channels using polarization microscopy.
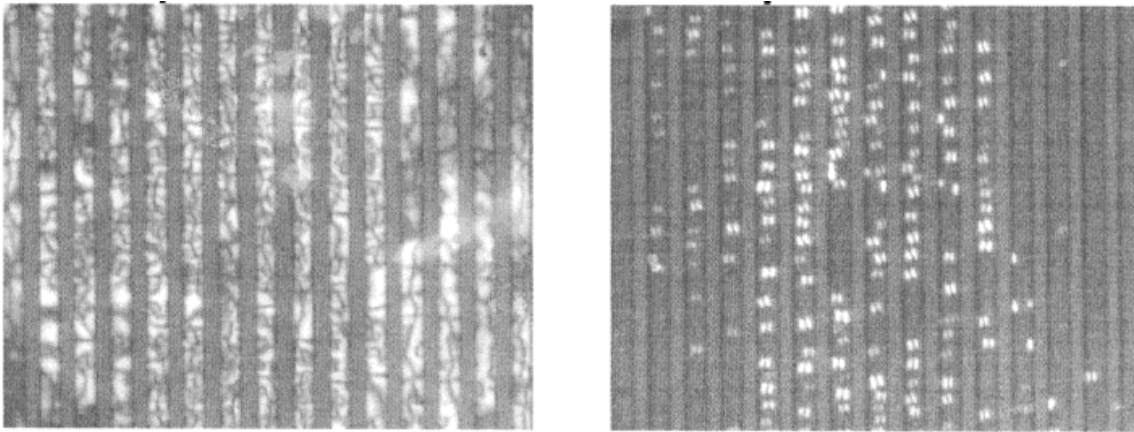
Figure 1.16: Polarization microscopy images of 8CB confined within 3 μm by 2 μm
channels on a silicon substrate coated with PEI. The nematic structure is pictured on the
left, and the smectic on the right. Reproduced from Pfhol[224].

While the smectic 8CB deposited on the unmodified silicon substrate formed the well-
known structures known as focal conics (see Figure 1.17 below for an example), and
within the 20 μm channels formed fairly uniform-sized toroidal and spherulite-like
(onionlike) defects (the latter being relatively rare in smectic-A materials), within the 3
μm channels the layers were found to align parallel to the bottom of the channels with the
long molecular axis perpendicular to the channel bottom. Spherulite-like and toroidal

defects occasionally interrupted this alignment, and were found to be very uniform in size[224].

Choi et al[225] confined smectic-A 8CB to silicon wafer microchannels etched by photolithography and studied the resultant defect domains using polarized microscopy and atomic force microscopy. Three channel widths (5, 10 and 20 μm) and two depths (5 and 10 μm) were used, and the walls were coated with polyethyleneimine (PEI) to orient the 8CB homeotropically. Three images taken using polarized light microscopy, clearly revealing focal conics, are shown in Figure 1.17.
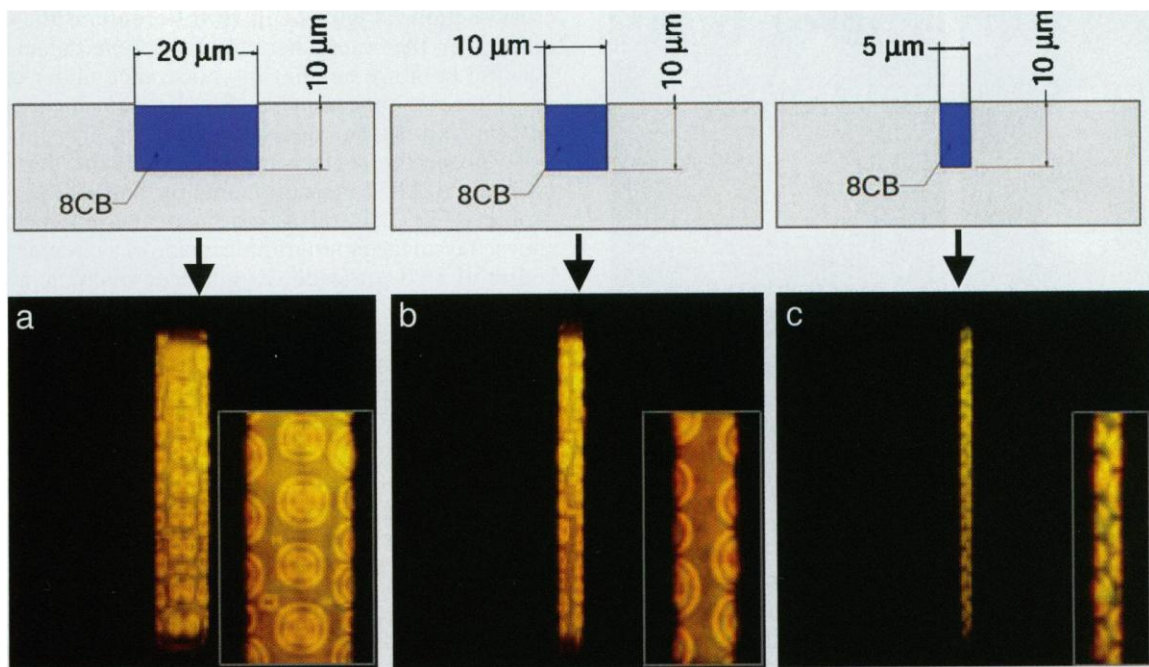
Figure 1.17: Polarized light microscopy images of 8CB confined to silicon wafer microchannels, illustrating the focal conic structures that form along the confining surfaces. Reproduced from Choi et al[225].

The defect domains were studied using tapping mode AFM, and were shown to be funnel-shaped toroids, in contrast to the lens-shaped defect structures that were observed by AFM in a droplet of 8CB atop a PEI-coated flat silica surface.
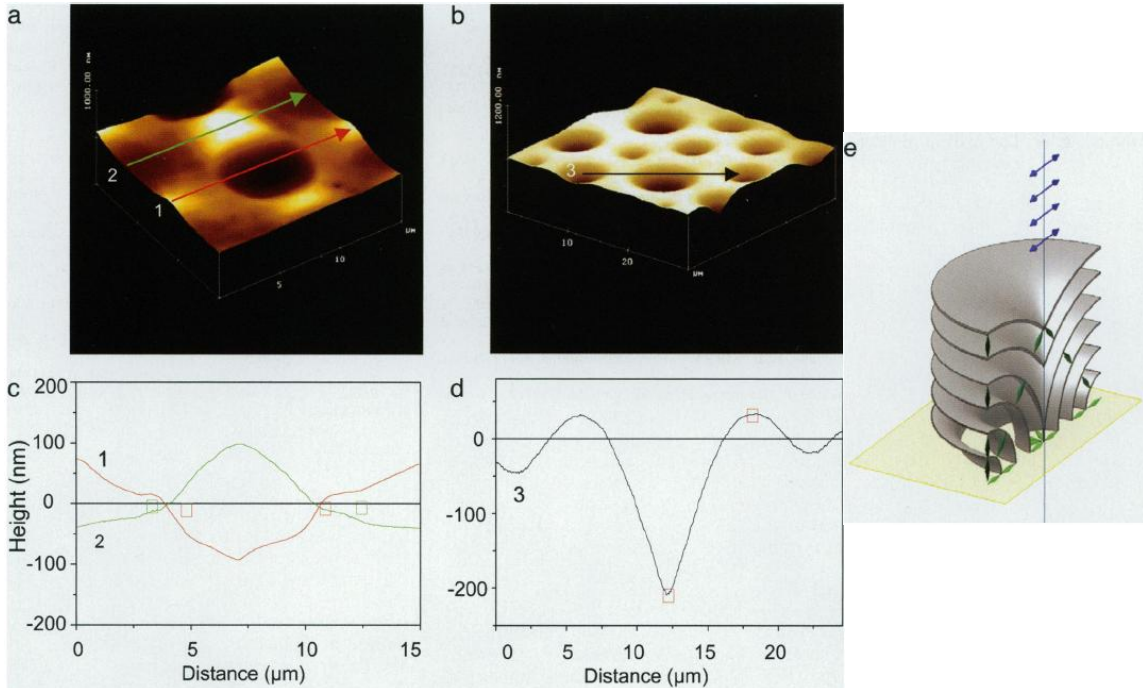
Figure 1.18: AFM images of a defect in smectic 8CB a) confined to a 20 μm wide, 10 μm deep silica microchannel; and b) on a flat silica surface. The AFM scans numbered in these images is shown in c) and d). A schematic of the toroidal structure is shown in e) with the green symbols representing the molecular orientation. Reproduced from Choi et al[225].

These toroidal structures must have stored energy and so would be stiffer than a similar volume of bulk 8CB[225]. Guo et al[226] have reported a simple and effective method of reliably generating focal conics using silicon substrates upon which a thin gold film has been evaporated, partially masked to create arbitrary regions of gold (which promotes homeotropic alignment) and bare substrate. When smectic layer covered by an air interface (which also promotes homeotropic alignment) is applied to the substrate, focal conics occur where the air and underlying interfaces promote different alignments (i.e. the bare substrate).

1.3.8 Broadband Dielectric Spectroscopy

Aliev, Nazario and Sinha[227] studied isotropic, nematic and smectic 8CB confined to 200 nm diameter cylindrical Anopores using broadband dielectric spectroscopy. Tests were first performed on nematic 8CB in a random porous structure, and a peak not found in bulk dielectric spectra was detected, corresponding to a slower relaxation process than that found in bulk material. It was attributed to rotation of 8CB near to the surface, slowed down due to an increased viscosity in the region. A second peak not found in bulk was attributed to polarization relaxation within the interfacial 8CB layer. Tests were also performed on lecithin-treated pores, as the coating promotes homeotropic alignment of the molecules. By placing the Anopore filter with pore axis either parallel or perpendicular to the electric field, one can thus obtain molecular alignment either perpendicular or parallel to the field, respectively. Spectra of the two orientations showed peaks higher in frequency than those found in bulk, with the radial orientation exhibiting peaks of such high frequency that they could only be attributed to the librational (tumbling) mode. This librational mode was also monitored as the sample was cooled from the isotropic phase down to below the bulk smectic-A phase lower temperature limit. The observed decrease in relaxation time throughout the nematic phase was interpreted as being due to an increase in order that facilitates the relaxation process, while the observed increase in the supercooled state was attributed to the increasing viscosity of the system, which would inhibit relaxation. Maier and Meier[15] provide a relationship between order parameter and dielectric strength,

$S \approx 1 - \Delta \varepsilon k_B T / \mu^2$ (where μ is the dipole moment parallel to the long molecular axis), so that by monitoring $\Delta \varepsilon T$ one can gauge changes in order parameter due to temperature.

Aliev et al[227] showed that the order parameter decreased gently throughout the smectic phase and most of the nematic phase, but dropped rapidly as the nematic-isotropic transition point was approached.

Aliev and Basu[228] performed dynamic light scattering experiments on the same system and found the autocorrelation functions for confined nematic 8CB followed a double stretched exponential decay curve, as opposed to bulk 8CB which followed a single exponential decay curve, and concluded that the longer relaxation of approximately one second was due to fluctuations of the director due to interactions between the liquid crystal and the pore surface. The stretch of the decay curve would then have been due to a distribution of liquid crystal to wall distances producing a distribution of relaxation rates, and the greater amplitude of the slower relaxation component for radial orientation ($A = 0.4$) than axial orientation ($A = 0.18$) indicates that the 8CB-wall interaction is stronger for the former orientation than the latter orientation. Similar tests on 5CB within an aerosol network produced similar results. Lowering the temperature from 306.7 K to 305.5 K only slightly changed the relatively flat, smectic-like results for the axially-oriented sample, but for the radially-oriented sample the relaxation dropped considerably with this temperature shift. As this early relaxation is characteristic of nematics, Basu and Aliev conclude that smectization of 8CB in a radial orientation transition from the nematic to smectic phase at a lower temperature than those in an axial orientation do. By varying the 8CB concentration (and hence the ratio of surface-affected to centrally-located 8CB) and finding an increase in the ratio of amplitudes of the slow to fast

relaxation rate, they were able to conclude that the slower rate must be associated with the surface[229].

Negita, Inoue and Kondo[140, 230] confined nematic and smectic 8CB to a 1 mm gap within the concentric cylinders of a viscometer and performed dielectric spectroscopic experiments upon them to understand the relationship between shear and structural changes in both phases. By comparing the temperature dependences of the viscosities and dielectric permittivities at a shear rate of 329.5 sec^{-1} they were able to assign various regimes of shear-induced orientations around the smectic-nematic transition temperature, as shown in Figure 1.19:
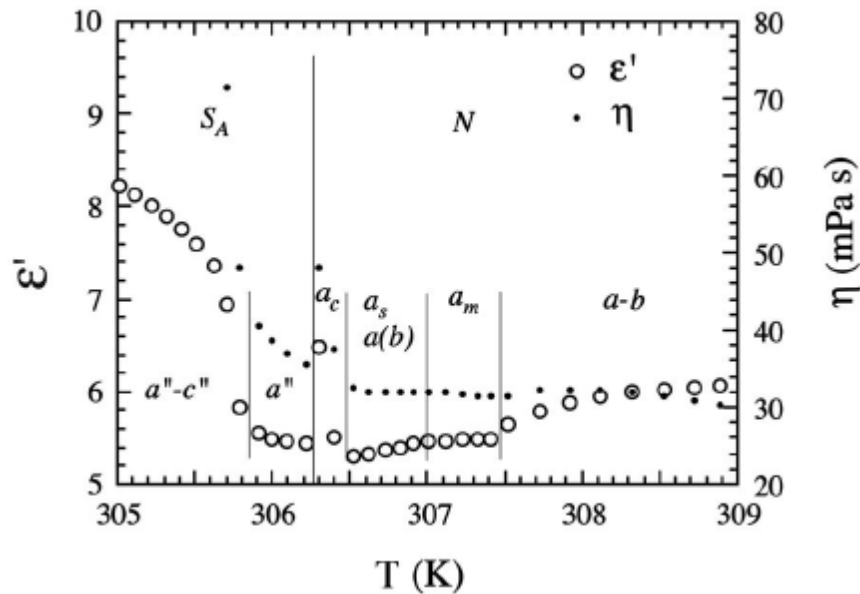
Figure 1.19: Dielectric permittivity, ε', and viscosity, η, as a function of temperature for confined 8CB (1 mm gap). State *a-b* refers to the coexistent Mięsowicz nematic 'a' and 'b' orientations and $a''-c''$ refers to the smectic Mięsowicz smectic 'a' and 'c' orientations, while *a(b)*, a_c, a_s and a_m refer to various shear-induced structures discussed by Safinya et al[52]. Reproduced from Negita, Inoue and Kondo[140].

The transition from the 'a-c' to 'a' orientation within the smectic state, reported by Panizza et al[172] and Negita et al[173] and mentioned within the review of x-ray studies above, was attributed to undulation instability[140].

Dielectric spectroscopy tests also performed by Ewiss, Moawia and Stoll[231] on isotropic, nematic and smectic-A 8CB containing 5% (by weight) nanoparticles of SiO_2 while within a 50 Hz alternating electric field. They found that a stronger field was necessary to align the material in the smectic-A phase (1.6 V/μm) than was needed for the nematic phase (0.2 V/μm).

1.3.9 Infrared and Raman Spectroscopy

Soga, Dhinojwala and Granick[232] reported on results obtained with sheared nematic 5CB under mesoscale confinement (9.5 μm) by three types of molecularly flat smooth surfaces (silicon, germanium and zinc selenide), all of which minimally attenuate infrared light, so that IR spectroscopy can be performed. The sample, oriented normal to the surface by the application of a DC voltage, was sheared sinusoidally with an amplitude of 240 nm and frequencies in the range of 25 to 400 Hz using a home-built device, and observed using FTIR. They concluded from their observations that so long as the frequency of oscillation exceeded the relaxation rate of the molecules in the sample, the shear response amplitude would be proportional to the shear amplitude, not the shear rate. A later experiment on the same setup showed that the 5CB aligned only slightly without the DC voltage compared to when the sample was homeotropically aligned prior to shear[233].

Boinovich and Emelyanenko[234] performed infrared spectroscopy experiments on nematic 5CB confined between fluorite (CaF_2) plates, using a confinement device built by them that allowed a range of gap sizes from tens of nanometers to tens of microns. Their results, analyzed using a two-fraction model that accounted for preferential orientation both on the inclination angle and on the direction in the film plane, showed that a more complete description of order within a nematic system should include not only the order parameter, S, but also information on the degree of ordering of various molecular fragments of the mesogen as well[235, 236].

Fehr et al[237] studied the polymorphism of solid 8CB confined to silica aerogel pores (of 10, 17 and 20 nm diameter) using Raman spectroscopy, and found that even at a temperature of 100 K, quenched from the isotropic phase, evidence of a possible smectic-like phase could be observed. Two distinct smectic mesophases were observed, one which they named K_S, and the other (occurring in pore sizes of 10 nm or less) they named $K_{S'}$. They argued that this is due to the sudden increase in viscosity associated with the quench preventing the director from relaxing to an equilibrium crystalline position, thereby freezing it in a metastable phase. A later report by Fehr et al using ^{13}C on nematic 5CB confined to silica aerogels (with pore sizes of from 10 to 50 nm diameter) indicates that the order parameter decreases with increasing confinement due to topological defects and to a larger number of distortions in the nematic ordering due to strong anchoring at the walls[238]

1.3.10 Other Methods of Studying Confinement

Several experimental methods have been developed to study liquid crystals in bulk and under confinement to understand their static and dynamic properties. While a complete discussion of each here is not given for the sake of space, a brief overview of some of the more successful and fruitful results obtained has been provided here.

Hsiung, Rasing and Shen[239] performed evanescent wave ellipsometry experiments on 5CB confined to silane-coated glass surfaces with a gap size of 130 μm, slightly above the isotropic-nematic transition. A weak nematic layer was found as the transition point was approached, with the correlation length defining the thickness of the layer varying with temperature as $\xi(T) \propto (T/T_c - 1)^{-1/2}$, where T is the temperature and T_C is the transition temperature, in nearly exact agreement with Mauger et al's prediction regarding isotropic liquid crystals close to the nematic-isotropic transition[240, 241] as developed from Landau-de Gennes theory[19, 21, 22], itself developed by de Gennes from Ginzburg-Landau theory[242].

Börzsönyi et al[243] studied homeotropically-aligned nematic 4-n-pentyl-4'-cyanobiphenyl (K15) confined between two parallel plates while undergoing oscillatory rectilinear Couette flow (resulting in displacements varying sinusoidally with time) using frequencies from 0.01 to 10 Hz and gap sizes of 10 to 130 μm. The sample was monitored by passing parallel beams of light through it and measuring the transmitted light intensity with a semiconductor one-dimensional detector, while the receiver plate was monitored by a set of three accelerometers to measure acceleration in all directions.

The observed response was found to compare favourably with theoretical predictions from Kozhevnikov[244], that instabilities in the system would occur above amplitudes of $A_c \approx d \big/ \left(\omega \sqrt{\tau_d \tau_v} \right)$, where τ_d is the director relaxation time, τ_v is the viscous damping time, d is the gap size and ω is the angular frequency of oscillation. In this instability regime spatially periodic rolls perpendicular to the shear velocity were observed with a period size on the order of the gap size[243]. By performing similar experiments with oscillatory elliptical Couette flow (obtained by oscillating both top and bottom sinusoidally and perpendicularly to each other) they were able to observe a slow precession of the director[245].

Guégan et al[246] performed neutron scattering experiments on smectic-A 8CB within aligned nanochannels of porous silicon films; the channels were approximately 30 nm in diameter and 30 μm in length, and had disordered surfaces with roughness on the order of 1 nm. They were able to track the correlation length associated with short-range smectic ordering from above the bulk isotropic phase transition temperature of 306.7 K (310 K) to more than 50 K below the bulk nematic-smectic-A transition (255 K). Incoherent quasielastic neutron scattering tests on a similar system showed that there is a strong reduction in molecular mobility due to the confining surfaces, which consistently increases with decreasing temperature[247]. Neutron and x-ray diffraction as well as small-angle neutron scattering (SANS) and DSC experiments were also performed on 8CB confined to porous aluminum and silicon with 30 nm nanochannels[248]. Fehr's K_S and $K_{S'}$ mesophases[237] were both observed (the $K_{S'}$ only in silicon channels), in addition to two crystalline phases, K and K' and the smectic-A phase[249].

1.4 Layered Systems under Shear

1.4.1 Energy and Entropy of Layered Systems

Layered systems under shear have been a focus of research since at least the early 1970's[47, 48, 50, 51, 250, 251], but the topic gained considerable popularity in the 1990's with studies of a wide variety of systems using a wide variety of techniques being published[42, 52, 172, 252-270], a trend that continues to this day[271, 272]. With their layers' ability to slide easily with respect to one another while undergoing shear, smectics have found considerable use as lubricants[273-277]. While the response to shear can vary depending on the material being studied, one common trend that emerges is that for many systems, low shear rates tend to orient the layers parallel to the confining walls while at higher shear rates the layers tend to either orient perpendicular to the walls or reorient into multilamellar vesicles, reminiscent of onions in the way the layers are organized[278]. Leist et al have reported that these reorientation effects are a function of shear rate, $\dot{\gamma} = 4\,A\,\nu/D$ (where A is the shear amplitude, D is the gap size and ν is the shear frequency) rather than shear frequency[257].

Using a similar approach to that which Ericksen used to describe the flow of nematics under shear (see Section 1.2.4), de Gennes presented a derivation of the dynamical equations for smectics and other lamellar materials under shear[19]. Beginning with conservation equations for mass, momentum and energy and assuming local equilibrium, while making use of entropy treatments applicable to simple fluids[250], he was able to express the entropy in terms of dissipative fluxes:

$$T \frac{dS}{dt} = -\frac{\partial T}{T} J_\alpha^{\varepsilon^d} + \sigma_{\alpha\beta}^d \partial_\beta \upsilon_\alpha + \partial_\beta \sigma_{\alpha\beta}^u \dot{u}_\alpha^d + h_\alpha \dot{\Omega}_\alpha^d \tag{31}$$

where T is the temperature, t is the time, S is the entropy density, J_α is the energy flux, ε^d is the energy density, σ is the stress tensor (with dummy variable α and β representing elements of the tensor), υ is the velocity tensor (and hence $\partial_\beta \upsilon_\alpha$ is the velocity gradient tensor), h is a measure of the flux in rotational order, $\dot{u}_\alpha$ is the rate of change of the layer displacement and $\dot{\Omega}$ is the rate of change of rotation of the system. The first term of the right-hand side represents the dissipation due to heat transport, the second due to friction, the third due to permeation (that is, the motion of fluid crossing the layers via imperfections and interstitials in the lamellae, described by Helfrich[50] and developed in Section 1.4.2 below) and the fourth due to rotational motion[19]. By assuming negligible external fields, the above entropy equation gives way to four relationships:

$$\sigma_{\alpha\beta}^d = \eta_{\alpha\beta\gamma\delta} \, \partial_\delta \upsilon_\gamma \tag{32a}$$

$$J_\alpha^{\varepsilon^d} = K_{\alpha\beta} E_\beta + \mu_{\alpha\beta} g_\beta \tag{32b}$$

$$\dot{u}_\alpha^d = \mu_{\alpha\beta} E_\beta + \lambda_{\alpha\beta} g_\beta \tag{32c}$$

$$\dot{\Omega}_\alpha^d = v_{\alpha\beta} h_\beta \tag{32d}$$

where $\eta_{\alpha\beta\gamma\delta}$ is the viscosity tensor containing the six components (five of them independent, as demonstrated by Parodi for a nematic system[83] and discussed in Section 1.2.4), $K_{\alpha\beta}$ is the thermal conductivity tensor, $\mu_{\alpha\beta}$ is the thermodiffusion tensor, $v_{\alpha\beta}^{-1}$ is the generalized twist viscosity tensor and $\lambda_{\alpha\beta}$ is the permeation tensor, while E_α, g_α and

h_α are the force tensor equivalents of the fluxes introduced earlier, $J_\alpha^{\varepsilon^d}$, $\dot{u}_\alpha^d$ and $\dot{\Omega}_\alpha^d$,

respectively. For a smectic-A system, the stress tensor equation simplifies to:

$$
\sigma_{\alpha\beta}^d = \alpha_0 \delta_{\alpha\beta} A_{\mu\mu} + \alpha_1 \delta_{\alpha z} \delta_{\beta z} A_{zz} + \alpha_4 A_{\alpha\beta} + \dots
$$
$$
+ \alpha_{56} \left(\delta_{\alpha z} A_{z\beta} + \delta_{\beta z} A_{z\alpha} \right) + \alpha_7 \left(\delta_{\alpha z} \delta_{\beta z} A_{\mu\mu} + \delta_{\alpha\beta} A_{zz} \right)
$$

$$(33)$$

where α_i are the Leslie coefficients and A_{xy} is the symmetric velocity gradient tensor

$A_{xy} = \dfrac{1}{2}\left(\partial_x \upsilon_y + \partial_y \upsilon_x \right)$. The five independent Leslie viscosities further reduce to three

using the assumption that the fluid is incompressible, leaving one with the three

Mięsowicz viscosities discussed in Section 1.3.1[81].

1.4.2 Distortion and Undulations

One smectic property that has received continued interest in modern research is that of

distortion, first discussed in theory by de Gennes in 1969[20], and demonstrated

experimentally by Clark et al in 1973[47, 48] by observing characteristic light scattering

effects in gently distorted smectic systems (in their case, p-butoxybenzyl-p-(β-

methylbutyl) aniline, or BBMBA). Two types of distortions are allowable in smectic-A

systems: Splaying of the director (equivalent to bending of the layers), and compression

of the layers[55]. From de Gennes, the energy distortion penalty is given by[19]:

$$
E_{smectic\ distortion} = E_{sd} = \frac{1}{2} B \left(\frac{\partial u}{\partial z} \right)^2 + \frac{1}{2} K_{Splay} \left(\nabla \cdot \vec{n} \right)^2
$$

$$(34)$$

where B is a compression modulus, u is the lamellar displacement relative to the original

unperturbed position along the z-axis, and z is the position coordinate parallel to $\vec{n}$ but

assumed to be perpendicular to the layer plane. By minimizing $\int E_{sd}\, dV$ using the

calculus of variations, an Euler-Lagrange solution yields[61]:

$$\frac{\partial}{\partial z}\frac{\partial E_{sd}}{\partial(\partial u/\partial z)} - \frac{\partial^2}{\partial x^2}\frac{\partial E_{sd}}{\partial(\partial^2 u/\partial x^2)} = 0$$

Combining the above solution with Equation (34) yields:

$$B\frac{\partial^2 u}{\partial z^2} - K_{Splay}\frac{\partial^4 u}{\partial x^4} = 0 \qquad\qquad (35)$$

which has a simple analytical solution of $u = e^{-\lambda k^2 z}\cos kx$, where $2\pi/k$ is the period of

undulation, and $\lambda = \sqrt{K_{Splay}/B}$ is the length scale known today as the *permeation length*,

first developed by de Gennes[23] and later by Martin et al[250]. This value is usually on the

order of the layer thickness, and its significance lies in the fact that it defines the length

scale at which the two competing forces, compression and splay, are equal to one another

in the event that a macroscopic distortion has been introduced into the smectic system;

that is, a bending of the layers will result in compression or dilation of the layers if the

bend radius falls below λ, or in splaying of the layers if the radius stays above λ[55]. From

the same solution's exponential decay constant one can define the *penetration depth* as

well, $\ell_p = 1/\lambda k^2$, which describes the length scale over which an undulation extends

from a surface before dying away[61]. The characteristic distortions observed in nematics

(represented by K_{Bend} and K_{Twist}), conspicuously absent here, aren't permitted in smectics

if one assumes the layers remain parallel[55]. A distortion of the layers in the form of a

thickness change of the smectic stack greater than $2\pi\lambda$ leads to *undulational instability*[55],

studied by Helfrich and discussed below[51]. This effect is independent of the stack

thickness, as shown by Delaye et al[251] and Clark and Meyer[48] in 1973, when the former

demonstrated experimentally that observable distortions could be created in p-cyano-benzilidene-p-octyl-oxy-aniline (CBOOA) in stacks above 50 μm thick with thickness changes of only 22 ± 0.3 Å, and so will potentially have significant influence on smectic dynamics.

1.4.3 Short and Long Range Order in Layered Liquid Crystals

One interesting property of multilayer membrane systems such as smectics is their inherent sensitivity to external conditions, leading to the aforementioned undulational instabilities. In addition to their dependence on dilatation, long-range van der Waals interactions and short-range repulsive hydration and screened electrostatic forces between the layers can lead to perturbations in long-range homogeneity in the layers and can cause instabilities as well[279, 280]. Upon joining RCA Laboratories in 1967 after a postdoctoral fellowship at the National Research Council (NRC) in Ottawa from 1964 to 1966[56], Wolfgang Helfrich tackled the problem of liquid crystals and membranes, and, spurred on by ideas from de Gennes[20], proposed in 1973 that lamellar materials with diamagnetic anisotropy exposed to an electromagnetic field will lead to undulations now known as *Helfrich undulations* or *Helfrich deformations*[51]. This notion of an oscillatory mechanism for turbulence within confined liquid crystals arose from communications with his colleague at RCA, George H. Heilmeier in 1969[49] who, with Helfrich, had observed the effect using light scattering with confined nematics perturbed by an ac signal[281, 282]. If one considers these fluctuations as one-dimensional waves either along the director (aligned with the z-axis) as would occur with smectic-A materials, or at some angle ϕ to it as one would see with smectic-C materials, the overall perturbation can be broken down into a longitudinal mode and transverse mode:
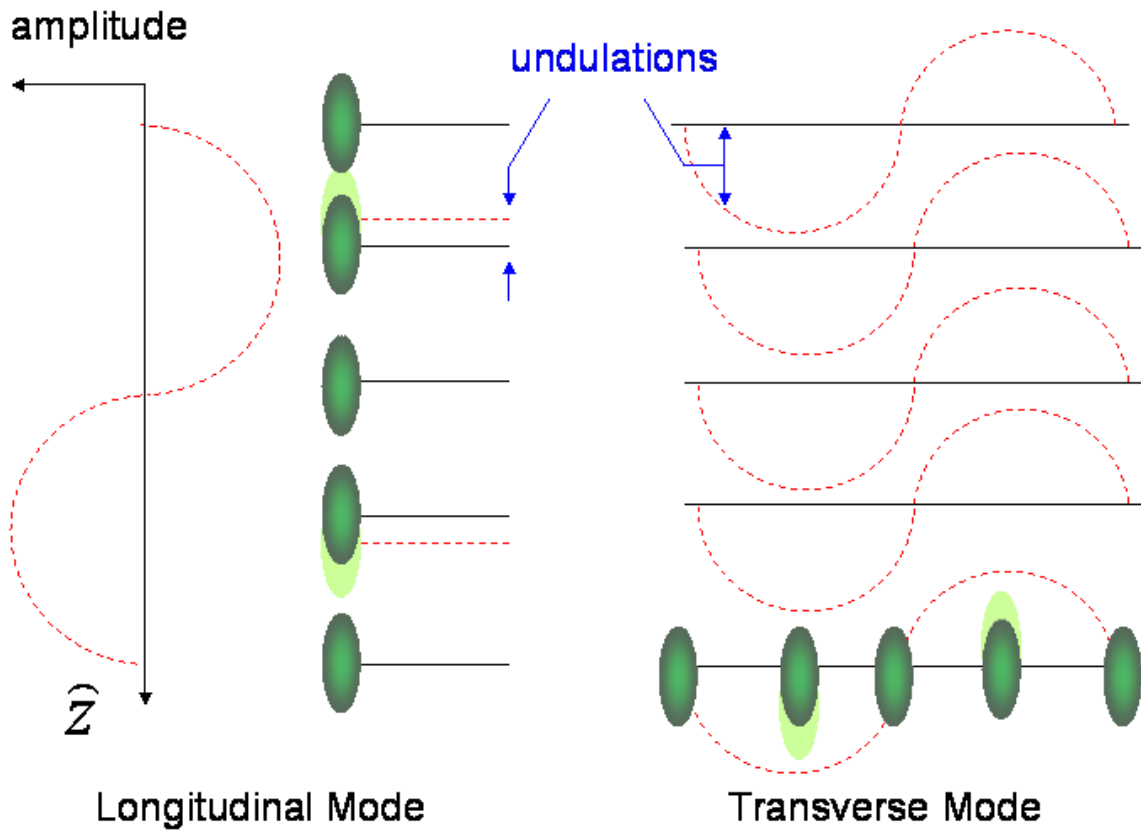
Figure 1.20: Longitudinal and transverse modes in layered liquid crystals

It should be noted that for a particular layer, the longitudinal mode experiences a net undulation, $u(\vec{q})$, where $\vec{q}$ is the displacement from equilibrium along the z-direction, while the overall amplitude in the transverse mode case averages to zero to second order. The overall energy contribution for the longitudinal mode is that of a simple spring oscillating about equilibrium:

$$E_{long} = \frac{1}{2} B q_{\parallel}^{2} u^{2}(\vec{q})$$

where B is the compressibility of the layer and $q_{\parallel}$ is the displacement in the longitudinal direction. To find the energy contribution from the transverse mode one must probe the free energy of the system (since, to first order, the layer fluctuation amplitude is zero), which yields the second-order term:

$$E_{trans} = \frac{1}{2} K q_{\perp}^{4} u^{2}(\vec{q})$$

where K is the nematic splay elastic constant. It is interesting to note that K is identical for nematics and smectics near the SmA·N transition[19]. An external magnetic field,

$\vec{H} = H\hat{z}$, will interact with the aforementioned lamellar volume diamagnetic susceptibility anisotropy (represented by χ_a) that arises from the nematic ordering so that the interaction energy is:

$$E_{mag} = \frac{1}{2} \chi_a H^{2} q_{\perp}^{2} u^{2}(\vec{q})$$

Note that both of the coefficients B and $\chi_a H^2$ have dimensions of energy per unit length, so that one can imagine the smectic phase as having a characteristic length associated with it. The total free energy will then be:

$$F = E_{long} + E_{trans} + E_{mag}$$

$$= \frac{1}{2} \left[B q_{\parallel}^{2} + \chi_a H^{2} q_{\perp}^{2} + K q_{\perp}^{4} \right] u^{2}(\vec{q}) \tag{36}$$

and the characteristic lengths associated with smectic-A materials are:

i)   The *Sample Dimension*, L

ii)   The *Density Wavelength*, d (represented in Fourier space by $q_0 = 2\pi/d$)

iii)   The *Penetration Depth* $\lambda = \sqrt{K/B}$ (as mentioned in Section 1.4.2)

iv)   The *Magnetic Coherence Length* $\xi_m = \sqrt{K/\chi_a H^2}$

It has been demonstrated that λ determines the decay of an undulation distortion, while ξ_a determines the long-wavelength cutoff of diverging fluctuations in u[19].

Equation (36) represents the Hamiltonian of a smectic system, and with it one can estimate long-range positional order. Assuming a negligible compressibility ($B \approx 0$):

$$F = \frac{1}{2}\left[\chi_a H^2 q_\perp^2 + Kq_\perp^4\right]u^2(\vec{q}) \tag{37}$$

The Equipartition Theorem reveals that the mean value of each quadratic term in the above equation must be $\frac{1}{2}k_B T$. That is:

$$\langle F \rangle = \frac{1}{2}k_B T = \frac{1}{2}\left\langle \chi_a H^2 q_\perp^2 + Kq_\perp^4 \right\rangle\left\langle u^2(\vec{q}) \right\rangle \tag{38}$$

One can now solve for the average of the squared undulation size to estimate the positional order of the smectic:

$$\left\langle u^2(\vec{q}) \right\rangle = k_B T \frac{1}{V}\int_V \left[\chi_a H^2 q_\perp^2 + Kq_\perp^4\right]^{-1} dq_\perp dq_\parallel$$

$$\propto T \int_{-q_0}^{q} dq_\parallel \int_{q_{min}}^{q_{max}} \left[\chi_a H^2 q_\perp^2 + Kq_\perp^4\right]^{-1} dq_\perp$$

And, recalling that $\xi_m = \sqrt{K/\chi_a H^2}$

$$\left\langle u^2(\vec{q}) \right\rangle \propto T \int_{q_{min}}^{q_{max}} \left[q_\perp^2 + \xi_m^{-2}\right]^{-1/2} dq_\perp$$

Integration at this point leads to two possible answers, depending on the magnitude of χ_a:

92

$$\left\langle u^2\left(\vec{q}\right)\right\rangle \tilde{\propto} \begin{cases} T \ln\left(q_{max}\, L/2\pi\right) & \text{for } \xi_m = 0 \\ T \ln\left(2\xi_m q_{max}\right) & \text{for } 0 < \xi_m < L \end{cases} \qquad (39)$$

where q_{max} is the cut-off wavevector, above which the initial assumption of the layers behaving elastically no longer realistically holds. From the above one can see that the mean squared displacement diverges logarithmically with length scales L and ξ_m. That is, they fall away slowly over large translations, and consequently, it may be concluded that there is no true long-range positional ordering within smectic systems in the absence of an external magnetic field. This conclusion is known as the *Landau-Peierls instability*[19, 283, 284]. It should be noted that similar calculations for crystalline and columnar systems yield results of:

$$\left\langle u^2\left(\vec{q}\right)\right\rangle \tilde{\propto} Tq_{max} \qquad (40)$$

for crystals and:

$$\left\langle u^2\left(\vec{q}\right)\right\rangle \tilde{\propto} T\sqrt{\frac{q_{max}}{\lambda}} \qquad (41)$$

for columnar liquid crystals. That is, within both systems the mean squared displacement stays finite for larger length scales and so is controlled by short-range forces[19], exempt from the Landau-Peierls instability. Sirota et al have measured the undulation amplitude directly in multimembrane systems via x-ray scattering for freestanding films of dymyristoylphosphotidylcholine (DMPC) and the ternary system of sodium dodecyl sulfate (SDS), pentanol and water[285].

1.4.4 Experiments with Smectics under Shear

Since the establishment of de Gennes' theories[20] and Clark, Martin, Delaye and Helfrich et al's early work on smectics under shear, several studies have built on their ideas[47, 48, 51, 250, 251]. Some of the more relevant experiments and extensions of the theory follow.

In 1978 Horn and Kléman[42] presented rheometry results showing large amplitude oscillatory shear tends to remove defects and align bulk smectic layers. Using two different geometries (simple planar as well as cone and plate) and homeotropically oriented (by lecithin) smectic-A 8CB as a sample, they found that while with perfectly smooth surfaces no structural changes were observed up to shear rates up to 60 sec^{-1}, even small surface defects produced 'textures' in the material that were visible at shear rates as low as 0.1 sec^{-1}. These textures resembled undulational modes resulting from dilatation. The nucleation of this texture (which was found to be rectangular in shape), however, differed from that arising from dilatations, in that it occurred locally rather than globally, as observed in optical micrographs taken of the sample[42]. These local seeds were found not to grow beyond a certain point, but rather to migrate, overlap and mesh together as shearing progressed; this inability to grow meant that the structures as a whole could be erased simply by shearing in the opposite direction. Finite yield stresses observed from the rheometry results demonstrated that in samples at rest shear must overcome immobilization forces (likely resulting from defects and impurities in the sample). In Horn and Kléman's experiments, this immobilization force was attributed to focal conics on the order of a micron in diameter which they observed in the 8CB[42].

In 1980 Cagnon and Durand[286] presented results on the shear response of homeotropically-aligned smectic-A and smectic-B butyloxy-benzylidene-octylanine (4O.8) confined between glass plates for frequencies between 1 Hz and 10 kHz. The stress strain relationship was established for both, and the former phase was found to behave viscously and the latter elastically, as determined from the observed shear modulus.

In 1982 Oswald and Ben-Abraham[287, 288] reported that shear forces on smectics that lie in the flow direction increase the dilatation threshold that leads to undulations. They started from the Navier-Stokes equation for an incompressible fluid as it applies to a lamellar system with molecules oriented homeotropically to the surface (and hence with layers parallel to shear flow):

$$\rho \, \frac{d\vec{v}}{dt} = \eta \nabla^2 \vec{v} - \nabla P + \vec{G} \tag{42}$$

where ρ, η and P are the mass density, viscosity (assuming that all Mięsowicz viscosities are identical) and pressure, respectively, while $\vec{v}$ and $\vec{G}$ are the velocity field and volume force density arising from elasticity of the layers, respectively. By assuming slow variations in functions perpendicular to the wall and negligible permeation, they were able to demonstrate that while in a static confinement case undulations may occur in any direction parallel to the surface (since all directions parallel to the surface are equivalent), under shear conditions this symmetry is broken and undulations will occur in a preferred direction, specifically, in the direction transverse to the shear. In the shear case where an additional dilation allows for two-dimensional undulations, the secondary undulation must be in the direction of shear as the undulations must be perpendicular to

one another[287, 288]. This effect was demonstrated by Oswald et al in the same year[289]. It should be noted that if permeation were allowed in the above treatment, then there would exist a critical velocity of shear dependent on the permeation depth above which dislocations would be unable to follow the shear flow, potentially leading to undulational instability[288].

In 1984 Ramaswamy[290] showed that, at low frequencies, four of the five Leslie viscosities diverge for smectic systems such that for a small velocity gradient:

$$\alpha_i(\dot{\gamma}) = \alpha_i^0 + \frac{b_i}{|\dot{\gamma}|} \qquad \text{for } i = 1,2,4,5 \tag{43}$$

where b_i is a coupling constant between the velocity field and the layer displacement field, $\dot{\gamma}$ is the shear rate and α_i^0 is the ith Leslie viscosity with no flow. Since $\alpha_i = \sigma/\dot{\gamma}$ this implies:

$$\sigma = \alpha_i^0 \dot{\gamma} + \left(\dot{\gamma}/|\dot{\gamma}|\right)b_i \tag{44}$$

which indicates that, unlike a fluid-like system, smectics require a certain minimum yield stress b_i in order to flow in the layers. The effect was presaged by Kim[291] et al and Bhattacharya[292], who found in capillary flow experiments that after an initial applied pressure was removed, the residual pressure in the system was non-zero in size[290]. The phenomenon of a minimum yield stress was not new to the scientific community at this time—Bingham had reported on viscoplastic materials, which exhibit solidlike behaviour at low stresses but liquidlike behaviour above a critical stress value as early as 1916[293]—but Ramaswamy's results indicated that the source of this behaviour may be the breakdown of hydrodynamics within the system rather than a solidlike resistance to

flow[61]. Ramaswamy also showed that shear promotes stability in smectic systems by rotating wave fronts from undulations, thereby shortening their wavelength and leading to a reduced undulation lifetime[290]. While the notion of shear-induced fluctuation suppression was first proposed in this context by de Gennes[24], the phenomenon has its origins with James Clerk Maxwell's experiments on refractive properties of sheared viscous materials, begun while he was an undergraduate student at the University of Edinburgh, and for this reason has been named the *Maxwell Effect*[294].

Ramaswamy[252] later, using Helfrich's theory of elasticity while considering the effects of steric repulsion from the confining surfaces, calculated that the undulation suppression regime has an upper shear limit such that $\dot{\gamma} \approx \dfrac{k_B^3 T^3}{K_{Bend}^2 \, \eta \, d^3}$, where T is the temperature, k_B is the Boltzmann constant, η is the viscosity and d is the layer spacing, above which point the layers compress and collapse. The phenomenon was later confirmed by Al kahwaji and Kellay using dynamic light scattering on a mix of the ionic surfactant bis-ethyl hexyl sulfosuccinate (AOT) and brine, creating a lamellar compound, confined to a Couette cell geometry[295]. Marlow and Olmsted demonstrated that shear in lyotropic smectic materials results in fluctuation reduction due to a combination of interlayer friction, convection and bilayer collisions which lead to an effective anisotropic surface tension. The exact consequence of shearing was found to depend on the level of permeability of the material[296]. They later demonstrated that strong shear flow can give rise to other effects in lamellar systems via couplings between the system parameters[297].

The frequency-dependent shear modulus of 8CB confined by aerosil gel (spherical 7 nm diameter hydrophilic SiO_2 particles sonicated with acetone to create the gel) was reported by Bandyopadhyay[298], using a temperature- and stress-controlled rheometer in the cone and plate geometry.
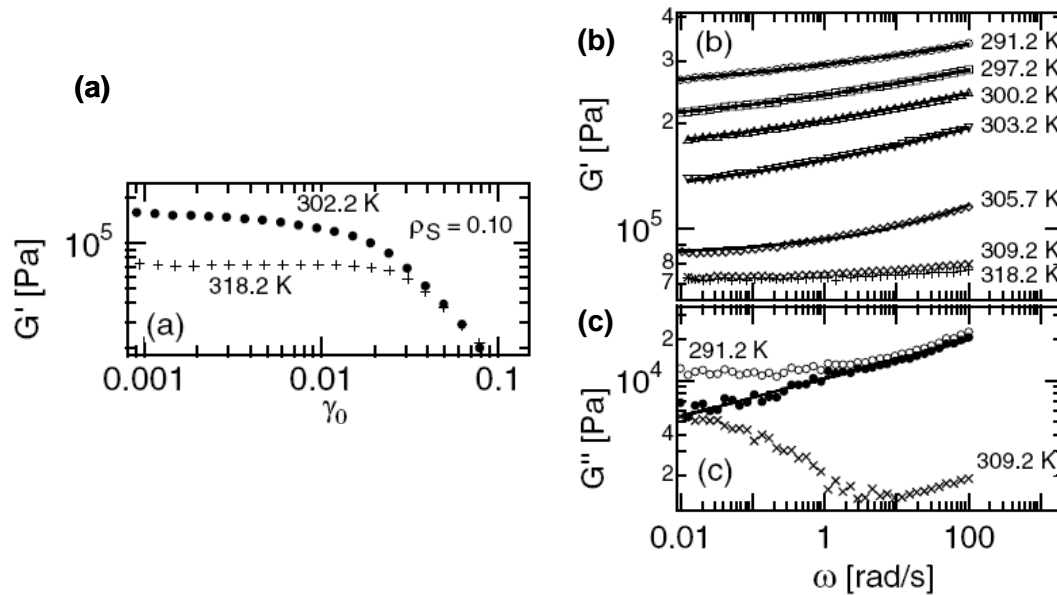
Figure 1.21: Storage and loss moduli for 8CB confined by aerosil gel. a) Storage modulus, G', as a function of shear amplitude γ_0 for a shear rate of 1 rad/sec, below (solid circles) and above (crosses) the nematic-smectic transition temperature of 306.97 K. b) Storage modulus, G', and c) loss modulus, G'', as a function of frequency for various temperatures. The solid circles in c) represent the difference between the spectra and are fitted with a power law function. Taken from Bandyopadhyay[298].

At low temperatures the storage modulus was found to be more than three orders of magnitude larger than those moduli reported in bulk 8CB. It also possessed a power law component with an exponent that diminished with increasing gel density but not temperature, characteristic of the 'soft glassy rheology' found in foams, emulsions and suspensions. While the nematic and isotropic 8CB exhibited predominantly elastic behaviour, the smectic 8CB at low temperatures was found to be elastic but dominated by

structural defects as determined by the amplitude, temperature- and gel density-variance of G'[298].

In 1993 Diat, Roux and Nallet[261] published a broad series of experiments on the influence of shear on bulklike lyotropic lamellar materials confined to concentric cylindrical shear cells (with gap sizes varying from 100 µm to a few millimeters), using light and neutron scattering, rheometry and microscopic techniques to observe their results. They were able to conclude that the prime difference between low and high shear (which are themselves defined relative to the concentration of the lyotropic) is the resultant orientation of the material: for low shears, domain orientation was found along not only the direction of flow but also the rotation axis as well, while with high shear the orientation is almost exclusively at a fixed angle from the 'c' orientation of Mięsowicz. An isotropic orientation was observed between the two extremes, with the notable presence of spherulites whose size was a function of the shear rate.

1.4.5 Smectics under Shear: Theoretical work

Building on previous work that demonstrated shear flow affected phase transition characteristics[95, 299-301], in 1992 Bruinsma and Rabin[302] stressed that Ericksen-Leslie Parodi theory (ELP) is incomplete in that the flow distortion of the structure factor leads to a torque on the director that cannot be explained solely with the Leslie viscosities. They redeveloped the theory near the nematic-smectic A transition by considering the observed phenomena geometrically, and by assuming constant relaxation times and a simple flow field unperturbed by fluctuations. With this ELP modification they showed

that fluctuations in lamellar systems under shear flow undergo a gradual shape change, from elliptical under very slow shear (that is, with shear rates much smaller than the longest characteristic relaxation rate of the shear system) to a very anisotropic one-dimensional shape at rapid shearing rates (greatly exceeding the relaxation rate of the system) by analyzing the structure factor, $s(\vec{q})$, as a function of the Deborah Number, D ($D = \dot{\gamma}\tau$, where τ is the relaxation rate). They also demonstrated that the shear-induced suppression of fluctuations, occurring at shear rates above a critical value of

$$\dot{\gamma} = \frac{T^{5/2}}{K_{Bend}^{3/2}\, \eta\, d^3}$$ (with temperature T, viscosity η and layer spacing d), leads to an

increased nematic-smectic transition temperature which will be dependent as well on the orientation of the layers. They indicated that because, at equilibrium, fluctuations change the layer spacing (as discussed by Ramaswamy[290]), they will necessarily increase K_{Bend} and K_{Twist} as well. Furthermore, because shearing tends to tilt layers in the 'b' orientation in the presence of fluctuations, it will also necessarily increase α_3. While under shear, however, K_{Bend} and K_{Twist} tend to decrease, and under the condition $\dot{\gamma}\tau q_0 \xi \sim 1$ (where

$q_0 = 2\pi/d$ with d being the layer spacing and ξ being the anisotropic correlation length), where the onset of distortion occurs, α_3 is reduced, an indication that shear thinning may be occurring and may lead to a mix of 'a' and 'b' orientations in the range of $\dot{\gamma}\tau q_0 \xi \sim 1$ to

$\dot{\gamma}\tau \sim 1$ [303].

   A later study by Bruinsma and Rabin[302] compared the Maxwell Effect (as developed in Section 1.4.4) to an opposing phenomenon, the *Reynolds Effect*, named for and first described by one of the pioneers of fluid dynamics, Osborne Reynolds[304]. The Reynolds

Effect (as it applies to lyotropic liquid crystals, or to any two component system with internal degrees of freedom) refers to the generation of instabilities due to shear and is due to the generation of viscous stresses, of order $\eta\dot{\gamma}$, in which fluctuations in flow arise due to fluctuations in concentration, which themselves arise from variable interlayer spacings, a topic first considered by Helfrich[305]. By combining Helfrich's free energy density with concepts developed by Martin, Parodi and Pershan[250] (and simplified by Nallet, Roux and Prost[306]) and integrating a concentration dependence, they demonstrated the Reynolds Effect for a two-component lyotropic system. From these findings they further demonstrated that shear-induced fluctuation suppression within thermotropic liquid crystals leads to their transforming to an orthorhombic solid state, while shear flow enhances short-wavelength concentration fluctuations within the lamellar, or L_α, lyotropic liquid crystals[302], in agreement with experimental results published by Nallet et al[306].

Auernhammer, Brand and Pleiner[278], following on the work described above[47, 48, 251, 288, 290, 302, 303, 307], reiterated that de Gennes' derivation for smectic hydrodynamics does not on its own adequately explain the reorientation of smectic layers that had been observed, and cited the reason as being de Gennes' assumption that each layer can be represented by a two-dimensional fluid. They reconsidered the sheared smectic problem from the point of view of irreversible thermodynamics under the condition that the layers remain of constant thickness and quantity, and stay parallel to the confining walls. By following Martin's[250] standard derivation and incorporating the Gibbs and Gibbs-Duhem relations involving both nematic order and smectic order to develop a dissipation

function, they were able to show that shear flow tends to reorient the director such that it tilts slightly in the direction of flow (x direction):

$$n_x = \frac{\dot{\gamma}\gamma_1}{B_1}\frac{1+\lambda}{2} \qquad (45)$$

where B_1 is a coupling constant between the director and layer normal, $\dot{\gamma}$ is the shear rate, γ_1 is the rotational viscosity and λ is the flow alignment parameter. The director component perpendicular to shear flow and parallel to the confining layer, n_y, is nil, and that perpendicular to both must be $n_z = \sqrt{1 - n_x^2} \approx 1 - \frac{1}{2}n_x^2$.
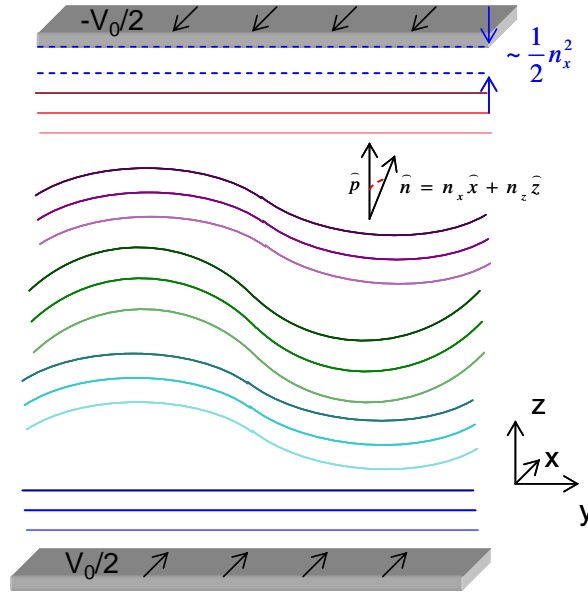
Figure 1.22: Shear in the x-direction causes a tilt to occur between the director, $\hat{n}$, and the layer normal, $\hat{p}$, leading to an effective dilatation of approximate size $n_x^2/2$ which is prevented by the confining walls. Adapted from Auernhammer[278].

The tilt to the director is equivalent to a dilatation of the layers, since n_z is less than unity, but the dilatation is prevented by the fixed confining layer boundary condition. The result is a critical tilt, $n_{x,c}$, and shear flow, $\dot{\gamma}_c$, which would induce undulations,

$$n_{x,c}^2 = \frac{4\,B}{B - 2\,B_1}\frac{\pi}{d}\sqrt{\frac{K_{Splay}}{B}} \quad \text{and} \quad \dot{\gamma}_c = \frac{4\,B_1}{(1+\lambda)\gamma_1}\sqrt{\frac{B}{B - 2\,B_1}}\frac{\pi}{d}\sqrt{\frac{K_{Splay}}{B}}$$, where B is the smectic

compression modulus and d is the gap size. The undulations are perpendicular to the

shear direction while the director is tilted in the direction of flow, prohibiting coupling

between the flow and fluctuation waves[278, 308].

Noirez[269] reported on shear experiments (using shear rates from 0.1 to 50 sec^{-1})

performed on a smectic side-chain liquid crystalline polymer system (PMA-OC$_4$H$_9$)

confined within a shear cell to mesoscopic scale gap sizes (the exact gap size is not

mentioned), studied using neutron scattering with a setup which allows observation of the

flow and layer normal directions, and observed a slight reduction in layer spacing (a

decrease of 2% of the initial layer spacing) compatible with Auernhammer et al's results.

In studies of sheared lamellar lyotropic systems by Müller et al[264] using polarizing

microscopy, viscometry, small-angle light scattering and deuteron NMR spectroscopy,

and by Zipfel et al[309] using rheology and small-angle neutron and light scattering, both

groups found that the transition from parallel alignment to vesicle exhibited an

intermediate state containing flow-oriented cylindrical structures that resemble the

undulations described by Auernhammer[308].

In a later analysis of the same system, but considering couplings between the velocity

field and orientational and positional order terms, Auernhammer et al[308, 310] found the

order parameter is most affected by undulations near to the confining surfaces. They also

found that by uncoupling the director field from the velocity field, certain anisotropic

viscosity conditions could lower the undulation instability threshold. Laurer et al[256] studied bulk lamellar diblock copolymer poly(styrene-b-isoprene) undergoing large amplitude shear (shear rate of 1 sec^{-1} and strain amplitude of 98%) using transmission electron microscopy (TEM) and small-angle x-ray scattering (SAXS) and found a uniform parallel-oriented lamellar structure extending 2 μm beyond the confining surfaces, consistent with Auernhammer et al's conclusions in that the order parameter peaked near to the surfaces. Soddeman and Auernhammer et al[311] reported on their investigations of smectics under shear using both molecular dynamics simulations and macroscopic hydrodynamic theory, and found that while they behave as predicted by Auernhammer et al's[278, 308, 310] analytical solution at low shear rates, both methods lead to shear-induced instabilities in the layers above a critical value, indicating that the director can have dynamics independent of the layer normal.

1.4.6 Static Smectics re-visited: A new analysis with some old ideas

Stewart[312] presented results on the equilibrium state of a smectic system where the layer normal does not coincide with the director. This layer normal-director orientation discrepancy, arising from Oseen's constraint that $\nabla \times a = 0$ (where a is the layer normal vector) in the absence of layer defects[11], cannot usually be handled by standard treatments, and so Stewart achieved this, taking a different approach from de Gennes' formulation[19], by considering the energy density of the smectic system. He presented results for three different configurations: A simple planar homeotropic orientation; a planar orientation away from the walls with a fixed orientation at the wall referred to as a 'fixed bookshelf' configuration; and a similar setup to the last but with the smectic layer

allowed to be incoincident with the wall, known as a 'variable bookshelf'

configuration[312]. Sketches of the three orientations are given in Figure 1.23:
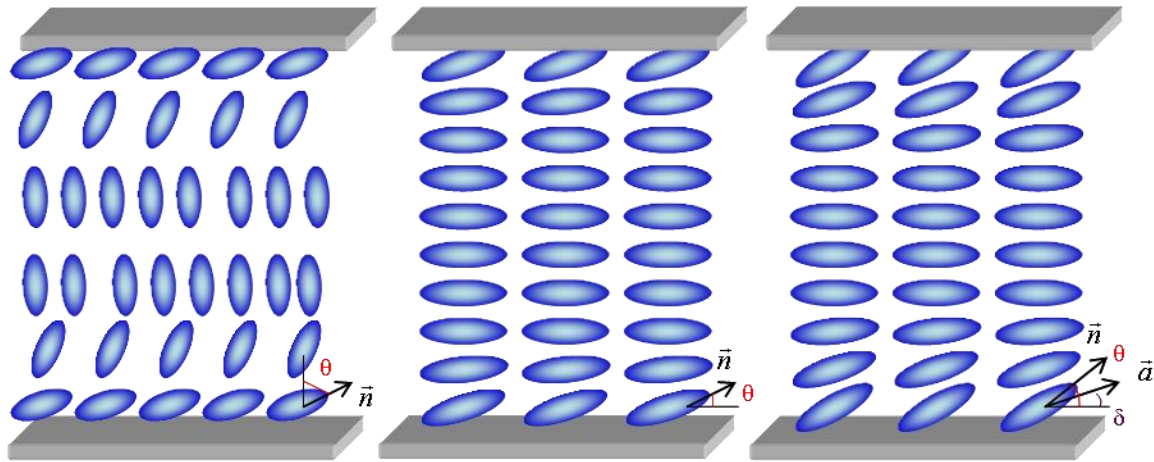
Figure 1.23: The three configurations considered by Stewart: (left) homeotropic; (middle) fixed bookshelf, and; (right) variable bookshelf, with θ the angle between the long axis and the wall and θ-δ the angle between the long axis and the layer normal. Reproduced from Stewart[312].

He found that in most cases the penetration depth as it pertains to the director (i.e. the

distance from the surface at which the director has changed direction from the surface-

induced tilt to being oriented with the layer normal) was on the order of the thickness of a

smectic layer (with dimensionless penetration depth $\xi = \sqrt{B_0/B_1}$, where B_1 is the

coupling constant between layer normal and director and B_0 is the layer compression

constant), in agreement with experimental results[313]. For the third case, however, with a

strongly anchored director tilt, he was able to show that two boundary effects, each at

different length scales, may exist: The first is the reorientation of the layer normal and

director to coincide with one another, occurring at a penetration depth of roughly five or

ten layer spacings following the $\xi = \sqrt{B_0/B_1}$ relation, and the second is a reorientation of

the layer normal and director to the bookshelf alignment, much further out from the

surface at a penetration depth of on the order of 200 layer spacings, typically

corresponding to approximately 0.4 µm.
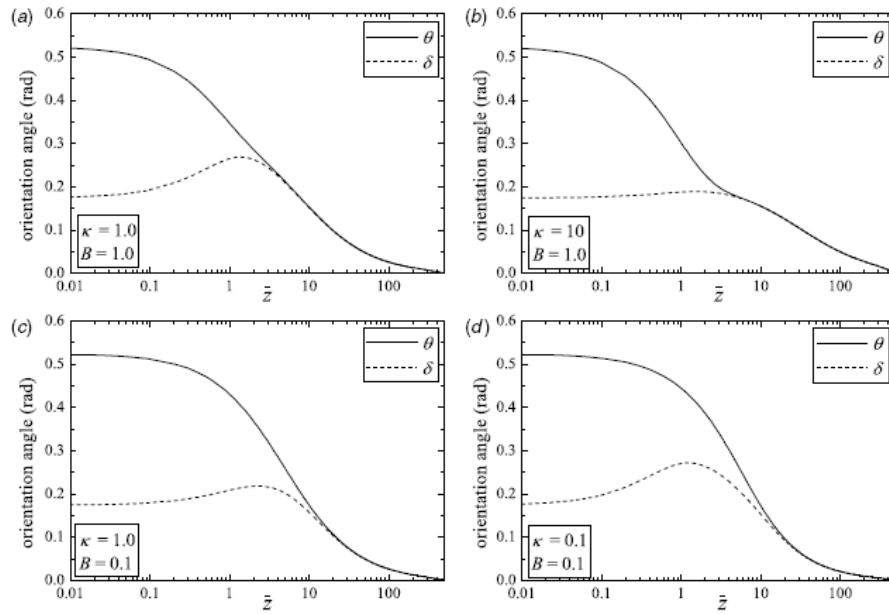
Figure 1.24: Director angle, θ, and layer normal, δ, as a function of number of layer spacings, $\bar{z}$, for various stiffnesses, k, and ratios, $B = B_1/B_0$ for a strongly anchored smectic system in which the layer normal and director are allowed not to coincide. Reproduced from Stewart[312].

This analysis has as of yet only been applied to the strong anchoring case, but may also

yield realistic results for the weak anchoring condition as well[312].

1.5 Confined 8CB Studies with the SFA and XSFA

1.5.1 Early X-Ray Work with Sheared 8CB Under Confinement

Safinya, Sirota and Plano[52, 53] performed synchrotron x-ray experiments on sheared 8CB (4-cyano-4'-octylbiphenyl) near the nematic to smectic-A transition. This system was considered an ideal candidate for a study of structural changes, since it was known that for values of $\dot{\gamma}\tau$ greater than unity, where $\dot{\gamma}$ is the shear rate and τ is the fluid's fluctuation relaxation time, the material should experience distortions in structure, and for larger molecules τ should be large enough for this to be accomplished with reasonably small shear rates. Furthermore, nematics near the smectic-A transition had been shown previously to have exhibited expanded correlation lengths, ξ[314], and that $\tau \approx \xi^{3/2}$[315]. A Couette cell geometry was chosen with gap sizes of 0.5, 1.0 and 1.5 mm; the inner cylinder had a 10 mm radius and was fixed, with the outer cylinder rotating at shear rates of 50 to 300 sec^{-1} [52, 53]. The group wished to study previously seen[316] pretransitional flow-induced fluctuational forces, and reported that steady state regimes occurring due to the combination of these forces with viscous frictional forces could be observed via x-ray scattering.

1.5.2 XSFA Investigations of Smectic 8CB Under Mesoscale Confinement

Idziak et al[54] performed several synchrotron x-ray experiments with 8CB under 'mesoscale' confinement (that is, with gap sizes in the range of roughly 0.1 to 10 μm) using an x-ray Surface Forces Apparatus (XSFA). The mesoscale range is distinguished by its spanning the gap between distinctly bulk-like behaviour and distinctly well-

confined behaviour. The XSFA allows scattering studies to be done at precise separations (± 1 Å) over several orders of magnitude (from a few Angstroms up to 10 μm), and in the first tests two crossed 2-mm diameter cylindrical capillary tubes with 10 μm thick back-silvered mica sheets glued to them were used as surfaces between which the sample was placed. The cylinders were placed 45° to the shear direction, and the gap of ~0.4 μm[317] was obtained by monitoring the Newton's Rings pattern created by passing sodium light through the cylinders. The triangular shear profile was generated by a piezoelectric bimorph lateral sliding device, and four shear rates were reported (0, 0.17, 10 and 30 sec^{-1}). Three orientation directions were seen in each case, one with the smectic director pointed towards the top surface, one towards the bottom, and one in the direction of shear corresponding to the 'b' orientation given by Mięsowicz (see Section 1.3.1). The latter had not been seen previously in large gap shear studies due to the large energy penalty associated with it[318], and was found to be made up not of a single well-defined orientation, but rather a mosaic of discrete domains centered about the expected peak. The 'b' orientation observed at zero shear, it was hypothesized, originated from the orienting inherent with the loading of the sample[317].

Koltover and Idziak et al[127, 319] used a similar device for the next study of confined 8CB (this time not under shear), but two new types of surfaces were used in addition to the aforementioned capillary tubes: Both resembled the standard cylindrical lenses used in SFA studies (20 mm diameter), but were made of aluminum and had a small (1 mm diameter) hole drilled through the center (perpendicular to the back plane), through which x-rays could pass. The hole in one was covered with a glued back-silvered thin (5-6 μm

thick) mica sheet, acting as a soft surface, while the other was first covered by a thin (4-8 µm thick) glued quartz sheet, which was covered in turn with a 3-5 µm thick glued mica sheet, acting together as a hard surface:
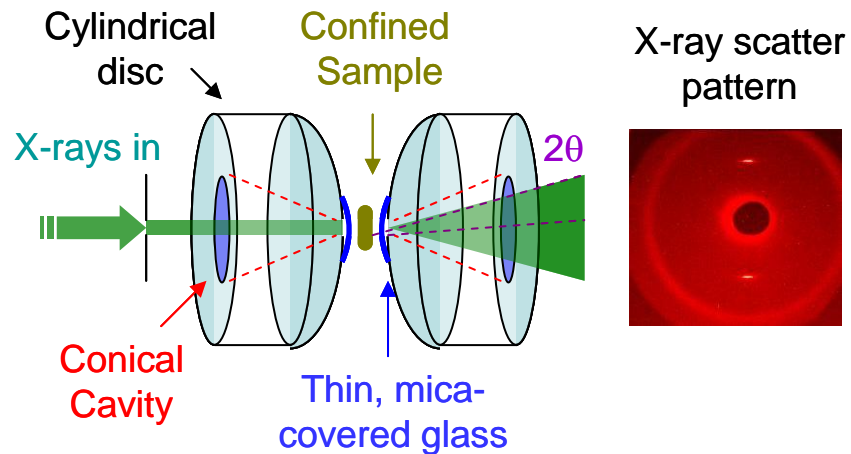
Figure 1.25: Diagram of the XSFA sample setup. Adapted from Idziak[317].

With the soft surfaces the 8CB alignment was continuous from gap sizes of 1 mm down to 3-4 µm, but broke up into multiple domains below this separation; this transition, it was reported, is reversible. With the hard surfaces, however, no transition was seen at any point. The reason for the difference, they proposed, is that while the hard surfaces can easily squeeze the 8CB out, the soft surfaces distort upon attempting to break up the 3 µm domains, in turn breaking them up into smaller and less oriented ones. Soft surfaces were also seen to have considerably smaller mosaicities (2°, as compared to 3.5° for hard surfaces), a result, they postulated, of soft surfaces being able to adjust to accommodate domain re-orientation, which in turn allows the domains to coalesce and orient themselves optimally.

Idziak et al[127] provided shear results on the same setup as above, with shear rates of 500 sec^{-1} and mesoscale gap sizes of 0.4 μm. Equally strong shear-induced ordering and alignment were found for both hard and soft surfaces, indicating flow-induced forces dominate over surface forces at the shear rate used. The study reinforced the notion that confinement-induced and flow-induced structures are distinct from one another, in that the former are static while the latter are not at equilibrium.

Koltover et al[320] presented further results of 8CB confined by atomically smooth surfaces with the XSFA. They compared force-measurements (that is, measurements of F/R as a function of gap size, where F is the normal force and R is the radius of the confining cylinders, based on experiments pioneered by Horn and Israelachvili[41, 129]) of the smectic and nematic states. In the nematic below gap sizes of 6 nm, the force was oscillatory with periodicity of 9-10 Å, the approximate diameter of an 8CB dimer[321]. The oscillations increased with decreasing gap size, indicating the molecules were positionally ordered as layers within 20-30 Å of the surface[143], and the last two layers (corresponding to 17 Å thickness) could not be removed. The smectic measurements were more difficult to obtain due to the high viscosity of the material causing a long-range force that obscured any squeeze-out forces above 35 Å, but faint kinks with similar periodicity to the nematic could be seen down to 25 Å, below which flattening of the surfaces due to their slight elasticity obscured the results.

X-ray results of smectic 8CB in bulk-like confinement (between two crossed cylinders) and confined to a 4 μm gap showed significantly different peaks; in bulk, the

peaks were broad, indicating the domains were only slightly oriented with the cylinders (possibly due to flow during loading), while the confined material showed sharp peaks, indicating the material was well-aligned with the cylinder walls. X-ray results were also shown of 8CB confined to a 1 μm gap, comparing stationary diffraction patterns to those obtained under 150 sec^{-1} shear rates. The stationary mosaicity was found to be ~30°, while four minutes of shear produced a mosaicity of less than 2°, a state which lasted for hours after the shear was complete.

Idziak[317] built on the previous studies by developing the X-ray Confinement Cell (XCC)[322], which uses capacitor feedback translation stages and high-precision optical encoders to gauge gap sizes between two crossed cylinders identical to those used with the XSFA. X-ray experiments were performed at two gap sizes, 0.5 μm and 5 μm, at various shear rates. The shear amplitude used for the former gap was 0.125 μm, and for the latter was 7.5 μm. For the larger confinement, at the higher shear rate (50 sec^{-1}) reorientation towards the 'a' orientation was rapid and a high degree of alignment was obtained, as indicated by the peak position, amplitude and mosaicity; within 5-7 minutes, all three had reached asymptotic values. For the lower shear rate (0.06 sec^{-1}) reorientation was much slower, and an asymptote is not reached by any of the measured parameters after 1200 seconds.
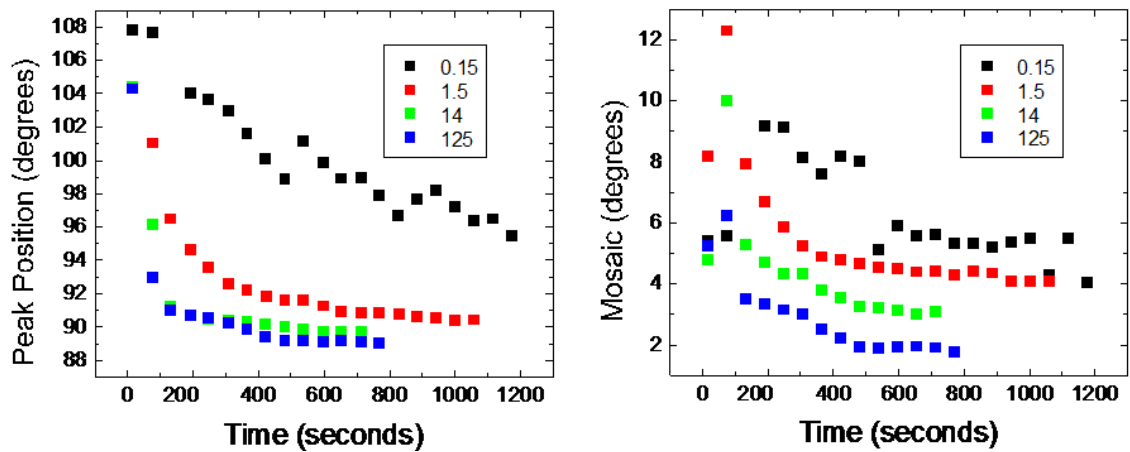
Figure 1.26: Peak Position and Mosaic for confined 8CB as a function of time for 5 μm gap size at various shear rates (shown in legend). Reproduced from Idziak[317]

Within the smaller gap size, reorientation was relatively slow at the higher shear rate (24.8 sec^{-1}), with an asymptote reached in peak position after roughly 1000 seconds, while for the lower shear rate (0.01 sec^{-1}) the asymptote did not appear to have occurred even after 6000 seconds.
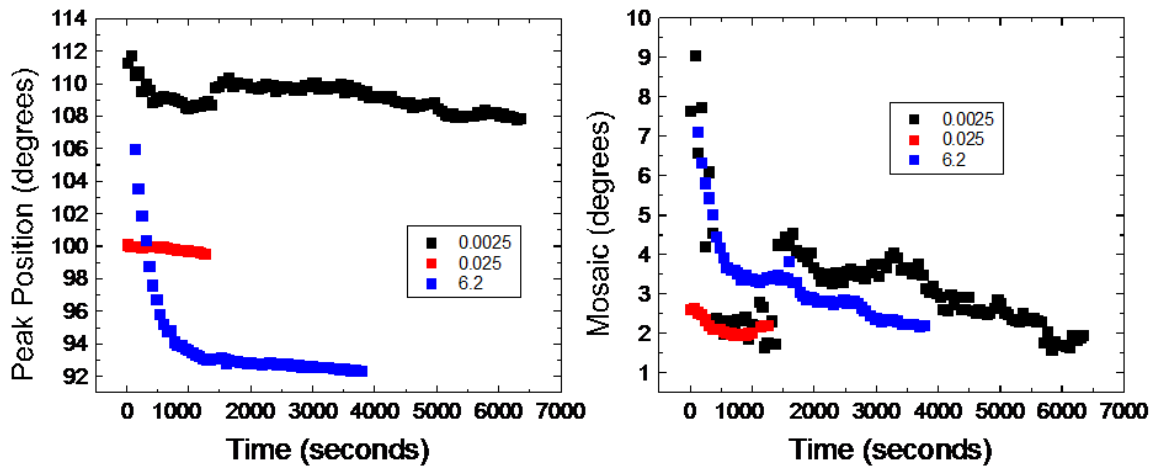
Figure 1.27: Peak Position and Mosaic for confined 8CB as a function of time for 0.5 μm gap size at various shear rates (shown in legend). Reproduced from Idziak[317]

For both shear rates, interestingly, the reorientation occurred in discrete steps rather than smoothly, as it had with the larger gap size, and it was theorized that these steps are due to domain reorientation. Furthermore, at the smaller gap size and at low shear, the diffraction peak amplitude oscillated from positive to negative with periodicity identical to the shear period.
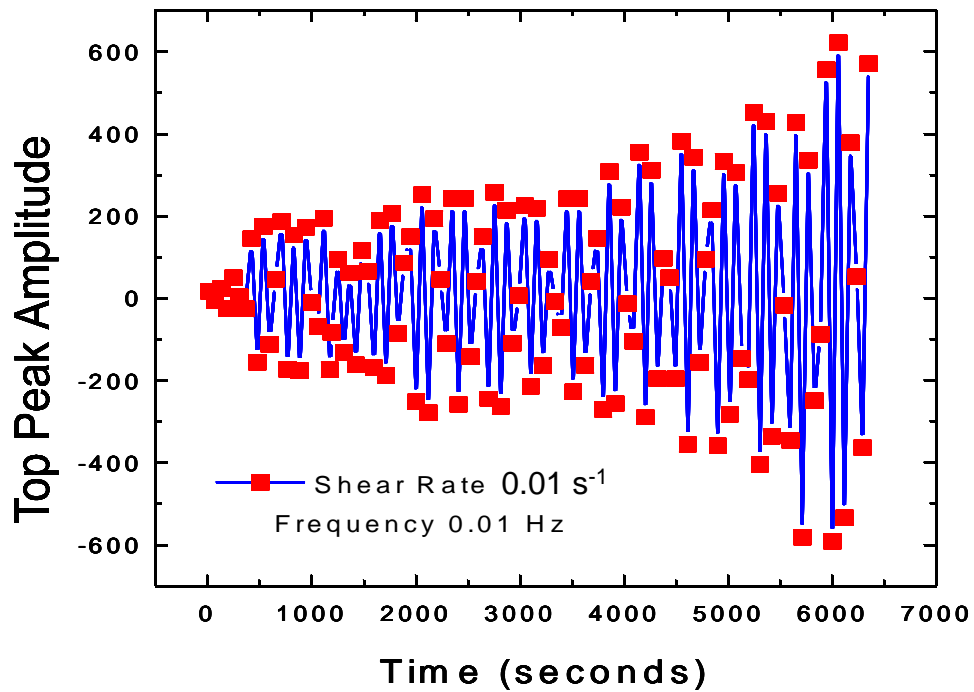
Figure 1.28: Diffraction peak amplitude as a function of time for sheared 8CB for 0.5 µm gap size and 0.01 sec^{-1} shear rate. Reproduced from Nieman and Idziak[323].

This, they theorized, indicated that the scattering plane was oscillating as well, which demonstrated that the domain were being gently 'massaged' back and forth due to shear. This behaviour was also responsible for the fluctuating intensities observed with the larger gap at low shear, but which was weaker due to the greater number of differently-oriented domains present in the x-ray beam radius. The effect was not seen at higher

shear rates because it would have been averaged out over the long (50 second) exposure times[323].

1.5.3 Later Shear Experiments with the SFA

Ruths, Steinberg and Israelachvili[125] performed experiments that examined both normal and frictional forces as well as the viscosity of nematic and smectic 8CB while highly confined by two mica surfaces in the SFA. Surface roughness and hydrophobicity were modified in order to study their effects on the resultant 8CB epitaxial ordering. Both parallel and perpendicular alignments (with respect to the confining surfaces) were studied, the former by using untreated surfaces, and the latter by using dihexadecyldimethyl ammonium acetate (DHDAA) and cadmium arachidate. It was known that DHDAA forms a loosely-packed monolayer on mica surfaces, while cadmium arachidate forms tightly packed monolayers. The group observed that ordering occurs even without previously shearing or bringing the surfaces into contact, as evidenced by FECO discontinuities near to the point of closest approach. By bringing the surfaces into contact or shearing the 8CB with large amplitudes (above 5000 nm), the discontinuities gradually diminish and disappear, and this domain uniformity remains even after the external stimulus is removed, until the surfaces are separated enough (on the order of microns) to allow randomly oriented domains to flow to the point of closest approach[125].

Force-measurements were performed on the samples of both orientations and both nematic and smectic mesophases, building on Koltover's[320] work. In all cases periodic

oscillations of amplitude near to the dimer length or width (depending on orientation) were seen extending from the surface: For parallel orientation, the nematic and smectic penetration depths were similar to those given by Koltover, while for the perpendicular orientation, the DHDAA monolayer resulted in penetration depths of 25 nm for the nematic and considerably further for the smectic (an exact value is not given). The cadmium arachidate monolayer led to penetration depths of at least 45 nm in the nematic and at least as far again in the smectic. Furthermore, the innermost layer of 8CB was reduced in size from the approximately 31 Å (or one dimer length) to 22-25 Å, attributable to the DHDAA's loosely packed monolayer allowing for interdigitation of the anchored layer of 8CB. This trait was not seen in experiments performed with the tightly packed cadmium arachidate[125].

The group also found that the parallel-oriented 8CB exhibits peculiar anisotropic optical properties: the wavelength of the ordinary component of the FECO fringe doublet, "β" varies with gap size as would an isotropic material, while the extraordinary component, "γ" shifts to longer wavelength more quickly than for an isotropic material. The crossing period (that is, the range over which γ shifts to the same relative position with respect to β_n as it had been to β_{n+1}) of this doublet splitting was found to occur over a separation change of approximately 1.6 μm. This differs with perpendicularly-oriented 8CB, which behaves as would an isotropic material in that the β-γ doublet splitting decreases as the gap size is increased[125].

Experiments were performed wherein one surface was vertically oscillated and the response of the other was measured, in order to gauge the radial viscosity. The parallel orientation in this type of experiment gives rise to some combination of the 'a' and 'b' Mięsowicz viscosities, while the perpendicular orientation leads to the 'c' Mięsowicz viscosity. Israelachvili previously derived an equation describing the viscosity, η, measured in such an experiment[38]:

$$\eta = \frac{k\overline{D}}{12\,\pi^2 R^2 v}\left[\left(\frac{A_0}{A}\right)^2 - 1\right]^{1/2} \tag{46}$$

where k is the stiffness of the surface mount, $\overline{D}$ is the average gap size, R is the hydrodynamic radius, v and A_0 are the applied frequency and amplitude of oscillations, and A is the amplitude of the response. Hence, by plotting $\dfrac{12\,\pi^2 R^2 v}{k}\left[\left(\dfrac{A_0}{A}\right)^2 - 1\right]^{-1/2}$

versus $\overline{D}$ one will obtain η^{-1} from the slope. Ruths et al presented such plots for various shear rates and found in each case that above a separation of approximately 300 nm the relation was linear, while below that point the curve exhibits continuously changing positive curvature. It was also noted that the linear portion of the responses had increasing slopes for increasing shear rates. Both situations indicate that viscosity η increases with v and D, and hence both are evidence of shear thinning[125].

The group[172] noted that the smectic form generally exhibited a viscosity an order of magnitude larger than the nematic form, unlike what is typically seen in bulk, where smectics and nematics have similar viscosities. They ascribed this to increased coupling of the surfaces, a result of the response being dependent on the bulk layer permeation

modulus in the smectic mesophase, a phenomenon reported also by Okano and Yamamoto[324, 325]. The modulus reduces the amount of permeation that occurs between layers, leading to stronger coupling between the surfaces in the smectic than in the nematic, and, they asserted, the long-range force reported in smectics by Koltover[320].
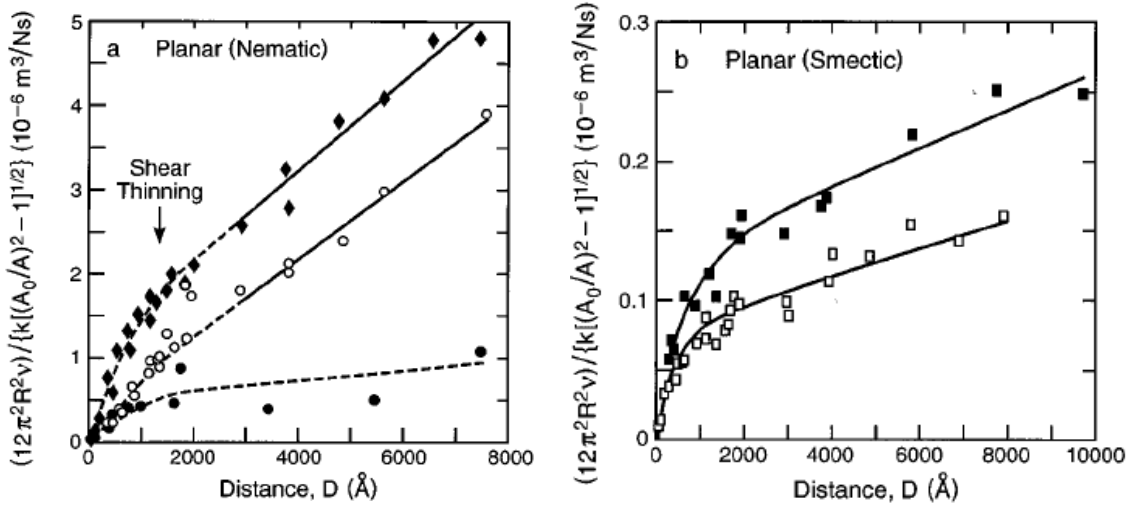
Figure 1.29: Viscosity curves for nematic and smectic parallel-oriented 8CB for various shear rates (Nematic: $v = 0.05$ sec^{-1} [closed circles]; $v = 0.1$ sec^{-1} [open circles]; $v = 0.2$ sec^{-1} [filled diamonds]. Smectic: $v = 0.1$ sec^{-1} [open squares]; $v = 0.2$ sec^{-1} [closed squares]). Reproduced from Ruths et al[125].

Lateral friction experiments were also performed by Ruths et al[125]. These experiments were performed on parallel-oriented two monolayer thick nematic and smectic 8CB systems at various speeds and loads, and it was found that the friction force measured in the smectic system was invariably much smaller than in the nematic (

$\mu_{nematic} \approx 0.21 - 0.24$, while $\mu_{smectic} \approx 0.08 - 0.09$), a result of the smectic's increased ordering leading directly to a more fluid system. The force decreased with shear speed, which they attributed to the molecules not having enough time to relax to an entangled

117

state during the shear. Significant friction forces were also observed even with no load applied, as seen below in Figure 1.30:
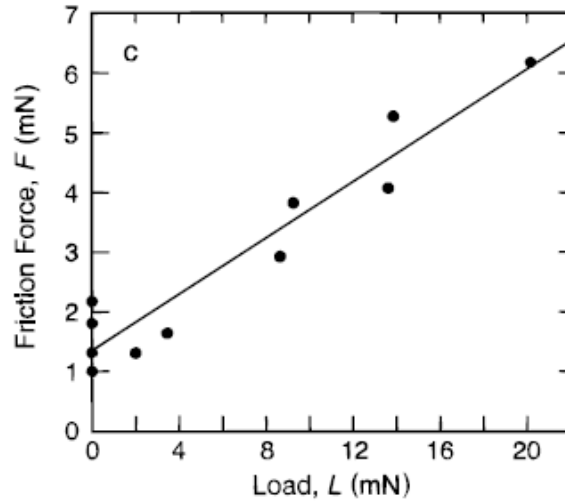
Figure 1.30: Friction force as a function of load for perpendicularly-oriented smectic 8CB confined to 2.2 nm, sheared at 60 nm/sec. Reproduced from Ruths et al[125].

Experiments performed on thin layers (22-30 Å thick) of perpendicularly-oriented 8CB revealed that such an orientation leads to deformation of the surfaces if oriented with DHDAA ($\mu \approx 0.6$), and stick-slip motion if oriented with cadmium arachidate ($\mu \approx 0.1$).

Herke, Clark and Handschy[326, 327] performed dynamic surface force measurements on homeotropically-aligned smectic-A 8CB to study its response to layer-normal stress using a surface forces apparatus modified to include capacitance micrometry and electronic detection to improve on normal force measurements[328]. Compressive and dilatory force-measurements were performed in increments of 1 to 8 nm at initial separations of 4 μm and 1.4 μm, respectively, and an incremental response was observed, indicating the 8CB stiffness was at least an order of magnitude larger than the spring mount used. By

calculating the effective spring constant of the sample, $K_{eff} = 2\pi RB \ln\left(1 + \dfrac{\rho_{max}^2}{2RD_0}\right)$, where

B is the average bulk compressibility of the 8CB, ρ_{max} is the effective radius, R is the

radius of the cylindrical surfaces and D_0 is the jump-in distance, they were able to

estimate the effective radius as being on the order of 50 μm in order to generate such a

large spring constant[326, 327].

Herke et al[326, 327] also studied the phenomenon of plastic flow in the normal direction

where, when the force on the sample exceeded a certain point, it momentarily stopped

resisting to its full extent and fell to a new level of resistive force. The response here was

sigmoidal with respect to time, and was often preceded by what the authors called a

'foreshock' event: a small perturbation in the resistive force a few seconds previous to the

drop, which, while it did not seem to be the cause of the drop, immediately preceded it.

The drops were usually found to be equivalent to the thickness of a single monolayer of

8CB (although several multilayer events were seen as well, especially at smaller gap

sizes), indicating it is analogous to the squeeze-out effects first documented at much

smaller separations by Horn and Israelachvili in 1981[129], and the force needed to cause

the plastic flow was similarly found to increase with decreasing gap size as well[326, 327].

Simulations of the various possible defects evolving with stress were performed, and the

Glaberson-Clem-Oswald-Kléman helical instability of screw dislocations model was

found to be in best agreement with the data obtained. The model, first proposed in 1974

by Glaberson in describing flow in superfluid vortex lines in liquid Helium II and later in

1977 by Clem in describing vortex flux lines in type II superconductors[329, 330], was

applied to smectic-A systems in 1984 by Oswald and Kléman[331]. It had been shown

previously that a screw dislocation evolves into a helical structure with the addition of a compression or dilatation force in order to remove or add layers of material, a unique property of layered systems where the energy cost in doing so is low[332].

Artsyukhovich et al[130] performed shear experiments on thinner layers of nematic 8CB at 23ºC, compressing the mica surfaces as much as reasonably possible and finding only a single monolayer (10.2 Å thick) of material remaining between them (determined optically via FECO) before applying the constant velocity shear (with shear rate approximately 300 sec^{-1} and period of 10 sec) at both high and low loads (controlled by a homogeneous magnetic field combined with a magnet affixed to double cantilever springs beneath the lower surface, a setup designed by Christenson and Salmeron et al[333, 334]). For all loads, the response behaved linearly up to a critical deflection at which point under low loads (1-1.5 MPa) a single small decrease in frictional force followed by continuous slipping was observed, while at higher loads (1.5-2.7 MPa) repeated stick-slip behaviour occurred until transitioning into continuous slip behaviour.
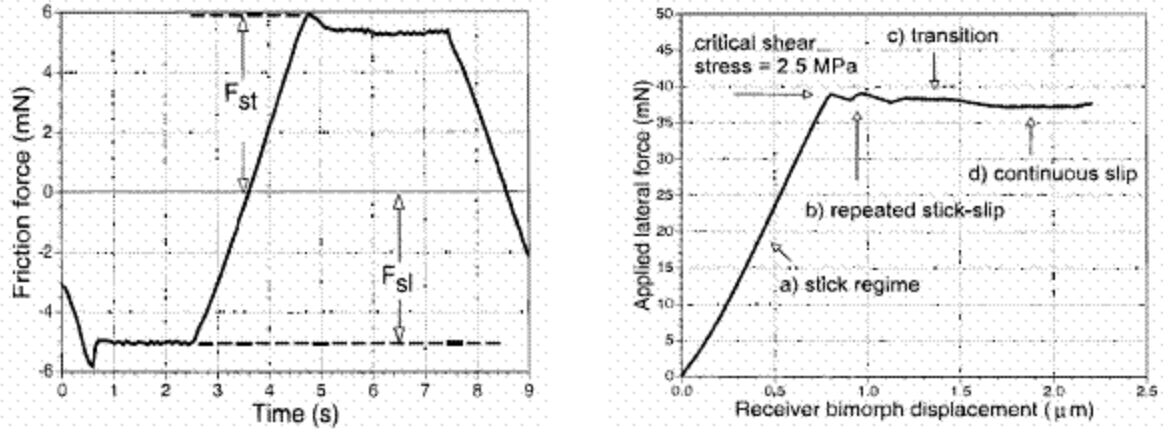
Figure 1.31: Monolayer 8CB SFA shear response data. (Left) Low load response as a function of time. F_{st} and F_{sl} refer to static and sliding friction, respectively. (Right) High load response as a function of receiver bimorph displacement, showing the various observed behaviours. 'Transition' refers to the transition period between the stick-slip regime and continuous slip regime. Reproduced from Artsyukhovich[130].

Differences between these low load results and those obtained under similar conditions

by Ruths et al[125] were explained as being due to differences in sample preparation and

maintenance of the sample during experimentation. Specifically, despite Ruths' purging

of the SFA with dry nitrogen to absorb residual water vapour, Artsyukhovich claimed the

method would not keep the sample completely dry, leading to their observed liquidlike

response. Artsyukhovich's group kept the SFA in a drybox and the sample over a

molecular sieve, and so, they claim, observed a distinctly non-liquidlike response[130].

Artsyukhovich[130] also found that while the first cycle exhibited viscous traits,

subsequent cycles exhibited more solidlike traits. Shear experiments performed parallel

to the molecular axis were found to have different critical shear stress levels (0.28 MPa at

low load and 0.6 MPa at high load) than those performed perpendicular to the molecular

axis (0.42 MPa at low load and 1.2 MPa at high load), demonstrating the anisotropy of

frictional properties. It was suggested that the increasing critical shear stress observed

121

with increasing load may have been due to an increasing pressure-induced dissociation of the 8CB dimer, leading to chemisorption of the 8CB with the mica surface and hence a different surface-8CB interaction[130].

Chapter 2

The Surface Forces Apparatus

The majority of results presented in this thesis were performed on the Surface Forces Apparatus (SFA). For this reason it is worth understanding the device in some detail, and the following chapter breaks the device down into its components to discuss each part individually. The SFA chamber and base are discussed first (Section 2.1.1), followed by the optics stand, which guides the light to the spectrometer (Section 2.1.2), the various micrometers, with which the level of confinement can be obtained (Section 2.1.3), the Force-measuring spring and piezo mount, which allow vertical forces to be determined precisely (Section 2.1.4), the bimorphs, which direct the bottom surface in various ways (Section 2.1.5), and the Friction Device, which allows horizontal forces to be measured precisely (Section 2.1.6).

Most SFA's are controlled via a control panel supplied by the manufacturer, which is connected to the SFA and its electronic equipment via several cables. Such a setup is impractical for tests that require long-term thermal stability, since the operator must, from time to time, be in the room with the SFA in order to run experiments. Because the confining surfaces are very delicate and typically only last a few weeks at most before degrading to the point where they are unusable, it is desirable to maximize the amount of time they can be used for testing and hence minimize the amount of user interference, which inevitably result in large thermal fluctuations that take hours to stabilize. For this reason the SFA has been fully automated and hence can be sealed off for weeks or

123

months at a time while being controlled outside the room via a desktop PC fitted with a National Instrument data acquisition card. Section 2.2 and Sections 2.4.1-2.4.5 discuss the electrical connections that were necessary to create such an automated system. Section 2.3 develops the equations that were used to calculate the gap sizes using the three-film interference relations that describe the optical path within the gap.

A calculation of the gap size can typically take several minutes, as fringes of equal chromatic order (FECO) must be counted and their wavelengths measured. This can be disadvantageous for experiments in which one must begin as quickly as possible after setting the positions of the confining surfaces. For the results presented here, following each shear test the sample was agitated to remove any prior shear-induced domain ordering. To begin each subsequent shear test with a consistent degree of post-agitation ordering, a method of calculating the gap size semi-automatically following the surface positioning was developed. Section 2.4.6 describes the methodology behind this novel preparation technique.

2.1 Overview

The Surface Forces Apparatus (SFA), developed by D. Tabor, R. Winterton and J. Israelachvili, has been used to investigate molecular, surface-surface and surface-medium interactions since its creation in 1972[335]. It distinguishes itself from other nanoscale measurement instruments, the Atomic Force Microscope (AFM) for example, by its ability to measure, over several orders of magnitude of distance (from Angstrom level up to tens or hundred of microns), the forces between two surfaces rather than between surface and tip.
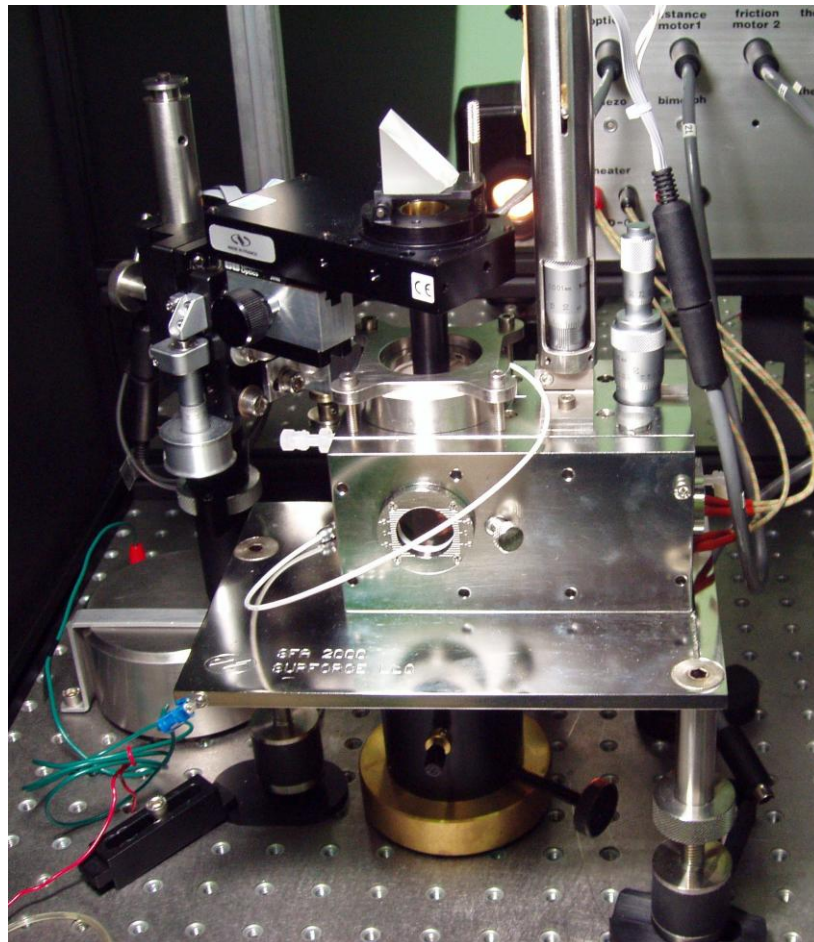
Figure 2.1: The SFA in its standard configuration

This complex instrument (a picture of which is shown above in Figure 2.1 and a diagram of which follows below in Figure 2.2) is made up of several components, each of which warrants a separate discussion, following below.
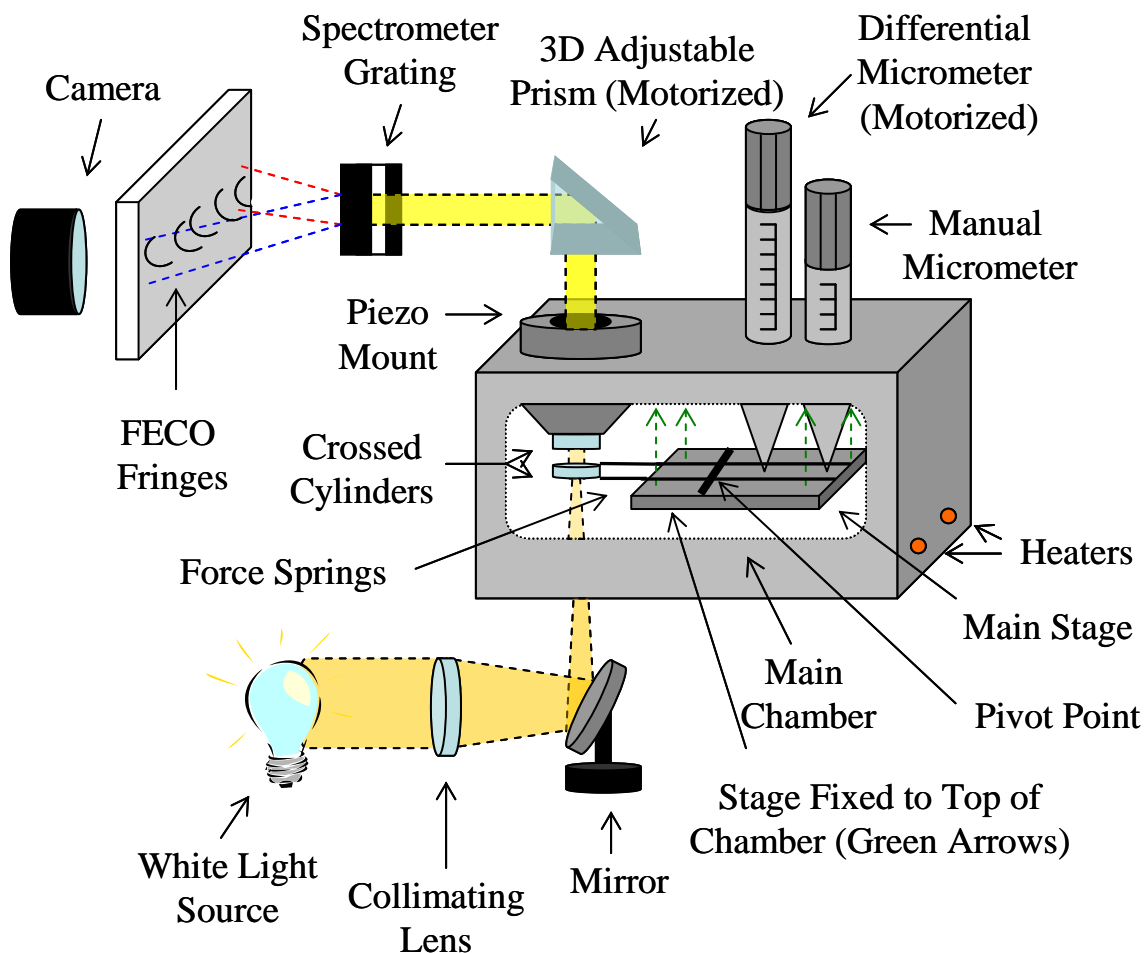
Figure 2.2: A diagram of the SFA and the light path from source to spectrometer

2.1.1 The SFA Chamber, Base and Legs

SFA experiments take place within the Main Chamber, a roughly cuboidal space 3×3×10 cm in size centered within the SFA body proper. The front of the chamber is

accessible by a front plate that screws into the rest of the SFA, creating a liquid-tight seal. There are several entry and exit ports providing access to the SFA chamber even while the front plate is in place: A Vapour Pressure Port, within which a plug recessed to contain a vapour bath can be inserted; an electric port through which various wires (most commonly those associated with the bimorph mounts) may be inserted; an air hole positioned near the surfaces through which screwdrivers and other tools may be passed to manipulate the surfaces and mounts; and a liquid port used to fill the chamber or to purge it with inert gas (typically dry nitrogen). A small circular window in the bottom of the chamber directly beneath the surfaces allows white light to pass into the chamber, and a large port at the top allows the top mount to be secured to the SFA and the light to exit the chamber. Two holes at the top allow the micrometers to be secured to the SFA as well. Two cylindrical holes running beneath and parallel to (but separate from) the length of the chamber allow for the insertion of two snugly-fitting heaters to alter and maintain the temperature within the chamber. The SFA body can be attached to a solid plate (the Base) which in turn can be attached to three adjustable legs that can set the height of the SFA so that the exit prism is at the same height as the spectrometer.

2.1.2 Optics Stand

The optics stand's primary purpose is to focus and direct the FECO interference pattern from the SFA and towards the spectrometer. It does this by the use of an optics tube which sits recessed into either the friction device or piezo mount (whichever is used to hold the upper surface) so that the objective lens can be close to the surfaces but still independent from it and adjustable in all directions. At the top of the tube sits a prism

which redirects the interference pattern from the vertical to horizontal direction (i.e. along

the spectrometer's diffraction plane); the prism stand has a tilt- and swivel-table, giving

the prism two more degrees of freedom to improve the precision of the light path. The

table is connected to a stepper motor, as is the vertical fine adjustment of the optics arm,

so they can be used remotely using the control box or by computer (both can also easily

be adjusted manually as well). The entire optics tube, tilt- and swivel-table and motor

casing is connected to the stand via a rotation clamp, allowing the entire arm to be

swiveled away from the SFA to allow for easier access to inspect the surfaces (in order,

for example, to locate Newton's Rings and, hence, the point of closest approach of the

confining surfaces) and to load the upper mount. The entire stand is clamped firmly to

the floating table surface to ensure that the prism remains motionless to avoid blurring of

the FECO pattern.

2.1.3 Differential and Fine Micrometers

   The SFA is usually equipped with three micrometers, with each having its own range

and turn/deflection ratios. In the standard set-up, the differential micrometer is manually-

controlled and is comprised of the coarse and medium micrometers, the former with a

positioning accuracy of 200 nm and the latter with a positioning accuracy of 50 nm. The

deflection is obtained by the shaft pushing on the lower mount's pivot stage (to which is

affixed a sapphire disk to protect both the mount and the micrometer). By pushing the

pivot stage downward and creating an angle, θ, between its original and new position

(with the pivot point as the center of the traced-out circle—see Figure 2.3), the lower

mount will deflect in the normal direction an amount $L\theta$, where L is the length between the pivot point and the surfaces.
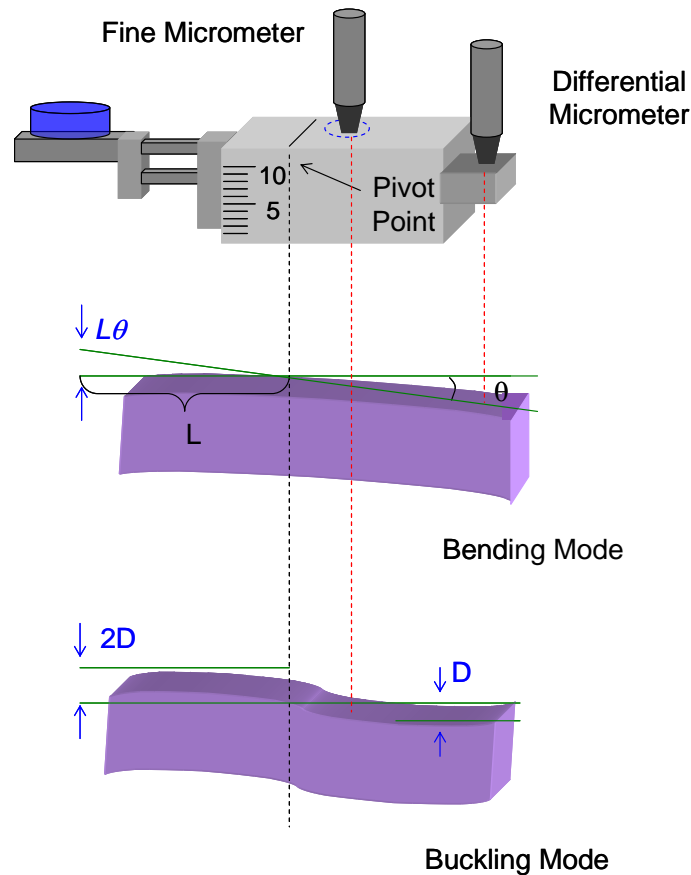
Figure 2.3: Bending and buckling modes implemented by the differential and fine micrometers, respectively. The lower mount depicted is the Force-measuring Spring mount, described in the section below, although the bending and buckling principles apply equally well to the Bimorph mounts. Here 2D and $L\theta$ refer to the deflection in the lower mount. Adapted from Israelachvili[336].

   The fine micrometer, conversely, is motor-controlled, pushing against a pivot stage closer to the pivot point of the lower mount. Unlike the differential micrometer, then, the deflection caused by the fine micrometer occurs as a result of buckling of the cantilever spring on the stage while the rear pivot stage remains in contact with the differential micrometer, leading to a deflection, D, that translates to a roughly *2D* deflection in the

surfaces. The fine micrometer has a spring in place between the pivot stage and the micrometer shaft, and so the ratio of turns/deflection can be adjusted for it by swapping one spring for one of different stiffness. By this method the surfaces can be deflected with a positioning accuracy of approximately 2 Å over a range of 5 mm[337].

The fine micrometer stepper motor allows the user to control the amount of surface deflection by way of the Control Box, resulting in the considerable accuracy mentioned above. To protect both the micrometer and the lower mount, limit switches are added to the stepper motor preventing the micrometer from turning beyond limits imposed by the user. The limit switches, each made up of a small strip of metal, are triggered by a single prong that sits between the minimum and maximum range points. The strips slide on a track along the length of the micrometer casing so that they can be set by the user, and if the strips are pressed beyond a critical point by the prong during operation they trigger, interrupting the stepper motor circuit and thereby stopping the micrometer from moving any further. The Friction Device described below has a similar stepper motor system, complete with limit switches, to those that have been described here.

In the experiments presented in this thesis, the traditional micrometer and DC motor setup has been altered in order to be able to perform experiments remotely for extended periods. The first and most noteworthy adjustment entails removing the stepper motor from the Friction Device and affixing it to the differential micrometer. The reason for this is to provide the user with as much variability in deflecting the bottom surface (and hence adjusting the gap size) as possible. To accomplish this, two couplers were

designed and manufactured in-house, to connect the stepper motor's flex coupler to either the head of the coarse micrometer (a stainless steel cylindrical cap approximately 2 mm in height and 10 mm in diameter) or to the fluted handle of the medium micrometer (which has no cap to it, as it sits at the bottom of the differential micrometer). The stepper motor sits above the differential micrometer in both configurations, connected by the coupler, and is attached to the floating table as well via a clamped retort stand in order to provide a fixed reference point by which it can turn. Both connectors were made from aluminum, with one end connected to the flex coupler by way of the latter's set screw, and with the other end connected to the differential micrometer by a set screw within the coupler itself. A schematic of the modified SFA setup is given below in Figure 2.4:
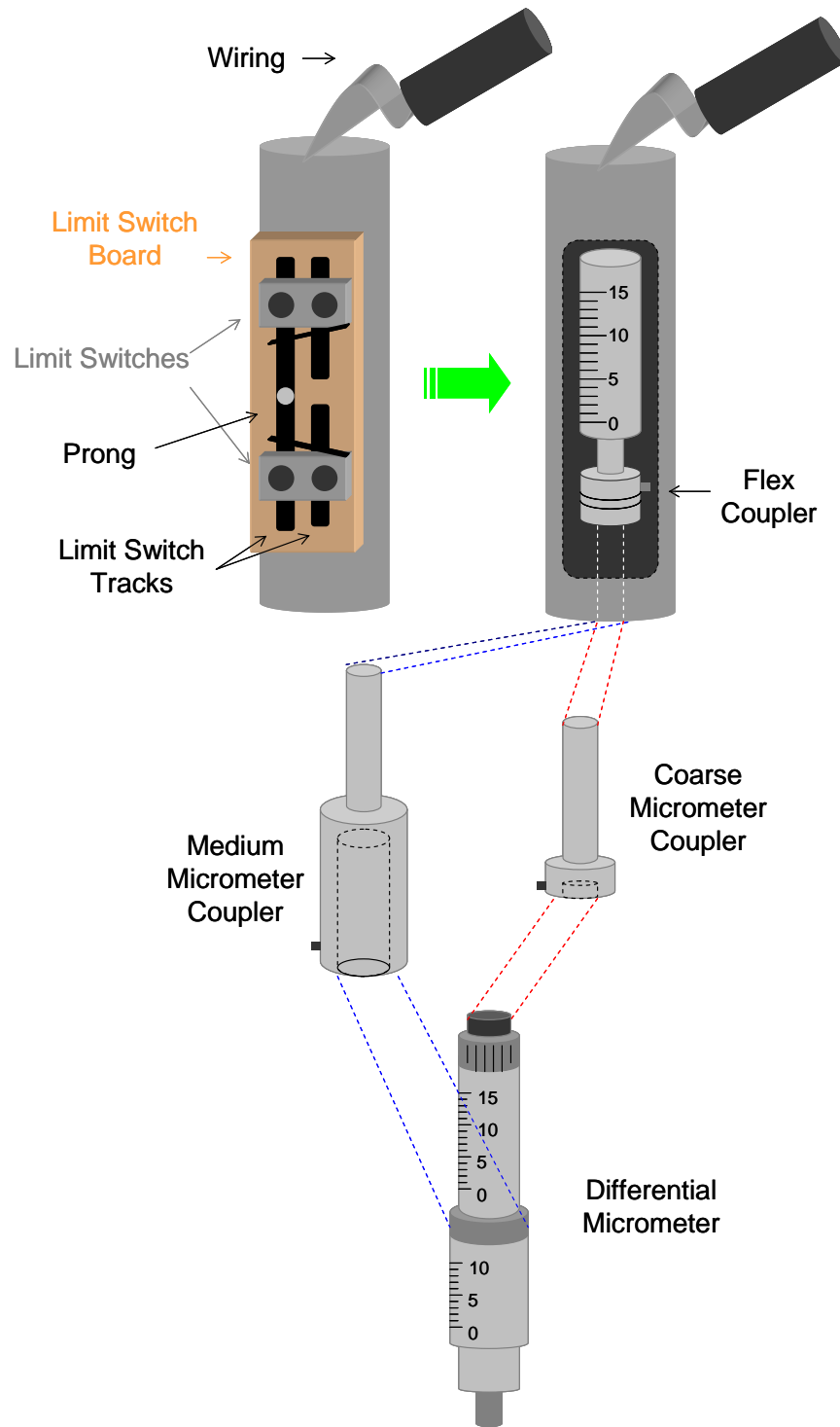
Figure 2.4: Schematic of the Differential Micrometer couplers and stepper motor limit switches.

With the differential micrometer only providing either medium or large deflections of the lower surface, the problem arises as to how to fine-tune the gap size quickly and relatively accurately at the separations used in the set of experiments presented. In the standard setup the fine micrometer can only adjust separations fairly slowly and with more accuracy than is needed at 500 or 5000 nm separations, and so a stiffer spring was inserted to give a more rapid determination of separation over a larger total range, at the expense of a slight decrease in accuracy (which would not likely be noticed at the separations used). A sketch of this change is presented in Figure 2.5:
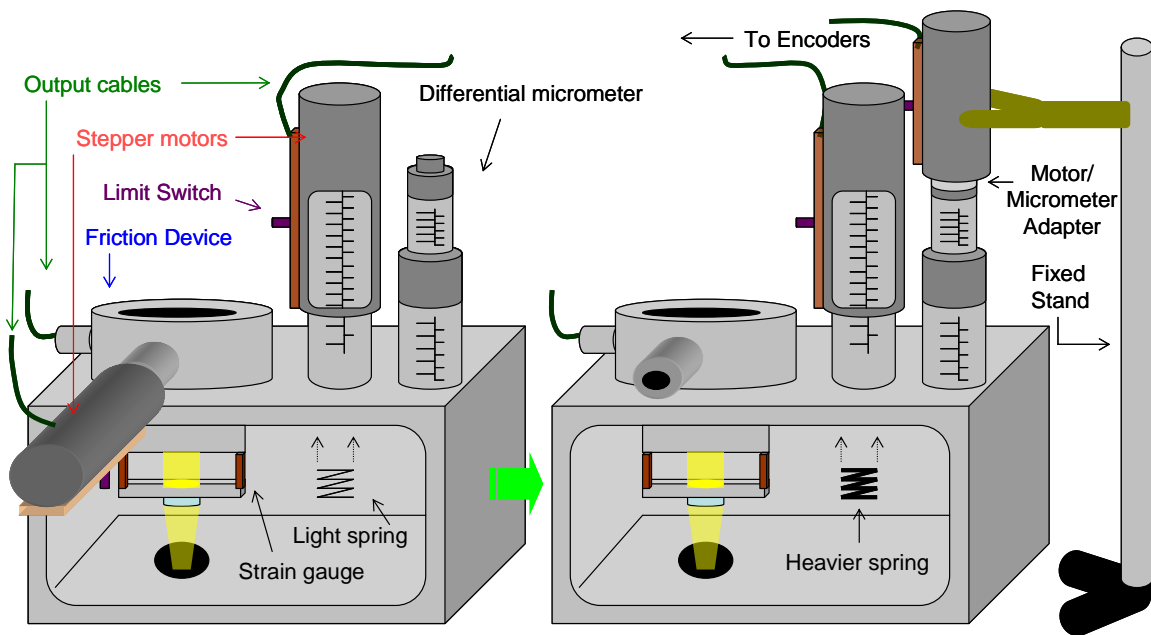
Figure 2.5: Conversion from the standard SFA setup to the remote operation setup.

2.1.4 Force-measuring Spring and Piezo Mount

The simplest option for holding the lower disk in place is the force-measuring spring, which, after having been calibrated and installed in the SFA (see the discussion of SFA

calibration in Section 3.1.1), will deflect normal loads exerted by the top surface and hence (since the stiffness of the mount is known) will give the normal force transferred through the sample.
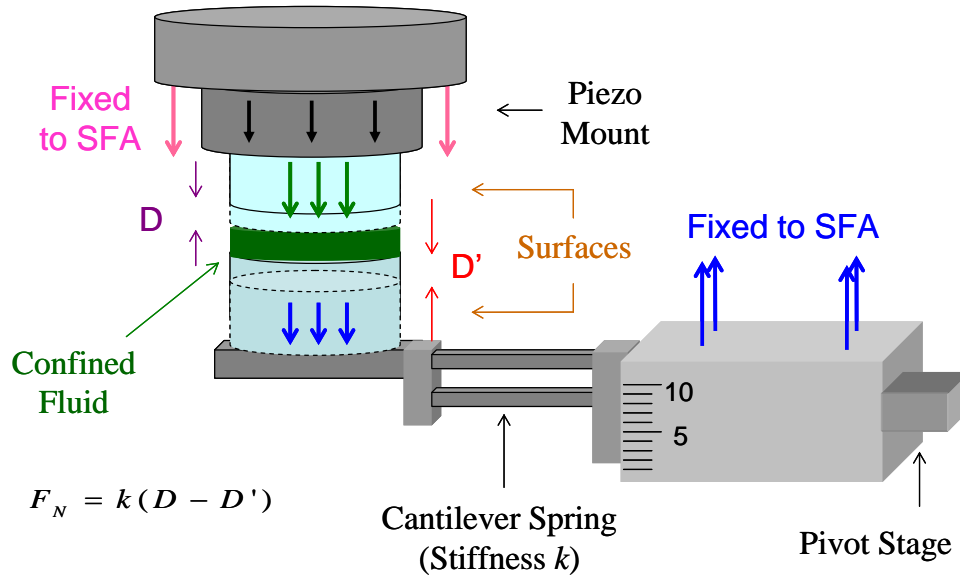
Figure 2.6: Force-measuring Spring and Piezo Mount performing a normal force test.

The stiffness of the cantilever spring to which the lower mount is attached can be varied over more than four orders of magnitude due to the spring's sturdy design and copper-beryllium composition. The Piezo Mount, holding the upper surface, is typically used in conjunction with the Force-measuring Spring to perform normal force measurements. It consists of a PZT-5A piezoelectric tube that is clamped by a butterfly ring to the top aperture of the SFA, allowing the tube itself lateral adjustment and rotation to align the surfaces as desired. The mount consists of two parts: The top cylindrical stainless steel chamber, which holds the piezo controls, and the bottom (separated from the top by a watertight Teflon bellows), another stainless steel piece which extends into the SFA Chamber and holds the surface disk in place. The Piezo Mount has a positioning

134

accuracy of less than one Angstrom, making it more accurate than the aforementioned micrometers[337]. A typical force-measurement experiment involves adjusting the separation by a known amount, D, using the calibrated piezoelectric crystal, and then measuring the amount the separation between the surfaces has changed, D', by noting the FECO positions before and after the shift. Since the stiffness of the cantilever spring is known, the change in force between the initial and final positions, F_N, can be determined using Hooke's Law: $F_N = k(D - D')$ [338].

2.1.5 Bimorph Components

There are two bimorph mounts typically used with an SFA: The Bimorph Slider and the Bimorph Vibrator. While the Bimorph Slider was used exclusively for the experiments presented in this thesis, both devices will be discussed here. The piezoelectric bimorphs used with the Slider consist of two thin, parallel sectored sheets set up in a double cantilever geometry; the bimorphs were obtained from Morgan Technical Ceramics (formerly Morgan Matroc). The sheets consist of two flexible piezoelectric ceramic elements glued to a central metal (or similarly conducting material) sheet, or vane, with each element glued with reverse polarization to the other, so that should an electric field be present, one of the sheets will expand and the other will contract. Since they are fixed together, this collective action will result in a net lateral displacement, A_B, as shown in Figure 2.7.
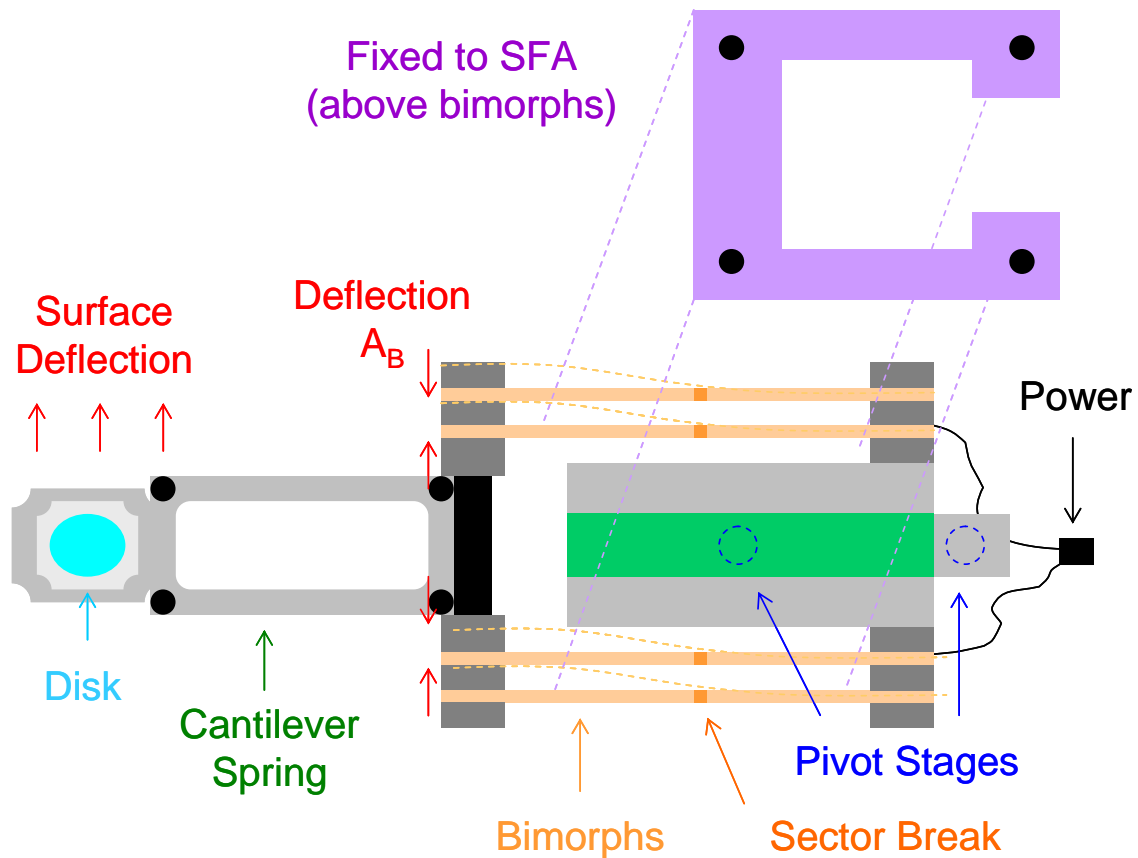
Figure 2.7: Schematic of the Bimorph Slider (Top View). Adapted from Luengo et al[339].

The outer portion of the bimorph is covered in a protective conducting coating which will provide a surface to which electrical connections can be attached. On its own, an applied voltage will create a pure bending motion in a bimorph coupler as described above. Sectoring the bimorphs—by scraping a small strip of the coating in the middle of the bimorph pair and reversing the wiring on the inner and outer sheets, thereby splitting the voltage between the two sectors—causes the two sectors to bend in opposite directions, creating a nearly linear (lateral) displacement. The field is provided by a voltage applied via wires at the back of the device, and can be either a dc offset or a more complex driving pattern chosen by the user when connected to a function generator. Surforce

Corporation, the maker of the SFA used in these experiments, recommends the bimorph move with constant speed for best results, which is equivalent to a triangular voltage profile. Triangular voltage profiles were used for all shear experiments presented in this thesis. The resonant frequency of the bimorphs, while it will vary depending on the number and length of the sheets used, is typically on the order of 250 Hz, and so periodic functions up to that frequency can be used to drive the Slider (Surforce Corporation recommends no higher than 200 Hz be used[337]). For potentials below 100 V the bending of the bimorphs is linear with voltage, and the maximum lateral displacement allowable is 1 mm[339].

The stiffness of the bimorph varies proportionally to the inverse cube of its active length (that is, the length between the clamps fixing the sheets in place) and to the square of the maximum lateral displacement of the surface. The stiffness of the cantilever spring holding the surface mount was reinforced in-house using a 3 mm thick stainless steel block screwed into the frame in order to increase the overall stiffness and thereby reduce possible vibrations in the experiments described in this dissertation. The piezoelectric effect can also work in reverse, so that a deflection to the bimorph (generated, for example, by a mechanical stress) will produce a voltage across the electrodes which can be measured; hence, the Bimorph Slider can also work as a force sensor, although for the experiments described in this thesis this particular application was not used.

The Bimorph Vibrator performs a function similar to the Bimorph Slider in that it provides a dynamic motion for the bottom surface, but while the Slider moves laterally,

137

the Vibrator moves exclusively in the vertical direction. As a result, while the sample experiences a *shear* flow with the Slider, it will experience a *squeeze* flow with the Vibrator. Despite this difference, both systems will give rise to similar equations of motion[337].
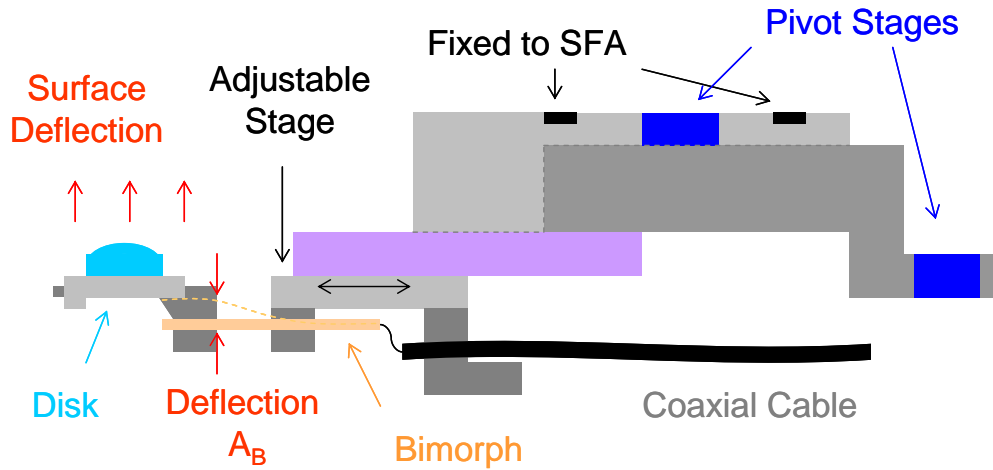
Figure 2.8: Schematic of the Bimorph Vibrator. Adapted from Israelachvili[336].

Bimorph Vibrators are generally used to perform oscillatory experiments, and the response is usually measured either by monitoring the FECO response with a camera[40, 340] or by using a lock-in amplifier to measure the amplitude and phase of the input signal with respect to the output signal[337]. The Bimorph Vibrator was not used for any of the experiments discussed in this dissertation.

2.1.6 Friction Device

The Friction Device, usually used in tandem with the either the Force-measuring Spring mount or the Bimorph Slider during oscillatory shear experiments, consists of top and bottom sections, the former consisting of the electronics protected by a cylindrical

stainless steel housing, and the latter consisting of an interchangeable friction barrel, to

which friction springs are attached. The friction springs in turn hold the disk mount plate

to which the top disk is affixed.
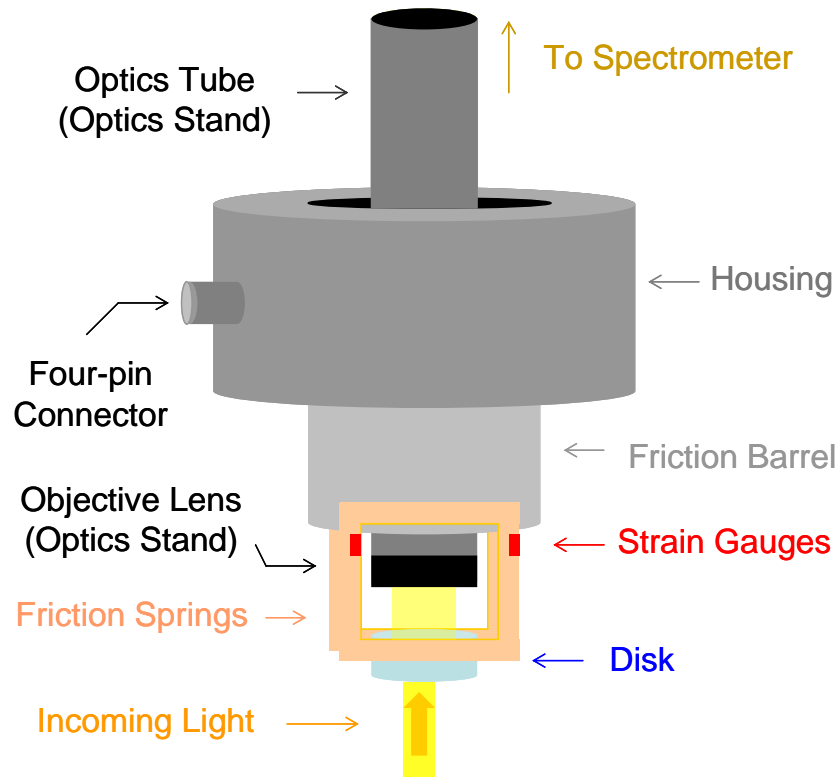
Figure 2.9: Schematic of the Friction Device, with the Optics Tube of the Optics Stand
in place. Adapted from Ishraelachvili[336].

The friction springs contain strain gauges, which can be of two different types: Resistive,

which are less sensitive but sturdy (obtained from Vishay Measurement Group), and

semiconductor, which are more sensitive but also more fragile than their resistive

counterparts (obtained from Micron Instruments). The strain gauges are set up in a

Wheatstone bridge configuration to improve their sensitivity. Strain gauge materials vary

in resistance as strain is applied to them, resulting in a bridge imbalance represented by

the strain sensitivity formula[341]:

$$S = \frac{R - R'}{R\,\varepsilon} \tag{1}$$

where R is the resistance of the unstrained material, R' is the resistance of the material undergoing strain, ε is the strain on the gauge and S, the strain sensitivity factor (also known as the Gauge Factor), is a dimensionless quantity representing the material's response to applied strain. A deflection of the friction springs will result in a small bridge voltage imbalance that is produced as an output voltage, V, given by (for the Wheatstone bridge configuration)[341]:

$$V = \frac{S\,\varepsilon V_B}{4} \tag{2}$$

where V_B is the bridge voltage supplied by the signal conditioning amplifier. The resultant signal is read and amplified by the signal conditioning amplifier, and then passed either directly to the connector block (and hence the DAQ card in the computer) or to the lock-in amplifier, where the signal is further processed. In this way the Friction Device can be used as a receiver for shearing motions generated, say, by the Bimorph Slider, as shown in Figure 2.10:
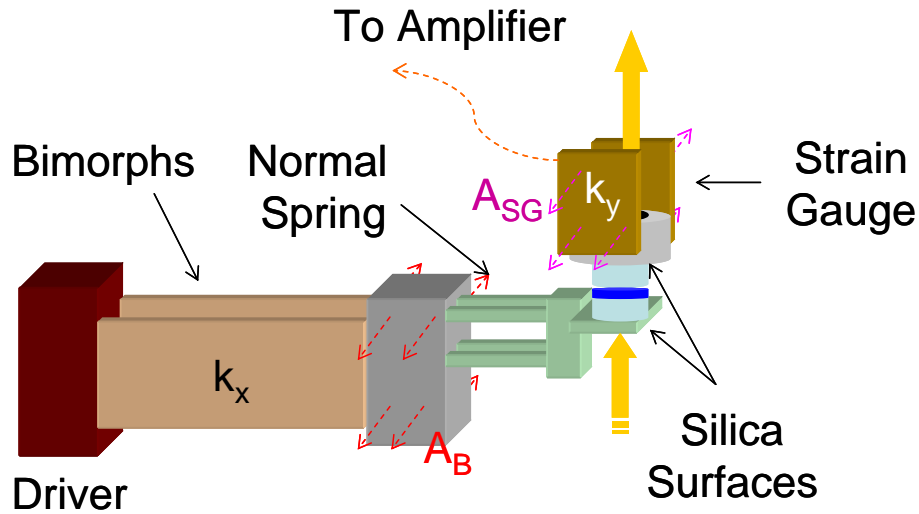
Figure 2.10: Bimorph Slider working in conjunction with the Friction Device. Adapted from Israelachvili[336].

Alternatively the Friction Device can be used to generate shear motion which can be monitored using, for example, the Bimorph Slider (see Section 2.1.5 for details on how the slider can be used as a receiver). It achieves this by the addition of a DC motor system with encoder similar to the one described above (see Section 2.1.3) which, by inputting the appropriate signal, can generate custom oscillatory shear patterns via the micrometer attached to the motor, which presses against the translation stage contained within the top section.

Equations of motion can be developed for the Bimorph Slider and Friction Device system by assuming an effective mass, *m*, and stiffness, *K*, for both components (where a B subscript stands for Bimorph and SG stands for Strain Gauge). Each component will, at any given time, have a lateral position, x, velocity, $\dot{x}$, and acceleration, $\ddot{x}$, and the shear will produce a friction force, κv, where v is the relative velocity $\dot{x}_B - \dot{x}_{SG}$ and κ is

the damping coefficient of the sample, as well as a damping force on each component. The bimorph will provide an external force F, so that the equations of motion for the bimorph and strain gauge components, coupled by the sample connecting them, will be[339]:

$$m_B \ddot{x}_B + K_B x_B + \kappa_B \dot{x}_B + \kappa \left(\dot{x}_B - \dot{x}_{SG} \right) = F \tag{3}$$

and

$$m_{SG} \ddot{x}_{SG} + K_{SG} x_{SG} + \kappa_{SG} \dot{x}_{SG} - \kappa \left(\dot{x}_{SG} - \dot{x}_{SG} \right) = 0 \tag{4}$$
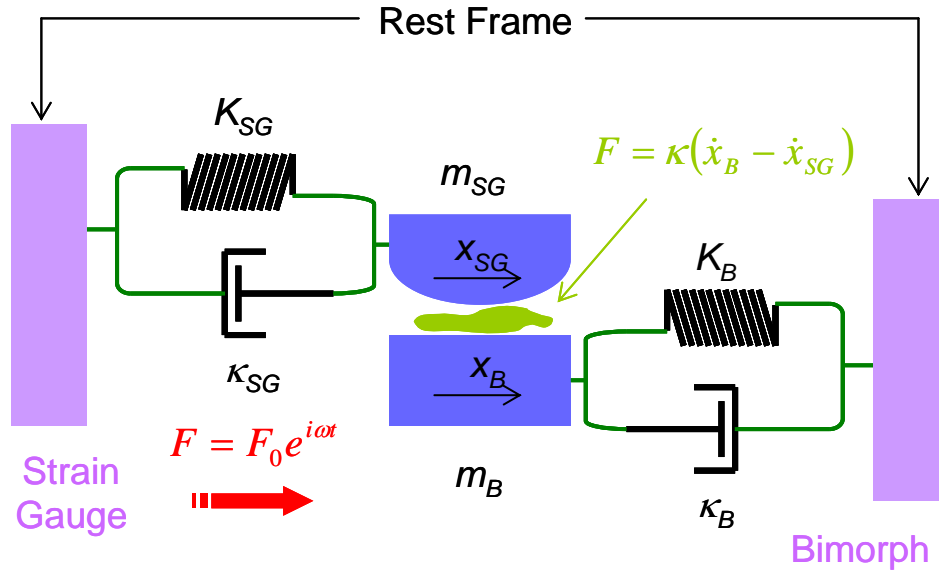
Figure 2.11: Schematic of the Friction Device (with Strain Gauge) and Bimorph Slider showing the various parameters used to set up the equations of motion for the system. Adapted from Luengo et al[339].

In most cases both the mass terms and component damping terms are negligible when compared to the other terms (although they may become a factor if oscillations are near to the resonant frequency of the Slider or Friction Device). Furthermore, since both the right-hand term and the spring-like term in Equation (3) are much greater than the liquid damping term in general, Equations (3) and (4) reduce to[339]:

$$x_B = \frac{F}{K_B} = \frac{F_0 e^{i\omega t}}{K_B} \tag{5}$$

and

$$x_{SG} = \frac{\kappa(\dot{x}_B - \dot{x}_{SG})}{K_{SG}} \tag{6}$$

where, in the rightmost term of (5) one assumes an oscillatory driving force with frequency $f = \omega/2\pi$ and amplitude F_0, providing a bimorph deflection amplitude of $A_B = F_0/K_B$. This demonstrates that the shear created by the Bimorph Slider manifests itself on the Friction Device by way of the friction force of the fluid, leading to deflection in the friction springs. Substituting Equation (5) into Equation (6) in turn leads to (with some further derivation)[339]:

$$x_{SG} = \frac{F_0 \exp[i(\omega t + \phi)]}{K_B \sqrt{[1 + K_{SG}^2/(\omega^2 \kappa^2)]}} = A_{SG} \exp[i(\omega t + \phi)] \tag{7}$$

where $\phi = \tan^{-1}\left(\frac{-K_{SG}}{\omega\kappa}\right)$. The above treatment has assumed a simple fluid, but quite often a sample may exhibit viscoelastic properties which will alter Equations (3) and (4) by the addition of an elastic component (assuming linear viscoelasticity), which will give rise to a complex viscoelasticity, $\eta = \eta' - i\eta''$, and complex shear modulus, $G = G' + iG''$, with components:

$$\eta' = \frac{K_{SG} A \sin\phi}{\omega\Omega[A^2 - (2A\cos\phi - 1)]} = \frac{G''}{\omega} \tag{8}$$

and

$$\eta'' = \frac{K_{SG}(A\cos\phi - 1)}{\omega\Omega[A^2 - (2A\cos\phi - 1)]} = \frac{G'}{\omega} \tag{9}$$

where Ω is a generalized surface geometry parameter and A is the ratio of amplitudes for

Bimorph and Friction Device, $A = A_B/A_{SG}$ The real viscosity component represents the

viscosity which is in phase with the rate of strain while the complex component

represents that which is 90° phase lagged to the rate of strain. The real component of

shear modulus represents the energy stored elastically in the sample while the complex

component represents the energy lost per cycle due to viscous dissipation[339].

2.2 SFA Control and Automation

2.2.1 Control Panel

Several of the components of the SFA can be controlled by a control panel provided by Surforce Corporation:

i) Both the prism swivel table and the optics arm can be controlled by the panel, the latter up and down to allow the objective lens to focus on the surfaces;

ii) The heaters mentioned in Section 2.1.1 can be controlled via a knob on the control panel;

iii) Both stepper motors (traditionally for the Friction Device and the Fine Micrometer) can be controlled separately by the panel. The micrometer shaft can be moved in or out at a rate adjustable by an analogue controller on the panel;

iv) The Piezo Mount can be set to a DC offset position or set to an AC oscillatory pattern and controlled externally;

v) The Bimorph Slider and Vibrator can both be controlled both by the control panel and externally via AC oscillatory patterns;

vi) Lights on the panel can also be turned on and off by a switch on the panel to illuminate it during experiments under poorly lit conditions (e.g. while optimizing FECO).

2.2.2 Electrical Connections

Because many of the cables leading to the control panel are only long enough to have it a few feet away from the SFA, most of the cables were extended to allow for more

mobility. Because the controls don't offer the flexibility needed to perform the experiments presented in this thesis (which require the ability to control the SFA whilst outside the SFA room, so that the thermal equilibrium is not disturbed), the panel was bypassed by developing software to emulate it on a desktop computer with the appropriate encoder and LabVIEW cards installed. The S&D 096 control box (described below in Section 2.4) was also designed to allow the user to switch between the control panel and the computer for any or all of the controls described above. The overall setup showing the flow of information to the SFA is given in Figure 2.12, while the setup showing the flow of information from the SFA is given in Figure 2.13:
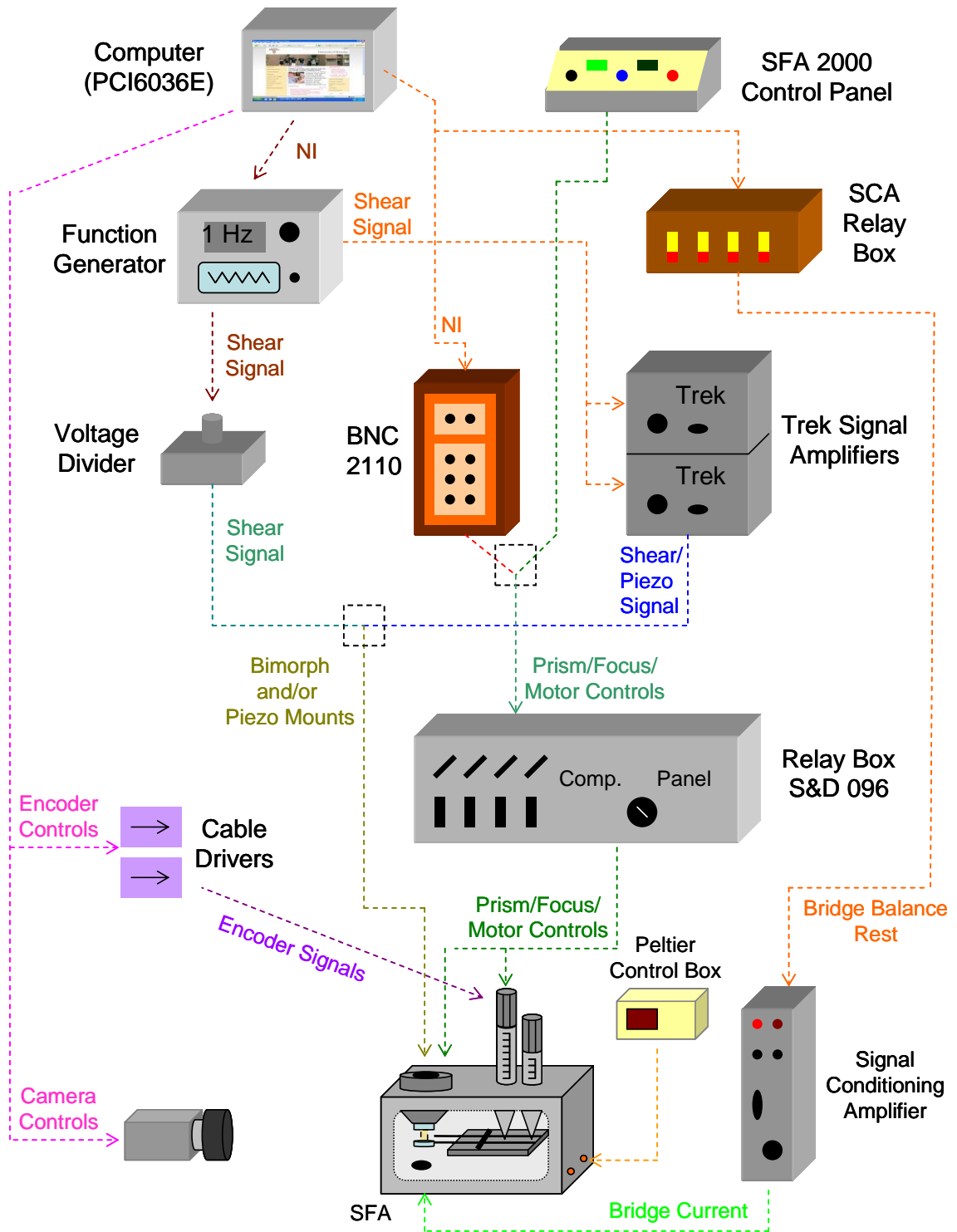
Figure 2.12: Schematic of the SFA setup showing information flow to the SFA.
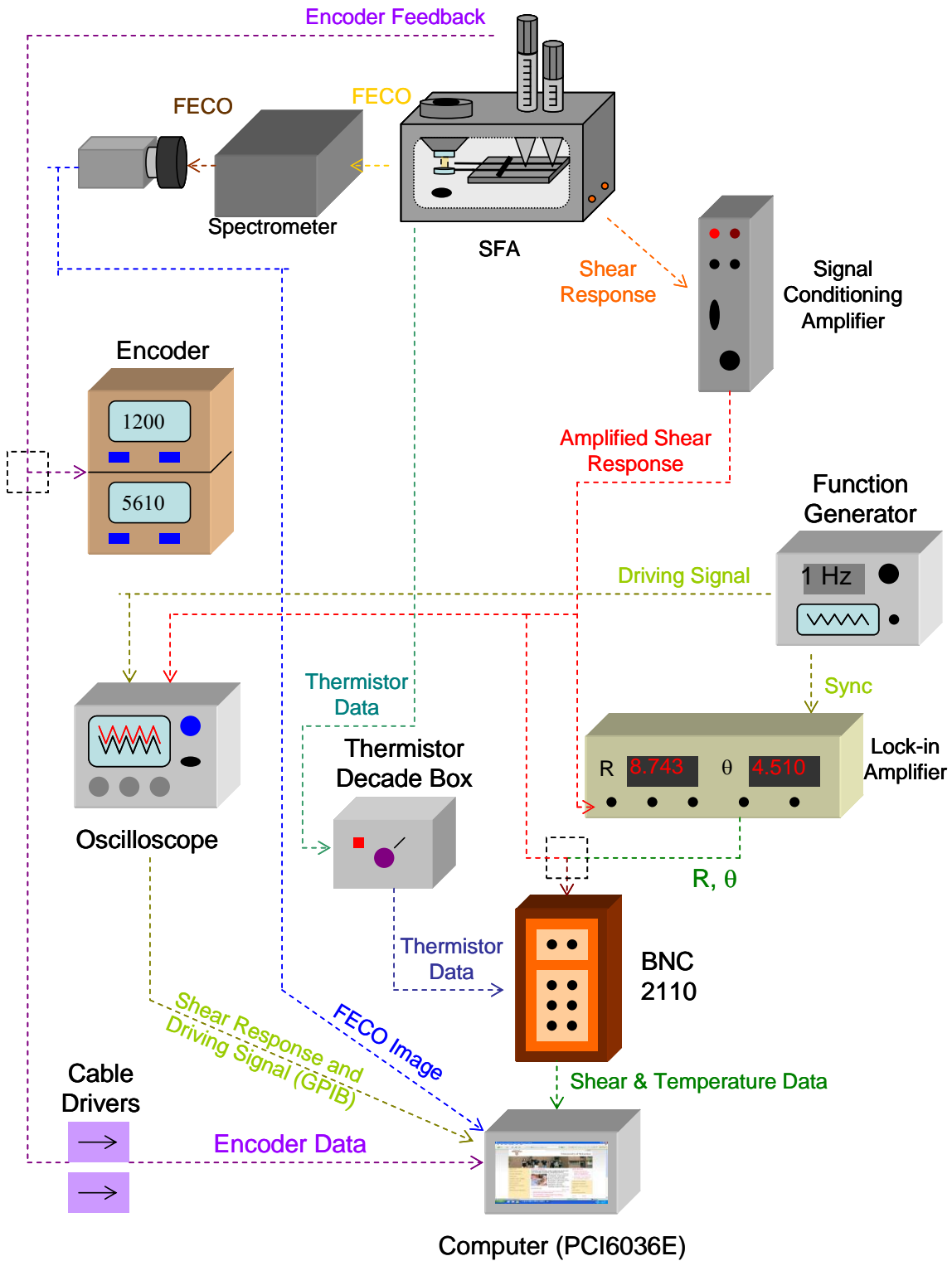
Figure 2.13: Schematic of the SFA setup showing information flow from the SFA.

2.3 Calculation of Gap Size and Optical Properties Using the SFA

2.3.1 A Simple Solution to the Three-Layer Symmetric Interferometer Using FECO

Very accurate calculations of a sample's index of refraction and of its thickness at the

point of closest approach can be made in situ with the SFA by using the principles of

interferometry, specifically, the interference pattern known as Fringes of Equal

Chromatic Order, or FECO. With identically thick and flat mica sheets on either side of a

sample, and each mica sheet coated with a thin reflective layer of silver (55 nm thickness

is considered optimal, corresponding to approximately 95% reflectivity[335]), the system

may be considered a three-film interferometer, as shown in Figure 2.14.
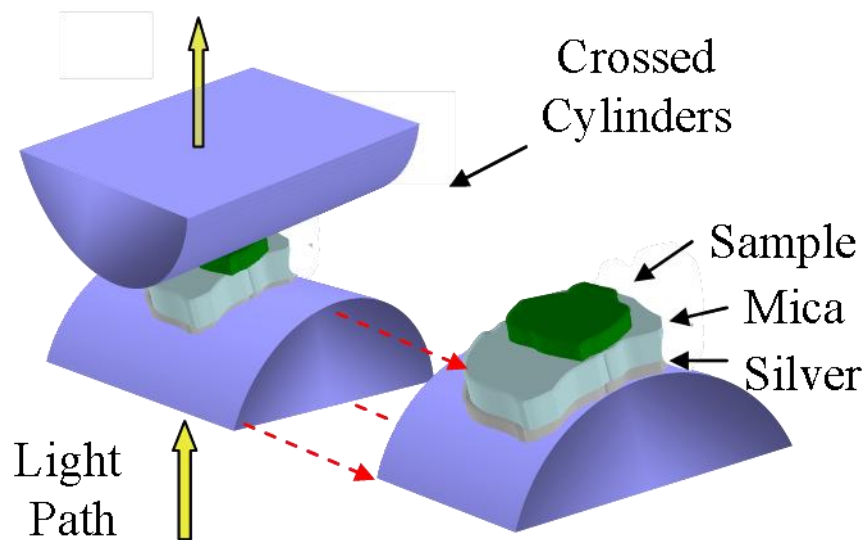
Figure 2.14: Diagram of the lens and sample configuration within the SFA

A derivation of the interference equation follows, using the method developed by Horn

and Smith[342] who follow Israelachvili's earlier derivation[335].

A schematic for a three-layer system is given below, with central (sample) layer of thickness D (in the case of crossed cylindrical geometry this would represent the point of closest approach between the cylinders) and index of refraction μ_S, and outer layers (mica) of equal thickness $Y = Y_1 = Y_2$ and index of refraction μ_m.
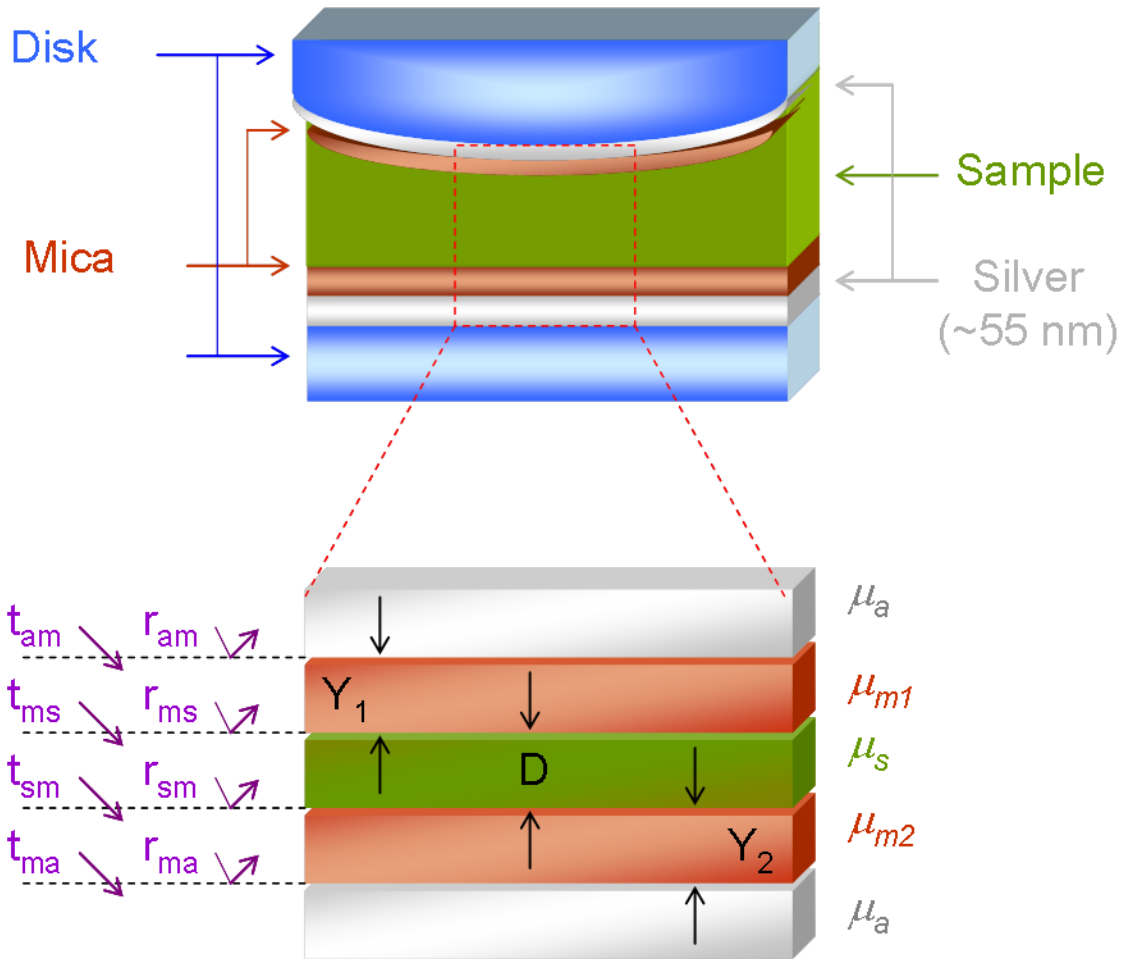
Figure 2.15: Schematic of the three-layer interferometer typically used in the SFA setup.

A thin transparent epoxy layer holds the mica to the disk substrate, with index μ_d. Using the matching rules for electric fields at optical interfaces, the three layer system (mica-sample-mica) yields the following set of equations for normal incident light:

$$i) \quad C = t_{am} A + r_{am} D$$

$$ii) \quad D \exp(-ik\mu_{m1}Y_1) = r_{ms} C \exp(ik\mu_{m1}Y_1) + \left(t_{ms}/M_1\right)G \exp(-ik\mu_s Y_1)$$

$$iii) \quad F \exp(ik\mu_s Y_1) = t_{ms} C \exp(ik\mu_{m1}Y_1) - r_{ms} G \exp(-ik\mu_s Y_1)$$

$$iv) \quad G \exp\left[-ik\mu_s(Y_1 + D)\right] = -r_{sm} F \exp\left[ik\mu_s(Y_1 + D)\right] + t_{sm} N \exp\left[-ik\mu_{m2}(Y_1 + D)\right]$$

$$v) \quad M \exp\left[ik\mu_{m2}(Y_1 + D)\right] = \frac{t_{sm}}{M_2} F \exp\left[ik\mu_s(Y_1 + D)\right] + r_{sm} N \exp\left[-ik\mu_{m2}(Y_1 + D)\right]$$

$$vi) \quad N \exp\left[-ik\mu_{m2}(Y_1 + Y_2 + D)\right] = r_{ma} M \exp\left[ik\mu_{m2}(Y_1 + Y_2 + D)\right]$$

$$vii) \quad W \exp\left[ik\mu_a(Y_1 + Y_2 + D)\right] = t_{ma} M \exp\left[ik\mu_{m2}(Y_1 + Y_2 + D)\right]$$

$$(10)$$

Where subscripts *am* and *ms* represent the air-mica and mica-sample interfaces on the entrance side of the system, and the reverse subscripts represent the same interfaces on the exit side of the system. as given in the above schematic. Variables *r* and *t* are the coefficients of reflection and transmission; specifically, $r_{ms} = \pm\left(\dfrac{\mu_{m1} - \mu_s}{\mu_{m1} + \mu_s}\right)$ and

$r_{sm} = \pm\left(\dfrac{\mu_{m2} - \mu_s}{\mu_{m2} + \mu_s}\right)$ (with the positive sign representing light passing into the sample

layer and the negative sign representing light passing from the sample layer), while

$t_{ms} = \dfrac{2\mu_{m1}}{\mu_{m1} + \mu_s}$ and $t_{sm} = \dfrac{2\mu_{m2}}{\mu_{m2} + \mu_s}$ [343]. Subscripts relating to the indices of refraction,

m1 and *m2*, represent the mica sheet on the entrance and exit side, respectively, while

$M_1 = \dfrac{\mu_{m1}}{\mu_s}$ and $M_2 = \dfrac{\mu_{m2}}{\mu_s}$. Variables *A*, *C*, *D*, *F*, *G*, *M*, *N* and *W* represent the wave

amplitudes at various stages in the system as shown in the above diagram, and $k\mu$ is the

medium's wavenumber (with the medium identified by μ's subscript).

Solving the above seven equations for the eight unknown coefficients yields the following[335, 342, 344]:

$$\left|\frac{W}{A}\right| = \left|\frac{t_{am}\,t_{ma}\,t_{sm}\,t_{ms}}{M_2\,\sigma}\right| \tag{11}$$

where:

$$\sigma = \exp\left[ik\,(\mu_a - \mu_{m1})Y_1\right]\exp\left[ik\,(\mu_a - \mu_{m2})Y_2\right]\exp\left[ik\,(\mu_a - \mu_s)D\right]\cdot$$

$$\cdot\left\{\left[1 - r_{ms}\,r_{am}\,e^{2ik\mu_{m1}Y}\right]\left[1 - r_{sm}\,r_{ma}\,e^{2ik\mu_{m2}Y_2}\right] - e^{2ik\mu_s D}\left[r_{ms} - r_{am}\,e^{2ik\mu_{m1}Y_1}\right]\left[r_{sm} - r_{ma}\,e^{2ik\mu_{m2}Y_2}\right]\right\}$$

The above equation can be simplified somewhat (Horn solves the general case[342], while Hunter et al and Israelachvili provide the simplified version[335, 344]) by the assumption that the mica surfaces are the same thickness and index of refraction (so that $Y = Y_1 = Y_2$ and $\mu_m = \mu_{m1} = \mu_{m2}$, which leads to the additional simplification of $r = r_{ms} = r_{sm}$, $t = t_{ms} = t_{sm}$ and $M = M_1 = M_2$) along with the assumption that the silver surface is 100% reflective (so that $r_{am} = r_{ma} \approx 1$ and $t_{am} = t_{ma} \approx 0$) which means σ reduces to:

$$\sigma = \exp\left[2ik\,(\mu_a - \mu_{m1})Y\right]\exp\left[ik\,(\mu_a - \mu_s)D\right]\left\{\left[1 - r\exp\left(2ik\mu_m Y\right)\right]^2 - \exp\left(2ik\mu_s D\right)\left[r - \exp\left(2ik\mu_m Y\right)\right]^2\right\}$$

Provisions are made during the surface preparation stage to ensure that the above conditions are satisfied (see Section 3.2 for more information). It should be noted that the transmitted amplitude, W, can only be finite for the silvered surface case ($r_{am} = r_{ma} \approx 1$ and $t_{am} = t_{ma} \approx 0$ as assumed above) when $\sigma \approx 0$ (in which case the approximately zero values for the numerator and denominator of Equation (11) balance one another), which corresponds to the constructive interference condition. Since this is only true when σ's braced term is zero, we have:

$$[1 - r \exp{(2 ik \mu_m Y)}]^2 = \exp{(2 ik \mu_s D)}[r - \exp{(2 ik \mu_m Y)}]^2$$

which, after taking the square root of both sides, simplifies to:

$$1 - r \exp{(2 ik \mu_m Y)} = \pm \exp{(ik \mu_s D)}[r - \exp{(2 ik \mu_m Y)}]$$

And with some further rearrangement:

$$\pm \exp{(ik \mu_s D)} = \frac{1 - r \exp{(2 ik \mu_m Y)}}{r - \exp{(2 ik \mu_m Y)}}$$

And, by using Euler's relation ($\exp(ix) = \cos{(x)} + i \sin{(x)}$):

$$\pm [\cos{(k \mu_s D)} + i \sin{(k \mu_s D)}] = \frac{1 - r[\cos{(2 k \mu_m Y)} + i \sin{(2 k \mu_m Y)}]}{r - [\cos{(2 k \mu_m Y)} + i \sin{(2 k \mu_m Y)}]} \tag{12}$$

Before continuing, it is wise to simplify the complex term on the right by multiplying it by the complex conjugate of the denominator to isolate complex components to the numerator:

$$\pm [\cos{(k \mu_s D)} + i \sin{(k \mu_s D)}] = \left\{ \frac{r - \cos{(2 k \mu_m Y)} + i \sin{(2 k \mu_m Y)}}{r - \cos{(2 k \mu_m Y)} + i \sin{(2 k \mu_m Y)}} \right\} \cdot$$

$$\cdot \left\{ \frac{1 - r[\cos{(2 k \mu_m Y)} + i \sin{(2 k \mu_m Y)}]}{r - \cos{(2 k \mu_m Y)} - i \sin{(2 k \mu_m Y)}} \right\}$$

$$\pm [\cos{(k \mu_s D)} + i \sin{(k \mu_s D)}] =$$

$$= \frac{2 r - r^2 \cos{(2 k \mu_m Y)} - i r^2 \sin{(2 k \mu_m Y)} - \cos{(2 k \mu_m Y)} + i \sin{(2 k \mu_m Y)}}{1 - 2 r \cos{(2 k \mu_m Y)} + r^2}$$

By taking the imaginary and real components of both sides of the above, one obtains the following two equations:

$$\pm \sin{(k \mu_s D)} = \frac{- r^2 \sin{(2 k \mu_m Y)} + \sin{(2 k \mu_m Y)}}{1 - 2 r \cos{(2 k \mu_m Y)} + r^2} \qquad \text{for the imaginary part, and;}$$

$$\pm \cos{(k \mu_s D)} = \frac{2 r - r^2 \cos{(2 k \mu_m Y)} - \cos{(2 k \mu_m Y)}}{1 - 2 r \cos{(2 k \mu_m Y)} + r^2} \qquad \text{for the real part.}$$

Dividing the imaginary component by the real component simplifies the relation somewhat:

$$\tan\left(k\mu_s D\right) = \frac{-r^2\sin\left(2k\mu_m Y\right) + \sin\left(2k\mu_m Y\right)}{2r - r^2\cos\left(2k\mu_m Y\right) - \cos\left(2k\mu_m Y\right)}$$

$$\tan\left(k\mu_s D\right) = \frac{\left(1 - r^2\right)\sin\left(2k\mu_m Y\right)}{2r - \left(1 + r^2\right)\cos\left(2k\mu_m Y\right)} \tag{13}$$

One can render the above equation more useful from an experimental point of view by converting the mica thickness (which often isn't known beforehand) to FECO wavelengths by noting that when the gap size, D (and hence the left hand side of Equation (13)), is zero, the sine term on the right hand side must also be zero also (note that $r^2 \neq 1$ generally) and therefore:

$$2k_0\mu_m Y = n\pi \tag{14}$$

where k_0 is angular wavelength of transmitted light at contact ($k_0 = 2\pi / \lambda_n^0$). Hence:

$$2\mu_m Y = n\pi/k_0 = n\lambda_n^0/2$$

If the mica surfaces are separated to a gap size of T, so that $k = 2\pi/\lambda$, the new interference condition must then be:

$$2k\mu_m Y = \left(2\mu_m Y\right)(k) = \left(\frac{n\lambda_n^0}{2}\right)\left(\frac{2\pi}{\lambda_n}\right)$$

$$2k\mu_m Y = n\pi\left(1 - \frac{\lambda_n - \lambda_n^0}{\lambda_n}\right) = n\pi\left(1 - \frac{\Delta\lambda_n}{\lambda_n}\right) \tag{15}$$

Recalling that Equation (15) represents the angle in the trigonometric functions of Equation (13) and noting that $\sin\left(n\pi - \theta\right) = \left(-1\right)^{n+1}\sin\theta$ while $\cos\left(n\pi - \theta\right) = \left(-1\right)^{n}\cos\theta$

for positive integer values of n, Equation (13) can then be simplified using the four

possible simplifications (i.e. odd and even values of n for each equation):

$$\tan\left(k\mu_s D\right) = \frac{\pm\left(1 - r^2\right)\sin\left(n\pi\Delta\lambda_n/\lambda_n\right)}{2r \pm \left(1 + r^2\right)\cos\left(n\pi\Delta\lambda_n/\lambda_n\right)}$$

Or, multiplying the right hand side of the above equation by $\pm 1/\pm 1$:

$$\tan\left(k\mu_s D\right) = \frac{\left(1 - r^2\right)\sin\left(n\pi\Delta\lambda_n/\lambda_n\right)}{\pm 2r + \left(1 + r^2\right)\cos\left(n\pi\Delta\lambda_n/\lambda_n\right)} \tag{16}$$

Recalling the definition of r, $r = \dfrac{\mu_m - \mu_s}{\mu_m + \mu_s} = \dfrac{\bar{\mu} - 1}{\bar{\mu} + 1}$, the above equation can be rewritten in

terms of indices of refraction:

$$\tan\left(k\mu_s D\right) = \frac{\left[1 - \left(\dfrac{\bar{\mu} - 1}{\bar{\mu} + 1}\right)^2\right]\sin\left(\dfrac{n\pi\Delta\lambda_n}{\lambda_n}\right)}{\pm 2\left(\dfrac{\bar{\mu} - 1}{\bar{\mu} + 1}\right) + \left[1 + \left(\dfrac{\bar{\mu} - 1}{\bar{\mu} + 1}\right)^2\right]\cos\left(\dfrac{n\pi\Delta\lambda_n}{\lambda_n}\right)} \tag{17}$$

By multiplying the right hand side by $\left(\bar{\mu} + 1\right)^2/\left(\bar{\mu} + 1\right)^2$ and noting that

$\left(\bar{\mu} + 1\right)^2 - \left(\bar{\mu} - 1\right)^2 = 4\bar{\mu}$, $\left(\bar{\mu} + 1\right)^2 + \left(\bar{\mu} - 1\right)^2 = 2\left(\bar{\mu}^2 + 1\right)$ and $2\left(\bar{\mu} - 1\right)\left(\bar{\mu} + 1\right) = 2\left(\bar{\mu}^2 - 1\right)$,

the above equation reduces to:

$$\tan\left(k\mu_s D\right) = \frac{2\bar{\mu}\sin\left(n\pi\Delta\lambda_n/\lambda_n\right)}{\pm\left(\bar{\mu}^2 - 1\right) + \left[1 + \bar{\mu}^2\right]\cos\left(n\pi\Delta\lambda_n/\lambda_n\right)} \tag{18}$$

The two solutions manifest themselves physically in the form of FECO doublets

representing the ordinary and extraordinary indices of refraction. An example of this

FECO pattern is shown in Figure 2.16:
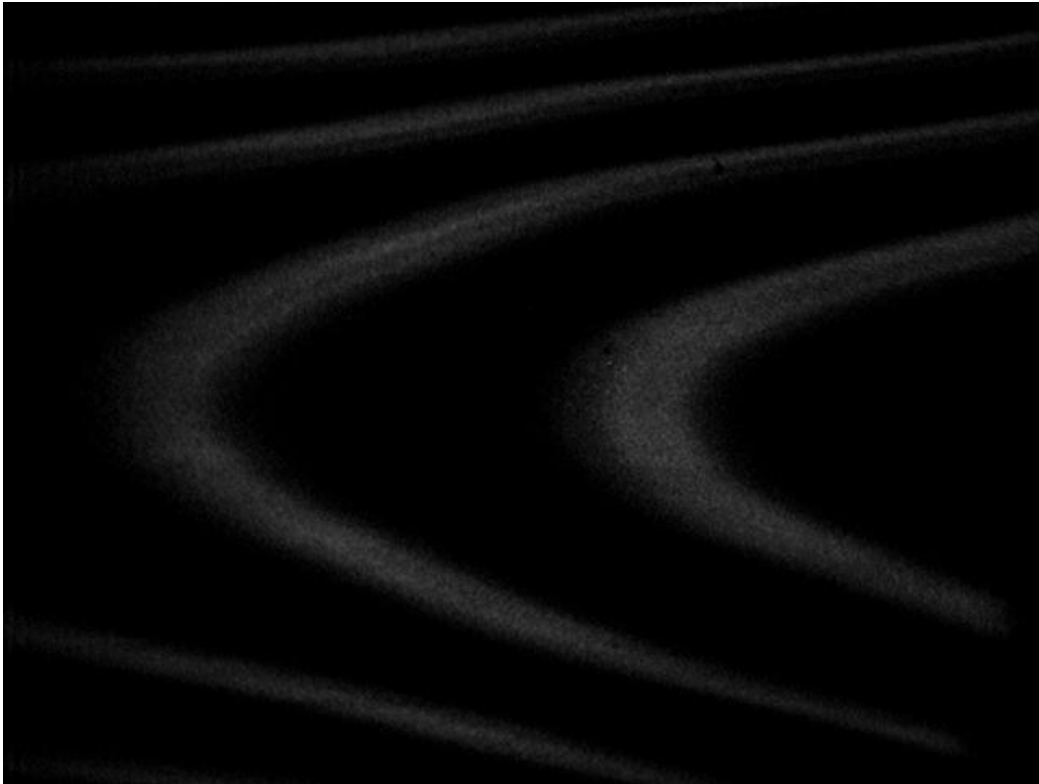
Figure 2.16: Example of Fringes of Equal Chromatic Order (FECO)

In the above figure, the doublet is not well defined, but can be discerned somewhat above the crests of each of the two pictured fringes, which represent the point of closest approach between the confining surfaces. In the above picture, the vertical direction represents the lateral distance from this point and the horizontal direction represents the wavelength of light passing through the surfaces. A diagram of FECO, showing them both with some separation between the surfaces and when the surfaces make contact with one another, is shown in Figure 2.17 (here the doublets are omitted for simplification):
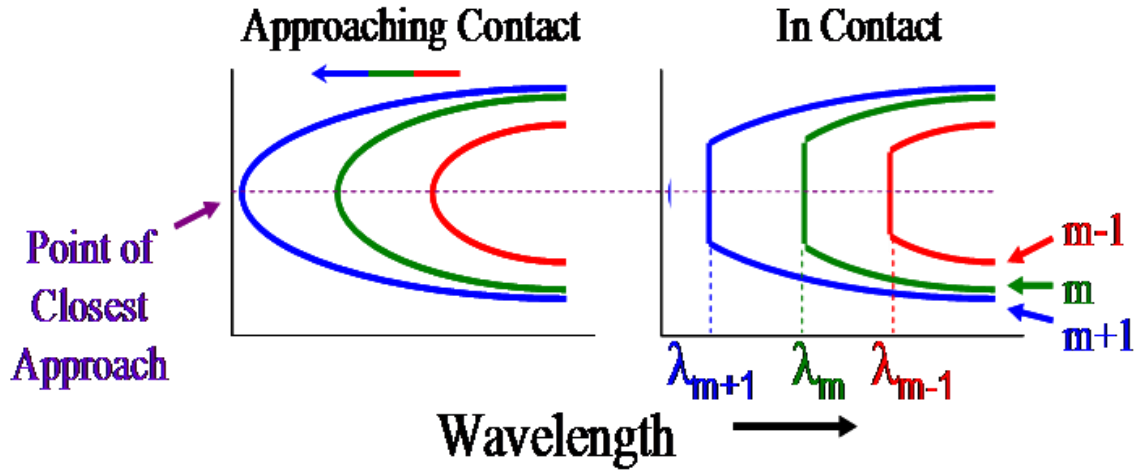
Figure 2.17: A Diagram of FECO for (left) surfaces that are out of contact and (right) surfaces that are in contact.

As can be seen in the diagram on the right, the FECO shift upward in wavelength (manifesting as a leftward shift on spectrometric output) and ultimately flatten upon coming into contact with one another. This latter effect is understandable since the surfaces are flattening at the point of closest approach, resulting in an expanding area within which all three-film interferometer parameters are identical and thereby produce identical interference patterns.

2.3 2 Calculation of Separation and Refractive Index Using the Three-Film Interferometry Equation

From the interferometry equation given by Israelachvili[335], first derived by Hunter and Nabarro[344] and re-derived in the previous section, the size of separation and index of refraction at the point of closest approach between two surfaces varies with FECO fringe position in the following way:

$$
\tan\left(\frac{2\pi\mu_s D}{\lambda_n^D}\right) = \frac{2\,\overline{\mu}\,\sin\left\{\left[\left(1 - \lambda_n^0/\lambda_n^D\right)\middle/\left(1 - \lambda_n^0/\lambda_{n-1}^0\right)\right]n\,\pi\right\}}{\left(1 + \overline{\mu}^2\right)\cos\left\{\left[\left(1 - \lambda_n^0/\lambda_n^D\right)\middle/\left(1 - \lambda_n^0/\lambda_{n-1}^0\right)\right]n\,\pi\right\} \pm \left(\overline{\mu}^2 - 1\right)}
\tag{19}
$$

157

where D is the size of separation between the surfaces, $\overline{\mu} = \dfrac{\mu_m}{\mu_s}$ is the ratio of indices of

refraction of mica, μ_m, and the sample at distance D, μ_s, and λ is the FECO wavelength all

measured at the point of closest approach. Wavelength subscripts refer to the order of the

measured fringe (note that the n and n-1 implies that two *neighbouring* fringes must be

tracked to obtain a value of D and μ_s), while superscripts 0 and D refer to wavelength

measurements with surfaces in contact and at the desired separation, respectively.

For small separations ($D \lessapprox 30$ nm) the small angle approximation ($\sin \theta \approx \tan \theta \approx \theta$

and $\cos \theta \approx 1$) may be applied, reducing the above equation to:

$$\frac{2\pi\mu_s D}{\lambda_n^D} \approx \frac{2\overline{\mu}\left[n\left(1 - \lambda_n^0/\lambda_n^D\right)/\left(1 - \lambda_n^0/\lambda_{n-1}^0\right)\pi\right]}{\left(1 + \overline{\mu}^2\right)(1) \pm \left(\overline{\mu}^2 - 1\right)}$$

Note that non-subscript n in the above equation comes about due to the N possible integer

solutions to the sine in the numerator, corresponding to the N FECO fringes in the

interference pattern. Here n represents one of the integer solutions, and hence the nth

fringe. With some factoring, the equation becomes:

$$\frac{2\pi\mu_s D}{\lambda_n^D} \approx \frac{2\overline{\mu}\left[n\lambda_{n-1}^0\left(1 - \lambda_n^0/\lambda_n^D\right)/\left(\lambda_{n-1}^0 - \lambda_n^0\right)\pi\right]}{\left(1 + \overline{\mu}^2\right)(1) \pm \left(\overline{\mu}^2 - 1\right)} \tag{20}$$

Introducing the ratio:

$$F_n = \frac{\lambda_{n-1}^0}{\lambda_{n-1}^0 - \lambda_n^0} \tag{21}$$

one can rewrite the above as:

$$\frac{2\pi\mu_s D}{\lambda_n^D} = \frac{2\overline{\mu}\left[nF_n\left(1 - \lambda_n^0/\lambda_n^D\right)\right]\pi}{1 + \overline{\mu}^2 \pm \left(\overline{\mu}^2 - 1\right)}$$

so that D becomes:

$$D = \frac{\overline{\mu}}{\mu_s} \left\{ \frac{nF_n \left(1 - \lambda_n^0 / \lambda_n^D \right) \lambda_n^D}{1 + \overline{\mu}^2 \pm \left(\overline{\mu}^2 - 1\right)} \right\}$$

$$D = \frac{\overline{\mu}}{\mu_s} \left\{ \frac{nF_n \left(\lambda_n^D - \lambda_n^0 \right)}{1 + \overline{\mu}^2 \pm \left(\overline{\mu}^2 - 1\right)} \right\} \tag{22}$$

And so, for n odd (that is, when ± is negative):

$$D = \frac{\overline{\mu}}{\mu_s} \left\{ \frac{nF_n \left(\lambda_n^D - \lambda_n^0 \right)}{1 + \overline{\mu}^2 + \overline{\mu}^2 - 1} \right\}$$

$$D = \frac{1}{\mu_s \overline{\mu}} \left\{ \frac{nF_n \left(\lambda_n^D - \lambda_n^0 \right)}{2} \right\}$$

$$D = \frac{nF_n \left(\lambda_n^D - \lambda_n^0 \right)}{2\mu_m} \tag{23}$$

while for n even (when ± is positive):

$$D = \frac{\overline{\mu}}{\mu_s} \left\{ \frac{nF_n \left(\lambda_n^D - \lambda_n^0 \right)}{1 + \overline{\mu}^2 - \overline{\mu}^2 + 1} \right\}$$

$$D = \frac{\overline{\mu} nF_n \left(\lambda_n^D - \lambda_n^0 \right)}{2\mu_s}$$

$$D = \frac{nF_n \left(\lambda_n^D - \lambda_n^0 \right) \mu_m}{2\mu_s^2} \tag{24}$$

So that, knowing the index of refraction of the mica being used and by measuring two adjacent fringe positions at contact and at the desired surface separation, one can make an accurate determination of the separation. For the most accurate results and for very small spacings, measuring the mica index of refraction directly (via Abbé Refractometer, say) is recommended, but in general mica will fall into one of two categories[337]: Reddish or brownish mica, with refractive indices of:

159

$$\mu_\gamma = 1.5846 + 4.76 \times 10^5 / \lambda^2$$

$$\mu_\beta = 1.5794 + 4.76 \times 10^5 / \lambda^2$$

and greenish mica, with refractive indices of:

$$\mu_\gamma = 1.5953 + 4.76 \times 10^5 / \lambda^2$$

$$\mu_\beta = 1.5907 + 4.76 \times 10^5 / \lambda^2$$

All wavelengths here are measured in Angstroms. The γ and β subscripts refer to the slow and fast components for light transmission within mica, which is birefringent. The mean values for reddish or brownish and greenish mica are $\mu_\gamma = 1.5820 + 4.76 \times 10^5 / \lambda^2$ and $\mu_\gamma = 1.5930 + 4.76 \times 10^5 / \lambda^2$, respectively.

The index of refraction of the sample can be calculated using Equations (23) and (24) by using two neighbouring fringes of order n and n-1, so that, while Equation (23) remains n^{th} order, Equation (24) shifts by one and so becomes

$$D = \frac{(n-1)F_{n-1}\left(\lambda_{n-1}^D - \lambda_{n-1}^0\right)\mu_m}{2\mu_s^2}.$$ Equating the distances for Equations (23) and (24) gives:

$$D = \frac{nF_n\left(\lambda_n^D - \lambda_n^0\right)}{2\mu_m} = \frac{(n-1)F_{n-1}\left(\lambda_{n-1}^D - \lambda_{n-1}^0\right)\mu_m}{2\mu_s^2}$$

$$\therefore \mu_s^2 = \frac{(n-1)F_{n-1}\left(\lambda_{n-1}^D - \lambda_{n-1}^0\right)}{nF_n\left(\lambda_n^D - \lambda_n^0\right)}\mu_m^2$$

$$\mu_s = \sqrt{\frac{(n-1)F_{n-1}\left(\lambda_{n-1}^D - \lambda_{n-1}^0\right)}{nF_n\left(\lambda_n^D - \lambda_n^0\right)}}\mu_m \tag{25}$$

It should be noted that since $F_{n-1} = \dfrac{\lambda_{n-2}^0}{\lambda_{n-2}^0 - \lambda_{n-1}^0}$, it is necessary for *three* neighbouring fringe wavelengths (n, n-1 and n-2) to be measured with surfaces in contact, along with

160

two fringe wavelengths (*n* and *n-1*) with surfaces separated, for a calculation of index of refraction to be done.

2.3.3 Phase Changes and Dispersion in the Three-Layer Interferometer

While Equation (18) is an adequate approximation of a three-layer system in theory, in practice it does not account for dispersion and phase changes upon reflection at the interfaces.   Israelachvili provides a method of determining gap separation by using the inherent dispersive quality of mica along with the phase change upon reflection of light at the mica-silver interface[335]. Together, the two will produce a shift in the fringe wavelengths that is indistinguishable from that produced by the gap separation, so that the interference condition given by the left hand side of Equation (14) must be re-written:

$$\frac{2\pi\mu_n d_n}{\lambda_n^0} = n\pi \tag{26}$$

and

$$\frac{2\pi\mu_{n+1} d_{n+1}}{\lambda_{n+1}^0} = (n+1)\pi \tag{27}$$

where *d* represents an effective distance made up of the total thickness of both mica sheets, *D*, added to the artificial distance due to the wavelength shift upon reflection, Φ:

$$d = D + \Phi$$

while subscripts *n* and *n+1* reinforce the notion that both μ and d are dispersive quantities depending on wavelength, the latter due solely to the dispersive nature of the phase change itself[335, 337].

One can handle the three experimental parameters' dispersive effects by constructing

equations incorporating their respective shifts. For example, the indices of refraction are

related in the following way:

$$\mu_{n+1} = \mu_n \left[1 + \frac{\mu_{n+1}}{\mu_n} - 1 \right]$$

$$= \mu_n \left[1 + \frac{(\mu_{n+1} - \mu_n)}{\mu_n} \right]$$

$$= \mu_n \left[1 + \frac{\Delta \mu}{\mu_n} \right] \tag{28}$$

where $\Delta \mu = \mu_{n+1} - \mu_n$ is the shift in index of refraction due to dispersion. A similar

derivation for the effective thickness gives:

$$d_{n+1} = d_n \left[1 + \frac{\Delta d}{d_n} \right] \tag{29}$$

while for wavelength:

$$\frac{1}{\lambda_{n+1}^0} = \frac{1}{\lambda_n^0} \left[1 + \frac{\lambda_n}{\lambda_{n+1}} - 1 \right]$$

$$= \frac{1}{\lambda_n^0} \left[1 + \frac{\lambda_n - \lambda_{n+1}}{\lambda_{n+1}} \right]$$

$$= \frac{1}{\lambda_n^0} \left[1 - \frac{\Delta \lambda}{\lambda_{n+1}^0} \right] \tag{30}$$

Substituting Equations (28) through (30) into Equation (27), the interference condition

may be written as:

$$\frac{2\pi\mu_{n+1} d_{n+1}}{\lambda_{n+1}^0} = \frac{2\pi\mu_n d_n}{\lambda_n^0} \left(1 + \frac{\Delta \mu}{\mu_n} \right) \left(1 + \frac{\Delta d}{d_n} \right) \left(1 - \frac{\Delta \lambda}{\lambda_{n+1}^0} \right)$$

which, assuming 1st and 2nd order terms dominate over others, approximates to:

$$\frac{2\pi\mu_{n+1}d_{n+1}}{\lambda^0_{n+1}} = \frac{2\pi\mu_n d_n}{\lambda^0_n}\left(1 + \frac{\Delta\mu}{\mu_n} + \frac{\Delta d}{d_n} - \frac{\Delta\lambda}{\lambda}\right)$$

and, substituting (19), simplifies to:

$$\frac{2\pi\mu_{n+1}d_{n+1}}{\lambda^0_{n+1}} = n\pi\left(1 + \frac{\Delta\mu}{\mu_n} + \frac{\Delta d}{d_n} - \frac{\Delta\lambda}{\lambda}\right)$$

$$= n\pi\left\{1 - \frac{\Delta\lambda}{\lambda}\left[1 - \frac{\lambda}{\Delta\lambda}\left(\frac{\Delta\mu}{\mu_n} + \frac{\Delta d}{d_n}\right)\right]\right\}$$

Making a further approximation that the index of refraction and effective thickness shifts are small and due solely to dispersion gives:

$$\frac{2\pi\mu_{n+1}d_{n+1}}{\lambda^0_{n+1}} = n\pi\left\{1 - \frac{\Delta\lambda}{\lambda}\left[1 - \frac{\lambda}{\mu_n}\cdot\frac{\partial\mu}{\partial\lambda} - \frac{\lambda}{d_n}\cdot\frac{\partial d}{\partial\lambda}\right]\right\}$$

The factor F (introduced previously as an arbitrary fringe shift) can here be inserted to more quantitatively define the dispersive nature of the interference pattern:

$$\frac{2\pi\mu_{n+1}d_{n+1}}{\lambda^0_{n+1}} = n\pi\left\{1 - \frac{\Delta\lambda}{\lambda}F\right\} \qquad (31)$$

where:

$$F = 1 - \frac{\lambda}{\mu_n}\cdot\frac{\partial\mu}{\partial\lambda} - \frac{\lambda}{d_n}\cdot\frac{\partial d}{\partial\lambda}$$

Bailey and Kay[345] and Eisner[346] give values for dispersive quantities $\frac{\partial\mu}{\partial\lambda}$ and $\frac{\partial d}{\partial\lambda}$, respectively, so that for the nth fringe at a wavelength of 5500 Å, F_n will be approximately[335]:

$$F_n \approx 1.024 + 1/n \qquad (32)$$

Combining the above estimation for F_n with the original definition from Equation (21):

$$F_n = \frac{\lambda^0_{n-1}}{\lambda^0_{n-1} - \lambda^0_n}$$

(33)

allows one, with a measurement of adjacent contact fringes λ^0_{n-1} and λ^0_n, to determine the fringe order, n[335, 337].

Comparing Equations (15) and (31) shows that in order to incorporate phase changes and dispersion effects (embodied in the corrective term, F_n), one need only multiply $\Delta\lambda/\lambda_n$ by F_n. With this in mind, Equation (18) can be easily modified to account for these factors, leading to:

$$\tan\left(k\mu_s D\right) = \frac{2\bar{\mu}\sin\left(n\pi\Delta\lambda_n F_n/\lambda_n\right)}{\pm\left(\bar{\mu}^2 - 1\right) + \left[1 + \bar{\mu}^2\right]\cos\left(n\pi\Delta\lambda_n F_n/\lambda_n\right)}$$

Noting that $\dfrac{\Delta\lambda_n F_n}{\lambda_n} = \left(\dfrac{\lambda_n - \lambda^0_n}{\lambda_n}\right)\left(\dfrac{\lambda^0_{n-1}}{\lambda^0_{n-1} - \lambda^0_n}\right) = \dfrac{\left(1/\lambda_n\right)\left(\lambda_n - \lambda^0_n\right)}{\left(1/\lambda^0_{n-1}\right)\left(\lambda^0_{n-1} - \lambda^0_n\right)} = \dfrac{1 - \lambda^0_n/\lambda_n}{1 - \lambda^0_n/\lambda^0_{n-1}}$, the above

equation becomes:

$$\tan\left(k\mu_s D\right) = \frac{2\bar{\mu}\sin\left(n\pi\left(1 - \lambda^0_n/\lambda_n\right)/\left(1 - \lambda^0_n/\lambda^0_{n-1}\right)\right)}{\pm\left(\bar{\mu}^2 - 1\right) + \left[1 + \bar{\mu}^2\right]\cos\left(n\pi\left(1 - \lambda^0_n/\lambda_n\right)/\left(1 - \lambda^0_n/\lambda^0_{n-1}\right)\right)}$$

(34)

which is identical to Equation (19), noting that $\lambda_n \equiv \lambda^D_n$. From Equation (34) various relatively simple methods of determining the gap size, D, and the sample's index of refraction, μ_s, may be derived, as explained in the previous section.

2.4 Automation of the Surface Forces Apparatus

Because of the considerable sensitivity of the strain gauge and surface position to temperature changes, it is desirable to have a well-configured PID temperature controller within the SFA room to ensure long-term stability. Such a system usually does little to control temperature on short time scales, however, and so for those tests which require a quick start after setup, even the brief presence of an experimenter in the SFA chamber can greatly compromise experimental results. Ultimately the simplest way to avoid thermal fluctuations of this sort is to avoid entering the SFA room altogether during testing, but to do this a fully automated system must be in place to control all instruments within the room by a computer located outside the room. Because of the relative sophistication of the Surface Forces Apparatus, this can be a daunting task. The following chapter details the equipment and software developed to automate the tests presented in this thesis.

2.4.1 The Electronics Relay Box

The standard SFA package provided by Surforce Corporation consists of several parts that are to be controlled electronically. Two stepper motors, one attached to the fine micrometer and one to the Friction Device, have as outputs five pin LEMO connectors, along with separate encoder outputs. Both the prism swivel motion and the focusing lens position are controlled via similar connections. Two electric heaters (not used in the present tests) each have a one pin connector. These devices are all to be controlled by a single unit, the SFA2000 control panel, supplied by Surforce Corporation. Because of

the shortness of the cables, the panel must stay near the SFA, making remote control of the machine impossible. It is therefore desirable for tests in which temperature must be maintained even at short times that a remote system be developed.

The S&D-096 relay box has been designed to accommodate all of the standard inputs and outputs to the SFA unit. A feed-through box with identical connectors on both sides passes cables through the insulation box to minimize the effect of the room's air currents on the SFA unit. There are three types of outputs from the relay box:

i)   A 25-pin D-connector, links the S&D-096 to the National Instruments BNC-2110 connector block, which in turn links it to the remote computer via a National Instruments 6036E Data Acquisition card, and handles all digital controls;

ii)   Two BNC analog controls also connect to the BNC-2110 and manage the speeds of the two stepper motors;

iii)   Various other connectors link the S&D-096 to the SFA2000 control panel and act as a feed-through should the user wish to control the SFA manually. A toggle on the S&D-096 allows the user to switch easily from manual to automatic operation.

The remote computer also controls the acquisition of data. The strain gauge output can be obtained either directly from the Signal Conditioning Amplifier, or from the Lock-in Amplifier. In both cases the output is fed into the BNC-2110 connector block; with the former setup, a single coaxial cable is used, and with the latter, two are used, one for the

amplitude channel and one for the phase channel. To obtain the phase information directly with the former setup, a cable splitter splits the driving signal both to the SFA (via the appropriate Trek Amplifier, if necessary) and to the BNC-2110 connector block so that it can be compared directly to the response.

2.4.2 Miscellaneous Equipment

There will usually be supplementary equipment present during an SFA experiment as well:

i)   Often a thermistor is placed near to the surfaces to measure temperature there, and so a thermistor line will frequently be present. Automation can easily be done by using a thermistor controller connected to the thermocouple line, with output readings sent directly to the BNC-2110 connector block via coaxial cable.

ii)   If a camera is being used, it too can be automated to provide video or snapshots of the FECO at whatever rate is desired. In the present setup, a Retiga Exi QImaging Fast 1394 camera with FireWire output has been used; it is connected to the remote computer via a single Sewell SW-1101 FireWire Active Extension cable. It should be noted that while IEEE 1394 specifications demand FireWire cables be less 4.5 meters in length, they are nevertheless still very reliable up to 18 meters when chained together.

iii)   A lock-in amplifier is often of considerable use in experiments where viscoelastic properties of sheared materials are being studied, in order to extract phase information from the shear response. The lock-in amplifier is

167

capable of extracting periodic signals as low as a few nanovolts from noisy input signals so long as the frequency of the signal is well-known[347]. It does this by use of the technique of phase-sensitive detection (PSD), which involves multiplying two signals (in the SFA's case, the amplified strain gauge output and the function generator's sync output, which contains the exact phase and frequency of the input signal) and filtering the resultant AC signal with a low-pass filter. The resultant filtered signal will be a DC signal output representing the amplitude occurring specifically at the sync frequency. A second PSD allows for the extraction of the phase between the two signals as well, and so the dual-phase lock-in amplifier can output both the shear response amplitude and phase. One significant drawback to this technique is that an accurate output is only possible after a full cycle has elapsed (since the PSD output is averaged over a full cycle), and so for low frequency tests like those presented in this thesis, in which intra-period phenomena may occur, especially early on, vital information from early on in the shearing process may be lost. As a result, the Stanford Research Systems SR830 lock-in amplifier programmed to run with the SFA was not used to collect the data presented in this thesis.

iv) An oscilloscope can also be used to collect shear data outputted from the Signal Conditioning Amplifier, and is particularly useful for higher frequency experiments (10-200 Hz), where the data rate needed to give detail to a single cycle may be greater than that capable by a standard data acquisition card. Large amounts of high frequency shear data can be collected by the

oscilloscope and outputted to the computer by GPIB. For the current setup, an

Agilent 54621A was available, which has two million data points per channel

available in memory.   Because the highest shear frequency used with the tests

presented here was 10 Hz and the DAQ card data rate was 500 points/second,

yielding a satisfactory 50 points per cycle at the highest shear frequency

tested, the oscilloscope was not needed and hence was not used.

v)   Finally, the two encoders located in the stepper motors can also be automated

and controlled directly by remote computer. This can be achieved by

installing a US Digital PCI-4E PCI Interface card in the remote computer and

reading the encoder output directly. It may be necessary to use cable drivers

to synchronize the encoders with the card.

The Signal Conditioning Amplifier's Wheatstone bridge tends to drift over time from

its perfectly balanced state, and so periodic re-balancing is recommended to optimize its

sensitivity. The amplifier can be balanced manually by toggling the AMP BAL switch

(note that the SFA must be connected to the Signal Conditioning Amplifier and the

desired Excitation must be selected during the balancing), but the switch cannot be

accessed remotely. Another balancing method does exist, however: Intertechnology Inc.

manufactures an Option Y Relay Kit that can be installed in the Signal Conditioning

Amplifier. The kit will allow not only the Bridge Balance to be reset, but will also allow

the Excitation to be toggled off and on, and will adjust the shunt calibration if necessary.

It should be noted that the Excitation toggle allows the user to check the amplifier

balance without entering the SFA room, since by switching it off one can see how well-zeroed the response is by checking via LabVIEW.

The Option Y Relay Kit requires a 5 Vdc (10 mA for Balance and Shunt Calibration, and 25 mA for Excitation) trigger. The RESET line (which governs the Balance switch) must be triggered for a minimum of 50 milliseconds, after which the Auto Balance will commence. A box has been designed which will trigger any of the three switches via the BNC-2110 connector block digital output.

2.4.3 Control Software

LabVIEW software has been developed to control each of the above components, each with its own asynchronous loop cycling every 200 ms (or faster, if needed). Five digital controls (5V TTL) are used to control the fine focusing control micrometer and prism turntable motors on the Optics Stand, as well as the fine micrometer and friction device motors (the latter of which has been converted to be used with the differential micrometer). Control of this equipment is achieved by passing the digital controls to the aforementioned S&D-096 unit via the BNC-2110 connector block, and then on to the various SFA components themselves. The table of correspondences between digital signals and device triggers is shown below, with Motor1 and Motor2 here referring to the stepper motors controlling the two micrometers and hence controlling the gap size:

Table 2.1: Digital settings for the SFA Focus, Prism and Motor controls

D1	D2	D3	D4	Focus Up	Focus Down	Prism Left	Prism Right	Motor 1 In	Motor 1 Out	Motor 2 In	Motor 2 Out
0	0	0	0	0	0	0	0	0	0	0	0
1	0	0	0	1	0	0	0	0	0	0	0
1	0	0	1	0	1	0	0	0	0	0	0
1	0	1	0	0	0	1	0	0	0	0	0
1	0	1	1	0	0	0	1	0	0	0	0
1	1	0	0	0	0	0	0	1	0	0	0
1	1	0	1	0	0	0	0	0	1	0	0
1	1	1	0	0	0	0	0	0	0	1	0
1	1	1	1	0	0	0	0	0	0	0	1

2.4.4 Automated Calculation of Fringes

The first step of the automation process involves a While Loop stepping through values of n that compares equations (32) and (33) and terminates when the ith iteration difference between equations is larger than that of the previous iteration, thereby finding the order of the fringes that are on screen. Once these are determined and the further experimental values λ^0_{n-2}, λ_n and λ_{n-1} are collected (the latter two by moving the surfaces to their non-contact positions), the separation and index of refraction may be calculated using equations (23) and (24). The calculation of the wavelengths from their on-screen position is easily achieved by first calibrating the camera's pixel to wavelength ratio, $C_{p\lambda}$, using a light source with a well-defined doublet, such as sodium's 5895.932 Å and 5889.963 Å doublet[348, 349] (see Section 3.1.2 for details). One must then compare the light source to a fixed point on the spectrometer to determine the offset, ϕ, between them. One can then, by recording the pixel positions of each fringe, N_p, find its wavelength by referencing it to the calibration wavelength:

$$\lambda = C_{p\lambda} N_p + \phi \tag{28}$$

2.4.5 LabVIEW Control of the SFA and its Peripherals

The SFA has several components and peripherals that are controllable remotely by a computer fitted with an encoder board (to monitor the stepper motors) and a connector block (to send and receive digital and analog signals). Software (entitled *SFA Control Panel*, with various suffixes to represent its stages of development) has been written to control the bimorph and piezo mounts (via a function generator), stepper motors, camera and lock-in amplifier, as well as to monitor the strain gauges (via the signal conditioning amplifier), camera, lock-in amplifier, thermistor and optical encoders for the stepper motors. The code was broken into four asymmetric control loops, one for the camera, one for the encoders, one for reading data from the equipment and one for the both the function generator and the various controls discussed in the table of correspondences above (Table 2.1). Each will be discussed briefly below.

Because each SFA trigger requires a unique digital signal, only one component can be used at any one time, and so the first step of the SFA controls loop is to construct a Boolean array made up of buttons from the front panel representing the various components. After a check to ensure only a single button has been pressed (if there are more than one, all digital signals are reset to zero, thereby stopping all digitally-controlled SFA components), the appropriate digital signal is sent to the S&D 096 unit via the connector block. An analog input for the stepper motor amplitude is also read in if the digital signature indicates either motor has been triggered, with a maximum voltage

of 10 V being allowed. A safety button can also be found on the front panel which will override all other controls and switch off all digital signals, setting all analog inputs to 0 V. The function generator controls also execute each time the loop cycles, if they are triggered by the user using controls available on the front panel. The user must input a waveform from a dropdown menu with eleven possible choices, the most popular being DC offset, sine wave, triangular wave and square wave. The user must also input a frequency, amplitude and offset if they are applicable to the waveform selected. To protect the SFA and its peripheral equipment, if the sum of the amplitude and the absolute value of the voltage offset selected is greater than that allowable for a given component (often needed for the Bimorph Slider, for example, which has a maximum applied voltage of ± 50 V[337]) a popup window will appear warning the user while the amplitude is reset to 0 V. A setting on the front panel allows the user to select what component they are using (e.g. Bimorph, Piezo Mount) so that the program knows which voltage limit to apply. The same provisions have been made for the input frequency, as some components have limits on this parameter (e.g. the Bimorph Slider, which has an effective upper limit of 200 Hz). All signals are sent to the function generator by GPIB cable and connectors.

The data-reading loop runs every 0.2 seconds by default, but this value is adjustable by the user using a control on the front panel. The thermistor, signal conditioning amplifier output (containing the amplified shear response), lock-in amplifier outputs R and θ, and the function generator output are all monitored and, if the user clicks a button on the front panel, records all input data to a text file in a folder selected by the user.

Alternate versions of the *SFA Control Panel* software allow the user to collect either the thermistor data or the strain gauge data using a Keithley multimeter (the data of which is sent to the computer via GPIB), which allows for some flexibility in the experimental setup. A toggle on the front panel allows the user to convert the incoming shear response data from voltage to deflection and, if the lock-in amplifier is being used, from the θ value outputted as a voltage to a value in degrees.

The camera control loop cycles by default every 0.2 seconds while the Camera Control button is switched off. When it is triggered the camera is initiated, with the exposure time, the number of bits (8-bit or 16-bit) and the binning set by the user from the front panel, and switches to a non-time delayed loop (to capture video in real time, if desired) after creating an image buffer. The camera settings can be changed at any time while it is running, and the user can take snapshots of the onscreen image showing on the front panel, which are saved to a location chosen by the user. The files are saved in Portable Network Graphics (png) format, which provides lossless data compression of the image, although other formats are available if desired.

The encoder control loop cycles every 0.2 seconds by default, but can be altered on the front panel. Once the encoders are activated by a button on the front panel, they are first either reset or left at their last-used value (chosen by the user via a button). The encoders are then prompted for their count position (out of a possible 30 000 counts) using software developed by the author. With the stepper motors attached to the fine and differential micrometers (the configuration used to collect the data used in this

dissertation as discussed in Section 2.1.3), the count values are converted to separation

values (see Figure 2.18) and the two micrometer encoder-read separation values are

added together to give the total separation, updated every cycle.
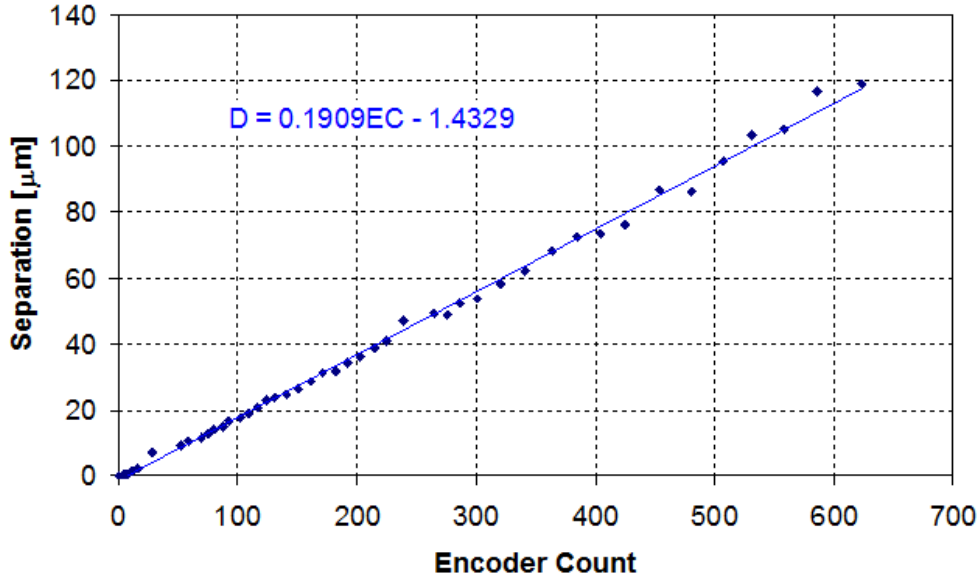
Figure 2.18: Plot of Separation as a Function of Encoder Count for the Encoders used in
the SFA

The encoders can be reset at any time during operation, and the separation is updated on a

graph displayed on the front panel and can be saved to a location provided by the user at

any time.

2.4.6 Agitation and Test Software

Two programs were written, borrowing liberally from the SFA Control Panel program

written by the author (discussed in the previous section), to agitate the liquid crystal

sample so that any orientation that may have occurred due to shear during the previous

run will be destroyed, and to set up the shear test discussed in the Experimental

Parameters and Procedure section. The first program, named *Sample Agitation*, contained three asynchronous loops. The first loop is an algorithm comprised of three sequences. The first sequence triggers the differential micrometer motor so that it separates the surfaces out to a point set by the user. The second reverses the motor and executes an in-out motion for the surfaces N times (N set by the user, typically 10 times for the experiments discussed here) with a preset amplitude. The third brings the surfaces back to 100 nm separation, the distance chosen as it was found to be close to surface-surface contact (where all test runs must necessarily begin, in order to establish a contact reference position) but far enough apart that if a malfunction was to occur the user would have enough time to stop the program before damage of the surface or equipment should occur. The second loop is identical to the encoder loop discussed in the Section 2.4.5, which cycles every 0.2 seconds and determines the separation of the surfaces, which is then compared to the set motor reversal point in the first loop so that it may determine the point at which to switch directions. The third loop is simply the camera loop also discussed in the previous section, with both loops triggered automatically at the onset of the program. The camera is used to observe the region between the surfaces. In general at the separations used throughout agitation (once the initial separation occurs) no FECO fringes should be visible due to the relative opacity of the sample. This provides an early warning sign of malfunctioning equipment or software so that if, during the agitation, FECO come into view the user should immediately click the Agitation Stop button to avoid having the surfaces come into contact and potentially damaging the micrometer shaft, the surfaces or the mounts themselves. In future versions of the software, fast

FECO detection software should be written so that any chance of operator error can be removed from the process altogether.

The second program performs the shear test discussed in Section 3.3.2 (Experimental Parameters and Procedures). It is intended that the program be started immediately after the desired gap size (as determined via one of the two techniques developed and described in Section 3.3.1) is established. The algorithm begins with a command sent to the function generator initiating the shear profile, the parameters of which have been entered on the front panel by the user. The program then moves immediately to four asynchronous loops. The first is the primary data collection loop, which cycles as at a rate set by the operator, typically once per 100 milliseconds; this rate should be maximized to provide as much intra-period data as possible. While in its current version it collects only data from the function generator and strain gauge output to minimize the output file size, it can easily be expanded to collect up to eight different signals from the BNC connector block if the analog input ports are available. A lock-in amplifier control section, running within its own control loop, can be found on the front panel in case that equipment is needed during testing, with the output saved to a separate file from the shear response file. A third loop, typically cycling more slowly than the previous two (once per second for the experiments described here), monitors the output voltage from the thermistor probe, converting it to a temperature value within the loop and saving this output in a third text file chosen by the user. A fourth loop controls the QCam camera, taking a snapshot at a rate chosen by the user and saving it to a folder chosen by the user, adding the time in seconds at which the snapshot was taken to the end of the filename.

The duration of the experiment is entered before the test begins by the user, and all loops in this stage of the program will terminate once the LabVIEW Stopwatch function timing the experiment exceeds this value. Once the loops have terminated, a command is sent to the function generator to switch the output from a shear profile to a DC offset of 0 V, stopping the shearing, and the program then terminates.

Chapter 3

Experimental Details

The Surface Forces Apparatus is a complex piece of machinery, and as such requires extensive preparation in order to be used effectively. This chapter discusses the setup and calibration process in detail, starting with a general overview of the SFA setup (Section 3.1 introduction), continuing with the calibration of the SFA components such as the bimorphs and strain gauges (Section 3.1.1), and finishing with the calibration of the spectrometer and camera (Section 3.1.2). Section 3.2 details the delicate and involved process of preparing the confining surfaces, including cleaving, silvering and gluing the mica (Sections 3.2.1-3.2.3).

Section 3.3 discusses the necessary steps to preparing the SFA chamber for a test, from loading the sample to readying the optical and electronic components. Section 3.3.1 discusses in more detail the method by which the gap size can be calculated quickly and automatically for both the smaller and larger gaps within the mesoscale regime (each has its own distinct process). Section 3.3.2 details the specific test parameters, such as shear frequency and amplitude, gap size, response gain and filter characteristics, sampling rate and test duration that were chosen for this set of experiments.

3.1 SFA Overview

Experiments were performed on a model SFA2000 Surface Forces Apparatus (SFA),
purchased from Surforce Corporation. The description of the SFA experimental set-up
and procedure is true of all tests included in this dissertation, unless otherwise noted.

All test runs were performed in a small (80×50×50 cm) enclosure with ventilation
sealed off to minimize air currents and thermal drift within the test chamber. The room
was climate-controlled by use of a thermostat, and the test chamber was enclosed within
a frame (0.5 m^3 volume) with panels of 0.5 cm thick insulated foam to further ensure
thermal stability. The temperature within the SFA chamber was monitored with a YSI
44004 Precision thermistor placed less than one-half centimeter from the surfaces
(typically 1-2 mm away), and temperatures for all tests were obtained via this thermistor
at a rate of once per second. The door to the room containing the SFA remained
unopened for the entirety of the test run to minimize thermal fluctuations and mechanical
vibrations during and between the experiments.

The SFA, light sources (white light and monochromatic sodium light) and
spectrometer were all located on a Melles Griot floating table to minimize vibrations
(using 50 PSI pressure on average). The SFA and both shelves containing the electrical
equipment used to control it were electrically grounded via a common wall receptacle to
avoid ground loops. The output from the SFA, containing the interferometric information
from the lens-sample system, was directed via a pair of prisms to a spectrometer grating,
which diffracted it into its component wavelengths. The resulting FECO spectrum was

then directed to a QImaging Retiga digital camera, where the image was recorded and stored on a computer. A discussion of FECO and the equations associated with them is given in Section 2.3.

3.1.1 Calibration of the SFA

Several parts of the system must be calibrated and aligned before an experiment can be performed. Both the resistive and semiconductor strain gauge must have their stiffnesses measured. To accomplish this, a calibration stage was built to allow the entire Friction Device, upper disc mount included, to be affixed to an L brace and suspended vertically, as shown here above.
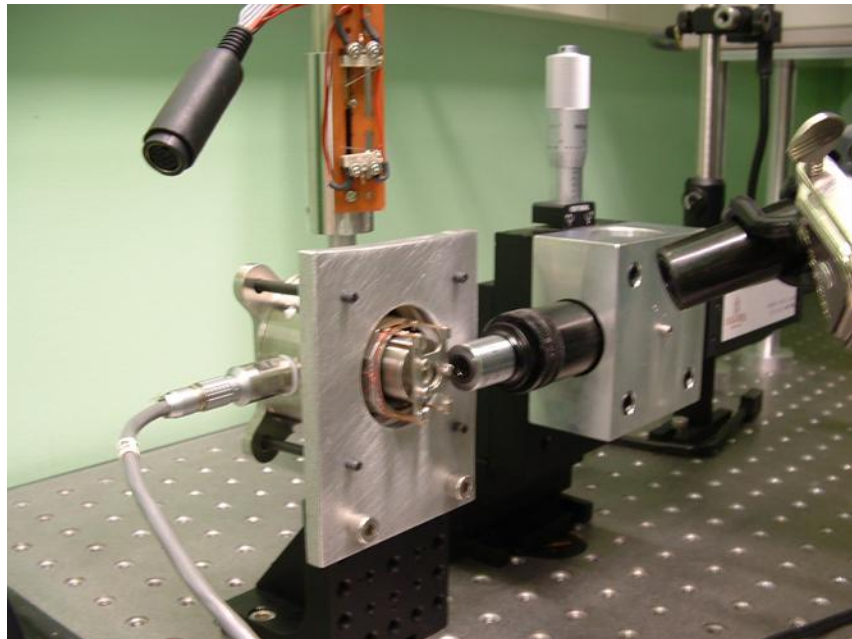
Figure 3.1: Picture of the Friction Device undergoing calibration, affixed to the calibration stage with a digital camera directly behind it.

The Friction Device was attached using the same adjustable level clamp that was used to secure it within the SFA, and the four pin strain gauge output cable was connected as

well. A high resolution camera, calibrated by graded reticule so that the distance per pixel at the focal length is known, was mounted in such a way that it was focused on the disc mount. Weights were then suspended from the disc mount and the disc mount deflection was measured by camera, so that the applied force $F = mg$ could be correlated to the deflection, x, to find the stiffness via Hooke's Law, $F = kx$. During this calibration, the disc mount's deviation from one-dimensional motion could also be ascertained by tracking its deflection in the y-direction (i.e., perpendicular to the hanging mass). The disc mount's lateral deflection was found to be negligible for the standard range of motion. Plots of the calibration data for each of the two strain gauges are provided in Figure 3.2, and show that the stiffnesses for the resistive and semiconductor gauges are $0.0034 \pm 2.9 \times 10^{-5}$ N/μm and $0.0107 \pm 1.7 \times 10^{-4}$ N/μm, respectively.
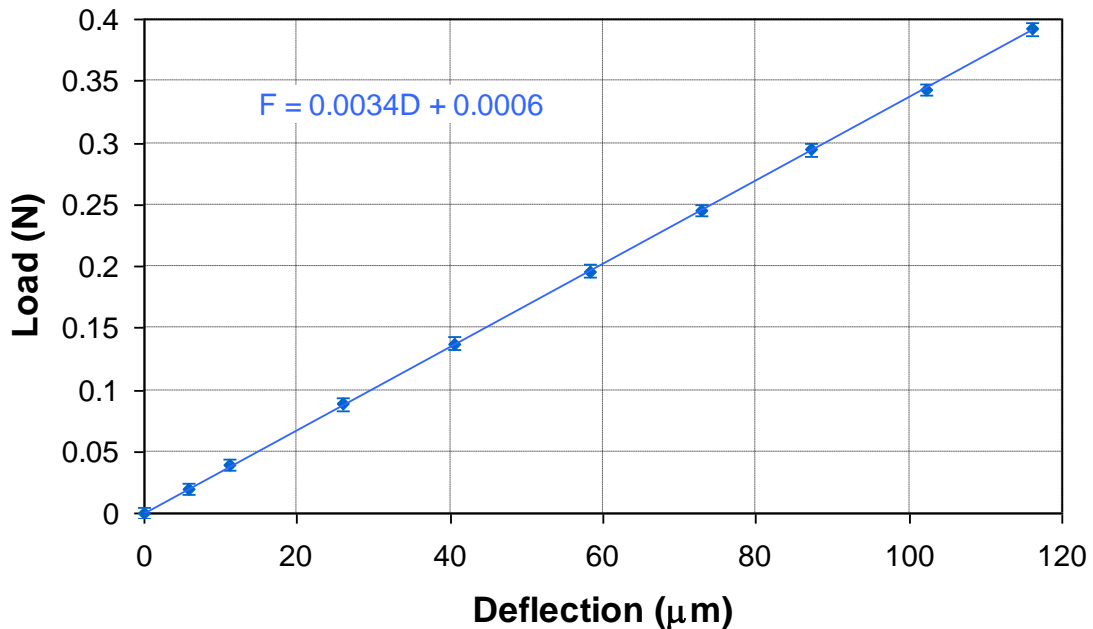
Figure 3.2: Plot of load vs. deflection for the resistive strain gauge
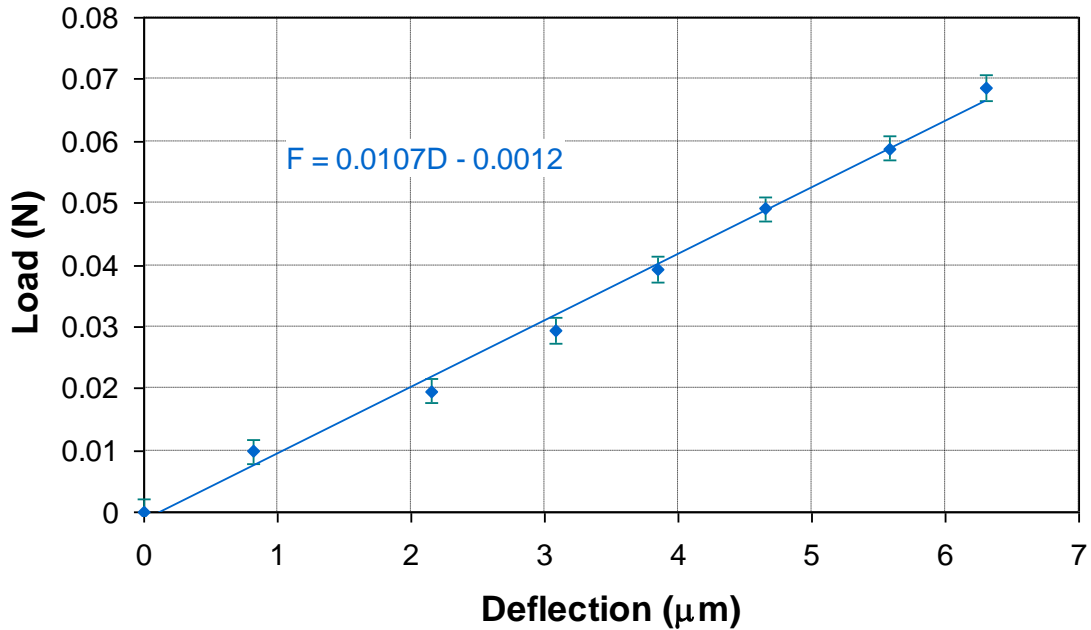
Figure 3.3: Plot of load vs. deflection for the semiconductor strain gauge

The Friction Device must also have its deflection response calibrated (that is, the voltage response registering on the strain gauges for a given deflection of the disc mount). This can and should be performed while the stiffness is being calibrated. With the strain gauge output cable connected, voltage readings were made (once the system had stabilized) with the addition of each suspended weight. Special note should be made of the Signal Conditioning Amplifier's Excitation setting, as the output signal is linearly proportional to the Excitation Voltage. As the output voltage is linearly proportional to the mount deflection, a plot of the former versus the latter will yield a slope equal to the deflection response. Plots of this calibration data for both strain gauges are given in Figures 3.4 and 3.5 below, and give values of 0.0426 ± 0.001 V/μm and 1.452 ± 0.04 V/μm (using a gain of 10 000 and an excitation of 1 V for both calibrations) for the resistive and semiconductor strain gauges, respectively.

183
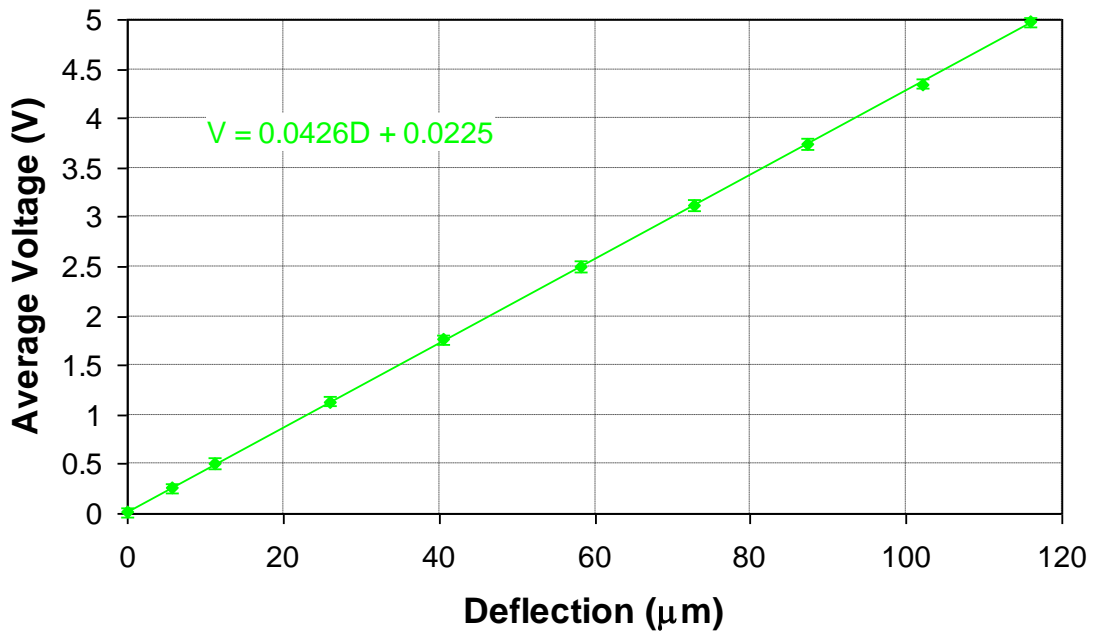
Figure 3.4: Plot of average measured voltage vs. deflection for the resistive strain gauge
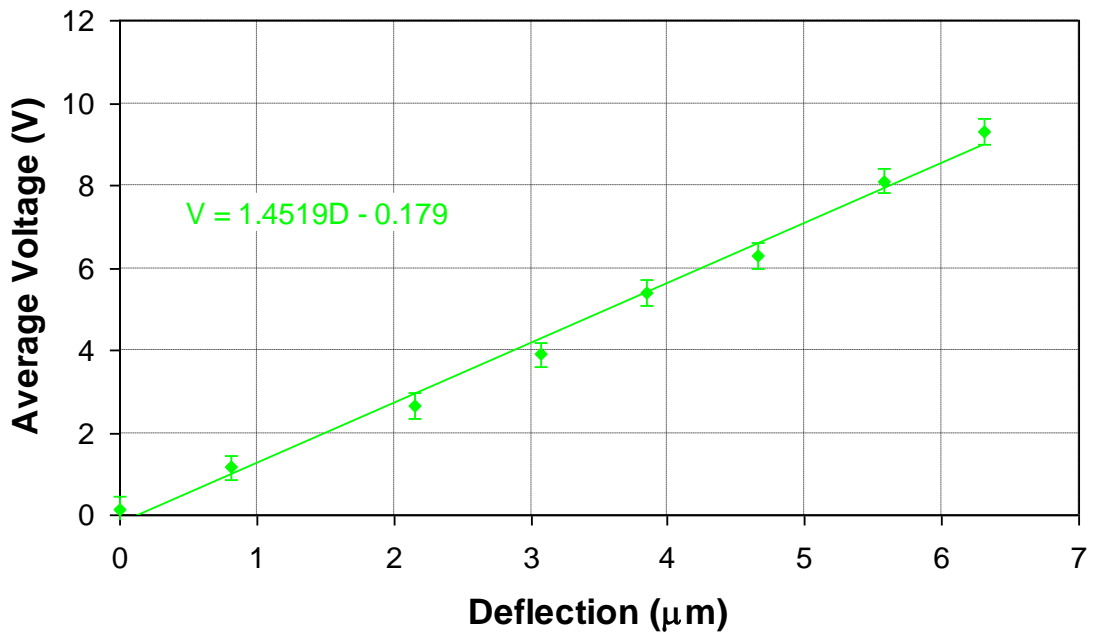
Figure 3.5: Plot of average measured voltage vs. deflection for the semiconductor strain gauge

Factoring out the gain and excitation from this measurement, then, will give non-amplified calibration factors of 4.26 ± 0.1 V/m and 145.2 ± 4.0 V/m for the resistive and semiconductor strain gauges, respectively.

The Bimorph Slider's stiffness and deflection response must be measured as well. This was accomplished in a manner similar to that used with the Friction Device, with the Bimorph Slider attached while on its side via calibration stage to an L brace, and connected to a function generator with the supplied LEMO adaptor cable. Weights could then be suspended and the resulting deflections measured by camera to obtain the stiffness as for the Friction Device. Passing a DC voltage to the bimorphs with the function generator and measuring the deflections will similarly give the deflection response, and this method was used to calibrate the Slider. Alternatively, the latter can be obtained with the bimorph slider in place within the SFA, so long as the Friction Device has been calibrated. By connecting the upper and lower discs with a very stiff substance (glue or modeling clay, for example), and by passing a DC or AC voltage to the bimorph, one can monitor the displacement amplitude occurring in the Friction Device (which, due to the resilient medium connecting it to the lower mount, should have the same amplitude as its mate), thereby relating a given voltage to a resulting deflection and hence producing a deflection response factor. Calibration plots for the bimorph slider are given in Figures 3.6 and 3.7, showing stiffness and voltage calibration factors of 1551 ± 14 N/V and 9897 ± 140 V/m, respectively.
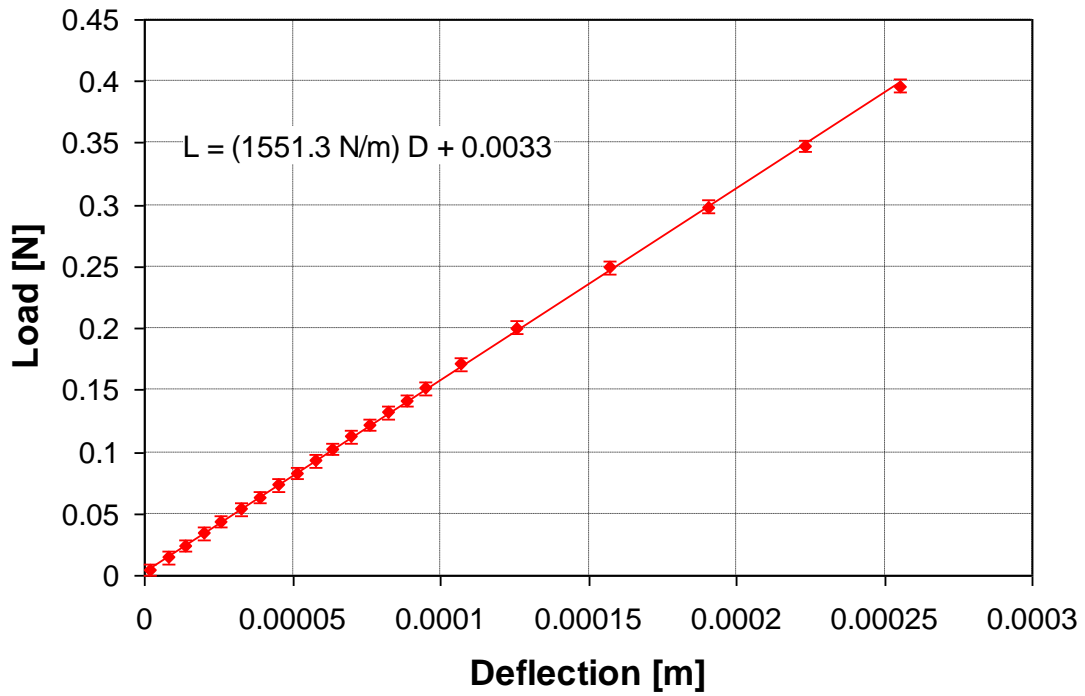
Figure 3.6: Plot of load vs. deflection for the bimorph slider
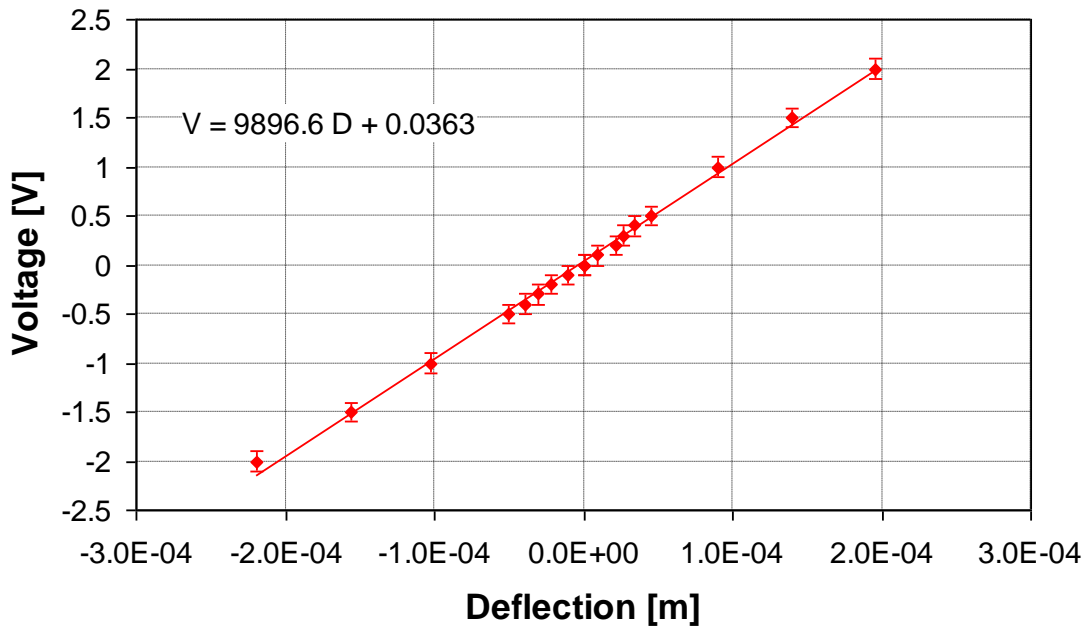
Figure 3.7: Plot of average measured voltage vs. deflection for the bimorph slider

The force-measuring spring stiffness (which measures forces perpendicular to the surface plane) can be calibrated in the same way as is given for the bimorph slider and for the Friction Device. It should be noted that the glue layers of the discs are not infinitely stiff in practice, and so it is better to consider the effective stiffness, k_{eff}, as being a result of the force-measuring spring in series with the glue, so that $\dfrac{1}{k_{eff}} = \dfrac{1}{k_{spring}} + \dfrac{1}{k_{glue}}$. An estimation of k_{glue} can be obtained by measuring the force required to separate two surfaces from adhesive contact while the force-measuring piece is fully secured and when it is loosely in place with respect to the SFA chamber. In the latter case, only the contact adhesion should resist the separation, so that k_{spring} is negligible and k_{glue} can be approximated. In this way a more exact value of k_{eff} can be determined. Since only lateral shear measurements were performed for the results discussed here, no calibration was necessary for the Force-measuring springs.

Both DC motors must be calibrated in terms of distance versus encoder reading. It should be noted that the SFA2000 has been modified so that one of the motors (originally intended as a fixture for the Friction Device) can be fitted to the differential micrometer with one of two couplers, one for the coarse control and one for the medium control as discussed in Section 2.1.3. In this way one of the two micrometers can be motorized at any given time. The second motor controls the fine control, as intended by the manufacturer. Because both motors control micrometers which themselves control the bottom disc mount, and because the top disk remains fixed, the distance calibration for each motor represents a separation of the disc pair (note that a separate calibration must

187

be done for each of the differential micrometer setups). As a result, calibration can be

easily done by setting up a FECO pattern with two fresh disks and adjusting the disk

separation via each motor-controlled micrometer, monitoring the FECO position (which

yields the separation as discussed in Sections 2.3.2 and 2.3.3) and the corresponding

encoder position, and plotting one versus the other to obtain the conversion ratio between

the two. This procedure was followed to obtain the conversion ratio for (and hence

calibrate) each micrometer. A plot of the surface separation as a function of the encoder

count is given in Figure 2.16.

With the calibration values given above one can easily convert from the voltage output

of the signal conditioning amplifier to a shear response force, R:

$$R = \frac{k \cdot C_{V \to D} \cdot V}{G \cdot E}$$

where G and E are the Gain and Excitation settings of the signal conditioning amplifier, k

is the stiffness of the strain gauge, $C_{V \to D}$ is the voltage to deflection calibration factor

and V is the output (in Volts) of the signal conditioning amplifier. Sample calculations

follow for semiconductor and resistive strain gauge responses, R_{SC} and R_{Res}, respectively.

Recall that in the tests presented here, gain and excitation values of 10 000 and 1V,

respectively, were used.

$$
\begin{aligned}
R_{SC} &= \frac{\left[(0.0107 \ \text{N}/\mu\text{m})(10^{6} \ \mu\text{m}/\text{m})\right] \cdot (1/145.2 \ \text{m}/\text{V}) \cdot V}{(10000) \cdot (5)} \\
&= 0.0014738 \quad \cdot V \quad (\text{in N}) \\
&= 1473.8 \cdot V \quad\quad (\text{in } \mu\text{N})
\end{aligned}
\tag{1}
$$

for the semiconductor strain gauge response, and:

$$R_{Re\ s} = \frac{\left[(0.0034\ \text{N}/\mu\text{m})(10^6\ \mu\text{m}/\text{m})\right]\cdot(1/4.26\ \text{m}/\text{V})\cdot V}{(10000)\cdot(5)}$$

$$= 0.0015962 \quad \cdot V \quad (\text{in N}) \tag{2}$$

$$= 15962 \quad \cdot V \quad (\text{in } \mu\text{N})$$

for the resistive strain gauge response. The uncertainty in a given measurement of response for each strain gauge (using the calibration uncertainties mentioned above) will then be:

$$\Delta R_{SC} = \pm \sqrt{\left(\frac{\Delta C_{V \to D}}{C_{V \to D}}\right)^2 + \left(\frac{\Delta k}{k}\right)^2}\ R_{SC}$$

$$= \pm \sqrt{\left(\frac{4}{145.2}\right)^2 + \left(\frac{1.7 \times 10^{-4}}{0.0107}\right)^2}\ (1473.8 \cdot V)$$

$$= \pm 47 \cdot V$$

for the semiconductor strain gauge, and:

$$\Delta R_{Re\ s} = \pm \sqrt{\left(\frac{\Delta C_{V \to D}}{C_{V \to D}}\right)^2 + \left(\frac{\Delta k}{k}\right)^2}\ R_{Re\ s}$$

$$= \pm \sqrt{\left(\frac{0.1}{4.26}\right)^2 + \left(\frac{2.9 \times 10^{-5}}{0.0034}\right)^2}\ (15962 \cdot V)$$

$$= \pm 400 \cdot V$$

for the resistive strain gauge.

3.1.2 Calibration of the Spectrometer and Camera

   The accurate measurement of sample thicknesses requires that the interference pattern wavelengths be measured precisely, and so calibration of the spectrometer is essential. This is accomplished by using a monochromatic light source, and for the results presented here, a sodium source was used, positioned as shown in Figure 3.4 so that the sodium light will pass through the SFA chamber and strike the spectrometer grating

normally. The resulting diffraction pattern passes to a cooled Retiga Exi QImaging Fast 1394 camera, which has 1392×1040 pixels, pixel dimensions of 6.45 μm $\times$ 6.45 μm and 12 bit digital output; images are saved to a computer via an extended FireWire cable and can be displayed there in real time. The sodium source has a doublet with wavelengths at 5895.932 Å and 5889.963 Å, and so by tracking these bands across the screen one can determine not only the offset of the spectrometer reading from the sodium position for a given position on the screen, but also the wavelength to pixel ratio. A plot determining the latter is shown in Figure 3.8, showing the wavelength to pixel ratio is 0.0316 nm/pixel Note that the negative value indicates the 'direction sense' of the band, in that the pixels move *left* along the screen for an increase of wavelength.
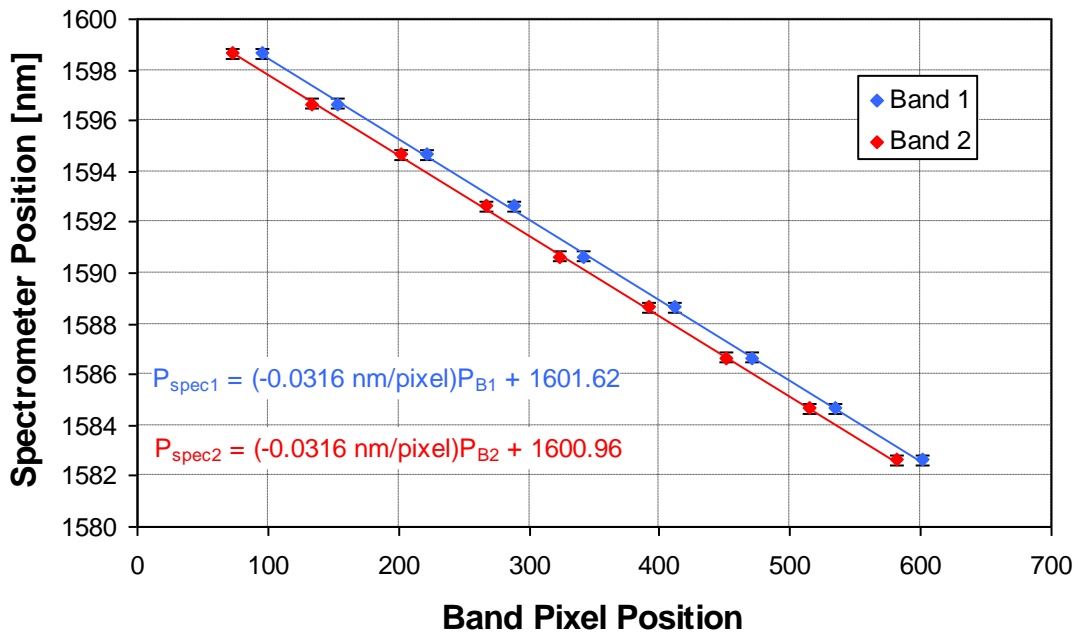
Figure 3.8: Calibration plot of spectrometer position vs. band pixel position for the sodium doublet, with uncertainty in spectrometer position of $\pm$ 0.2.

3.2 Preparation of the Surfaces

The preparation of high quality mica-covered surfaces for SFA use has been a topic of some debate in recent years, with several groups developing and refining their techniques with various levels of success[335, 337, 350-361]. The techniques used in these experiments and described here generally follow those laid down by Israelachvili[337], although the method of obtaining mica sheets more closely follows the simple procedure described by Perkin et al, as explained below. An overview of the mica preparation process is shown in Figure 3.2:
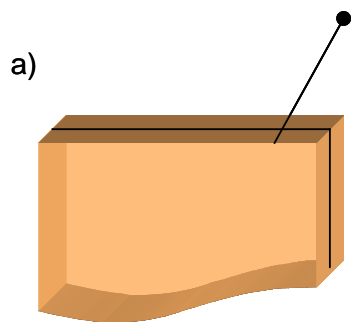
a) Cleave the mica with a pin
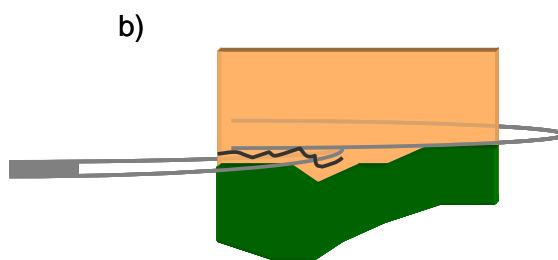
b) Grip firmly with one pair of tweezers, and tear off the desired piece with another
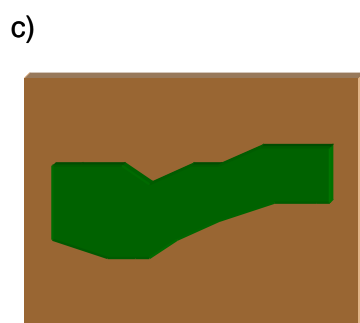
c) Place the piece on a backing sheet

d)
Mica

QCM

Boat

+   -
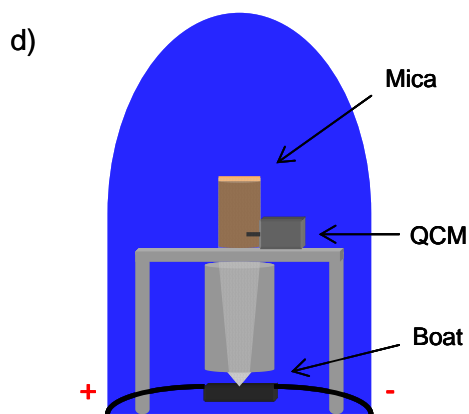
Deposit silver layer on the mica within an evacuated chamber
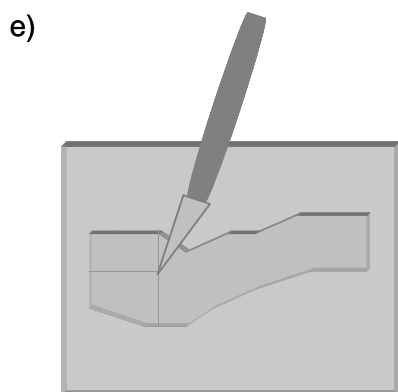
e) Cut the silvered mica to disk-sized pieces
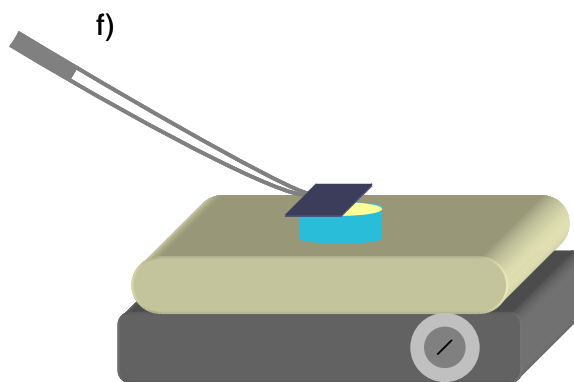
f) Melt and smooth epoxy to a disk on a hotplate and apply the mica

Figure 3.9: The various steps leading to the creation of a disk used with the SFA.

The surfaces themselves, obtained from Esco Products, are fused silica plano-convex (PCX) circular discs; the base is 9.9 mm in diameter, while the radius of curvature of the cylindrical surface is 2 cm. It is crucial that a disc of proper body thickness (i.e. not counting thickness from the raised cylindrical top) be used, as the lower mount should be as close to parallel with the top mount for ease of surface alignment. For the mounts used in the experiments presented (the Friction Device and Bimorph Slider) a body thickness of 3.5 mm was used, but surfaces of 4.5 mm body thickness are available and have been found to be more appropriate for use with the Piezo Mount.

3.2.1 Cleaving the Mica

The thickness of the mica sheets used on SFA surfaces have several criteria that they must adhere to in order to be suitable for experiments. First and foremost, they must be molecularly smooth, and so must be free of steps, spots and other impurities (for example, dust, oils and, if possible, an excess of atmospheric water). For this reason it is necessary to perform as much of the surface preparation as possible in an environment shielded as well as possible from contamination, and for the experiments described here the mica sheets were processed in a Labconco Horizontal Cleaning Bench, a laminar flow hood which consists of a stainless steel workspace with sides, back and top shielded. The entire back wall is made up of a filtered fan that blows air towards the front of the enclosure at a rate chosen by the user in order to remove dust and other particulates from the environment. A mask must be worn whenever mica or disks are handled as well to avoid airborne contaminants from breathing, and whenever possible gloves should be

worn to minimize the chances of leaving fingerprints on the mica being cleaved. Several standard tools should always be present during the processing:

- Scissors for cutting thick sheets of mica. These should be replaced or sharpened fairly frequently as they can wear down quickly;

- Biological-grade tweezers of various types and tip sizes, including standard tweezers, spatular flat-tipped tweezers, curved-tip tweezers and tweezers that have rounded flat tips large enough to grip the 9.9 mm diameter disks firmly;

- Scalpels, both flat-edged and curve-edged, to cut the mica during the gluing stage, with the former used for small, precision cuts and the latter rolled over larger silvered sections to be cut in order to minimize flaking of silver and mica;

- A spray bottle of ethyl alcohol to wipe down all surfaces and equipment to remove contaminants;

- Lint-free swabs, pipe cleaners and lens paper, to clean tools and surfaces quickly, used in conjunction with the ethyl alcohol;

- One or more covered carrying trays for the disks, preferably with a secured inset that contains disc-sized recesses containing set screws that hold the discs in place so they don't slide or flip over, and;

- A selection of pins or other pointed tools with various tip sizes, to cleave mica of various thicknesses and to apply epoxy to the surfaces smoothly.

A wire is normally strung from one side wall to the other near to the top of the flow hood, with small clips strung along the length of it in order to hold sheets of mica while the user is occupied with other tasks. To keep the bench surface clean and dust-free, a transparent plastic sheet is affixed to the front of the bench with Velcro covering the open space completely while the bench is not in use. The entire working area should be wiped down with alcohol before and after every use.

The surface preparation process begins with cleaving the mica, which generally comes from the retailer (Grade IV ruby red muscovite obtained from S&J Trading Inc. was used in the experiments discussed here) in the form of 1-2 millimeter thick blocks 500-1000 cm^2 in area. Before cleaving, a smaller block (100-200 cm^2 in area) should be cut from the original section, since the cleaving process involves pulling two sheets apart and that action tends to cause steps and tears in the sheets if they are of a larger area than this. Gloves may or may not be used at this stage; while any section of mica touched by an ungloved hand will *always* be unusable, so long as only the corners are touched most of the mica will still remain uncontaminated. The use of gloves is actually often counter-productive at this stage, as gloves tend to accumulate fragments of mica very quickly during the cleaving stage so that mica touched with them, while they will be oil-free, will still have particulate contamination on them. The electrostatic buildup on the sheets prevents these fragments from being removed easily, and having gloves may give a false sense of security to the cleaver in addition to reducing their manual dexterity, resulting in a lower yield of usable mica with the gloves than without them. Protective glasses and a facemask should be used at all times during the cleaving process, however, as inhalation

of fine mica particles is a health hazard[337], and introduction of mica shards to the eye can lead to eye damage such as corneal abrasion.

The cleaving itself should begin with a thicker, less pointed pin in order to split the thicker sheets apart (Figure 3.2a). A typical cleave is initiated by holding the sheet firmly at a corner with one hand while thrusting the pin into the mica along the plane of the sheet with the other. Often with thinner sheets this can be difficult to do, and to assist in the penetration it is advisable to abrade the edge to be cleaved using the side of the pin, scuffing or 'fozzing' it (cf. the Scottish term *fozy*, an adjective meaning spongy and loose-textured, which describes the mica edge if done properly when the process is complete) in the process. By doing this, the softened edge will be thicker, giving it a larger cross-section to penetrate, and softer, making it easier to penetrate gently with the pin. Care should be taken while fozzing the edge to keep the worked edge down, so that mica particles fall away from the surfaces and do not contaminate them, and towards the cleaver, so that the airflow from the hood will blow mica shards away from the surface. Cleaves should generally be close to the center of the layer if possible to avoid splitting one side too thin, as cleaving a thin sheet from a much thicker sheet often produces tears in the thinner slice, making them too small in area to be used easily.

Unused halves should be either suspended from the clips above the user (as described earlier) or placed carefully against one of the flow hood walls at an angle so that neither side touches any surface that may be contaminated (nevertheless, any area where mica is temporarily stored should be wiped down frequently). Due to the asymmetric molecular

196

ordering in planes of mica, cleavage in one direction (that which is parallel to the step lines) will usually be easier than cleavage orthogonal to that direction. This is evident immediately after the mica block splits: If the cleave goes against the plane the increased resistance to the split is perceptible, and if the sheets are pulled apart too quickly one may even see a small electrostatic discharge. Since cleaving *against* the step lines generally creates sheets with more step lines, it is recommended that all cleaving be done *with* the step lines to maximize the production of step-free surfaces[337].

The cleaving should be repeated as described above until the sheets are too thin (roughly 0.3 to 0.5 mm thick) to be cleaved easily with the thicker pin, at which point a thinner, smaller-tipped pin should be used to reduce the thickness to less than 10 μm. This thickness of mica is characterized by a considerable loss of rigidity; a simple test to verify this is to hold the mica from one corner, making sure not to bend the sheet to artificially bolster its resilience, with the sheet parallel to the ground. If the mica sags or bends significantly due to gravity, it is likely in the range of thicknesses that are usable for SFA surfaces. Another indication of thinness is a change of colour; mica is strongly pleochroic when in thin sections, meaning it changes colour depending on the angle at which it is viewed[362, 363]. As the mica sheet loses its rigidity it also takes on a few characteristic colours. For ruby muscovite, the dull brown colour characteristic of thick sections is replaced by vibrant forest and emerald green, sapphire blue and ruby red colours, with the exact colour dependent on the thickness of the sheet; forest green pieces are thickest (as judged by the rigidity test mentioned above) while the sapphire blue pieces are so thin as to crumple during cleaving, rendering them useless. The range of

mica thicknesses typically used with SFA surfaces are 1-5 μm, with pleochroism occurring around 2-3 μm and considerable loss of rigidity around 1-2 μm[337]. As FECO fringe spacing is inversely proportional to the mica thickness, it is desirable to have as thin a piece as possible, although the extreme delicateness of thin mica sheets generally prevents the use of sections less than one micron in thickness in practice.

Once one obtains a mica sheet thin enough be used, one must detach it from the surrounding mica that likely contains steps and contamination. A few techniques have been developed to liberate the desired mica. Israelachvili pioneered the platinum wire technique which entails using a 3D translation stage to which is attached a mount holding a seven millimeter long piece of 0.2 mm diameter platinum wire which can be electrified to heat it[335]. With enough current the wire can grow hot enough to melt mica, and so the wire can be used to cut rectangular sections large enough to cover SFA disks. The mica must be placed between mounting blocks (without touching the section to be removed, of course) at the height of the platinum wire and pulled taut to facilitate the cutting process[337]. Once the sections are cut (remembering to clasp one corner with a pair of tweezers, since the breeze from the laminar flow hood can unexpectedly detach the piece near the end of the cutting), the sections should be placed on a pre-prepared, freshly cleaved substrate of thicker (~0.5 mm) mica so that it can be later mounted for silvering. To minimize birefringence effects in the FECO fringes, it is important to keep the mica planes parallel to one another for all pieces obtained. This is achieved by cutting an equal number of rectangles with their long axes perpendicular to one another, with one of the sets flipped over before placed on the backing sheet; this will allow the surfaces to,

198

when they are glued to the SFA disks, be in crystallographic register with one another[337]. An accurate, dated sketch of the backing sheet and mica pieces should be made in a lab manual, making note of any wrinkles, steps, blemishes or contaminated areas, along with the overall quality and colour of each usable section, so that the appropriate sections of mica can be easily found later after silvering and problem areas can be avoided. The mica pieces should be placed as centrally as possible on the backing sheet (which, in the current setup, should not exceed 10×10 cm in size, so that it can properly fit on the evaporation chimney, described in Section 3.2.2) so that shadow effects from the chimney wall and QCM can be avoided during the evaporation process (again, see Section 3.2.2).

While the platinum wire technique is effective in producing mica pieces of regular size and shape, problems with the method have been reported in recent years[354, 358, 364], leading to other techniques being developed[359, 365]. In practice, the heat required to melt mica makes the platinum fragile, often making the cutting process difficult. Frequently the wire can break during the cutting, particularly if the wire hits a section that is thicker than 5 μm, and often damaging the mica in the process. Of more concern to experimentalists, particularly those using the SFA with very small gap sizes, is the frequent presence of particles 20-150 nm in diameter and 2-3 nm high that can be found on the mica surfaces following a platinum wire cut. While the particles were originally thought to be solidified pieces of mica that had melted during the cut[364], it has recently been confirmed that they are in fact globules of platinum that accumulate on the surface, a result of the platinum evaporating at temperatures lower than the melting point of mica

(with $T_{Pt-evap} = 1300 \ °C$ [366], while $T_{m-mica} = 1320 \ °C$ [358]). One alternate method for obtaining mica, originated by Frantz and Salmeron[355], involves cleaving mica to a thickness of between 4 and 8 microns, silvering and gluing it in the traditional way (described in section 3.2.3) and then, immediately before using the surfaces in the SFA, placing a small piece of adhesive tape on each surface and removing the top layer of mica to produce a very fresh, clean surface. The disadvantage of this method is that there is no guarantee that the remaining mica layers are of the same thickness, so that recalibration of the system must be performed with each new pair of surfaces. This method of mica preparation was attempted prior to the results presented in this thesis with only moderate success and so the technique was eventually abandoned.

A very simple and effective method of mica preparation, developed by the author in 2005 and identical to a method first published by Perkin et al in 2006[359], involves placing the sheet containing the desired section of mica between two mounting blocks in the same fashion as the platinum-cutting method or holding the body of the mica by a sturdy pair of tweezers, and then carefully tearing away the desired piece whole with tweezers rather than cutting it with a wire. One disadvantage to this method is that, unlike the platinum-cutting method, which leaves the mica edges partially melted and thick and thereby making them easier to pick up after silvering, the tearing method leaves the mica edges extremely thin and nearly impossible to pick up without tearing the mica. Simple solutions to this problem, all tried successfully by the author, are:

- to either place one edge of the desired mica hanging over an edge of the substrate where it is easily retrieved;

- to place it with one edge upon a step on the backing sheet (either naturally-occurring or deposited by the cleaver) which provides a lip under which tweezers can reach to retrieve the mica, or;

- to tear the piece such that a thicker section remains attached, which can be used to remove the entire piece once silvering is complete (as discussed in the paragraph below) as shown in Figure 3.2b;

Disk-sized sections of the mica can be obtained by cutting them with a scalpel after the silvering process is complete. Perkin et al report that results obtained via this method of mica preparation are not observably different from those obtained using the other techniques[359], and this is the method used for the experiments presented in this thesis. One minor difference between the two methods is that while Perkin et al removes only the desired mica section and adds a substrate to provide a lip, the author removes not only the desired section but also an adjacent, stepped section which, due to its increased thickness and possible wrinkles, is easily discernable from the thin section and does not usually stick as well to the backing sheet. For these reasons the adjacent piece can act as a tab which can be handled by tweezers to peel off the thin sections, and makes the mica easier to handle during the gluing process as well.

3.2.2 Silvering the Mica Sheet

Immediately after cleaving the mica and placing it on a substrate as shown in Figure 3.2c, the latter is placed in a covered Petri dish (to protect the former from airborne contaminants), which is in turn placed in a desiccating jar. The jar is evacuated right

away by a twin diaphragm vacuum pump obtained from Neuberger, Inc., and left under vacuum until it can be placed in the evaporation unit's bell jar; the pump is oil-free and the desiccating jars are grease-free to prevent contamination of the samples. The evaporation unit, a sketch of which is shown in Figure 3.2d, has been built in-house and is made up of a roughing and turbo pump unit connected to an evaporation chamber that is covered by the bell jar. The chamber consists of a platform, below which two electrodes are set, connected by a tungsten wire evaporation boat in which two or three 99.999% pure silver pellets are placed. The electrodes are attached to a Variac power supply outside the chamber so that the current through the boat, and hence the heat emitted by it, can be controlled. Above the melting point of the evaporated metal, the Variac setting varies roughly linearly with the evaporation rate of the metal. The platform has a central hole approximately 10 cm in diameter through which evaporated metals can pass to deposit on the mica surface. The hole can be quickly covered by a shutter attached to a lever outside the chamber, so that the substrate can be protected from spattering materials while the boat and evaporating material heat up. The boat and platform are only about 20 cm apart, and Israelachvili reports that the mica should be kept at least 30 cm from the boat since exposure to high heat for prolonged periods can discolour the mica, which can in turn adversely affect the optical properties of the mica. For this reason, a removable 10 cm long metal chimney with the same diameter as the hole has been added directly above the hole to increase the distance to 30 cm; the mica substrate is placed atop the chimney with the thin mica pieces placed as centrally as possibly to minimize shadowing from the passage walls and QCM crystal (discussed below). Cut into the side of the bottom of the chimney is an aperture, through which an

exposed 10 MHz Quartz Crystal Microbalance (QCM) crystal disk protrudes. The crystal is connected to a small controller box which is wired to a 200 MHz electronic counter, so that the frequency change in the QCM crystal can be monitored. According to the Sauerbrey equation (first derived by Günter Sauerbrey in 1959[367]) the frequency shift in a thin piezoelectric crystal is proportional to the change in mass of material deposited on it, and if the density of that material is known, to the thickness of the deposited surface as well[367, 368]:

$$\Delta f = \frac{-2 f_0^2}{A \sqrt{\rho_q \mu_q}} \Delta m \tag{1}$$

where Δf is the frequency shift, f_0 is the resonant frequency of the crystal, A is the exposed area of the crystal, ρ_q and μ_q are the density and shear modulus of quartz, and Δm is the change in mass of the deposition layer. The area of the QCM used in the setup is circular so that the deposition layer will be cylindrical, and since the mass of a cylinder is $\Delta m = \rho_{Ag} A \Delta d$, where ρ_{Ag} is the density of silver and Δd is the change in cylinder height (i.e. the thickness of the layer):

$$\Delta f = \frac{-2 \rho_{Ag} f_0^2}{\sqrt{\rho_q \mu_q}} \Delta d \tag{2}$$

As a result, by monitoring the change in frequency one can determine the thickness of the deposition layer on the QCM and hence the mica itself.

Calibration of the QCM involves placing a glass slide on the chimney and performing an evaporation on it while measuring the frequency shift, Δf. The thickness on the slide can be measured easily using an AFM, and so by performing several glass slide

evaporations while varying Δf, one can create a plot of Δf vs. Δd, from which one may determine the required frequency change for a desired deposition thickness with the evaporator. A calibration plot demonstrating the linear relationship between Δd and Δf is given in Figure 3.3:
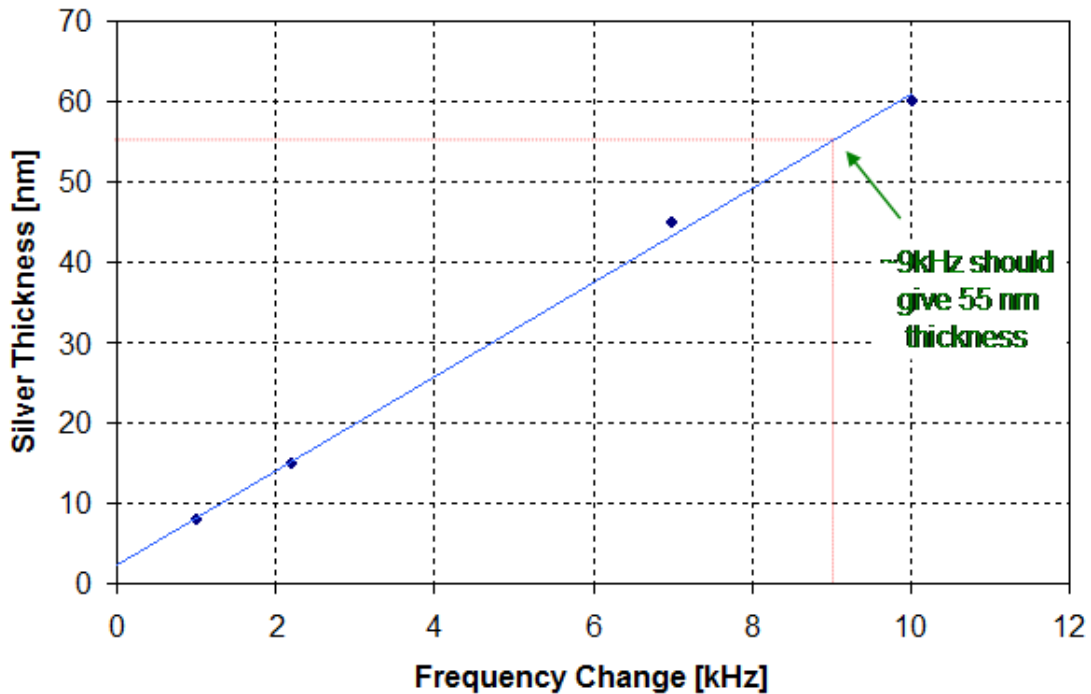
Figure 3.10: Plot of silver thickness (as deposited using the home-built evaporator) vs. QCM crystal frequency change. The desired 55 nm silver thickness that will give optimal FECO fringe sharpness has been denoted on the graph as occurring with a frequency change of approximately 9 kHz.

As some of the QCM circuitry is exposed to the evaporation, a small plank covering all parts of the QCM except for the crystal itself (a small hole was drilled in the plank to accomplish this) has been added beneath the unit to avoid forming a conductive layer on the QCM and ruining the electronics. Since changing the alignment between the QCM and plank will alter A in equation (1) and hence the calibration using equation (2), it is

imperative that the QCM/plank alignment be moved as little as possible in between evaporations. Any time a significant change to the bell jar setup occurs (including, of course, a change of the material to be evaporated), a new calibration must be performed. Generally, despite the presence of the masking plank, the QCM will stop functioning due to the gradually increasing presence of a silver conducting layer (the plank only delays this inevitable effect) which will ultimately short circuit the exposed electronics near the crystal, a phenomenon that usually occurs around a silver thickness of 1.2 μm, corresponding to a total frequency shift (from start of life of the crystal) of approximately 200 kHz. Since both sides of the QCM used work equally well and the crystal can be detached easily from the electronics box into which it is plugged, its lifetime can be nearly doubled by flipping it around to expose the second side before the conducting layer fully forms on the first side used.

The pressure within the chamber was monitored by an ionization pressure gauge obtained from Veeco. While Israelachvili recommends a pressure of ~10^{-6} torr, the lowest pressure typically attainable in this lab is 1.8×10^{-6} torr, after pumping and degassing for 6-12 hours (or 24-36 hours if the bell jar is not kept under vacuum while not in use). The ionization element (purchased from Scientific Instruments, Inc.) was usually degassed at least twice during the pumping down of the bell jar to improve the gauge's pressure measurement. The pumping system consisted of a rotary pump working in tandem with a turbo pump controlled by a Turbotronik NT 20 pump controller. The standard deposition layer thickness used for SFA studies is 55 nm, corresponding to approximately 98% reflectivity[335, 337], and so this was the thickness adhered to as closely

as possible for the results presented in this thesis. Below this thickness the FECO fringes can blur significantly, making an accurate determination of gap size difficult, and above this thickness the reflectivity is often too high to be able to detect FECO at all. The Premion silver pellets used were obtained from Alfa Aesar and were rated to 99.999% purity. The recommended evaporation rate[337] of 1 Å/sec was also followed for the surfaces used, so that the approximate total evaporation time was usually 10 minutes. All thicknesses were determined using the QCM procedure mentioned above. The jar was left evacuated for at least 30 minutes following the evaporation before bleeding in pressurized nitrogen via a needle valve to allow the silver to cool, which in turn minimized the reaction between the silver and nitrogen. All silvered mica sheets were returned to their original covered Petri dishes and immediately placed into a desiccating jar which was evacuated by the twin diaphragm pump mentioned above until they were ready to be glued, to avoid a reaction between the silver and the atmosphere. Reactions between the silver layer and water and oily vapours have been reported to reduced adherence between the mica and disks by Israelachvili[337].

3.2.3 Gluing of the Mica to the Cylindrical Discs

   Gluing took place on a Corning Hot Plate, always within the laminar flow hood and always with a mask and powder-free gloves to eliminate particulate contamination. Several epoxies were provided by Surforce Corporation, and prior to the first gluing attempts, a few grains of each epoxy were fractured by applying pressure to them via spatula scoop, and the fractured pieces were then heated on the stage (with two glass slides beneath them to simulate an SFA disk) to determine their material and optical

properties. A table of the various epoxies, their melting onset temperatures and wetting temperatures (as determined by eye) as well as their characteristics during the melting process is provided below:

Table 3.1: Common epoxies used with the SFA and their mechanical and optical properties

Epoxy Type	Solid Characteristics	Melting Onset Temperature (±15 °C)	Wetting Onset Temperature (±15 °C)	Characteristics during Melting
EPON 1004F	Whitish, semi-transparent granules that fracture easily	105.2	155.0	Bubbles form as the epoxy begins wetting; clear and bubbly
EPON 1007	Yellowish granules that fracture easily	115.5	140.7	Never becomes fully wettable below 241 °C; clear with no bubbles
EPON 1009	Shiny, silvery white and difficult to fracture	131.4	182.3	Clear with bubbles
Sym-DPC	Off-white powder	182.3	214.4	Red popping bubbles form upon melting; clear yellow liquid
White Sugar	Small white granules	229.2	241.0	Dark yellow at first, becomes bright yellow; no bubbles

All temperatures were determined by a thermistor placed slightly off-center on the hot plate, and due to the large temperature variation across the surface, may under-represent the temperature of the grains themselves. Fourteen temperatures were tested (with an average increase of 10-15°C per test, giving the uncertainty in temperature), with the

heater allowed to sit at each temperature for approximately five minutes to allow slower melting processes to occur. A plot of hot plate setting vs. temperature (as measured by a thermistor resting on the hot plate) is given in Figure 3.4, showing the ratio between the two to be 0.014:
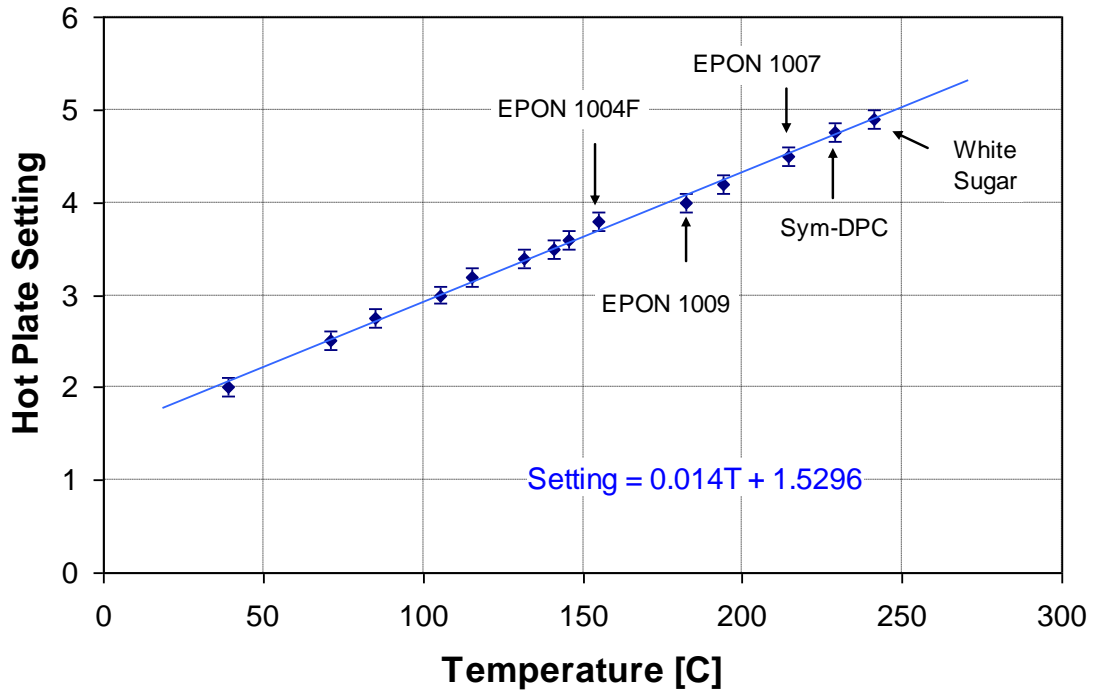
Figure 3.11: Calibration plot of hot plate setting vs. temperature, showing the melting points of the tested epoxies candidates.

In general, smaller granules were observed to melt more quickly than larger granules of the same substance. Granules that fractured easily were found to break into small, relatively equal-sized pieces, while those that fractured poorly allowed only a few small pieces to be chipped away while the bulk of the grain remained intact, or tend to squash flat upon applying pressure. Sym-diphenylcarbazide (sym-DPC), a powder at room temperature, was found to be already of sufficient size for melting in amounts needed for gluing. The ideal epoxy should have a low melting point (to protect the mica from

discoloration) and a relatively high wetting temperature as well, so that there is a wide range of temperatures over which the gluer can form the epoxy layer easily, without much leaking over the sides of the disk (too much epoxy leakage can prevent the disk from fitting in the SFA mounts). It should also be bubble-free if possible, since bubbles may create local rough spots if they become trapped under the mica sheet, and, since it satisfied all of the criteria mentioned above, EPON 1007 was chosen as the ideal candidate for gluing the silvered mica to the glass disks.

The gluing process begins with placing several disks flat side down near the center of the hot plate. The plate should be turned to the desired setting for gluing and left for a few minutes to allow the temperature to equilibrate. During this time the surfaces should be checked for blemishes and, if any are found, they should be cleaned or removed for future cleaning. A cleared surface on the laminar flow surface should be cleaned thoroughly so that one or two pieces of epoxy can be placed on it and broken by a blunt tool (one either dedicated for the task, or a thoroughly cleaned tweezers handle, for example). When the pieces are small enough to be used (roughly 0.5-1.0 mm^3 or less) they can be deposited directly on one of the surfaces (preferably with the spatular flat-tipped tweezers, as they can collect the epoxy dust as well), which should be nudged to the center of the plate to get the target heat and to give the gluer space to work with the disk. If the temperature is high enough, the grains should melt to a semi-wettable, moldable state within about thirty seconds. At this point the user should clasp the disk firmly with the rounded-tip tweezers, being careful not to leave the tweezers exposed to the epoxy so that the disk does not bond with the tweezers. With the other hand, the

gluer should, in one slow, fluid motion, sweep across the disk surface either with curved tweezers (if available) or with a thick, straight pin or similar tool, making sure to maintain a constant pressure so as to distribute the epoxy evenly across the surface; if curved tweezers are used, the smoothing motion should be along the length of the cylinder, whereas if a pin is used the length of the pin should be aligned as closely as possible to the length of the cylinder, as any deviation will likely lead to an uneven distribution. The gluer should inspect at the surface at an angle (so that the sheen of the glue can be seen), checking for thin or thick patches, or bubbles, and if any are seen, the surface should be re-smoothed as many times as is necessary to create a smooth, evenly layered glue layer; if *any* contamination is seen, the disk should not be used. If the right amount of epoxy is used, the amount that is pushed over the side of the disk should be minimal. As the fingers and thumbs come close to touching the hot plate during this procedure, the latex gloves mentioned above serve a double purpose as they partially shield the gluer's fingers from the heat. Wearing a facemask is also essential at this stage to avoid contaminating the surfaces and the mica.

At an opportune moment (usually either while the disks are heating or while the epoxy is melting) the mica backing sheet should be removed from the desiccating jar and Petri dish and placed on a recently cleaned area of the laminar flow hood. If it hasn't been done already during the cleaving stage (see the Section 3.2.1 for details on the various mica preparation methods) the desired section of mica should be cut into sheets the right size (roughly 1×0.7 cm) as shown in Figure 3.2e, making sure if possible to cut an equal number of pieces with the long rectangular axis in each of two chosen directions

perpendicular to one another. The cut should be made with a round-edged scalpel, starting at one corner of the rectangle and *rolling* the blade over the section to be cut, not dragging it across, as a dragging motion may tear the mica or break off silver shards that could contaminate the surface. It should be noted that macroscopic silver shards do not stick to the surface and so can be removed fairly easily by flipping the mica piece over and allowing them to drop off. A firm rolling motion should be enough to cut through the desired mica piece. Rolling too hard or repeatedly over the same cut could cut through the backing sheet, making removal of the desired section difficult or impossible, so this should be avoided if possible. The tip of a flat-edged scalpel is best used to free corners or any other stubborn sections, but should be used sparingly as it can easily penetrate the backing sheet. If the 'lip method' (described in the Section 3.2.1) is used, cutting should be *around* the lip leaving it attached so that the desired section can be easily raised from the backing sheet. Before continuing, it should be made certain that every side of the rectangle is completely free from the rest of the sheet, as any snags during the lifting process may tear the piece. A corner or edge of the mica should be slightly and very gently raised from the backing sheet using needle nose tweezers; as the mica is extremely fragile it may be a good idea to continue raising the piece by blunter tweezers (possibly even the spatular tweezers) to increase the surface contact between the two and minimize the chance of tearing the mica. All contact, of course, should be along the extreme edge or corners to avoid contaminating the central section of the piece.

The first mica piece removed should be gently placed centrally and silver-side down on the disk as shown in Figure 3.2f, with the long axis of the rectangle along the

cylindrical axis. The second piece of mica should be rotated 90° (unless this has already been done in the cleaving process using Israelachvili's method) and then flipped over to be placed silver-side down on the second disk. This is done to minimize mica birefringence by aligning them crystallographically. To avoid mounting the disks with the mica 180° with respect to one another, a small mark can be placed on the side of each disk with a felt-tipped pen if possible to keep track of their alignment during the mounting process. The gluer should place the mica gently on the disk center first, letting the glue draw the rest of the piece onto it by capillary action, and under *no* circumstances should the mica be dragged into place once it has contacted the disk, as this will cause the glue to redistribute unevenly and cause stress on the system. Once the mica is set in place, the corners of the mica may need to be tamped down at the corners and edges gently so that the mica fully takes the form of the cylinder, and this can be done very carefully using the tweezers tip. Tamping should not be done nearer the center of the mica, as this will likely contaminate it; if the mica center does not conform to the cylindrical surface well, it should be discarded altogether.

The disks should next be removed from the hot plate as soon as possible, as excess heating of the mica can discolour and hence damage it, and be placed in a covered container immediately. The surface should be checked for bubbles or wrinkles, particularly any that stick up from the rest of the surface and especially along the topmost part of the cylindrical axis, as this will be the section in closest contact with the other surface. If any aberrations are observed, the disk should not be used and a replacement disk should be prepared with the same mica sheet so that it matches with the other disk.

Any fleck of mica that is found to be sticking up from the surface that looks like it could be removed without compromising the disk should only be detached after the glue has fully set (several minutes after removing from the hot plate), to avoid pulling the entire sheet along the disk and ruining the surface.

Once the disks are done being used, the mica can be removed by leaving them in a sealed vessel containing either chloroform or acetone for at least twelve hours to dissolve the glue. Once the mica has been removed the disks should be rinsed thoroughly in distilled water. If pure water is not used there is a strong likelihood the glass will develop water deposits which can be very difficult to remove. Once the disks are clean they can be dried by blowing them with pressurized nitrogen or air until all water beads are removed. Repeated immersions in solvent may be necessary to remove all glue from the surfaces.

3.3 Pre-experimental SFA setup

Samples of 8CB are loaded using a syringe which, after a single small drop of the liquid crystal (approximately three to five cubic millimeters in volume, estimated by eye) has been collected on the tip, is swept across the bottom lens in the SFA while taking care to touch the surface with the sample only. The surfaces are then brought near to contact (within a few microns), to allow the sample to coat both surfaces. This must be done rapidly to avoid dust contamination on the surfaces, and during the loading process a surgical mask must be worn for the same reason.

The point of contact between the surfaces is found by directing monochromatic light normally through the surfaces and observing (with an objective lens) the Newton's Rings pattern that result from the close proximity of the surfaces. A clear, well-defined, round series of concentric circles will result if the surfaces are near or exactly perpendicular to one another well away from any local surface defects, and if the tilt between the surfaces is minimized; the latter is accomplished by varying the tightness of the four set screws securing the adjustable level clamp to the Friction Device. A Teflon O-ring recessed in the SFA separates the Friction Device from the SFA's top, facilitating tilt variations due to its slight flexibility; a bellowed O-ring can also be used for more flexibility if necessary. The monochromatic light is usually generated by using a monochromatic source (a sodium lamp as pictured in Figure 3.4, for example). Alternatively, a white light source can be used in combination with a monochromatic filter placed above the surfaces and before the objective in the optical path. The filter allows the operator to see

only a single wavelength (or very narrow range of wavelengths) and hence observe the

Newton's Rings phenomenon.
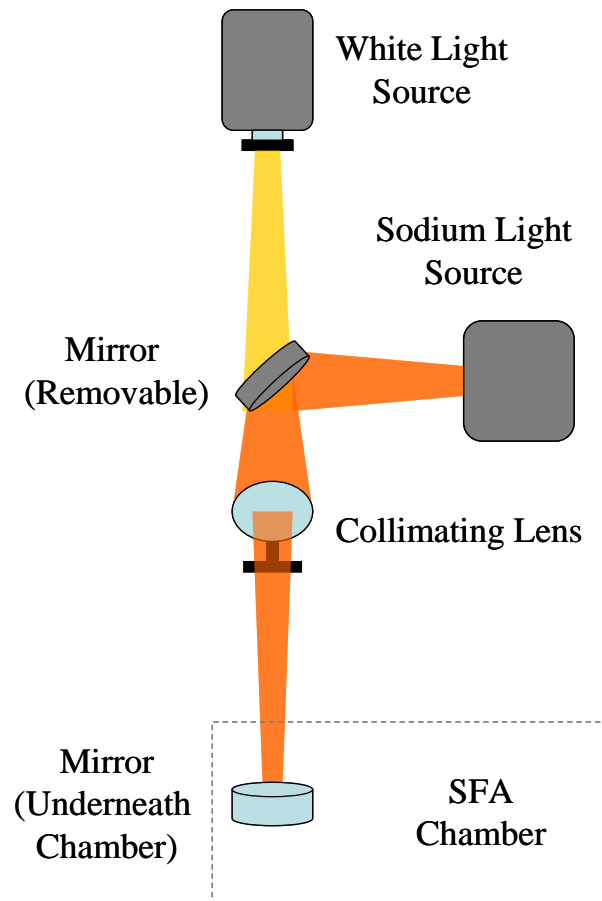
Figure 3.12: White light and sodium light source setup.

Once the surfaces are properly set in place and secured, the optics stand, mounted with

a prism, can be set in place and fine adjustments to lateral position, focus and tilt of the

latter can be performed. Optimal positioning occurs when the prism's exit beam

(comprised of white light from a standard halogen source that has passed normally

through the surfaces, the focusing lens and the prism) strikes the spectrometer slit

normally and is centered both vertically and horizontally on the slit. Further adjustments

to the optical path are often necessary so that light emerging from the point of contact

strikes normal to and centered on the spectrometer slit. The resultant interference pattern, comprised of Fringes of Equal Chromatic Order (FECO), should appear sharp and well-defined (this is more important for small separations). They should also move horizontally across the screen (i.e., the wavelength axis; see Section 3.1.2 for more details) when the surface separation is varied, and if they do not, the camera must be rotated in its sleeve until they do.

Once the optical path has been properly aligned and a circular set of Newton's Rings has been found, the following preparations should be done before actual testing begins:

1) The thermistor tip should be carefully placed as close as possible to the surfaces without touching or disturbing the mounts or the surfaces. In the experiments presented here, the thermistor-surface distance was approximately 1-2 millimeters, after the wire was fed through the vapour pressure port.

2) All ports to the SFA must be sealed in order to minimize air currents near the surfaces. In the experiments presented here, the vapour pressure port was closed, but not fully screwed in to avoid damaging the thermistor wire.

3) The front panel to the SFA outer chamber must be put in place to minimize air currents around the SFA.

4) The floating table's resistance to vibrations should be checked by pushing down gently on each corner and gauging the response; if the table doesn't cushion the disturbance adequately, air pressure to the table should be increased or decreased as appropriate.

5) All extraneous electrical equipment should be turned off to minimize the generation of heat and vibrations within the room.

6) All electrical equipment should be checked to make sure that it is functioning properly and is running optimally. All remote controls that are to be used, in particular, should be checked to make sure they respond properly.

7) The Signal Conditioning Amplifier Balance should be checked by turning the Excitation switch off while the gain is set to X100 and then checking the output lamps. The amplifier is balanced if the lights are extinguished. If the lamps are even slightly lit, the AMP BAL adjustment should be turned (using a small flathead screwdriver) until they are fully extinguished. The Excitation must be turned back on and the Gain set to the desired level when this procedure is complete.

8) The Signal Conditioning Amplifier Bridge should be balanced, if necessary, by using the Auto Balance Reset knob (for large adjustments) and/or the Trim knob (for small adjustments) until the lamps are extinguished. Once the balancing is finished, the amplifier should be monitored for an hour afterward, while keeping temperature in the room as stable as possible, to see if it drifts significantly. If it does (that is, if one of the lamps becomes a solid or semi-solid red), this step should be repeated until the amplifier remains relatively stable over the monitoring period.

9) Ensure that the Signal Conditioning Amplifier filter is set to as low a filter level as possible without adversely affecting the experiments that will follow (typically at least five times the anticipated maximum shearing frequency to be used, so that

higher harmonics remain unfiltered as well), to maximize the output's signal to noise ratio. The filter used here is a two-pole Butterworth filter and the experiments involve frequencies up to 10 Hz, and so a filter setting of 100 Hz has been used with the data presented.

10) Any limit switches to be used must be set to ensure the safety of the SFA. This is achieved by gently bringing the surfaces near to contact using the coarse control (preferably using the motor while set to a very slow setting) while the medium control is near its upper position. Then bring the surfaces slightly out of contact using the coarse control (again, this is best achieved using the coarse motor on a very slow setting), and once the surfaces are near to but not in contact, bring them back into gentle contact with the medium control. Both micrometers should ultimately sit near the center of their operating range in case further adjustments need to be made later. Once the micrometers and surfaces are both positioned optimally, the limit switches should gently be brought as near to triggering as possible. This will ensure that the surfaces will press no further beyond contact during testing than has been allowed by the final medium control adjustment in the event of motor or software failure. It should be noted that any adjustment to the fine micrometer will offset the limit position of the coarse micrometer, and so the former should be used sparingly during testing and returned to its original position whenever convenient to avoid cumulative error in the limit position. Generally, though, the fine micrometer correction should not make much difference overall because of its miniscule range, and so is not a major concern. The limit switches should be tested several times with the coarse control on a

slow setting to ensure it is functioning properly and returning to the same point with each approach. If it is not, the limit switches should be adjusted to maximize their sensitivity to the triggering mechanism.

11) The methods of determining the gap size discussed in the following section both require a foreknowledge of the index of refraction, μ, and so a run tracking the index of refraction as a function of gap size using traditional optical methods discussed in Section 2.3 should be performed. Because both the extraordinary and ordinary fringes must necessarily yield the same separation either can be used (as per Israelachvili[335, 337]), and in the experiments discussed here the ordinary fringe was used. Because the refractive index was not found to vary substantially over the range of separations tested (specifically, $\Delta\mu/\mu$ was found to be $\pm 3\%$, smaller than the $\pm 10\%$ estimated accuracy for the methods described below), a single value for μ of 1.56 was used, obtained with the spectrometer centered at 5850 Å.

12) Because the testing should begin as soon after the sample agitation is complete as possible, and because an accurate calculation of gap size can be time-consuming, a rapid method of separation determination has been developed for both gap sizes. Since it requires precise knowledge of the final FECO fringe placement or separation (depending on which gap size, 0.5 µm or 5 µm, is desired), markers must be placed on the LabVIEW camera image so that both can be determined very quickly by eye. This technique and the markers that are used with it are described in more detail in the following section.

3.3.1 Calculation of Surface Separations for Remote Experiments

Israelachvili et al and other groups have developed several techniques for the determination of gap separation using the principles of three-layer thin film interferometry, as described in Section 2.3[335, 337, 342, 369]. Many of these methods, however, involve the tracking of fringes by spectrometer and recording their respective changes in wavelength, which is not possible when the SFA is being used remotely, as the spectrometer used in the current experiments cannot be operated remotely. Furthermore, because the experiments are to be begun as quickly as possible after the sample is agitated and specific gap sizes are required, it is necessary to have a quick method of determining the surface separation without sacrificing its accuracy. Consequently, the aforementioned conventional methods have been adjusted and LabVIEW software has been developed that will accomplish this.

The basic equation to be used is given by Israelachvili[337]:

$$ D = \frac{1}{\left(\lambda_{p-1} - \lambda_p \right)} \left[\frac{\lambda_p \lambda_{p-1}}{2\mu} + \lambda_{p-1} T_p - \lambda_p T_{p-1} \right] \tag{3} $$

where D is the gap size, λ_p and λ_{p-1} are two adjacent fringe wavelengths that lie between two previously measured adjacent contact fringe wavelengths λ_n^0 and λ_{n-1}^0, μ is the sample index of refraction, and T_p and T_{p-1} are hypothetical distances representing a wavelength shift of λ_n^0 and λ_{n-1}^0 to λ_p and λ_{p-1}. This equation is exact and is ideal for measuring separations remotely, as the ideal fringe wavelengths, λ_p and λ_{p-1}, can be calculated beforehand using a pre-measured value of μ and the automated LabVIEW script developed (as described in Sections 2.4.4 through 2.4.6). The appropriate

positions, with the required fringe separation considered, can then be overlaid on the camera image for rapid gap separation determination during testing. To obtain the desired gap size, then, the operator need only adjust the coarse micrometer to approach the right separation, and then fine tune the separation using the fine micrometer setting until λ_p and λ_{p-1} match the markers on the screen. This method is ideal for remote determination of large separations such as the 5 µm gap size studied in the experiments presented in this thesis.
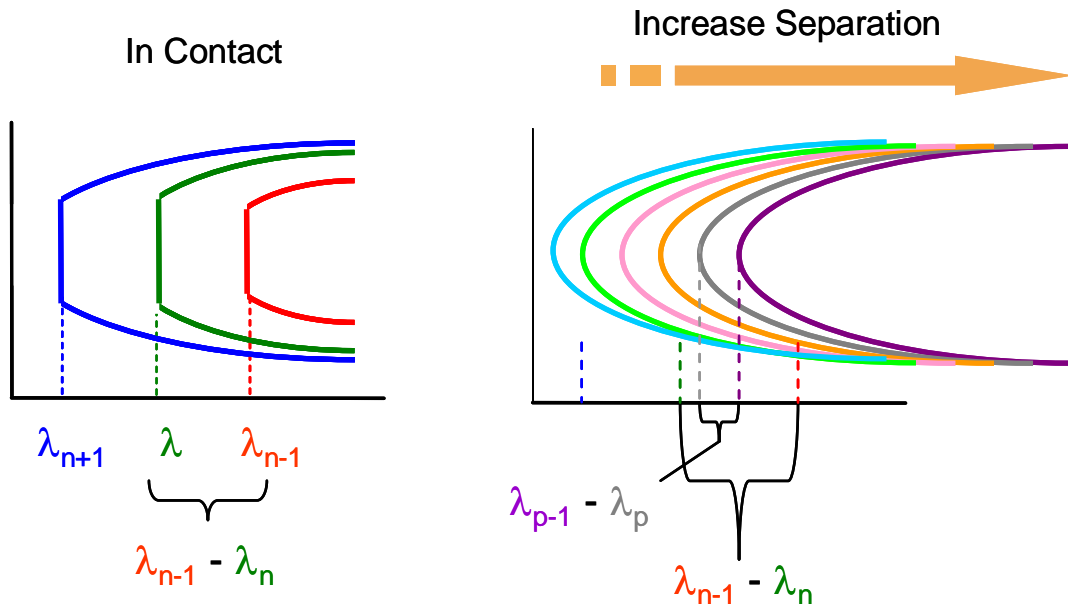
Figure 3.13: Sketch of the fast determination of the 5.0 µm separation. The process starts on the left, with surfaces in contact, where λ_{n-1} and λ_n are recorded. It ends on the right, when two fringes spaced exactly λ_{p-1} - λ_p apart lie between the former λ_{n-1} and λ_n positions. The λ_{p-1} - λ_p spacing is defined such that $D = 5.0$ µm in Equation (3).

The speed at which one can obtain the desired gap size will vary, but if the user has a general idea of how long it takes for the surfaces to separate at maximum stepper motor speed, the proper separation can often be found within about twenty seconds and the shearing can begin shortly thereafter.

For smaller separations (like the 0.5 μm gap size also studied in the experiments presented here) the above method is not sufficiently accurate, as the change in adjacent fringe separation is not large enough over such a range. One can, however, use the simple but effective approximation described by Israelachvili[337] in which one counts the fringes passing by a contact point fringe, λ_n^0, upon separating the surfaces, as each one represents a separation of $D_{fringe} = \lambda_n^0 / 2\mu$. Therefore, by working backward from this equation with a gap size, D, (which, for the present experiments, is 0.5 μm), and pre-measured values of μ for various separations, one can determine the number of fringes and where the final fringe must be positioned for the desired separation D:

$$N_{fringe} = \frac{2\mu D}{\lambda_n^0} \tag{4}$$

where the whole portion of N_{fringe} represents the number of fringes passing the λ_n^0 position and the fractional portion represents the fraction of one fringe separation the final fringe comes to reaching the λ_{n+1}^0 position. As with the previously mentioned larger separation method, the necessary fringe positions to attain the desired gap size can be overlaid on the camera image in order to determine the separation quickly.
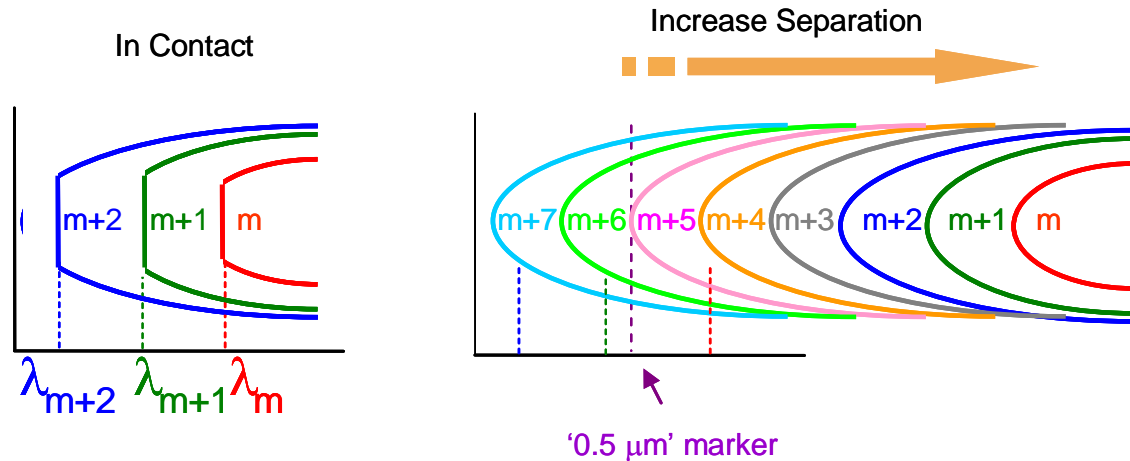
Figure 3.14: Sketch of the fast determination of the 0.5 µm separation. The process starts on the left, with surfaces in contact, and ends on the right, when a set number of fringes have passed the contact position (here, λ_{m+1}) and the last fringe has reached a predetermined point representing the 0.5 µm separation.

One notable limitation on this method is that the surfaces must be moved apart slowly enough that the fringes can be counted precisely before the final fringe position is sought. By advancing too quickly, the fringes temporarily blur making tracking them difficult. Nevertheless, with due care and some practice before the test run begins, a methodology can be adopted whereby the surfaces can be separated from contact and in place within about fifteen seconds.

3.3.2 Experimental Parameters and Procedure

Once the surfaces are in place, the optical path has been optimized and the final SFA, electronics and room preparations have been completed as outlined above, the door to the room can be closed and the testing can begin. Experiments were performed on smectic 8CB for two separations (0.5 µm and 5 µm), the former nearer to the calculated de Gennes penetration depth[312] and the latter further into the mesoscopic regime; the gap

sizes approximately correspond to those used by Koltover and Idziak in their series of experiments[54, 127, 128, 317, 319, 320, 370] so a comparison can be made between the results as well. The Bimorph Slider was used as the lower mount, in order to create a shear constant velocity oscillatory shear pattern (with velocity reversing direction at the extremes), and the Friction Device was used as the upper mount in order to gauge the shear response. For each gap size, experiments were performed at three different shear amplitudes (62.5, 625 and 6250 nm) and four different shear frequencies (0.01, 0.1, 1 and 10 Hz). Many of the tests were performed at three different temperatures (approximately 20.5°C, 22°C and 27°C), although the focus of the analysis was on those results obtained at 20.5°C, as the shear response was largest and best-defined at that temperature due to the greater stiffness of the material. The experiments were performed in the following general order:

Table 3.2: List of experiments grouped by experimental parameters

Group #	Experiments
1	1st round of 20.5°C tests (62.5 and 625 nm amplitudes, all frequencies and both gap sizes)
2	All 22°C tests (62.5 and 625 nm amplitudes, 0.01 and 0.1 Hz frequencies, and both gap sizes)
3	All 27°C tests (62.5 and 625 nm amplitudes, 0.01 and 1.0 Hz frequencies, and both gap sizes)
4	2nd round of 20.5°C tests (62.5 and 625 nm amplitudes, 0.01 and 0.1 Hz and both gap sizes)
5	3rd round of 20.5°C tests, after the semiconductor strain gauge mount is switched to the resistive strain gauge mount (6.25 μm amplitude, all frequencies and both gap sizes)

As indicated in the table above, for the smaller two amplitudes the semiconductor strain gauge mount was used within the Friction Device, as it is the more sensitive of the

two possible mounts. For the largest amplitude the resistive strain gauge mount was used, as it is more robust and so can handle larger deflections with less risk of breaking it. The bridge voltages used for the semiconductor and resistive strain gauge experiments were 5 V and 10 V, respectively (a lower semiconductor strain gauge bridge voltage was used to avoid damaging the gauge under high strain conditions, as per instructions given by the manufacturer). During each series of tests performed shown in Table 3.2, the only time the SFA room was entered was to either change the room temperature or to switch the mounts, so that the temperature fluctuations during each test run were kept to a minimum throughout. The same pair of surfaces was used for all tests.

Before each test, any shear-related ordering in the sample from the previous test was removed by bringing the surfaces far out of contact (approximately 1 mm) and oscillating the sample in the normal direction repeatedly with a large amplitude (0.5 mm); this technique has been found to remove ordering in previous studies by Ruths et al[125]. The process has been LabVIEW-automated and is discussed in Section 2.4.6. Immediately following the agitation of the sample, the surfaces were brought into contact, where an image was captured via the main LabVIEW SFA-controlling software. The contact point was ascertained optically, by decreasing the separation until the normally-rounded FECO fringes flattened, indicating that the surfaces were on the verge of being deformed. Previous experiments have shown that the last one or two monolayers of 8CB remain even after considerable normal pressure has been applied[125], so that a perfect mica-mica contact point would not likely have occurred, but the difference from contact is expected

to have been negligible, especially considering the large separations used in the experiments performed.

Once brought into contact, the surfaces were separated to one of the two gap sizes being studied using the methods discussed above, as quickly as possible (generally within twenty seconds). The FECO was monitored using the *SFA Control Panel* software, upon whose QCam image both the necessary 0.5 μm and 5 μm lines were overlaid so that the appropriate gap sizes could be determined as quickly as possible. Immediately after ascertaining the gap size, the shear experiments were begun. As mentioned above, the Bimorph Slider provided a constant velocity shear (except at the path extremes, where the velocity was abruptly reversed) and the shear response was measured by the Friction Device as a voltage. The response voltage was sent via a shielded cable to the Signal Conditioning Amplifier (SCA), where the signal was amplified 11 000-fold and then filtered using a 2-pole 10 Hz low-pass Butterworth filter. The SCA output signal was sent directly to the BNC 2110 shielded connector block, which was in turn read by the data acquisition card using LabVIEW software. Because the experiments were performed with frequencies orders of magnitude different from one another and tests were to be performed for as long as possible, different data collection rates were used depending on the frequency, with a targeted total number of points per experiment of roughly 10^6. The data rates used were:

Table 3.3: List of data rates used for the various shear frequencies tested

Shear Frequency (Hz)	Experiment Duration (sec)	Data Collection Rate (points/sec)	Total Points Collected	Points per Shear Cycle
0.01	25 200	50	1.26×10^6	5000
0.1	10 800	50	5.4×10^5	500
1	10 800	100	1.08×10^6	100
10	1800-3600	500	$9 \times 10^5 - 1.8 \times 10^6$	50

It should be noted that because of the many processes running on the computer during any given experiment, collecting at data rates higher than 500 points per second runs the risk of overloading the system and so this number was used as an upper limit for tests running longer than a few minutes with the LabVIEW automation software, despite the data acquisition card's limit being 1000 points per second. The air temperature 1-2 mm from the surfaces was measured by a thermistor and the temperature data was collected every second. An image of the FECO fringes was collected by the QCam camera attached to the spectrometer, and an image was saved every 60 seconds. The entire process, including control of all components used before and during the experiment, was controlled by LabVIEW programs coded by the author, described in Section 2.4.

Chapter 4

Results

    Results for the tests described in Chapter 3 are presented below, beginning with preliminary data collected using a rheometer to compare its shear response profile of smectic 8CB with that obtained from the SFA (Section 4.1); a characteristic non-linear behaviour for both is observed and reported. A survey of the various response characteristics observed for different shear parameters is then provided, with attention paid to a kink that is present both during moderate and aggressive shearing (Section 4.2). A discussion of the reproducibility of the results follows, along with the dependence of the response amplitude on temperature and shear rate (Sections 4.2.2-4.2.3). Of particular interest is the observed transition from shear-induced thickening to thinning behaviour that occurs with increasingly aggressive shearing, for which a schematic summarizing the phenomenon and plots showing the amplitude-shear rate relationship for large amplitude shear are provided. The response amplitude is found to decay according to a two-exponential curve, and the time constants of the resultant fits are plotted as a function of shear rate, shown alongside x-ray results of smectic 8CB sheared under similar conditions from Nieman et al[323]. A discussion is also given of the method used to eliminate noise from the collected data via high-pass post-acquisition filtration and extraction of the first harmonic values to allow for easier fitting of the results (Section 4.2.4), followed by a corresponding plot of two-exponential time constant vs. shear rate, this time using the filtered data. Both shear-induced time thickening and thinning time

228

constants were found to fall on the same lines, indicating a single direct cause for both phenomena.

A comparison is then made between the measured shear responses at the two gap sizes, 0.5 μm and 5.0 μm (Section 4.2.5). The ratios of these response amplitudes are themselves compared to those predicted by a simple approximation given by Newton's Theory integrated over the crossed-cylindrical geometry of the SFA confinement volume, and it is shown that while the theory and measured values agree fairly well at asymptotic times, early on the measured value can greatly exceed the theoretical ratio. This is followed by a discussion of the shape of the shear response curve itself and the various possible models that could potentially represent it (Section 4.2.6). Ultimately two models are selected: A Burgers Model, which has historically been used to describe viscoelastic materials undergoing shear, and a Split Model, made up of two steps, a Kelvin-Voigt curve for points preceding the observed kink occurring mid-period, and a simple cubic for post-kink data. The latter model originates from the theory that the aforementioned kink represents the point at which the viscoelastic limit has been reached, beyond which essentially viscous flow is occurring. Various other observed intra-period features are also discussed, the most important of which are frequent jumps in response that exceed that measured from noise contributions (Section 4.2.8). It is proposed that these jumps are a direct result of domain reorientations. The frequency of jumps is found to decrease slightly with higher frequency shearing, but persist to the end of the test for all tested shear parameters.

The topic of Large Amplitude Oscillatory Shear (LAOS) is introduced next (Section 4.2.8). Storage and loss moduli G' and G'' obtained from rheology tests are shown as a function of percent strain in an effort to understand the shear dynamics of confined smectic 8CB, and the harmonic ratio (A_N/A_1, with A being the transformed response amplitude) of the Fourier Transformed SFA shear data are compared to those expected from a perfectly triangular response, the difference in theoretical and measured values giving evidence that the viscoelastic limit has, in fact, been exceeded for the larger amplitude shear cases. This ratio is shown to increase for a short period following the onset of shear only in the tightly confined condition.

4.1 Rheology Results

Preliminary experiments were performed on smectic 8CB using a rheometer obtained from Rheometric Scientific Ltd. Both dynamic tests and tests of steady vs. oscillatory shear were performed, the former over a frequency range of from 0.1 to 100 rad/sec and strain amplitude range of 0.01% to 100%, and the latter from 0.011 sec^{-1} to 237 sec^{-1}. All tests were performed using a cone-and-plate geometry with a 56 μm gap, a cone diameter of 25 mm and a cone angle of 0.0988 radians. The data was collected at three temperatures: 20.5°C, 22°C and 27°C. The time domain shear response shows a slight elbow (or kink) that is most prominent for larger strains, as demonstrated below for a strain of approximately 10%:
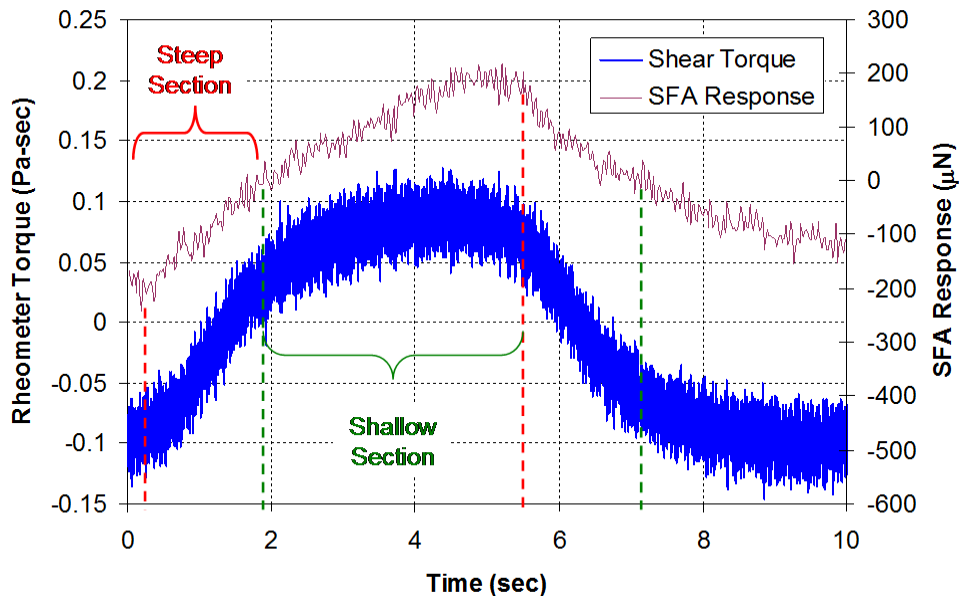
Figure 4.1: Overlay of the applied shear stress and resultant torque for 8CB confined to a 56 μm gap (for the rheometer) and 5 μm gap (for the SFA), sheared with (for the rheometer sample) 10% and (for the SFA) 12.5% strain.

As can be seen in the figure above, a similar elbow can be observed with smectic 8CB sheared using the SFA under similar conditions. The SFA has an advantage over most

rheometers in that it can easily explore smaller gap sizes and percent strains with customizable shear patterns and thereby provide a fuller picture of the transition from microscopic to bulk smectic 8CB dynamics. It should be noted that because the shear profiles for the rheometry and SFA measurements are slightly different (sinusoidal for the former and triangular for the latter) one should not expect an exact match in the overall shape of the response. The elbow does persist with both shear profiles, however, and the overall shear sweep can be thought of as being made up of two sections, an early steep part and a later shallow part. This feature will be discussed in the sections that follow.

4.2 SFA Shear Experiment Results

The shear responses that were obtained differed markedly in appearance depending on the shear parameters used. A schematic showing the distribution of the observed response shapes is given below:
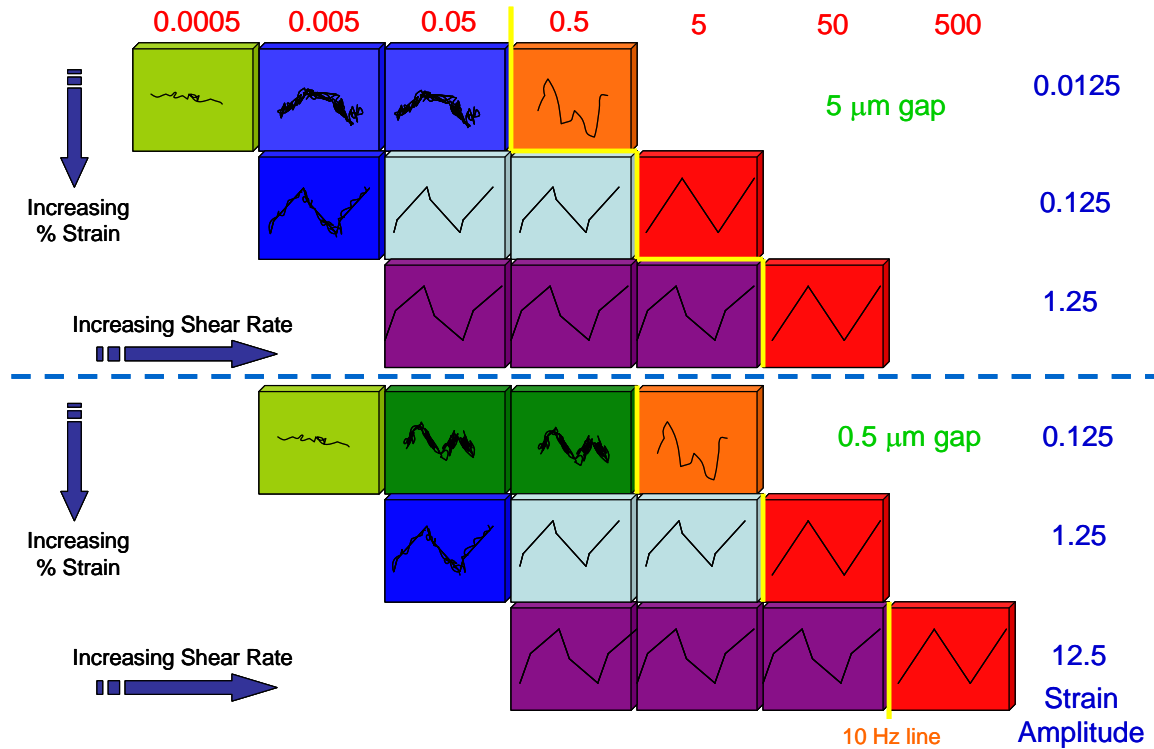
Figure 4.2: Summary of the various shear response effects observed for smectic 8CB under mesoscale confinement using the SFA.

Each square colour in the diagram above represents a response qualitatively different from other coloured squares in some way, while the pictographs within the squares represent the shape of the response corresponding to that colour, as described in the table below:

Table 4.1: Shear Response Characteristics

Square Colour	Shear Response Characteristics
Lime Green	Very noisy with no obvious response trends observed
Light Blue	Very noisy response, with a vaguely oscillatory response that is susceptible to thermal and electronic drift
Forest Green	Very noisy response, with a triangular response that is somewhat susceptible to thermal and electronic drift
Dark Blue	Slightly noisy triangular response that sometimes contain a small elbow early on in the shear sweep
Cyan	Well-defined triangular response that clearly exhibits a small elbow early on in the shear sweep
Purple	Well-defined largely triangular response with a smoothly changing slope throughout
Orange	Noise-free vaguely oscillatory response
Red	Very well-defined triangular response with slight blunting at the peaks

All plots related to these shear experiments, showing the response for the first five periods, are presented in Appendix 1.

It should be noted that response curves to the right of the yellow line (labeled the '10 Hz filter line'), corresponding to the orange- and red-coloured squares in Figure 4.2, have been significantly altered by the presence of a 10 Hz low-pass post-amplification filter within the signal conditioning amplifier. The filter was necessary to remove signals observed beforehand at 37-38 Hz due to vibrations from an air conditioning fan within the test room (which, in turn, was necessary to maintain a near-constant temperature within the test chamber, to minimize voltage drift in the strain gauge's Wheatstone bridge). The filter attenuation graph provided by the manufacturer indicates that the first harmonic of a 10 Hz triangular response will be attenuated by approximately 40%, while higher harmonics will be attenuated by 90% (for the second harmonic) or more (96% for

the third harmonic, 98% for the fourth harmonic, etc.). Since the Fourier series of a

triangular wave consists of a series of sine waves of decreasing amplitude, such an

attenuation profile will lead to a blunted triangular response, matching the pattern

observed for the 10 Hz shear responses. The shapes of the 10 Hz curves, therefore, do

not accurately describe physical phenomena and cannot be interpreted as being the result

of a shear-related dynamic or structural shift in the 8CB. A reconstruction of the

response curve is possible by inverting the transfer function of the post-amplifier filter

and applying it to the measured response, but because it may be inaccurate due to the

small post-filter signals it has been omitted. The *amplitudes* of the 10 Hz curves,

however, can be easily reconstructed since the fine details of the response curve will not

contribute greatly to its overall amplitude, and so have been used in the analysis that

follows. All 10 Hz response amplitudes have been increased by a factor of $5/3$,

corresponding to the aforementioned first harmonic attenuation factor, which should

reestablish the magnitude obtained before filtering.

4.2.1 Reproducibility of Results

   The SFA surfaces tend to deteriorate over time as shear is applied (a process that can

be monitored by observing the concomitant deterioration of the quality of the FECO

fringes from which the gap size is determined), making the optimization of the number

and length of experiments critical. One unfortunate byproduct of this property is that it is

often difficult to perform multiple identical experiments to ensure the results are

reproducible without sacrificing experiments that may yield more valuable results.

Because of the inherently qualitative nature of the results and the overall sensitivity of

these results to varying experimental parameters, reproducing the experiment with a new pair of surfaces can also be unreliable and hence undesirable. Even with great care, changes in surface quality, surface alignment, the amount of material being tested, and the strain gauge bridge balance will occur, all of which can alter the overall output data from experiment to experiment. For this reason, it is essential to perform the entire set of experiments using a single pair of surfaces in order to minimize the variation between tests. Nevertheless, duplicate experiments were performed following the initial series of tests in an attempt to reproduce the original results for the set of 625 nm shear amplitude tests. A fresh set of surfaces were used, and the resistive strain gauge was used in place of the semiconductor strain gauge that had been used with the original tests. The results were found to be quite similar in both shape and amplitude, and two examples are presented below in Figure 4.3:
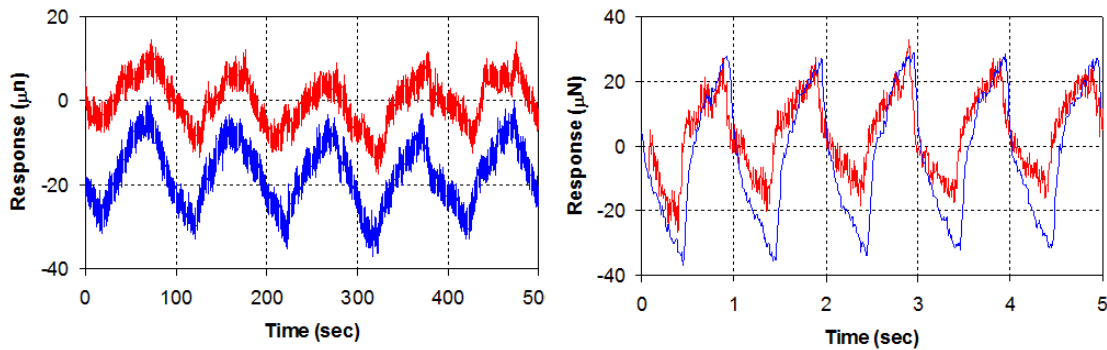
Figure 4.3: Overlay of shear responses from the original set of experiments (in blue) and experiments performed later (in red), showing the similarity between the two, for shear frequencies of (Left) 0.1 Hz and (Right) 1 Hz. A driving amplitude of 625 nm was used in both cases.

Note that the data from the second set of experiments (in red) is visibly noisier than that obtained from the later experiments (in blue), particularly for the 1 Hz results. This is a consequence of the 10 Hz low-pass post-amplifier filter mentioned earlier, which was

236

used for the original tests but not for the subsequent tests, and of having used the less sensitive resistive strain gauge for the subsequent tests.

4.2.2 Temperature Dependence of the Response

The shear experiments were performed at three separate temperatures: Most were performed at 20.5°C, and the results in the sections that follow were taken at this temperature. Subsequent tests were performed at 22°C and 27°C, and all temperature readings had an uncertainty of ±0.1°C. All tests were performed with the same pair of surfaces and setup, and the test room was allowed to adjust to each temperature over a period of ten to twelve hours. The responses obtained at the two higher temperatures were generally weaker than those obtained at 20.5°, indicating, as expected, that the viscosity has decreased with increasing temperature. An example of this response deterioration is shown below in Figure 4.4:
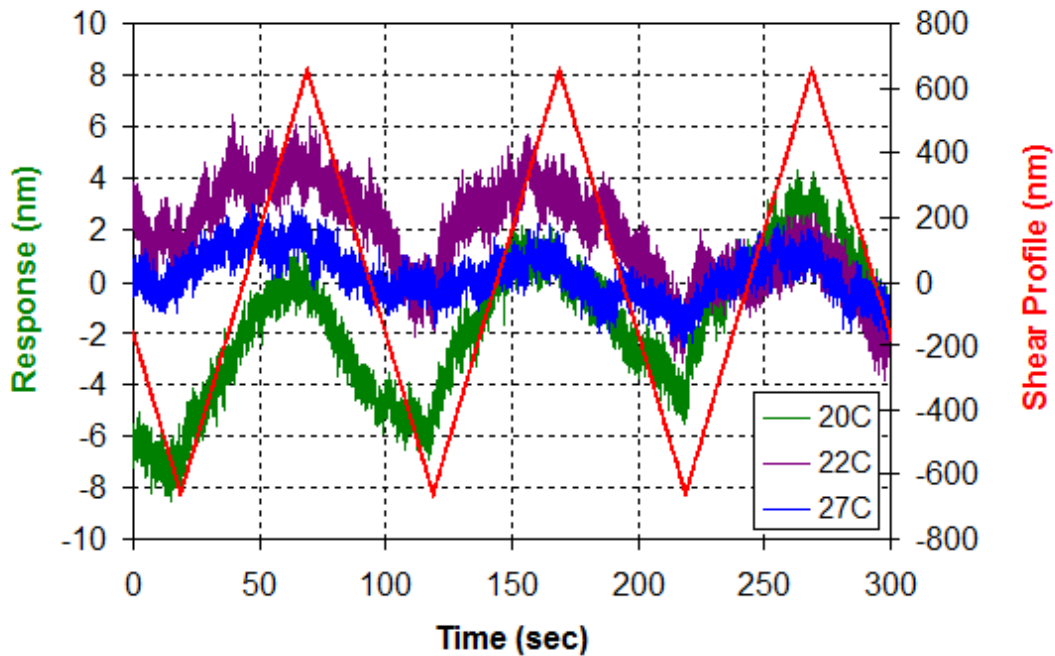
Figure 4.4: Initial shear response obtained at three different ambient temperatures, for 8CB confined to a 500 nm gap, sheared at a frequency of 0.01 Hz and with an amplitude of 625 nm. The shear profile is shown in red.

The rapid drop in viscosity with temperature underscores the importance of maintaining a low, stable temperature within the SFA, so that the response will be large enough to keep the signal to noise ratio high.

4.2.3 Shear Rate Dependence of the Shear Response Amplitude

The amplitudes of each shear response cycle were obtained by calculating the difference between the data extremes and converting it from voltage to shear force using the Friction Device calibration data (sample calculations for which have been provided in Equations (1) and (2) in Chapter 3). For the gentle shear tests only slight changes in amplitude were observed, while under more aggressive shearing, particularly with large shear amplitudes, the amplitude change was much more apparent. In the latter case, the

amplitude was found to decrease over time, indicating that the viscosity of the system

was decreasing and hence that shear-induced time thinning was occurring. An example

of this behaviour is shown in Figure 4.5:
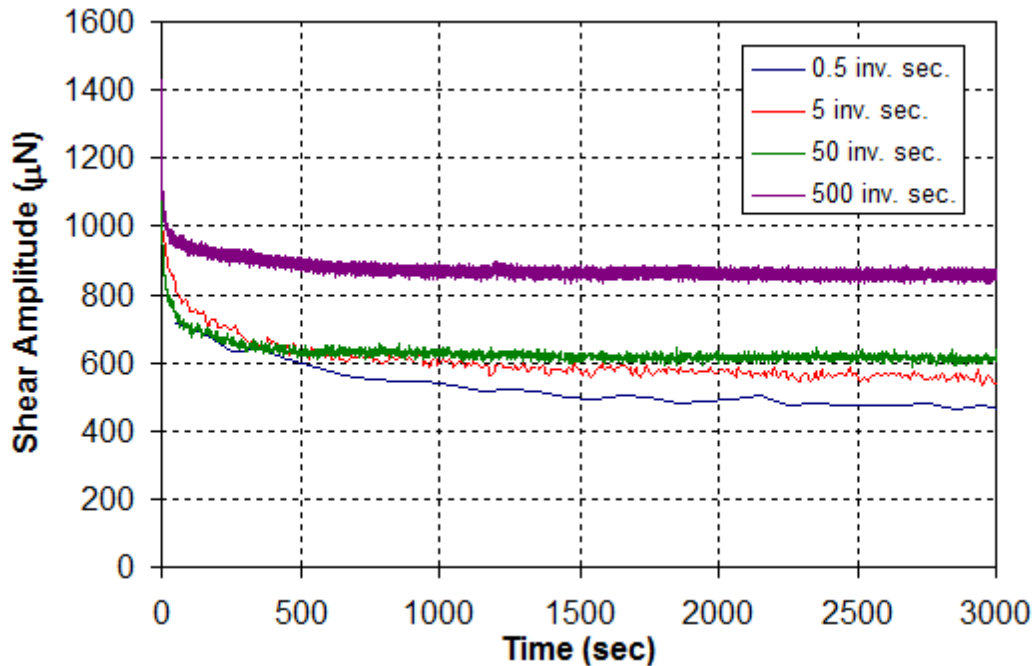
Figure 4.5: Plot of shear response as a function of time for 8CB sheared at various
frequencies (blue 0.01 Hz, red 0.1 Hz, green 1 Hz and violet 10 Hz) using a shear
amplitude of 6.25 μm and a gap size of 500 nm.

Both upward and downward shifts in response (the latter corresponding to shear-induced

time thickening) were observed, as summarized in Figure 4.6 below:
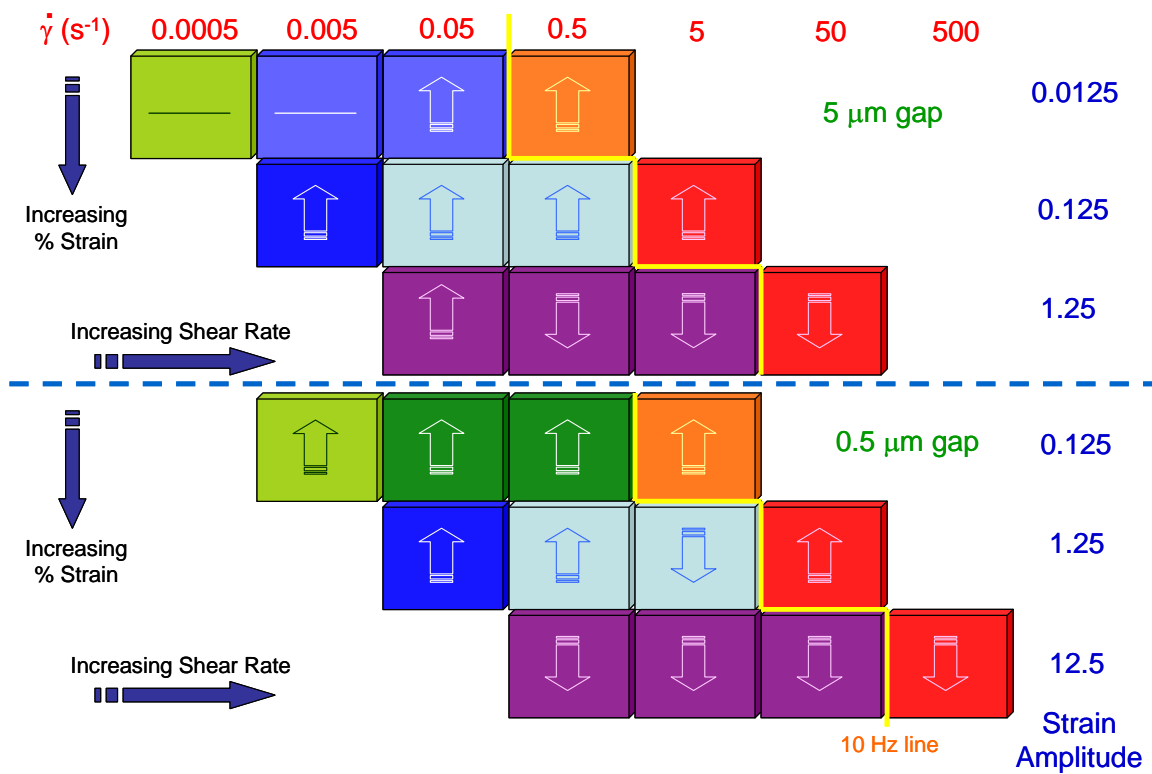
Figure 4.6: Summary of the changes in shear response amplitude for various shearing parameters. The square colours represent the shape of the shear response, as given in Table 4.1. Upward pointing arrows represent an observed increase in amplitude with time, while downward pointing arrows represent a decrease in amplitude with time and flat lines represent responses that were indeterminate due to the low signal to noise ratio.

The extent of thinning and thickening was generally found to be more pronounced in tests using a 0.5 μm gap size than for those using a 5 μm gap size, particularly during large amplitude shearing. A plot of the shear response amplitude as a function of shear rate for both gap sizes, both shortly after the onset of shear and at asymptotic times (from one hour for 10 Hz shear tests to eight hours for 0.01 Hz shear tests), is shown below:
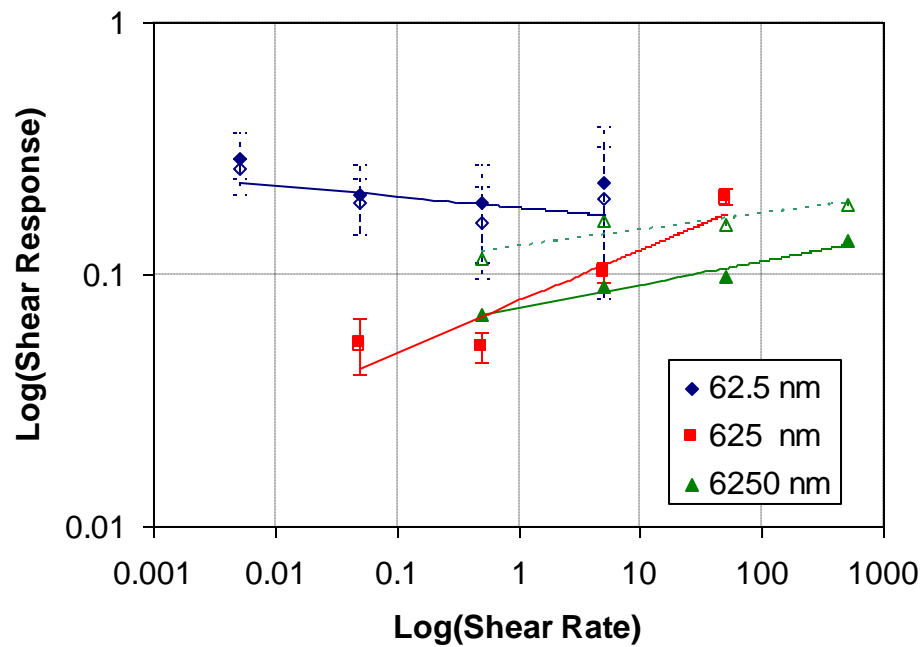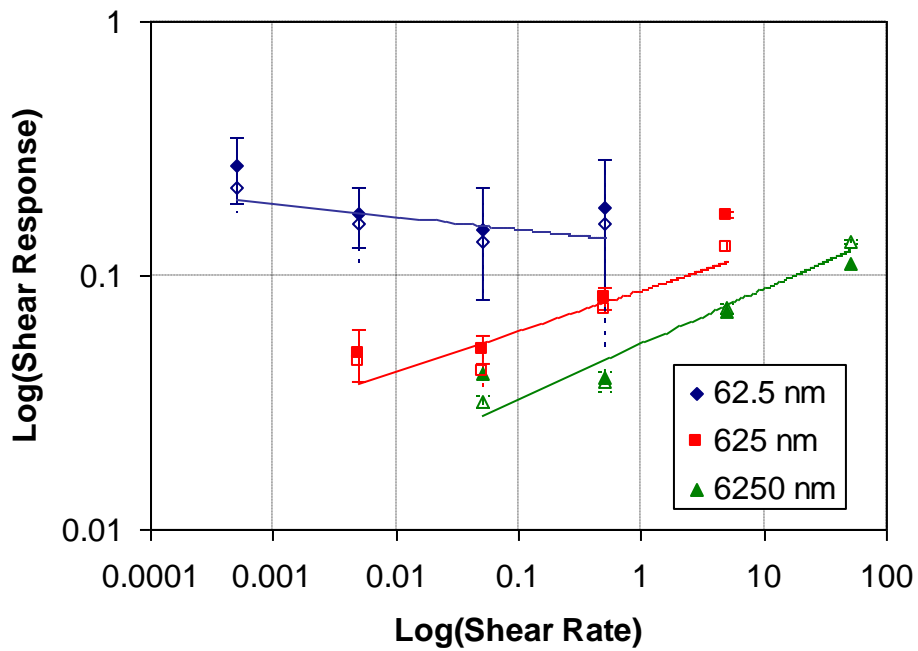
Figure 4.7: Log-log plots of shear response amplitude as a function of shear rate for gap sizes of (Top) 5 μm and (Bottom) 0.5 μm. Empty symbols represent the response during the first few (one to five) shear cycles and have solid error bars, while solid symbols represent the response at asymptotic times and have dotted error bars. Responses are normalized by shear amplitude for direct comparison.

The shear response uncertainty values shown in the figures above were estimated by assuming that over short time intervals (approximately five shearing periods) at asymptotic times (after hundreds or thousands of shearing periods, by which point changes in response amplitude were found to be minimal) the test conditions had changed only minimally, so that the variance in shear response can be accounted for only by uncertainty in the fitting, not in changes to the structure or dynamics of the sheared sample.

The change in shear response amplitude, A, as a function of time can also be modeled for the various test parameters. The following models were attempted:

i) A single exponential fit, $A = Ce^{-t/\tau} + A_0$ (where A is the shear amplitude, C is a proportionality constant, A_0 is the asymptotic response amplitude, t is time and τ is the time constant), indicating a single response time is sufficient to characterize the shear response, was found to be acceptable (that is, having a coefficient of determination, R^2, consistently above 0.9) for some test cases, but failed frequently both at early and asymptotic times for other test cases;

ii) A stretched polynomial with offset fit, $A = C \exp{(-t/\tau)^{\alpha}} + A_0$ (where α is a stretching exponent, ranging from 0 for a line, to 1 for an ideal exponential), representing a smooth distribution of shear responses (the response time envelope of which is characterized by α), was attempted next. It produced reasonable results, but also produced fitting parameters that showed no sustainable trends and consistently failed to reproduce the sharp curvature observed at early times for large amplitude shear tests, examples of which can

be seen in the purple and, to a lesser extent, the green curves in Figure 4.5.

And;

iii) A two exponential fit, $A = C_1 e^{-t/\tau_1} + C_2 e^{-t/\tau_2} + A_0$, representing two distinct shear responses each with its own response time (themselves represented by time constants τ_1 and τ_2), was attempted and was found to be acceptable in all cases where amplitude shifts were observed.

A sample two exponential fit is given below:
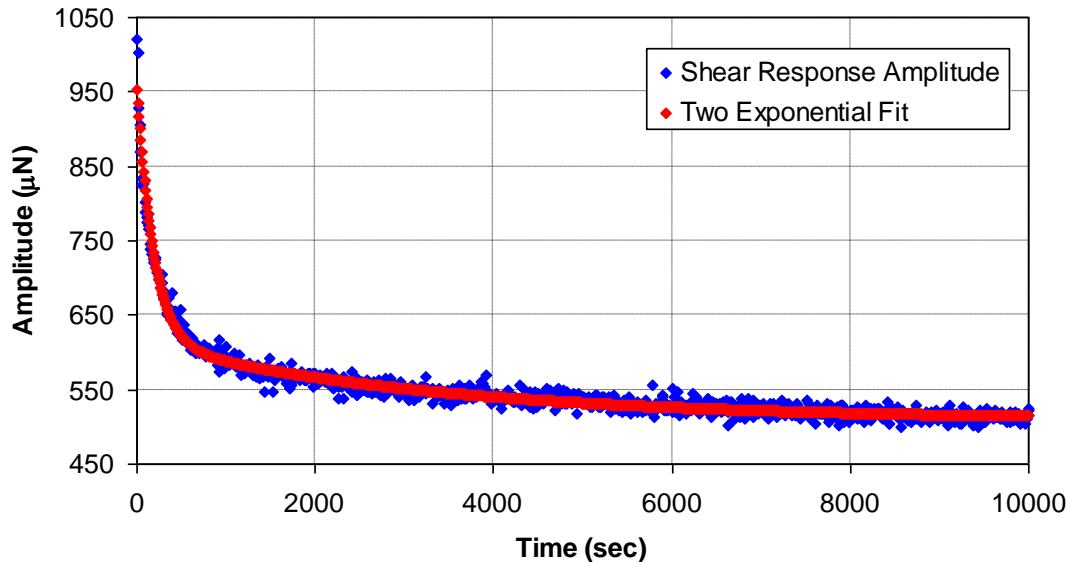
Figure 4.8: Shear response amplitude as a function of time for smectic 8CB sheared at 0.1 Hz frequency, 6.25 μm amplitude and gap size 0.5 μm, with an overlay of the two exponential fit reconstruction line shown in red.

A plot of the two exponential time constants as a function of shear rate for the two gap sizes is given below for the largest shear amplitude:
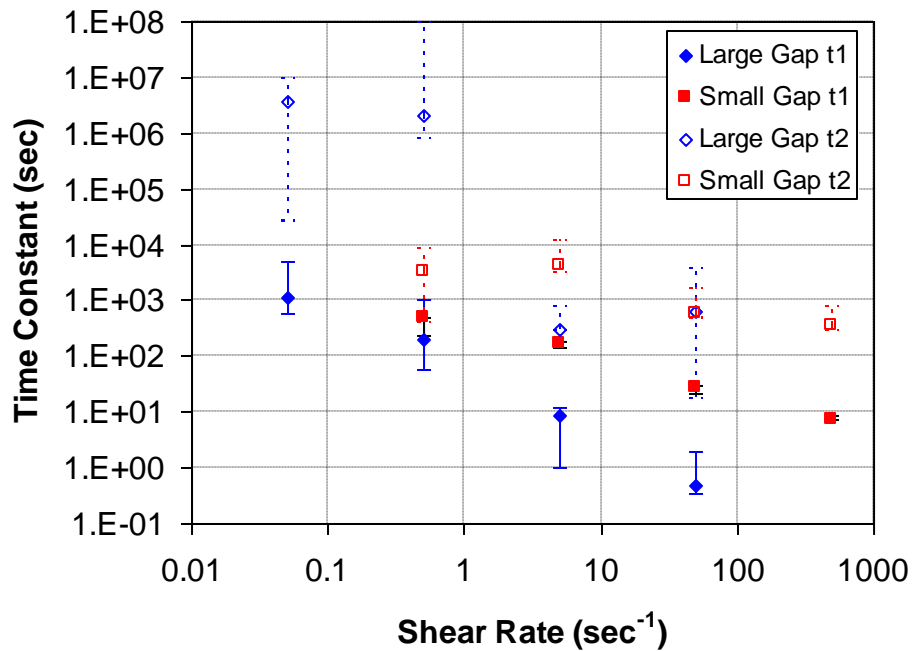
Figure 4.9: Plot of relaxation time constant vs. shear rate for shear amplitudes of 6.25 μm. Small and large gaps refer to 0.5 μm and 5 μm gaps, respectively. 't1' and 't2' refer to the 1st and 2nd time constants in the fitting equation $A = C_1 e^{-t/\tau_1} + C_2 e^{-t/\tau_2} + A_0$, respectively.

In several cases, the shear response data above a cutoff value was excised so that a stable asymptotic response could be obtained for fitting purposes. This cutoff point was determined by overlaying the response data with the accompanying temperature data (note that the response lags the temperature data by 600-700 seconds). Whenever significant fluctuations in the asymptotic response were found to correspond to thermal fluctuations (as determined by eye), a cutoff point was established before the fluctuation. Error bars on the above plot were estimated after the best nonlinear fit was determined, by fixing the time constant at a value shifted a set amount above the best fit value and then refitting. The process was repeated until either the R^2 value fell below 80% of the best fit R^2 value or the fit failed altogether by not converging (whichever occurred first),

and the time constant, τ_{upper}, was then recorded. The process was then repeated for time constants below the best fit value, τ_{lower}, and the difference between the two was used as a rough estimate of time constant uncertainty. Before a more rigorous analysis can be done, though, further processing of the noisier data sets is necessary, the method of which will be discussed in the following section.

4.2.4 Data Reproduction in Frequency Space

For smaller shear amplitudes, noise accompanying the response often makes the determination of amplitude difficult, and so further data processing is necessary to assist in the analysis. In order to improve the signal to noise ratio, Discrete Fourier Transforms (DFTs) and Power Spectra were generated for each data set using software written in LabVIEW by the author. Spectra were generated for one, two, five and ten cycle bins of data and the results were compared to ensure that no extraneous peaks were created due to the data processing. No such peaks were found even for the single cycle transforms; furthermore, only the single cycle transforms properly maintained the rapidly changing changes to the curve that sometimes occurred early on in the more aggressive shearing process. A sample overlay of the Fourier Transform reconstructions for the bin sizes tested is given in Figure 4.10:
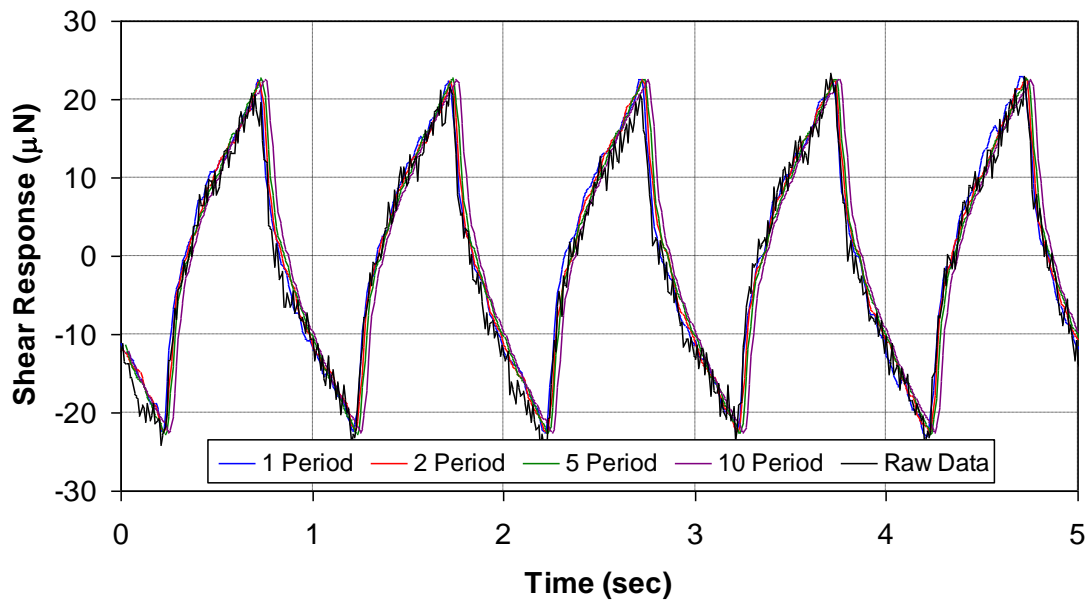
**Figure 4.10**: Overlay plot of shear response as a function of time for smectic 8CB sheared at 1 Hz frequency, 625 nm amplitude and gap size 5 μm.

A simple low-pass filtration of the signals at a cutoff frequency of $10f_0$ (where f_0 is the fundamental frequency of the triangular driving force) reduced the noise considerably, as shown in Figure 4.9 (leftmost plot). As a result, any fast and non-periodic events that may occur as a result of shearing must necessarily be filtered out. By assuming the responses are roughly triangular (visually ascertainable from the shear response in most cases) like the driving force, a further filtration was performed wherein all non-harmonic frequencies in addition to all frequencies above the 10th harmonic within the DFTs were removed, and an inverse DFT was then performed to recreate the original responses, including only their ten lowest harmonics. The noise in the resultant response was largely suppressed, and in some cases the characteristic 'elbow' observed in large (6.25 μm) amplitude shear responses were more distinguishable for the medium (625 nm)

246

amplitude shear responses as well. An example of this filtered signal is shown in Figure

4.11 (rightmost plot).
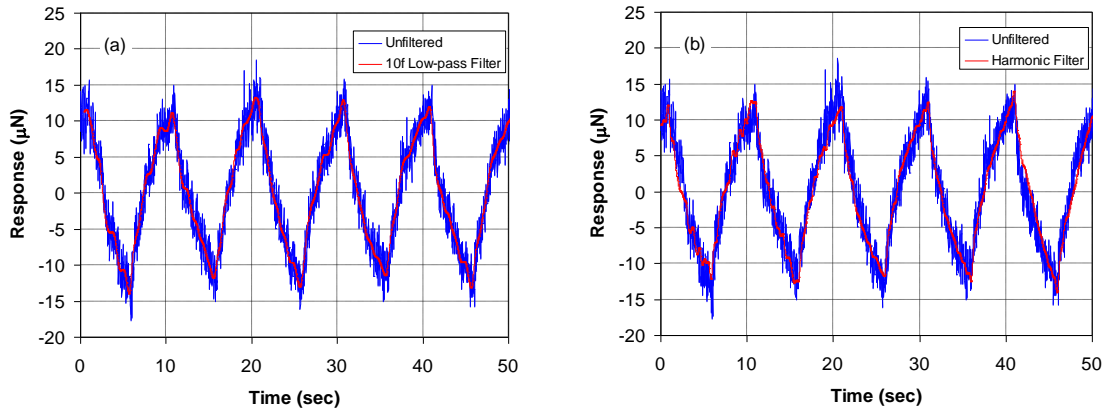
Figure 4.11: Plot of (left) an overlay of unfiltered data and data with a $10f_0$ low-pass filter, and (right) an overlay of unfiltered data and data with the harmonic filter used.

Since the first harmonic has an amplitude of $8/\pi^2 \approx 81\%$ of the overall amplitude as

given by its Fourier expansion (assuming a perfectly triangular response), it should track

the overall signal well and should be more easily discernable than the unprocessed data as

most of the noise across the frequency spectrum will have been removed. An example of

this is shown in Figure 4.12, where the response and the first harmonic are overlaid to

show their similarity.
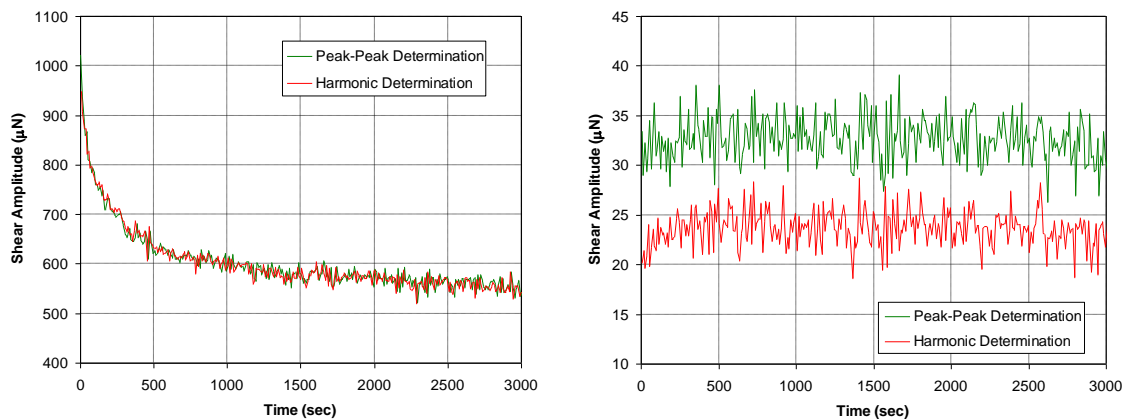
Figure 4.12: Overlay of a typical peak-peak amplitude vs. time curve and its corresponding first harmonic vs. time curve. On the left, an exact overlay is shown to demonstrate the similarity of the curves for a relatively noise-free response, while on the right the original data (in green) and the first harmonic data (in red) have been vertically offset by 10 μN from one another to more clearly illustrate the difference in signals at early times for a noisier response.

The magnitude of the first harmonic-determined amplitude was determined by finding the average peak-peak amplitude of the unfiltered data and the average amplitude of the first harmonic magnitude, then multiplying the latter by the ratio of amplitudes. As can be seen from the examples in Figure 4.12, the shape of the amplitude curve is well-preserved in the first harmonic curve both for the well-defined and noisier results, but with periodic artifacts removed, giving a slightly smoother curve that can be more easily fitted and interpreted.

The one-cycle DFT first harmonic responses exhibited a measurable change in amplitude during their first few shear oscillations for most of the experiments performed. Only the weakest shear experiments (62.5 nm shear amplitude and 5000 nm gap size for both 0.01 and 0.1 Hz shear frequencies) showed no significant and persistent amplitude

change, which is likely due to the exceptionally low signal to noise ratios masking the response for those tests. These harmonics can be fitted to a double exponential curve, $A(\omega_1) = C_1 e^{-t/\tau_1} + C_2 e^{-t/\tau_2} + A_0$, as was discussed in Section 4.2.3 for the raw shear response; a sample overlay plot of data and fit is given in Figure 4.8. Overlay plots of shear response and fitted curve for all tested shear parameters are presented in Appendix A1, Section 5. By plotting the smaller time constant, τ_1, as a function of shear rate on a log-log plot, the relationship between the two becomes clearer:
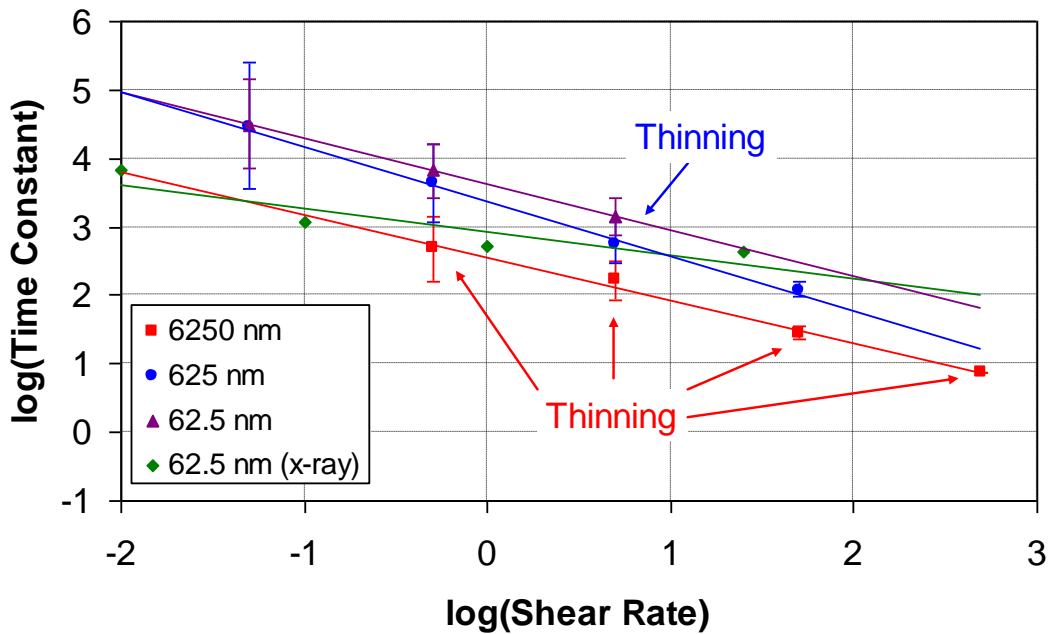
Figure 4.13: Plot of shear response time constants as a function of shear rate for 0.5 μm gap shear experiments for various shear amplitudes. Responses involving shear-induced time thinning responses have been marked; all others involve shear-induced time thickening. Also included are the peak shift time constants from similar experiments using an XCC[323].
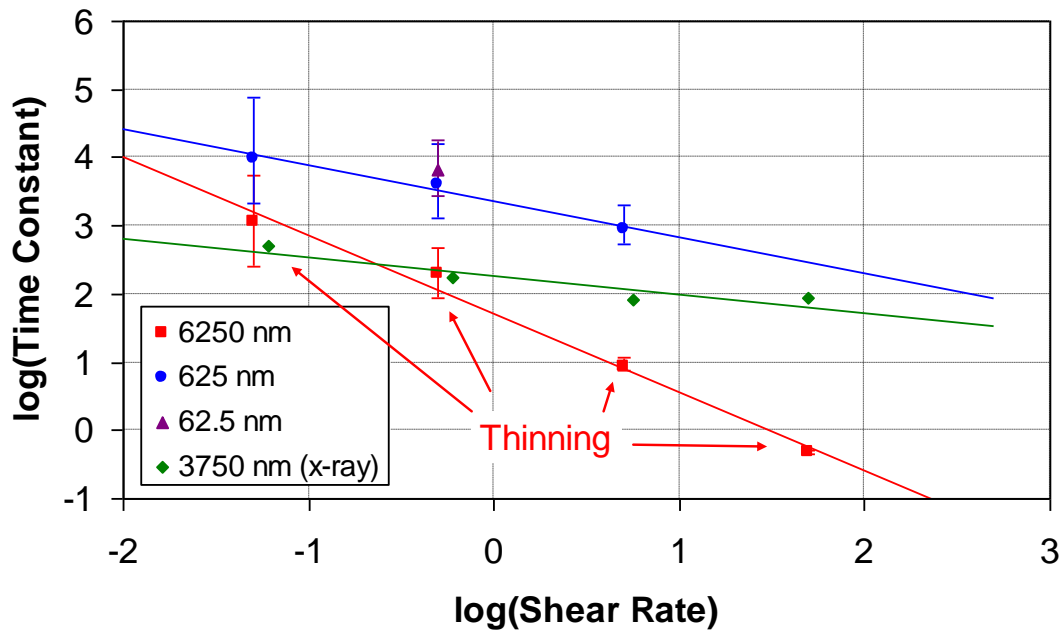
Figure 4.14: Plot of shear response time constants as a function of shear rate for 5.0 μm gap shear experiments for various shear amplitudes. Responses involving shear-induced time thinning responses have been marked; all others involve shear-induced time thickening. Also included are the peak shift time constants from similar experiments using an XCC[323].

The time constant uncertainties shown in the above two plots were estimated as they were

with the data presented in Figure 4.9, by refitting the curves with increasingly deviating

time constant values until either the constant of determination, R^2, fell below 80% of its

best fit value or the fit failed to converge altogether, and by using the resultant total

variation in time constant as the uncertainty.

It should be noted that the above graphs indicate the time constants for observed

shear-induced time thickening (as discussed in Section 4.2.3 and summarized in Figure

4.6) fall on the same line as those observed for shear-induced time thinning. The τ_2

values are often orders of magnitude larger than their corresponding τ_1 values, and in

many cases contribute little enough to the fit that the response effectively follows a single exponential curve, $A(\omega_1) \approx C_1 e^{-t/\tau_1}$. Because the secondary time constants are often on the order of several thousand seconds and as such are comparable in time to measurable temperature changes within the SFA chamber (<0.25°C), it is likely the τ_2 values correspond to a combination of thermal signal drift and long-term electronic instability rather than a shear effect. Time constants obtained by fitting the peak position data from x-ray data obtained previously[323] have been included in Figures 4.13 and 4.14 to show that the crystallographic observables follow similar time dependent behaviour.

4.2.5 Comparison of Shear Responses for Large and Small Gap Sizes

Figure A5.10, presented in Appendix 5, shows the magnitude of shear response generated by a crossed cylindrical geometry of *chosen* gap size, relative to a response due to a fixed parallel-plane geometry of *fixed* gap size (0.005 μm). This theoretical value has been calculated by integrating the response predicted by Newton's Theory of Viscosity over the crossed cylindrical surfaces and assuming a perfectly cylindrical sample (with ends distorted due to the crossed cylindrical confining surfaces) of constant volume and constant, single-valued viscosity, with fluid motion occurring entirely in the shear plane. Since all response lines are calculated relative to the same fixed planar shear conditions (including gap size), any two lines can be compared to one another easily by simply dividing the normalized geometric constants, $g_{0.005}C_{CC}/g_x$, for the gap sizes g_x, using an experimentally-determined sample radius, following the relationship established by equation (12) in Appendix 5. For the gap sizes used in the present study, 0.5 μm and 5.0 μm, the ratio of shear responses has been calculated to be approximately 1.57. That

is, for a sample of constant volume being sheared with a set frequency and magnitude, by adjusting the gap size from 5.0 μm to 0.5 μm the theory predicts the shear response will increase by a factor of 1.57, assuming the viscosity of the sample remains constant. Figure 4.16 shows this ratio for the three shear amplitudes tested as a function of time, with $t = 0$ corresponding to the onset of shear.
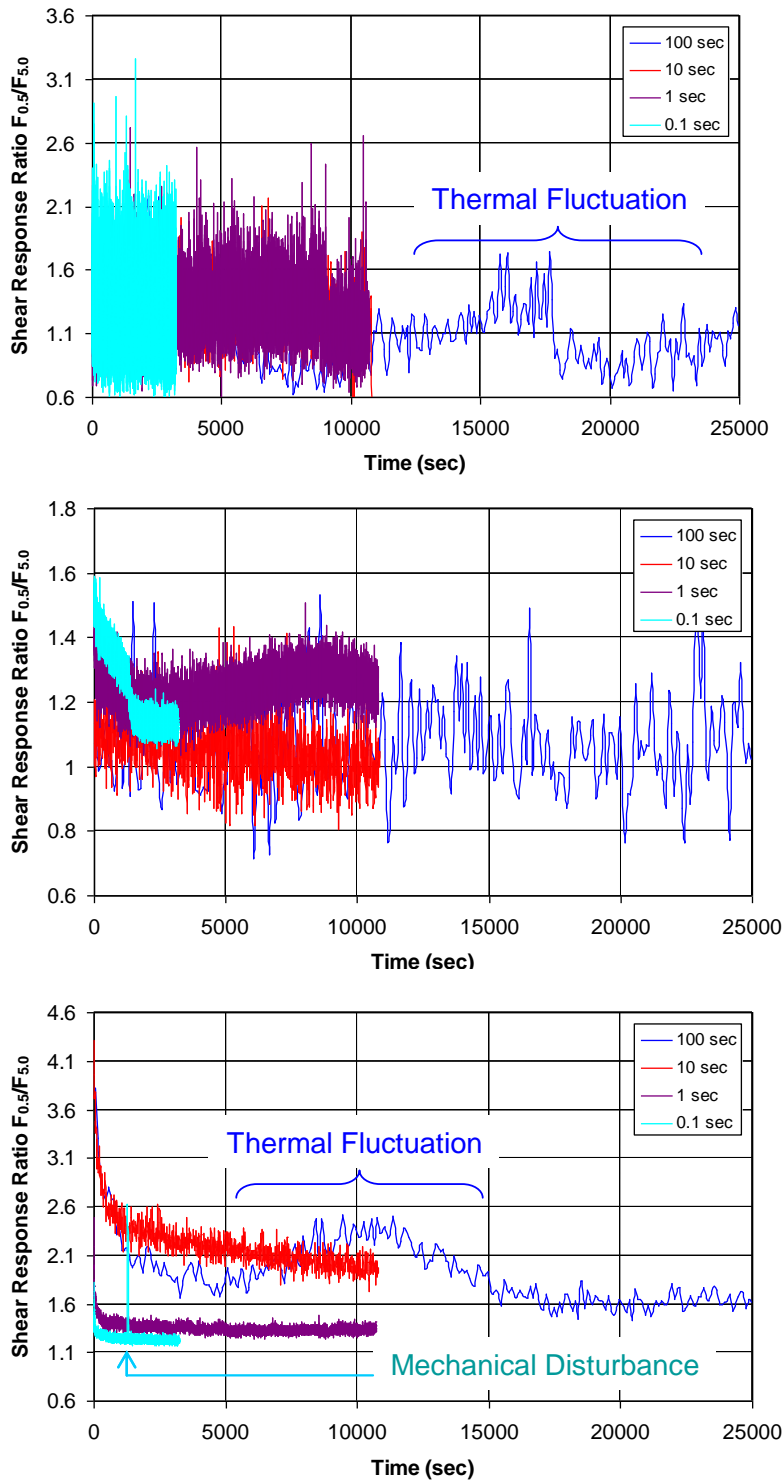
Figure 4.15: Plots of Shear Response Ratio $F_{0.5}/F_{5.0}$ as a function of time for shear amplitudes of (Top) 62.5 nm, (Middle) 625 nm and (Bottom) 6.25 μm for various shear frequencies.

Figure 4.15 shows that while the average response ratios for both the 62.5 nm and 625 nm shear amplitude all tend to begin between 1.0 and 1.6, those for the 6.25 µm shear amplitude begin noticeably higher, ranging from 1.82 for the 10 Hz shear test to 4.3 for the 0.1 Hz shear test, before settling to values below 2.0. An interpretation of this behaviour is presented in the Discussion chapter.

4.2.6 Intra-period Fitting Results

   With each experiment, the response from thousands of shear cycles was collected, with each period consisting of a half period of shear in one direction and a half period of shear in the other direction. Each half-period was fitted to several different model equations using LabVIEW-programmed fitting tools with varying degrees of success, with an acceptable fit considered to be one in which the coefficient of determination, R^2, frequently exceeds 0.9. All nonlinear models were fitted using a Levenberg-Marquardt algorithm. The following models, similar to those used during the inter-period fitting, were attempted during the fitting process:

   i)   Polynomial fits of up to third order (i.e. $\varepsilon = \sum_{k=1}^{n} C_k t^k + \varepsilon_0$ where n is 1, 2 and

            3 for the linear, quadratic and cubic fits, respectively; ε_i represents the intra-

            period shear response) were attempted and were found to be inadequate for all

            reasonably well-defined shear responses, both at early and asymptotic times.

            Polynomials above third order were not attempted as there was no obvious

            physical interpretation for such a model. An example of a linear fit is given in

            the left-hand graph of Figure 4.16.

254

ii) Both single and stretched single exponentials ($\varepsilon = Ce^{-t/\tau} + \varepsilon_0$ and

$\varepsilon = C\exp\left(-t/\tau\right)^\alpha + \varepsilon_0$) were also attempted, but yielded poor fits, particularly

for those responses that contained a sharp elbow at either early or late times

within the shear period. A sample exponential fit is given as the right-hand

graph of Figure 4.16.

iii) A two exponential model, $\varepsilon = C_1 e^{-t/\tau_1} + C_2 e^{-t/\tau_2} + \varepsilon_0$, generally fit the data

well, including those data sets containing elbows, with R^2 values typically

exceeding 0.90, but it was unclear what the physical mechanism would be that

could be described by such a model. A sample two exponential fit is given as

the left-hand graph of Figure 4.17.

iv) The data was then fitted to a more physically realizable model, the Burgers

Model (derived in Appendix 2):

$$\varepsilon = \sigma\left[\frac{1}{k_1} + \frac{t}{\eta_1} + \frac{1}{k_2}\left(1 - e^{-k_2 t/\eta_2}\right)\right] \tag{1}$$

where ε is the deformation of the system (here representing the deflection of

the bridge as measured by the strain gauges of the SFA's Friction Device), k_1

and k_2 are the elastic components of the system, η_1 and η_2 are the viscous

components and t is time after the strain is first applied. A sample Burgers

Model fit is given as the right-hand graph of Figure 4.17, and shear

response/Burgers Model fit overlay plots for all tested parameters are

presented in Appendix 1, Section 2.

v) To accommodate the elbow at time t_e that is believed to represent the smectic

8CB's transition from viscoelastic medium to plastic flow (as discussed in

Sections 5.4 through 5.6), data sets involving shear amplitudes of 6.25 μm have been modeled with a two-step equation, with points before the elbow fitted to a Kelvin-Voigt model and the points following the elbow fitted to a simple cubic:

$$\varepsilon\left(t < t_e\right) = \frac{\sigma}{k}\left(1 - e^{-kt/\eta}\right) + \varepsilon_{01}$$

$$\varepsilon\left(t > t_e\right) = \sigma\left(C_C t^3 + C_Q t^2 + C_L t\right) + \varepsilon_{02}$$

where C_C, C_Q and C_L are cubic fitting coefficients and ε_{01} and ε_{02} are offset values. The t_e initial value was determined by eye for each data set and was allowed to float during fitting by ±10%. Fits were performed at each prospective t_e value, and the final t_e value was determined by which set of pre- and post-elbow fits produced the highest summed R^2 values. A sample Split Model fit is given in Figure 4.18, and shear response/Split Model fit overlay plots for all tested parameters are presented in Appendix 1, Section 6.
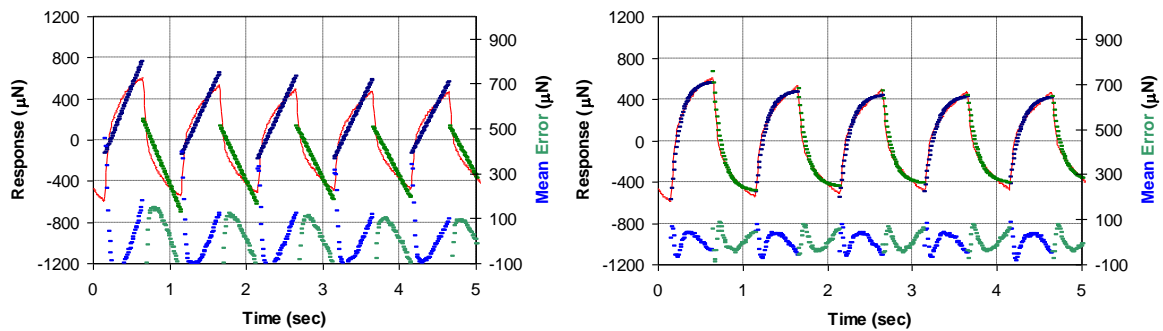
Figure 4.16: Overlay plot of shear response and (Left) a linear best fit curve and (Right) a single exponential best fit curve using a variable offset. The raw data is presented in red while the best fit curves are presented in blue and green. The difference between each overlain set of points is shown on the lower portion of the graph in light blue and teal, labeled as Mean Error on the right axis.

256
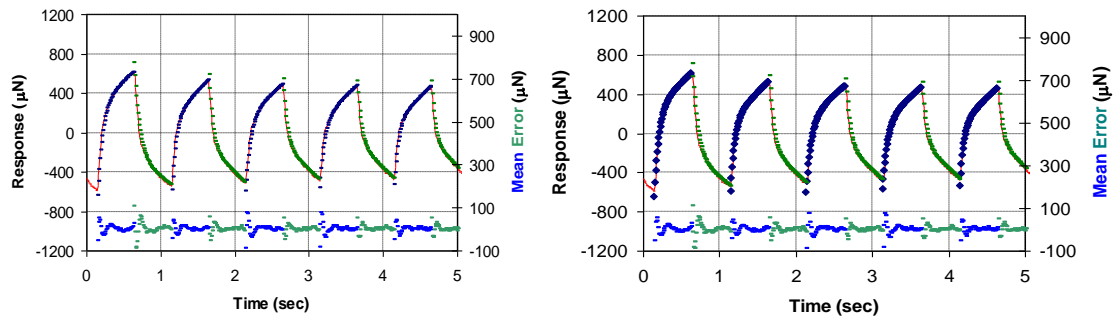
Figure 4.17: Overlay plot of shear response and (Left) a two exponential best fit curve using a variable offset and (Right) a Burgers Model best fit curve. The raw data is presented in red while the best fit curves are presented in blue and green. The difference between each overlain set of points is shown on the lower portion of the graph in light blue and teal, labeled as Mean Error on the right axis.
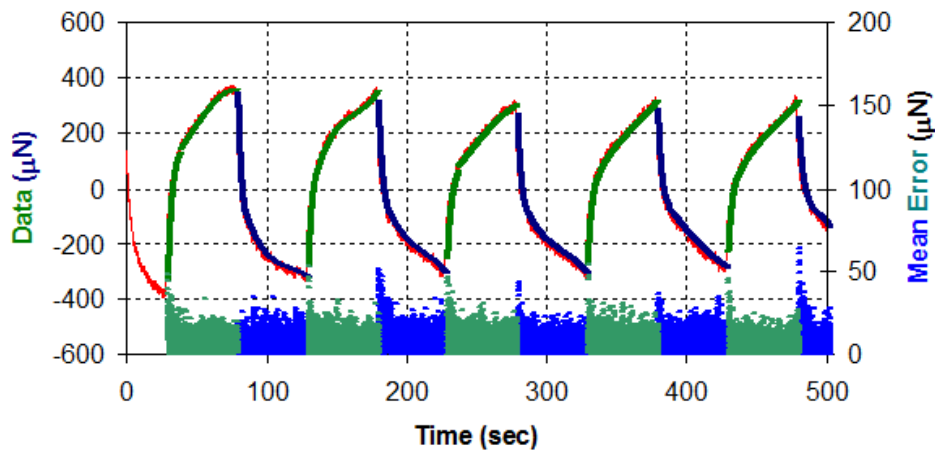
Figure 4.18: Overlay plot of shear response and a Split Model best fit curve using a variable offset. The raw data is presented in red while the best fit curves are presented in blue and green. The difference between each overlain set of points is shown on the lower portion of the graph in light blue and teal, labeled as Mean Error on the right axis.

A physical interpretation of the two exponential and Burgers Model fit is proposed in

Section 5.3. Plots of the Burgers Model and Split Model fitting parameters as a function

of time are given in Appendix 1, Sections 3 and 7, respectively.

4.2.7 Intra-period Features

One notable phenomenon that was observed for gentle shearing conditions was the 'jump': a frequent, spontaneous, brief deviation from the typical response path that sometimes occurred more than once in any given period. The deviations, typically 3-5 µN in size and sometimes larger, were often considerably larger than the 1-2 µN fluctuations attributed to noise (as determined by recording responses while the system was not undergoing shear), and had a large range of durations (typically 30% to 80% of the half-period) that lasted longer than fluctuations typical of system noise (up to 0.1 seconds) and much shorter than that observed due to electrical and thermal drift (typically several minutes or longer). An example of this behaviour is given below:
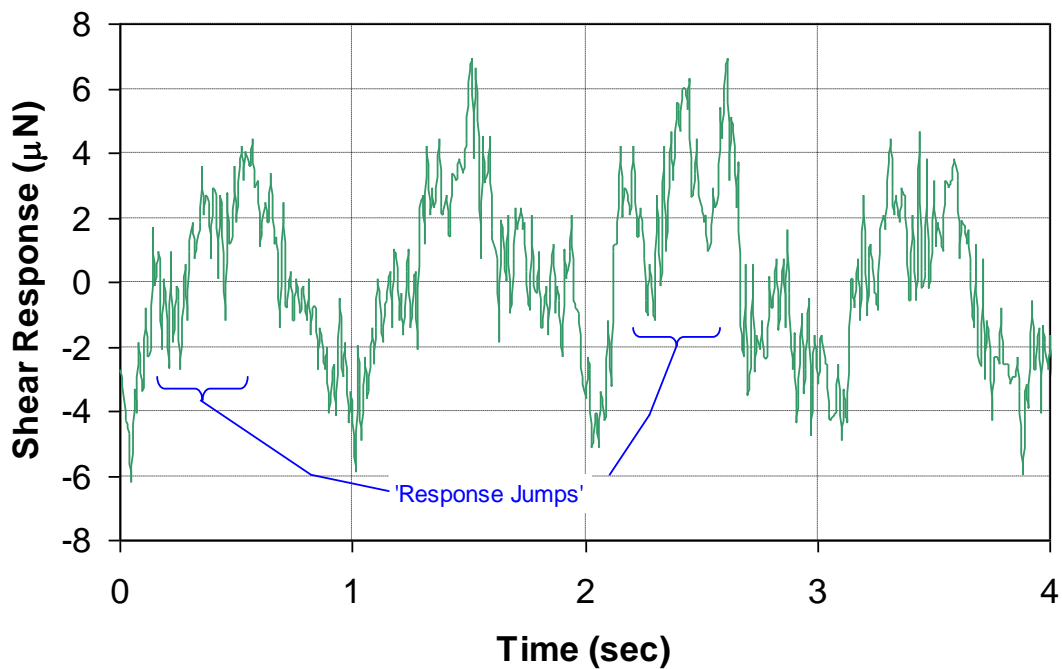
Figure 4.19: An example of the 'jump' behaviour observed under gentler shearing conditions. Here, the sample is being sheared with an amplitude of 62.5 nm, a frequency of 1 second, and a gap size of 0.5 µm.

The results of Nieman et al demonstrated a fundamental difference in behaviour between sheared 8CB samples confined to 0.5 μm and those confined to 5.0 μm[323]. While at the larger gap shifts in peak amplitude and mosaic were seen to be smooth, when confined to the smaller gap, and particularly when the shear frequency is low, shifts in peak amplitude and mosaic were found to occur discretely. Assuming changes in domain reorientation will slightly alter the local viscosity, which may in turn alter the shear response, it is possible that this behaviour will also manifest itself in the SFA data in the form of these sudden jumps and drops in amplitude.

By selecting an appropriate cutoff level for cycle to cycle changes in shear response, one can filter out those amplitudes that are conspicuously above the expected noise level, and which are therefore candidates for evidence of punctuated domain reorientation. The level is defined as being the response shift at which only a small number of outlying points (eight to fifteen) remains unfiltered over the entire data set. To avoid jumps due to random noise within a single cycle or a small number of cycles, rather than choosing a single outlying point, groups of ten averaged together have been chosen for comparison instead to demonstrate a sustained change in response.
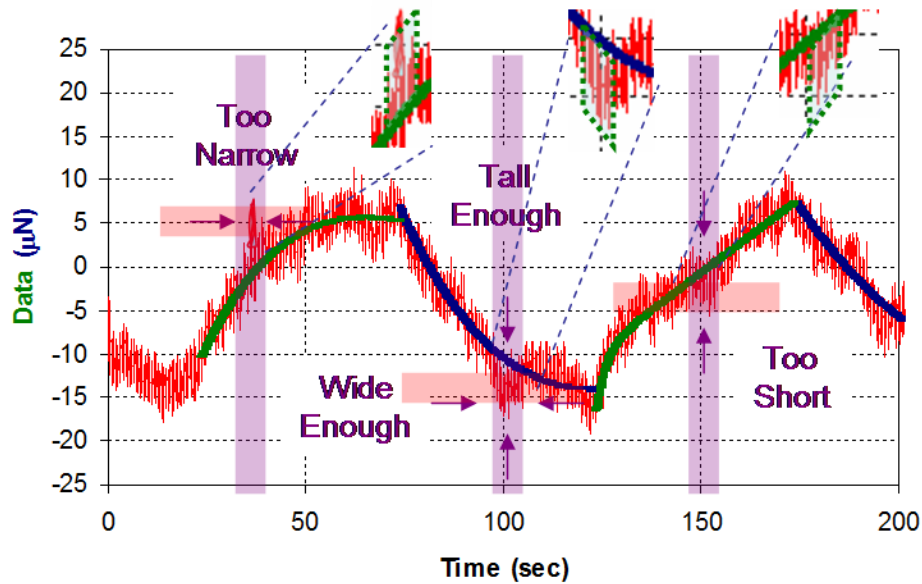
Figure 4.20: Diagram of how jump criteria are implemented. A window of fixed width (10 data points) sweeps each section. If the difference between a data point and its Burgers fit point exceeds a set value for ten consecutive points, the block is counted as a 'jump'. No further blocks can be counted until at least one data point passes to the opposite side of the Burgers curve to avoid double-counting.

This 'jump' criterion tends to be higher for smaller periods and for larger shear amplitudes, suggesting that in higher shear rate experiments any jumps due to domain reorientation are masked by larger random jumps due to the aggressive shearing and not necessarily to domain reorientation. To determine whether there is indeed a decreasing frequency of response shifts, the number of these occurrences has been counted and binned in 1800 second windows, as shown in the figure below:
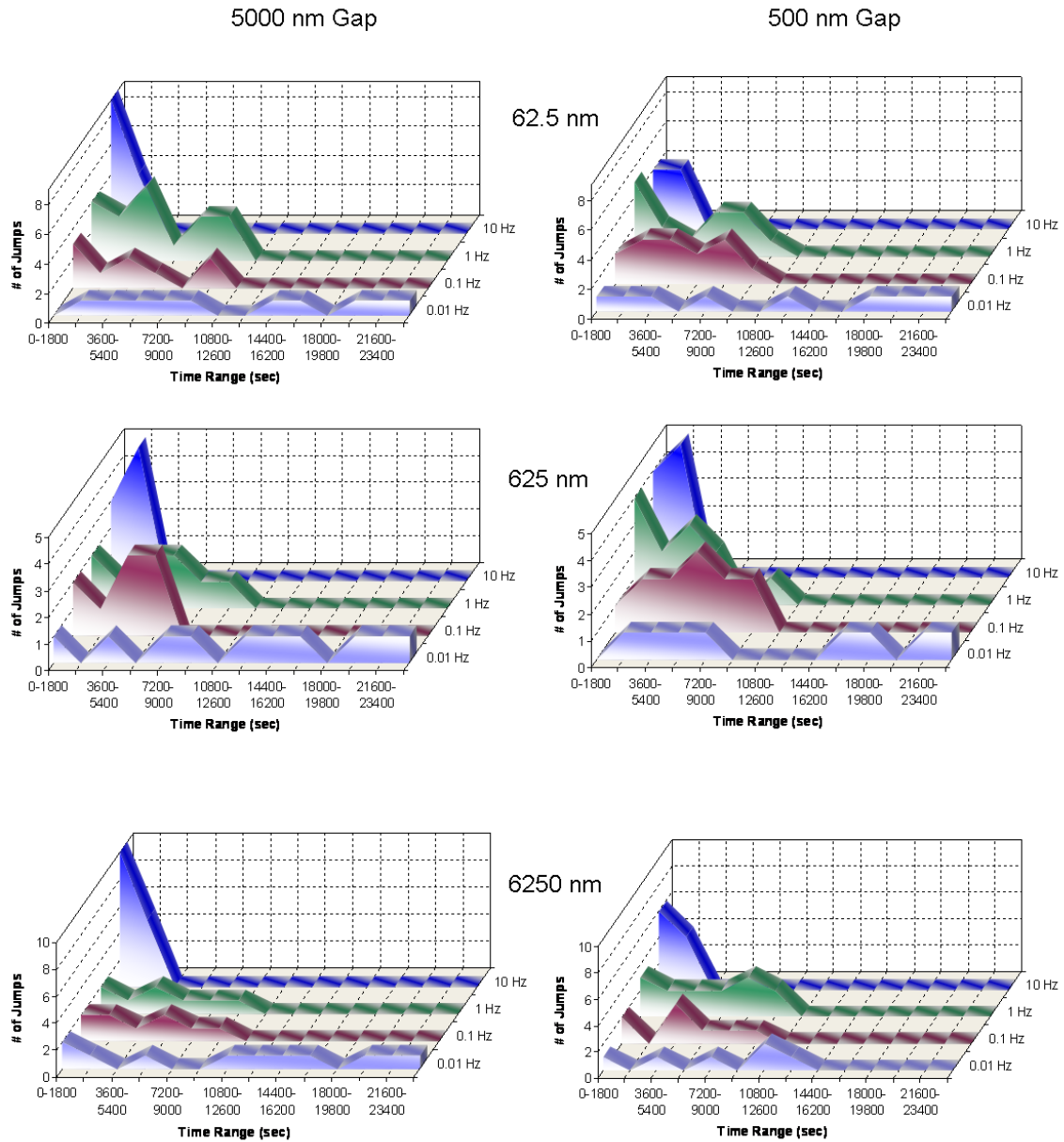
Figure 4.21: Plots of the number of jumps as a function of time for 8CB confined to a (Left) 5000 nm gap and a (Right) 500 nm gap, with shear amplitudes of (Top) 62.5 nm, (Middle) 625 nm and (Bottom) 6.25 μm and shear frequencies from 0.01 Hz to 10 Hz.

It is important to note that the data sets for 10 Hz shear data ran only for 3600 seconds, and so only the first two time bins in that row of Figure 4.17 contain relevant data. Similarly, the 0.1 and 1.0 Hz data sets ran for 10 800 seconds, so that only the first three

time bins are relevant. Only the 0.01 Hz data sets run for the full 23 400 seconds and hence use all the time bins.

For 8CB sheared at higher shear frequency (1 Hz and 10 Hz) the number of jumps generally tends to fall fairly rapidly, although for experiments performed with 625 nm shear amplitude the number of jumps actually increased slightly with time. Conversely, for 8CB sheared at lower frequency (0.01 Hz and 0.1 Hz) the number of jumps tends to stay fairly constant throughout the shear process. This may be an indication that for faster shearing, the entire domain reorientation process (which manifests itself as these 'jumps' in the shear response) is occurring rapidly while for slower shearing domain reorientation it is still occurring even after several hours. In general, though, the low sample size making up the statistics and the overall lack of strong trends in the graphs above make it difficult to draw firm conclusions as to whether the domain reorientation occurs smoothly or in discrete events. It is also important to recall that, because the 10 Hz data was filtered, its intra-period behaviour may not be truly representative of the number of jumps actually occurring. Groups that have studied bulk smectic 8CB under shear have noted the presence of defects that persist for many hours during aggressive large amplitude oscillatory shearing (LAOS, with $\gamma = 1.0$ and $\omega = 10 \ \sec^{-1}$)[371]. Recalling Horn and Kléman's report of a correlation between the removal of defects and domain reordering[42] (albeit during LAOS), and that Choi et al have demonstrated a greater stiffness and stored energy associated with these defects[225], which would necessarily be released by their removal, their presence and persistence further suggest a link between them and the response jumps observed in the present study which, while slightly

diminished over time, are present throughout the tests regardless of the shear parameters used.

4.2.8 Large Amplitude Oscillatory Shear

A proper analysis of the results must consider the relative length scales of the shear amplitudes and the material being sheared: While the 8CB dimer is 3.17 nm in length[327, 372] and may form domain structures bounded in length by the gap sizes of 0.5 μm and 5.0 μm, the total shearing distance varies from $2 \times 62.5 = 125$ nm to $2 \times 6.25 = 12.5$ μm. Because the shear amplitudes often exceed the maximum domain lengths, simple oscillatory shear theory may no longer apply, and the system is more accurately described using the techniques developed in the field of Fourier-Transform rheology, which have had success in dealing with large-amplitude oscillatory shear phenomena[373-375]. This method of shearing materials at amplitudes far beyond their fundamental length scales is often abbreviated to LAOS (Large Amplitude Oscillatory Shear).

One technique developed by Wilhelm et al involves studying the behaviour of storage and loss moduli, G' and G'', as they vary with strain during LAOS[376]. The smectic 8CB moduli were calculated from the dynamic rheology tests presented in Section 4.1 and are presented below as a function of percent strain:
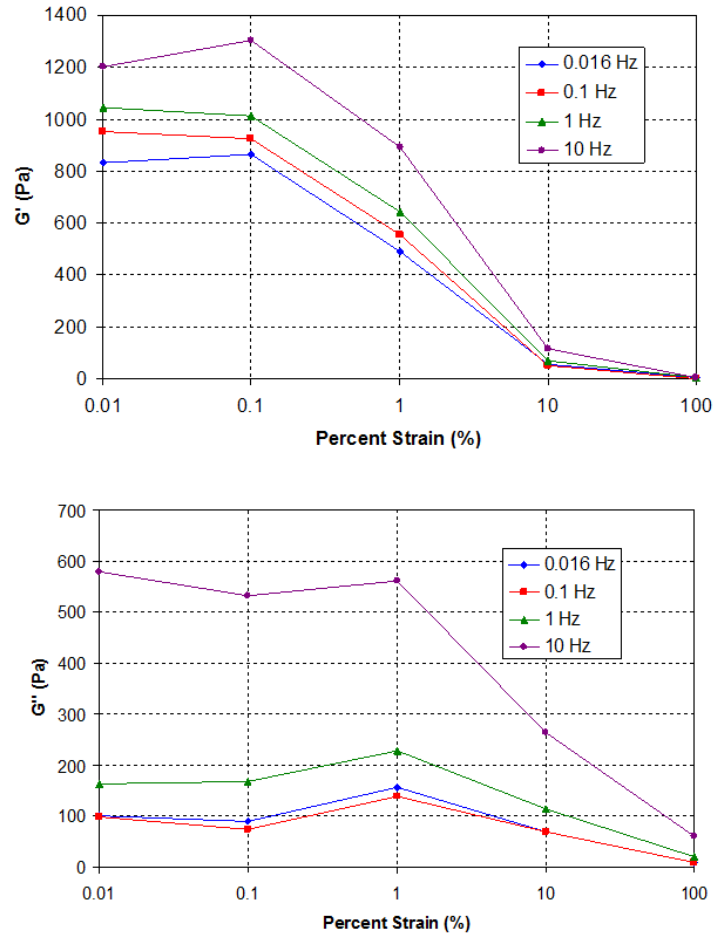
Figure 4.22: Storage and loss moduli, G' and G'', for 8CB under 56 μm confinement and various shear frequencies.

These results will be discussed in Section 5.5.

Another technique developed by Wilhelm involves examining the deviation of shear response from its sinusoidal shape while the material undergoes LAOS. In an effort to extend this technique to triangular shear tests as were used with the SFA, plots of the ratio of higher harmonics to the fundamental are thus presented for each of the three tested shear amplitudes in Figures 4.23 to 4.25. The values were obtained by performing a Discrete Fourier Transform on the raw SFA shear response data, the details of which

are presented in Section 4.2.4, extracting the harmonic components, and calculating the

relevant ratios from them.
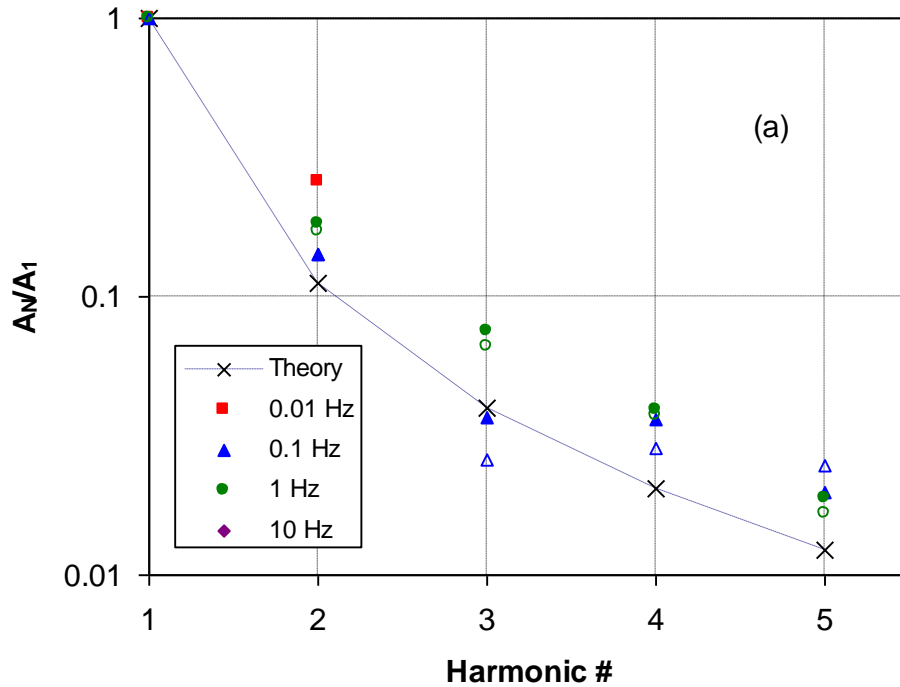
Figure 4.23: Plots of the ratio of harmonic amplitude to the fundamental amplitude A_N/A_1 as a function of harmonic number, for 62.5 nm amplitude shear. Solid symbols indicate tests performed using a 0.5 μm gap size and open symbols indicate tests performed using a 5.0 μm gap size. The expected values for a perfectly triangular response are shown as dotted lines on each graph.
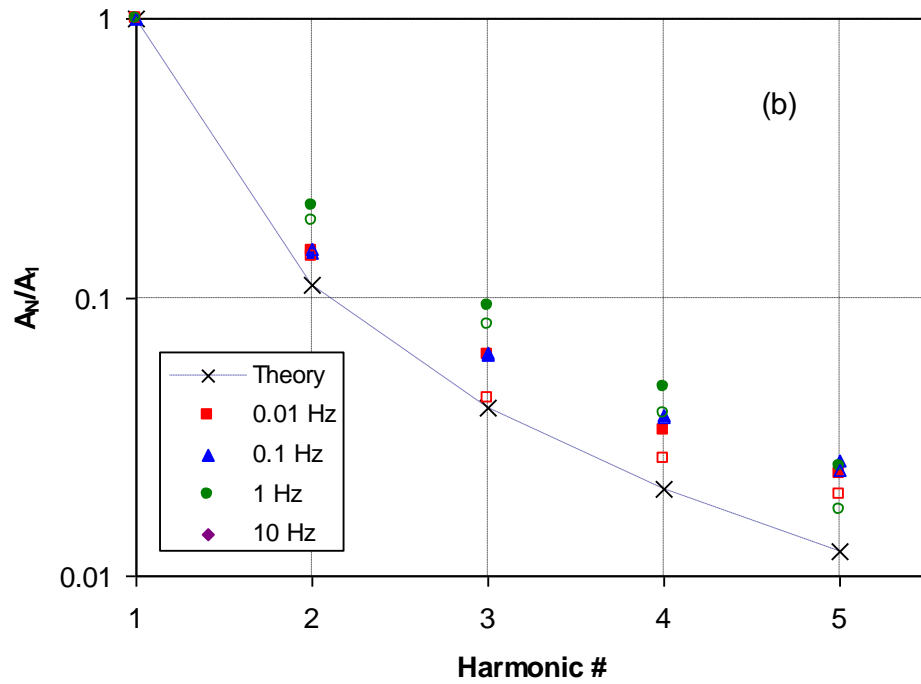
Figure 4.24: Plots of the ratio of harmonic amplitude to the fundamental amplitude A_N/A_1 as a function of harmonic number, for 625 nm amplitude shear. Solid symbols indicate tests performed using a 0.5 μm gap size and open symbols indicate tests performed using a 5.0 μm gap size. The expected values for a perfectly triangular response are shown as dotted lines on each graph.
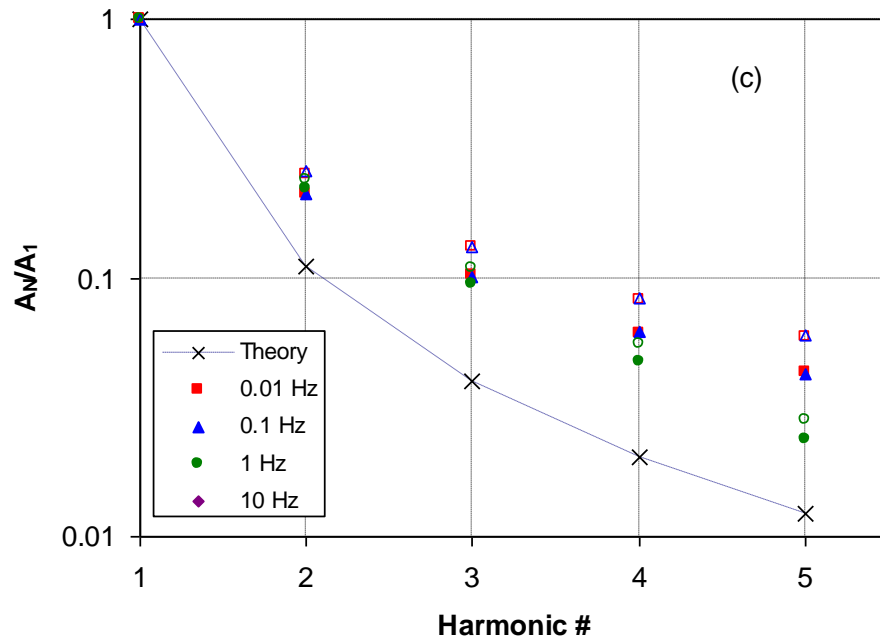
Figure 4.25: Plots of the ratio of harmonic amplitude to the fundamental amplitude A_N/A_1 as a function of harmonic number, for 6.25 μm amplitude shear. Solid symbols indicate tests performed using a 0.5 μm gap size and open symbols indicate tests performed using a 5.0 μm gap size. The expected values for a perfectly triangular response are shown as dotted lines on each graph.

It is interesting to note that, while under gentler test conditions, the ratio A_N/A_1 remains relatively constant over time (as exemplified by A_3/A_1 , which provides the clearest values since the first harmonic, A_3, is larger than all other higher harmonic intensities), in some tests, particularly those involving more aggressive shearing at large amplitudes and the smaller gap size, a slight increase in the value was noted early into the shearing process. The most pronounced example of this effect was observed in tests using the largest shear rate (shear frequency of 10 Hz, shear amplitude of 6.25 μm and gap size of 0.5 μm). Results for this shear amplitude at the shearing frequencies tested are shown for gap sizes of 0.5 μm and 5 μm in Figure 4.26, and a direct comparison of

the 10 Hz results is given in Figure 4.27, showing the marked difference in behaviour

shortly after the onset of shear. The ratios displayed in these plots have been offset from

one another so that they may be more easily compared with one another.
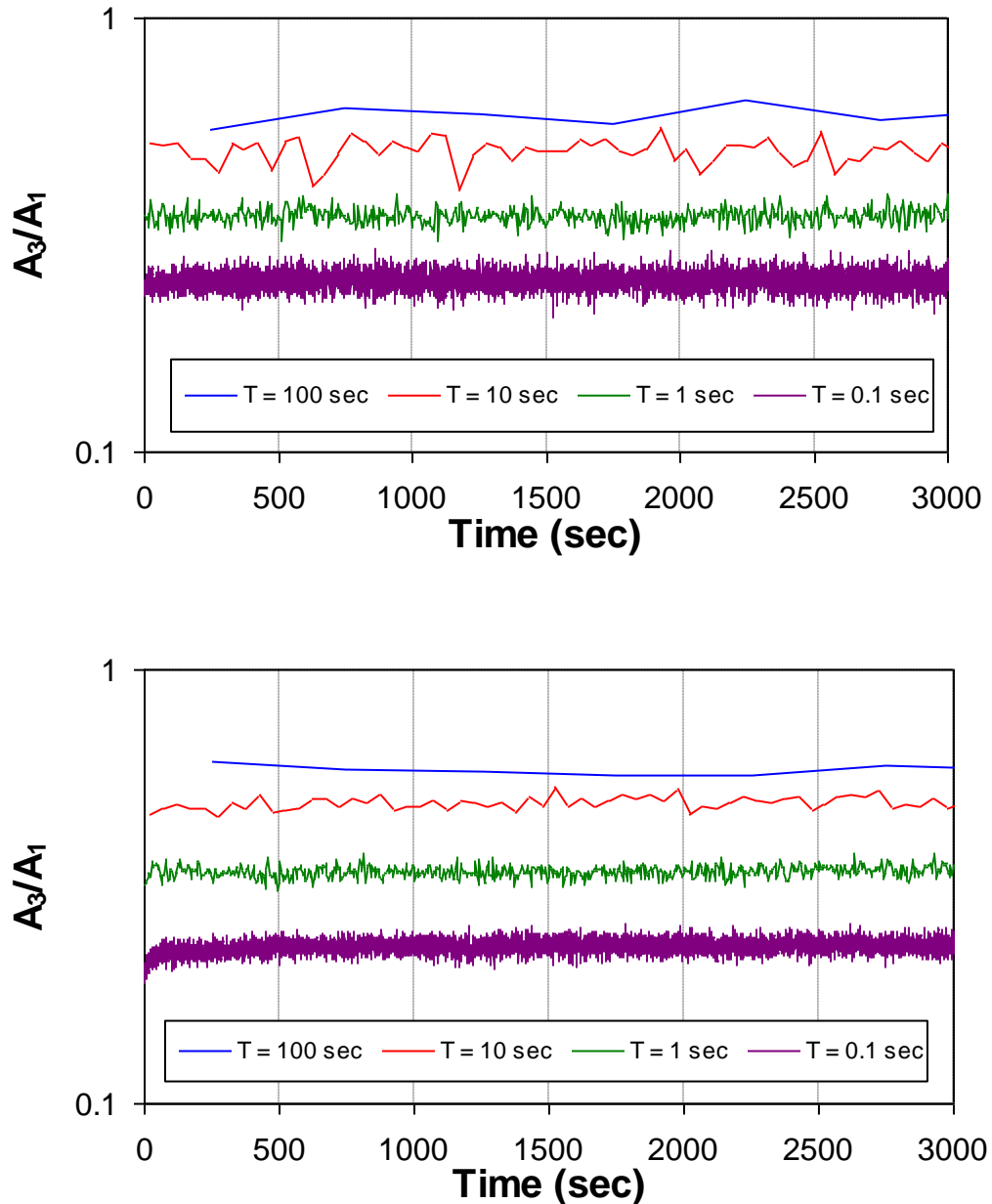
Figure 4.26: Ratio of amplitudes, A_3/A_1 , as a function of shearing time for shear
parameters $A = 6.25$ μm , (Top) $D = 5$ μm and (Bottom) $D = 0.5$ μm , and various shear
frequencies.
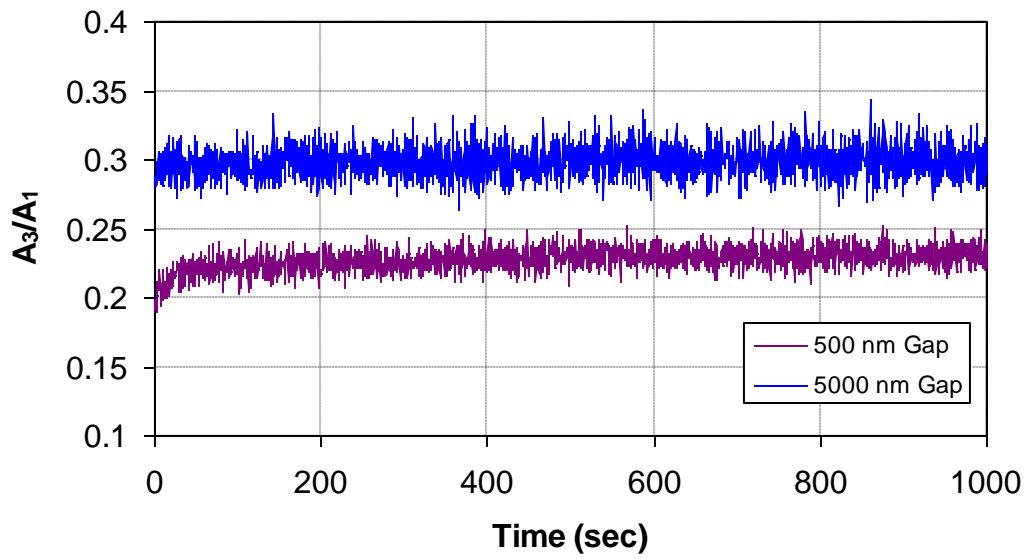
Figure 4.27: Ratio of amplitudes, A_3/A_1, as a function of shearing time for shear amplitude $A = 6.25\ \mu m$ and shear frequency 10 Hz for 0.5 μm and 5 μm gap sizes.

The relevance of this time dependence is explained in Section 5.5.

Chapter 5

Discussion

The following chapter will discuss how the results presented in Chapter 4 compare to the current body of knowledge, and what new conclusions can be obtained from them. It begins with a brief review of the recent findings particular to smectic 8CB under shear, and introduces the idea that domains may be spanning the 0.5 μm gap but not the 5.0 μm gap (Section 5.1). It stresses as well that SFA results include contributions from the entire sample volume, not just a small region as with the XSFA, a fact that must be considered when comparing the two sets of data. The viscoelastic response is found to follow a simple power law viscoelastic model that varies somewhat with the shear amplitude applied (Section 5.2). Contrary to results obtained in bulk, shear thinning is only observed for small amplitudes (as indicated by the 62.5 nm amplitude mesoscale results), while larger amplitudes (625 nm amplitude and higher) result in slight shear thickening. The yield stress characteristic of smectic materials under shear is also reported here for smectic 8CB, a property that has been associated with defects within the material.

The dependence of viscosity change on gap size is explored next, and the shear-induced thickening over time that occurs with smaller shear amplitudes and lower shear rates is discussed, in particular for the smaller gap (Section 5.3). When considered in combination with prior x-ray results that show an increase in mosaic near the area of tightest confinement, it is concluded that while the sample in this region undergoes

considerable domain reorientation (discretely), the majority of material under shear, which is more bulklike due to the crossed cylindrical geometry, contains domains that are unable to reorient but which are strained and deformed enough to stiffen the material overall. It is also noted that, while undergoing LAOS, smectic 8CB confined to the smaller gap fully reorients the sample domains more quickly than the larger gap. It is proposed that this may be due to single domains spanning the smaller gap (but not the larger gap) in the vicinity of tightest confinement, thereby hastening the process of domain reorientation due to the sample being stiffer in this region. The process is also hastened due to the smaller viscoelastic limit associated with a smaller gap size, and this suggests shearing the sample beyond this point is more effective in realigning domains confined to mesoscale gaps than in shearing with smaller amplitudes.

The role of shear amplitude on viscosity change is discussed next, and a model is developed to equate the two (Section 5.4). It is proposed that the influence of shear amplitude is due to the sample having been sheared beyond its viscoelastic limit, forcibly dislodging the domains from their neighbours and thereby facilitating their reorientation in the shear direction. The type of LAOS behaviour exhibited by smectic 8CB is then determined via rheological results, and the increase of harmonic ratio with time during large amplitude shearing shown in Figures 4.26 and 4.27 is linked to observations by Wilhelm, who attributes the behaviour to domain reordering[376] due to LAOS in similar smectic materials.

The shear dynamics of smectic 8CB under mesoscale confinement are then compared to those of bulk smectic 8CB (Section 5.6). The storage and loss moduli are found to vary similarly with shear frequency for the two levels of confinement, while the large amplitude behaviour that is reported by Larson to destroy alignment in bulk[371] is found to promote alignment in the mesoscale regime. Time constants associated with sheared bulk smectic 8CB are found to greatly exceed those observed at mesoscale levels of confinement, reinforcing the importance of gap size in determining its shear-related behaviour. Reports of defects persisting even within aggressively sheared smectic materials are ascribed to smectic 8CB as well, and for this reason are linked to the intermittent jumps in response discussed in Section 4.2.7.

A discussion of the observed intra-period features follows (Section 5.7). The discussion includes:

- The fitting of the shear response profile to a Burgers Viscoelastic Model, whose fitting parameters are found to vary exponentially with time;

- The intra-period elbow occurring roughly at 1.2 ± 0.3 μm that, it is theorized, is a result of the transition from viscoelastic behaviour to purely viscous behaviour as the viscoelastic limit is exceeded;

- The frequent jumps in response, which are attributed to defects within the sample and domain reorientation due to the shearing process.

A discussion of the parameters' behaviour over time follows (Section 5.8). Specifically, the observed decreasing effective viscosity terms coupled with an

272

increasing Kelvin-Voigt viscosity term indicate that the smectic 8CB is overall becoming less resistant to flow due to aggressive shearing during LAOS (6.25 μm shear amplitude), despite its post-viscoelastic limit state tending to stiffen over time. In addition, an observed drop in the Kelvin-Voigt time constant is attributed to a softening of the viscoelastic limit itself. For shear tests with smaller amplitudes (625 nm and less), a slight rise in the Burgers' viscosity parameters are noted, along with a softening of the viscoelastic limit, similar to but less prominent than that observed during LAOS. A discussion of the Split Model fits used for LAOS follows; the model represents a system which obeys simple Kelvin-Voigt behaviour up to a transition point and beyond which plastic flow occurs, indicating the 8CB has exceeded its viscoelastic limit under this aggressive shearing. These findings are then summarized and discussed (Section 5.9), and finally topics for future work in this area are suggested (Section 5.10).

5.1 Comparison to Earlier Work with Confined 8CB Under Shear

The results presented in the previous chapter when taken together indicate that a complex assortment of behaviours is occurring over the range of shear conditions tested. The work of Safinya et al[52, 53], Idziak et al[54, 127, 128, 317] and Ruths et al[125] have laid the groundwork for understanding the structure and dynamics for sheared 8CB under confinement, as discussed in Section 1.5. A brief review of the conclusions relevant to the present study is summarized below.

With the X-ray Confinement Cell (XCC), Idziak et al demonstrated that while under mesoscale confinement (corresponding to gap sizes of from 0.1 to 10 μm) by mica surfaces, sheared smectic 8CB takes on the three possible orientations[317] previously defined by Mięsowicz[34-36], shown pictorially in Figure 5.1:
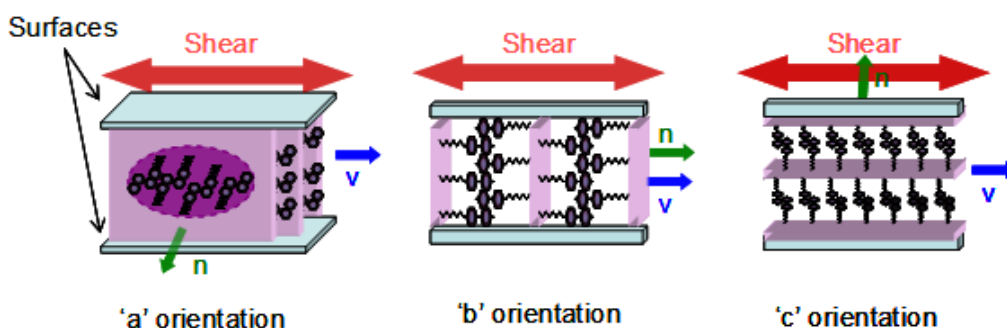
Figure 5.1: The three possible confined liquid crystal orientations as defined by Mięsowicz, using the modern a-b-c nomenclature for smectic liquid crystals. Here, 'v' is the shear (velocity) direction and 'n' is the director of the smectic layer.

The 'b' orientation, in which the smectic's director aligns with the direction of shear flow, was believed to have arisen due to the loading of the sample into the confinement space. The degree of 8CB alignment was found to increase down to a gap size of 3.4 μm

when soft surfaces were used, below which it fell off considerably. With hard surfaces similar to those used in the tests presented here, however, this effect was not observed, and the ordering of the 8CB decreased only slightly from 7 μm down to the smallest gap size tested (below 0.5 μm). These results indicate that the surfaces have a significant influence on the ordering of 8CB at this level of confinement, even without the added influence of shearing. The peak in ordering at 3.4 μm indicates that, given the opportunity to re-order, 8CB domains have the capacity to span confinement gaps of this approximate size, and so it is reasonable to conclude that this is the case for the smaller of the two gap sizes tested in the present study (0.5 μm), but may not necessarily be the case for the larger of the two gap sizes tested (5.0 μm). Ruths et al report domains of size 2-5 μm are observed in smectic 8CB confined to gaps in the vicinity of the mesoscale regime, confirming this hypothesis[125].

Because their test conditions are very similar, it is worthwhile comparing the results of the present experiments with those performed by Nieman et al using the XCC[323]. Both experiments focused on 8CB confined to two gap sizes, 0.5 μm and 5.0 μm, and both included a wide range of shear amplitudes (62.5 nm to 6.25 μm for the SFA, and 62.5 nm and 3.75 μm for the XCC) and shear frequencies (from 0.01 Hz to 10 Hz for both devices). One critical difference between the two experiments is that with the XCC one probes a sheared sample's structural properties via x-ray diffraction, while with the SFA one measures the same sample's physical properties mechanically via strain gauges. This difference leads to an important distinction in the sample size being tested: While the XCC's sample size is defined by the beam size (in Nieman et al's case, 50 μm^2), the SFA

275

measures the shear response generated by the sample *as a whole*. It is assumed that contributions from the most constrained sample (i.e. nearest the point of closest approach of the confining surfaces) dominate the response, but in practice some contribution from the more bulklike sample will likely also be present.

Figure 5.2 provides a rough guide as to the cumulative shear response contribution as a function of the distance from the point of closest approach for a sample volume of 4 mm^3 (similar to the sample volume, as judged by eye), assuming the sample behaves similarly at all levels of confinement. For the tested gap size of 0.5 μm, for example, a contact circle of 0.65 mm radius (representing 4.7% of the total contact area covered by the sample) makes up approximately 50% of the total shear response contribution.
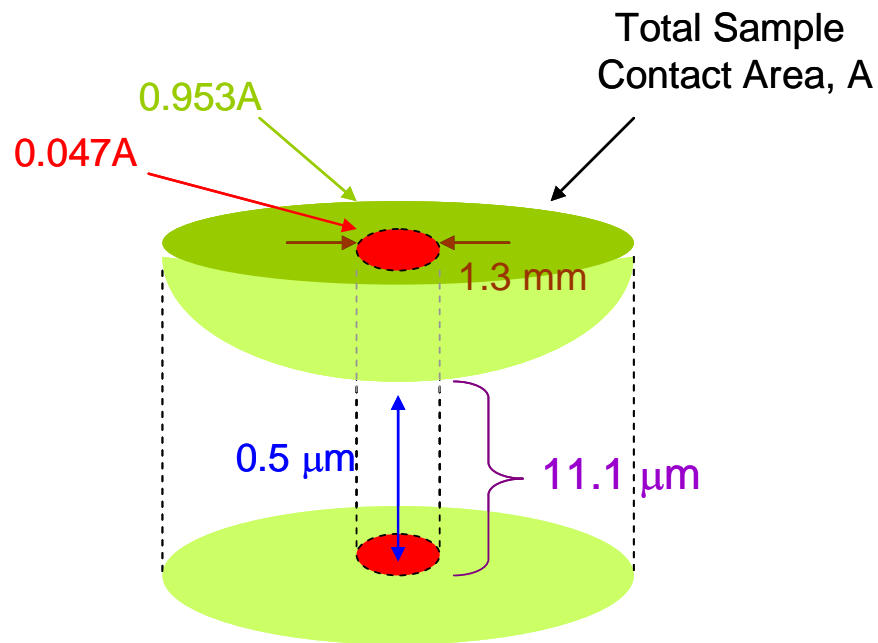
Figure 5.2: Sketch of the contact area (in red) representing 4.7% of the total sample contact area between the surfaces and approximately 50% of the shear response contribution as predicted in Appendix 5 for a sample volume of 4 mm^3. The area encompasses all gap sizes from 0.5 μm to 11.1 μm, spanning the entire mesoscale regime.

This contact circle represents the ring over which the gap size has increased to 11.1 μm, according to Equation (5) from Appendix 5, beyond what is generally considered the mesoscale regime (0.1 to 10 μm). Consequently, on the order of 50% of the response may be due contributions from the bulklike portion of the sample. While the numbers here may vary considerably depending on how the 8CB dynamics depend on confinement, the rough estimates above indicate that the bulklike response contribution should not be disregarded outright.

5.2 Shear Rate Dependence of Viscosity

Figure 4.7 shows the viscosity (represented by shear response) as a function of shear rate for the three shear amplitudes and two gap sizes tested. The straight lines on these log-log graphs demonstrates that each data set on its own follows a simple power law viscoelastic model (also referred to as the Ostwald-de Waele power law)[377]:

$$\eta(\dot{\gamma}) = K \dot{\gamma}^{\,n-1} \tag{1}$$

where K is known as the flow consistency index (or consistency) and n is the flow behaviour index (or power law index)[378]. Interestingly, while the shear tests at the two gap sizes have fairly similar K and n values for a given shear amplitude, the shear amplitudes themselves actually produce distinct power law relationships. As power index values greater than unity indicate a shear thickening material, and less than unity indicate a shear thinning material, of even more interest is that 625 nm and 6.25 μm amplitude shear tests result in fundamentally different behaviour, with their gentle but positive slopes ($n > 1$) indicating shear *thickening* may be occurring, unlike the 62.5 μm amplitude tests, whose negative slopes indicate slight shear *thinning* is occurring. Ruths et al report that the viscosity of sheared, highly confined (1.6-1.7 nm gap size) smectic 8CB decreases with increasing shear frequency[125]. This discrepancy may be due to the mix of mesoscale and bulk material being sheared; while 8CB domains near the point of closest approach align in the shear direction, the large amplitude shearing may have an opposite, disruptive effect on bulk 8CB, an effect reported by Larson[371] and discussed in Section 5.6, which may in turn increase the overall viscosity due to domain entanglement in this regime. The table below gives the complete set of K and n values for all tests, both at the onset of shear (subscript '0') and at asymptotic times (subscript '∞'):

Table 5.1: Power Law parameters for smectic 8CB

Shear Amplitude (nm)	0.5 μm Gap				5.0 μm Gap			
	K_0 (N·s^n)	K_∞ (N·s^n)	n_0 [±0.05]	n_∞ [±0.05]	K_0 (N·s^n)	K_∞ (N·s^n)	n_0 [±0.05]	n_∞ [±0.05]
62.5	11.6 ±2	13.4 ±2	0.96	0.97	8.46 ±4	9.43 ±4	0.95	0.94
625	4.91 ±0.5	4.97 ±0.5	1.20	1.20	5.47 ±0.5	6.79 ±0.5	1.16	1.18
6250	8.04 ±0.1	4.59 ±0.1	1.06	1.09	3.36 ±0.2	3.51 ±0.2	1.22	1.16

Interestingly, previous shear results on bulk smectic 8CB (under cone-and-plate geometry with gap spacing of 48 μm) at 25°C show a stronger dependence of viscosity on shear rate for a wide range of shear rates, from about 0.005 sec^{-1} to 100 sec^{-1}, with $n \approx 0$ below 0.1 sec^{-1}, $n \approx 0.54$ between 10 sec^{-1} and 100 sec^{-1}, and a plateau ($n \approx 1$) in the region of 5 sec^{-1} [379]. The present results, being consistently in the vicinity of $n \approx 1$, indicate that this plateau widens considerably in the vicinity of mesoscale confinement. Panizza et al report that the viscosity of bulk smectic 8CB varies with temperature and shear rate as

$\eta \propto \left(T_C - T\right)^{1/2} \cdot \dot{\gamma}^{-1/2}$ for temperatures down to 30.8°C, with T_C being a critical point lying near the nematic-smectic-A transition point ($T_C = 31.83\,°C$ and $T_{A/N} = 33\,°C$) [172]. The relative invariance of viscosity with shear rate at the temperatures used for the results presented ($T \approx 20.5\,°C$) may indicate that they were performed in the vicinity of a second critical point, this one near the smectic-crystalline transition point ($T_{Cr/Sm} \approx 19.5\,°C$, as measured by DSC and discussed in Appendix 4).

Figure 4.7 and the widely varying flow consistency values, K, of Table 5.1 demonstrate that the viscosity of smectic 8CB is not only shear rate dependent, but, for a

fixed shear rate, is shear amplitude dependent as well. This is further indication of a behavioral change that occurs between shear amplitudes of 62.5 nm and 625 nm for both gap sizes tested, as the 8CB switches from being a shear thinning to shear thickening material. Smectic A 8CB has been observed previously to undergo shear thinning at gap sizes of 0.1 mm[380, 381], 0.15 mm[382] and 1.0 mm[172] for lower shear rates, but the present large amplitude shear thickening results that take place within the mesoscale regime have not, to the author's knowledge, been observed previously. As they coincide with an increase of the shear amplitude well beyond the length scale of the 8CB dimer, it is proposed that this behavioral change is a product of the material being brought beyond its viscoelastic limit and not necessarily a characteristic specific to the mesoscale range being tested. One possible interpretation of this effect is that the act of bringing the sample beyond its viscoelastic limit tends to strain and deform the 8CB domains, thereby reducing their mobility and thereby producing an extra drag that results in the apparent 'stiffness' of the sample as measured by the strain gauge. Also evident from Figure 4.7 are the non-zero stresses at zero shear rates for both gaps and all shear amplitudes that result from an extrapolation to the point of zero shear rate. This yield stress is characteristic of a Bingham plastic[383], and has been observed for smectic 8CB previously[172, 382]. The yield stress has been attributed to defects in the smectic layers that exist even at low shear rates[42], and its variance with shear amplitude is likely due to the increase in domain stiffness that occurs beyond the viscoelastic limit mentioned earlier.

5.3 Gap Size Dependence of Viscosity Change

To provide a more comprehensive picture of the response amplitude changes over time, the change in response data can be presented as a three-dimensional column graph with the amplitudes represented by columns and the other two axes representing the shear frequency and amplitude. Snapshots of the relative response amplitudes for all shear amplitudes and periods at a given number of oscillations can then be compared. The columnar plots in Figures 5.3 and 5.4 show the evolution of the response amplitudes for both gap sizes:
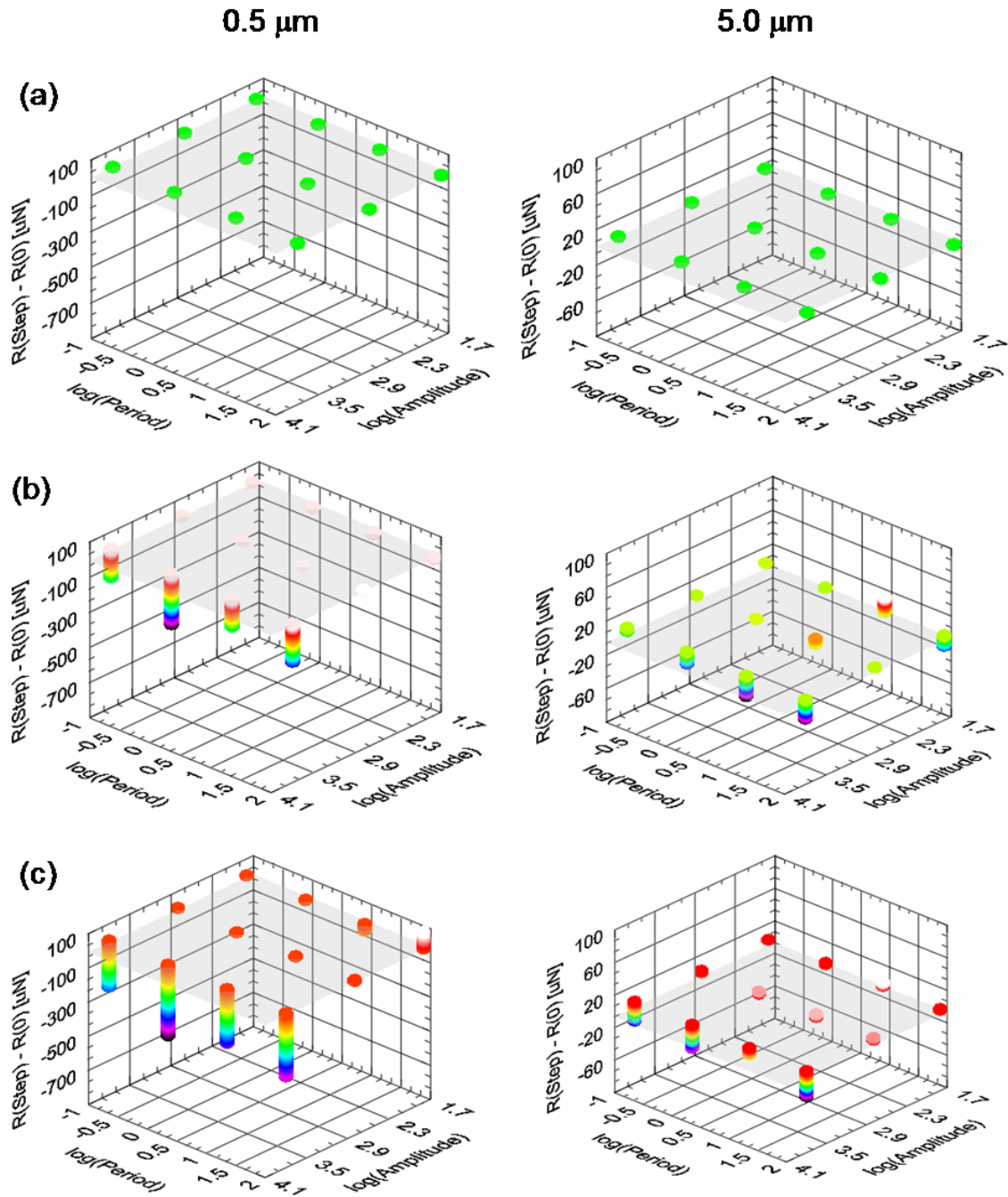
Figure 5.3: Column graphs of the shear response amplitude (relative to the initial, or 0th shear cycle amplitude) as a function of both shear frequency and amplitude, with the 0.5 μm gap size results on the left and 5.0 μm gap size results on the right, a set number of cycles into the test: (a) 0th cycle; (b) 2nd cycle; (c) 5th cycle.
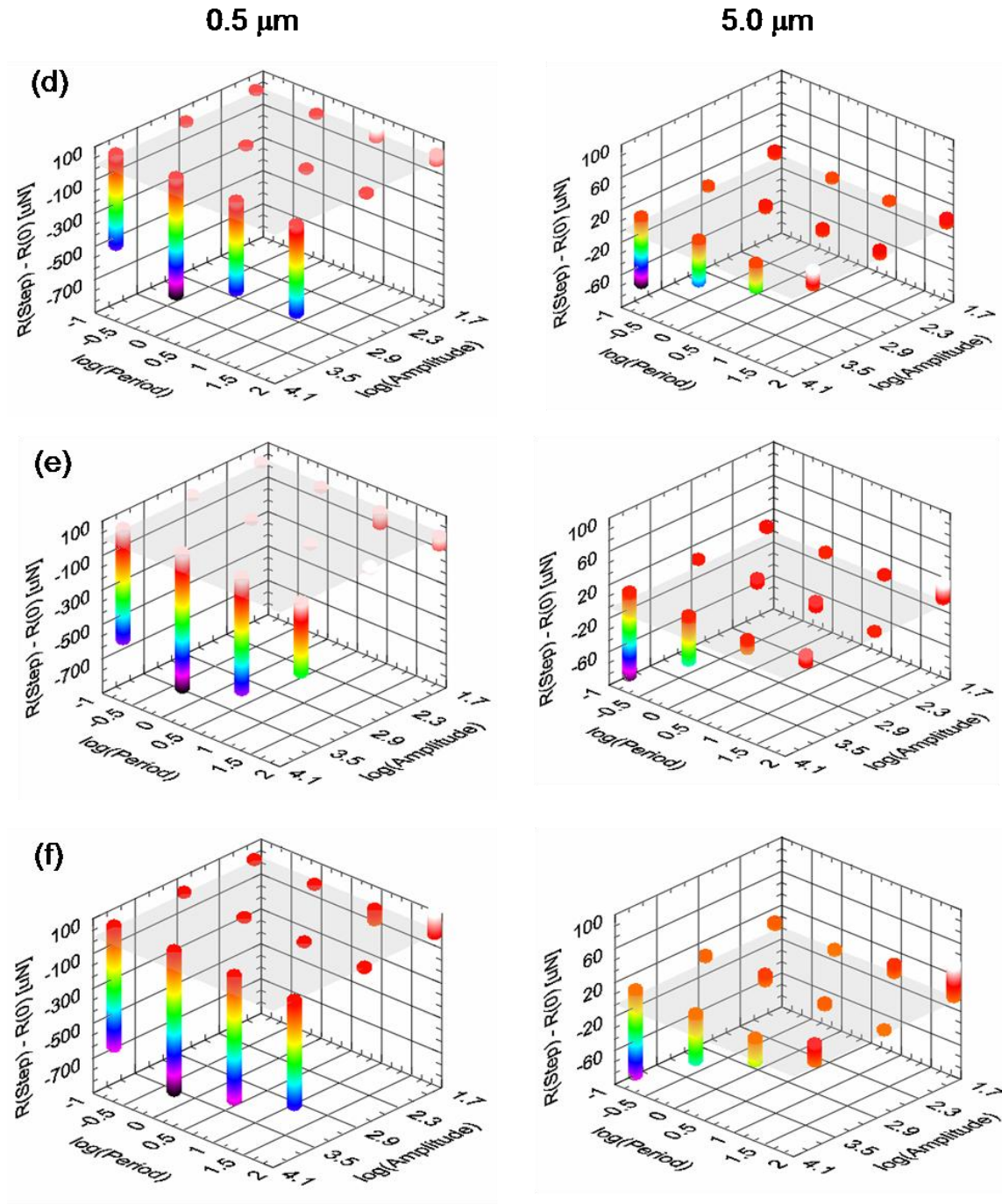
Figure 5.4: Column graphs of the shear response amplitude (relative to the initial, or 0th shear cycle amplitude) as a function of both shear frequency and amplitude, with the 0.5 μm gap size results on the left and 5.0 μm gap size results on the right, a set number of cycles into the test: (d) 40th cycle; (e) 99th cycle; (f) 193rd cycle.

Columns representing aggressive shear tests show a definite negative trend over time. This shear-induced time-dependent change in viscoelastic response has been noted previously for high molecular weight polymers in solution, and instabilities in viscosity similar to those discussed in Section 4.2.7 were also observed in these systems as well[371]. The drop represents a reorientation of domains in the shear direction. The instabilities were found to be transient phenomena lasting several minutes and were attributed to the formation and destruction of domain-like aggregates within the solution. Interestingly, at both levels of confinement under gentle shearing conditions, for samples sheared at the lower rates tested (0.05 sec^{-1} and 0.5 sec^{-1} for both gaps) and the smallest shear amplitude (62.5 nm), as represented by the two rightmost columns in Figures 5.3 and 5.4, the response actually *increases* slightly over time, indicating that thickening may be occurring with these specific test conditions. The extent of thickening is more prominent for the smaller gap than the larger gap, and its onset has the time dependence that shear thinning does, as indicated in Figures 4.13 and 4.14. The former fact indicates that the increase in viscosity is due at least in part to the level of confinement, and the latter suggests that the effects are related processes that share a common cause, specifically, the shearing of the material.

Tests performed by Nieman et al[323] under conditions similar to those of the present study (i.e. within the mesoscale regime) showed discrete, stepped decreases in mosaic, a property that is correlated to the uniformity in domain orientation, spaced by roughly 1000 to 2000 seconds. It is proposed that the 'gentle shear' effect observed with the SFA is a result of the shear not imparting sufficient energy to domains away from the tightest

level of confinement to allow them to shift and fully reorient to minimize their interfacial energy, but providing enough to grow, elastically deform and entangle, leading in turn to a stiffer state that increases the local viscosity and, therefore, the overall shear response. Domains in the region of the point of closest surface approach, conversely, to which the x-ray beam is localized (50 μm square) will have enough energy imparted to them to gradually realign to the shear direction, albeit discretely, leading to the mosaic increase reported by Nieman[323]. Sporadic reorientation of these stressed and deformed domains lead to the intra-period viscosity jumps discussed in Section 4.2.7. The gently-sheared sample as a whole, then, consists largely of a mix of confined, reoriented domains near the region of tightest confinement and more bulklike, disordered domains away from this region, which results in the slight overall increase in shear response observed with the SFA and the observed step-like increase in mosaic observed by Nieman under the same shear conditions. A schematic of this process is shown in Figure 5.5:
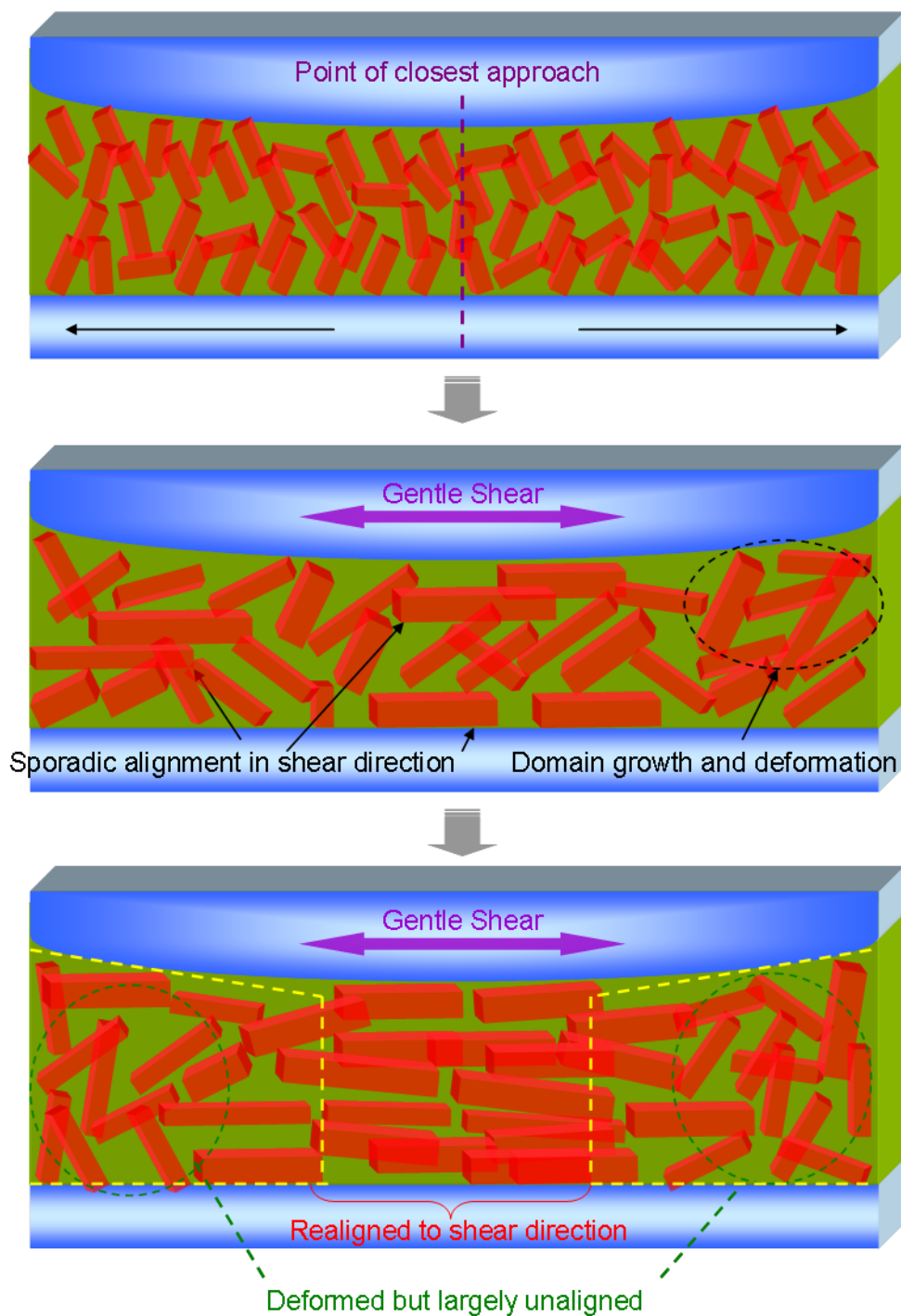
Figure 5.5: Schematic of the 8CB reorientation process during gentle shearing. Domains begin (Top) disordered, with epitaxial ordering of molecules near the confining surfaces. At the onset of gentle shear (Middle) they tend to grow and deform generally and align sporadically in the shear direction near the point of closest approach. After some time (Bottom) the domains near the point of closest approach are largely reoriented in the shear direction, while away from this point the deformed domains are unable to reorient easily, leading to an increase in viscosity. Gaps and domain sizes are not drawn to scale.

The x-ray results, then, show one aspect of a broader phenomenon: While near the point of closest approach of the surfaces the domains slowly and discretely become larger and better-oriented in time, in the more bulklike regime away from the point of closest approach the slow, periodic reordering of individual randomly-oriented domains results in larger strained domains that are being weakly jostled and distended with each sweep, but not fully reoriented in the shear direction. A similar phenomenon is reported by Ruths et al using vertical oscillations on bulklike (gap size greater than 0.5 mm) smectic 8CB, with uniform orientation in the vicinity of the point of closest approach and numerous disclination lines and domain boundaries observed outside of this region[125]. The effect was repeated using lateral shear both on bulklike smectic 8CB (again, with a gap size in excess of 0.5 mm) and on tightly confined smectic 8CB (1.6-1.8 nm gap size, with sliding velocity 0.2 μm/sec), demonstrating that a mix of confined, ordered domains and bulklike, disordered domains can result from shear with smectic 8CB regardless of gap size.

   It is also apparent from Figures 5.3(c) and 5.4(f) that, for large amplitude shearing (6.25 μm), the sample confined to the smaller gap exhibits a viscosity change that is relatively period-independent while the viscosity change of the more loosely-confined sample decreases markedly with increasing period. One interpretation of this phenomenon is that it is a result of the domain reorientation having been completed for the smaller gap tests, but remaining incomplete for the larger gap tests, based on the assumption that, regardless of shear frequency, the domains will ultimately reorient to the same extent given enough time. Since more aggressive shearing is necessarily involved

with the smaller gap tests, the domains all fully reorient in the shear direction, leading to a roughly equal total change in viscoelastic response for all periods. Conversely, for the larger gap tests, the less aggressive shearing leads to only partial domain reorientation by the 193rd sweep (the last shown in Figure 5.4), with faster (and hence more aggressive) shear tests leading to greater overall reorientation than slower shear tests. This further demonstrates that when the tightest gap is nearer to the upper limit of the mesoscale regime, the domain reorientation in this region can be complete while away from the region it can remain incomplete even after several aggressive shear sweeps.

This behavioral distinction may be due to more than just the difference in gap size alone; it may also be an indication that single domains are spanning the confining surfaces for the smaller gap, but not for the larger gap as discussed in Section 5.1. This spanning effect may facilitate domain reorientation, as the domains, in direct contact with the relatively inflexible surfaces, are more forcefully reoriented than if they were nudged more indirectly via other relatively flexible domains, leading to the considerable differences observed for the two gap sizes tested. It should be noted that the smaller amplitude tests result in viscosity changes too small to be able to make definite conclusions, suggesting that the bulk viscosity contribution is a significant component of the overall viscosity, and remains largely unaffected by the shearing process.

Figure 4.15 shows a considerable drop in the ratio of small gap to large gap shear response amplitudes for samples sheared at 6.25 µm amplitude, dropping from as much as 4.5 at the onset of shear to roughly 1.3-1.6 asymptotically, more in line with the

modified Newton's theory developed in Appendix 5, which predicts a value of 1.57 for a Newtonian fluid undergoing simple shear in a crossed cylindrical geometry. For samples sheared at 625 nm amplitude, the drop is much less pronounced (typically from 1.4-1.6 to 1.0-1.2), and for samples sheared at 62.5 nm amplitude the responses are noisy enough that it is not clear whether a change in ratio occurs at all (although the ratio itself seems to be about 1.2-1.6). The effect cannot be explained entirely by the tenfold ratio of percent strain values for the two gap sizes, since the maximum strain amplitude does not change with time. It can, however, be understood by considering the structure near the point of closest approach of the confining surfaces. Within the smaller gap size in the absence of shear, the epitaxial smectic layers extend far enough from these surfaces to form a dual-oriented span (that is, with epitaxially-ordered molecules extending from the top and bottom surfaces forming domains oriented differently from one another due to misalignment of the top and bottom mica substrates) connecting them, as introduced in Section 5.1. Within the larger gap, these epitaxial layers may not fully connect, or if they do, the connection will necessarily be more tenuous than it must be for the smaller gap. At the onset of shear, those domains bridging or nearly bridging the larger gap will have a significant amount of flexibility compared to those making up the smaller gap. The initial stiffness of the latter will increase the overall resistance to the applied shear, an effect which will be largely absent for the larger gap, thereby boosting the $F_{0.5}/F_{5.0}$ value early on in the shearing process. The drop in $F_{0.5}/F_{5.0}$ over time, therefore, is due to the domain reorientation, which will be more significant for the smaller gap than the larger gap (again, due to direct manipulation of the small-gap bridge by the confining walls),

289

thereby leading to the larger drop in $F_{0.5}$ than $F_{5.0}$. A diagram of this phenomenon is

show below:
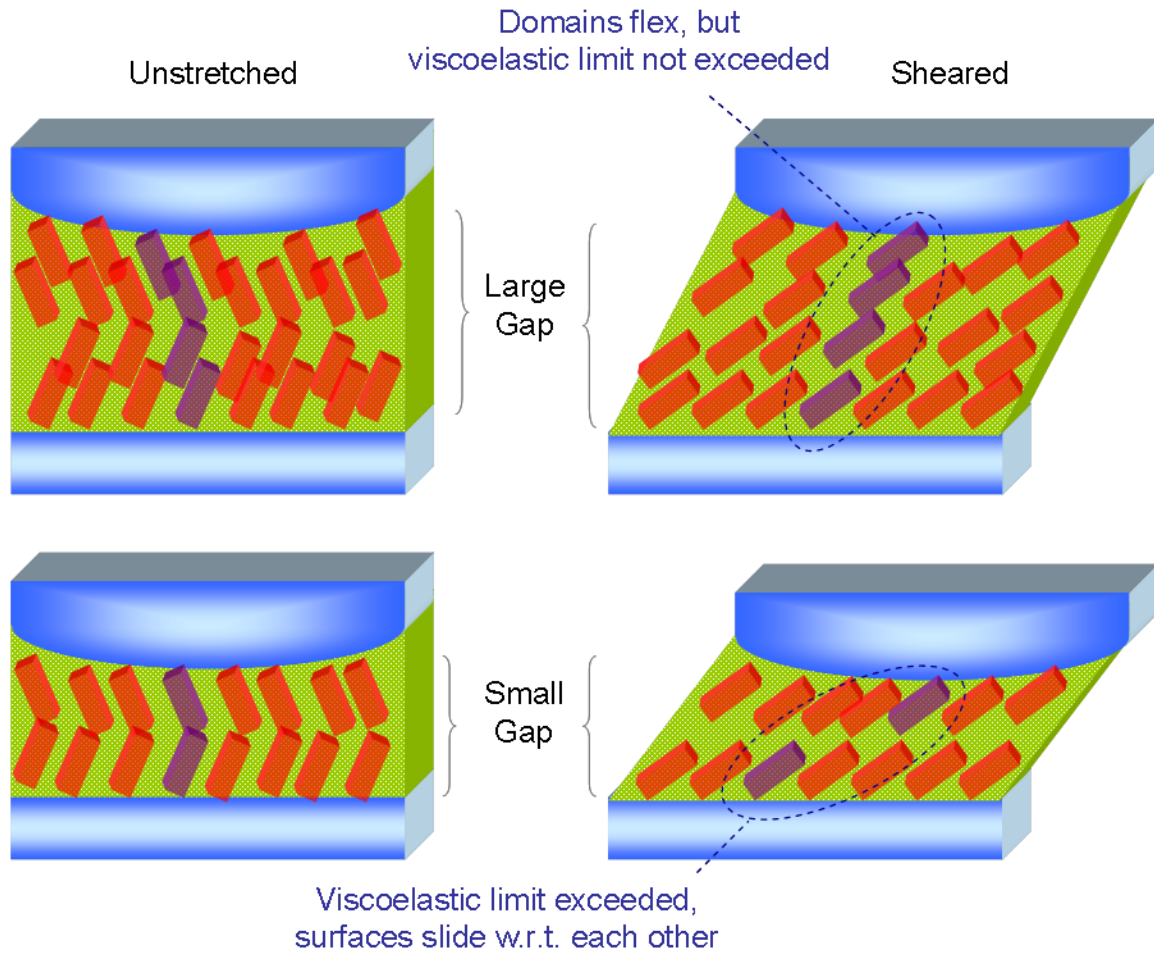
Figure 5.6: Illustration of the shearing of domains (shown in orange) for (Top) large and (Bottom) small gaps. A single pair of domains is highlighted in violet in each diagram showing how domains spanning larger gaps can better accommodate shearing due to their greater flexibility. Gaps and domain sizes are not drawn to scale.

The higher percent strain ratio of the smaller gap system, when considered alongside the

possibility that the domain stiffness is greater for small gaps than for larger gaps in the

vicinity of the mesoscale regime, introduces the notion that the viscoelastic limit for the

smaller gap will be much smaller than that of the larger gap. It is proposed that the

resultant increase of rigidity associated with the tighter confinement produces the

observed time-dependent shift in response ratios.

5.4 Viscosity Change as a Function of Shear Amplitude

Recalling that shear response F and viscosity η are, to a first approximation, related by Equation (6) (or, by assuming a simplified sphere-plane geometry, by Equation (7)) from Appendix 5, a cursory study of the various shear response plots presented in Appendix 1.4 reveals that the 8CB viscosity evolves with time from the onset of shear until it reaches an asymptotic level that can vary considerably depending on the aggressiveness of the shearing, with higher shear frequencies requiring less time to reach an asymptote. This effect has been reported previously by Ruths et al on molecularly thin (1.6-1.7 nm gap size) planar-oriented smectic 8CB[125]. The evolution can be described using a simple two exponential model (as reported in Section 4.2.3), with one term largely dominant for most of the viscosity change, and the other only becoming somewhat significant after several hundred shear oscillations have occurred. This is evident from the large difference in time constants, which is typically two or more orders of magnitude. The larger time constant is subtle enough that it can often be omitted without seriously affecting the quality of fitting, and it is proposed that the behaviour it is describing it simply the drift in response curve due to environmental effects. Ultimately, then, the viscosity changes exponentially with time, and it is worth exploring the relationship these fitting parameters have with one another.

Figures 4.13 and 4.14 demonstrate clearly that the rate of change of shear response (and hence rate of viscosity change) depends not only on shear rate, but also on shear amplitude, independently of shear rate, as well. The logarithmic relationship between the time constant and shear rate indicates that the following general relation can be written:

$$\tau = A\,\dot{\gamma}^{\,C} \tag{2}$$

where τ and $\dot{\gamma}$ are the time constant and shear rate, respectively, while A and C are

parameters dependent on the shear amplitude and gap size, extracted from the intercept

and slope of the log-log plots in Figures 4.13 and 4.14, respectively. A semi-log plot of A

as a function of shear amplitude (shown in Figure 5.7) demonstrates that the time

constant intercept varies semi-logarithmically with shear amplitude, that is:

$$A = \tau_S \, \log\, S + \tau_0$$

where τ_0 is a theoretical time constant for a system undergoing shear at 1 nm amplitude,

and τ_S is a variable describing the extent to which the shear amplitude affects the rate of

change of viscosity. Figure 5.7 may also suggest that these two variables are a function

of the level of confinement of the lamellar system when larger shear amplitudes are

applied, but not necessarily when smaller shear amplitudes are applied. More

experimentation is needed to confirm this observation, however.
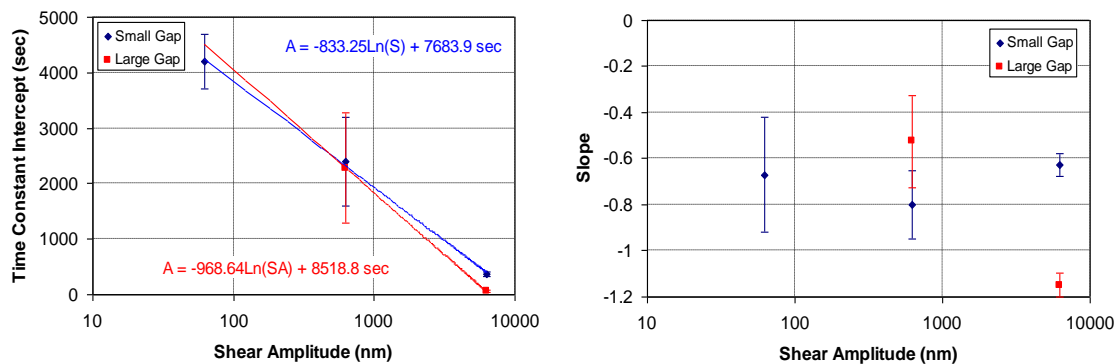
Figure 5.7: (Left) Time constant intercept, *A*, and (Right) Slope, *C*, as function of Shear Amplitude (SA) for 8CB, using data from Figures 4.13 and 4.14. 'Large Gap' and 'Small Gap' refer to 5.0 μm and 0.5 μm gap sizes, respectively.

293

In practice, the model presumably breaks down before τ_0 is reached, but this value cannot be determined due to the limits of the experimental equipment and because of long-term fluctuations in temperature and strain gauge balance. For the small gap experiments τ_0 and τ_s were found to be 7700 and -830 seconds, respectively, while for large gap experiments they were 8500 and -900 seconds, respectively, with an estimated uncertainty of ±1000 and ±30 seconds for both. A plot of C versus shear amplitude shows no obvious trend for either gap size, but in all cases it appears the slope tends to lie between -0.5 and -1.2 (or roughly -0.85 ± 0.35), so that the shear rate dependence will be, in very general terms, $\dot{\gamma}^{-0.85 \pm 0.35}$, and the time constant can then be expressed in terms of experimental parameters as:

$$\tau \propto \frac{\tau_S \, \log \, S + \tau_0}{\dot{\gamma}^{\,0.85 \pm 0.35}} \tag{3}$$

Specifically, for small gaps the time constant will be:

$$\tau_{small \; gap} \propto \frac{-\left(830 \;\; \sec\right)\log \, S + \left(7700 \;\; \sec\right)}{\dot{\gamma}^{\,0.85 \pm 0.35}} \tag{3a}$$

And for large gaps the time constant will be:

$$\tau_{l\arg e \; gap} \propto \frac{-\left(900 \;\; \sec\right)\log \, S + \left(8500 \;\; \sec\right)}{\dot{\gamma}^{\,0.85 \pm 0.35}} \tag{3b}$$

Overlaying the time constants predicted by equations (3a) and (3b), using the mean value of 0.85 for the shear rate exponential, with the time constants presented in Figures 4.13 and 4.14, one obtains the following predictive curves to align with the data:
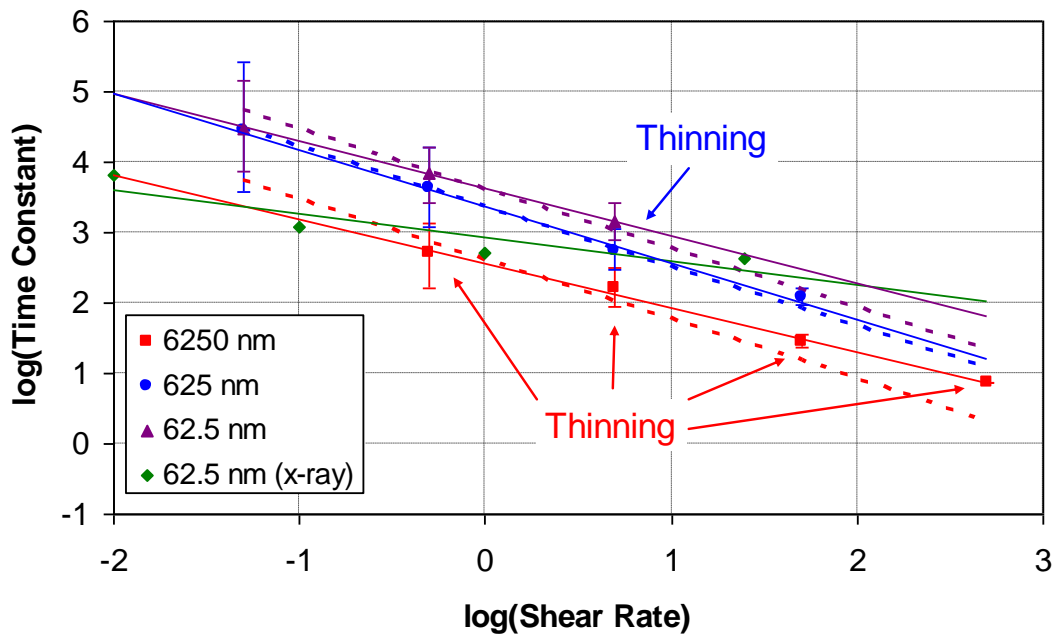
Figure 5.8: Plot of shear response time constants as a function of shear rate for 0.5 μm gap shear experiments for various shear amplitudes, with time constant predictions from Equation (3a) shown as dotted lines. Responses involving shear-induced time thinning responses have been marked; all others involve shear-induced time thickening. Also included are the peak shift time constants from similar experiments using an XCC[323].
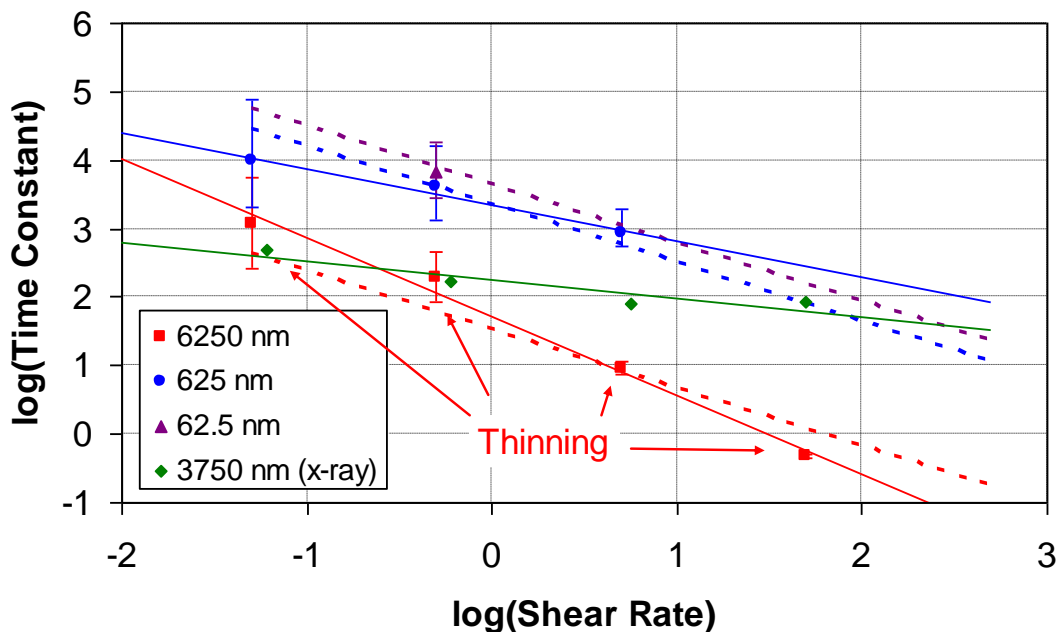
Figure 5.9: Plot of shear response time constants as a function of shear rate for 5.0 μm gap shear experiments for various shear amplitudes, with time constant predictions from Equation (3b) shown as dotted lines. Responses involving shear-induced time thinning responses have been marked; all others involve shear-induced time thickening. Also included are the peak shift time constants from similar experiments using an XCC[323].

As can be seen from Figures 5.8 and 5.9, the lines of predicted time constant agree reasonably well with the experimental values. The only notable deviation occurs for the largest shear amplitude at the largest shear rates, where the model predicts a low value for the smaller (0.5 μm) gap and a slightly high value for the larger (5.0 μm) gap. This may be a result of the considerable uncertainty in the model's current shear rate exponent given by $C_{,}$, and efforts to reduce this uncertainty would be a worthwhile focus for future experiments. Again, the thinning observed with more aggressive shearing (indicated in Figures 5.8 and 5.9) is indicative of considerable domain reorientation throughout the sample, while the thickening observed with gentler shearing represents the domain stretching and stiffening associated with partial domain reorientation.

296

Recalling that the two exponential fitting equation is given by

$\eta = C_1 e^{-t/\tau_1} + C_2 e^{-t/\tau_2} + \eta_0$, the rate at which the viscosity of the sample evolves, then, is

found by taking its time derivative, $\dfrac{d\eta}{dt} \approx \dfrac{C_1}{\tau_1} e^{-t/\tau_1}$ (for large τ_2), and so for early times (

$t \ll \tau$, with τ in this analysis representing τ_1) the viscosity will be:

$$\eta \; \tilde{\propto} \; \exp\left[- t\dot{\gamma}^{\,0.85 \pm 0.35} \Big/ \left(\tau_0 - \tau_S \, \log \, S\right)\right] \tag{4}$$

while the rate of change of viscosity will be:

$$\frac{d\eta}{dt} \; \tilde{\propto} \; \frac{\dot{\gamma}^{\,0.85 \pm 0.35}}{\tau_0 - \tau_S \, \log \, S} \exp\left[- t\dot{\gamma}^{\,0.85 \pm 0.35} \Big/ \left(\tau_0 - \tau_S \, \log \, S\right)\right] \tag{5}$$

Though it is difficult to draw firm conclusions because of the sparseness of data points, it

is interesting to note that in addition to varying roughly linearly with shear *rate*, as one

might expect (analogously to the power law relationship discussed in Section 5.2), it

further depends inversely on the shear *amplitude* as well, *independently* of the shear rate.

In physical terms, one interpretation of this behaviour is that the 8CB domains are more

strongly influenced by larger-amplitude shearing, beyond the expected scaling factor that

is incorporated into the shear rate. This may be a result of domain structures being

brought beyond their viscoelastic limit, thereby forcibly dislodging them from one

another and allowing them to reorient and align more quickly than they would while in a

continuous state of interconnectedness. A sketch of this is shown in Figure 5.10:
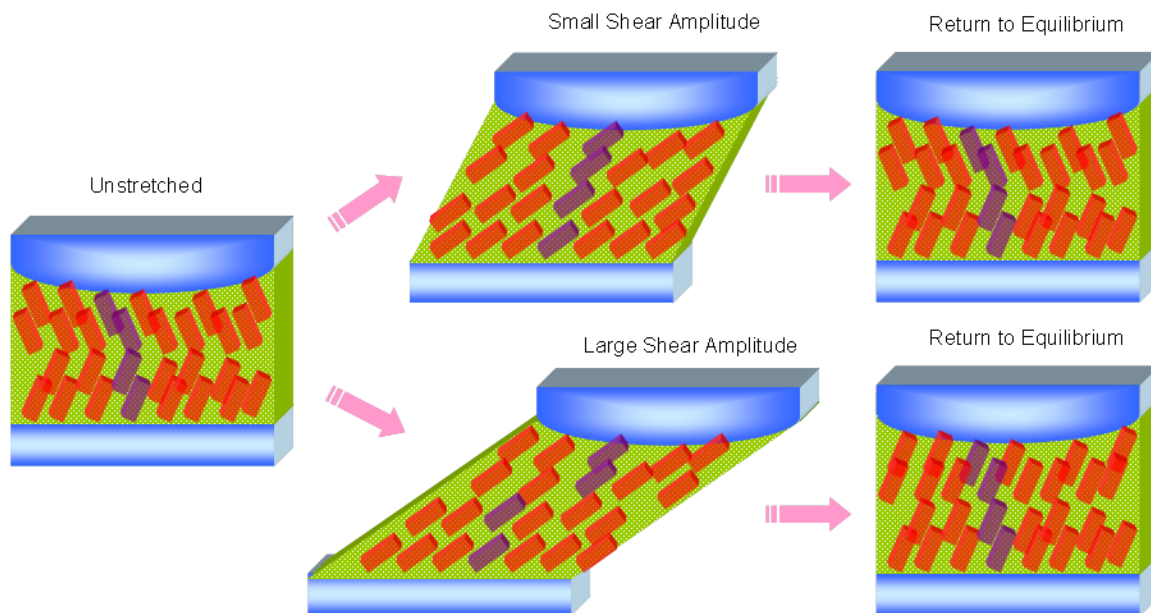
Figure 5.10: A sketch of 8CB being brought beyond its elastic limit. In the leftmost diagram, shearing has not yet begun and no domain reorientation has yet occurred. In the middle diagrams, shearing initiated by the bottom surface has caused the topmost domains to reorient, with (top) topmost and bottommost domains remaining in contact with one another and (bottom) topmost and bottommost domains disjoined. In the rightmost diagrams, the surfaces have returned to equilibrium, with (top) topmost domains returning largely to their original orientation and (bottom) topmost domains largely reoriented in the shear direction. Gaps and domain sizes are not drawn to scale.

Extracting the time constants and slopes for large and small gap shear from Nieman et al's x-ray experiments, one finds τ_0 values of 185 seconds and -0.27, respectively, for the large gap (3750 nm shear amplitude) and 850 seconds and -0.34 for the small gap (62.5 nm shear amplitude)[323]. Both pairs of values fall an order of magnitude below what is predicted by the above graphs, a discrepancy that may be explained by differences in temperature, surface texture and in the volume of 8CB being sheared. More importantly, though, these values represent the reorientation in the immediate vicinity of the point of closest approach of the confining surfaces, which may well occur much more quickly than in the mesoscale and bulk regimes as a whole. The qualitative similarity in shear rate dependence between the two experiments, nevertheless, demonstrates conclusively

that the shifts in mosaic, peak position and amplitude observed using x-ray and the viscosity changes observed using the SFA are very likely products of the same physical changes occurring in the system, specifically, a shear-induced reorientation of the domains.

5.5 Testing the Viscoelastic Limit via Large Amplitude Oscillatory Shear (LAOS)

The notion that large shear amplitudes may lead to complex rheological behaviour arises naturally from the premise that viscosity may vary with shear rate. In Wilhelm's treatment[376] of the problem, for which he assumes small sinusoidal shear rates and demonstrates a power law dependence of viscosity on shear rate, he concludes that the associated viscous-force response, F, will be:

$$F \propto A \cos \omega_1 t + B \cos 3\omega_1 t + C \cos 5\omega_1 t + ... \tag{5}$$

where A, B, C… are proportionality constants, ω_1 is the fundamental shear frequency and t is the time. That is, odd harmonics are created from a shear-dependent viscosity, and the phenomenon manifests itself experimentally in such a way that, while applying a sinusoidal driving shear to a material, the shear response tends to take on a non-sinusoidal shape, at odds with the conventional assumption of a sinusoidal output[373, 375]. This technique was first demonstrated successfully by Reiter et al using an SFA for self-assembled monolayers of octadecyltriethoxysilane (OTE) and the lubricant squalane ($C_{30}H_{62}$), both of which were confined to gaps of up to 10 nm thickness[384]. In Appendix 3 a similar derivation by the author for small triangular shear patterns (which, it will be recalled, are equivalent to an infinite series of diminishing sinusoidal waves according to Fourier Theory) has been provided.

A technique for classifying the types of LAOS behaviour using both the storage and loss moduli as well as the shear response's Fourier signature was developed by Hyun et

al[373, 374], and four distinct types were discussed with examples presented using various viscoelastic materials[373, 374]:

i)   Type I: Strain thinning (G' and G'' decrease with increasing strain);

ii)   Type II: Strain hardening (G' and G'' increase with increasing strain);

iii)   Type III: Weak strain overshoot, (G' decreases while G'' increases initially and later decreases with increasing strain); and

iv)   Type IV: Strong strain overshoot, (G' and G'' both increase initially and later decrease with increasing strain).

The results presented in Figure 4.22 indicate that, since both G' and G'' decrease, smectic 8CB by the above definition is best classified as a Type I (strain thinning) viscoelastic material under the conditions tested. The slight increase in G' at 0.1% strain and G'' at 1% strain may indicate the system is undergoing a strong strain overshoot, and thus would be better characterized as a Type IV viscoelastic material; more extensive testing to better define the G' and G'' curves would be needed before firm conclusions can be made, however. The latter relatively rare category has previously been associated with polymer solutions, with the behaviour attributed to micellar network-forming microstructures within the material, and possibly with the relaxation rate of the constituent molecules themselves[373, 385]. Similar behaviour is likely occurring within sheared smectic 8CB, with domain formation and reorientation representing the microstructure formation within this medium. Further rheological research is needed, however, to confirm this hypothesis.

Although the Fourier Transform technique is not directly applicable to the work presented here, since Wilhelm[376], Collyer[375] and Hyun's[373] work involves demonstrating the appearance of odd-harmonic response overtones arising from a simple (single frequency) sinusoidal input shear profile and analyzing their relative amplitudes, the technique can nevertheless prove to be useful in determining whether one is shearing with what one may consider to be large amplitude even while shearing with a triangular profile (as was used with the SFA). The SFA shear response, being the product of a triangular shear profile, is expected to contain harmonic overtones (at $3f_0$, $5f_0$, etc.) descending in harmonic ratios as per the coefficients of the triangular Fourier expansion series given by Equation (1) of Appendix 3 (1/9 at $3f_0$, 1/25 at $5f_0$, etc.) if the system is undergoing small-amplitude oscillatory shear (SAOS). That is, under ideal Newtonian conditions the shape of the response should be identical to that of the shear profile. In the case of non-Newtonian systems undergoing LAOS, however, the viscosity dependence on shear rate will also naturally give rise to signals at the harmonic overtone frequencies[376], and so by observing the divergence of harmonic ratios from the pure triangular ratios, one can assess the extent to which the system is being brought from ideal oscillatory conditions. Plots (a) and (b) of Figure 4.21, corresponding to shear amplitudes of 62.5 and 625 nm, show only a slight divergence from 'triangularity' (as defined by their triangular Fourier components, represented by the dotted line in each plot), while plot (c) (6.25 μm shear amplitude) shows a considerable divergence, particularly with its higher harmonic ratios, typically by a factor of from two to five. This discrepancy reinforces the notion that the LAOS phenomenon can be extended to

layered systems like smectic 8CB, and may be useful in determining the amplitude limits of oscillatory shear tests in future studies.

The increase of A_3/A_1 shown in Figure 4.26 and highlighted in Figure 4.27 represents, equivalently, an increasing non-linearity of the response signal with time. Furthermore, the increase is exponential with a time constant approximately the same rate as that of the response signals, A_1, found in Figures 4.13 and 4.14. It should be noted that, for most of the tests, the size of A_3 is small enough that the error of A_3/A_1 is too large to determine overall trends over time, and so this effect may be present to lesser extents generally, particularly for slower shearing frequencies where the amplitude changes occur over much longer times, as mentioned previously. A similar time-dependent effect was observed by Wilhelm[376] (in which A_3/A_1 *decreased* with time) while shearing a polystyrene/polyisoprene diblock copolymer at 0.1 Hz with a shear-strain amplitude of 2.0. It was attributed to the reordering of disordered copolymer material into a homogeneously-ordered domain several centimeters in size due to shear; the time of the reordering varied depending on the shear parameters, ranging from minutes to hours. The change in mobility of the copolymers during shear was proposed as the mechanism by which the A_3/A_1 shift occurs. Analogously, in the case of 8CB, this A_3/A_1 shift is likely due to growth and reorientation of domains, leading to their being less mobile and hence more susceptible to non-Newtonian, non-linear behaviour, ultimately giving rise to the increase in harmonic ratio. This novel technique represents a potentially valuable and as yet rarely-used method of determining the dynamics of domain reorientation mechanically using the SFA.

5.6 Comparison with Bulk Smectic 8CB Under Shear

It is worthwhile comparing the rheology results here with those obtained for bulk smectic 8CB. Larson et al reports that even with small shear-strain amplitudes of 0.01, non-linear responses are observable, similar to the results shown in Figure 4.1, for smectic 8CB at 27.5°C sheared using a cone-and-plate geometry (with a cone diameter and angle of 50 mm and 0.0988 radians, respectively)[371]. The exact level of confinement for these tests is not given, but tests for other materials presented in the same paper indicate a shear gap of 0.94 mm, well into the bulk regime; it should be recalled that the rheology results presented in Section 4.1 used a cone-and-plate geometry with a minimum gap of 56 μm, considerably closer to (although not within) the mesoscale regime, whose upper limit is generally given as approximately 10 μm. Plots of storage and loss moduli G' and G'' vs. shear frequency for the two configurations (Larson's bulk results followed by mesoscale results from the present study) are given in the figures below:
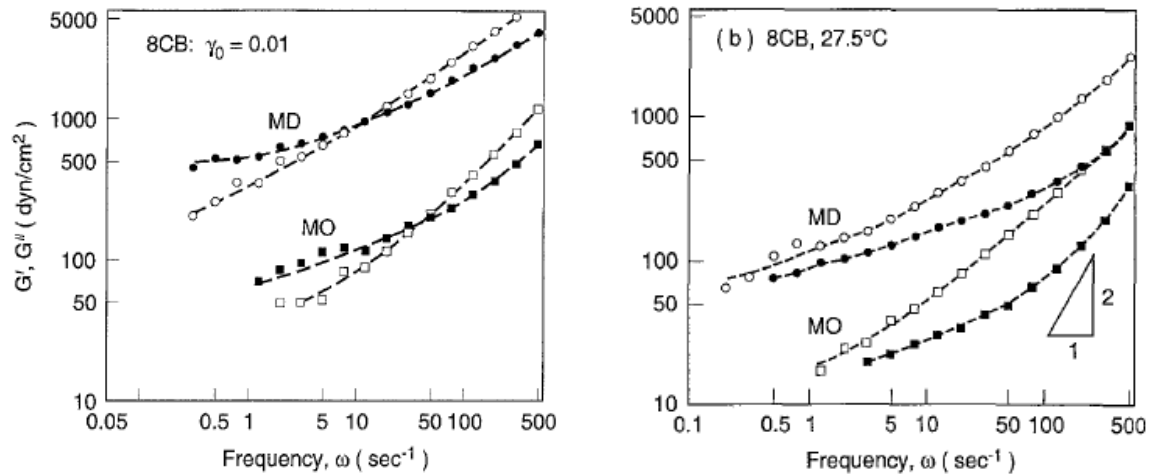
Figure 5.11: Plots of G' (solid symbols) and G'' (open symbols) vs. shear frequency for bulk smectic 8CB sheared at 27.5°C with shear-strain amplitudes, γ_0, of (Left) 0.01 and (Right) 0.1. MD refers to samples quenched from the isotropic phase before shearing (and hence molecularly disordered), and MO refers to samples sheared using LAOS before shearing (and hence molecularly ordered in the shear direction). Reproduced from Larson et al[371].
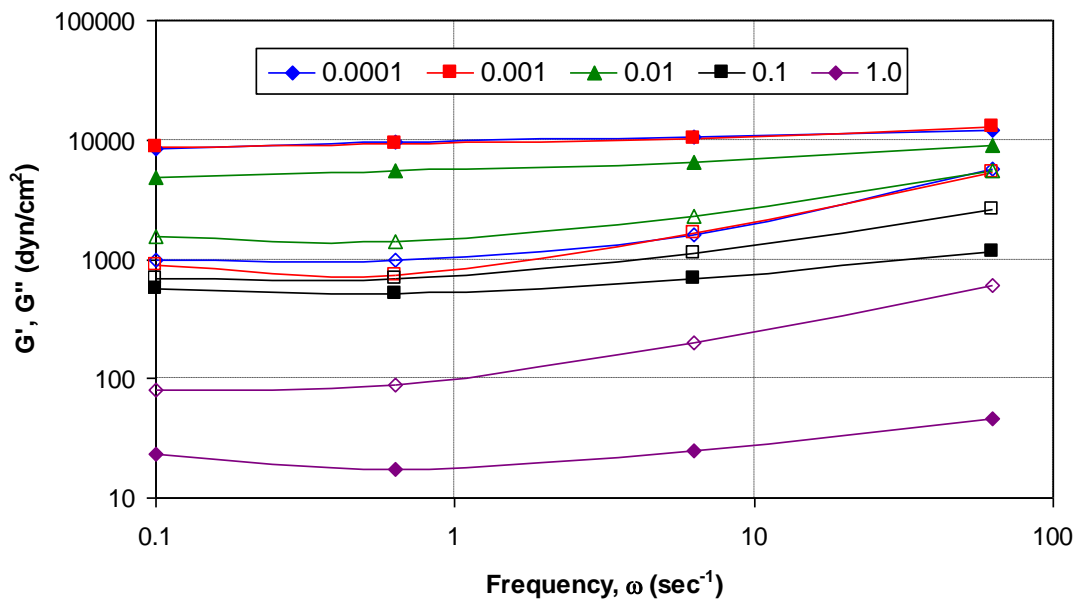

Figure 5.12: Plots of G' (solid symbols) and G'' (open symbols) vs. shear frequency for smectic 8CB at nearly mesoscale confinement sheared with shear-strain amplitudes, γ_0, of from 0.0001 to 1.0.

305

It is important to note that the absolute numbers between the two experiments cannot be reliably compared, since the temperatures and level of confinement used were different. What is interesting, though, is the qualitative similarity between the two, in the change of behaviour of G' and G'' as the shear-strain amplitude increases from 0.01 to 0.1. For both bulk and confined samples, G' exceeds G'' (for frequencies roughly below 50-100 sec^{-1}) when $\gamma_0 = 0.01$ and transitions to a situation where G'' exceeds G' for all tested frequencies when $\gamma_0 = 0.1$, with the difference between the two parameters increasing with increasing frequency. In this regard the bulk shear response behaviour is very similar to that of the sample confined more closely to the mesoscale regime (56 μm at the point of closest approach).

Larson's group also found that bulk samples required a shear-strain amplitude of unity to effectively shear-align the sample[371]; that is, it was necessary to shear the sample with an amplitude equal to the gap size at $\omega = 10 \ \sec^{-1}$ in order to shift from the MD to MO curve presented in Figure 5.11. This tends to agree with the present findings, in which the largest drops in viscosity (which, presumably, accompanies a shift in domain alignment) occur with the larger shear-strain amplitudes, while little to no viscosity changes were visible for the smaller shear-strain amplitudes, regardless of the shear frequency. More interesting, however, is Larson's comment that the use of shear-strain amplitudes of $\gamma_0 = 5.0$ "massively disrupts alignment, so that the sample becomes visibly turbid."[371] In the present study, no obvious qualitative differences in shear response have been observed with the two large amplitude shear cases, with shear amplitude 6.25 μm for the 0.5 μm and 5.0 μm gap sizes (and hence amplitudes of

$\gamma_0 = 12.5$ and $\gamma_0 = 1.25$, respectively). Since it is unlikely that the effectiveness of

domain alignment resumes once again above the $\gamma_0 = 5.0$ parameter tested by Larson et

al, or that the domain misalignment under these conditions results in a significant

lowering of the viscosity as observed, this may be an indicator that, at this tighter level of

confinement, LAOS tends not to disrupt domain alignment but rather to reinforce it even

at shear-strain amplitudes of 12.5.

Larson et al report that, due to similarities in moduli characteristics between 8CB and

other, longer molecule-chain smectics they studied (specifically, that they follow a

power-law with shear frequency that tails off at low frequency), that their similar moduli

must be determined by this smectic structure common to them[371]. This conclusion can

likewise be extended to smectic 8CB restricted to mesoscale confinement, as evidenced

by the similar moduli characteristics shown in Figures 5.11 and 5.12. They further note

that changes in magnitude to low frequency moduli were observed even after seven hours

of LAOS at 10 sec^{-1} shear frequency. If one is to assume that both moduli and viscosity

changes are due to shifts in domain alignment, this result differs somewhat from what has

been observed in the present study. For the tests involving shear frequencies

$\omega = 2\pi f = 2\pi (1\,Hz) = 6.28 \text{ sec}^{-1}$ and amplitudes of 6.25 μm at 0.5 μm and 5.0 μm, the

viscosity reached an asymptotic level at about 800 and 1200 seconds, respectively (see

Figures A1.5c and A1.5f). This difference is presumably due to the increased

confinement associated with the current set of tests, and demonstrates the importance of

gap size on the achieving domain alignment.

Other studies of bulk smectic 8CB under oscillatory shear give time constants of moduli G' and G'' that are considerably larger than those observed nearer to the mesoscale regime. For example, using rheology with a cone-and-plate geometry, Larson et al found an asymptotic drop in complex modulus $G^* = |G' + iG''|$ of roughly 6000 seconds by applying a shear force with shear-strain amplitude and frequency of $\gamma = 1.0$ and $\omega = 10 \ \sec^{-1}$, respectively[371]. Using a combined rheology and x-ray scattering technique with a plate-plate geometry (gap size 8 mm), Struth et al found an asymptotic drop in both G′ and G″ of at least 3600 seconds (and it is not clear from their plot that a true asymptote has been obtained) by applying a shear with shear-strain amplitude and frequency of $\gamma = 1.0$ and $\omega = 6.3 \ \sec^{-1}$, respectively[386]. This compares to time constants typically on the order of 10 to 100 seconds for LAOS shear parameters at both gap sizes and higher shear frequencies (1 or 10 Hz) using the SFA (see Figures 4.13 and 4.14). Three possible reasons for this are that the moduli and response do not decay at the same rate, that the reorientation of domains is more efficient at lower temperatures, and that the viscoelastic parameters of smectic 8CB are strongly gap-size dependent beyond the mesoscale regime. The latter seems more likely since shearing with a smaller gap size (and hence more aggressively) will likely align domains more efficiently and hence more quickly, but further cross-experimentation with the rheometer and SFA will be necessary to better understand this phenomenon.

Finally, Larson reports that, unlike with the block copolymer smectics they tested, the smaller-molecule smectic 8CB exhibited strong strain-amplitude-dependent moduli, which they interpreted as being indicative of the presence of defects that are not easily

removed through shearing[371]. Tests in which smectic 8CB confined between two glass sheets underwent steady-shear LAOS were also undertaken by the group, and light-scattering patterns indicative of defects were observed in these bulk samples[371]. The presence of yield stresses in smectics was a property first predicted by Ramaswamy[290], while defects were observed by Horn and Kléman to give rise to yield stresses in smectic 8CB[42], an effect observed in various other smectic materials as well[379, 387-390]. As yield stresses have been observed for smectic 8CB in the present study (discussed in Section 5.2), this indicates that defects are likely present during tests performed at mesoscale confinement as well. One possible product of these persistent domain defects, the intra-period jumps observed in the small amplitude SFA shear response data, is discussed in the following section.

5.7 Intra-period Fitting and Features

The shear response of smectic 8CB under mesoscale confinement exhibits a variety of features that can occur depending on the shear parameters used. At lower shear levels, for example, intra-period jumps that indicate discontinuities in the relative motion of the shearing surfaces have been observed (discussed in Section 4.2.7), which may be a result of smaller events occurring within the liquid crystal structure. The frequency of these events does not decrease even after hours of shearing has occurred, indicating that this is a regularly occurring phenomenon that is either a direct result of domain reorientation or a process that is contributing to the onset of domain reorientations at early shear times. The XSFA work of Nieman et al indicates that smectic normals tilt periodically with the shear frequency during gentle, low amplitude shearing within the mesoscale regime[323], and so one possible interpretation of the discontinuities is that it is a direct result of this sudden and regular tilting effect (but due to larger amplitude shearing). Another possible related source for the jumps is the reorientation of domain clusters. As domains reorient and coalesce in the direction of shearing, the sudden change in alignment may cause a slight disturbance in the response. Alternatively, these jumps may be due to the reduction of defects during the domain reorientation process. Larson reports the presence of domain defects within bulk smectic 8CB that persist during oscillatory shearing[371]. As indicated in Section 4.2.7, these jumps (while diminishing somewhat in frequency) also persist for the entirety of the shear process, suggesting there may be a link between them. Horn and Kléman, in their research involving LAOS of bulk smectic 8CB, note that defects tend to be removed as domains reorient[42]. Choi et al report that domain defects have stored energy associated with them due to their greater stiffness[225]; it is possible that

the jumps observed are a result of the sudden release of this stored energy as adjacent domains forming defects reorganize and aggregate with their neighbours during the reorientation process. Tests to confirm the long term falloff of these jumps in moderately sheared smectic 8CB is warranted to confirm these hypotheses, however.

Under gentle shear conditions, particularly those that are due to small shear amplitudes, the response was found to be approximately linear. That is, a triangular shear pattern resulted in a triangular response. It should be noted, however, that for these conditions the signal to noise ratio was often low enough that any but the most conspicuous details of the pattern (such as the jumps in response discussed in Sections 4.2.7 and 5.3), were lost. By contrast, more aggressive shearing generally resulted in a distinctly non-linear response, with the most prominent feature being an elbow occurring at a fairly consistent point (for a given set of shear parameters) within each sweep. The onset, definition, and angularity of this elbow depends on the shear characteristics, and was found to fit best using a Burgers Model (as introduced in Section 4.2.6 and derived in Appendix 2), which has been used previously with success to model a wide variety of viscoelastic systems under shear[391-396]. The model assumes that the response consists of a Kelvin-Voigt (solidlike) component and a Maxwell (liquidlike) component acting in series. The elastic components of both contributors primarily describe instantaneous and early behaviour and the Maxwell viscosity component dominates at asymptotic times, while the transitional regime is best described by an approximately exponential decay curve composed of a combination of the Maxwell and Kelvin-Voigt terms. The fits for each shear experiment are given in Appendix 1.

The most prominent intra-period feature observed, as mentioned earlier, is the 'elbow' or kink that appears with varying degrees of prominence in tests using moderate to large shear rates. The pre- and post-elbow sections of response are typically either linear or exhibit modest curvature, and it is the kinked section that often displays considerable curvature depending on the shear parameters used. The kink represents a clear change in the mechanical properties of the 8CB, and it is proposed that this point corresponds to the viscoelastic limit discussed in previous sections. Before the limit is reached, the liquid crystal exhibits both viscous and elastic components, but beyond the limit it is dominated by purely viscous behaviour, corresponding to the Burgers Model's η_1 component (as introduced in Section 4.2.6 and derived in Appendix 2). The kink is absent during gentler shearing, typically involving a shear amplitude of 62.5 nm, because the viscoelastic limit has not yet been reached. With the 6.25 μm shear amplitude tests the kink is shallower and wider and occurs early on in the shear sweep, while with the 625 nm shear amplitude tests the kink generally occurs beyond the midway point in the shear sweep. This indicates that the viscoelastic limit is reached after several hundred nanometers, so that one sees the entire change in behaviour with the former shear profile, but only *begins* to see the change in behaviour at the end of the shear period for the latter shear profile. Using data sets where the elbow is more sharply defined as a reference, this viscoelastic limit has been determined by eye to occur roughly at 1.2 ± 0.3 μm; the broad uncertainty associated with this value is a result not only of variance in the limit from sweep to sweep, but also that the limit itself is dependent on the shear parameters being used. The

effect this viscoelastic limit has on the smectic 8CB model will be discussed in the following section.

Figures 4.2 and 4.6 show a marked similarity to one another; with few exceptions, those experiments in which an elbow has been observed a short distance into each shear direction (typically associated with more aggressive shearing) also exhibit drops in viscosity over time. Conversely, those systems undergoing gentler shearing typically show a more linear shear response and occasionally undergo a slight *increase* in viscosity (or, more commonly, no discernable change in viscosity at all—the small signal to noise ratio coupled with long-term signal drift makes the determination of these slight changes of viscosity difficult). There is not a sharp delineation between the two regions, however, and across the phase diagram there exist some responses wherein the two phenomena sometimes tend to overlap. This fact, combined with what has been discussed earlier about the role of large amplitude shearing and domain reorientation, suggests that the act of drawing the sample beyond its viscoelastic limit plays a vital role in reorienting those domains within the mesoscale regime and beyond; Larson reports for bulk 8CB that only strain-shear amplitudes of near unity tend to produce domain reorientation, reinforcing this idea[371]. Gentle shearing, then, tends only to reorient domains in the immediate vicinity of the point of closest approach of the confining surfaces (as observed by Nieman et al[323]), leading to local ordering in the shear direction and thinning of the sample. The bulk of the sample, however, remains largely disoriented, leading to an overall thickening of the sample over time, as evidenced by the response increase measured via strain gauge.

With the response amplitude known to vary as a function of time, particularly for more aggressive shearing, it is natural to inquire how the Burgers Model parameters vary with time, in an effort to connect the intra-period features to the inter-period properties. While the parameters associated with tests involving shear amplitudes of 62.5 nm and 625 nm fluctuated too much with time to be able to be able to determine a definite long-term time dependence, the parameters arising from the 6.25 µm shear amplitude were found to fit well to exponential decay functions, like the inter-period response functions themselves, not surprisingly since it is the variance of one or more of these parameters that must lead to the variation in response. The corresponding decay constants of these Burgers Model parameters, which have been rewritten for convenience, are as follows:

$$\varepsilon = \sigma \left[\frac{1}{k_1} + \frac{t}{\eta_1} + \frac{1}{k_2}\left(1 - e^{-k_2 t/\eta_2}\right) \right] = A(t = 0) + B(t)t + C(t)\left(1 - e^{-Dt}\right) \tag{6}$$

This decay constant may be plotted as a function of shear rate, as shown below:
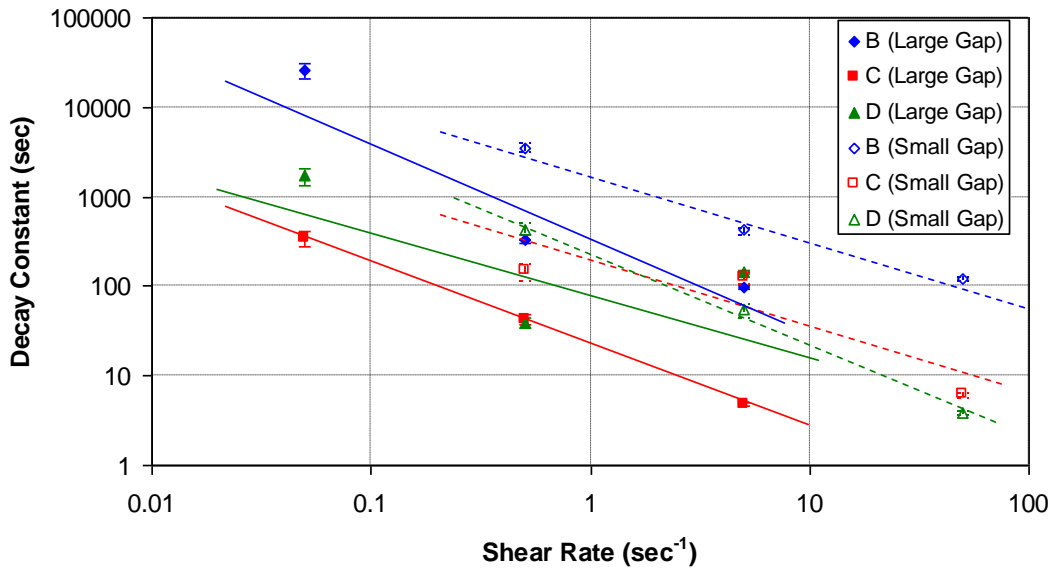
Figure 5.13: Intra-period Burgers Model fitting parameter decay constants as a function of shear rate for 8CB sheared at 6.25 μm amplitude, various frequencies and both gap sizes. Here the large gap refers to 5.0 μm, and the small gap refers to 0.5 μm.

Note that the constant *A*, being an offset and hence coupled with other experimental parameters such as electrical and thermal drift, is potentially misleading and so has been omitted. Also note that because this data has not had the benefit of a filter, the data to be fitted is noisier and so only the more trustworthy large amplitude fitting data have been presented. As can be seen in Figure 5.13, the decay constants vary in the same way with shear rate that the shear responses shown in Figures 4.9, 5.8 and 5.9 do. That is,

$X_{B-D} \approx \chi_{B-D} e^{-t/\tau_{B-D}}$, where X_{B-D} are the three Burgers Model parameters, *B*, *C* and *D*, while χ_{B-D} and τ_{B-D} are the corresponding proportionality constants and time constants for each parameter, respectively. A table of decay constants for the Burgers fitting results alongside the shear response decay constants from Figures 5.8 and 5.9 is presented below.

Table 5.2: Decay time constants for smectic 8CB with various shearing parameters

Large Gap (5.0 μm)			Burgers Variable Decay Constants			Viscosity Decay Constants
Period (sec)	Amplitude (μm)	Shear Rate (sec^{-1})	τ_B (sec)	τ_C (sec)	τ_D (sec)	τ (sec)
100	6.25	0.05	25920 ± 5500	345 ± 72	1695 ± 350	1141 ± 150
10	6.25	0.5	334.7 ± 37	43.35 ± 5.5	39.60 ± 5.0	194.4 ± 15
1	6.25	5	98.81 ± 5.2	4.888 ± 0.22	142.6 ± 6.3	8.857 ± 0.7
Small Gap (0.5 μm)			Burgers Variable Decay Constants			Viscosity Decay Constants
Period (sec)	Amplitude (μm)	Shear Rate (sec^{-1})	τ_B (sec)	τ_C (sec)	τ_D (sec)	τ (sec)
100	6.25	0.5	3536 ± 360	148.7 ± 33	420.0 ± 93	499.8 ± 60
10	6.25	5.0	420.2 ± 36	124.7 ± 20	54.35 ± 9.0	166.6 ± 15
1	6.25	50	121.8 ± 5.0	6.150 ± 0.33	3.911 ± 0.21	27.55 ± 2.0

The evolution of these parameters with time and their physical interpretations will be discussed in the following section.

5.8 Physical Interpretation of Intra-period and Inter-period Phenomena

The Burgers model represents a system in which both viscous and elastic components are both prominent at the beginning of each half-period (that is, when the shear direction is reversed). If one considers a system undergoing large amplitude shearing, that is, where the shear amplitude is much larger than the molecular length scale (which, for the 8CB dimer, is 3.17 nm), it is also worth considering a model wherein a viscoelastic component describes the response from the point when the shear reverses direction up until the viscoelastic limit is reached at time, t_k (when, as described in the previous section, the 'kink' of the curve is reached), while a purely viscous, essentially linear component describes the response beyond this limit. A sketch of the two regions is shown in Figure 5.14:
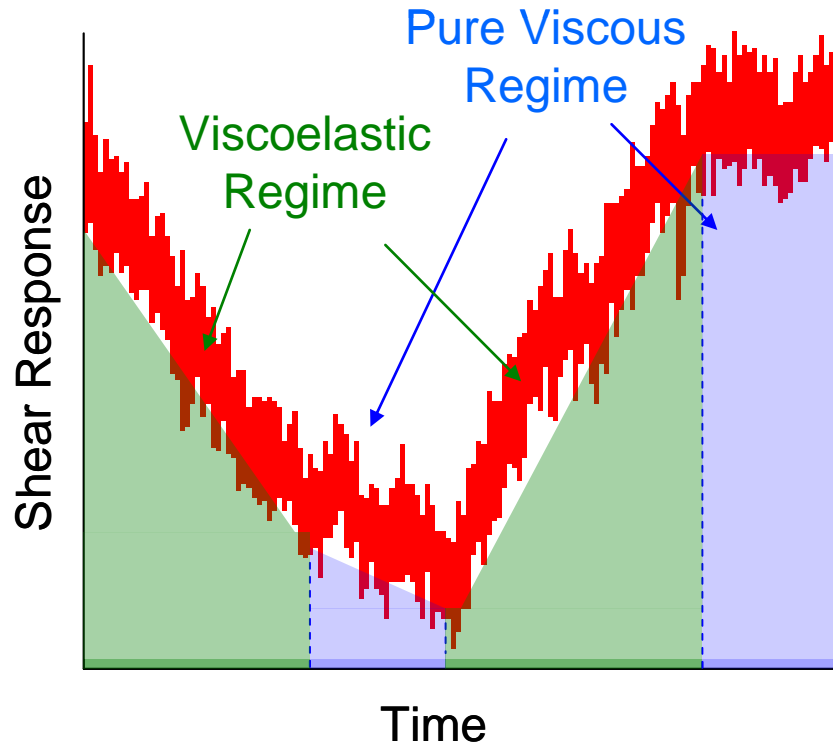
Figure 5.14: Sketch of shear response versus time for a shear amplitude of 625 nm, showing (in green) the viscoelastic regime and (in blue) the purely viscous regime.

The model is bolstered by the observation that at times following t_k the shear response tends to be fairly linear, which one would expect for an oscillatory system that has been drawn beyond its viscoelastic limit into a purely viscous, near-Newtonian regime. In such a model, the pre-limit data can be represented as a simple Kelvin-Voigt material following the result derived in Appendix 2 (The Burgers Model):

$$\varepsilon_2 = \frac{\sigma}{k_2}\left(1 - e^{-k_2 t/\eta_2}\right) \tag{7}$$

where σ is a constant stress while k_2 and η_2 are the elastic and viscous components of the material being studied. The post-limit data can be represented by a line or, to accommodate thermal and strain gauge fluctuations following the crossing of the viscoelastic limit, a simple cubic function. These fits are presented in Appendix 1 for

shear amplitudes of 6.25 μm; since the elbow occurs late enough with the 625 nm data and is fairly broad, the fitting was not felt to be necessary for the 625 nm data sets and the Burgers model alone was deemed sufficient.

   In most tests involving gentler shear (those with 62.5 nm and 625 nm shear amplitudes, particularly at low shear frequencies and larger gap sizes) the uncertainty associated with all fitting parameters largely prevented estimations of short- and long-term trends from being determined. Tests with 6.25 μm shear amplitude (and 625 nm shear amplitude with higher shear frequencies) were more telling. Figure 5.13 gives the most notable examples, shown as a function of shear rate, but a complete set of plots of Burgers parameters as a function of time are given in Appendix 1.1. A sample plot of the Burgers parameters for this shear amplitude is given below:
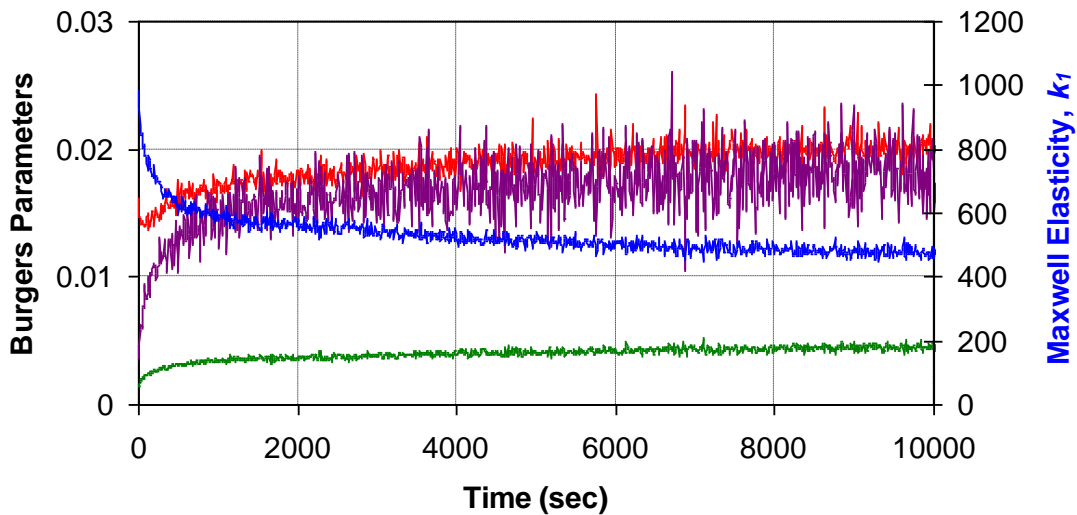

Figure 5.15: Smectic 8CB Burgers Model fit parameters as a function of time for shear amplitude 6.25 μm, shear frequency 0.1 Hz and gap 0.5 μm. Blue and green symbols represent k_1 and k_2 in equation (6), respectively, while red and purple symbols represent η_1 and η_2, respectively.

319

The Burgers intercept term, $\varepsilon(0) = 1/k_1$, because it represents the extremes of the shear cycle, will be proportional to the amplitude of response (although more susceptible to drift in the response than a straight peak to peak amplitude measurement), and so indicates the effective viscosity. It should be mentioned that the k_1 values presented are absolute values of negative raw data, and so show the opposite trend of their physical representation. The effective viscosity can therefore be seen to fall sharply early on in the shear process, indicating that the material is becoming more flexible from the shearing, a result of domain alignment in the shear direction. During this same period the viscosity parameter η_1 increases, offsetting this decrease in stiffness of the sample. The increasing viscosity term indicates that the sample, while stressed beyond the viscoelastic limit (where the η_1 term dominates), is actually becoming less viscous over time.

It is worth noting that the Kelvin-Voigt time constant k_2/η_2 drops during this first minute, since k_2 rises only slightly while η_2 rises sharply. The coincidence of this drop with the drop in viscosity and rise in η_1 indicates they are likely all caused by the same physical phenomenon, specifically, the growth and reorientation of 8CB domain structures. Because the exponential Burgers term is most prominent at the transition from viscoelastic to plastic behaviour, this dropping time constant is likely due to a blurring of the viscoelastic limit that may be a precursor to the drop in response observed later on during shearing. It is interesting to note that Ruths et al observed a similar initial period of non-equilibrium in shear response (18-60 sec) while shearing ultrathin (1.6-1.7 nm) planar-oriented layers of smectic 8CB at 0.1-0.2 μm/sec, attributing this behaviour to a 'greater fluidity' of the system[125]. This agrees with the aforementioned observation that,

at mesoscale confinement and aggressive enough shear levels, the viscosity tends to decrease, resulting in a 'more fluid' smectic 8CB. Beyond this early shift, the time constant remains unchanged and does not account for the overall 8CB shift in viscoelasticity with time.

While the weaker shear tests were too noisy to allow for the extraction of trends from the fitting parameters, some tests with moderate levels of shearing (in which the viscoelastic limit was either barely exceeded or not exceeded at all) yielded information about the dynamics at early times for cases in which the sample thickened as shear progressed. Figures 5.16 and 5.17 show the Burgers parameters for the larger gap, with 625 nm shear amplitude and 1 Hz shear frequency:
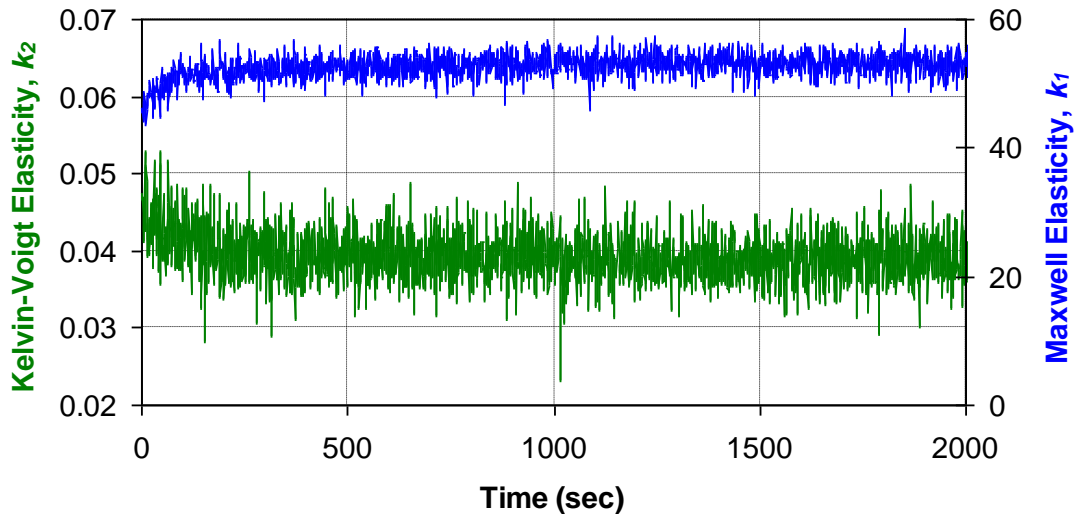

Figure 5.16: Smectic 8CB Burgers Model fit elasticity parameters as a function of time for shear amplitude 625 nm, shear frequency 1 Hz and gap 5 μm. Blue and green symbols represent k_1 and k_2 in equation (6), respectively.
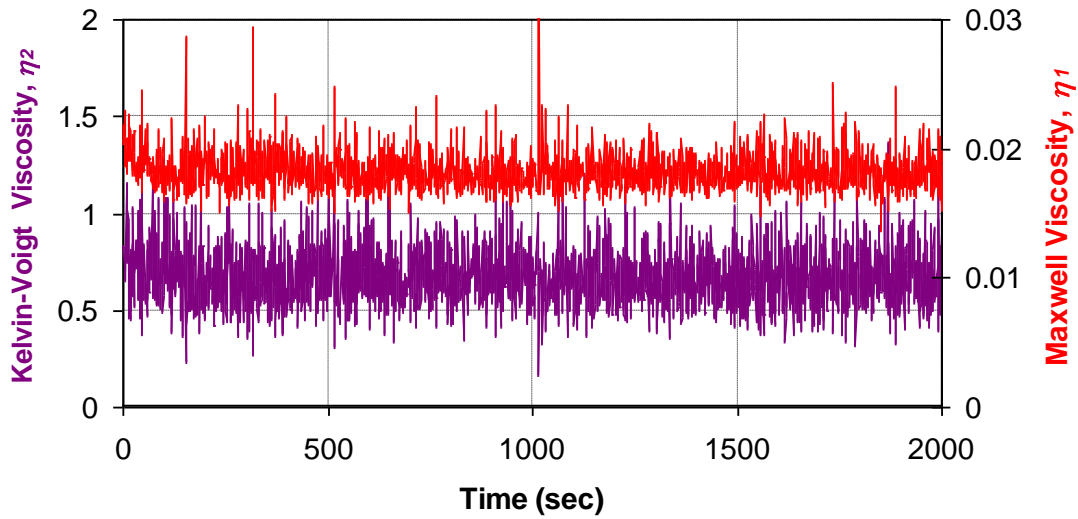
Figure 5.17: Smectic 8CB Burgers Model fit viscosity parameters as a function of time for shear amplitude 625 nm, shear frequency 1 Hz and gap 5 μm. Red and purple symbols represent η_1 and η_2, respectively.

The Maxwell and Kelvin-Voigt elasticity components for these moderate shear tests

(shown in Figure 5.16) clearly have the opposite trends established for the more

aggressive shearing case shown in Figure 5.15, indicating a stiffening of the liquidlike

component and a loosening of the solidlike component, respectively. The increase in k_1

indicates that the effective viscosity given by $\varepsilon(0) = 1/k_1$ increases slightly during the

shear. The viscosity components, meanwhile, both decrease only slightly over the same

time frame, indicating the extent of viscous flow of the 8CB remains more or less

constant throughout the shearing process. This differs from the behaviour observed

during aggressive shearing, wherein the viscous components tended to increase, and

demonstrates that the aggressive, large amplitude shearing is the main contributing factor

to the viscous component changes. The slight shift in the viscosity components early on

during moderate shearing accounts for the correspondingly slight increase in overall

shear response observed for gently and moderately sheared samples, and may be characteristic of the condition discussed in Section 5.3, in which gentle shearing leads to a sample oriented in the area of tightest confinement but remaining disordered elsewhere. The drop in k_2 is furthermore indicative of a softening of the intra-period curvature and hence a slight shift towards response linearity. If, as Wilhelm suggests, the non-linearity is a product of the process of domain aggregation[376], it suggests the early shearing has, to a very limited extent (perhaps only in the region of tightest confinement) completed this domain reorientation process.

As mentioned earlier, all 10 Hz shear tests were excluded from the intra-period fitting and the resultant analysis, as higher order parameters of the shear response were filtered away (as discussed in Section 4.2), in turn removing the features being studied here.

The large amplitude Split Model fitting shows a similar effect (see Figure A1.7b), with its Kelvin-Voigt time constant remaining relatively invariant, save for a sharp decrease in the first hundred seconds or so. This effect further demonstrates that changes to the dynamics of the system are occurring early on following the reversal of the shear direction, while the fairly linear component representing the post-elbow plastic flow tends to decrease steadily for the duration of shearing, indicating an overall thinning of the material, the product of significant domain reorientation.

5.9 Conclusions: An Overall Picture of Smectic 8CB at Mesoscale Confinement Under Shear

The results and discussion above describe a system in which smectic 8CB domains under confinement are induced to reorient by oscillatory shear stresses. The complex and varied behaviour observed depends considerably on the shear parameters applied. A table of the observed phenomena and their proposed physical interpretations and causes is given below:

Table 5.3: Shear properties and their proposed physical interpretations and causes

Condition	Phenomenon	Proposed Physical Interpretation/Cause
Gentle shear with small gap	Roughly linear but noisy response; frequent jumps in response	Jumps may indicate a discrete domain reorientation in the shear direction[323]
	Slight increase in response over time	Response increase may be due to domains that have grown and been stretched by the shearing process, but which have not fully reoriented, resulting in an overall increase in viscosity over time
	Shear thinning at low shear amplitudes	Shear thinning has been observed previously[380, 381] in bulk smectic 8CB
Gentle shear with large gap	Frequent jumps in response	Jumps may represent a discrete domain reorientation in the shear direction
	Shear thinning at low shear amplitudes	Shear thinning has been observed previously in bulk smectic 8CB[380, 381]
Moderate shear	Variously slight increases or decreases in response over time	Shear response will depend on the extent of domain reorientation, which in turn will depend on the specific shear parameters used
	Drop in Maxwell viscosity component	Response becomes more linear, suggesting domains have aggregated and reoriented[376]
	Slight kink in the shear period	Kink is caused by the material being brought beyond its viscoelastic limit, with post-kink

Condition	Phenomenon	Proposed Physical Interpretation/Cause
		regime representing plastic flow
Aggressive shear with small gap	Shear thickening at large shear amplitudes	Shear thickening is a product of the 8CB being brought beyond its viscoelastic limit
	Sharp kink shortly after reversal of shear direction	Viscoelastic limit is exceeded after small shear distance because of the relatively large percent strain due to the smaller gap
	Sharp decrease in elasticity Burgers component, slight increase in viscosity Burgers components	Repeatedly exceeding the viscoelastic limit quickly reorients the domains into the shearing direction, lowering the energy dissipation in the shearing process; rapid decrease in effective viscosity
	Long-term change in response is period-independent during LAOS	All domains have been reoriented in the shear direction due to the more aggressive shear effect created by gap-spanning domains within the smaller gap
Aggressive shear with large gap	Shear thickening at large shear amplitudes	Shear thickening is a product of the 8CB being brought beyond its viscoelastic limit
	Broad and gentle kink	Relatively small percent strain allows the 8CB to deform over a larger deformation distance before the viscoelastic limit is reached
	Sharp decrease in elasticity Burgers component, slight increase in viscosity Burgers components	Repeatedly exceeding the viscoelastic limit quickly reorients the domains into the shearing direction, lowering the energy dissipation in the shearing process; effective viscosity decreases
	Long-term change in response diminishes with increasing period during LAOS	This may be an indication that domains have not fully reordered for the larger period tests. Possible evidence that the domains are not fully spanning the larger gap and are thereby being reoriented less aggressively during shearing.

From the above table an overall picture of the system can be established, in which subtle differences can be seen between the shear response behaviour at the extremes of the mesoscale regime. Comparisons of the response amplitudes for the two extremes show that at the onset of shear, the material is stiffer within the 0.5 μm gap than the 5.0 μm, but drops in effective viscosity after several cycles, indicating the reorientation process is more efficient at the lower end of the mesoscale than at the higher end. This is

attributed to the former gap being on the order of the length scale of the domains, so that the hard confining surfaces contribute more directly to the domain reorientation than they would within the latter gap, in which many domains are reoriented by their more flexible domain neighbours and only indirectly affected by the hard confining surfaces. It also underscores the importance of the gap size in determining the viscoelastic limit; a smaller gap will have a smaller viscoelastic limit than a larger gap because the shear-strain amplitude will be proportionally larger. The inherently stiffer material within the smaller gap intensifies this effect by further reducing the viscoelastic limit within the smaller gap.

Dynamical and structural differences are also apparent between samples sheared while confined to mesoscale gaps and those sheared while in bulk. Turbidity indicative of disoriented domains due to particularly large shear-strain amplitude shearing (for shear-strain amplitudes of 5 or more), is observed within bulk smectic 8CB[371]. Within the mesoscale, however, rapid domain orientation is observed at both ends of the mesoscale regime (0.5 µm and 5.0 µm gap sizes), as evidenced by the sharp drop in shear response for each. This effect may be the result of the gap approaching the length scale of the domains, leading to hindered motion of the domains by the confining surfaces. Complete domain reorientation and aggregation during LAOS (with more moderate shear-strain amplitude) also occurs much more quickly at mesoscale confinement (within seconds or minutes) than it does for bulk samples (remaining incomplete even after several hours).

The differing intra-period fitting results for gentle and aggressive shearing indicates that different mechanisms are behind the observed behaviour: During gentle shearing,

slight increases in the Burgers viscosity components, likely the result of domains being unable to fully reorient into the shear direction (except near the point of tightest confinement, where ordering has previously been observed to increase in a stepwise manner), drive the increase in response during gentle shearing. Under more aggressive shearing the domain reorientation is much more rapid and thorough, leading to a drop in effective viscosity that is the result of an overall decrease in the Burgers elastic components accompanied by a moderate decrease in Burgers viscosity components. The drop in Maxwell viscosity indicates that the material is sliding with less resistance once the viscoelastic limit is exceeded, a direct result of the reorientation of domains over time.

Similarly, differences in behaviour can be seen between 8CB sheared with smaller and greater amplitudes relative to the viscoelastic limits of the material. Different shear amplitudes, for example, produce unique Ostwald-de Waele power law curves, such that at the lowest tested amplitude the expected shear thinning behaviour was observed, while at higher amplitudes slight shear thickening behaviour was observed, a result of the sample being brought beyond its viscoelastic limit. The viscosity evolution over time, in fact, was found to depend not only on shear rate, but also in part on shear amplitude as well. This is further indication that large amplitude shearing is more efficient at reorienting the domain structures. The sample is being brought beyond its viscoelastic limit, which forcibly separates neighbouring domains from one another and thereby provides them with more opportunity to reorient than if shearing had been kept to within this limit, where flexibility of the domains mitigates the effect of shearing. The viscosity

vs. time curves, when fitted to a two exponential model, yield a smaller time constant that varies logarithmically with shear rate. Furthermore, varying shear amplitude yields similar but distinct logarithmic relationships that, when their respective fitting parameters are plotted vs. shear amplitude, provide an equation describing the evolution of effective viscosity with time as a function not only of shear rate, but also independently of shear amplitude as well.

A method to determine the extent to which the viscoelastic limit has been exceeded, by way of calculating the harmonic ratios of the response, A_N/A_1, and determining the point at which (and the extent to which) they diverge from the expected triangular harmonic ratios. This divergence has, in prior research on other materials, yielded information on the construction and destruction of structures due to the large amplitude shearing. Changes in the second harmonic ratio over time has, in prior tests on lamellar materials, been demonstrated to be correlate to mobility changes in network structures due to their aggregation and reorientation[376] and so establishes a basis for similar studies using the SFA. A rise in third harmonic ratio during aggressive shearing of smectic 8CB indicates, similarly, that domains are annealing in the sample early on in the shearing process.

While the results presented require further testing to fully understand the phenomena presented here, they nevertheless provide tantalizing evidence of the unique behaviour characteristic of smectic dynamics at mesoscale confinement.

5.10 Future Work

Shear studies with the SFA require a great deal of patience due to the delicate and short-lived nature of the surfaces. As a result, the number and extent of test runs is necessarily limited and this, combined with the complex behaviour of smectic 8CB under shear leaves several areas where more extensive data gathering would be useful. Listed below are specific areas where further investigation would be warranted, and improvements to the test procedure could be made:

- Longer tests (over multiple days) at very low shear rates in order to ensure asymptotic viscosities have occurred, and compare the number of response discontinuities (discussed in Section 4.2.7) early and later in the shearing process.

- Further investigation into the transition zone seen in Figures 4.2 and 4.6, and discussed in Section 5.4, in which the shear-induced time-dependent viscosity change switches from clear thickening to weak thickening behaviour.

- Further investigation into the viscosity power law dependence to establish the nature of amplitude dependence of consistency, K, and power law index, n, particularly at different levels of confinement, both within and outside the mesoscale window, to determine whether confinement has an added influence to these parameters.

- Reduction or removal of noise between 10 Hz and 100 Hz so that high pass filtering of the strain gauge data is not necessary and, consequently, so that more accurate high frequency measurements can be made without the loss of intra-period features.

- Improvement of the temperature control within the SFA room and SFA chamber to minimize long-term thermal drift, which in turn would assist in the establishment of asymptotic shear response.

- Improvements to the sensitivity of the measurement of shear response can be made, for example, by replacing the semiconductor strain gauge system currently in place with a piezoelectric tube (PZT) measurement device, such as that developed by Klein and Kumacheva, which has a quoted lateral measurement resolution of 0.1 μN[43, 397].

- Investigation of the viscoelastic limit's dependence on intra-period shear parameters. By varying shear amplitude, frequency and gap size and monitoring the point within the shear period at which the aforementioned response kink occurs, information can be obtained on the length scales within the system.

- The installation and implementation of an improved data acquisition card capable of acquiring at a faster rate, allowing for better definition of the observed kink and potentially allowing for accurate measurement of the response phase shift.

References

[1]   F. Reinitzer, Monatshefte fur Chemie (Wien) **9**, 421 (1888).

[2]   G. Friedel, Annales de Physique **18**, 273 (1922).

[3]   O. Lehmann, in *Flussige Kristalle*, Leipzig, 1904).

[4]   C. Mauguin, Bull. Soc. Franc. Miner. **34**, 71 (1911).

[5]   C. Mauguin, Comptes rendus de l'Academie des Sciences **152**, 1680 (1911).

[6]   F. Grandjean, Bull. Soc. Fr. Miner. **39**, 164 (1916).

[7]   F. Grandjean, Comptes rendus de l'Academie des Sciences **164**, 280 (1917).

[8]   V. Fréedericksz and V. Zolina, Trans. Am. Electrochem. Soc. **55**, 85 (1929).

[9]   H. Zocher and K. Coper, Z. Phys. Chem. **132**, 295 (1928).

[10]   H. Zocher, Transactions of the Faraday Society **29**, 0945 (1933).

[11]   C. W. Oseen, Transactions of the Faraday Society **29**, 0883 (1933).

[12]   V. Tsvetkov, Acta Physicochim **15**, 132 (1942).

[13]   F. C. Frank, Discussions of the Faraday Society, 19 (1958).

[14]   W. Maier and A. Saupe, Zeitschrift Fur Naturforschung Part a-Astrophysik Physik Und Physikalische Chemie **13**, 564 (1958).

[15]   W. Maier and G. Meier, Zeitschrift Fur Naturforschung Part a-Astrophysik Physik Und Physikalische Chemie **16**, 262 (1961).

[16]   A. Saupe and G. Englert, Physical Review Letters **11**, 462 (1963).

[17]   A. Saupe and W. Maier, Zeitschrift Fur Naturforschung Part a-Astrophysik Physik Und Physikalische Chemie **16**, 816 (1961).

[18]   H. Lippmann, Annln. Phys. **1**, 157 (1958).

[19]   P. G. De Gennes and J. Prost, *The Physics of Liquid Crystals* (Oxford University Press, 1993).

[20]   P. G. De Gennes, J. Phys. (Paris) **4**, 65 (1969).

[21]   P. G. Degennes, Physics Letters A **A 30**, 454 (1969).

[22]   P. G. Degennes, Molecular Crystals and Liquid Crystals **12**, 193 (1971).

[23]   P. G. Degennes, Solid State Communications **10**, 753 (1972).

[24]   P. G. Degennes, Molecular Crystals and Liquid Crystals **34**, 91 (1976).

[25]   P. G. Degennes and C. Taupin, Journal of Physical Chemistry **86**, 2294 (1982).

[26]   J. F. Dreyer, in *3rd Int. Liquid Crystal Conf.*, Berlin, Germany, 1970).

[27]   P. Sheng, Physical Review Letters **37**, 1059 (1976).

[28]   P. Sheng, Physical Review A **26**, 1610 (1982).

[29]   B. Jerome, Reports on Progress in Physics **54**, 391 (1991).

[30]   B. Jerome, J. Bechhoefer, A. Bosseboeuf, et al., Molecular Crystals and Liquid Crystals **192**, 69 (1990).

[31]   B. Jerome and P. Pieranski, Europhysics Letters **13**, 55 (1990).

[32]   B. Jerome and Y. R. Shen, Physical Review E **48**, 4556 (1993).

[33]   P. Pieranski and B. Jerome, Physical Review A **40**, 317 (1989).

[34]   M. Miesowicz, Nature **136**, 261 (1935).

[35]   M. Miesowicz, Bull. Acad. Pol. A, 228 (1936).

[36]   M. Miesowicz, Nature **158**, 27 (1946).

[37]   J. Israelachvili and R. Pashley, Nature **300**, 341 (1982).

[38]   J. N. Israelachvili, Journal of Colloid and Interface Science **110**, 263 (1986).

[39] J. N. Israelachvili, Colloid and Polymer Science **264**, 1060 (1986).

[40] J. N. Israelachvili and S. J. Kott, Journal of Colloid and Interface Science **129**, 461 (1989).

[41] R. G. Horn, J. N. Israelachvili, and E. Perez, Journal De Physique **42**, 39 (1981).

[42] R. G. Horn and M. Kleman, Annales De Physique **3**, 229 (1978).

[43] J. Klein and E. Kumacheva, Journal of Chemical Physics **108**, 6996 (1998).

[44] J. Klein, E. Kumacheva, D. Perahia, et al., Acta Polymerica **49**, 617 (1998).

[45] J. Klein, Journal of Non-Crystalline Solids **235**, 422 (1998).

[46] J. Klein and E. Kumacheva, Physica A **249**, 206 (1998).

[47] N. A. Clark and P. S. Pershan, Physical Review Letters **30**, 3 (1973).

[48] N. A. Clark and R. B. Meyer, Applied Physics Letters **22**, 493 (1973).

[49] W. Helfrich, Journal of Chemical Physics **51**, 4092 (1969).

[50] W. Helfrich, Physical Review Letters **23**, 372 (1969).

[51] W. Helfrich, Zeitschrift Fur Naturforschung C-a Journal of Biosciences **C 28**, 693 (1973).

[52] C. R. Safinya, E. B. Sirota, and R. J. Plano, Physical Review Letters **66**, 1986 (1991).

[53] C. R. Safinya, E. B. Sirota, R. Plano, et al., Journal of Physics-Condensed Matter **2**, SA365 (1990).

[54] S. H. J. Idziak, C. R. Safinya, R. S. Hill, et al., Science **264**, 1915 (1994).

[55] R. G. Larson, *The Structure and Rheology of Complex Fluids* (Oxford University Press, 1999).

[56] T. J. Sluckin, D. A. Dunmur, and H. Stegemeyer, *Crystals that Flow: Classic Papers from the History of Liquid Crystals* (Taylor & Francis, 2004).

[57] M. de Broglie and E. Friedel, Comptes rendus de l'Academie des Sciences **176**, 738 (1923).

[58] H. Sackmann, Liquid Crystals **5**, 43 (1989).

[59] H. Sackmann and D. Demus, Molecular Crystals and Liquid Crystals **21**, 239 (1973).

[60] S. Chandrasekhar, *Liquid Crystals* (Cambridge University Press, 1992).

[61] A. Jakli and A. Saupe, *One- and Two-Dimensional Fluids: Properties of Smectic, Lamellar and Columnar Liquid Crystals* (CRC Press, Boca Raton, FL, 2006).

[62] S. Chandrasekhar, B. K. Sadashiva, and K. A. Suresh, Pramana **9**, 471 (1977).

[63] K. Kishikawa, S. Furusawa, T. Yamaki, et al., Journal of the American Chemical Society **124**, 1597 (2002).

[64] A. Krowczynski, D. Pociecha, J. Szydlowska, et al., Chemical Communications, 2731 (1996).

[65] A. J. Paraskos, Y. Nishiyama, and T. M. Swager, Molecular Crystals and Liquid Crystals **411**, 1405 (2004).

[66] R. Williams, Journal of Chemical Physics **39**, 384 (1963).

[67] R. A. L. Jones, *Soft Condensed Matter* (Oxford University Press, 2002).

[68] T. Carlsson and F. M. Leslie, Liquid Crystals **26**, 1267 (1999).

[69] E. Bose, Physikalische Zeitschrift **8**, 513 (1907).

[70] E. Bose, Physikalische Zeitschrift **9**, 708 (1908).

[71] E. Bose, Physikalische Zeitschrift **10**, 230 (1909).

72	M. Born, Sitzungsberichte Der Koniglich Preussischen Akademie Der Wissenschaften, 614 (1916).
73	G. P. Crawford, D. W. Allender, and J. W. Doane, Physical Review A **45**, 8693 (1992).
74	D. W. Allender, G. P. Crawford, and J. W. Doane, Physical Review Letters **67**, 1442 (1991).
75	P. Chatelain, Comptes rendus de l'Academie des Sciences **213**, 875 (1941).
76	G. W. Gray, *Molecular Structure and Properties of Liquid Crystals* (Academic Press, Inc., 1962).
77	A. Anzelius, Uppsala Univ. Arsskr., Mat. Naturv. **1**, 1 (1933).
78	J. L. Ericksen, Archive for Rational Mechanics and Analysis **4**, 231 (1960).
79	J. L. Ericksen, Transactions of the Society of Rheology **5**, 23 (1961).
80	J. L. Ericksen, Archive for Rational Mechanics and Analysis **9**, 371 (1962).
81	M. Kleman and O. D. Lavrentovich, *Soft Matter Physics: An Introduction* (Springer-Verlag, New York, 2003).
82	F. M. Leslie, Quarterly Journal of Mechanics and Applied Mathematics **19**, 357 (1966).
83	O. Parodi, Journal De Physique **31**, 581 (1970).
84	F. M. Leslie, Archive for Rational Mechanics and Analysis **28**, 265 (1968).
85	W. R. Burghardt, Journal of Rheology **35**, 49 (1991).
86	L. R. P. de Andrade Lima and A. D. Rey, Physical Review E **70** (2004).
87	L. R. P. De Andrade Lima and A. D. Rey, Rheologica Acta **45**, 591 (2006).
88	I. W. Hamley, V. Castelletto, and P. Parras, Physical Review E **74** (2006).
89	A. P. Krekhov, T. Borzsonyi, P. Toth, et al., Physics Reports-Review Section of Physics Letters **337**, 171 (2000).
90	A. P. Krekhov, L. Kramer, A. Buka, et al., Journal De Physique Ii **3**, 1387 (1993).
91	A. P. Krekhov and L. Kramer, Physical Review E **53**, 4925 (1996).
92	A. P. Krekhov and L. Kramer, Journal De Physique Ii **4**, 677 (1994).
93	P. T. Mather, D. S. Pearson, and W. R. Burghardt, Journal of Rheology **39**, 627 (1995).
94	K. Nakano, Tribology Letters **14**, 17 (2003).
95	P. D. Olmsted and P. Goldbart, Physical Review A **41**, 4578 (1990).
96	H. Siebert, I. Ouijada-Garrido, J. Vermant, et al., Macromolecular Chemistry and Physics **208**, 2161 (2007).
97	O. S. Tarasov, Liquid Crystals **31**, 1235 (2004).
98	O. S. Tarasov, A. P. Krekhov, and L. Kramer, Molecular Crystals and Liquid Crystals Science and Technology Section a-Molecular Crystals and Liquid Crystals **328**, 573 (1999).
99	P. Toth, A. P. Krekhov, L. Kramer, et al., Europhysics Letters **51**, 48 (2000).
100	V. M. Ugaz and W. R. Burghardt, Macromolecules **31**, 8474 (1998).
101	W. J. Zhou, J. A. Kornfield, and W. R. Burghardt, Macromolecules **34**, 3654 (2001).
102	W. R. Burghardt and G. G. Fuller, Macromolecules **24**, 2546 (1991).
103	W. R. Burghardt and G. G. Fuller, Journal of Rheology **34**, 959 (1990).
104	P. Chatelain, Bull. Soc. Fr. Miner. Crist. **78**, 262 (1955).

105 S. Jen, N. A. Clark, P. S. Pershan, et al., Journal of Chemical Physics **66**, 4635 (1977).

106 H. Moryson, D. Bauman, W. Hilczer, et al., Zeitschrift Fur Naturforschung Section a-a Journal of Physical Sciences **54**, 299 (1999).

107 S. H. Lee, V. Surendranath, Y. C. Kim, et al., Liquid Crystals **18**, 495 (1995).

108 J. W. Emsley, NATO ASI Ser, C (1985).

109 P. Diehl and C. L. Khetrapal, Canadian Journal of Chemistry **47**, 1411 (1969).

110 J. Courtieu, D. W. Alderman, D. M. Grant, et al., Journal of Chemical Physics **77**, 723 (1982).

111 F. M. Leslie, Luckhurs.Gr, and H. J. Smith, Chemical Physics Letters **13**, 368 (1972).

112 D. M. Grant and R. K. Harris, (John Wiley, Toronto, 1996), Vol. 1.

113 P. Diehl and C. L. Khetrapal, Molecular Physics **14**, 283 (1967).

114 P. Diehl, C. L. Khetrapal, H. P. Kellerhals, et al., J. Mag. Res. **1**, 527 (1969).

115 F. J. Kahn, G. N. Taylor, and Schonhor.H, Proceedings of the Ieee **61**, 823 (1973).

116 D. W. Berreman, Physical Review Letters **28**, 1683 (1972).

117 S. Kralj, S. Zumer, and D. W. Allender, Physical Review A **43**, 2943 (1991).

118 N. A. Tikhomirova and A. V. Guinsberg, edited by L. Bata (Pergamon Press - Akademiai Kiado, Oxford/New York/Budapest, 1980), Vol. 2, p. 651.

119 N. A. Tikhomirova, L. I. Dontsova, S. A. Pikin, et al., Kristallografiya **23**, 1239 (1978).

120 E. K. Frolova, O. G. Sarbey, and A. S. Sybashvily, Molecular Crystals and Liquid Crystals **104**, 111 (1984).

121 L. M. Blinov and A. A. Sonin, Molecular Crystals and Liquid Crystals **179**, 13 (1990).

122 E. Dubois-Violette and P. G. Degennes, Journal De Physique Lettres **36**, L255 (1975).

123 J. Janik, R. Tadmor, and J. Klein, Langmuir **13**, 4466 (1997).

124 J. Janik, R. Tadmor, and J. Klein, Langmuir **17**, 5476 (2001).

125 M. Ruths, S. Steinberg, and J. N. Israelachvili, Langmuir **12**, 6637 (1996).

126 M. Ruths and S. Granick, Langmuir **16**, 8368 (2000).

127 S. H. J. Idziak, I. Koltover, J. N. Israelachvili, et al., Physical Review Letters **76**, 1477 (1996).

128 S. H. J. Idziak, I. Koltover, K. S. Liang, et al., International Journal of Thermophysics **16**, 299 (1995).

129 R. G. Horn and J. N. Israelachvili, Journal of Chemical Physics **75**, 1400 (1981).

130 A. Artsyukhovich, L. D. Broekman, and M. Salmeron, Langmuir **15**, 2217 (1999).

131 J. Bechhoefer, B. Jerome, and P. Pieranski, Physical Review A **41**, 3187 (1990).

132 J. Bechhoefer, B. Jerome, and P. Pieranski, Phase Transitions **33**, 227 (1991).

133 L. Lejcek, J. Bechhoefer, and P. Oswald, Journal De Physique Ii **2**, 1511 (1992).

134 R. Barberi, N. Scaramuzza, V. Formoso, et al., Europhysics Letters **34**, 349 (1996).

135 J. Z. Xue, C. S. Jung, and M. W. Kim, Physical Review Letters **69**, 474 (1992).

136 S. Bardon, R. Ober, M. P. Valignat, et al., Physical Review E **59**, 6808 (1999).

137 B. Alkhairalla, H. Allinson, N. Boden, et al., Physical Review E **59**, 3033 (1999).

138 S. D. Evans, H. Allinson, N. Boden, et al., Faraday Discussions, 37 (1996).

139 I. D. Olenik, K. Kocevar, I. Musevic, et al., European Physical Journal E **11**, 169 (2003).

140 K. Negita, M. Inoue, and S. Kondo, Physical Review E **74** (2006).

141 S. Granick, Science **253**, 1374 (1991).

142 J. A. Pryde, *The Liquid State* (Hutchinson University Library, London, 1966).

143 J. N. Israelachvili, *Intermolecular and Surface Forces* (Academic Press, 1991).

144 V. Kitaev and E. Kumacheva, Journal of Physical Chemistry B **104**, 8822 (2000).

145 M. Ruths, M. Heuberger, V. Scheumann, et al., Langmuir **17**, 6213 (2001).

146 L. Moreau, P. Richetti, and P. Barois, Physical Review Letters **73**, 3556 (1994).

147 P. Richetti, L. Moreau, P. Barois, et al., Physical Review E **54**, 1749 (1996).

148 L. J. D. Frink and F. van Swol, Journal of Chemical Physics **108**, 5588 (1998).

149 E. J. Wanless and H. K. Christenson, Journal of Chemical Physics **101**, 4260 (1994).

150 H. K. Christenson and V. V. Yaminsky, Langmuir **9**, 2448 (1993).

151 H. K. Christenson, D. W. R. Gruen, R. G. Horn, et al., Journal of Chemical Physics **87**, 1834 (1987).

152 P. Attard and J. L. Parker, Journal of Physical Chemistry **96**, 5086 (1992).

153 P. M. McGuiggan and J. N. Israelachvili, Journal of Materials Research **5**, 2232 (1990).

154 J. Peachey, J. Vanalsten, and S. Granick, Review of Scientific Instruments **62**, 463 (1991).

155 J. Vanalsten and S. Granick, Physical Review Letters **61**, 2570 (1988).

156 Y. K. Cho and S. Granick, Journal of Chemical Physics **119**, 547 (2003).

157 B. Zappone, P. Richetti, R. Barberi, et al., Physical Review E **71** (2005).

158 G. Barbero and R. Barberi, Journal De Physique **44**, 609 (1983).

159 M. Mizukami, K. Kusakabe, and K. Kurihara, Progress in Colloid and Polymer Science **128**, 105 (2004).

160 J. Alsnielsen, R. J. Birgeneau, M. Kaplan, et al., Physical Review Letters **39**, 1668 (1977).

161 J. Alsnielsen, J. D. Litster, R. J. Birgeneau, et al., Physical Review B **22**, 312 (1980).

162 L. Gunthen, Y. Imry, and J. Lajzerowicz, Physical Review A **22**, 1733 (1980).

163 P. Sens and M. S. Turner, European Physical Journal E **4**, 115 (2001).

164 A. Caille, Comptes Rendus Hebdomadaires Des Seances De L Academie Des Sciences Serie B **274**, 891 (1972).

165 P. M. Chaiken and T. C. Lubensky, *Principles of Condensed Matter Physics* (Cambridge University Press, 2000).

166 J. Alsnielsen, R. J. Birgeneau, M. Kaplan, et al., Physical Review Letters **39**, 352 (1977).

167 C. R. Safinya, M. Kaplan, J. Alsnielsen, et al., Physical Review B **21**, 4149 (1980).

168 C. R. Safinya, W. A. Varady, L. Y. Chiang, et al., Physical Review Letters **57**, 432 (1986).

169 C. R. Safinya, D. Roux, G. S. Smith, et al., Physical Review Letters **57**, 2718 (1986).

170	J. T. Mang, K. Sakamoto, and S. Kumar, Molecular Crystals and Liquid Crystals **222**, 133 (1992).
171	N. A. Clark, T. Bellini, R. M. Malzbender, et al., Physical Review Letters **71**, 3505 (1993).
172	P. Panizza, P. Archambault, and D. Roux, Journal De Physique Ii **5**, 303 (1995).
173	K. Negita and S. Uchino, Molecular Crystals and Liquid Crystals **378**, 103 (2002).
174	E. Smela and L. J. Martinezmiranda, Journal of Applied Physics **73**, 3299 (1993).
175	L. J. Martinez-Miranda, Journal of Applied Physics **91**, 6452 (2002).
176	R. L. Leheny, S. Park, R. J. Birgeneau, et al., Physical Review E **67** (2003).
177	A. D. Rey, Journal of Rheology **44**, 855 (2000).
178	A. D. Rey, Journal of Rheology **46**, 225 (2002).
179	E. Fukushima and S. B. W. Roeder, *Experimental Pulse NMR: A Nuts and Bolts Approach* (Addison-Wesley Publishing Company, Reading, 1981).
180	C. P. Slichter, *Principles of Magnetic Resonance* (Springer-Verlag, New York, 1996).
181	J. Benson, in *Physics* (University of Waterloo, Waterloo, 2000), p. 82.
182	M. J. Stephen and J. P. Straley, Reviews of Modern Physics **46**, 617 (1974).
183	M. Vilfan and N. Vrbancic-Kopac, in *Liquid Crystals in Complex Geometries Formed by Polymer and Porous Networks* (Taylor & Francis, Bristol, PA, 1996), p. 159.
184	R. D. Spence, H. A. Moses, and P. L. Jain, Journal of Chemical Physics **21**, 380 (1953).
185	R. D. Spence, H. S. Gutowsky, and C. H. Holm, Journal of Chemical Physics **21**, 1891 (1953).
186	W. Haller, Nature **206**, 693 (1965).
187	W. Haller, Journal of Chemical Physics **42**, 686 (1965).
188	M. Vilfan, T. Apih, P. J. Sebastiao, et al., Physical Review E **76** (2007).
189	J. W. Doane, in *Magnetic Resonance of Phase Transitions*, edited by F. J. Owens (Academic Press, New York, 1979), p. Ch. 4.
190	G. P. Crawford, M. Vilfan, J. W. Doane, et al., Physical Review A **43**, 835 (1991).
191	G. P. Crawford and S. Zumer, *Liquid Crystals in Complex Geometries Formed by Polymer and Porous Networks* (Taylor & Francis, Bristol, PA, 1996).
192	A. Abragam, *Principles of Nuclear Magnetism* (Oxford University Press, Toronto, 1961).
193	J. F. Martin, R. R. Vold, and R. L. Vold, Journal of Chemical Physics **80**, 2237 (1984).
194	G. P. Crawford, R. Ondriscrawford, S. Zumer, et al., Physical Review Letters **70**, 1838 (1993).
195	M. Vilfan, N. Vrbancic-Kopac, P. Ziherl, et al., Applied Magnetic Resonance **17**, 329 (1999).
196	C. Cramer, T. Cramer, F. Kremer, et al., Journal of Chemical Physics **106**, 3730 (1997).
197	S. Kralj, A. Zidansek, G. Lahajnar, et al., Physical Review E **57**, 3021 (1998).
198	G. S. Iannacchione and D. Finotello, Physical Review E **50**, 4780 (1994).

199 S. Kralj, G. Cordoyiannis, A. Zidansek, et al., Journal of Chemical Physics **127** (2007).

200 H. Ogaki, K. Okumoto, A. Sugimura, et al., Thin Solid Films **499**, 249 (2006).

201 G. R. Luckhurst, B. A. Timimi, M. Nakatsuji, et al., Molecular Crystals and Liquid Crystals **398**, 235 (2003).

202 W. L. McMillan, Physical Review A **4**, 1238 (1971).

203 D. L. Johnson, C. F. Hayes, R. J. Dehoff, et al., Physical Review B **18**, 4902 (1978).

204 P. F. Sullivan and G. Seidel, Physical Review **173**, 679 (1968).

205 T. Bellini, N. A. Clark, C. D. Muzny, et al., Physical Review Letters **69**, 788 (1992).

206 V. G. Puglielli and N. C. Ford, Physical Review Letters **25**, 143 (1970).

207 I. D. Olenik, A. Mertelj, and M. Copic, Physical Review E **57**, 6732 (1998).

208 G. S. Iannacchione and D. Finotello, Physical Review Letters **69**, 2094 (1992).

209 M. Kuzma and M. M. Labes, Molecular Crystals and Liquid Crystals **100**, 103 (1983).

210 G. Iannacchione and D. Finotello, Liquid Crystals **14**, 1135 (1993).

211 Z. Kutnjak, S. Kralj, G. Lahajnar, et al., Physical Review E **68** (2003).

212 G. S. Iannacchione, S. H. Qian, G. P. Crawford, et al., Molecular Crystals and Liquid Crystals Science and Technology Section a-Molecular Crystals and Liquid Crystals **262**, 13 (1995).

213 G. S. Iannacchione, G. P. Crawford, S. Zumer, et al., Physical Review Letters **71**, 2595 (1993).

214 S. H. Qian, G. S. Iannacchione, D. Finotello, et al., Molecular Crystals and Liquid Crystals Science and Technology Section a-Molecular Crystals and Liquid Crystals **265**, 395 (1995).

215 S. H. Qian, G. S. Iannacchione, and D. Finotello, Physical Review E **53**, R4291 (1996).

216 S. H. Qian, G. S. Iannacchione, and D. Finotello, Physical Review E **57**, 4305 (1998).

217 K. Kocevar, R. Blinc, and I. Musevic, Physical Review E **62**, R3055 (2000).

218 K. Kocevar and I. Musevic, Physical Review E **65** (2002).

219 B. V. Derjaguin, V. M. Muller, and Y. P. Toporov, Journal of Colloid and Interface Science **53**, 314 (1975).

220 G. Carbone, R. Barberi, I. Musevic, et al., Physical Review E **71** (2005).

221 K. Kocevar and I. Musevic, Physical Review E **6405** (2001).

222 K. Kocevar and I. Musevic, Chemphyschem **4**, 1049 (2003).

223 A. B. Bracic, K. Kocevar, I. Musevic, et al., Physical Review E **68** (2003).

224 T. Pfohl, J. H. Kim, M. Yasa, et al., Langmuir **17**, 5343 (2001).

225 M. C. Choi, T. Pfohl, Z. Y. Wen, et al., Proceedings of the National Academy of Sciences of the United States of America **101**, 17340 (2004).

226 W. Guo, S. Herminghaus, and C. Bahr, Langmuir **24**, 8174 (2008).

227 F. M. Aliev, Z. Nazario, and G. P. Sinha, Journal of Non-Crystalline Solids **305**, 218 (2002).

228 F. Aliev and S. Basu, Journal of Non-Crystalline Solids **352**, 4983 (2006).

229 S. Basu and F. M. Aliev, Molecular Crystals and Liquid Crystals **421**, 49 (2004).

230 K. Negita, T. Nishikawa, and Y. Inamasu, Journal of Chemical Physics **125** (2006).

231 M. A. Z. Ewiss, F. Moawia, and B. Stoll, Liquid Crystals **34**, 127 (2007).

232 I. Soga, A. Dhinojwala, and S. Granick, Langmuir **14**, 1156 (1998).

233 I. Soga, A. Dhinojwala, and S. Granick, Japanese Journal of Applied Physics Part 1-Regular Papers Short Notes & Review Papers **38**, 6118 (1999).

234 L. B. Boinovich and A. M. Emelyanenko, Russian Chemical Bulletin **50**, 319 (2001).

235 L. B. Boinovich, A. M. Emel'yanenko, and E. I. Kochetkova, Colloid Journal **63**, 402 (2001).

236 L. B. Boinovich and A. M. Emelyanenko, European Physical Journal E **6**, 359 (2001).

237 C. Fehr, P. Dieudonne, J. L. Sauvajol, et al., Physical Review E **67** (2003).

238 C. Fehr, C. Goze-Bac, E. Anglaret, et al., Europhysics Letters **73**, 553 (2006).

239 H. Hsiung, T. Rasing, and Y. R. Shen, Physical Review Letters **57**, 3065 (1986).

240 A. Mauger, Physical Review Letters **54**, 2552 (1985).

241 A. Mauger, G. Zribi, and D. L. Mills, Physical Review Letters **53**, 2485 (1984).

242 V. L. Ginzburg and L. D. Landau, Zhurnal Eksperimentalnoi I Teoreticheskoi Fiziki **20**, 1064 (1950).

243 T. Borzsonyi, A. Buka, A. P. Krekhov, et al., Physical Review E **58**, 7419 (1998).

244 E. N. Kozhevnikov, Zhurnal Eksperimentalnoi I Teoreticheskoi Fiziki **91**, 1346 (1986).

245 T. Borzsonyi, A. Buka, A. P. Krekhov, et al., Physical Review Letters **84**, 1934 (2000).

246 R. Guegan, D. Morineau, C. Loverdo, et al., Physical Review E **73** (2006).

247 R. Guegan, R. Lefort, W. Beziel, et al., European Physical Journal-Special Topics **141**, 29 (2007).

248 R. Guegan, D. Morineau, R. Lefort, et al., European Physical Journal E **26**, 261 (2008).

249 R. Lefort, D. Morineau, R. Guegan, et al., Physical Chemistry Chemical Physics **10**, 2993 (2008).

250 P. C. Martin, O. Parodi, and P. S. Pershan, Physical Review A **6**, 2401 (1972).

251 M. Delaye, R. Ribotta, and G. Durand, Physics Letters A **A 44**, 139 (1973).

252 S. Ramaswamy, Physical Review Letters **69**, 112 (1992).

253 Z. R. Chen, A. M. Issaian, J. A. Kornfield, et al., Macromolecules **30**, 7096 (1997).

254 V. K. Gupta, R. Krishnamoorti, Z. R. Chen, et al., Macromolecules **29**, 875 (1996).

255 U. Wiesner, Macromolecular Chemistry and Physics **198**, 3319 (1997).

256 J. H. Laurer, B. S. Pinheiro, D. L. Polis, et al., Macromolecules **32**, 4999 (1999).

257 H. Leist, D. Maring, T. Thurn-Albrecht, et al., Journal of Chemical Physics **110**, 8225 (1999).

258 J. L. Zryd and W. R. Burghardt, Macromolecules **31**, 3656 (1998).

259 D. L. Polis, S. D. Smith, N. J. Terrill, et al., Macromolecules **32**, 4668 (1999).

260 O. Diat, D. Roux, and F. Nallet, Journal De Physique Iv **3**, 193 (1993).

261 O. Diat, D. Roux, and F. Nallet, Journal De Physique Ii **3**, 1427 (1993).

262 J. I. Escalante and H. Hoffmann, Rheologica Acta **39**, 209 (2000).

263 J. I. Escalante and H. Hoffmann, Journal of Physics-Condensed Matter **12**, A483 (2000).

264 S. Muller, C. Borschig, W. Gronski, et al., Langmuir **15**, 7558 (1999).

265 J. Zipfel, J. Berghausen, P. Lindner, et al., Journal of Physical Chemistry B **103**, 2841 (1999).

266 J. Zipfel, J. Berghausen, G. Schmidt, et al., Macromolecules **35**, 4064 (2002).

267 J. Zipfel, J. Berghausen, G. Schmidt, et al., Physical Chemistry Chemical Physics **1**, 3905 (1999).

268 J. Zipfel, P. Lindner, M. Tsianou, et al., Langmuir **15**, 2599 (1999).

269 L. Noirez, Physical Review Letters **84**, 2164 (2000).

270 L. Noirez and A. Lapp, Physical Review Letters **78**, 70 (1997).

271 S. Rendon, W. R. Burghardt, M. L. Auad, et al., Macromolecules **40**, 6624 (2007).

272 S. Rendon, W. R. Burghardt, and R. A. Bubeck, Rheologica Acta **46**, 945 (2007).

273 J. Cognard, Acs Symposium Series **441**, 1 (1990).

274 R. Eidenschink and A. M. Hager, Molecular Crystals and Liquid Crystals Science and Technology Section a-Molecular Crystals and Liquid Crystals **304**, 513 (1997).

275 K. Boschkova, J. Elvesjo, and B. Kronberg, Colloids and Surfaces a-Physicochemical and Engineering Aspects **166**, 67 (2000).

276 B. Wazynska and J. A. Okowiak, Tribology Letters **24**, 1 (2006).

277 M. D. Bermudez, G. Martinez-Nicolas, and F. J. Carrion-Vilches, Wear **212**, 188 (1997).

278 G. K. Auernhammer, H. R. Brand, and H. Pleiner, Rheologica Acta **39**, 215 (2000).

279 E. A. Disalvo and S. A. Simon, *Permeability and Stability of Lipid Bilayers* (CRC Press, Inc., New York, 1995).

280 E. Ruckenstein, Journal of Chemical Physics **109**, 6995 (1998).

281 G. H. Heilmeier and W. Helfrich, Applied Physics Letters **16**, 155 (1970).

282 G. H. Heilmeier and J. E. Goldmacher, Proceedings of the Ieee **57**, 34 (1969).

283 L. D. Landau, Phys. Z. Sowjetunion **11**, 26 (1937).

284 R. E. Peierls, Annales de l'I.H.P. **5**, 177 (1935).

285 E. B. Sirota, G. S. Smith, C. R. Safinya, et al., Science **242**, 1406 (1988).

286 M. Cagnon and G. Durand, Physical Review Letters **45**, 1418 (1980).

287 P. Oswald and M. Kleman, Journal De Physique Lettres **43**, L411 (1982).

288 P. Oswald and S. I. Benabraham, Journal De Physique **43**, 1193 (1982).

289 P. Oswald, J. Behar, and M. Kleman, Philosophical Magazine a-Physics of Condensed Matter Structure Defects and Mechanical Properties **46**, 899 (1982).

290 S. Ramaswamy, Physical Review A **29**, 1506 (1984).

291 M. G. Kim, S. Park, M. Cooper, et al., Molecular Crystals and Liquid Crystals **36**, 143 (1976).

292 S. Bhattacharya and S. V. Letcher, Physical Review Letters **44**, 414 (1980).

293 E. C. Bingham, U.S. Bureau of Standards Bulletin **13**, 309 (1916).

294 D. J. Evans, H. J. M. Hanley, and S. Hess, Physics Today **37**, 26 (1984).

295 A. Al Kahwaji and H. Kellay, Physical Review Letters **84**, 3073 (2000).

296   S. W. Marlow and P. D. Olmsted, European Physical Journal E **8**, 485 (2002).

297   S. W. Marlow and P. D. Olmsted, Physical Review E **66** (2002).

298   R. Bandyopadhyay, D. Liang, R. H. Colby, et al., Physical Review Letters **94** (2005).

299   P. D. Olmsted and P. M. Goldbart, Physical Review A **46**, 4966 (1992).

300   G. H. Fredrickson, Journal of Chemical Physics **85**, 5306 (1986).

301   M. E. Cates and S. T. Milner, Physical Review Letters **62**, 1856 (1989).

302   R. Bruinsma and Y. Rabin, Physical Review A **45**, 994 (1992).

303   R. F. Bruinsma and C. R. Safinya, Physical Review A **43**, 5377 (1991).

304   O. Reynolds, Philos. Mag. **20**, 469 (1885).

305   W. Helfrich, Zeitschrift Fur Naturforschung Section a-a Journal of Physical Sciences **33**, 305 (1978).

306   F. Nallet, D. Roux, and J. Prost, Journal De Physique **50**, 3147 (1989).

307   A. G. Zilman and R. Granek, European Physical Journal B **11**, 593 (1999).

308   G. K. Auernhammer, H. R. Brand, and H. Pleiner, Physical Review E **66** (2002).

309   J. Zipfel, F. Nettesheim, P. Lindner, et al., Europhysics Letters **53**, 335 (2001).

310   G. K. Auernhammer, H. R. Brand, and H. Pleiner, Physical Review E **71** (2005).

311   T. Soddemann, G. K. Auernhammer, H. Guo, et al., European Physical Journal E **13**, 141 (2004).

312   I. W. Stewart, Continuum Mechanics and Thermodynamics **18**, 343 (2007).

313   W. Chen, Y. Ouchi, T. Moses, et al., Physical Review Letters **68**, 1547 (1992).

314   J. D. Litster and R. J. Birgeneau, Physics Today **35**, 26 (1982).

315   P. C. Hohenberg and B. I. Halperin, Reviews of Modern Physics **49**, 435 (1977).

316   W. L. McMillan, Physical Review A **9**, 1720 (1974).

317   S. H. J. Idziak, in *Soft Materials: Structure and Dynamics*, edited by J. Dutcher and A. Marangoni (CRC Press, 2004), p. 39.

318   C. R. Safinya, E. B. Sirota, R. F. Bruinsma, et al., Science **261**, 588 (1993).

319   I. Koltover, S. H. J. Idziak, C. R. Safinya, et al., Mat. Res. Soc. Symp Proc. **366**, 101 (1995).

320   I. Koltover, S. H. J. Idziak, P. Davidson, et al., Journal De Physique Ii **6**, 893 (1996).

321   A. J. Leadbetter, J. C. Frost, J. P. Gaughan, et al., Journal De Physique **40**, 375 (1979).

322   B. Nieman, X. Commeinhes, N. S. Babcock, et al., Review of Scientific Instruments **75**, 936 (2004).

323   B. Nieman, J. Benson, M. Sutton, et al., (Submitted).

324   K. Okano and J. Yamamoto, Japanese Journal of Applied Physics Part 1-Regular Papers Short Notes & Review Papers **29**, 1149 (1990).

325   J. Yamamoto and K. Okano, Japanese Journal of Applied Physics Part 1-Regular Papers Short Notes & Review Papers **30**, 754 (1991).

326   R. A. Herke, N. A. Clark, and M. A. Handschy, Science **267**, 651 (1995).

327   R. A. Herke, N. A. Clark, and M. A. Handschy, Physical Review E **56**, 3028 (1997).

328   A. Tonck, J. M. Georges, and J. L. Loubet, Journal of Colloid and Interface Science **126**, 150 (1988).

329   J. R. Clem, Physical Review Letters **38**, 1425 (1977).

330 W. I. Glaberson, W. W. Johnson, and R. M. Ostermeir, Physical Review Letters **33**, 1197 (1974).

331 P. Oswald and M. Kleman, Journal De Physique Lettres **45**, L319 (1984).

332 L. Bourdon, M. Kleman, L. Lejcek, et al., Journal De Physique **42**, 261 (1981).

333 P. Frantz, F. Wolf, X. D. Xiao, et al., Review of Scientific Instruments **68**, 2499 (1997).

334 A. M. Stewart and H. K. Christenson, Measurement Science & Technology **1**, 1301 (1990).

335 J. Israelachvili, Journal of Colloid and Interface Science **44**, 259 (1973).

336 J. Israelachvili, Y. Min, M. Akbulut, et al., Reports on Progress in Physics **73** (2010).

337 J. Israelachvili, *Introduction to the SFA 2000 and its Attachments* (SurForce Corporation, 2003).

338 J. N. Israelachvili and P. M. McGuiggan, Journal of Materials Research **5**, 2223 (1990).

339 G. Luengo, F. J. Schmitt, R. Hill, et al., Macromolecules **30**, 2482 (1997).

340 J. N. Israelachvili, S. J. Kott, and L. J. Fetters, Journal of Polymer Science Part B-Polymer Physics **27**, 489 (1989).

341 A. L. Window, *Strain Gauge Technology* (Elsevier Science Publishers Ltd., Essex, 1992).

342 R. G. Horn and D. T. Smith, Applied Optics **30**, 59 (1991).

343 G. R. Fowles, *Introduction to Modern Optics* (Dover Publications, 1989).

344 S. C. Hunter and F. R. N. Nabarro, Philos. Mag. **43**, 538 (1952).

345 A. I. Bailey and S. M. Kay, British Journal of Applied Physics **16**, 39 (1965).

346 E. Eisner, Research **4**, 183 (1951).

347 SRS, *Model SR830 DSP Lock-in Amplifier Manual* (Stanford Research Systems, Sunnyvale, CA, 2004).

348 R. W. Wood, Physikalische Zeitschrift **15**, 313 (1914).

349 I. Solc, Czechoslovak Journal of Physics **15**, 532 (1965).

350 S. Ohnishi and A. M. Stewart, Langmuir **18**, 6140 (2002).

351 J. N. Israelachvili, N. A. Alcantar, N. Maeda, et al., Langmuir **20**, 3616 (2004).

352 J. N. Israelachvili and G. E. Adams, Journal of the Chemical Society-Faraday Transactions I **74**, 975 (1978).

353 J. Israelachvili, N. Maeda, and M. Akbulut, Langmuir **22**, 2397 (2006).

354 Y. Zhu and S. Granick, Langmuir **19**, 8148 (2003).

355 P. Frantz and M. Salmeron, Tribology Letters **5**, 151 (1998).

356 F. Ostendorf, C. Schmitz, S. Hirth, et al., Nanotechnology **19** (2008).

357 M. M. Kohonen and H. K. Christenson, Langmuir **16**, 7285 (2000).

358 M. M. Kohonen, F. C. Meldrum, and H. K. Christenson, Langmuir **19**, 975 (2003).

359 S. Perkin, L. Chai, N. Kampf, et al., Langmuir **22**, 6142 (2006).

360 H. Jaeger, P. D. Mercer, and R. G. Sherwood, Surface Science **6**, 309 (1967).

361 D. Tabor and R. H. Winterton, Proceedings of the Royal Society of London Series a-Mathematical and Physical Sciences **312**, 435 (1969).

362 S. W. Bailey, in *Reviews in Mineralogy*, edited by P. H. Ribbe (BookCrafters, Inc., Chelsea, MI, 1984), Vol. 13, p. 584.

363   H. Pichler and C. Schmitt-Riegraf, *Rocks Forming Minerals in Thin Section* (Chapman & Hall, New York, 1997).

364   S. Ohnishi, M. Hato, K. Tamada, et al., Langmuir **15**, 3312 (1999).

365   T. Becker and F. Mugele, Molecular Simulation **31**, 489 (2005).

366   V. S. Smentkowski and J. T. Yates, Journal of Vacuum Science & Technology a-Vacuum Surfaces and Films **12**, 224 (1994).

367   G. Sauerbrey, Zeitschrift Fur Physik **155**, 206 (1959).

368   F. Caruso, T. Serizawa, D. N. Furlong, et al., Langmuir **11**, 1546 (1995).

369   M. T. Clarkson, Journal of Physics D-Applied Physics **22**, 475 (1989).

370   S. H. J. Idziak, I. Koltover, P. Davidson, et al., Physica B **221**, 289 (1996).

371   R. G. Larson, K. I. Winey, S. S. Patel, et al., Rheologica Acta **32**, 245 (1993).

372   D. Davidov, C. R. Safinya, M. Kaplan, et al., Physical Review B **19**, 1657 (1979).

373   K. Hyun, S. H. Kim, K. H. Ahn, et al., Journal of Non-Newtonian Fluid Mechanics **107**, 51 (2002).

374   K. Hyun, J. G. Nam, M. Wilhelm, et al., Korea-Australia Rheology Journal **15**, 97 (2003).

375   A. A. Collyer, (Chapman & Hall, London, 1993).

376   M. Wilhelm, Macromolecular Materials and Engineering **287**, 83 (2002).

377   M. Reiner, *Deformation and Flow* (H. K. Lewis, London, 1949).

378   N. Phan-Thien, *Understanding Viscoelasticity: Basics of Rheology* (Springer-Verlag Berlin Heidelberg, Berlin, 2002).

379   R. H. Colby, C. K. Ober, J. R. Gillmor, et al., Rheologica Acta **36**, 498 (1997).

380   C. Meyer, S. Asnacios, C. Bourgaux, et al., Rheologica Acta **39**, 223 (2000).

381   C. Meyer, S. Asnacios, and M. Kleman, European Physical Journal E **6**, 245 (2001).

382   S. Fujii, Y. Ishii, S. Komura, et al., Epl **90** (2010).

383   E. C. Bingham, *Fluidity and Plasticity* (McGraw-Hill Book Company Inc., New York, 1922).

384   G. Reiter, A. L. Demirel, J. Peanasky, et al., Journal of Chemical Physics **101**, 2606 (1994).

385   V. Tirtaatmadja, K. C. Tam, and R. D. Jenkins, Macromolecules **30**, 1426 (1997).

386   B. Struth, K. Hyun, E. Kats, et al., Langmuir **27**, 2880 (2011).

387   L. L. Chapoy and R. W. Duke, Rheologica Acta **18**, 537 (1979).

388   R. W. Duke and L. L. Chapoy, Rheologica Acta **15**, 548 (1976).

389   I. Lelidis, C. Blanc, and M. Kleman, Physical Review E **74** (2006).

390   T. Narumi, H. Uematsu, and T. Hasegawa, in *Xvth International Congress on Rheology - the Society of Rheology 80th Annual Meeting, Pts 1 and 2*, 2008), Vol. 1027, p. 484.

391   J. Webster, R. M. Laing, and R. L. Enlow, Textile Research Journal **68**, 881 (1998).

392   C. A. Tovar, C. A. Cerdeirina, L. Romani, et al., Journal of Texture Studies **34**, 115 (2003).

393   P. Ravindran, J. M. Krishnan, and K. R. Rajagopal, International Journal of Engineering Science **42**, 1973 (2004).

394   V. A. Iktisanov, Colloid Journal **64**, 406 (2002).

395   J. M. Burgers, Verh. K. Akad. Wet. Amsterdam **15**, 5 (1935).

396   U. H. Faul and I. Jackson, Earth and Planetary Science Letters **234**, 119 (2005).
397   E. Kumacheva and J. Klein, Journal of Chemical Physics **108**, 7010 (1998).
398   G. W. Gray, K. J. Harrison, J. A. Nash, et al., *Liquid Crystals and Ordered Fluids* (Plenum Press, New York, 1974).
399   P. P. Karat and N. V. Madhusudana, Molecular Crystals and Liquid Crystals **36**, 51 (1976).
400   G. P. Crawford, R. Stannarius, and J. W. Doane, Physical Review A **44**, 2558 (1991).

Appendix 1

Plots of Shear Response, Amplitude, First Harmonic, Fit Curves and Fit Parameters as a Function of Time

The plots below represent the collected data and analysis of the primary 24 experiments discussed in the Results and Conclusions chapters. The plots are organized in the following way: Each page contains four plots of data from test conditions of identical percent strain, more specifically, with constant gap size and shear amplitude. Shear frequency (and hence shear rate) will vary over the four plots, from 0.01 Hz to 10 Hz. With three distinct shear amplitudes and two gap sizes, then, each section will make up six pages of data.

There are seven sections presented in this appendix:

   i)   Plots of shear response (first five periods only) as a function of time to show the general shape of the response curves.

   ii)   Overlays of response and Burgers Model fits (first five periods only) as a function of time

   iii)   Plots of the Burgers Model fitting parameters obtained from the fits presented in section (ii) as a function of time

   iv)   Plots of noise-reduced amplitude (as obtained from the first harmonic) as a function of time, overlain with the response amplitude

   v)   Overlays of noise-reduced amplitude and two exponential fits to the response curve

vi)   Overlays of response and Split Model fits (first five periods only) as a

function of time

vii)   Plots of the Split Model fitting parameters obtained from the fits presented in

section (vi) as a function of time

Response data was converted from the raw data values (measured in Volts) to their

corresponding force values, and the bridge balance offset removed so that the response

will lie about the zero line to aid the eye. Note that because the qualitative features of the

response curve were removed by the post-acquisition filter (as discussed in the Results

section), Burgers Model and Split Model fits were not performed on the 10 Hz data and

so those plots are not provided. Also, the graphs of those smaller shear rate tests that

were too noisy to yield a reasonable fit have been omitted as well.
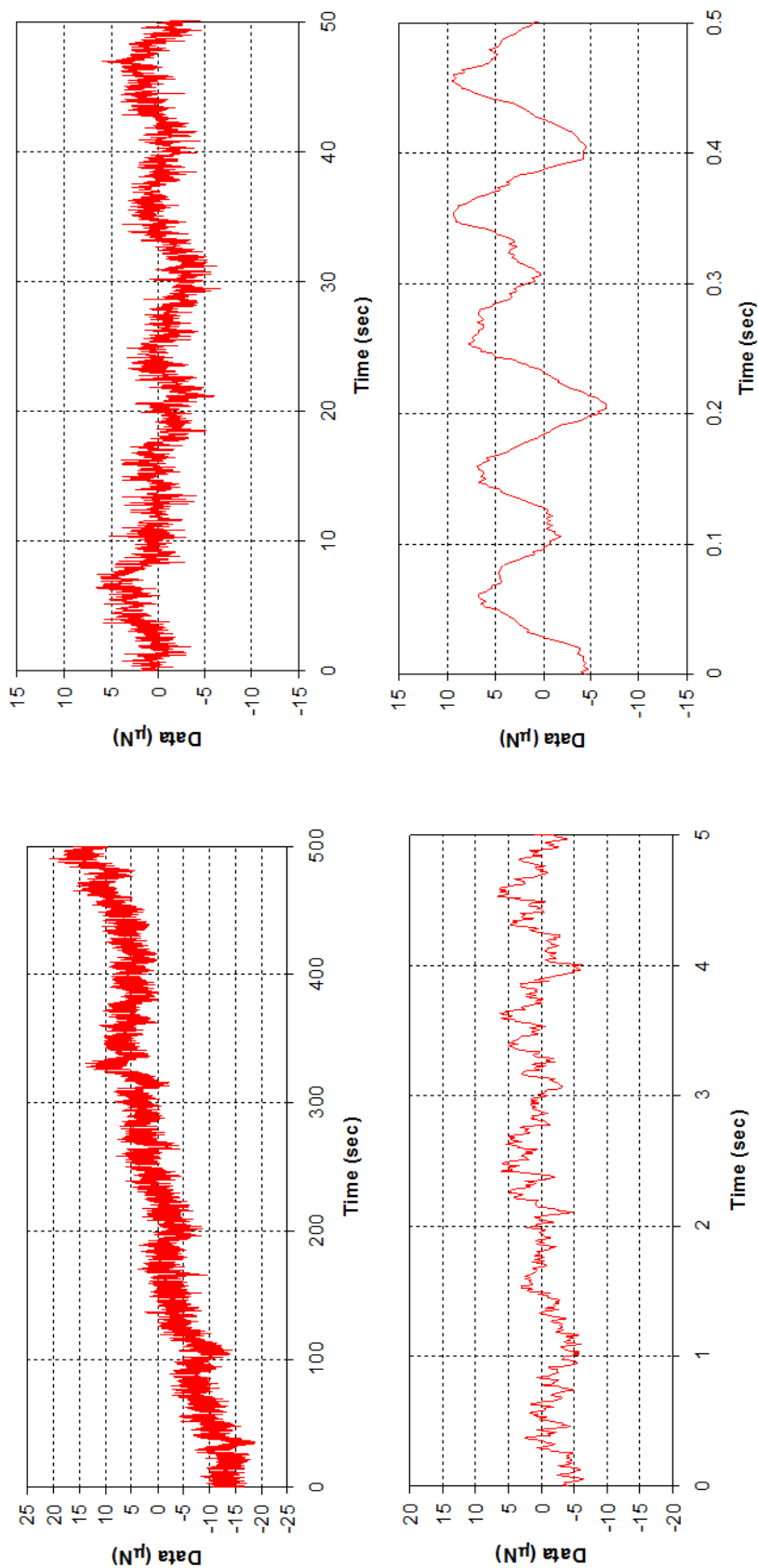
Figure A1.1a: Shear response over the first five shear cycles for smectic 8CB confined to a gap size of 5000 nm, with a shear amplitude of 62.5 nm and a shear frequency of (top left) 0.01 Hz, (top right) 0.1 Hz, (bottom left) 1.0 Hz and (bottom right) 10 Hz.
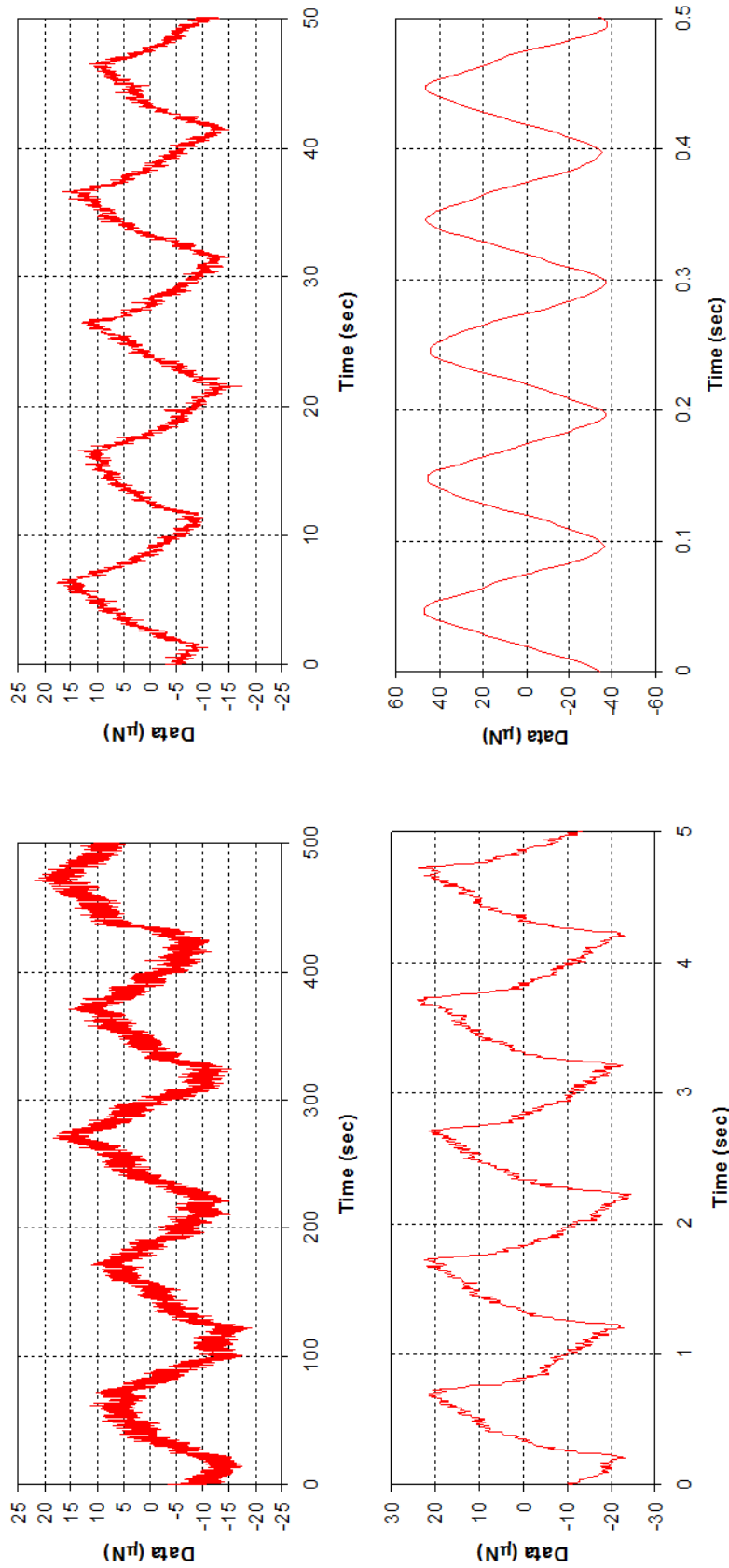
Figure A1.1b: Shear response over the first five shear cycles for smectic 8CB confined to a gap size of 5000 nm, with a shear amplitude of 625 nm and a shear frequency of (top left) 0.01 Hz, (top right) 0.1 Hz, (bottom left) 1.0 Hz and (bottom right) 10 Hz.

347
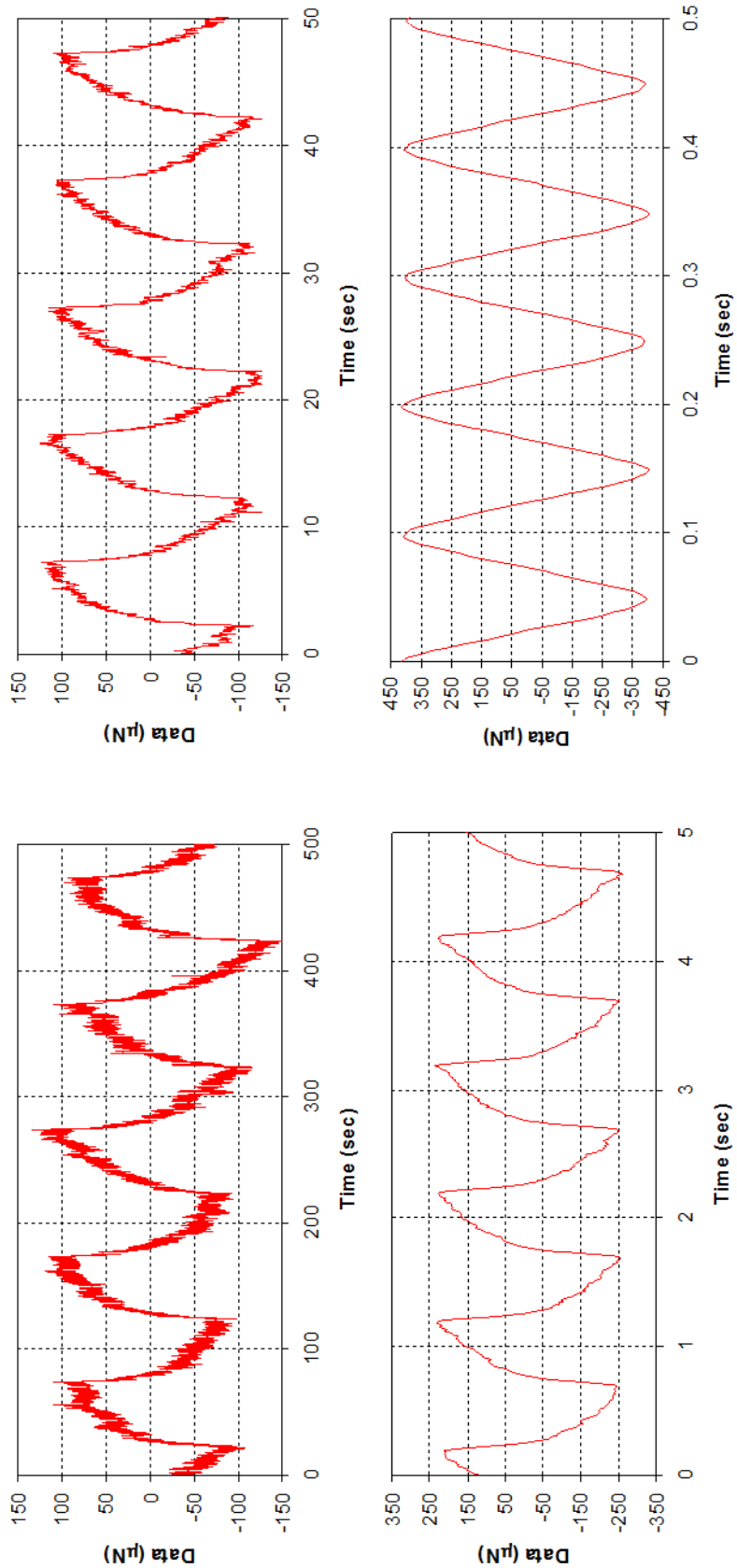
Figure A1.1c: Shear response over the first five shear cycles for smectic 8CB confined to a gap size of 5000 nm, with a shear amplitude of 6250 nm and a shear frequency of (top left) 0.01 Hz, (top right) 0.1 Hz, (bottom left) 1.0 Hz and (bottom right) 10 Hz.
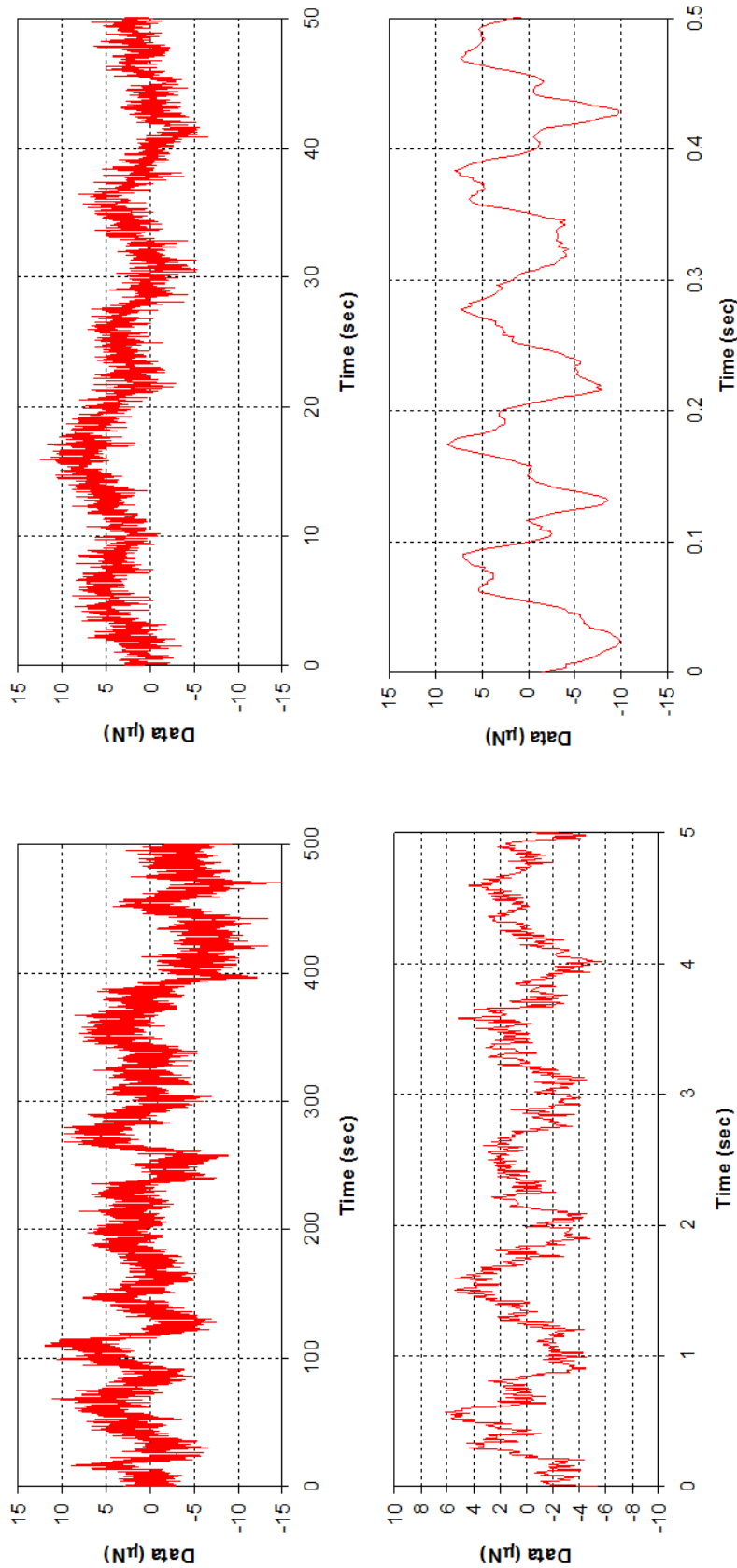
Figure A1.1d: Shear response over the first five shear cycles for smectic 8CB confined to a gap size of 500 nm, with a shear amplitude of 62.5 nm and a shear frequency of (top left) 0.01 Hz, (top right) 0.1 Hz, (bottom left) 1.0 Hz and (bottom right) 10 Hz.

349
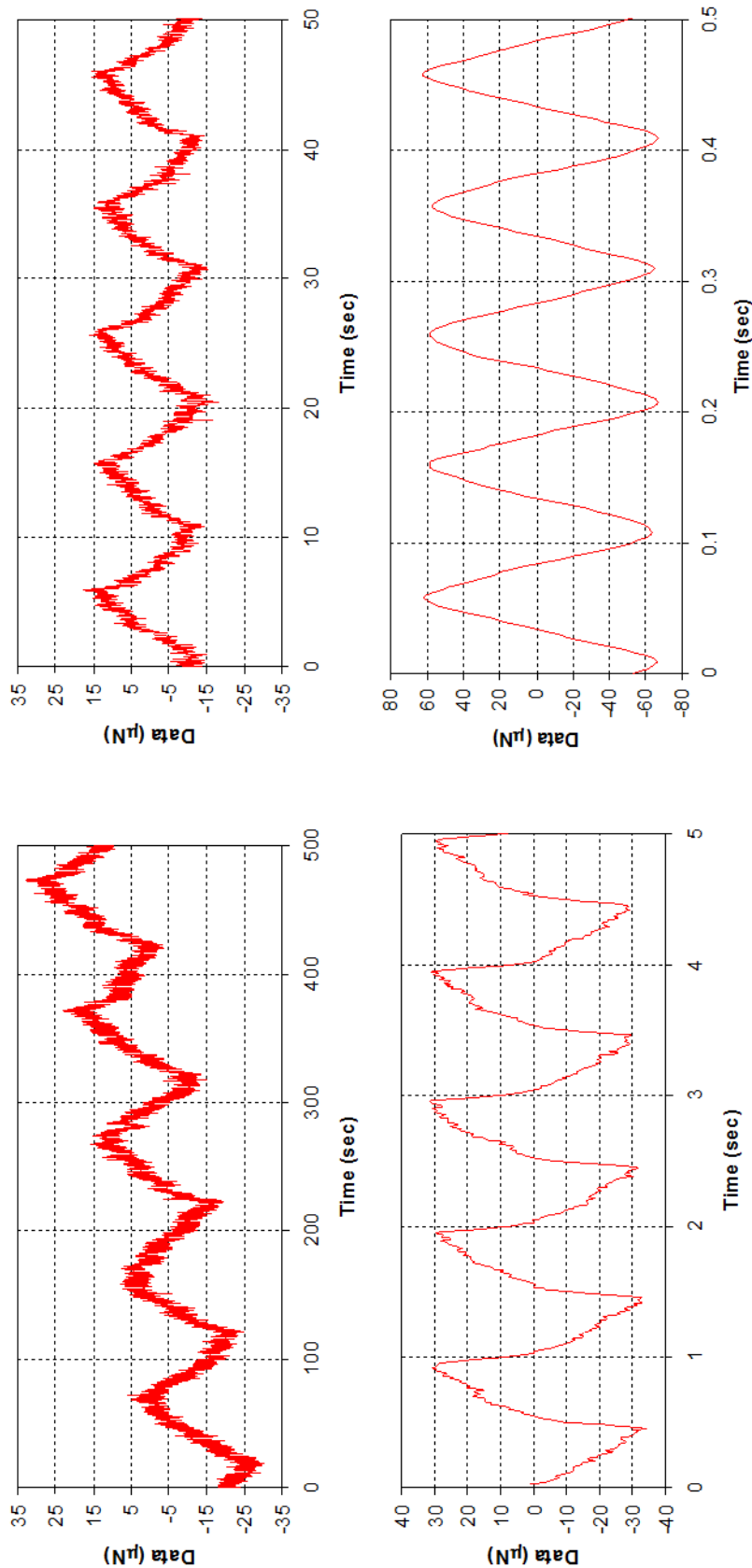
Figure A1.1e: Shear response over the first five shear cycles for smectic 8CB confined to a gap size of 500 nm, with a shear amplitude of 625 nm and a shear frequency of (top left) 0.01 Hz, (top right) 0.1 Hz, (bottom left) 1.0 Hz and (bottom right) 10 Hz.
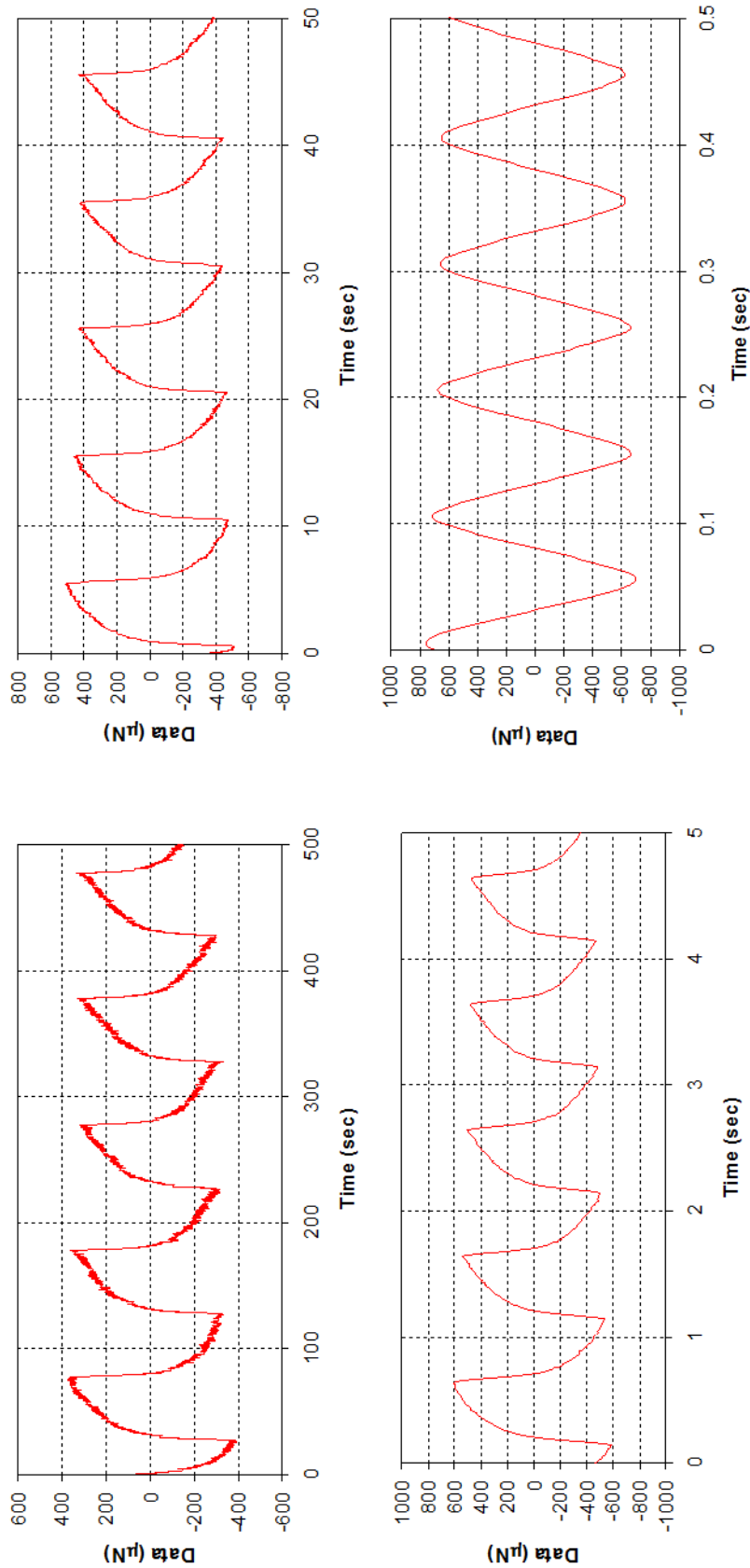
Figure A1.1f: Shear response over the first five shear cycles for smectic 8CB confined to a gap size of 500 nm, with a shear amplitude of 6250 nm and a shear frequency of (top left) 0.01 Hz, (top right) 0.1 Hz, (bottom left) 1.0 Hz and (bottom right) 10 Hz.

351
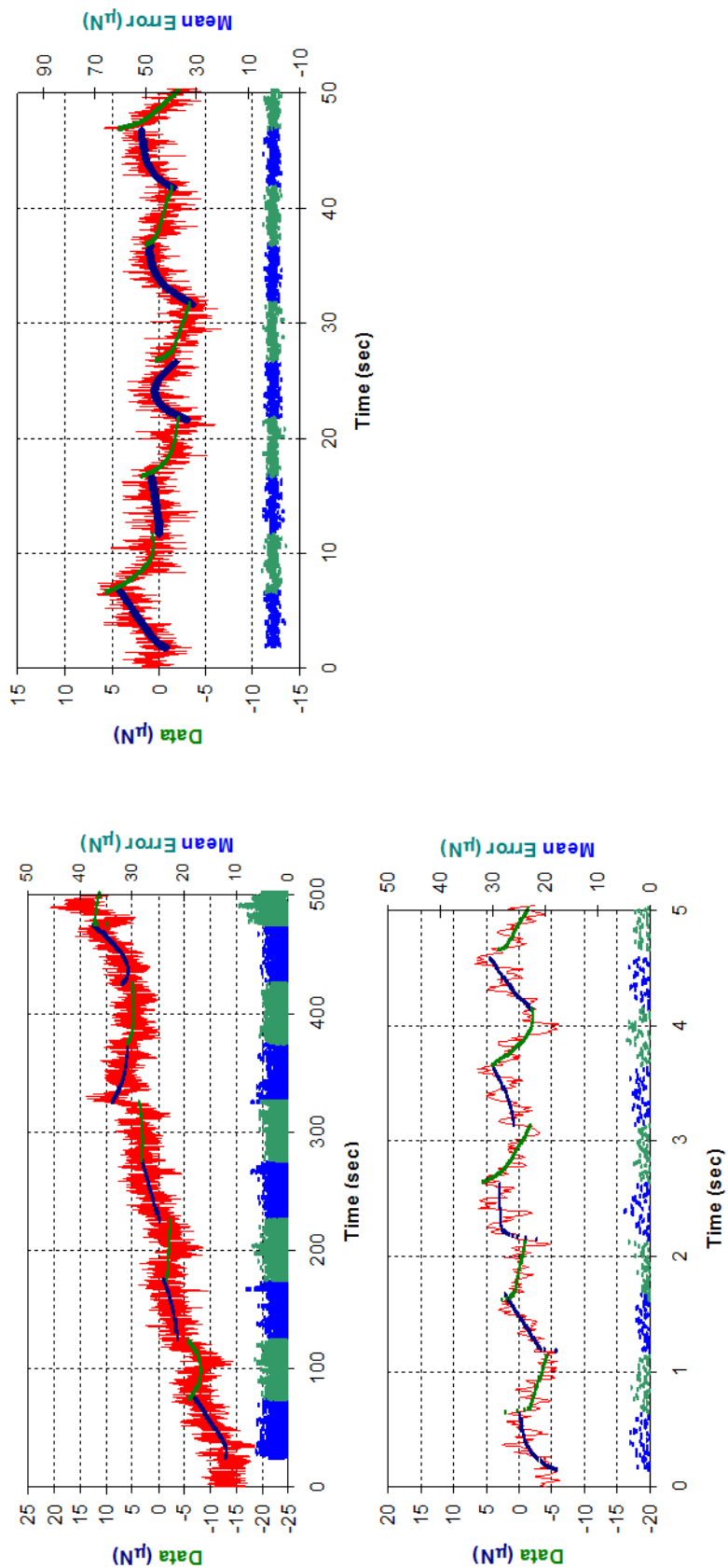
Figure A1.2a: Shear response (in red) and corresponding Burgers Model fit (in dark blue and green) for the first five shear cycles of smectic 8CB confined to a gap size of 5000 nm, with a shear amplitude of 62.5 nm and a shear frequency of (top left) 0.01 Hz, (top right) 0.1 Hz and (bottom left) 1.0 Hz. The difference between the fit and the data is given below the response in light blue and green.

352
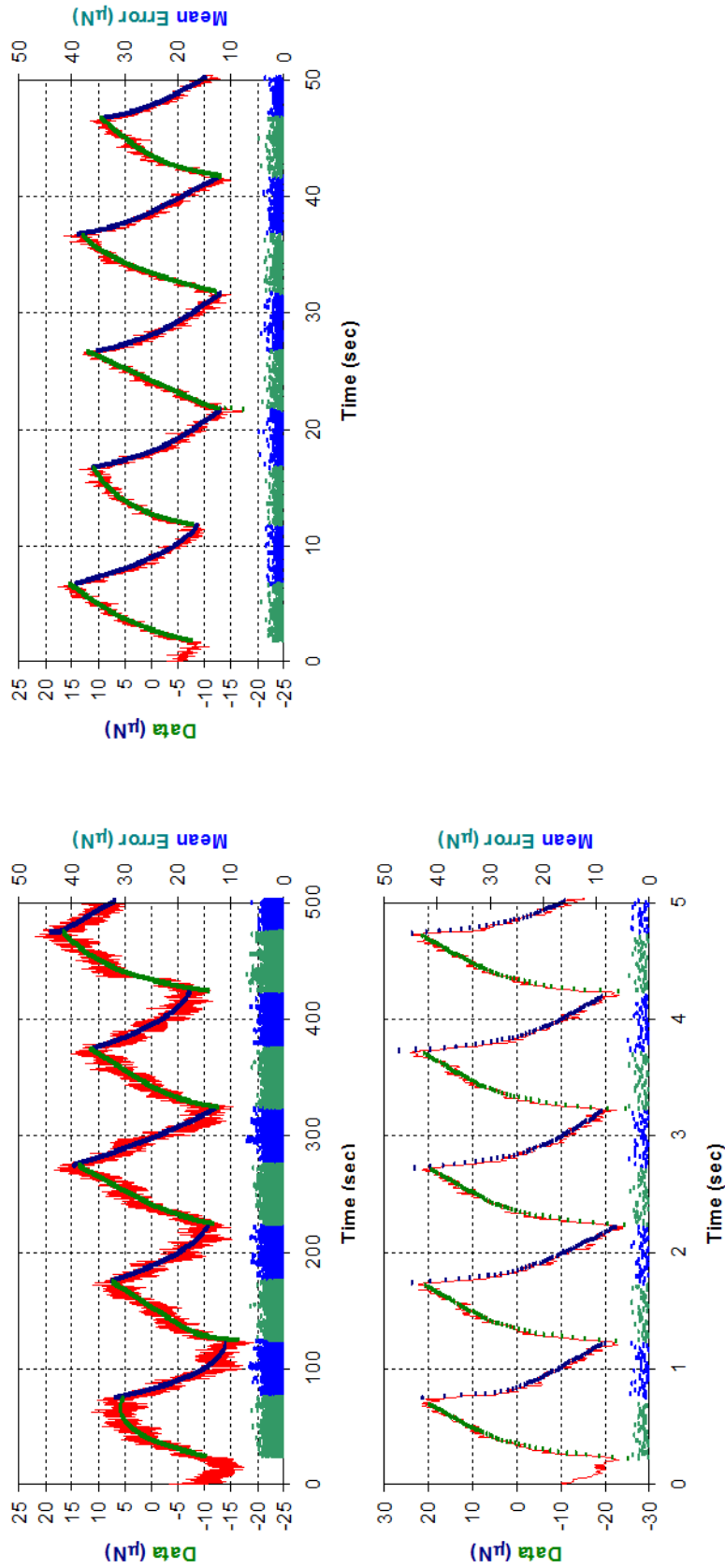
Figure A1.2b: Shear response (in red) and corresponding Burgers Model fit (in dark blue and green) for the first five shear cycles of smectic 8CB confined to a gap size of 5000 nm, with a shear amplitude of 625 nm and a shear frequency of (top left) 0.01 Hz, (top right), 0.1 Hz and (bottom left) 1.0 Hz. The difference between the fit and the data is given below the response in light blue and green.

353
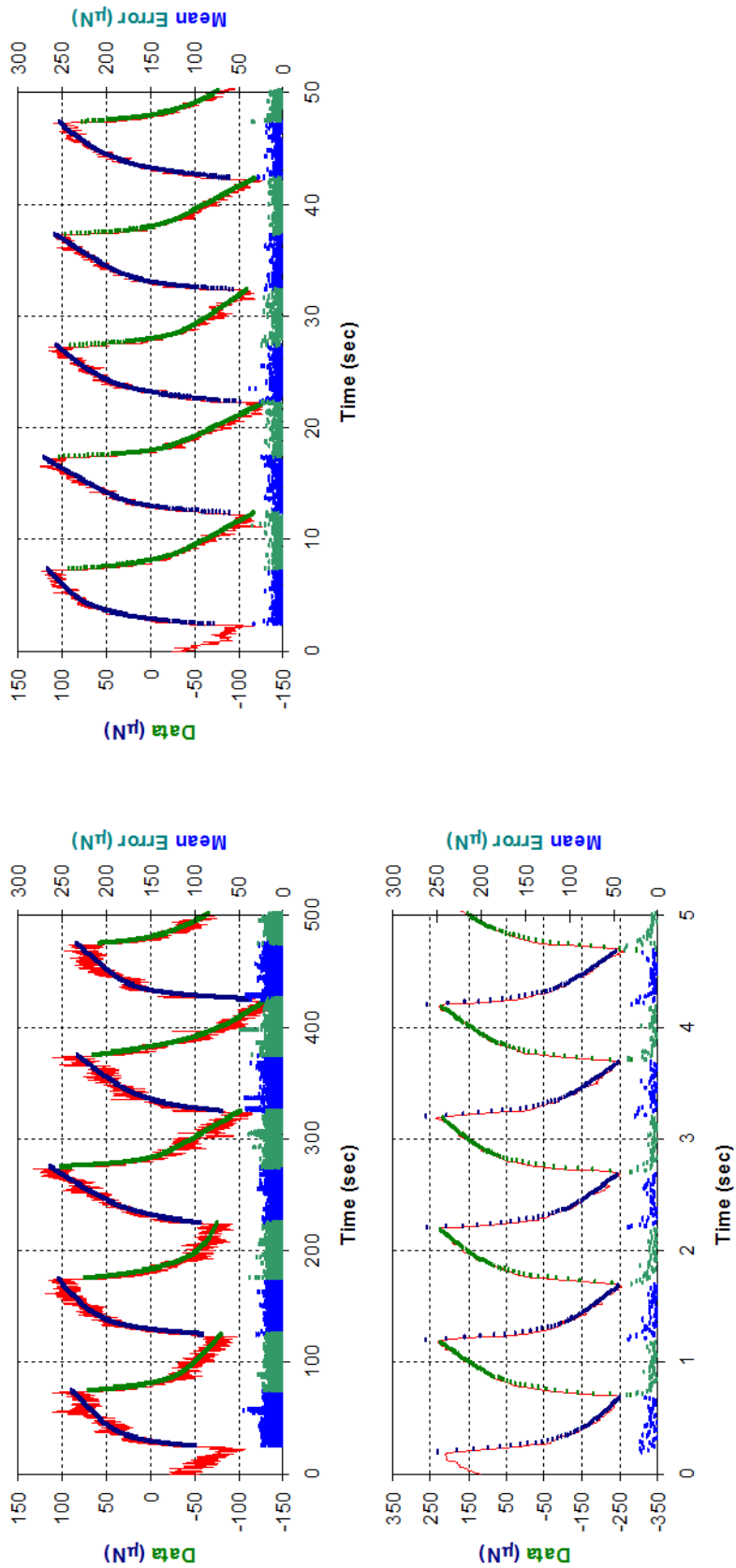
Figure A1.2c: Shear response (in red) and corresponding Burgers Model fit (in dark blue and green) for the first five shear cycles of smectic 8CB confined to a gap size of 5000 nm, with a shear amplitude of 6250 nm and a shear frequency of (top left) 0.01 Hz, (top right) 0.1 Hz and (bottom left) 1.0 Hz. The difference between the fit and the data is given below the response in light blue and green.

354
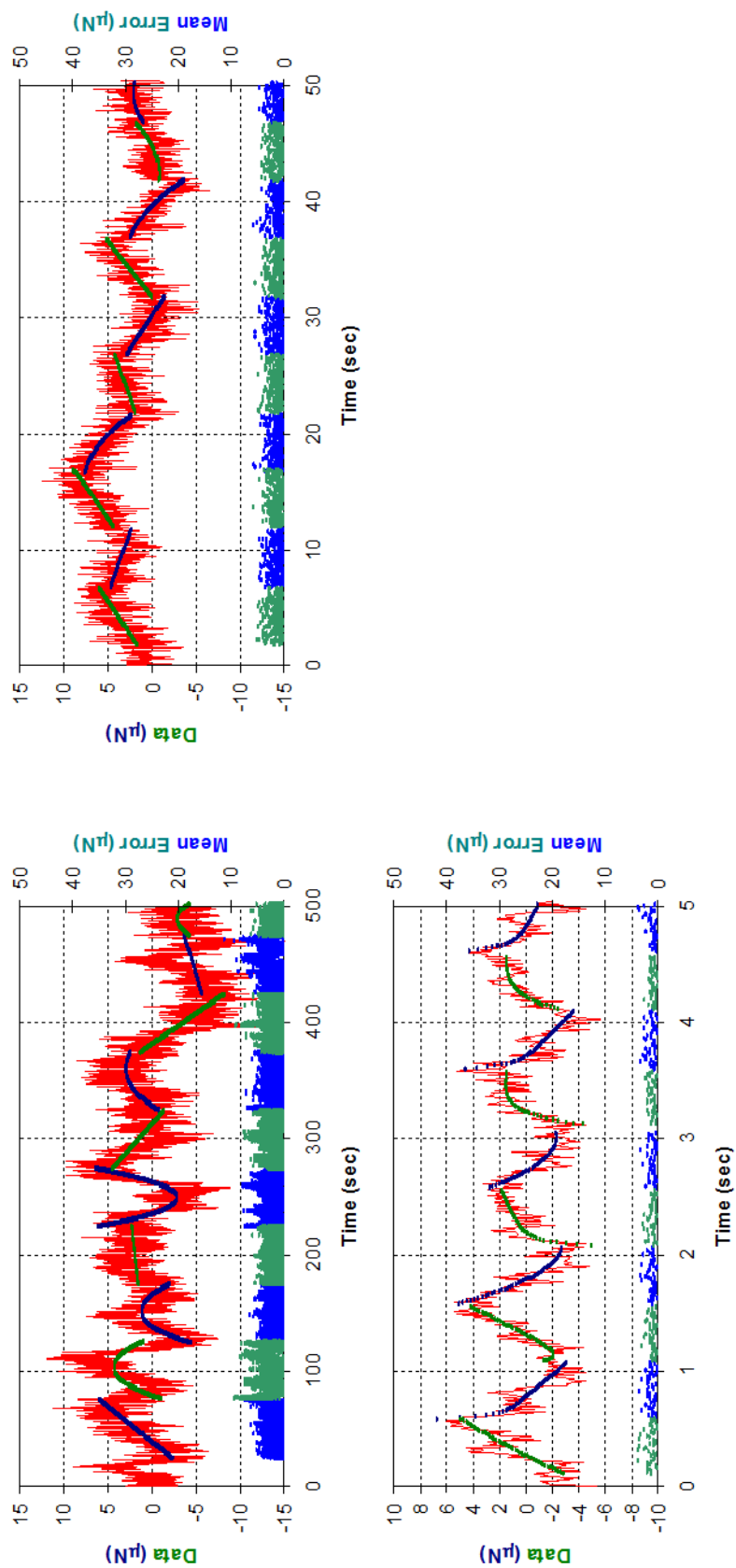
Figure A1.2d: Shear response (in red) and corresponding Burgers Model fit (in dark blue and green) for the first five shear cycles of smectic 8CB confined to a gap size of 500 nm, with a shear amplitude of 62.5 nm and a shear frequency of (top left) 0.01 Hz, (top right), 0.1 Hz and (bottom left) 1.0 Hz. The difference between the fit and the data is given below the response in light blue and green.
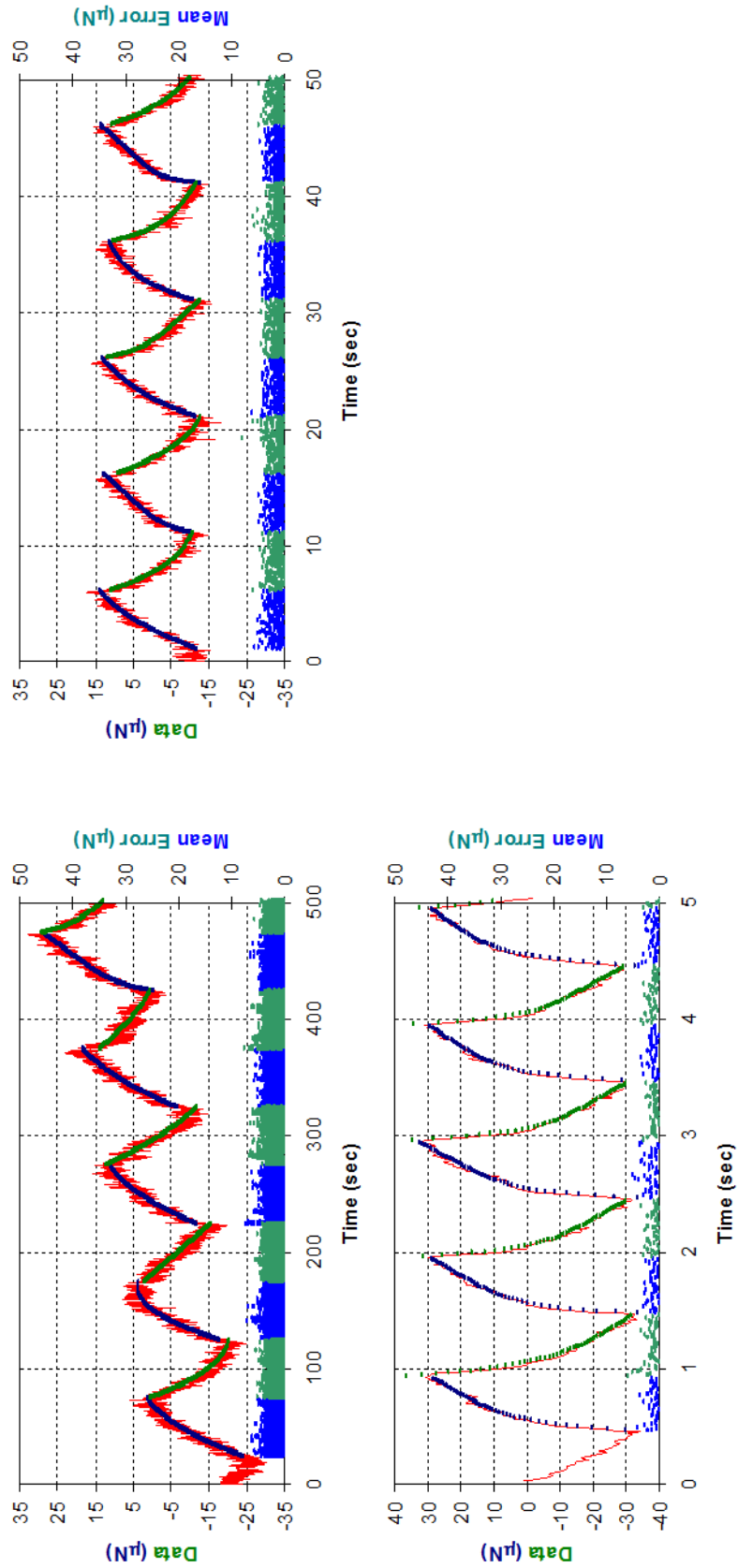
Figure A1.2e: Shear response (in red) and corresponding Burgers Model fit (in dark blue and green) for the first five shear cycles of smectic 8CB confined to a gap size of 500 nm, with a shear amplitude of 625 nm and a shear frequency of (top left) 0.01 Hz, (top right), 0.1 Hz and (bottom left) 1.0 Hz. The difference between the fit and the data is given below the response in light blue and green.
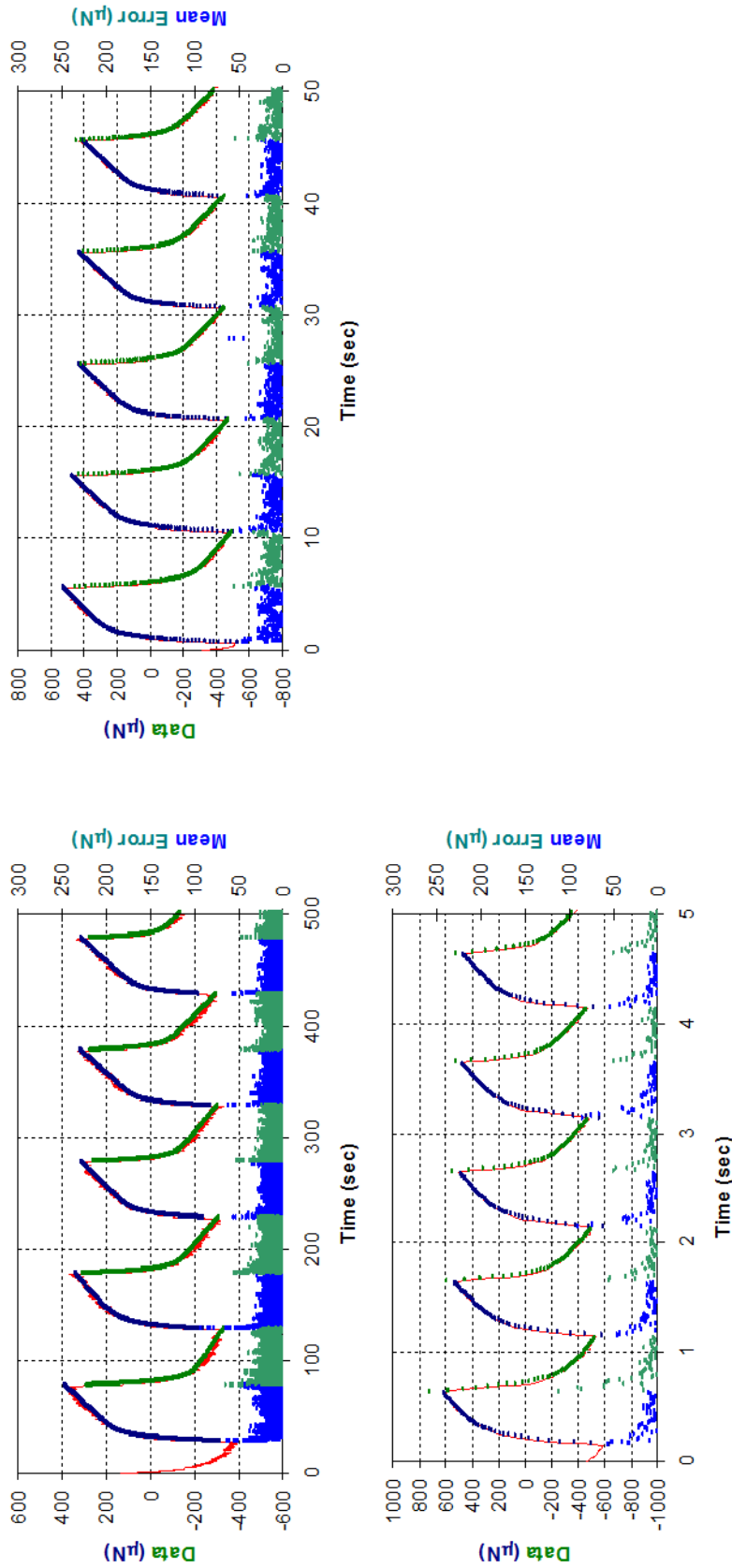
Figure A1.2f: Shear response (in red) and corresponding Burgers Model fit (in dark blue and green) for the first five shear cycles of smectic 8CB confined to a gap size of 500 nm, with a shear amplitude of 6250 nm and a shear frequency of (top left) 0.01 Hz, (top right), 0.1 Hz and (bottom left) 1.0 Hz. The difference between the fit and the data is given below the response in light blue and green.
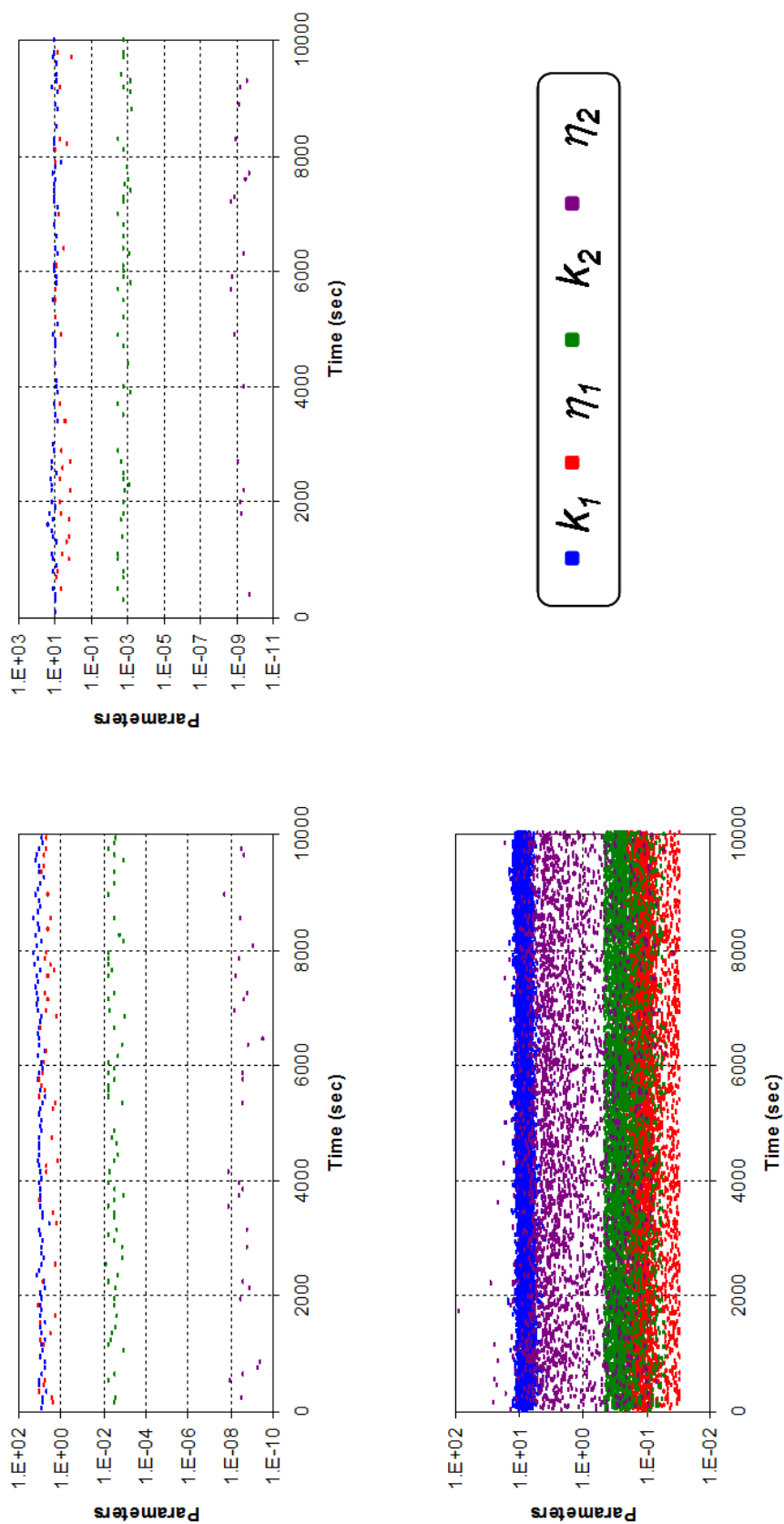
Figure A1.3a: Burgers Model fit parameters as a function of time for smectic 8CB confined to a gap size of 5000 nm, with a shear amplitude of 62.5 nm and a shear frequency of (top left) 0.01 Hz, (top right) 0.1 Hz and (bottom left) 1.0 Hz.

358
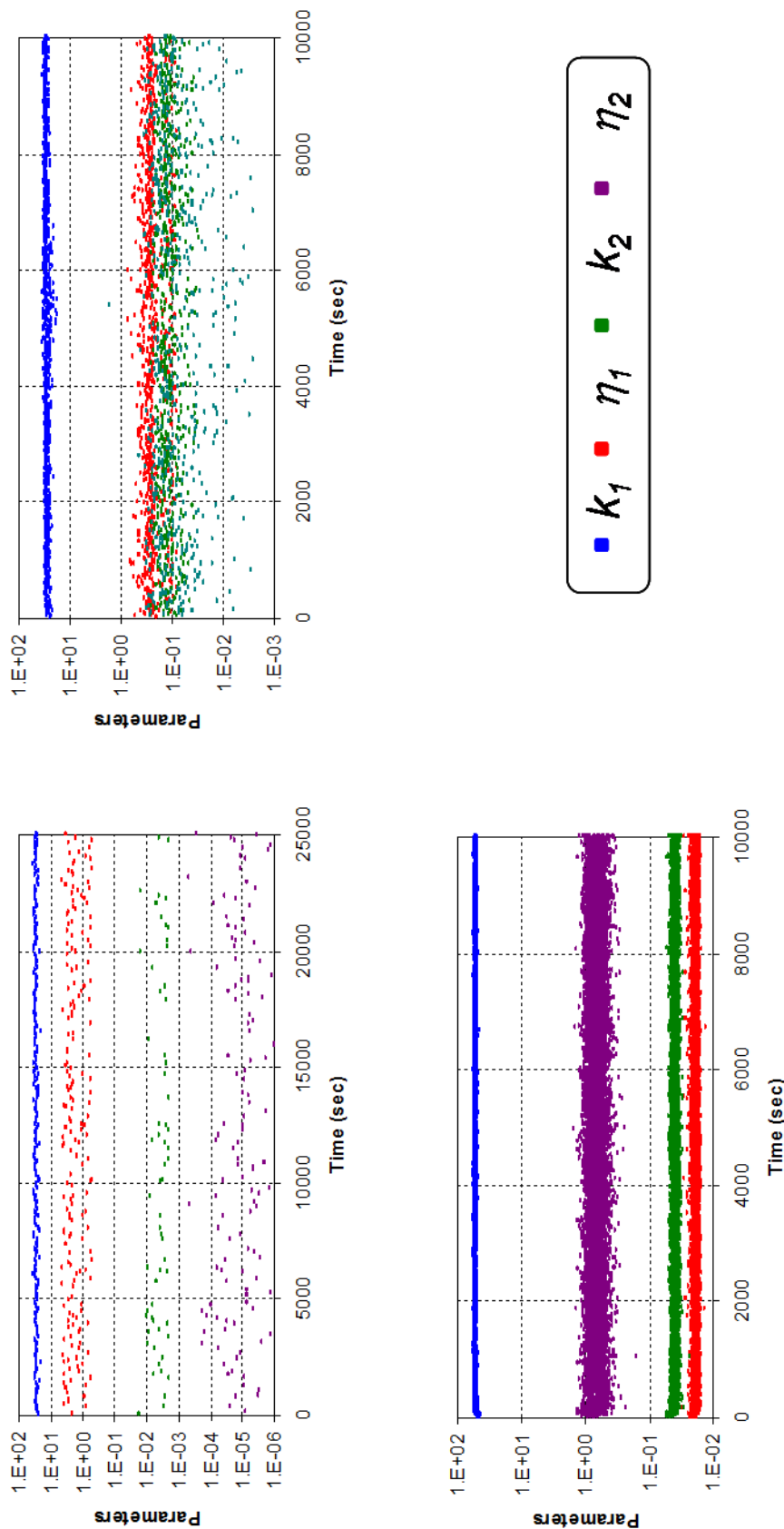
Figure A1.3b: Burgers Model fit parameters as a function of time for smectic 8CB confined to a gap size of 5000 nm, with a shear amplitude of 625 nm and a shear frequency of (top left) 0.01 Hz, (top right) 0.1 Hz and (bottom left) 1.0 Hz.
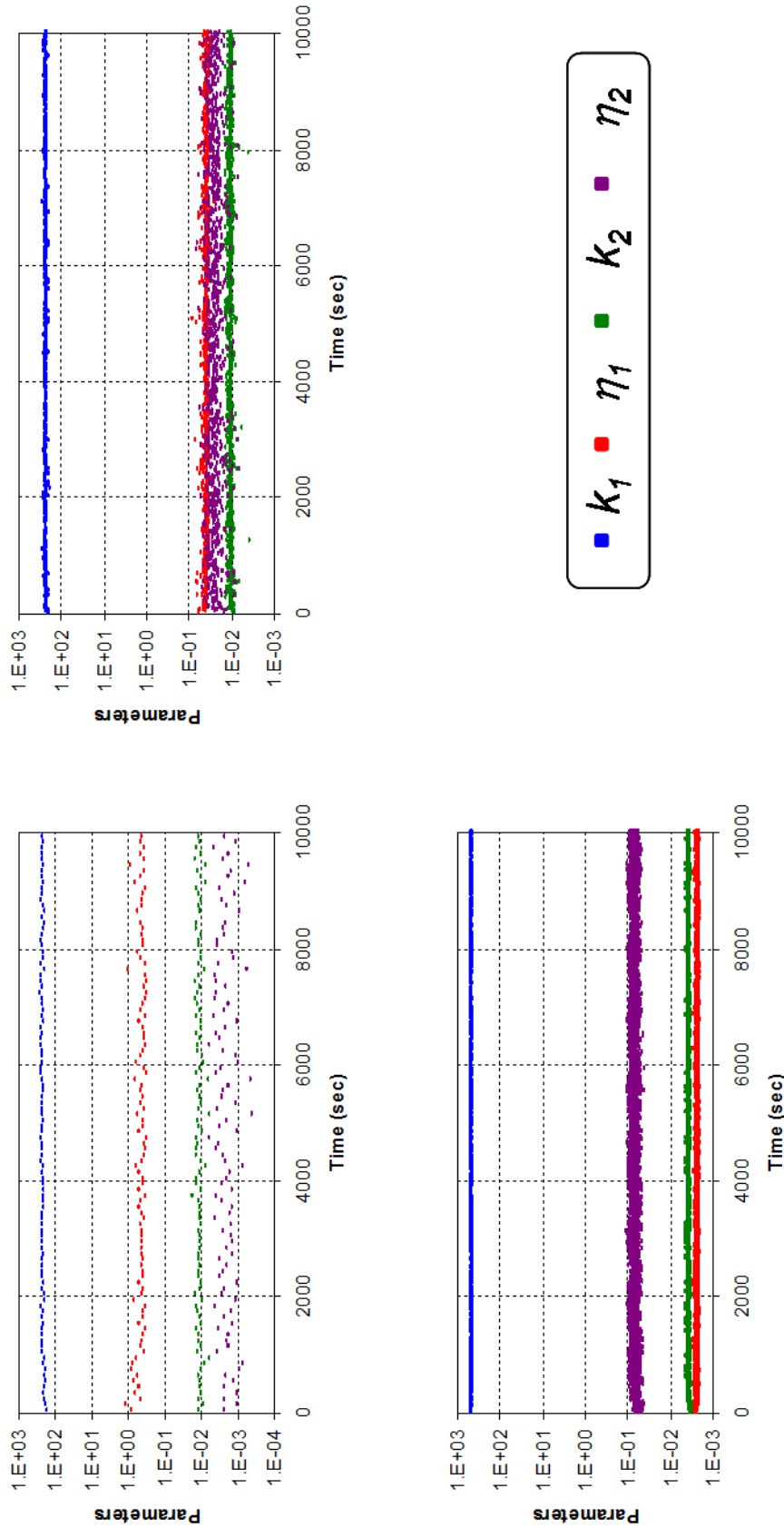
**Figure A1.3c:** Burgers Model fit parameters as a function of time for smectic 8CB confined to a gap size of 5000 nm, with a shear amplitude of 6250 nm and a shear frequency of (top left) 0.01 Hz, (top right) 0.1 Hz and (bottom left) 1.0 Hz.
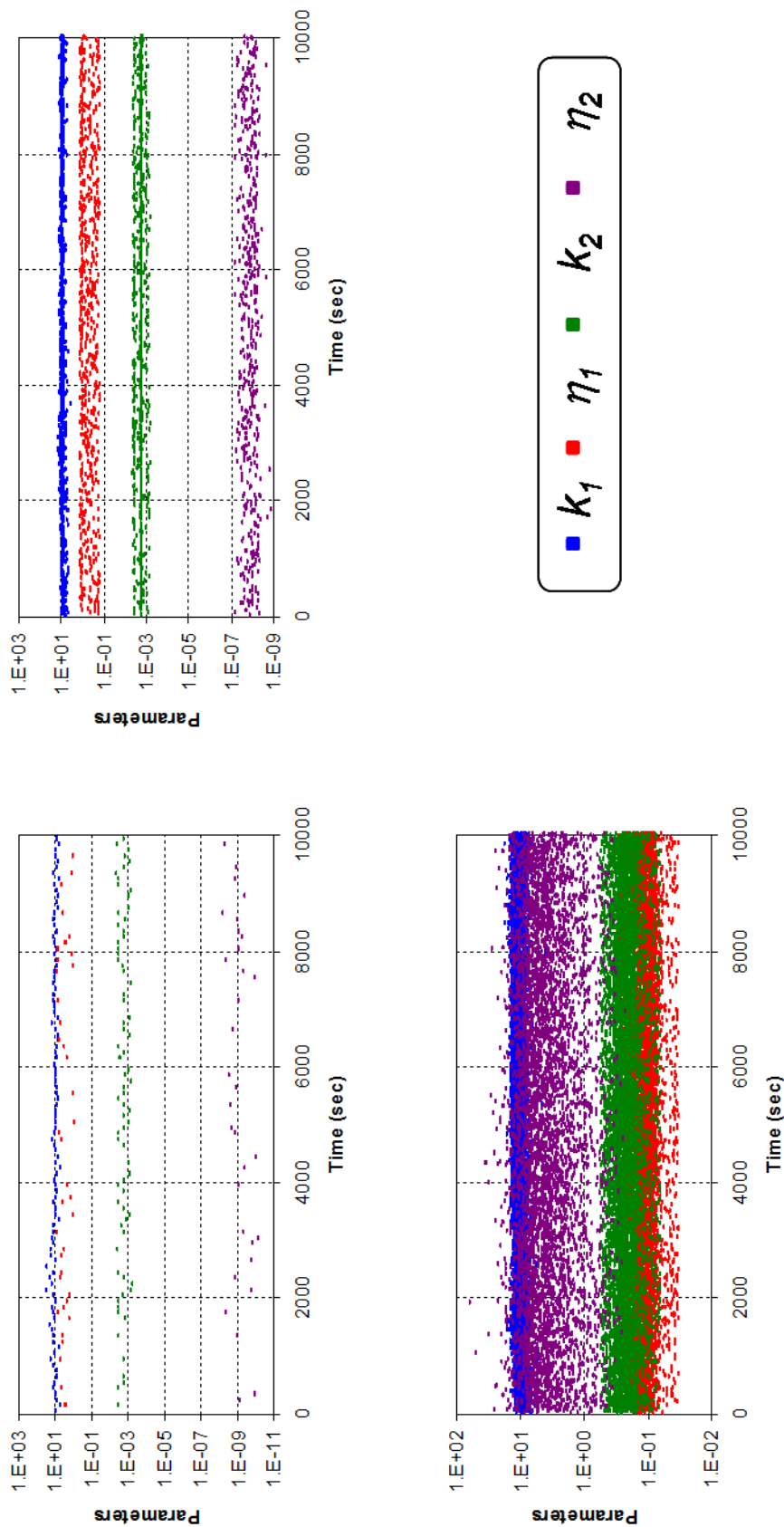
Figure A1.3d: Burgers Model fit parameters as a function of time for smectic 8CB confined to a gap size of 500 nm, with a shear amplitude of 62.5 nm and a shear frequency of (top left) 0.01 Hz, (top right) 0.1 Hz and (bottom left) 1.0 Hz.
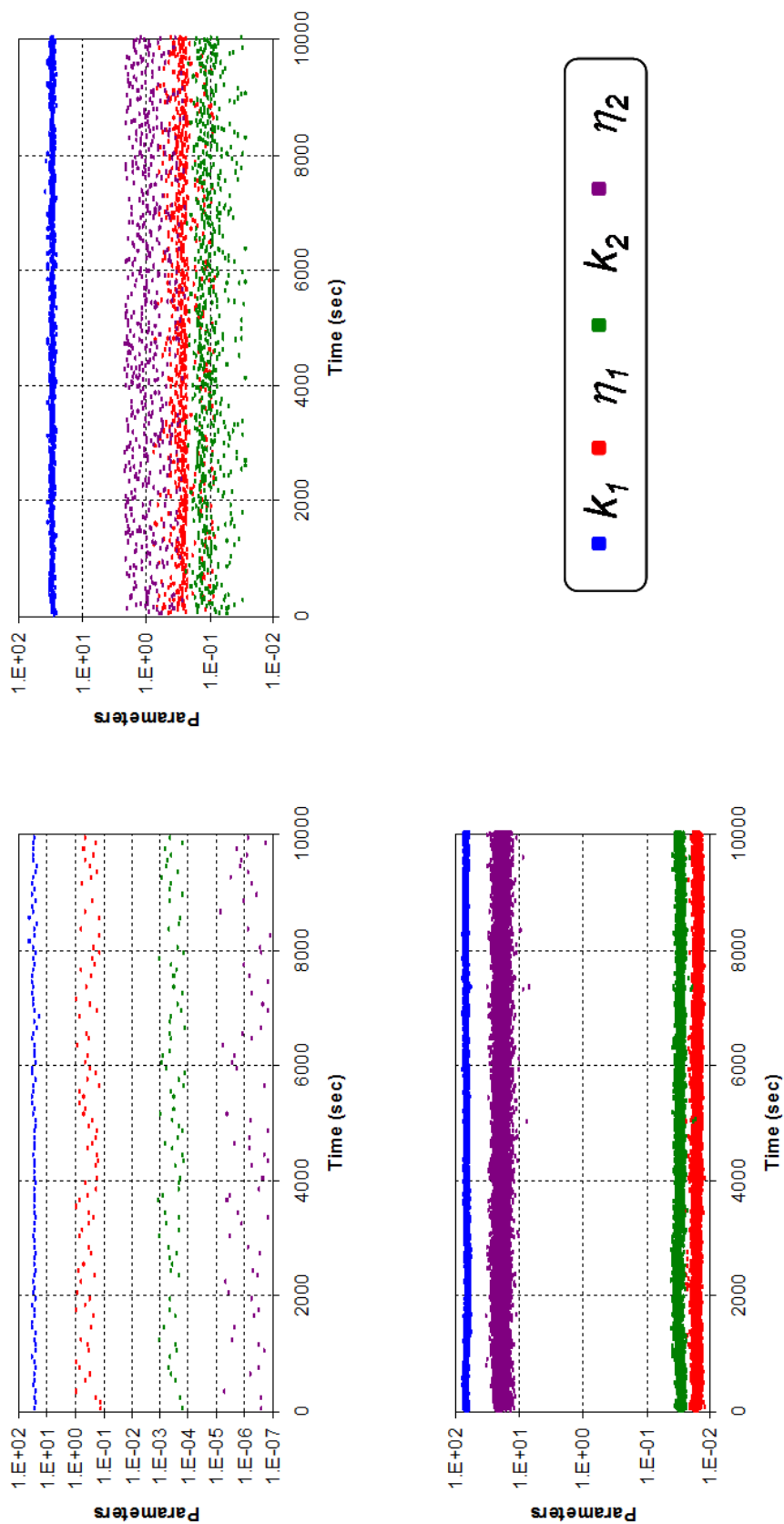
**Figure A1.3e**: Burgers Model fit parameters as a function of time for smectic 8CB confined to a gap size of 500 nm, with a shear amplitude of 625 nm and a shear frequency of (top left) 0.01 Hz, (top right) 0.1 Hz and (bottom left) 1.0 Hz.

362
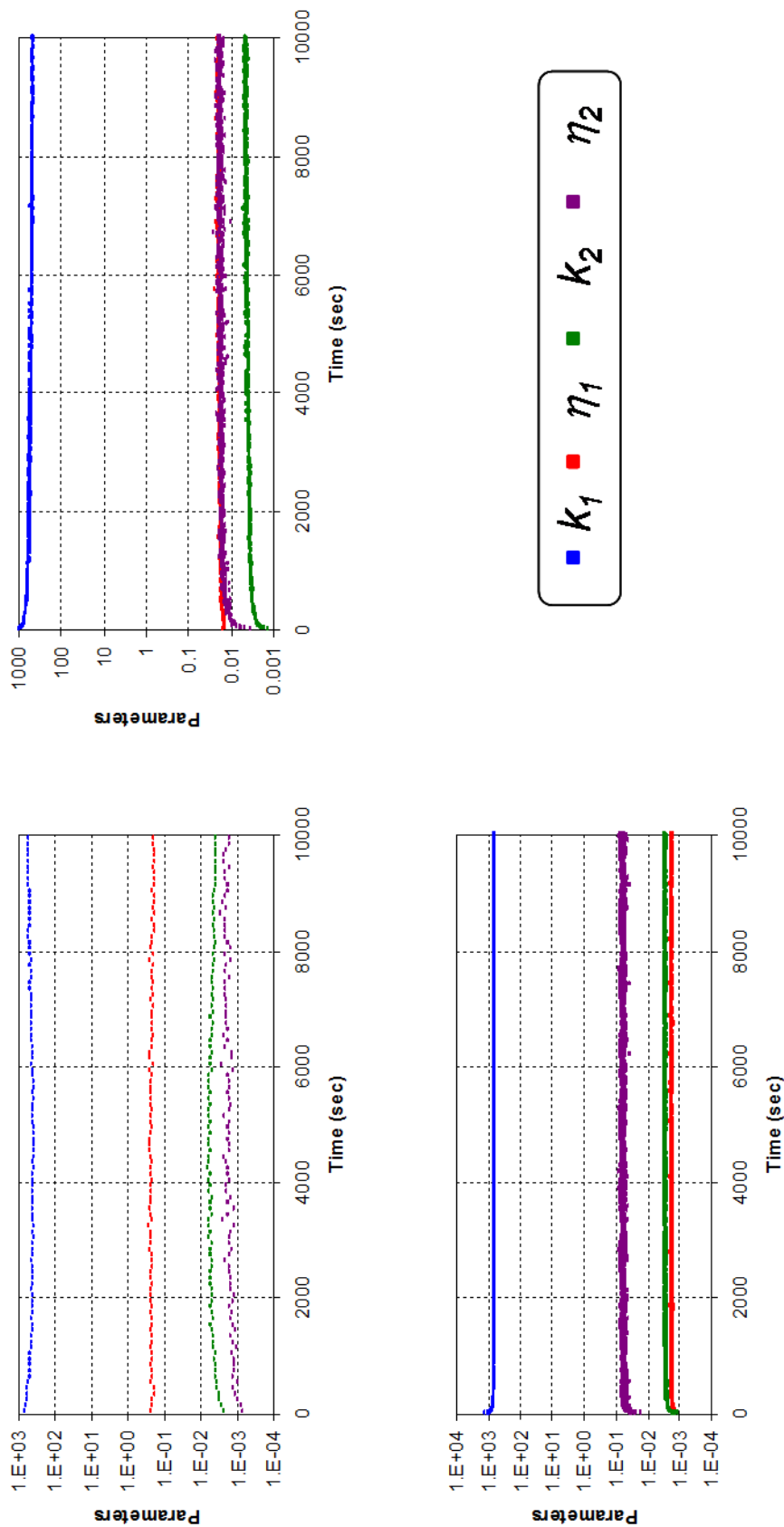
Figure A1.3f: Burgers Model fit parameters as a function of time for smectic 8CB confined to a gap size of 500 nm, with a shear amplitude of 6250 nm and a shear frequency of (top left) 0.01 Hz, (top right) 0.1 Hz and (bottom left) 1.0 Hz.

363
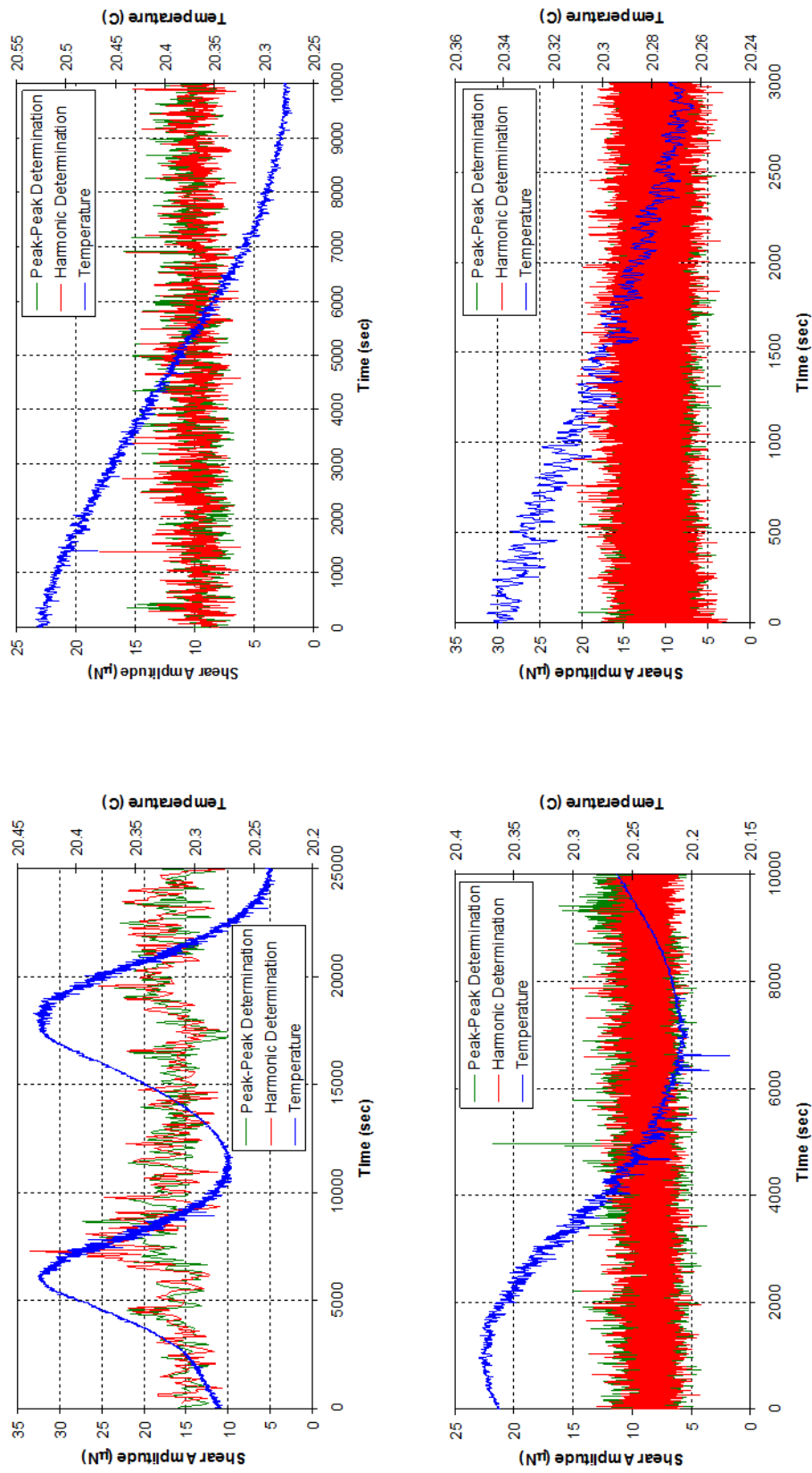
Figure A1.4a: Overlay of peak to peak amplitude and first harmonic amplitude as a function of time for smectic 8CB confined to a gap size of 5000 nm, with a shear amplitude of 62.5 nm and a shear frequency of (top left) 0.01 Hz, (top right) 0.1 Hz, (bottom left) 1.0 Hz and (bottom right) 10 Hz.

364
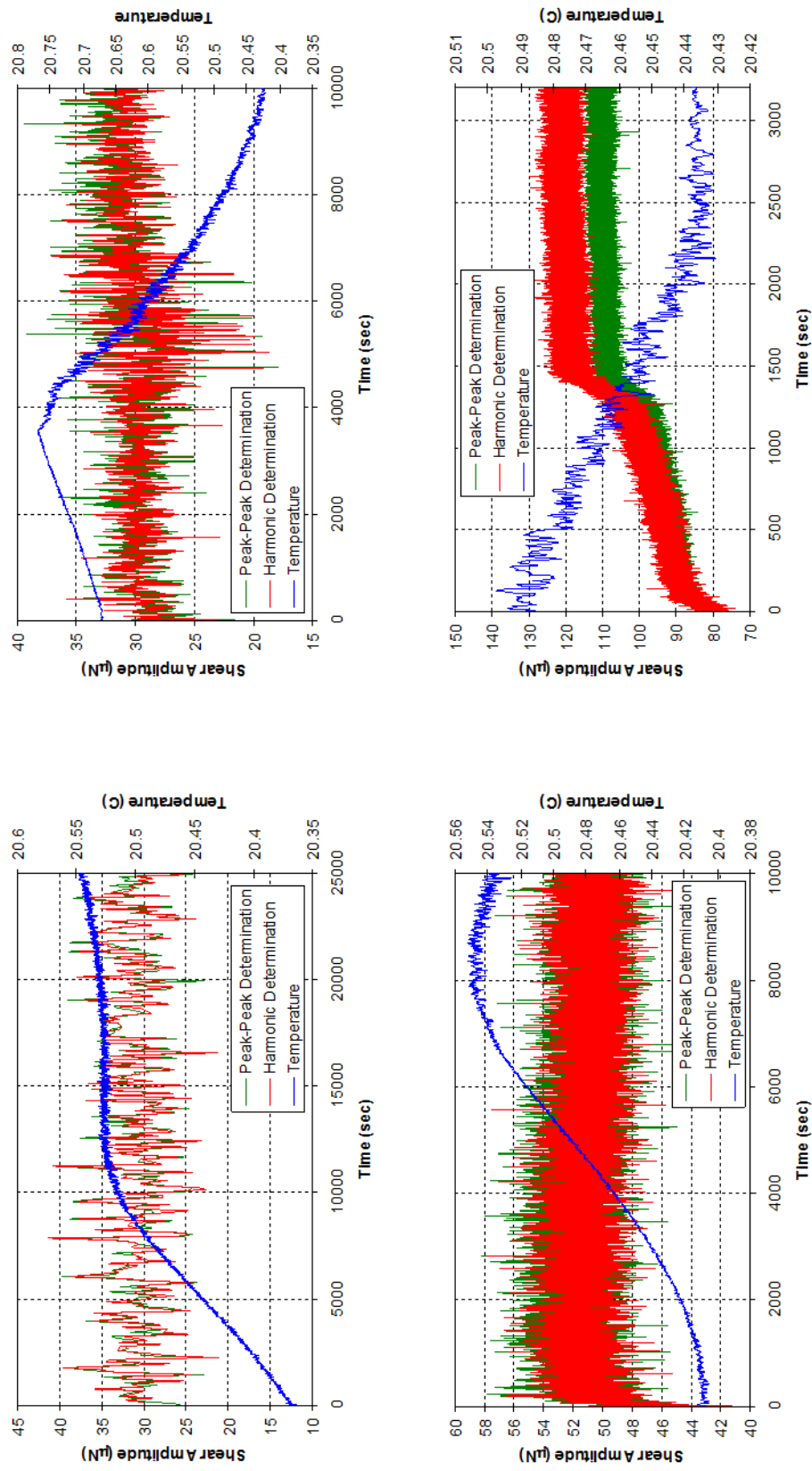
Figure A1.4b: Overlay of peak to peak amplitude and first harmonic amplitude as a function of time for smectic 8CB confined to a gap size of 5000 nm, with a shear amplitude of 625 nm and a shear frequency of (top left) 0.01 Hz, (top right) 0.1 Hz, (bottom left) 1.0 Hz and (bottom right) 10 Hz.

365
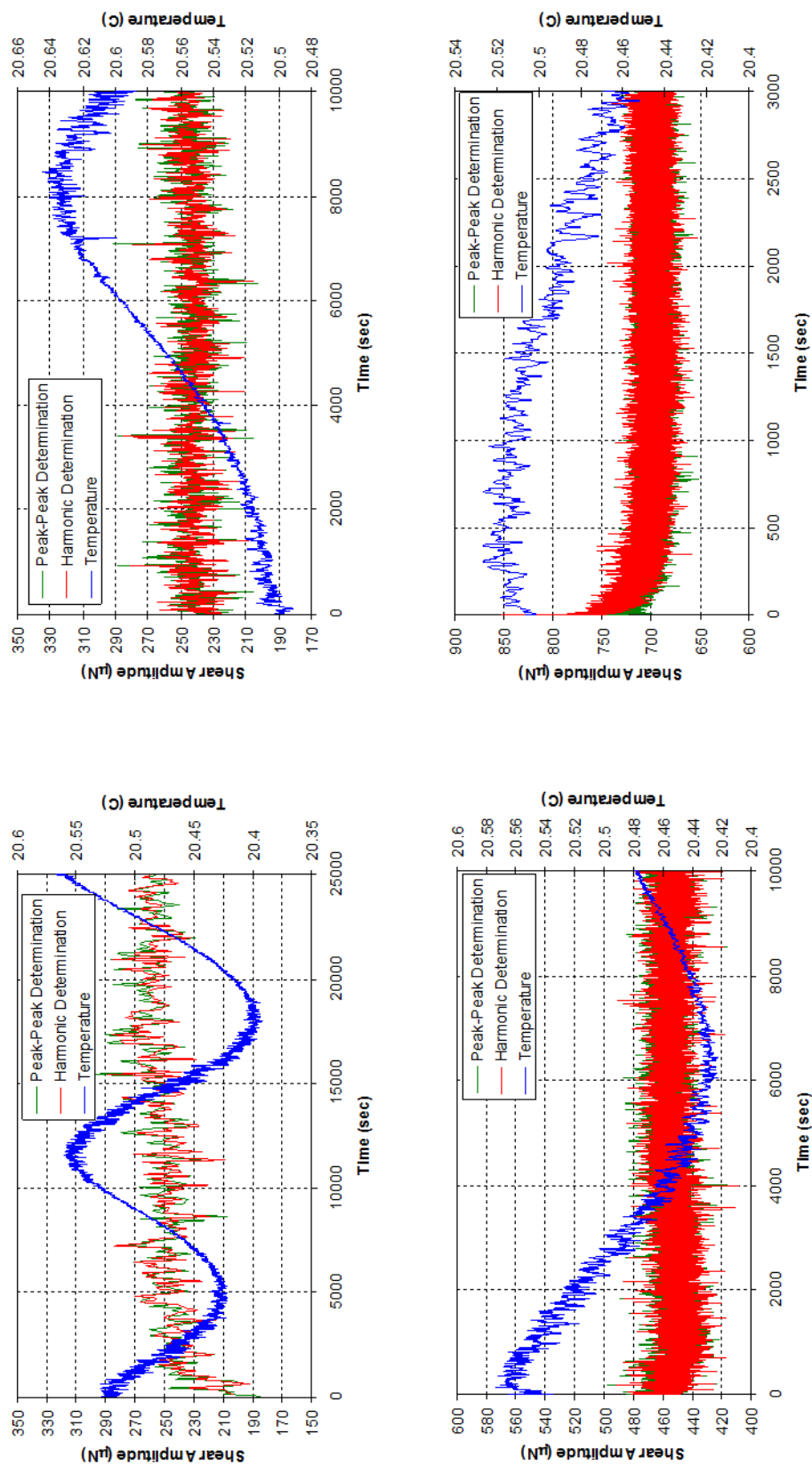
Figure A1.4c: Overlay of peak to peak amplitude and first harmonic amplitude as a function of time for smectic 8CB confined to a gap size of 5000 nm, with a shear amplitude of 6250 nm and a shear frequency of (top left) 0.01 Hz, (top right) 0.1 Hz, (bottom left) 1.0 Hz and (bottom right) 10 Hz.
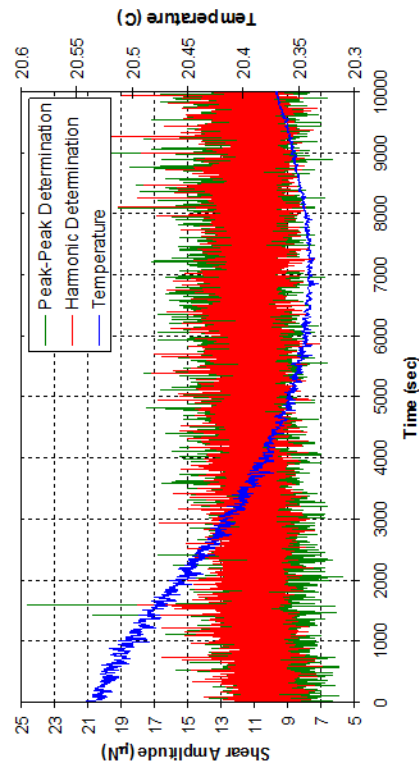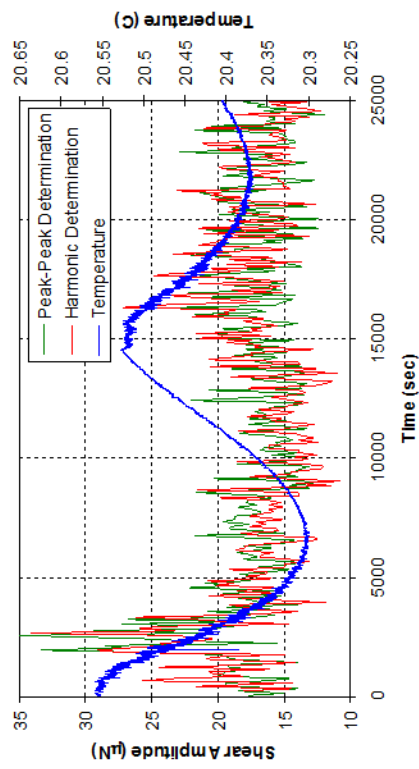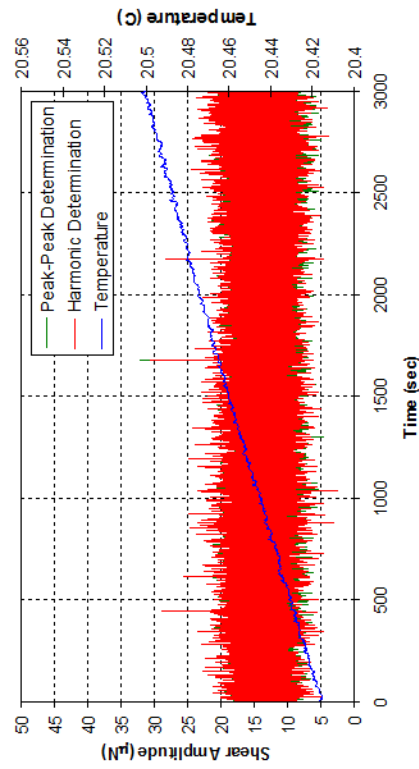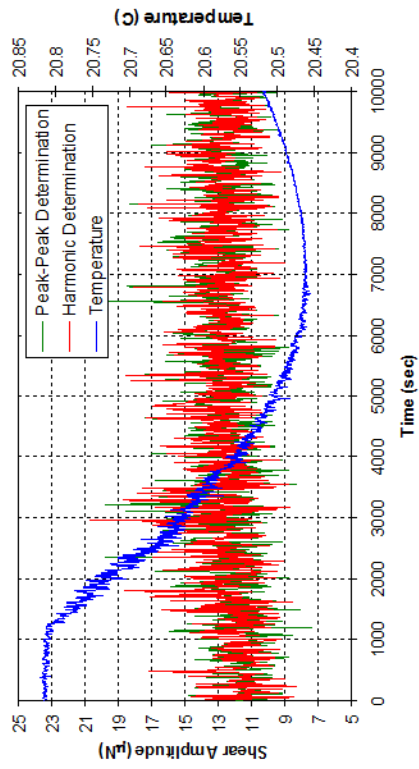
Figure A1.4d: Overlay of peak to peak amplitude and first harmonic amplitude as a function of time for smectic 8CB confined to a gap size of 500 nm, with a shear amplitude of 62.5 nm and a shear frequency of (top left) 0.01 Hz, (top right) 0.1 Hz, (bottom left) 1.0 Hz and (bottom right) 10 Hz.

367
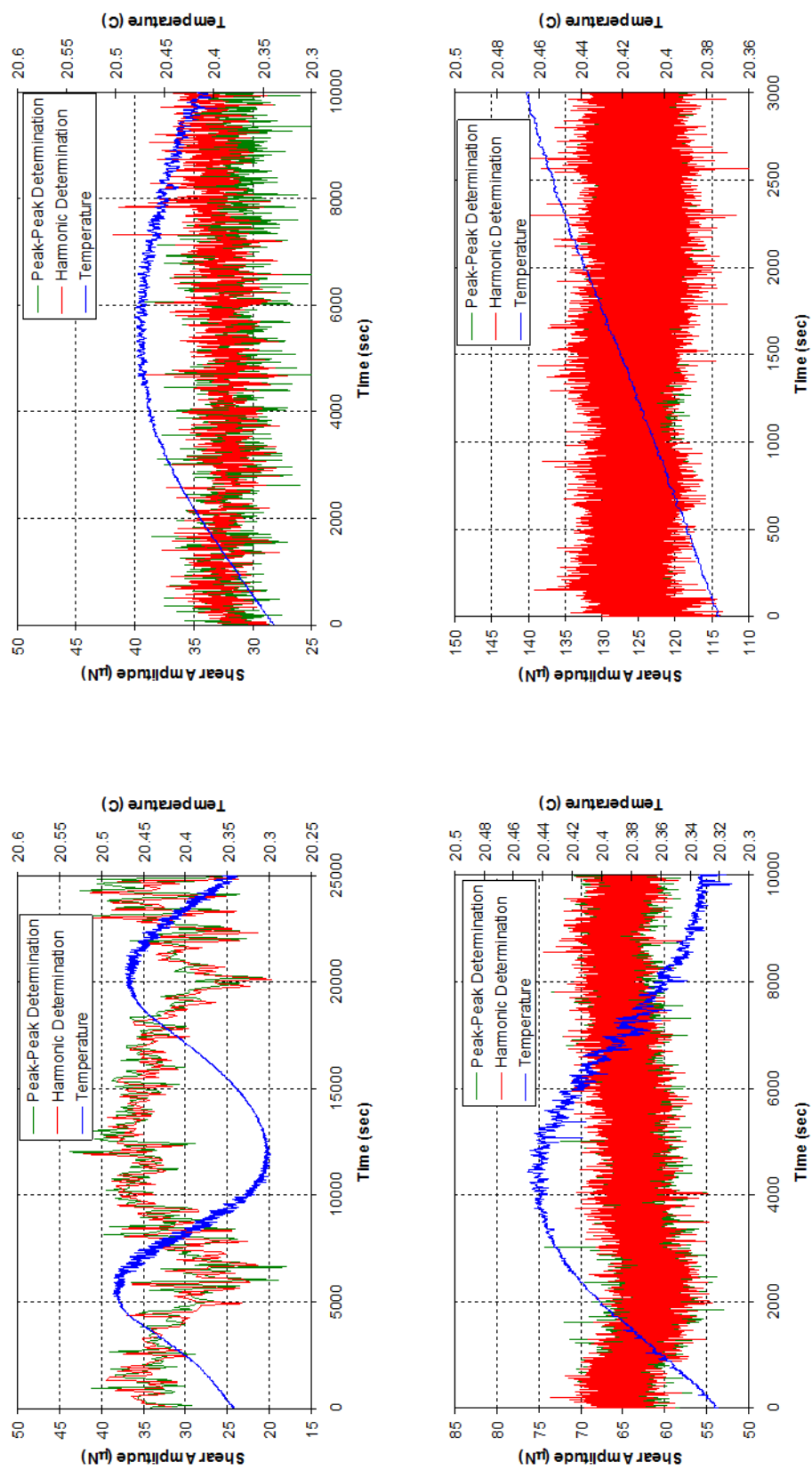
Figure A1.4e: Overlay of peak to peak amplitude and first harmonic amplitude as a function of time for smectic 8CB confined to a gap size of 500 nm, with a shear amplitude of 625 nm and a shear frequency of (top left) 0.01 Hz, (top right) 0.1 Hz, (bottom left) 1.0 Hz and (bottom right) 10 Hz.

368
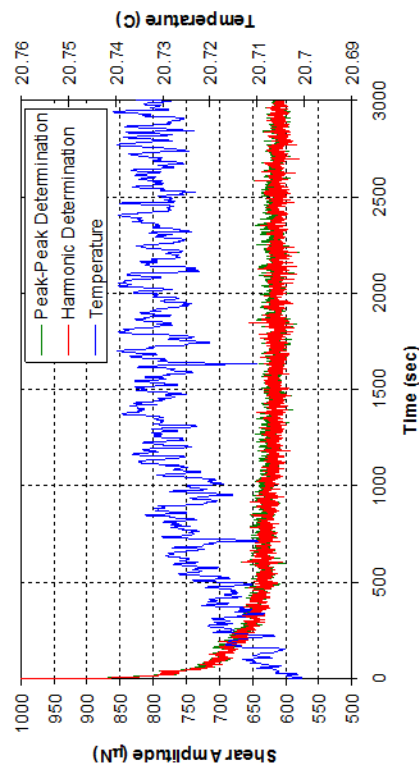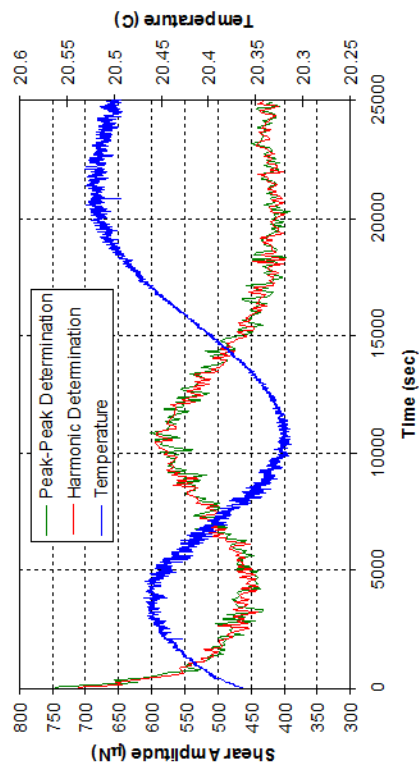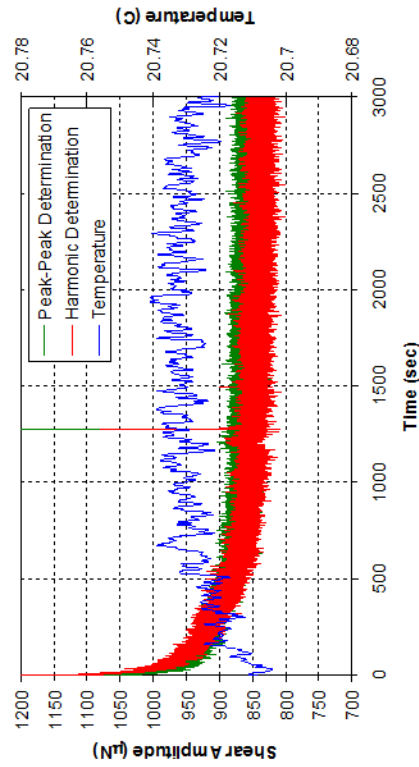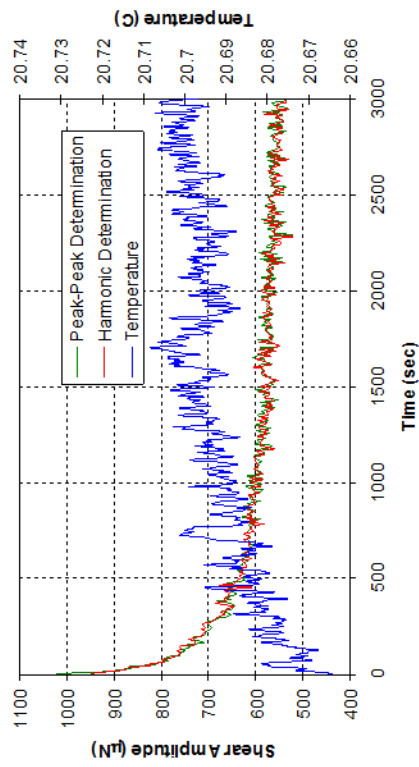
Figure A1.4f: Overlay of peak to peak amplitude and first harmonic amplitude as a function of time for smectic 8CB confined to a gap size of 500 nm, with a shear amplitude of 6250 nm and a shear frequency of (top left) 0.01 Hz, (top right) 0.1 Hz, (bottom left) 1.0 Hz and (bottom right) 10 Hz.

369
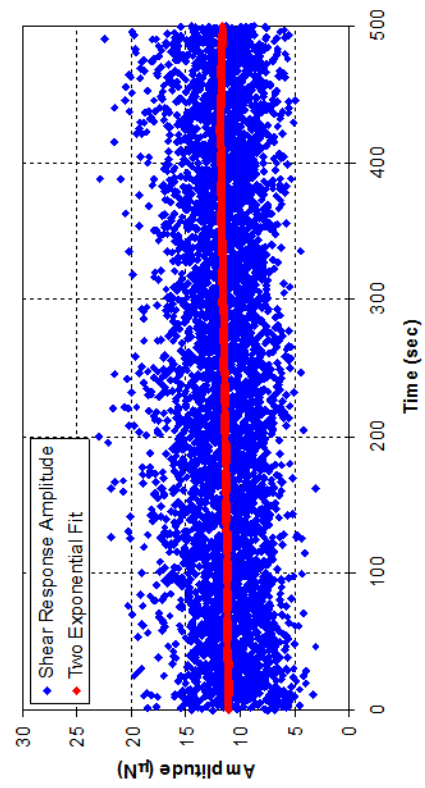
Figure A1.5a: Overlay of peak to peak amplitude and two-exponential fit as a function of time for smectic 8CB confined to a gap size of 5000 nm, with a shear amplitude of 62.5 nm and a shear frequency of 10 Hz.
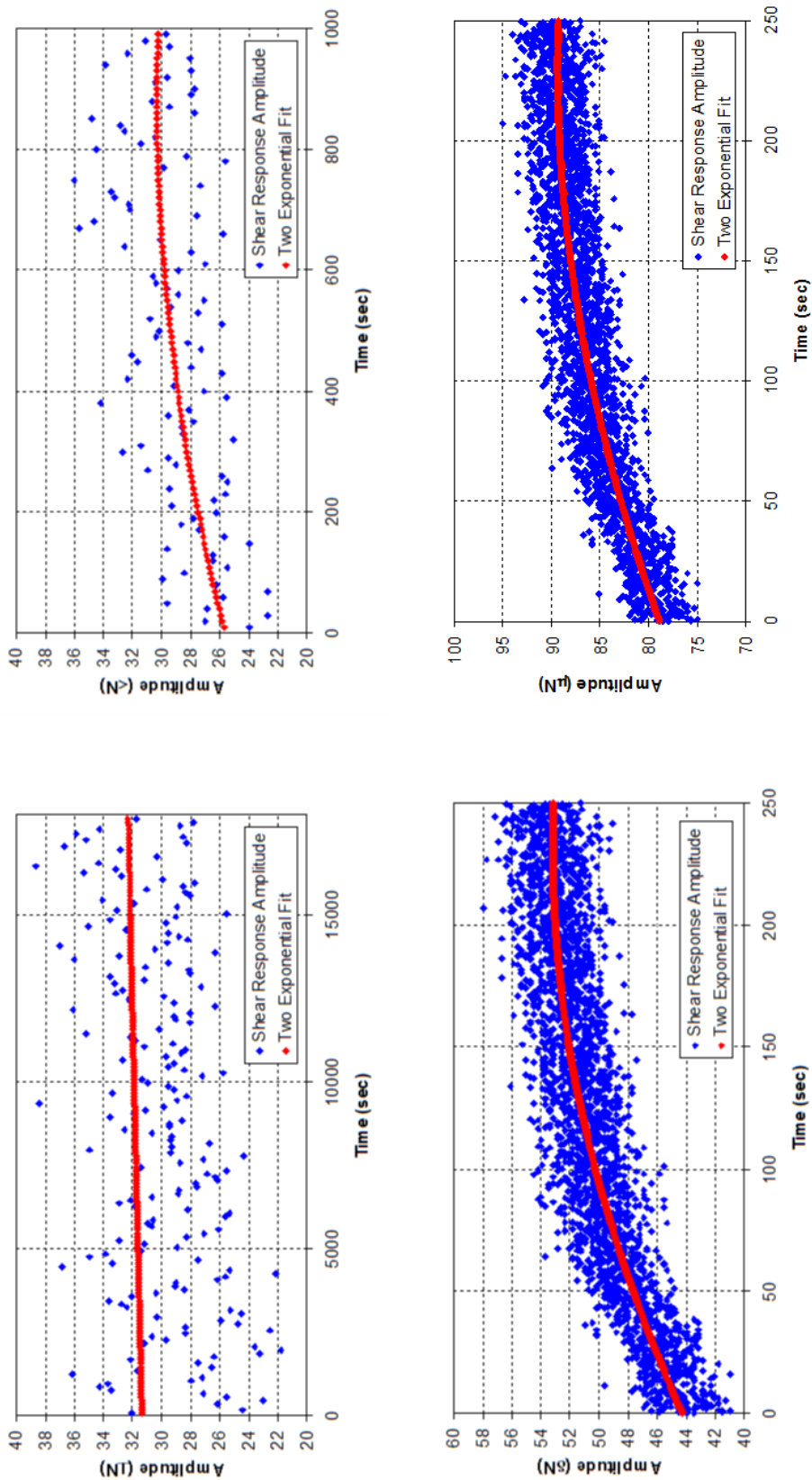
Figure A1.5b: Overlay of peak to peak amplitude and two exponential fit as a function of time for smectic 8CB confined to a gap size of 5000 nm, with a shear amplitude of 625 nm and a shear frequency of (top left) 0.01 Hz, (top right) 0.1 Hz, (bottom left) 1.0 Hz and (bottom right) 10 Hz.

371
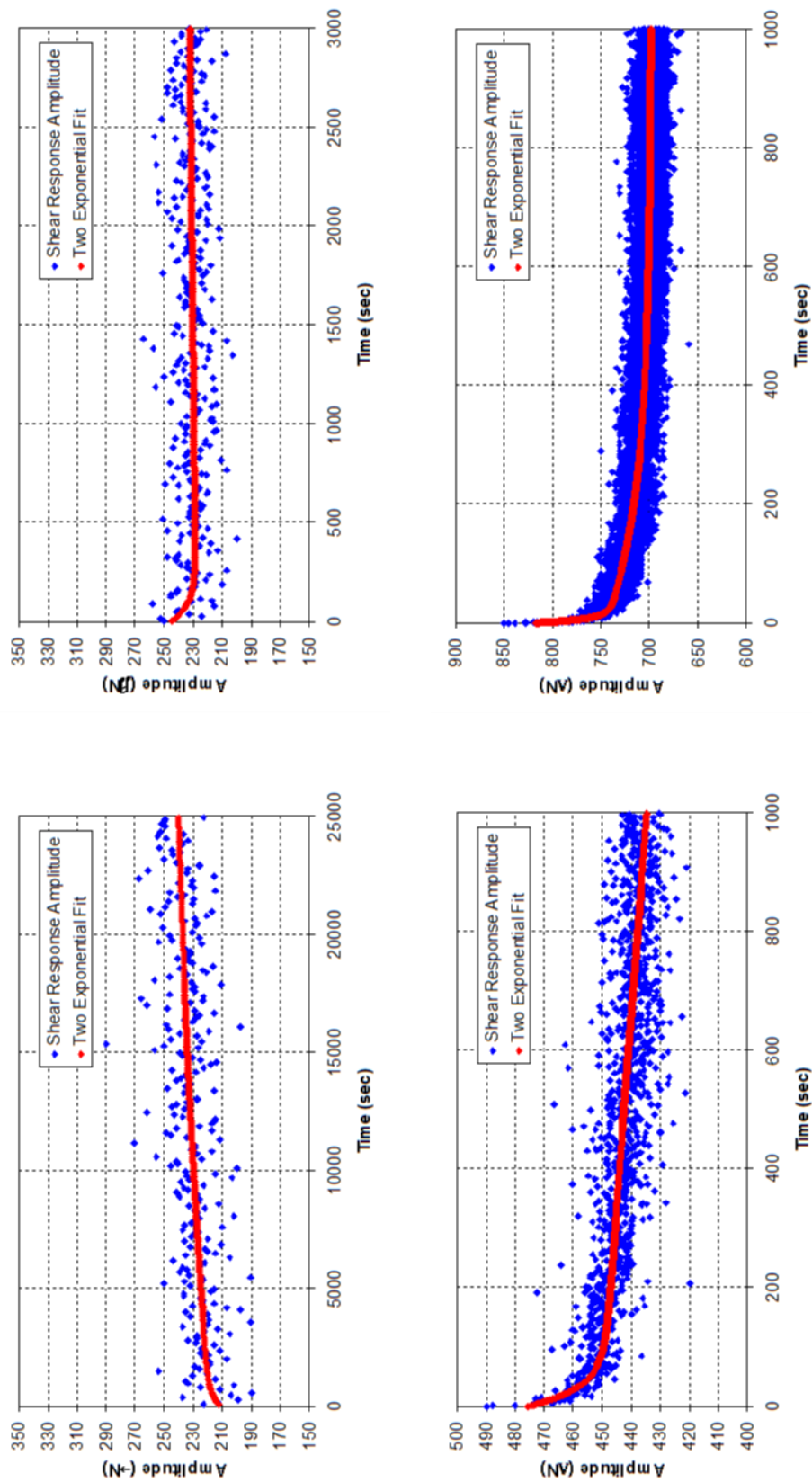
Figure A1.5c: Overlay of peak to peak amplitude and two-exponential fit as a function of time for smectic 8CB confined to a gap size of 5000 nm, with a shear amplitude of 6250 nm and a shear frequency of (top left) 0.01 Hz, (top right) 0.1 Hz, (bottom left) 1.0 Hz and (bottom right) 10 Hz.
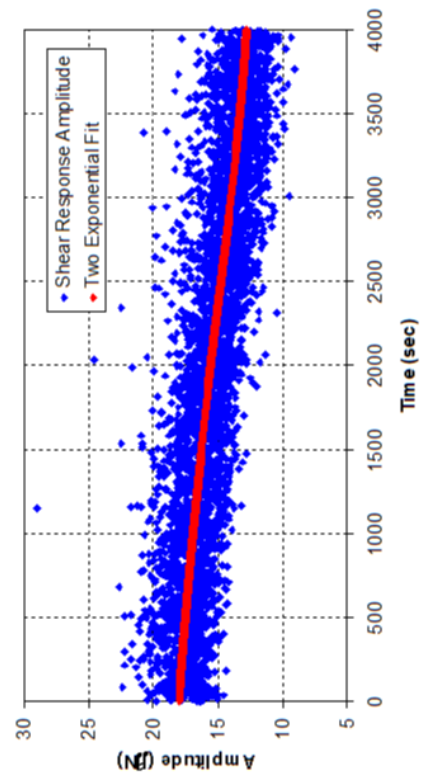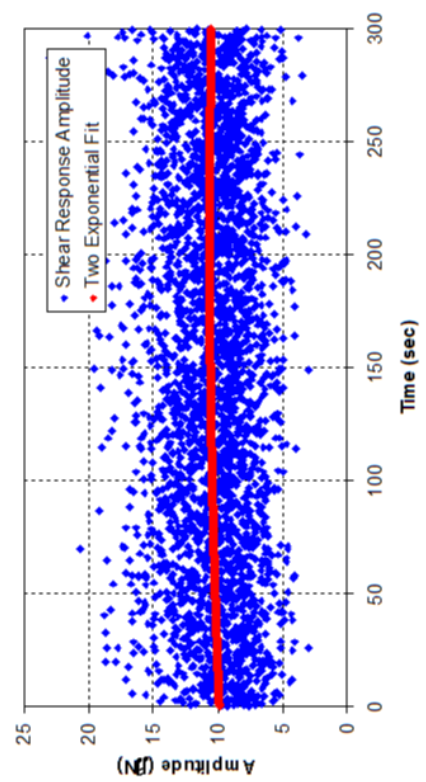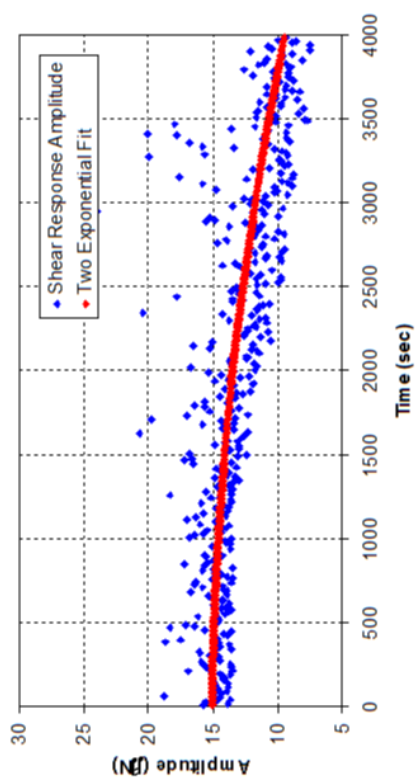
Figure A1.5d: Overlay of peak to peak amplitude and two-exponential fit as a function of time for smectic 8CB confined to a gap size of 500 nm, with a shear amplitude of 62.5 nm and a shear frequency of (top left) 0.01 Hz, (top right) 0.1 Hz, (bottom left) 1.0 Hz and (bottom right) 10 Hz.

373

Figure A1.5e: Overlay of peak to peak amplitude and two-exponential fit as a function of time for smectic 8CB confined to a gap size of 500 nm, with a shear amplitude of 625 nm and a shear frequency of (top left) 0.01 Hz, (top right) 0.1 Hz, (bottom left) 1.0 Hz and (bottom right) 10 Hz.

374

Figure A1.5e: Overlay of peak to peak amplitude and two exponential fit as a function of time for smectic 8CB confined to a gap size of 500 nm, with a shear amplitude of 6250 nm and a shear frequency of (top left) 0.01 Hz, (top right) 0.1 Hz, (bottom left) 1.0 Hz and (bottom right) 10 Hz.

375

Figure A1.6a: Shear response (in red) and corresponding Split Model fit (in dark blue and green) for the first five shear cycles of smectic 8CB confined to a gap size of 6250 nm, with a shear amplitude of 5000 nm, with a shear frequency of (top left) 0.01 Hz, (top right), 0.1 Hz and (bottom left) 1.0 Hz. The difference between the fit and the data is given below the response in light blue and green.

376
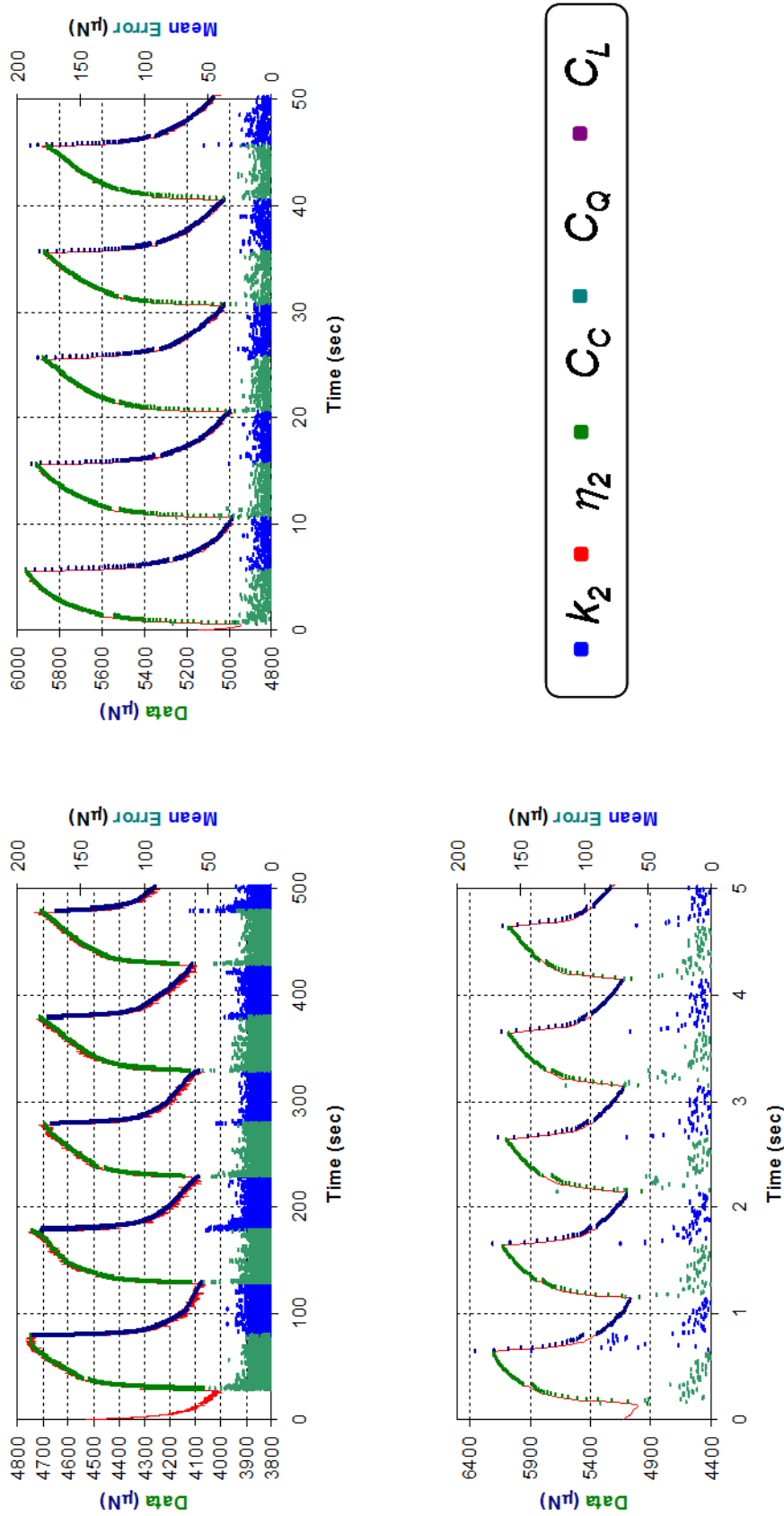
Figure A1.6b: Shear response (in red) and corresponding Split Model fit (in dark blue and green) for the first five shear cycles of smectic 8CB confined to a gap size of 500 nm, with a shear amplitude of 6250 nm and a shear frequency of (top left) 0.01 Hz, (top right), 0.1 Hz and (bottom left) 1.0 Hz. The difference between the fit and the data is given below the response in light blue and green.
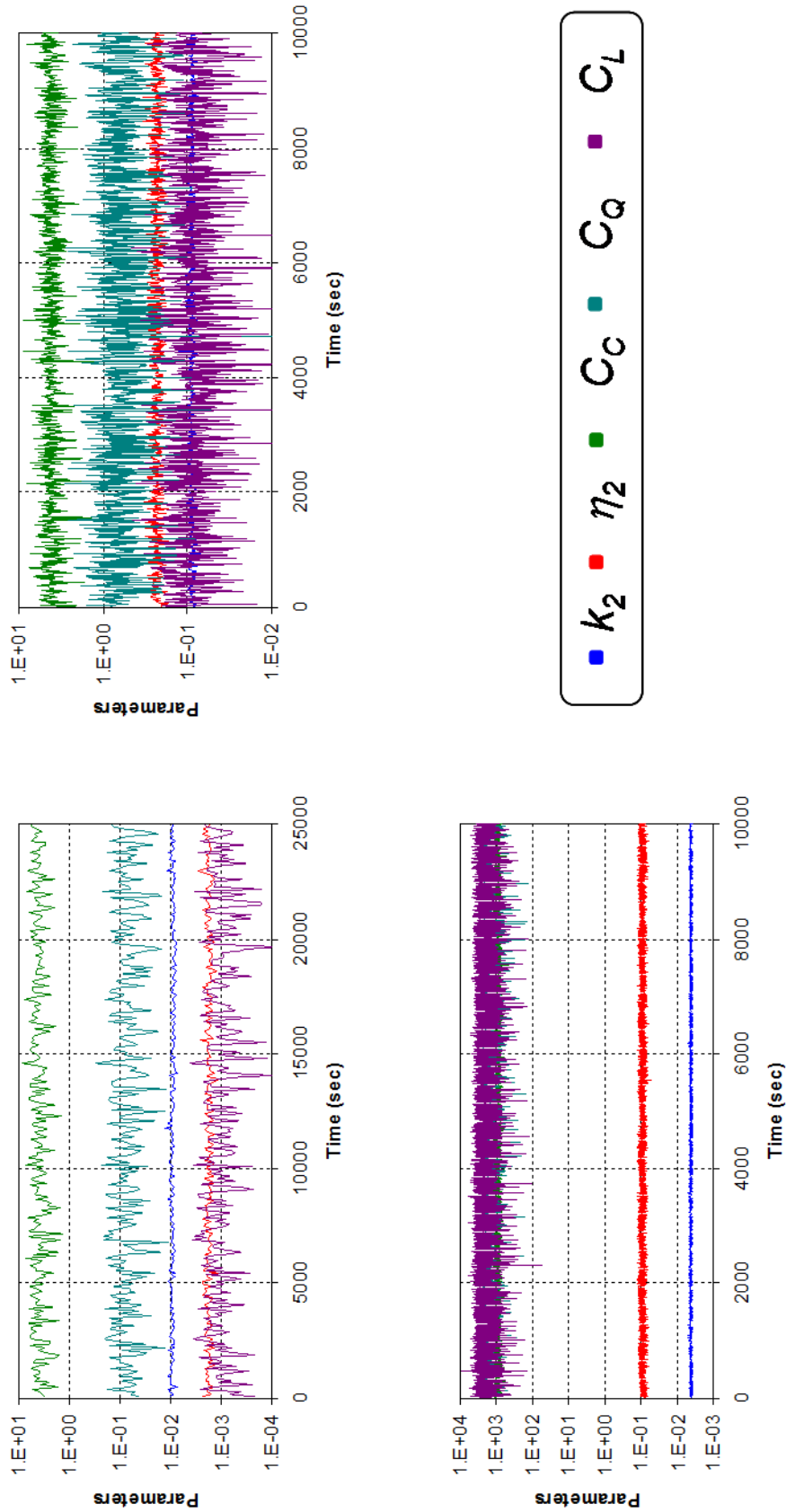
Figure A1.7a: Split Model fit parameters as a function of time for smectic 8CB confined to a gap size of 5000 nm, with a shear amplitude of 6250 nm and a shear frequency of (top left) 0.01 Hz, (top right) 0.1 Hz and (bottom left) 1.0 Hz.
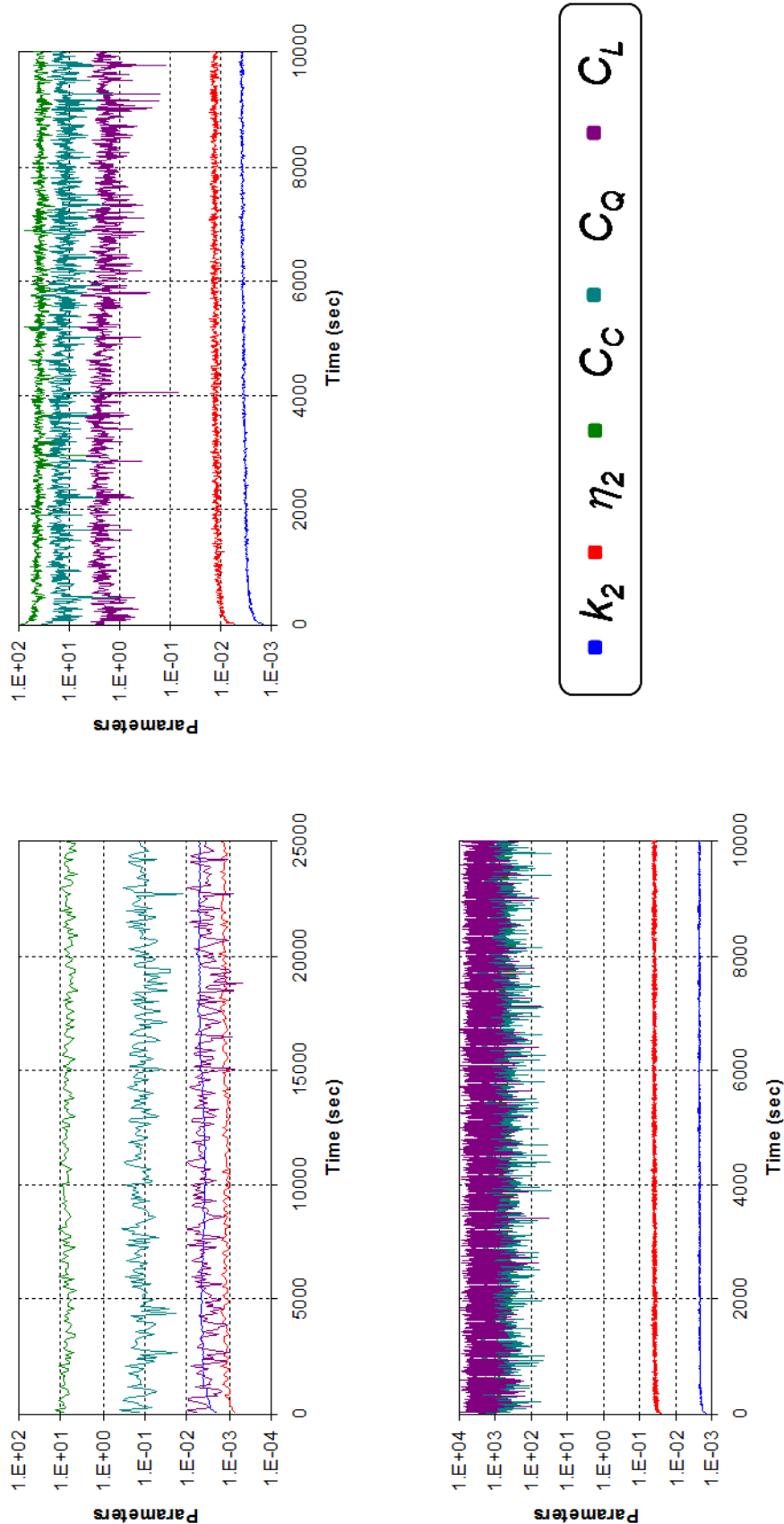
Figure A1.7b: Split Model fit parameters as a function of time for smectic 8CB confined to a gap size of 500 nm, with a shear amplitude of 6250 nm and a shear frequency of (top left) 0.01 Hz, (top right) 0.1 Hz, and (bottom left) 1.0 Hz.

Appendix 2

The Burgers Model

Often viscoelastic materials under shear exhibit prominent elastic and viscous components in their dynamic response. One common way of representing this characteristic behaviour is by using the Burgers Model[394], introduced by Johannes Martinus Burgers in 1935[395]. The model consists of a combination of Kelvin-Voigt and Maxwell Models in series as shown in Figure A2.1:
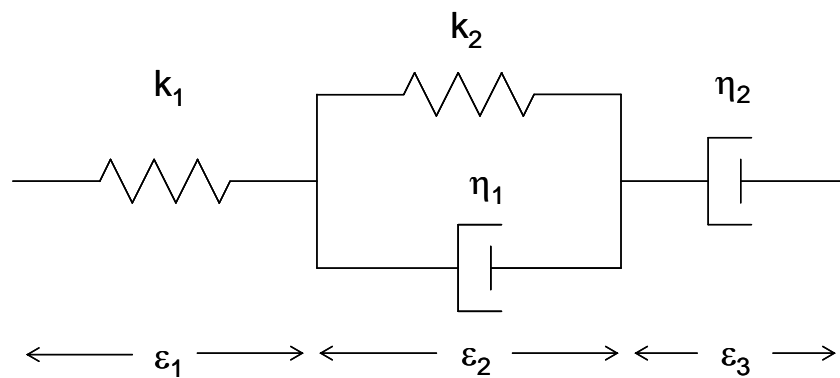
Figure A2.1: The Burgers Model, consisting of a Kelvin-Voigt component (with a spring and dashpot in parallel, comprising the central portion with stretch ε_2), in series with a Maxwell component (with a spring and dashpot in series, comprising the left and right portions with combined stretch $\varepsilon_1 + \varepsilon_3$).

The above system is made up of two springs, both of which follow Hooke's Law $F = k\varepsilon$, where F is the force, k is the spring stiffness and ε is the extension, and two dashpots, both of which resist force proportionally to their velocity. That is, $F = \eta\dot{\varepsilon}$, where η is the viscosity and $\dot{\varepsilon}$ is the rate of change of extension. It should be noted that while the relationships above consider an applied force and the resultant extension in a system, the

same reasoning can be extended to a simple stress-strain relationship, with the equivalent

Hooke's Law being $\sigma = k\varepsilon$, with σ as an applied stress and ε now as the resultant strain.

The leftmost spring and rightmost dashpot, together as they are in series, make up a

Maxwell component, and the central portion of spring and dashpot in parallel constitute a

Kelvin-Voigt component. The latter system, being in parallel, would yield an overall

stress of $\sigma = \eta\dot{\varepsilon} + k\varepsilon$. Each of the three sections may undergo a unique strain of ε_i, but

together they must sum to a total strain of $\varepsilon = \sum\limits_{i=1}^{3} \varepsilon_i$; each component, furthermore, can

be assumed to be unstretched initially, and so $\varepsilon_1(0) = \varepsilon_2(0) = \varepsilon_3(0) = 0$. Because the

springs and dashpots are all massless, the shear stress, σ, will be the same throughout the

chain, and this leads to a relationship between the components of:

$$\sigma = k_1\varepsilon_1 = k_2\varepsilon_2 + \eta_2\dot{\varepsilon}_2 = \eta_1\dot{\varepsilon}_3 \tag{1}$$

From equation (1) three separate equations may be formed:

$$\varepsilon_1 = \frac{\sigma}{k_1} \tag{1a}$$

$$\dot{\varepsilon}_2 = \frac{\sigma}{\eta_2} - \frac{k_2\varepsilon_2}{\eta_2} \tag{1b}$$

$$\dot{\varepsilon}_3 = \frac{\sigma}{\eta_1} \tag{1c}$$

From (1c) we may find ε_3:

$$\varepsilon_3 = \frac{1}{\eta_1}\int \sigma\, dt$$

$$= \frac{\sigma t}{\eta_1} + const\ .$$

and since $\varepsilon_3(0) = 0$,

$$\varepsilon_3 = \frac{\sigma t}{\eta_1} \qquad\qquad\qquad (1d)$$

Together, equations (1a) and (1d) give the solution to the Maxwell component, a plot for which is provided below given a constant shear stress:
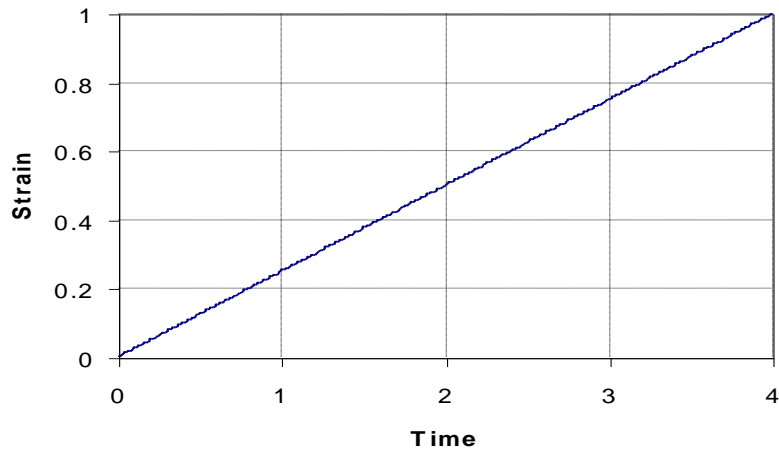
Figure A2.2: Strain as a function of time for a Maxwell component undergoing constant shear stress. Note that the yield stress here, indicated by the intercept $1/k_1$, is zero, but in general it does not have to be.

Note that the Maxwell component alone is not able to describe a viscoelastic material sufficiently since it does not take creep into consideration (as indicated by the linear strain vs. time).

From (1b), similarly, we may determine ε_2. It is best solved using the standard solution for linear first order equations. That is, for $\frac{dy}{dx} + P(x)y = Q(x)$ a solution exists such that $ye^{\int Pdx} = \int Qe^{\int Pdx} dx + const$. In the present case we may substitute $y = \varepsilon$, $x = t$, $P(x) = k_2/\eta_2$ and $Q(x) = \sigma/\eta_2$ so that:

$$\varepsilon_2 e^{\int \frac{k_2}{\eta_2} dt} = \int \frac{\sigma}{\eta_2} e^{\int \frac{k_2}{\eta_2} dt} dt + const \quad .$$

$$\varepsilon_2 e^{k_2 t/\eta_2} = \frac{\sigma}{\eta_2} \int e^{k_2 t/\eta_2} dt + const \quad .$$

$$\varepsilon_2 e^{k_2 t/\eta_2} = \frac{\sigma}{k_2} e^{k_2 t/\eta_2} + const \quad .$$

$$\varepsilon_2 = \frac{\sigma}{k_2} + Ce^{-k_2 t/\eta_2}$$

and, noting that $\varepsilon_2(0) = 0$, $C = -\sigma/k_2$ so that:

$$\varepsilon_2 = \frac{\sigma}{k_2}\left(1 - e^{-k_2 t/\eta_2}\right) \tag{1e}$$

which is the standard result for the Kelvin-Voigt model, applicable to some simple

viscoelastic materials. A plot is given below showing the solution to the Kelvin-Voigt

model for a constant stress:
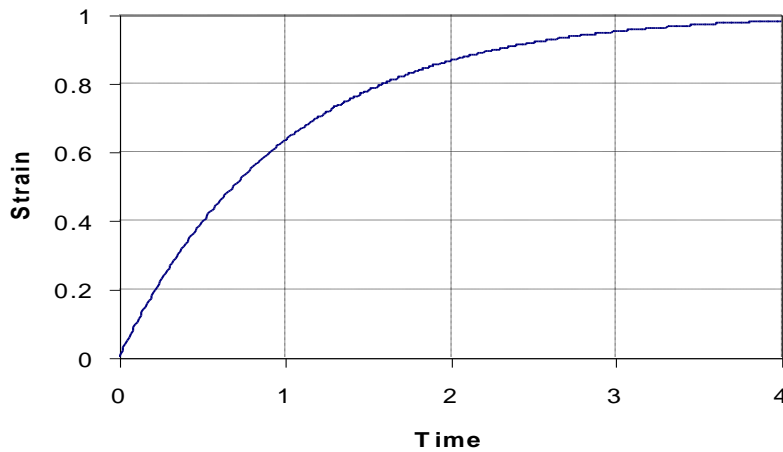
**Figure A2.3**: Strain as a function of time for a Kelvin-Voigt component undergoing constant shear stress.

Taking equations (1a), (1d) and (1e) and summing them, an analytical solution for the overall extension ε can be obtained:

$$\varepsilon = \sigma \left[\frac{1}{k_1} + \frac{t}{\eta_1} + \frac{1}{k_2} \left(1 - e^{-k_2 t / \eta_2} \right) \right]$$ (2)

The above equation represents the Burgers Model, describing the time-dependent change of strain under constant stress. The leftmost term on the right hand side represents the instantaneous strain that occurs as a result of stressing the system, the rightmost term represents the viscoelastic behaviour that follows shortly after, and the central term represents the viscous flow that occurs after the material has been stressed beyond its elastic limit. A plot of the Burgers Model solution for a system under constant stress is given below:
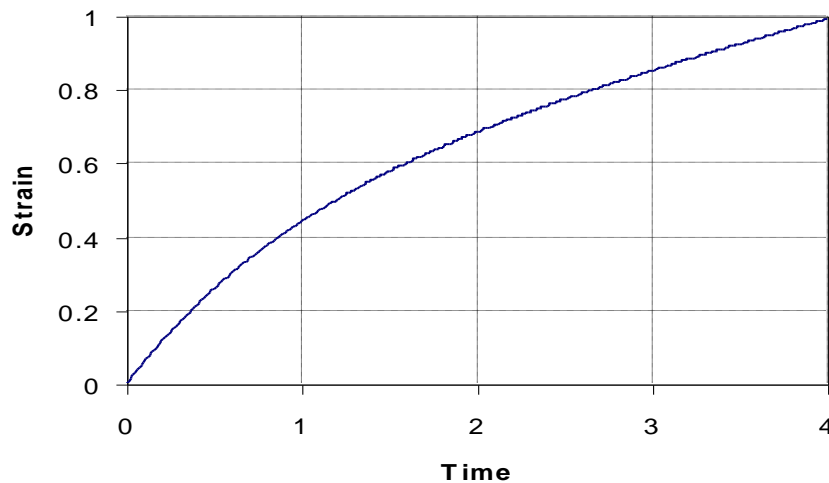
Figure A2.4: Strain as a function of time for the Burgers Model for a system undergoing constant shear stress. Note that the yield stress here, indicated by the intercept $1/k_1$, is zero, but in general it does not have to be

The Maxwell and Kelvin-Voigt components in series allow for more flexibility in modeling viscoelastic systems, in which the material exhibits both liquidlike (Maxwell)

and solidlike (Kelvin-Voigt) behaviour. This model has been applied to the smectic 8CB

shear response data presented in the Results section, describing the material as it is

sheared beyond its viscoelastic limit.

Appendix 3

Demonstration of the Odd-Harmonic Nature of a Non-Newtonian Response to a Triangular Shear Profile

Following Wilhelm's derivation of a non-Newtonian response to a sinusoidal shear profile[376], an extension can be made to the slightly more complicated case of a triangular shear profile to demonstrate that it too yields a response made up purely of odd-harmonic components, due in part to the triangular input (which is made up entirely of odd-harmonic components) and in part to the non-Newtonian nature of the viscosity dependence on shear rate. One begins by assuming the material's viscosity depends on shear rate alone and is independent of direction (a fact not necessarily true for layered systems, as demonstrated by Mięsowicz[36], but applicable here assuming the shearing direction remains parallel to a single Mięsowicz viscosity) so that $\eta = \eta(|\dot{\gamma}|)$, and the shear rate is small enough that the viscosity can be approximated as a Carreau Model polynomial series:

$$\eta = \eta_0 + c_1|\dot{\gamma}| + c_2|\dot{\gamma}|^2 + \ldots$$

where c_n are proportionality constants. The triangular shear pattern can be expanded in a Fourier series so that the strain it exerts is:

$$\gamma = A\left[\sin\omega_1 t - \frac{1}{9}\sin 3\omega_1 t + \frac{1}{25}\sin 5\omega_1 t - \ldots\right] = \sum_{n=1}^{\infty}\frac{A(-1)^{n-1}\sin\left\{[2n-1]^2\omega_1 t\right\}}{(2n-1)^2} \tag{1}$$

where A is the strain amplitude, ω_1 is the fundamental shearing frequency and t being time. The strain rate will then be:

$$\dot{\gamma} = A\,\omega_1\left[\cos\,\omega_1 t - \frac{3}{9}\cos\,3\omega_1 t + \frac{5}{25}\cos\,5\omega_1 t - ...\right] = A\,\omega_1\sum_{n=1}^{\infty}\frac{(-1)^{n-1}\cos\left\{[2n-1]^2\,\omega_1 t\right\}}{(2n-1)}$$

So that:

$$\left|\dot{\gamma}\right| = A\,\omega_1\left|\sum_{n=1}^{\infty}\frac{(-1)^{n-1}\cos\left\{[2n-1]^2\,\omega_1 t\right\}}{(2n-1)}\right|$$

This being a triangular wave (with the periodicity doubled from the previous expression due to the absolute value signs), it can be expanded in a Fourier series expansion of a triangular wave, so that it can be written as:

$$\left|\dot{\gamma}\right| = A\,\omega_1\left[\frac{\pi}{2} - \frac{4}{\pi}\left(\frac{\cos\,2\omega_1 t}{1^2} + \frac{\cos\,6\omega_1 t}{3^2} + \frac{\cos\,10\,\omega_1 t}{5^2} + ...\right)\right] = A\,\omega_1\left[\frac{\pi}{2} - \frac{4}{\pi}\sum_{n=1}^{\infty}\frac{\cos\left\{2(2n-1)\omega_1 t\right\}}{(2n-1)^2}\right]$$

which simplifies, in general terms, to:

$$\left|\dot{\gamma}\right| \propto c_0' + c_1'\cos\,2\omega_1 t + c_2'\cos\,6\omega_1 t + c_3'\cos\,10\,\omega_1 t + ...$$

where c_n' are proportionality constants ($c_0' = \pi A\,\omega_1/2$, $c_1' = -4A\,\omega_1/\pi$, $c_2' = 4A\,\omega_1/9\pi$, etc.). The viscosity-related force can now be easily calculated by substituting the relations derived above into the viscosity-strain rate equation:

$$F \propto \eta\dot{\gamma}$$

$$F \propto \left(\eta_0 + c_1\left|\dot{\gamma}\right| + c_2\left|\dot{\gamma}\right|^2 + ...\right)\left\{\left[\cos\,\omega_1 t - \frac{3}{9}\cos\,3\omega_1 t + \frac{5}{25}\cos\,5\omega_1 t - ...\right]\right\}$$

$$F \propto \left\{\begin{array}{l}\eta_0 + c_1\left[\dfrac{\pi}{2} - \dfrac{4}{\pi}\left(\dfrac{\cos\,2\omega_1 t}{1^2} + \dfrac{\cos\,6\omega_1 t}{3^2} + \dfrac{\cos\,10\,\omega_1 t}{5^2} + ...\right)\right] + \\[4mm] c_2\left[\dfrac{\pi}{2} - \dfrac{4}{\pi}\left(\dfrac{\cos\,2\omega_1 t}{1^2} + \dfrac{\cos\,6\omega_1 t}{3^2} + \dfrac{\cos\,10\,\omega_1 t}{5^2} + ...\right)\right]^2 + ...\end{array}\right\}\bullet$$

$$\bullet\left\{\left[\cos\,\omega_1 t - \frac{3}{9}\cos\,3\omega_1 t + \frac{5}{25}\cos\,5\omega_1 t - ...\right]\right\}$$

$$F \propto \left\{ \left[\frac{\pi}{2} \left(c_1 + \frac{\pi}{2} c_2 \right) + \eta_0 \right] \cos \omega_1 t - \left[\frac{4c_1}{\pi} + 4c_2 \right] \cos 2\omega_1 t \cos \omega_1 t - \right.$$

$$- \frac{4c_2}{\pi} \cos^2 2\omega_1 t \cos \omega_1 t - \frac{3}{9} \left[\frac{\pi}{2} \left(c_1 + \frac{\pi}{2} c_2 \right) + \eta_0 \right] \cos 3\omega_1 t +$$

$$\left. + \frac{5}{25} \left[\frac{\pi}{2} \left(c_1 + \frac{\pi}{2} c_2 \right) + \eta_0 \right] \cos 5\omega_1 t - \frac{12 c_1}{9\pi} \cos 2\omega_1 t \cos 3\omega_1 t + ... \right\}$$

$$F \propto \left\{ \left[\frac{\pi}{2} \left(c_1 + \frac{\pi}{2} c_2 \right) + \eta_0 \right] \cos \omega_1 t - \frac{1}{2} \left[\frac{4c_1}{\pi} + 4c_2 \right] [\cos \omega_1 t + \cos 3\omega_1 t] - \right.$$

$$- \frac{2c_2}{\pi} \cos 2\omega_1 t [\cos \omega_1 t + \cos 3\omega_1 t] - \frac{3}{9} \left[\frac{\pi}{2} \left(c_1 + \frac{\pi}{2} c_2 \right) + \eta_0 \right] \cos 3\omega_1 t +$$

$$\left. + \frac{5}{25} \left[\frac{\pi}{2} \left(c_1 + \frac{\pi}{2} c_2 \right) + \eta_0 \right] \cos 5\omega_1 t - \frac{2c_1}{3\pi} [\cos \omega_1 + \cos 5\omega_1 t] + ... \right\}$$

$$F \propto \left\{ \left[\frac{\pi}{2} \left(c_1 + \frac{\pi}{2} c_2 \right) + \eta_0 \right] \cos \omega_1 t - \frac{1}{2} \left[\frac{4c_1}{\pi} + 4c_2 \right] [\cos \omega_1 t + \cos 3\omega_1 t] - \right.$$

$$- \frac{c_2}{\pi} [2 \cos \omega_1 t + \cos 3\omega_1 t + \cos 5\omega_1 t] - \frac{1}{3} \left[\frac{\pi}{2} \left(c_1 + \frac{\pi}{2} c_2 \right) + \eta_0 \right] \cos 3\omega_1 t +$$

$$\left. + \frac{5}{25} \left[\frac{\pi}{2} \left(c_1 + \frac{\pi}{2} c_2 \right) + \eta_0 \right] \cos 5\omega_1 t - \frac{2c_1}{3\pi} [\cos \omega_1 + \cos 5\omega_1 t] + ... \right\}$$

$$F \propto \left\{ \left[\left(\frac{\pi}{2} - \frac{2}{\pi} - \frac{2}{3\pi} \right) c_1 + \left(\frac{\pi^2}{4} - 2 - \frac{2}{\pi} \right) c_2 + \eta_0 \right] \cos \omega_1 t + \right.$$

$$- \left[\left(\frac{2}{\pi} + \frac{\pi}{6} \right) c_1 + \left(2 + \frac{1}{\pi} + \frac{\pi^2}{12} \right) c_2 + \eta_0 \right] \cos 3\omega_1 t +$$

$$\left. \left[\left(\frac{\pi}{10} - \frac{2}{3\pi} \right) c_1 + \left(\frac{\pi^2}{20} - \frac{1}{\pi} \right) c_2 + \eta_0 \right] \cos 5\omega_1 t + ... \right\}$$

$$F \propto C_1 \cos \omega_1 t + C_3 \cos 3\omega_1 t + C_5 \cos 5\omega_1 t + ...$$

where C_n are the proportionality constants defined by the lengthy coefficients shown in the previous line.

As can be seen from the lower order terms, in general the viscosity, being composed of even cosine terms (plus the offset zero shear-rate term), when multiplied by the shear rate, being composed entirely of odd cosine terms, must necessarily result in a function composed entirely of odd cosine terms. Consequently, the response due to a triangular shear wave will be composed entirely of odd-harmonic terms.

Appendix 4

Demonstration of the Crystallization Point of 8CB via Differential Scanning Calorimetry

To maximize the shear response the sample should be as viscous as possible, which is easily obtained by lowering the temperature of the sample near to the smectic-crystalline bulk transition point, which is reported by various groups to be approximately 20.5°C to 21.5°C[125, 130, 321, 398, 399]. In order to approach the transition point without crossing it, it is necessary to know the exact transition point for the sample being used, and so a DSC test was performed on the sample with temperature steps of 0.1°/min from 60°C to -10°C, holding there for 30 minutes and then raising the temperature back to 60°C in 0.1°/min increments. The results of the test are shown below:
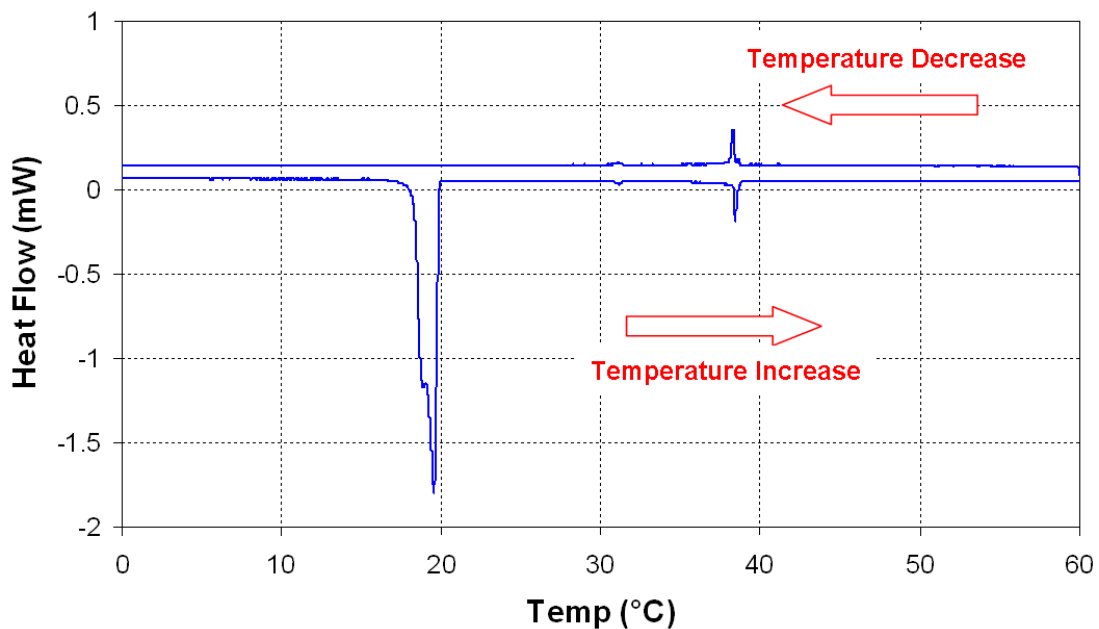

Figure A4.1: Heat flow as a function of temperature for 8CB as obtained by DSC.

The heat flow spike spanning 18°C to 20°C and peaking at 19.5°C clearly shows the

crystalline to smectic-A transition, along with the nematic-smectic-A transition at 38.2°C

to 38.4°C. For this reason, the SFA sample temperature was chosen to be 20.5°C to

ensure that the sample would be in the smectic-A state but with as high a viscosity as

possible (and hence as high a shear response signal to noise ratio as possible) within that

phase.

Appendix 5

The Relation of Shear Response to Viscosity in the Surface Forces Apparatus

Viscosity is commonly defined as the measure of resistance of a fluid to deformations such as (but not limited to) shear and stress. For a fluid between two flat surfaces moving relative to one another, this resistance is known specifically as *shear viscosity*, and can, with most simple fluids and for low velocities, be described reasonably using Newton's Theory, that the applied shear stress will be proportional to the velocity gradient perpendicular to the surfaces. This gives rise to the constitutive equation:

$$\sigma = \eta \frac{\partial v}{\partial z}$$

where σ is the shear stress, $\partial v / \partial z$ is the velocity gradient between the surfaces (with z, therefore, being the direction perpendicular to the plates) and η is the viscosity of the fluid. If the force generating the shear stress is F and the surfaces have area A, the shear stress may be expressed as $\sigma = F/A$. Likewise, the velocity gradient in this simple scenario can be simplified to $\partial v / \partial z \approx v/z$, with z as the distance between the surfaces, leading to an equivalent equation to the one above:

$$\frac{F}{A} = \eta \frac{v}{z} \tag{1}$$

A schematic of this simple situation is shown below:
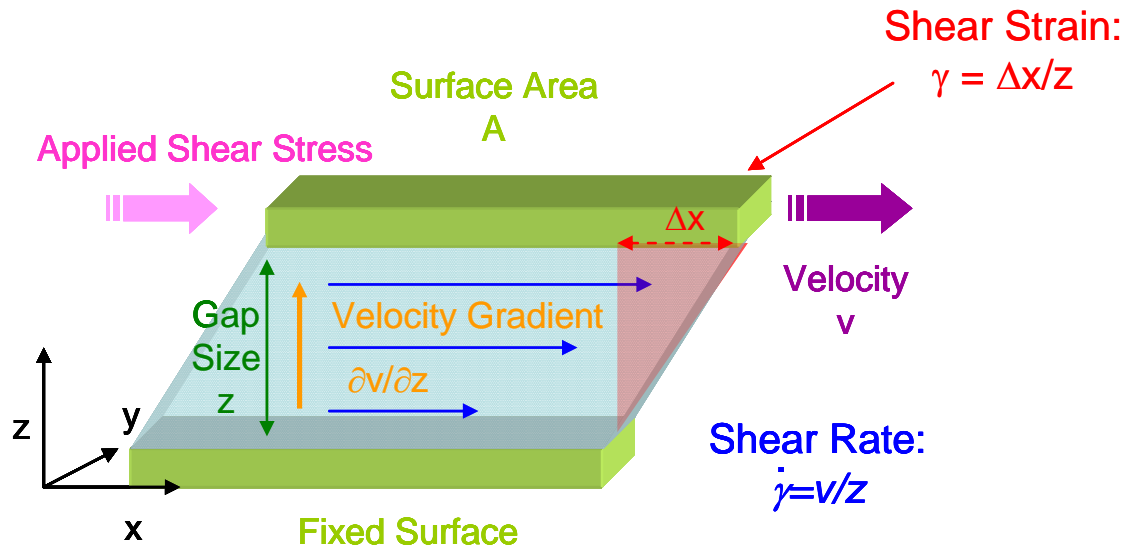
Figure A5.1: A fluid being deformed by two plates moving relative to one another, giving rise to a velocity gradient within the fluid which, in simple scenarios, is proportional to the shear stress with proportionality constant η, the shear viscosity.

The configuration is somewhat more complicated within a Surface Forces Apparatus, since the fluid is confined not by two flat surfaces but typically by two crossed cylinders. The shear stress equation given above will apply only for infinitesimal points across from one another on the crossed cylinder geometry, since only for two infinitesimals will the surfaces be effectively 'flat' relative to one another, but by integrating this equation over the sheared area one can obtain an approximate relation between shear stress and viscosity (again, of a Newtonian fluid), albeit a more complicated one. These infinitesimals can be integrated over the surface of contact to give the total shear force. Starting with Equation (1) and, again, assuming flow is primarily directed parallel to the surfaces, Newton's Theory is re-written:

$$\int dF = \int_A \eta \frac{v}{z} dA$$

Assuming a uniform viscosity throughout the fluid and a steady driving relative velocity between the surfaces, the above becomes:

$$F = v\eta \int_A \frac{dA}{z}$$

Once the sample has been deposited between the cylinders, it typically takes on a columnar shape with the ends conforming to the confining cylinders' geometry (defined by its radius, R). For this reason, converting the above integration to cylindrical polar coordinates is useful to continue the derivation, with the radius coordinate corresponding to the radius of the sample column and the axis passing perpendicularly through the point of closest approach of the crossed cylinders. In converting to this system, it is worth noting that flow will likely be chiefly in the plane of contact as pictured in Figure A5.1, so that $dz \approx 0$ to first approximation and the differential area in cylindrical coordinates reduces to that of an infinitesimally thin annular ring $dA \approx r dr d\theta$. The shear equation then becomes:

$$F = v\eta \int_A \frac{r}{z} dr d\theta \tag{2}$$

It is now a matter of defining the surface to surface distance in terms of cylindrical coordinates so that the crossed cylinder shear equation can be determined. This will be discussed in the following paragraph.

When the surfaces are in contact, the distance between surface points, z, will be a function of the radial distance from this point (that is, the distance between the axial center, or origin, and the projection of the surface on the contact plane). A schematic of the geometry is given below:

394
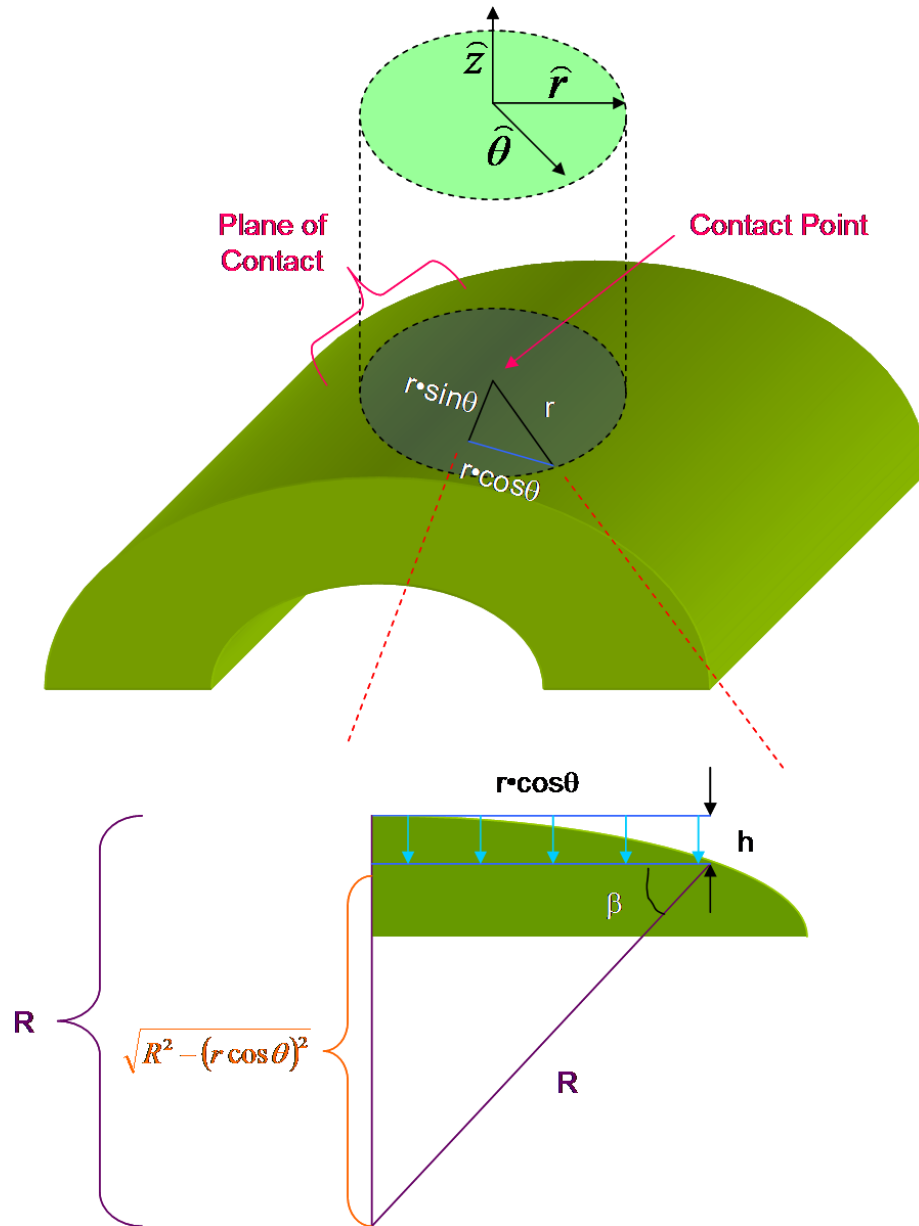
Figure A5.2: A schematic of the geometry for a single cylinder, from which the distance between the cylinder surface and the plane of contact, *h*, can be calculated as a function of *r*, *R* and *θ*.

The distance between this point and the nearest point on the plane of contact, *h*, will be:

$$h = R - \left\{ \left[R^2 - (r \cos\theta)^2 \right] \right\}^{1/2}$$

In a similar way, the value of h can be calculated for the second cylinder. Since it is aligned perpendicularly to the first cylinder, the equation will be shifted by exactly 90°, and the distance between crossed cylindrical surfaces in contact at the point of closest approach, at an arbitrary radial distance from center, r, will be:

$$h_{tot} = \left(R - \left\{\left[R^2 - (r\cos\theta)^2\right]\right\}^{1/2}\right) + \left(R - \left\{\left[R^2 - (r\cos(\theta + \pi/2))^2\right]\right\}^{1/2}\right)$$

$$h_{tot} = 2R - \left[R^2 - (r\cos\theta)^2\right]^{1/2} - \left[R^2 - (r\sin\theta)^2\right]^{1/2}$$

$$h_{tot} = R\left\{2 - \left[1 - \left(\frac{r}{R}\cos\theta\right)^2\right]^{1/2} - \left[1 - \left(\frac{r}{R}\sin\theta\right)^2\right]^{1/2}\right\} \tag{3}$$

And hence, for cylinders with a gap size g, the total distance between cylinders at a radial distance r from the point of closest approach will then be:

$$z = h_{tot} + g \tag{4}$$

Alternatively, an approximation to the above can be made by assuming the geometry of the system consists of a plane and sphere of radius R separated at the point of closest approach by a distance g; this geometry approximates the crossed-cylindrical geometry to second order and, because of the symmetry of the sphere, greatly simplifies the angular integration term in Equation (2). The distance between a point on the sphere a radial distance r from the point of closest approach and its projection on the plane is given by:

$$z_{sphere - plane} = \frac{r^2}{2R} + g \tag{5}$$

The distance relation from Equation (3) can be incorporated into equation (2) to simplify the treatment of the shear equation:

$$F = v\eta \int_A \frac{r\,dr\,d\theta}{R\left\{2 - \left[1 - \left(\dfrac{r}{R} \cdot \cos\theta\right)^2\right]^{1/2} - \left[1 - \left(\dfrac{r}{R} \cdot \sin\theta\right)^2\right]^{1/2}\right\} + g}$$

By noting that the bounds of integration for θ and r will be [400] and $\{0, r\}$ (the radial upper limit remains undefined to accommodate different sizes of the drop of sample between the cylinders) the following relation emerges after some minor rearrangement:

$$F = \frac{v\eta}{g} \int_0^r \int_0^{2\pi} \frac{gr}{R\left\{2 - \left[1 - \left(\dfrac{r}{R} \cdot \cos\theta\right)^2\right]^{1/2} - \left[1 - \left(\dfrac{r}{R} \cdot \sin\theta\right)^2\right]^{1/2}\right\} + g}\,dr\,d\theta \tag{6}$$

And, for the sphere-plane approximation, since Equation (5) has no angular dependence, the differential annular ring becomes $dA \approx r\,dr\,d\theta \approx 2\pi r\,dr$ and so Equation (2) becomes:

$$
\begin{aligned}
F_{Sphere-Plane} &= 2\pi v\eta \int_0^r \frac{r}{z}\,dr \\
&= 2\pi v\eta \int_0^r \frac{r}{r^2/2R + g}\,dr \\
&= 2\pi v\eta \left[R \ln\left(2gR + r^2\right)\right]_0^r \\
&= 2\pi v\eta R \ln\left(1 + \frac{r^2}{2gR}\right)
\end{aligned}
\tag{7}
$$

Equation (7) provides a quick way to estimate the force contribution at a given distance from the point of closest approach (which coincides with the axis of the cylindrical coordinate system shown in Figure A5.2). Expressed as a fraction of the total force (i.e. the force at radial point r_s, the sample radius), this relation will be:

$$
\begin{aligned}
\frac{F_{Sphere-Plane}(r)}{F_{Sphere-Plane}(r_s)} &= \frac{2\pi v\eta\ R \ln\left(1 + r^2/2gR\right)}{2\pi v\eta\ R \ln\left(1 + r_s^2/2gR\right)} \\
&= \frac{\ln\left(1 + r^2/2gR\right)}{\ln\left(1 + r_s^2/2gR\right)}
\end{aligned}
$$

For the present study, the sample radius was estimated by eye to be approximately 3 mm while the surfaces were near contact. A figure showing the cumulative force as a function of distance from the origin (i.e. the point of closest approach between the surfaces) is given below for this sample size:
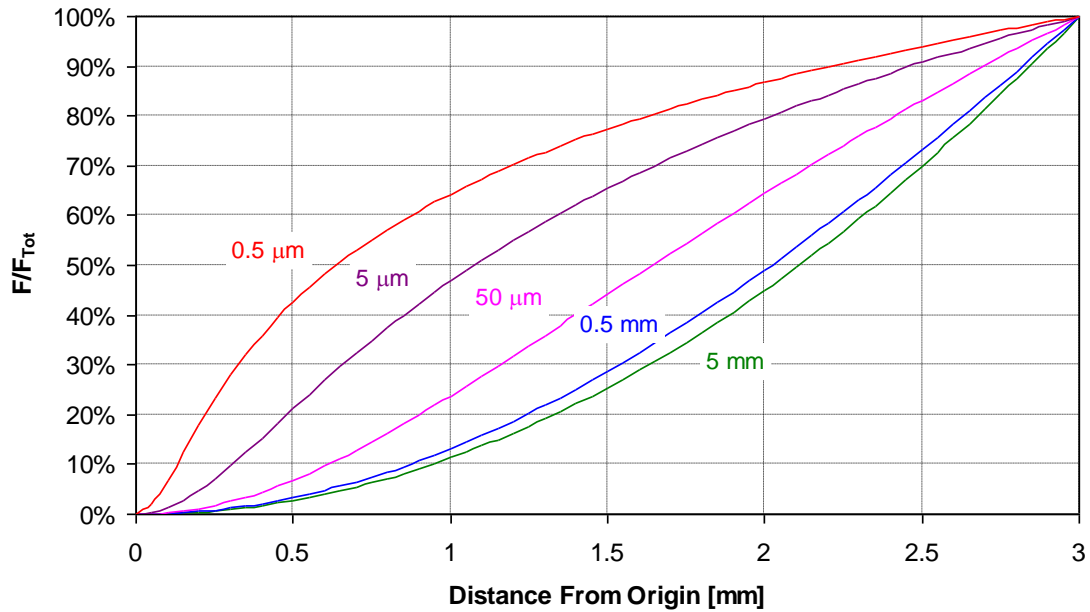

Figure A5.3: Fraction of total shear force as a function of radial distance from the origin with a sample radius of 3 mm.

The above plot assumes that force contributions at all distances from the origin are of equal magnitude. This is likely a considerable simplification of actual complex fluid systems under varying levels of confinement, in which more tightly-confined domains may behave differently from domains that are located further from the point of closest approach and are hence less tightly-confined. Nevertheless, the plot provides a rough estimate of the extent to which radial distances should be assumed to contribute to the overall shear response for a given gap size.

Regardless of the values of R and g, Equations (6) and (7) will, of course, only make physical sense while $r < R$. Note that, in the limiting case where the cylinders are of infinite size, so that $R \rightarrow \infty$, one would expect these equations to reproduce the planar case described by Newton's Theory (Equation (1)). Similarly, in the limiting case where $r \rightarrow 0$, the planar case should again be reproduced since r has reduced to a point and therefore lost its curvature. Since the integration is in cylindrical coordinates, one can divide equations (6) and (7) by the area of a radial planar projection of the cylinder, $A = \pi r^2$, to give, for the sphere-plane approximation:

$$
\lim_{R \rightarrow \infty \vee r \rightarrow 0} \frac{F_{Sphere - Plane}}{A} = \lim_{R \rightarrow \infty \vee r \rightarrow 0} \left[\frac{2\pi v\eta R}{\pi r^2} \ln \left(1 + \frac{r^2}{2gR} \right) \right]
$$

$$
= \lim_{R \rightarrow \infty \vee r \rightarrow 0} \left\{ \frac{2\pi v\eta R}{\pi r^2} \left[\frac{r^2}{2gR} - \frac{1}{2} \left(\frac{r^2}{2gR} \right)^2 + ... \right] \right\}
$$

$$
= \lim_{R \rightarrow \infty \vee r \rightarrow 0} \left[\frac{v\eta}{g} \left(1 - \frac{r^2}{4Rg} + ... \right) \right]
$$

$$
= \frac{v\eta}{g}
$$

And for the crossed cylindrical geometry:

$$\lim_{R \to \infty \vee r \to 0} \frac{F}{A} = \lim_{R \to \infty \vee r \to 0} \left\{ \frac{v\eta}{g\pi r^2} \int_0^r \int_0^{2\pi} \frac{gr}{R\left\{2 - \left[1 - \left(\frac{r}{R}\cdot\cos\theta\right)^2\right]^{1/2} - \left[1 - \left(\frac{r}{R}\cdot\sin\theta\right)^2\right]^{1/2}\right\} + g} \, dr d\theta \right\}$$

$$= \frac{v\eta}{g\pi r^2} \int_0^r \int_0^{2\pi} \frac{gr}{R\{2 - 1 - 1\} + g} \, dr d\theta$$

$$= \frac{v\eta}{g\pi r^2} \int_0^r \frac{2\pi grdr}{g}$$

$$= \frac{2v\eta}{gr^2}\left[\frac{1}{2}r^2\right]$$

$$= \frac{v\eta}{g}$$

That is, in the limiting case of two cylinders of infinite radius, an equivalent geometry to two flat planes, Equation (1) is reproduced as it should, with the gap size at the point of closest approach becoming equivalent to the gap size, z, of the planar case.

In general, though, the right hand side of Equation (6) has no simple analytic solution, but it can be related to the planar case easily in its present form. Since the integration is in cylindrical coordinates with the radial direction along the confining surfaces (see Figure A5.2), the equivalent planar force must have a circular area so that $F_{Planar} = v\eta\left(\pi r^2\right)/g$, and Equation (6) becomes:

$$\frac{F_{Crossed\ Cylinders}}{F_{Planar}} = \frac{\eta_{CC}}{\pi\eta_P r^2} \int_0^r \int_0^{2\pi} \frac{gr}{R\left\{2 - \left[1 - \left(\frac{r}{R}\cdot\cos\theta\right)^2\right]^{1/2} - \left[1 - \left(\frac{r}{R}\cdot\sin\theta\right)^2\right]^{1/2}\right\} + g} \, dr d\theta$$

$$\frac{F_{Crossed\ Cylinders}}{F_{Planar}} = C_{CC} \frac{\eta_{CC}}{\eta_P} \tag{8}$$

400

where C_{CC} is the crossed cylinder geometric constant:

$$C_{CC} = \frac{1}{\pi r^2} \int_0^r \int_0^{2\pi} \frac{gr}{R\left\{2 - \left[1 - \left(\dfrac{r}{R} \cdot \cos\theta\right)^2\right]^{1/2} - \left[1 - \left(\dfrac{r}{R} \cdot \sin\theta\right)^2\right]^{1/2}\right\} + g} \, dr d\theta \qquad (9)$$

and subscripts P, CC and (used later) SP refer to the planar, crossed cylindrical, and sphere-plane geometry, respectively. Note that since the relative velocity of the surfaces, v, will be identical regardless of the surfaces' shape, these terms for the crossed cylindrical and planar geometries will cancel. For the sphere-plane approximation, this relationship simplifies to:

$$\frac{F_{Sphere - Plane}}{F_{Planar}} = \frac{2 g \eta_{SP} R}{\eta_P r^2} \ln\left(1 + \frac{r^2}{2 gR}\right)$$

so that:

$$\frac{F_{Sphere - Plane}}{F_{Planar}} = C_{SP} \frac{\eta_{SP}}{\eta_P} \qquad (10)$$

with:

$$C_{SP} = \frac{2 gR}{r^2} \ln\left(1 + \frac{r^2}{2 gR}\right) \qquad (11)$$

The constant, C_{CC}, then, represents the fractional reduction in shear force for a given radius of sample size in a crossed cylindrical geometry (with cylinders of radius R) compared to an equivalent planar configuration with the same projected cross-sectional area, A, and a planar gap size, z, equal to the crossed cylinder point of closest approach, g. Since the velocity and gap size are fixed for a given set of test parameters, C_{CC} manifests itself, according to the left hand side of Equation (6), in terms of the apparent viscosity of the sample as measured by the shear response. C_{SP} represents a simpler,

analytical equation that can give very accurate predictions of the fractional reduction

under certain shear conditions, as will be discussed later.

Constant C_{CC} can be evaluated numerically via Maple software, using typical

experimental parameters for constants R and g. Plots of both C_{CC} and C_{SP} as a function

of sample radius with various g values and constant R (2 cm) are given below:
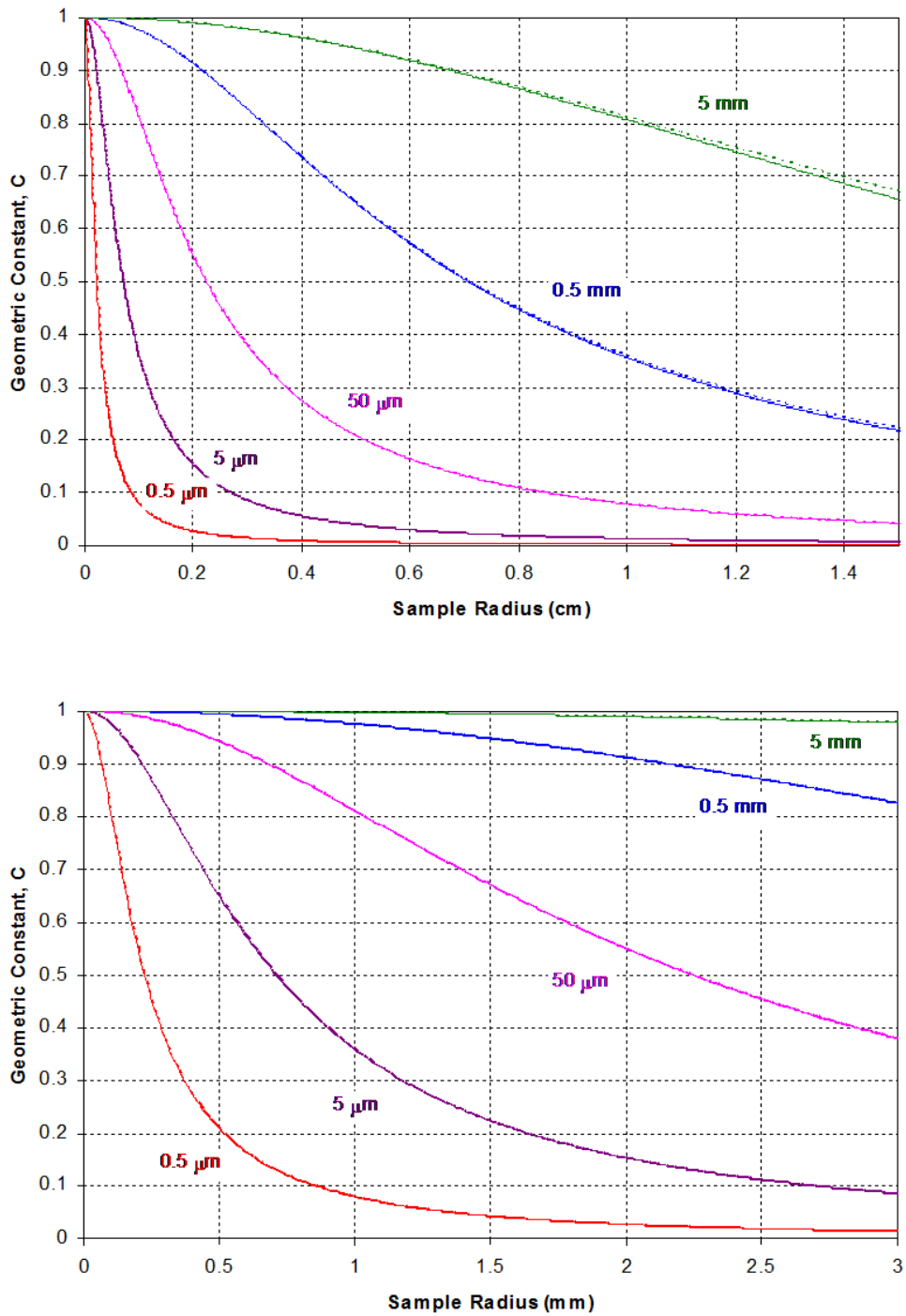
Figure A5.4: Geometric constant, C, as a function of sample radius, r, for various gap sizes, g, and constant cylinder radius R (2 cm), for (Top) larger sample radii and (Bottom) a more detailed view with smaller sample radii. C_{CC} is presented as a solid line while C_{SP} is presented as a dotted line. Recall that gap sizes of 0.5 μm and 5.0 μm, corresponding to the red and violet curves, were used to obtain the results presented in this thesis.

The trend featured above makes physical sense, in that as the gap size increases the curvature of the cylinders impacts the overall shear response less (that is, the relative drop-off in gap size due to curvature is less drastic when the point of closest approach is increased) and so it behaves more similarly to the planar shear configuration, indicated by the approach of *C* to unity for larger values of *r*. Even for small gap sizes, the small sample radii values of *C* remain close to unity, as one would expect since, as one approaches an infinitesimal sample radius, one also approaches an approximate planar configuration; for a point radius, curvature is negligible and Newton's Theory is obtained regardless of gap size, with $C = 1$ and $F_{CC} = F_{SP} = F_P$. In general, though, for a given sample size, $C < 1$ since, for a given gap size, flat planes with $A = \pi r^2$ will always produce a shear force larger than will two crossed cylinders with a similar projected area between the surfaces due to their curvature. Note that in Figure A6.4 the dotted lines are indistinguishable from the solid lines for all but the largest gap sizes and sample radii, indicating that Equation (11) gives a very good approximation for small gap sizes, so long as one takes care to minimize the amount of sample inserted into the SFA and thereby reduce the sample radius. A plot of the percent difference between predictions of *C* for crossed cylinder and sphere-plane geometry is given below:
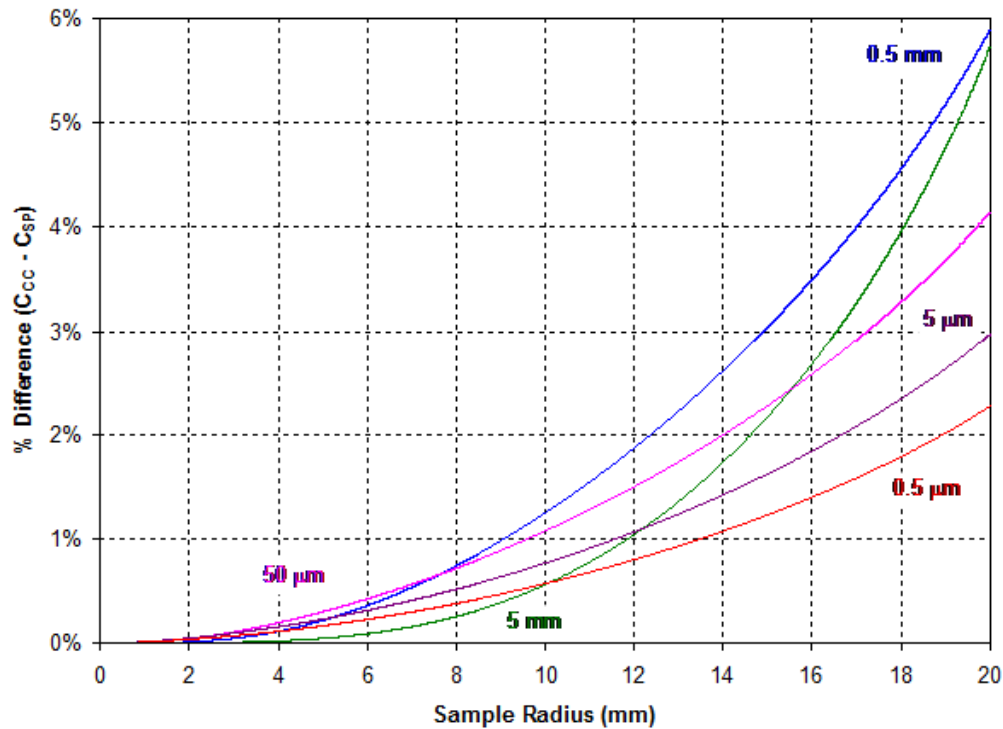
Figure A5.5: Plot of the percent difference in calculated geometric constant values, C, for crossed cylinder and sphere-plane geometries as a function of sample radius, r.

As can be seen from the above graph, the sphere-plane approximation is an accurate one for all sample radii associated with the SFA, as the discs used with them normally do not exceed 5 mm radius, for which the geometric constants differ by less than about 0.3%. For the estimated 4 mm sample radius observed for the results presented in this thesis, the 0.5 μm and 5.0 μm gap sizes would yield geometric constants that differ by 0.111% and 0.155%, respectively.

Plots of the geometric constant for various cylinder radii and the two gap sizes used with the reported results (0.5 μm and 5.0 μm) are shown below:
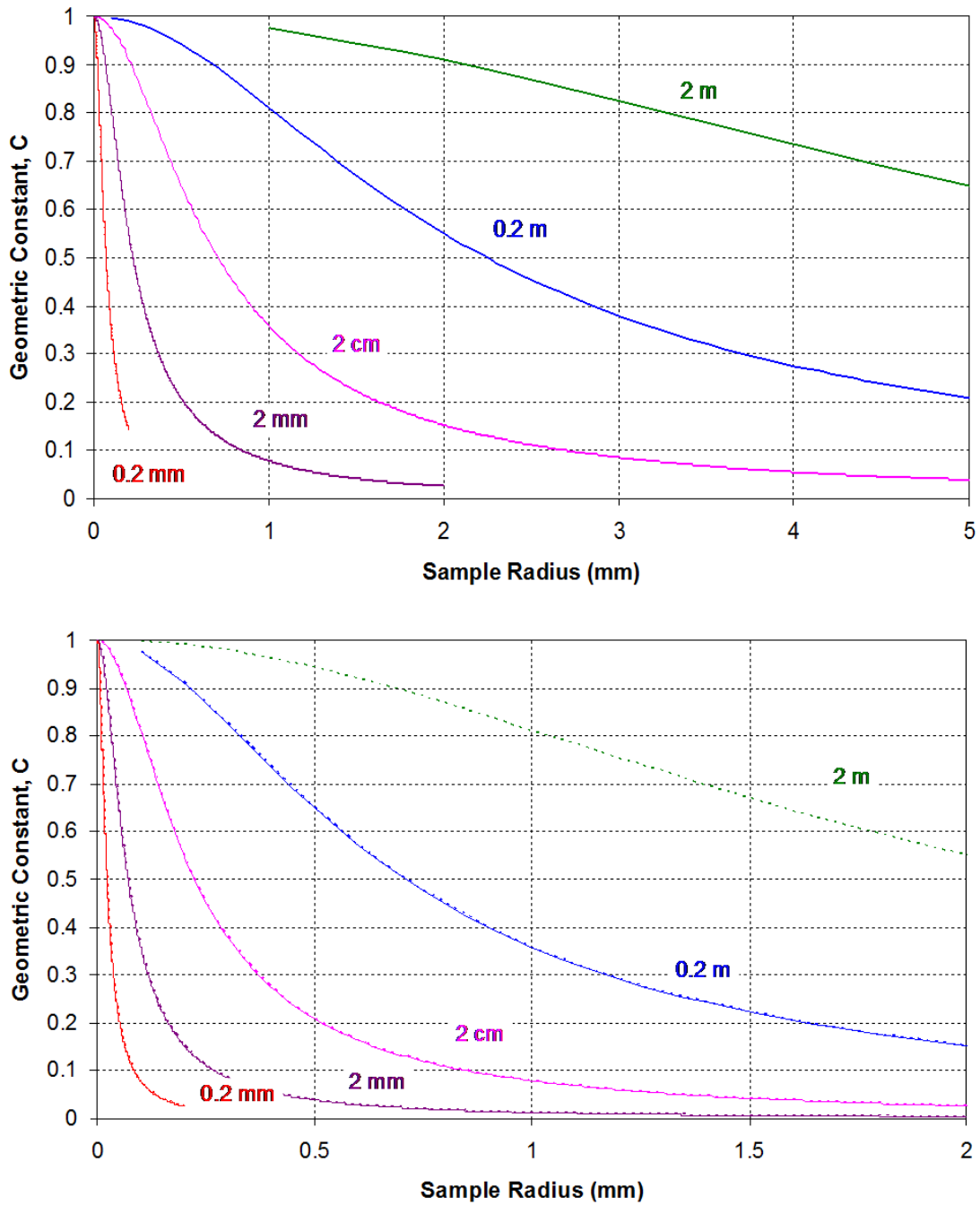
Figure A5.6: Geometric constant, C_{CC}, as a function of sample radius, r, for various cylinder radii, R, and the two constant gap sizes, g, of (Top) 5.0 μm and (Bottom) 0.5 μm, that were used in the results presented in this thesis. C_{CC} is presented as a solid line while C_{SP} is presented as a dotted line.

Once again, as expected, the geometric constant converges to unity as the sample radius drops to zero, due to the point particles' inherent lack of curvature and consequent similarity to the planar configuration. Also, as the cylinder size increases, the configuration increasingly approximates a planar configuration, thereby leading to values of C_{CC} approaching unity for larger sample radii. As with the results shown in Figure A5.4, the dotted and solid lines overlap well enough to be virtually indistinguishable from one another, regardless of the cylinder radius. The one exception is for very large cylinder radius (2m) and small sample radius (<3mm), as for these test conditions Equation (9) predicts a complex C while Equation (11) predicts a real C. For this reason, only the calculated results from the latter are shown in the plot.

Figure A5.4 is limited in its use, since each C_{CC} line represents a ratio of the shear force between crossed cylinders of gap size g and that between planes of the same area and gap size, shown schematically in Figure A5.7:
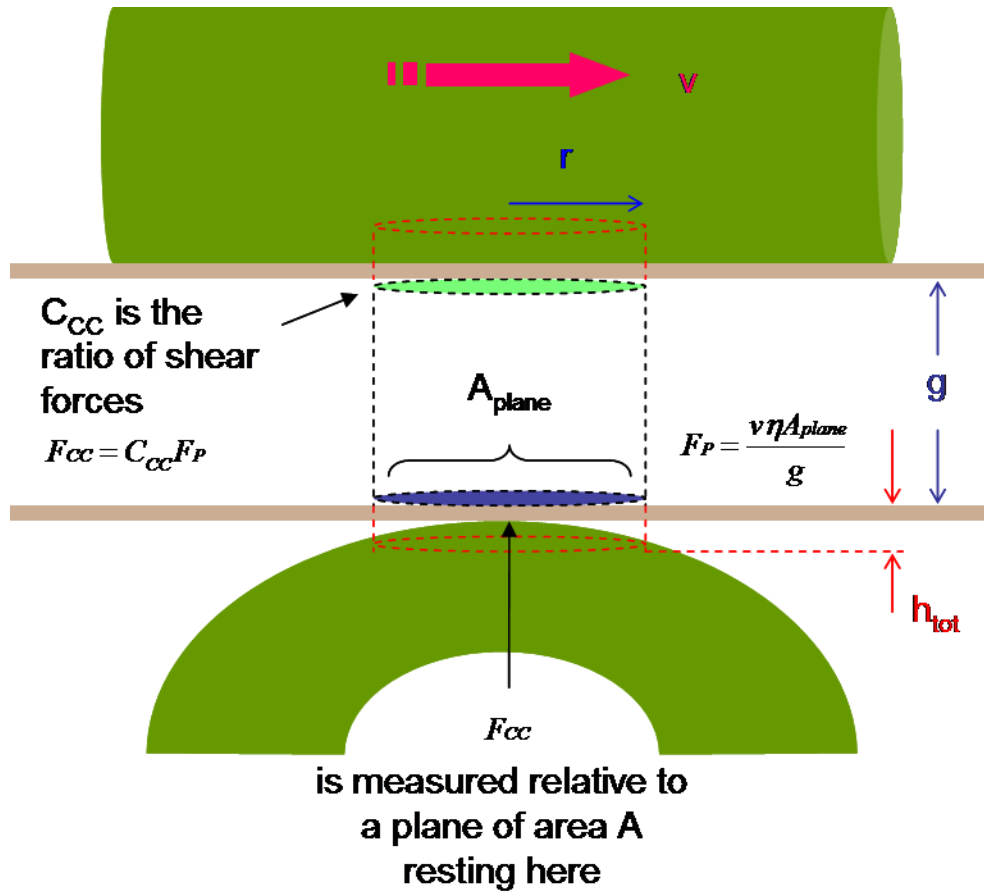
Figure A5.7: Schematic of the crossed cylindrical geometry and how its shear force, F_{CC}, relates to the planar shear force of Newton's Theory, F_P.

Any two lines in Figure A5.6 cannot be directly compared because they are measured relative to different planar conditions. The C_{CC} curves for 0.5 μm and 5.0 μm gap sizes, for example, are calculated relative to planar shear configurations with gap sizes of 0.5 μm and 5.0 μm, respectively. This is easily remedied by assuming the relative velocity and viscosity are identical for the two configurations (the latter assumption is, of course, not necessarily true, and will be discussed later in the derivation) and noting that according to Newton's Theory, shear stress is inversely proportional to gap size. Hence, by dividing each C_{CC} line by its gap size, all planar conditions will be identical and any

two lines will become comparable. That is, geometric constants with gap sizes g_1 and g_2, their ratio gives:

$$\frac{C_{cc\,1}}{C_{cc\,2}} = \frac{F_{cc\,1}/F_{P1}}{F_{cc\,2}/F_{P2}}$$

$$= \frac{F_{cc\,1}\left(g_1/\eta_1 vA\right)}{F_{cc\,2}\left(g_2/\eta_2 vA\right)}$$

$$= \frac{F_{cc\,1}g_1\eta_2}{F_{cc\,2}g_2\eta_1}$$

And therefore, by dividing both sides by the ratio of gap sizes gives:

$$\frac{C_{cc\,1}/g_1}{C_{cc\,2}/g_2} = \frac{F_{cc\,1}\eta_2}{F_{cc\,2}\eta_1} \tag{12}$$

Hence, a comparison can be made between shear responses at different gap sizes, F_{CC}, by comparing their C_{cc}/g_x values, and deviations from the ratio given by (12) can indicate relative viscosity changes. Figure A5.8 shows these 'normalized' lines using $g_{0.005}$ as a baseline (that is, multiplying Equation (12) by $g = 0.005$ m to recover the same curve as was presented in Figure A5.4):
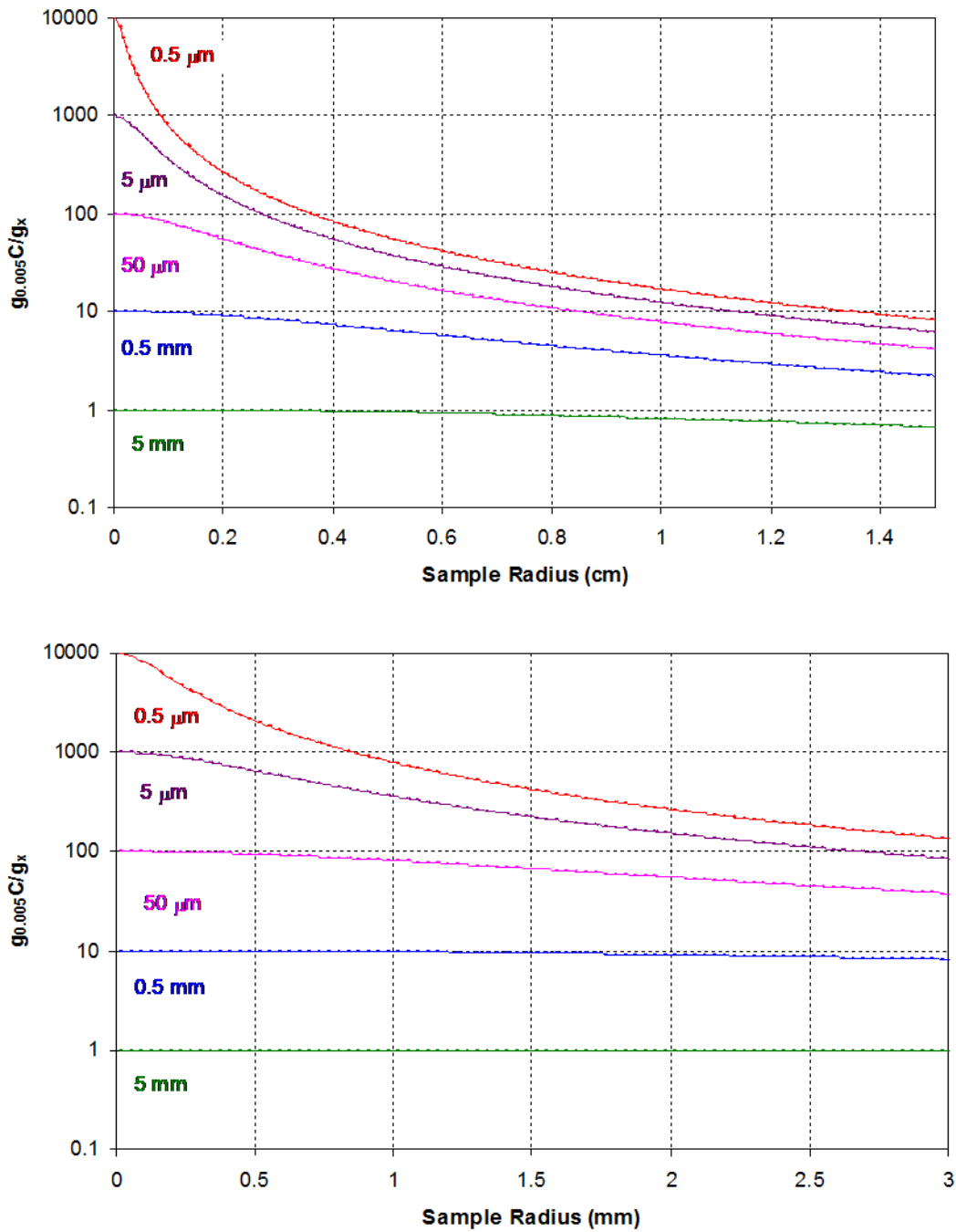
Figure A5.8: Plot of $g_{0.005}C_{CC}/g_x$ as a function of sample radius, r, for various gap sizes, g, and constant cylinder radius R (2 cm), for (Top) larger sample radii and (Bottom) a more detailed view with smaller sample radii. C_{CC} is presented as a solid line while C_{SP} is presented as a dotted line.

It is readily apparent from the intercepts of the above plots that while the point particle

($r = 0$) case, equivalent to a planar configuration as discussed previously, will produce

viscosities that are exactly inversely proportional to the gap size as Newton's Theory

predicts (since they are exact decade-multiples of the $g_{0.005}$ case), this proportionality fails

even at relatively small r, particularly for smaller values of g. Changing the gap size by a

factor of 10 from 5 µm to 0.5 µm, for example, will yield a shear force that is only a

factor of 1.6 larger, according to the plot. Once again, the sphere-plane approximation

yields results that are close enough to the crossed-cylinder geometry that the pairs of lines

in Figure A5.8 are virtually indistinguishable for all g and r presented.

One must still be careful with making direct comparisons between r-values on the

line, however, since a direct comparison of gap sizes with identical r-values implies that

the column of sample spanning the gap retains its radius despite a potentially large

change in gap size, which in turn implies, incorrectly, that the sample volume has

changed. For that reason, one further adjustment must be made to the curves in Figure

A5.8: Specifically, lines of constant volume must be overlain on the plot so that

comparisons between different gap sizes can be made while assuming a constant *volume*

of sample, not a constant *radius*.

To construct the constant volume lines, one must first determine the sample volume as

a function of the sample radius, cylinder radius and gap size. This is easily done by

noting that the volume can be approximated as a cylinder with ends shaped according to

the confining cylinders, and so the total volume, V, can be broken down into two parts:

$$V = V_{ends} + V_{gap}$$

where V_{gap} is the volume of the sample's columnar portion and V_{ends} is the volume contained beyond the column's imaginary end points. While formulating V_{gap} is trivial (it being a cylinder), V_{ends} requires some integration. For a radial distance r the distance between crossed cylinders (with gap size zero, since this portion is accounted for by V_{gap}) is given simply by Equation (3) as before, integrated over an area defined in terms of cylindrical polar coordinates $dA = rdrd\theta$, so that:

$$V = R\int_0^r\int_0^{2\pi} r\left\{2 - \left[1 - \left(\frac{r}{R}\cos\theta\right)^2\right]^{1/2} - \left[1 - \left(\frac{r}{R}\sin\theta\right)^2\right]^{1/2}\right\}drd\theta + \pi r^2 g \tag{13}$$

To create lines of constant volume for a given gap size, one must solve for g:

$$g = \frac{1}{\pi r^2}\left(V - R\int_0^r\int_0^{2\pi} r\left\{2 - \left[1 - \left(\frac{r}{R}\cos\theta\right)^2\right]^{1/2} - \left[1 - \left(\frac{r}{R}\sin\theta\right)^2\right]^{1/2}\right\}drd\theta\right) \tag{14}$$

The sphere-plane approximation leads to a simpler gap size-volume relationship. Starting from Equation (5) and proceeding in the same way as for the crossed-cylinder case:

$$V = \int_0^r\int_0^{2\pi}\left(\frac{r^2}{2R}\right)rdrd\theta + \pi r^2 g$$

$$= 2\pi\left(\frac{r^2}{4R}\right) + \pi r^2 g$$

And so, solving for g:

$$g_{SP} = \frac{V}{\pi r^2} - \frac{r^2}{4R} \tag{15}$$

Equation (14) can be solved numerically to model the gap size as a function of sample radius for various sample volumes. Examples of these curves are shown in Figure A5.9:
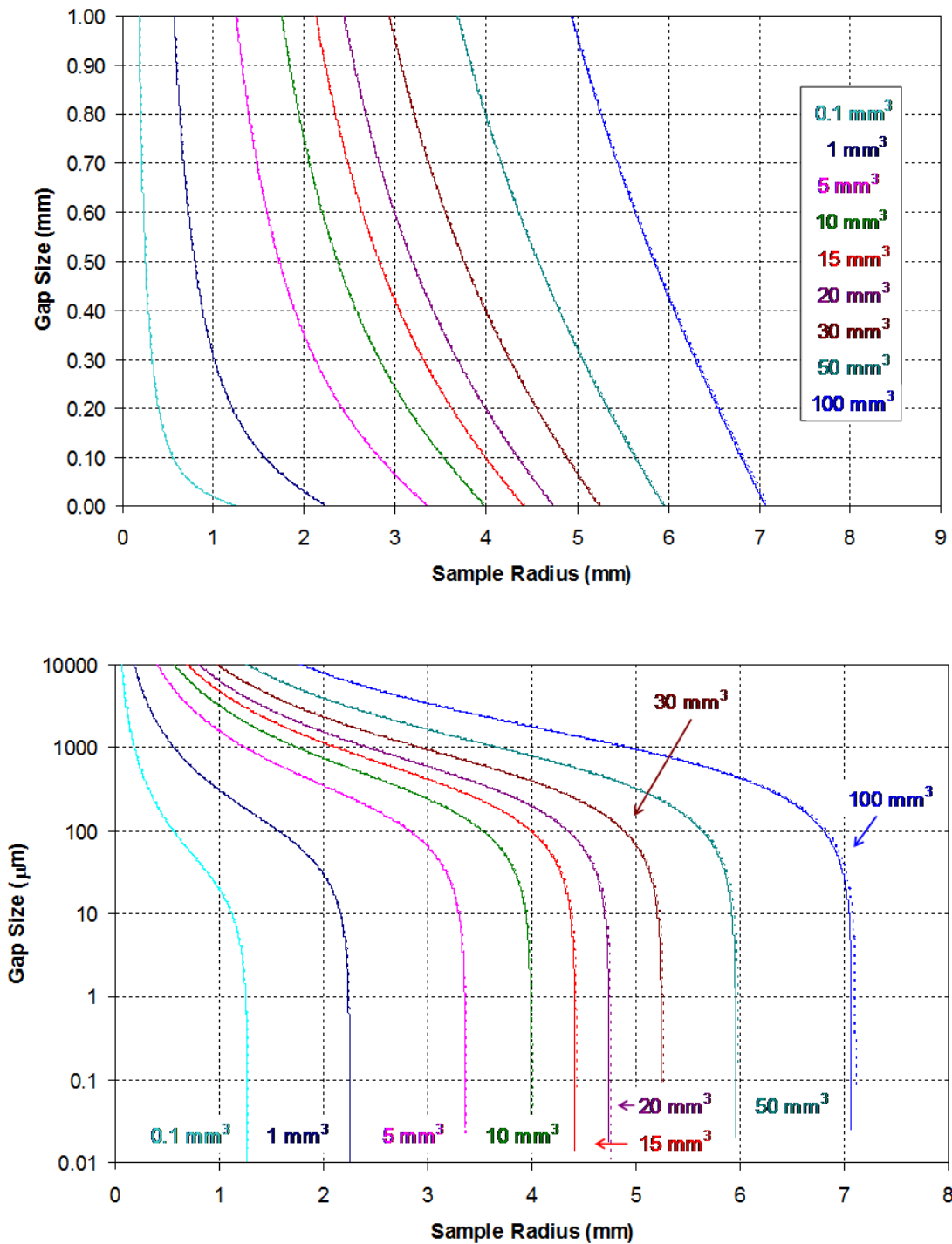
Figure A5.9: Plot of gap size as a function of sample radius for various sample volumes presented as (Top) a linear plot and (Bottom) a semi-logarithmic plot. The cylinder radius, R, was kept constant at 2 cm. Gap size g_{CC} is presented as a solid line while g_{SP} is presented as a dotted line.

The top plot shows that the gap size falls off nearly with the inverse square of the sample radius as one would expect for a cylinder (that is, $g = V/\pi r^2$) but with a well-defined lower limit determined not by an asymptotic sample radius but by the radius of the confining surfaces, as the rightmost term in Equation (11) dominates the leftmost term. Again, the sphere-plane approximation matches closely with the crossed cylinder geometry, only diverging slightly for the larger sample volumes presented when the gap size has diminished nearly to zero.

By plotting the curves semi-logarithmically, as is shown in the bottom plot, one can observe the behaviour for small gap sizes that were used in the present study. The sharp downward turn that occurs for the volumes plotted in Figure A5.8 indicates that, below a gap size of roughly 10 µm and above a sample volume of 0.1 mm^3, the sample radius is determined unambiguously by the sample volume and not the gap size. Using this plot, then, one can quickly and easily determine the sample volume by noting the point at which, as the surfaces are brought closer together, the period of rapid radial expansion ceases, and making a measurement or estimate of the radius. This value can then be read off the plot above and the volume determined. For the present study, the sample radius near contact was estimated to be roughly 3 mm, for example, corresponding to a sample volume of about 4 mm^3.

The volume curves above can now be overlain on the plots of Figure A6.8 so that a realistic comparison can be made between the geometric coefficients of different gap sizes. An overlay plot is shown in Figure A5.10:
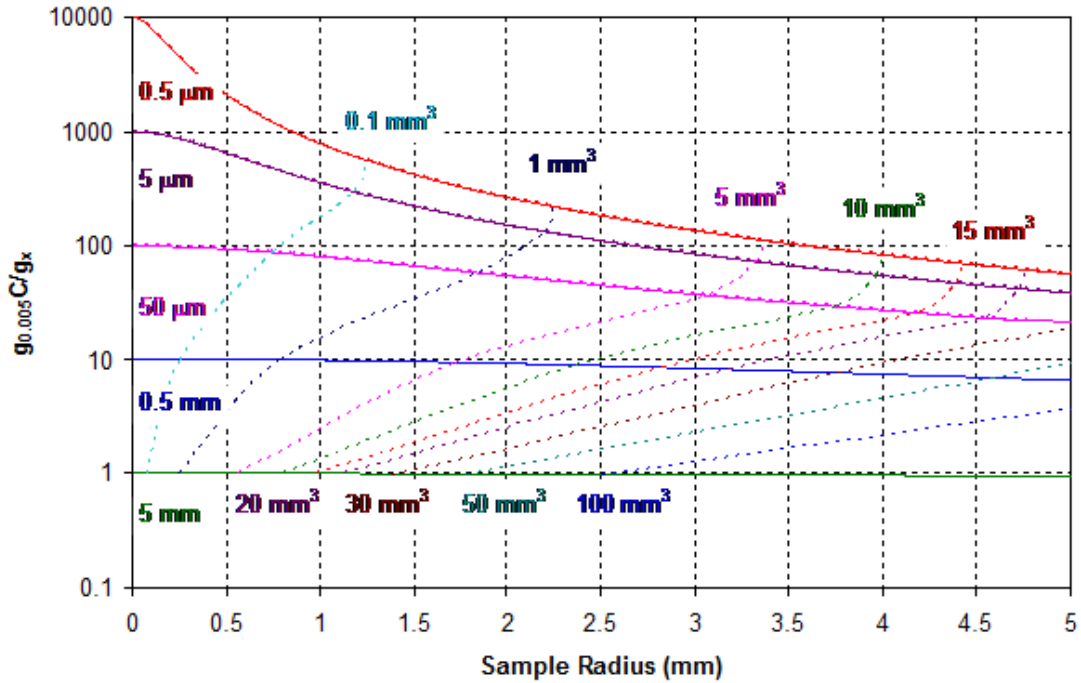

Figure A5.10: Plot of $g_{0.005}C/g_x$ as a function of sample radius, r, for various gap sizes, g, and constant cylinder radius R (2 cm), with overlays of constant volume lines to show how the radius of a sample will change as the gap size is varied. Two geometries are given: C_{CC} is presented as a solid line (——) and C_{SP} is presented as a dashed line (-----), while the lines of constant volume are represented as dotted lines (·······).

The plot above shows that the sample radius increases very little while the gap size falls from 5 μm to 0.5 μm, by only about 26 to 39 μm depending on the exact sample volume. From Figure A5.9 and by direct observation, the sample volume was found to be approximately 4 mm³, so that when comparing the solid red and violet $g_{0.005}C_{CC}/g_x$ lines representing the normalized geometric factors for 0.5 μm and 5.0 μm gap sizes,

respectively, the ratio of values should fall between the navy and pink dotted lines, representing the volumes 1 mm^3 and 5 mm^3. The ratios of geometric factors for these volumes are 1.652 and 1.547, respectively, and since 4 mm^3 falls three-quarters of the way from 1 mm^3 and 5 mm^3, the best estimate for the normalized geometric ratio between gap sizes of 0.5 μm and 5.0 μm with a cylinder radius of 2 cm and sample volume of 4 mm^3 is $1.547 + 0.25\,(1.652 - 1.547) \approx 1.5732$. Hence, assuming a similar sample viscosity, one should expect the shear response using a gap size of 0.5 μm to be only a factor of 1.57 larger than that using a gap size of 5.0 μm, rather than the tenfold factor predicted by Newton's Theory. And, as mentioned previously, a deviation from this ratio may be an indication that the viscosity ratio appearing in Equation (12) is no longer unity and hence that the viscosity has changed with gap size. The equivalent ratio for the sphere-plane geometry is $1.546 + 0.25\,(1.653 - 1.546) \approx 1.5728$, differing only by 0.025% from the crossed cylinder result, and so demonstrating that this approximation is extremely accurate for the surface radius and sample volume used.

The above derivation relies on several assumptions, any of which could lead to potentially significant deviations from the predicted behaviour. Examples include:

i)   Shear-induced flow occurs only in the radial direction. Dissipation of energy along the axial direction will produce extra terms in Equation (2) and hence extra terms in Equation (9).

ii)   Viscosity of the sample is uniform. This is particularly relevant for smectic liquid crystals, since they have the property of viscous anisotropy (the *Mięsowicz viscosities*, discussed in Section 1.3.1).

iii) The crossed cylinders are perfectly perpendicularly aligned. Any skew from perpendicularity will also skew Equation (3) and complicate the derivation considerably. Similarly, perfect axial alignment is also assumed and any tilt from this geometry will also affect the results.

iv) The surfaces are perfectly smooth. As with the planar shear case, imperfections in the surface or the accretion of sample at the surface will lead to deviations in Equation (3), complicating the derivation of Equation (9).

v) The sample fills the gap between the crossed cylinders in a perfectly cylindrical column. Menisci formed due to sample-surface interaction, or to domain structures near the surface within smectic liquid crystals (see *Grandjean terracing* in Section 1.2.1), may well have an effect on the central sample column joining the surfaces, skewing Equations (13) and (14) and thereby shifting the 'equal volume' lines in Figure A5.10 and hence altering the normalized geometric ratio.

In performing experiments involving lateral shear with the SFA it is important to minimize the effects of above sources of error wherever possible.